The Neutron Electric Form Factor to $Q^2 = 1.45$ (GeV/c)^2

MASSACHUSETTS INSTITUTE OF TECHNOLOGY
APR 07 2004
LIBRARIES

by

Bradley Robert Plaster

Submitted to the Department of Physics
in partial fulfillment of the requirements for the degree of

Doctor of Philosophy

at the

MASSACHUSETTS INSTITUTE OF TECHNOLOGY

February 2004

© Massachusetts Institute of Technology 2004. All rights reserved.

ARCHIVES

Author .....
Department of Physics
November 5, 2003

Certified by .....
Stanley B. Kowalski
Professor of Physics
Thesis Supervisor

Certified by .....
Richard Madey
University Professor Emeritus, Kent State University
Thesis Supervisor

Accepted by .....
Thomas J. Greytak
Associate Department Head for Education

The Neutron Electric Form Factor to $Q^2 = 1.45$ (GeV/c)^2

by

Bradley Robert Plaster

Submitted to the Department of Physics
on November 5, 2003, in partial fulfillment of the
requirements for the degree of
Doctor of Philosophy

Abstract

The nucleon elastic electromagnetic form factors are fundamental quantities needed for an understanding of nucleon and nuclear electromagnetic structure. The evolution of the Sachs electric and magnetic form factors with Q^2, the square of the four-momentum transfer, is related to the distribution of charge and magnetization within the nucleon. High precision measurements of the nucleon form factors are essential for stringent tests of our current theoretical understanding of confinement within the nucleon.

Measurements of the neutron form factors, in particular, those of the neutron electric form factor, have been notoriously difficult due to the lack of a free neutron target and the vanishing integral charge of the neutron. Indeed, a precise measurement of the neutron electric form factor has eluded experimentalists for decades; however, with the advent of high duty-factor polarized electron beam facilities, experiments employing polarization degrees of freedom have finally yielded the first precise measurements of this fundamental quantity.

Following a general overview of the experimental and theoretical status of the nucleon form factors, a detailed description of an experiment designed to extract the neutron electric form factor from measurements of the neutron's recoil polarization in quasielastic $^2\mathrm{H}(\vec{e}, e'\vec{n})^1\mathrm{H}$ scattering is presented. The experiment described here employed the Thomas Jefferson National Accelerator Facility's longitudinally polarized electron beam, a magnetic spectrometer for detection of the scattered electron, and a neutron polarimeter designed specifically for this experiment. Measurements were conducted at three Q^2 values of 0.45, 1.13, and 1.45 (GeV/c)^2, and the final results extracted from an analysis of the data acquired in this experiment are reported and compared with recent theoretical predictions for the nucleon form factors.

Thesis Supervisor: Stanley B. Kowalski
Title: Professor of Physics

Thesis Supervisor: Richard Madey
Title: University Professor Emeritus, Kent State University

Acknowledgments

I intentionally delayed writing this section of the thesis until the document was essentially complete as I knew that thanking everyone who has helped me during my career as a graduate student would bring a fitting conclusion to my many years at MIT as an undergraduate and graduate student.

I would like to begin by thanking my two advisors, Stanley Kowalski and Dick Madey. Words cannot say enough for the appreciation I have for the many opportunities Stanley and Dick gave me over the past several years. I am especially grateful to Stanley for the large amount of independence I enjoyed and the innumerable resources I had at my disposal. During my first year of graduate school, Stanley presented me with the opportunity to work on this experiment; no doubt, many advisors would have been very hesitant to put a first-year graduate student only four months into graduate school in such a position, and perhaps there were those who thought it was not the best idea. I am grateful Dick was agreeable to the idea, and I think Stanley, Dick, and I are pleased to report everything worked out for the very best in the end.

I have been fortunate to "travel the world" during my time as a graduate student, and I thank Stanley for the trips to Germany to participate in the parity violation experiment at Mainz and the opportunities to attend conferences in Brazil and Greece. This is not to mention the nearly limitless opportunities I had to travel back and forth from Boston to Newport News during crucial stages of the analysis after I had returned to MIT to finish my coursework and the opportunities to attend a number of conferences in the U.S. Also, I thank Stanley and Connie for Easter dinner and for their gracious hospitality at their home on Cape Cod.

I thank Dick for serving as my second advisor and inspiring me to achieve a high degree of excellence in my work. Dick pushed me harder than anyone has ever pushed me in my life (yes, even harder than an MIT undergraduate education) and, strangely enough, I am extremely thankful for this — you never know what you can accomplish until you are challenged to do so. Dick endeavored to train me to think like a physicist, and I am fortunate to have worked with and learned from someone who pioneered

the recoil polarization technique for measurements of the nucleon form factors. I admire Dick's unwavering dedication to a goal, and I know he must be thrilled that the results from the experiment he first considering doing 18 years ago have now been published.

I thank the other members of my thesis committee, Bill Donnelly and Dick Yamamoto, for agreeing to serve on my committee and for providing a number of useful commments on this document.

Next, I would like to thank those who I credit most for my development: Jim Kelly and Andrei Semenov. At times, I found Jim's extremely high standards and desire for rigor to be exasperating, especially during the development of our simulation code and discussions of formalism (e.g., the "dreaded" Wigner rotation!), but, in retrospect, I am glad that I was constantly challenged to do something in an even better way and never permitted to give up. Indeed, I didn't fully appreciate the rigor of our analysis until our results were final, but hindsight is always 20/20. Also, I thank Jim for numerous comments and suggestions on this thesis; it is much better and much more complete because of his many suggestions. Andrei was the true guru (read: czar) of our analysis efforts, and he instilled in me the importance of careful work. I especially appreciate Andrei's timely responses to the numerous questions I always had concerning the analysis and the various analysis tools that we used; if there was someone who was sure to know the answer, that person was Andrei. Without Andrei, our analysis efforts would never have gotten off the ground. I also offer thanks to Irina Semenova; I am extremely grateful she was willing to bear some of our analysis load.

I offer special thanks to Simon Taylor. Simon and I endured one of the most painful experiences of the experiment, the mapping of the Charybdis magnet at the conclusion of the experiment, but we survived. I greatly enjoyed the many long conversations Simon and I had while in Newport News, Germany, and at Bates, and I thank Simon for the great time we had during the trip we took to London the last time I was at Mainz (do your feet still hurt?).

I would like to thank Calvin Howell for taking the time to provide me with excellent

input and suggestions for the section of this thesis describing the NPOL electronics; it is much better because of the highly detailed comments he provided me.

Hartmuth Arenhövel deserves a large amount of recognition. Hartmuth was kind enough to send me more than 10,000 of his calculations via email, and he was always quick to respond to my many (naive) questions concerning his calculations.

I especially would like to thank the other thesis students on this experiment: Aram Aghalaryan, Erick Crouse, Glen MacLachlan, Shige Tajima, Will Tireman, and Chenyu Yan. Will, in particular, deserves special recognition; he was my officemate in Trailer City, and we endured a long summer (that of 2001) together (especially right before PAC 20), and I thank Will for helping to keep things in perspective. Shige deserves special recognition for the many helpful discussions I had with him during the various stages of the analysis. Also, I thank all of the students for all of the help they provided me after I arrived at JLab.

Several Hall C staff members deserve special recognition. I am very appreciative of the great deal of help I received from Mark Jones shortly after my arrival at JLab, and I have always enjoyed the witty conversations I have had with Dave Mack. I very much enjoyed Bill Vulcan's rather unique sense of humor, and I thank Steve Hickson for his constant good-natured "harrassment".

Joanne Gregory, the Medium Energy Group's secretary, has helped me a great deal during my time here (including numerous pizza lunches), and I very much appreciate her efforts. I thank Joanne for making all of my travel arrangements over the years which saved me a considerable amount of time.

It brings me great pleasure to thank all of the friends I have made during my time at MIT. During my years in graduate school, I would especially like to thank several of my fellow colleagues in nuclear physics, Ben Clasie, Peter Monaghan, and Jason Seely, for making the "Penthouse" a slightly more tolerable place and for much mutual commisseration during the many long nights we all spent there before general exams and, especially, field theory(!). Jason deserves special thanks; he and Jen helped me find a place to live after I returned to MIT from JLab, and we've been through a lot during our time in graduate school.

My friends from my undergraduate days at MIT know me better than almost anybody, and I especially thank Jon Robinson and Jason Timpe for all of their encouragement and support especially during the writing of this thesis. I also thank Keith Battocchi, Miki and Spencer Behr, Jon Chang, Christine Chiou, Dave Hausman, Doug Kriner, Matt Lahaie, and Matt Monteleone for being the good friends they have been ever since our undergraduate days here at MIT.

Turning back to my roots in North Dakota, I thank Dennis Friestad at Valley City High School for sparking my interest in the physical sciences and mathematics; without Dennis's guidance and efforts, I most likely would never have ended up at MIT. Also, I thank Rory Mulvaney for his friendship over the years.

Finally, I thank those to whom I am most appreciative: my parents, my sister, and my grandmothers. Although they have not always understood what or why it is I am doing/studying the things I am (one of my relatives recently asked one of my grandmothers if nuclear physics implied I was developing nuclear weapons), they have always encouraged me in my pursuits. We all still remember the day I was dropped off at MIT as a freshman (having grown up in rural North Dakota and not having seen MIT prior to arrival), and it is hard to believe that all of this time has now passed us by. I love you all very much, and it is to you that I dedicate this thesis.

Brad Plaster
October 29, 2003
Cambridge, Massachusetts

Contents

List of Figures

List of Tables

Chapter 1

Introduction

The electromagnetic interaction, in particular, electron scattering, has proven to be an extremely valuable tool for the study of nucleon and nuclear structure over the past 50 years. There are two primary reasons electron scattering has proven to be such an indispensable tool for experimental nuclear physics [1]:

- The electromagnetic interaction is well known and understood within the context of Quantum Electrodynamics (QED); therefore, precise calculations are possible as the small value of the electromagnetic coupling constant ($\alpha \approx 1/137$) suppresses higher-order processes other than the lowest-order process of one-photon exchange. Accordingly, electron scattering is a clean probe of nucleon and nuclear structure.

- For a fixed electron energy loss, the square of the four-momentum transfer, Q^2, carried by the virtual photon can be varied (unlike that for real photons in which the square of the four-momentum is identically zero). Variation of the square of the four-momentum transfer permits the virtual photon to probe the nucleon or nuclear target at different length scales as the spatial resolution of the virtual photon is proportional to Q^{-1}.

The origins of electron scattering can be traced to the early experiments conducted by Lyman, Hanson, and Scott [2] in 1951 with a 15.7 MeV electron beam extracted from a 20 MeV betatron at the University of Illinois. Cross sections were measured

for elastic scattering from aluminum, carbon, copper, gold, and silver nuclear targets, and on the basis of their measurements, Lyman, Hanson, and Scott concluded that the "...observed deviations from Coulomb scattering are consistent with the picture of a nuclear charge whose ... density distribution is uniform or possibly slightly greater at the center of the nucleus".

Soon thereafter, electron scattering experiments began in earnest at several different facilities. Some of the most notable early experiments were the pioneering elastic electron-proton scattering experiments conducted by Hofstadter and others (see, e.g., [3–5]) at the Stanford Mark III accelerator in the mid-1950s which revealed that the proton is not a point particle but is, instead, a complex object with an extended electromagnetic structure and the pioneering MIT-SLAC deep-inelastic electron scattering experiments conducted by Friedman, Kendall, Taylor, and others (see, e.g., [6, 7]) at the Stanford Linear Accelerator in the early 1960s which verified the quark substructure of the nucleon.

Indeed, we now know that nucleon is a very complicated object that can, in principle, be described in terms of the quark and gluon degrees of freedom of the underlying theory of the strong interaction, Quantum Chromodynamics (QCD). Although QCD cannot be solved analytically, the theory is asymptotically free as the strong coupling constant $\alpha_s \propto [\log(Q/\Lambda)]^{-1}$, where the momentum scale Λ is on the order of a few hundred MeV; therefore, at very high energies, or very large values of Q^2, α_s is small and QCD can be solved perturbatively. At the other extreme of very low energies, such as the ground state of the nucleon, QCD cannot be solved perturbatively and understanding the structure of the nucleon in terms of the QCD quark and gluon degrees of freedom in this non-perturbative region remains one of the outstanding challenges in nuclear physics. One of the best tests to which a model of confinement can be subjected is the requirement that the model accurately reproduce the electromagnetic structure of the nucleon as probed in elastic electron-nucleon scattering.

As will be discussed in extensive detail in the next chapter, the electromagnetic structure of the nucleon can be probed via elastic electron-nucleon scattering, and the deviation of the nucleon's electromagnetic structure from that of a point particle can

be quantified in terms of *electromagnetic form factors.* Experimental measurements of these form factors are of a fundamental intellectual interest in their own right as the electric and magnetic form factors are related to the distribution of charge and magnetization within the nucleon; however, in addition, comparisons of experimental results for these form factors with those predicted by QCD-inspired models of confinement provide a crucial test for our current theoretical understanding of confinement within the nucleon.

The proton electric and magnetic form factors have been been measured up to Q^2 values of $\sim$8 and $\sim$30 $(\mathrm{GeV}/c)^2$, respectively; however, as will be discussed in detail in the next chapter, measurements of the proton electric form factor are less precise than those of the magnetic form factor, and significant discrepancies exist between older and more recent measurements. The situation for the neutron is even less satisfying; due to the lack of a free neutron target (as the neutron beta-decays after approximately 15 minutes), the neutron form factors are known with significantly less precision than the proton form factors and existing measurements are restricted to considerably smaller ranges of Q^2. In fact, until recently, very little was known about the Q^2 dependence of the neutron electric form factor; due to the vanishing integral charge of the neutron, this quantity is very small and a precise measuremement of this quantity at any value of $Q^2 > 0$ has eluded experimentalists for decades.

The focus of the remainder of this thesis is the proper description of an experiment designed to extract the neutron electric form factor from measurements of the neutron's recoil polarization in quasielastic $^2\mathrm{H}(\vec{e}, e'\vec{n})$ scattering at three Q^2 values of 0.45, 1.13, and 1.45 $(\mathrm{GeV}/c)^2$. This experiment, conducted in Hall C of the Thomas Jefferson National Accelerator Facility, employed a longitudinally polarized electron beam, a magnetic spectrometer for detection of the scattered electron, and a neutron polarimeter designed specifically for this experiment. A brief overview of the layout of this thesis is as follows. We begin in Chapter 2 with an overview of the nucleon form factors; we introduce and discuss the concept of a nucleon electromagnetic form factor, we review the various experimental techniques that have been used for measurements of the form factors, we review the status of experimental measurements of

the nucleon form factors, and we discuss a number of different theoretical calculations of the form factors. We continue in Chapter 3 with a discussion of the accelerator and the experimental equipment in Hall C, and we then provide an overview of the neutron polarimeter in Chapter 4. Next, we continue in Chapters 5 through 7 with a discussion of the analysis procedures that were employed for the extraction of the neutron electric form factor from the data acquired in this experiment, and our final results are presented in Chapter 7. Finally, we conclude with a very brief summary in Chapter 8.

Chapter 2

Nucleon Form Factors: An Overview

In this chapter, we provide an overview of the nucleon elastic electromagnetic form factors.

We begin in Section 2.1 by deriving the differential cross section for unpolarized elastic electron scattering from unpolarized pointlike (i.e., structureless) charged fermions. We then proceed to discuss unpolarized elastic electron scattering from unpolarized nucleons; we introduce the concept of a nucleon form factor, and we derive the differential cross section for this process. Finally, we conclude Section 2.1 by introducing the Sachs electric and magnetic form factors and discussing how the electric and magnetic form factors are related to the distribution of charge and current within the nucleon.

In Section 2.2, we survey the status of nucleon form factor measurements conducted with unpolarized electron beams. We begin by discussing the various techniques that have been employed in extractions of the nucleon form factors from unpolarized elastic electron-proton, quasielastic electron-deuteron, and elastic electron-deuteron cross section measurements. Following an overview of these techniques, we present the results of these measurements. Henceforth, we will refer to the results from nucleon form factor measurements conducted with unpolarized electron beams as "*unpolarized results*".

Next, in Section 2.3, we survey the status of nucleon form factor measurements conducted with polarized electron beams. We begin by discussing the formalism that has motivated measurements of the nucleon form factors using polarized electron beams, polarized nuclear targets, and recoil nucleon polarimeters. Following an overview of this formalism and the various experimental techniques that have been developed for these measurements, we compare the results of these measurements with those presented in Section 2.2. Again, we will for the remainder of this thesis refer to the results from nucleon form factor measurements conducted with polarized electron beams as "*polarized results*".

We continue, in Section 2.4, by discussing various theoretical calculations of the nucleon form factors. Following a brief overview of the methods, we compare the results of these calculations with the experimental data presented in Sections 2.2 and 2.3. Finally, we conclude this chapter in Section 2.5 by arguing why further high precision measurements of the nucleon form factors are important and needed for a more complete understanding of nucleon and nuclear structure.

2.1 Nucleon Elastic Electromagnetic Form Factors

2.1.1 Notation and Units

Throughout this chapter and the remainder of this thesis, we will primarily follow the convention for relativity adopted by Peskin and Schroeder [8]; that is, we will use the metric tensor

$$g_{\mu\nu} = g^{\mu\nu} = \begin{pmatrix} 1 & 0 & 0 & 0 \\ 0 & -1 & 0 & 0 \\ 0 & 0 & -1 & 0 \\ 0 & 0 & 0 & -1 \end{pmatrix}, \tag{2.1}$$

with Greek indices (μ, ν, etc.) running over all components of a four-vector (i.e., 0, 1, 2, and 3). Where applicable, Roman indices (i, j, etc.) will run over the spatial components of a four-vector (i.e., 1, 2, and 3). Four-vectors will be denoted by light

italic type (e.g., A^μ), while three-vectors will be denoted by boldface type (e.g., $\mathbf{A}$); for example, the four-momentum of a particle with energy E and three-momentum $\mathbf{p}$ will be denoted

$$p^\mu = (E, \mathbf{p}) \ , \qquad p_\mu = g_{\mu\nu} p^\nu = (E, -\mathbf{p}) \ , \tag{2.2}$$

and for a particle of mass m,

$$p^2 = p^\mu p_\mu = E^2 - |\mathbf{p}|^2 = m^2 \ . \tag{2.3}$$

As is customary, we will primarily employ "natural units" (i.e., $\hbar = c = 1$) in derivations and during discussions of formalism; however, we will restore units when discussing and presenting experimental results. Finally, traces will be denoted "tr".

2.1.2 Electron Scattering by Pointlike Charged Fermions

As a preliminary to our consideration of elastic electron-nucleon scattering, we consider a simpler case: unpolarized elastic electron scattering by unpolarized pointlike charged (spin-$\frac{1}{2}$) fermions. Henceforth, e and m_e will denote, respectively, the charge and mass of the electron; also, for the purposes of this subsection, we assume the charge of the pointlike fermions is e, and we use m to denote their mass. In what follows, we derive the differential cross section for this process.

As shown schematically in Fig. 2-1, the electromagnetic (Coulomb and magnetic) interaction between the electron and the fermion proceeds (at tree-level) via the exchange of a single virtual photon. Here, k^μ (k'^μ) and p^μ (p'^μ) denote the initial (final) four-momentum of the electron and the fermion, respectively. The *four-momentum transfer* (i.e., the four-momentum carried by the virtual photon), q^μ, is defined to be

$$q^\mu = k^\mu - k'^\mu = p'^\mu - p^\mu \ . \tag{2.4}$$

According to the Feynman rules for Quantum Electrodynamics (QED) [9,10], the

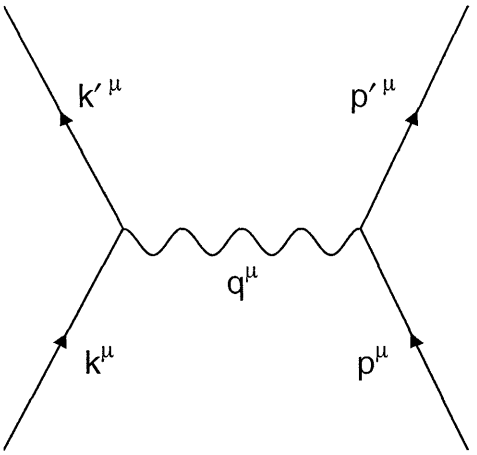

Figure 2-1: Tree-level Feynman diagram for elastic electron-pointlike fermion scattering.

matrix element, $\mathcal{M}$, or amplitude, for the tree-level diagram can be written as [8]

$$i\mathcal{M} = J^{\mu}(p',p)\frac{-ig_{\mu\nu}}{q^2}j^{\nu}(k',k) \ , \tag{2.5}$$

where

$$J^{\mu}(p',p) = \overline{u}^{s'}(p')(-ie\gamma^{\mu})u^{s}(p) \ , \tag{2.6}$$

$$j^{\mu}(k',k) = \overline{u}^{r'}(k')(-ie\gamma^{\mu})u^{r}(k) \ , \tag{2.7}$$

are, respectively, the fermion and electron currents and $-ig_{\mu\nu}/q^2$ is the virtual photon propagator. Here, $u^{s}(p)$ $[u^{s'}(p')]$ and $u^{r}(k)$ $[u^{r'}(k')]$ denote, respectively, Dirac spinors for the initial-state [final-state] fermion and electron, $-ie\gamma^{\mu}$ is the electromagnetic vertex function for a *pointlike* fermion of charge e, and γ^{μ} is the usual notation for a Dirac matrix.

The unpolarized (i.e., spin-averaged) differential cross section $\mathrm{d}\sigma$ can be calculated from the initial- and final-state spin-averaged matrix element according to [8]

$$\mathrm{d}\sigma = \frac{\mathrm{d}\Pi_2}{4E_eE_f|\beta_e - \beta_f|}\ \frac{1}{4}\sum_{\text{spins}}|\mathcal{M}|^2 \ , \tag{2.8}$$

where $d\Pi_2$ is a product of phase-space factors,

$$d\Pi_2 = \frac{d^3\mathbf{p}_{e'}}{(2\pi)^3 2E_{e'}} \frac{d^3\mathbf{p}_{f'}}{(2\pi)^3 2E_{f'}} (2\pi)^4 \delta^{(4)}(k + p - k' - p') \ , \tag{2.9}$$

and E_e (E_f), β_e (β_f), $\mathbf{p}_{e'}$ ($\mathbf{p}_{f'}$), and $E_{e'}$ ($E_{f'}$) denote the initial-state energy, initial-state velocity, final-state three-momentum, and final-state energy of the electron (fermion). Using the completeness relation for Dirac spinors,

$$\sum_s u^s(p)\overline{u}^s(p) = \not{p} + m \ , \tag{2.10}$$

the square of the spin-averaged (i.e., averaged over the initial-state spins and summed over the final-state spins) matrix element is

$$\frac{1}{4}\sum_{\text{spins}} |\mathcal{M}|^2 = \frac{e^4}{4q^4} \text{tr}\left[(\not{p}' + m)\gamma^\mu(\not{p} + m)\gamma^\nu\right] \text{tr}\left[(\not{k}' + m_e)\gamma_\mu(\not{k} + m_e)\gamma_\nu\right] \ , \tag{2.11}$$

where $\not{p}$ is the usual notation for the product $\gamma^\mu p_\mu$. The evaluation of the traces is straightforward, and the result is

$$\frac{1}{4}\sum_{\text{spins}} |\mathcal{M}|^2 = \frac{8e^4}{q^4}\left[(k \cdot p')(k' \cdot p) + (k \cdot p)(k' \cdot p') - m^2(k \cdot k') - m_e^2(p \cdot p')\right] \ . \tag{2.12}$$

The above expression for the spin-averaged matrix element is most easily evaluated in the center-of-mass (CM) frame (defined by $\mathbf{p}_e = -\mathbf{p}_f$ and $\mathbf{p}_{e'} = -\mathbf{p}_{f'}$); however, experimentalists are, in general, interested in the laboratory frame conditions such as those shown schematically in Fig. 2-2. Using four-momentum conservation, the four-momenta in the laboratory frame can be written explicitly as

$$k^\mu = (E_e, \mathbf{p}_e) \ , \qquad p^\mu = (m, \mathbf{0}) \ , \tag{2.13}$$

$$k'^\mu = (E_{e'}, \mathbf{p}_{e'}) \ , \qquad p'^\mu = (E_{f'}, \mathbf{p}_{f'}) = (E_e + m - E_{e'}, \mathbf{p}_e - \mathbf{p}_{e'}) \ . \tag{2.14}$$

Evaluation of the dot products for ultra-relativistic electrons (i.e., $\beta_e = 1$ and $m_e = 0$)

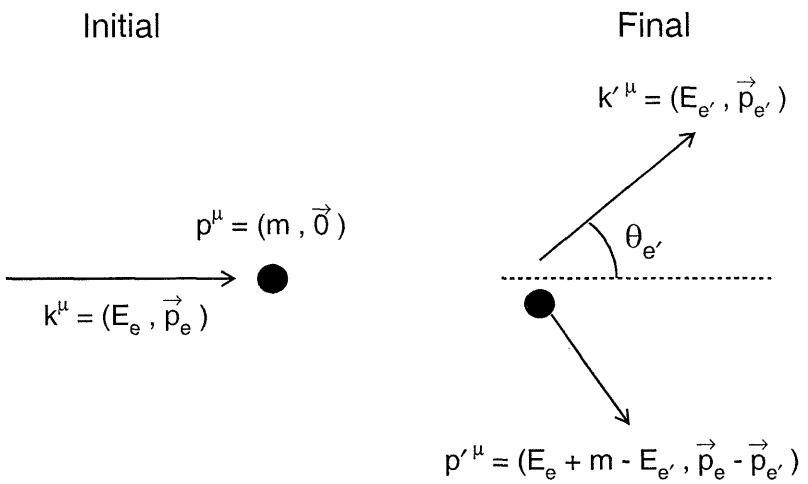

Figure 2-2: Initial- and final-state kinematics for elastic electron scattering from a stationary target.

permits us to rewrite Eq. (2.12) as

$$\frac{1}{4}\sum_{\text{spins}}|\mathcal{M}|^2 = \frac{2e^4}{q^4\sin^2\frac{\theta_{e'}}{2}}\left[q^4\sin^2\frac{\theta_{e'}}{2} - 2q^2m^2\cos^2\frac{\theta_{e'}}{2}\right] , \tag{2.15}$$

where $q^2 = -4E_eE_{e'}\sin^2\frac{\theta_{e'}}{2} < 0$ is the square of the (spacelike) four-momentum transfer and, as indicated in Fig. 2-2, $\theta_{e'}$ is the laboratory frame electron scattering angle.

As a final step in our derivation, the phase-space factor $d\Pi_2$ must be evaluated in the laboratory frame; this is most readily accomplished by partially evaluating the phase-space integral

$$\int d\Pi_2 = \int \frac{d^3\mathbf{p}_{e'}}{(2\pi)^3 2E_{e'}}\frac{d^3\mathbf{p}_{f'}}{(2\pi)^3 2E_{f'}}(2\pi)^4\delta^{(4)}(k+p-k'-p') \tag{2.16}$$

in the laboratory frame. First, integrating the three components of $\mathbf{p}_{f'}$ over the delta function enforces three-momentum conservation and reduces the phase-space integral to

$$\int d\Pi_2 = \int \frac{dE_{e'}d\Omega\ E_{e'}^2}{(2\pi)^3 4E_{e'}E_{f'}}(2\pi)\ \delta(E_e + m - E_{e'} - E_{f'}) . \tag{2.17}$$

Second, rewriting the delta function as

$$\delta(E_e + m - E_{e'} - E_{f'}) = \left| \frac{E_{f'}}{E_{f'} + E_{e'}(1 - \cos\theta_{e'})} \right| \delta \left(E_{e'} - \frac{E_e}{\left[1 + \frac{E_e}{m}(1 - \cos\theta_{e'}) \right]} \right) , \tag{2.18}$$

and integrating over the final delta function gives

$$\mathrm{d}\Pi_2 = \frac{4E_e \, \mathrm{d}\Omega}{m \left[1 + \frac{2E_e}{m} \sin^2 \frac{\theta_{e'}}{2} \right]} . \tag{2.19}$$

Finally, substituting Eqs. (2.15) and (2.19) into Eq. (2.8) gives

$$\left(\frac{\mathrm{d}\sigma}{\mathrm{d}\Omega} \right)_{\text{Dirac}} = \frac{\alpha^2}{4E_e^2 \sin^4 \frac{\theta_{e'}}{2} \left[1 + 2\frac{E_e}{m} \sin^2 \frac{\theta_{e'}}{2} \right]} \left[\cos^2 \frac{\theta_{e'}}{2} - \frac{q^2}{2m^2} \sin^2 \frac{\theta_{e'}}{2} \right] . \tag{2.20}$$

This result is known as the *Dirac cross section.* The term with the $\cos^2 \frac{\theta_{e'}}{2}$ factor represents the contribution of the electric (helicity-preserving) interaction, while the term with the $\sin^2 \frac{\theta_{e'}}{2}$ factor represents the contribution of the magnetic (helicity-flipping) interaction.

To conclude this subsection, we note that the derivation of the differential cross section for the elastic scattering of unpolarized electrons by unpolarized pointlike spin-0 particles is similar; however, the derivation is simpler as there is no magnetic contribution. The result for the differential cross section, known as the *Mott cross section*, is

$$\left(\frac{\mathrm{d}\sigma}{\mathrm{d}\Omega} \right)_{\text{Mott}} = \frac{\alpha^2 \cos^2 \frac{\theta_{e'}}{2}}{4E_e^2 \sin^4 \frac{\theta_{e'}}{2} \left[1 + 2\frac{E_e}{m} \sin^2 \frac{\theta_{e'}}{2} \right]} . \tag{2.21}$$

2.1.3 Electron Scattering by Nucleons

In this subsection, we consider the elastic scattering of unpolarized electrons by unpolarized nucleons. As stated in Chapter 1, nucleons are not pointlike particles; instead,

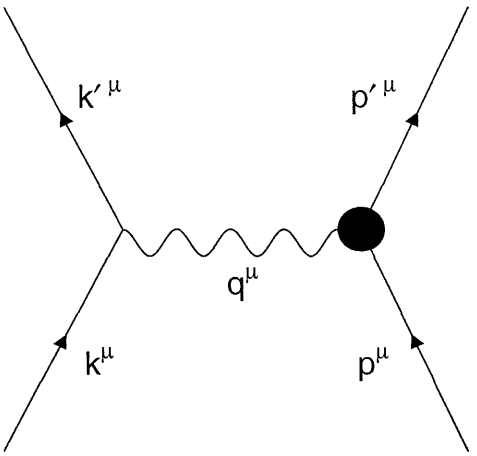

Figure 2-3: Tree-level Feynman diagram for elastic electron-nucleon scattering.

as has been confirmed by numerous experiments, nucleons are complex objects with an extended electromagnetic and spin structure.

A schematic diagram of the tree-level electron-nucleon electromagnetic interaction is shown in Fig. 2-3; here, the shaded circle represents the finite electromagnetic structure of the nucleon. As the electromagnetic structure of the nucleon differs from that of a pointlike particle, the nucleon electromagnetic vertex function is not equivalent to the pointlike fermion electromagnetic vertex function, $-ie\gamma^\mu$. A derivation of the nucleon electromagnetic vertex function based on general arguments was first given by Foldy [11,12] and Salzman [13]; our discussion below closely follows the pedogical overview of this problem given by Peskin and Schroeder [8].

As stated in the previous subsection, the Feynman rules for QED state that the electromagnetic vertex function for a pointlike fermion is $-ie\gamma^\mu$. Analogously, the nucleon electromagnetic vertex function can be written quite generally as $-ie\Gamma^\mu$, where Γ^μ is some expression that must involve p^μ, p'^μ, q^μ, γ^μ, and physical constants. This list is exhaustive; no other mathematical entities appear in the Feynman rules for fermions in QED. The only other entity that could appear is γ^5; however, γ^5 is excluded as we are considering a parity-conserving process.

The functional form for Γ^μ can be deduced based on general arguments. First, we appeal to Lorentz invariance; Γ^μ must transform in exactly the same manner as γ^μ.

This restriction requires Γ^μ to be linear in p^μ, p'^μ, q^μ and γ^μ; therefore, Γ^μ can be written as

$$\Gamma^\mu = \gamma^\mu \cdot A + (p'^\mu + p^\mu) \cdot B + (p'^\mu - p^\mu) \cdot C \ , \tag{2.22}$$

where A, B, and C are unknown functions. A, B, and C could, in principle, involve Dirac matrices dotted into four-vectors (e.g., $\not{p}$ or $\not{p}'$); however, as $\not{p}u(p) = mu(p)$ and $\overline{u}(p')\not{p}' = \overline{u}(p')m$, A, B, and C can be written solely in terms of physical constants and real numbers. Further, as $p \cdot p = p' \cdot p' = m^2$, the only non-trivial scalar that is available is

$$p \cdot p' = -\frac{1}{2}q^2 + m^2 \ ; \tag{2.23}$$

therefore, it follows that A, B, and C can only be functions of $p \cdot p'$ (or, equivalently, of q^2) and physical constants.

Second, the functional form for Γ^μ can be simplified further by imposing the requirement that Γ^μ must satisfy the Ward identity, $q_\mu \Gamma^\mu = 0$; the Ward identity is a statement of current conservation in quantum field theory. The first two terms of Γ^μ in Eq. (2.22) satisfy the Ward identity, but the third term, in general, does not; therefore, C must equal zero. No further simplications can be made beyond those that follow from Lorentz invariance and the Ward identity; however, using the Gordon identity,

$$\overline{u}(p')\gamma^\mu u(p) = \overline{u}(p') \left[\frac{p'^\mu + p^\mu}{2m} + \frac{i\sigma^{\mu\nu}q_\nu}{2m} \right] u(p) \ , \tag{2.24}$$

where, as usual, $\sigma^{\mu\nu} = \frac{i}{2}[\gamma^\mu, \gamma^\nu]$, Γ^μ can be rewritten as

$$\Gamma^\mu(p', p) = \gamma^\mu F_1(q^2) + \frac{i\sigma^{\mu\nu}q_\nu}{2m} F_2(q^2) \ , \tag{2.25}$$

where A and B have been replaced by $F_1(q^2)$ and $F_2(q^2)$. $F_1(q^2)$ and $F_2(q^2)$ are known as the *Dirac and Pauli form factors*, respectively, and quantify the deviation of the nucleon's electromagnetic structure from that of a point particle with a Dirac magnetic moment, $\mu_{\text{Dirac}} = e/2m$; clearly, for a point particle with a Dirac magnetic moment, $F_1 = 1$ and $F_2 = 0$ for all values of q^2. A physical interpretation for $F_1(q^2)$

and $F_2(q^2)$ in terms of the nucleon's extended electromagnetic structure will be given in the next subsection.

The procedure for the derivation of the unpolarized elastic electron-nucleon scattering differential cross section is identical to that used in the previous subsection for the calculation of the unpolarized cross section in elastic electron scattering by pointlike charged fermions; therefore, in what follows, we only highlight the salient features of the derivation. Using the nucleon current,

$$J^{\mu}(p',p) = \overline{u}(p') \left[-ie \left(\gamma^{\mu} F_1(q^2) + \frac{i\sigma^{\mu\nu} q_{\nu}}{2m} F_2(q^2) \right) \right] u(p) \ , \tag{2.26}$$

the result for the spin-averaged matrix element is

$$\begin{aligned} \frac{1}{4} \sum_{\text{spins}} |\mathcal{M}|^2 = \frac{e^4}{4q^4} \Bigg\{ & (F_1 + F_2)^2 \text{tr} \left[(\not{p}' + m) \gamma^{\mu} (\not{p} + m) \gamma^{\nu} \right] \text{tr} \left[\not{k}' \gamma_{\mu} \not{k} \gamma_{\nu} \right] \\ & - 2(F_1 + F_2) F_2 \left(\frac{p'^{\nu} + p^{\nu}}{2m} \right) \text{tr} \left[(\not{p}' + m) \gamma^{\mu} (\not{p} + m) \right] \text{tr} \left[\not{k}' \gamma_{\mu} \not{k} \gamma_{\nu} \right] \\ & + \frac{F_2^2}{4m^2} (p'^{\mu} + p^{\mu})(p'^{\nu} + p^{\nu}) \text{tr} \left[(\not{p}' + m)(\not{p} + m) \right] \text{tr} \left[(\not{k}' \gamma_{\mu} \not{k} \gamma_{\nu}) \right] \Bigg\} \ . \end{aligned} \tag{2.27}$$

The evaluation of the traces is again straightforward, albeit tedious, and the result is

$$\frac{1}{4} \sum_{\text{spins}} |\mathcal{M}|^2 = \frac{2e^4}{q^4} \left[4(F_1 + F_2)^2 \cdot \mathbf{I} + \left(-4(F_1 + F_2) F_2 + \frac{p \cdot p'}{m^2} F_2^2 \right) \cdot \mathbf{II} \right] \ , \tag{2.28}$$

where

$$\begin{aligned} \mathbf{I} &= (k \cdot p)(k' \cdot p') + (k \cdot p')(k' \cdot p) - m^2 (k \cdot k') \ , \\ \mathbf{II} &= (k \cdot p)(k' \cdot p) + (k \cdot p)(k' \cdot p') + (k \cdot p')(k' \cdot p) \\ &\quad + (k \cdot p')(k' \cdot p') - (k \cdot k')(p \cdot p') - m^2 (k \cdot k') \ . \end{aligned} \tag{2.29}$$

We are again interested in the unpolarized laboratory frame differential cross section, $\mathrm{d}\sigma/\mathrm{d}\Omega$, for ultra-relativistic electrons. Evaluation of the dot products for the same

kinematics as in the previous subsection (i.e., those shown in Fig. 2-2) reduces the spin-averaged matrix element to

$$\frac{1}{4}\sum_{\text{spins}}|\mathcal{M}|^2 = \frac{2e^4m^2}{q^2\sin^2\frac{\theta_{e'}}{2}}\left[-2\left(F_1^2 - \frac{q^2}{4m^2}F_2^2\right)\cos^2\frac{\theta_{e'}}{2} + \frac{q^2}{m^2}(F_1+F_2)^2\sin^2\frac{\theta_{e'}}{2}\right] . \tag{2.30}$$

After substituting the above result for the spin-averaged matrix element and the result for the phase-space factor $\mathrm{d}\Pi_2$ given in Eq. (2.19) into the general equation for the differential cross section, Eq. (2.8), the result for the differential cross section in the laboratory frame is

$$\frac{\mathrm{d}\sigma}{\mathrm{d}\Omega} = \frac{\alpha^2}{4E_e^2\left[1+2\frac{E_e}{m}\sin^2\frac{\theta_{e'}}{2}\right]\sin^4\frac{\theta_{e'}}{2}}\left[\left(F_1^2+\tau F_2^2\right)\cos^2\frac{\theta_{e'}}{2} + 2\tau(F_1+F_2)^2\sin^2\frac{\theta_{e'}}{2}\right] , \tag{2.31}$$

where $\tau \equiv -q^2/4m^2$. This result was first derived by Rosenbluth [14], and the result is now known as the *Rosenbluth formula.* As expected, we recover the Dirac cross section if $F_1 = 1$ and $F_2 = 0$.

2.1.4 Sachs Electric and Magnetic Form Factors

Henceforth, as is customary, in lieu of q^2, we will use

$$Q^2 \equiv -q^2 = 4E_eE_{e'}\sin^2\frac{\theta_{e'}}{2} > 0 \tag{2.32}$$

as the square of the four-momentum transfer in electron scattering is spacelike.

Early attempts to relate $F_1(Q^2)$ and $F_2(Q^2)$ to the distribution of charge and current (or magnetization) within the nucleon were undertaken by Yennie, Lévy, and Ravenhall [15], Walecka [16], Ernst, Sachs, and Wali [17], and Sachs [18]. Prior to these analyses, it was assumed that F_1 and F_2 were related to the nucleon's charge and magnetization distributions; however, as will be seen in what follows, it is, instead, certain linear combinations of F_1 and F_2 that are related to the distribution of charge and magnetization within the nucleon.

First, we consider the normalization of F_1 and F_2. In the limit $Q^2 \to 0$, the virtual photon cannot resolve the electromagnetic structure of the nucleon, and $F_1(0)$ and $F_2(0)$ must describe the integral electromagnetic properties of the nucleon. As previously discussed, the electromagnetic vertex function for a pointlike fermion of charge e with a magnetic moment $e/2m$ is $-ie\gamma^\mu$, while the electromagnetic vertex function for a nucleon with an extended electromagnetic structure is

$$-ie\Gamma^\mu = -ie\left[\gamma^\mu F_1(q^2) + \frac{i\sigma^{\mu\nu}q_\nu}{2m}F_2(q^2)\right] \; ; \tag{2.33}$$

therefore, it is obvious that for the proton (p) and the neutron (n), F_1 must be normalized at $Q^2 = 0$ to

$$F_{1p}(0) = 1 \; , \qquad F_{1n}(0) = 0 \; . \tag{2.34}$$

The normalization of $F_2(0)$ can be deduced via a calculation of the nucleon's magnetic moment, μ, from the current operator in a state in which the nucleon is at rest. Such a calculation was first carried out by Ernst, Sachs, and Wali [17], and their results showed that μ is related to $F_1(0)$ and $F_2(0)$ by

$$\mu = \frac{e}{2m}\left[F_1(0) + F_2(0)\right] = \mu_{\text{Dirac}} + \mu_{\text{Pauli}} \; , \tag{2.35}$$

where $(\mu_{\text{Pauli}})_{p,n} = eF_{2p,n}(0)/2m = \kappa_{p,n}$ is the Pauli, or anomalous, magnetic moment. Further, Ernst, Sachs, and Wali [17] showed that the second moment of the nucleon's charge distribution, $\langle r^2_{\text{ch}}\rangle$, is related to F_1 and F_2 according to

$$-\frac{1}{6}\langle r^2_{\text{ch}}\rangle = \left.\frac{\mathrm{d}F_1}{\mathrm{d}Q^2}\right|_{Q^2=0} - \frac{1}{4m^2}F_2(0) \; . \tag{2.36}$$

These results for μ and $\langle r^2_{\text{ch}}\rangle$ in terms of F_1 and F_2 suggested the introduction of two new form factors, the *Sachs charge (or electric), G_E, and magnetic, G_M, form*

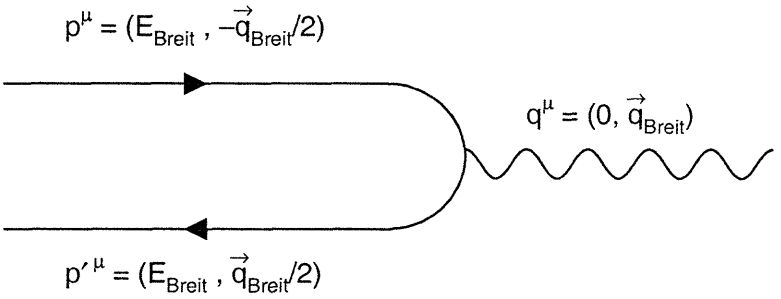

Figure 2-4: Schematic representation of the Breit frame.

factors, defined according to

$$G_E(Q^2) = F_1(Q^2) - \tau F_2(Q^2) \ , \tag{2.37}$$

$$G_M(Q^2) = F_1(Q^2) + F_2(Q^2) \ , \tag{2.38}$$

where $\tau = Q^2/4m^2$. With this redefinition of the form factors, the Rosenbluth formula, Eq. (2.31) can be written as

$$\frac{\mathrm{d}\sigma}{\mathrm{d}\Omega} = \frac{\alpha^2}{4E_e^2\left[1+2\frac{E_e}{m}\sin^2\frac{\theta_{e'}}{2}\right]\sin^4\frac{\theta_{e'}}{2}}\left[\frac{G_E^2+\tau G_M^2}{1+\tau}\cos^2\frac{\theta_{e'}}{2}+2\tau G_M^2\sin^2\frac{\theta_{e'}}{2}\right] \ . \tag{2.39}$$

We see that this expression contains no interference terms between G_E and G_M.

Sachs [18] showed that a physical interpretation of G_E and G_M is simplest if $Q^2 = \mathbf{q}^2$ (i.e., if the energy transfer vanishes). This condition is satisfied in a particular frame of reference known as the Breit frame (or the "brick-wall frame"). In the Breit frame, shown schematically in Fig. 2-4, the initial four-momentum of the nucleon is $p_{\mathrm{Breit}} = (E_{\mathrm{Breit}}, -\mathbf{q}_{\mathrm{Breit}}/2)$, and the final four-momentum of the nucleon is $p'_{\mathrm{Breit}} = (E_{\mathrm{Breit}}, \mathbf{q}_{\mathrm{Breit}}/2)$; therefore, the four-momentum transfer in the Breit frame is $q_{\mathrm{Breit}} = (0, \mathbf{q}_{\mathrm{Breit}})$. In the laboratory frame, the initial four-momentum is $p = (m, \mathbf{0})$, and for a four-momentum transfer of $q = (\omega, \mathbf{q})$, it follows that the final four-momentum is $p' = (m+\omega, \mathbf{q})$. As Q^2 is Lorentz invariant, $Q^2 = \mathbf{q}^2_{\mathrm{Breit}} = \mathbf{q}^2 - \omega^2 = 2m\omega$; therefore,

$$Q^2 = \mathbf{q}^2_{\mathrm{Breit}} = \frac{\mathbf{q}^2}{1+\tau} \tag{2.40}$$

uniquely defines the nucleon momentum in the Breit frame. With this definition, it is clear that a unique Breit frame exists for each value of Q^2.

Sachs [18] demonstrated that in the Breit frame (i.e., for a particular value of Q^2) the nucleon current, $J^\mu(p',p) = (J^0, \mathbf{J}) = \overline{u}(p')(-ie\Gamma^\mu)u(p)$, separates into individual contributions from G_E and G_M,

$$J^0(p',p) = -ie\overline{u}(p')(G_E)u(p) \ , \tag{2.41}$$

$$\mathbf{J}(p',p) = -ie\overline{u}(p')\left[\left(\frac{i\boldsymbol{\sigma}\times\mathbf{q}_{\rm Breit}}{2m}\right)G_M\right]u(p) \ , \tag{2.42}$$

where $\boldsymbol{\sigma}$ denotes the nucleon spin vector; henceforth, we shall define the nucleon current operator in the Breit frame to be

$$\begin{aligned}\hat{J}_\mu &= \left(G_E, \frac{i\boldsymbol{\sigma}\times\mathbf{q}_{\rm Breit}}{2m}G_M\right) \\ &= \left(G_E, \ i\frac{|\mathbf{q}_{\rm Breit}|}{2m}\sigma_y G_M, \ -i\frac{|\mathbf{q}_{\rm Breit}|}{2m}\sigma_x G_M, \ 0\right) \ ,\end{aligned} \tag{2.43}$$

where we have taken the z-axis to be along $\mathbf{q}_{\rm Breit}$.

With this identification for the nucleon current, Sachs [18] argued that $G_E(Q^2)$ and $G_M(Q^2)$ can be interpreted as the Fourier transforms of the nucleon's charge, $\rho_{\rm ch}$, and magnetization, $\rho_{\rm mag}$, densities

$$G_E(Q^2) = \frac{4\pi}{Q}\int r{\rm d}r \ \rho_{\rm ch}(r) \ \sin Qr \ , \tag{2.44}$$

$$G_M(Q^2) = \frac{4\pi}{Q}\int r{\rm d}r \ \mu\rho_{\rm mag}(r) \ \sin Qr \ ; \tag{2.45}$$

therefore, according to this argument, the nucleon charge and magnetization densities could be extracted from an inverse Fourier analysis of experimental data on G_E and G_M. Unfortunately, this interpretation of charge and magnetization densities in terms of G_E and G_M is somewhat naive; a simple Fourier inversion does not account for the variation of the Breit frame with Q^2. Any attempt to interpret G_E and G_M in terms of the nucleon's charge and magnetization densities must account for this relativistic effect. Relativistic prescriptions relating G_E and G_M to the nucleon charge and

magnetization densities have recently been developed by Kelly [19, 20]. Space does not permit discussion of this model here; therefore, we refer the reader to the original references.

Neglecting relativistic corrections, at (very) low Q^2, G_E and G_M can be related to the nucleon's charge and magnetization radii; at $Q^2 \approx 0$, the integrands of the Fourier integrals can be expanded in a power series, with the result that

$$\begin{aligned} G_E(Q^2) &= \int 4\pi r^2 \mathrm{d}r\ \rho_{\mathrm{ch}}(r) - \frac{1}{3!}Q^2 \int 4\pi r^2 \mathrm{d}r\ r^2 \rho_{\mathrm{ch}}(r) + \dots , \\ &= 1 - \frac{1}{3!}Q^2 \langle r_E^2 \rangle + \dots , \end{aligned} \tag{2.46}$$

and

$$\begin{aligned} G_M(Q^2)/\mu &= \int 4\pi r^2 \mathrm{d}r\ \rho_{\mathrm{mag}}(r) - \frac{1}{3!}Q^2 \int 4\pi r^2 \mathrm{d}r\ r^2 \rho_{\mathrm{mag}}(r) + \dots \\ &= 1 - \frac{1}{3!}Q^2 \langle r_M^2 \rangle + \dots , \end{aligned} \tag{2.47}$$

where μ denotes the nucleon magnetic moment. It follows that the charge and magnetization radii,

$$\langle r_E^2 \rangle = -6 \frac{\mathrm{d}G_E}{\mathrm{d}Q^2}\bigg|_{Q^2=0} , \qquad \langle r_M^2 \rangle = -6 \frac{1}{\mu} \frac{\mathrm{d}G_M}{\mathrm{d}Q^2}\bigg|_{Q^2=0} , \tag{2.48}$$

are proportional to the slope of $G_E(Q^2)$ and $G_M(Q^2)$, respectively, at $Q^2 = 0$.

2.2 Nucleon Form Factor Measurements with Unpolarized Electrons

In this section, we survey the status of nucleon form factor measurements conducted with unpolarized electron beams. We begin with the proton form factors; we discuss how the proton electric and magnetic form factors have been extracted from measurements of the unpolarized elastic electron-proton cross section, and we present

the results of these measurements. After discussing the proton form factors, we turn to the neutron form factors. Due to the lack of a free neutron target, the neutron form factors have been extracted from measurements of the unpolarized elastic and quasielastic electron-deuteron cross section. Such measurements have proven to be difficult as the extraction of the neutron form factors from these cross section measurements is complicated by the structure of the deuteron and the presence of the proton. To further complicate matters, as the neutron's integral charge is zero, the neutron electric form factor, G_{En}, is very small. Indeed, as we shall see, measurements of G_{En} have proven to be even elusive than measurements of G_{Ep} with unpolarized electron beams.

2.2.1 Proton Form Factors via Unpolarized Elastic ^{1}H(e,e') and ^{1}H$(e,e'p)$ Cross Section Measurements

As discussed in the previous section, the unpolarized differential cross section in the laboratory frame for elastic unpolarized-electron, unpolarized-proton scattering in the one-photon exchange approximation is given by the Rosenbluth formula, Eq. (2.39), which can be rewritten as

$$\frac{\mathrm{d}\sigma}{\mathrm{d}\Omega} = \left(\frac{\mathrm{d}\sigma}{\mathrm{d}\Omega}\right)_{\mathrm{Mott}} \left(\frac{1}{1+\tau}\right) \left[G_{Ep}^2(Q^2) + \frac{\tau}{\epsilon} G_{Mp}^2(Q^2)\right] , \tag{2.49}$$

where

$$\epsilon = \left[1 + 2(1+\tau)\tan^2\frac{\theta_{e'}}{2}\right]^{-1} \tag{2.50}$$

is the transverse polarization of the virtual photon for an electron scattering angle $\theta_{e'}$. With the cross section written in this form, it is clear that for a fixed value of τ (i.e., Q^2), the cross section is linear in ϵ^{-1}; therefore, G_{Ep}^2 and G_{Mp}^2 can be extracted from the ϵ^{-1} dependence of the reduced cross section,

$$\sigma_R \equiv \frac{\mathrm{d}\sigma}{\mathrm{d}\Omega} \Big/ \left[\left(\frac{\mathrm{d}\sigma}{\mathrm{d}\Omega}\right)_{\mathrm{Mott}} \left(\frac{1}{1+\tau}\right)\right] = G_{Ep}^2(Q^2) + \frac{\tau}{\epsilon} G_{Mp}^2(Q^2) , \tag{2.51}$$

on ϵ^{-1} at fixed Q^2. Such an extraction of the form factors is termed a *Rosenbluth separation.* A Rosenbluth separation of G_{Ep}^2 (G_{Mp}^2) becomes increasingly difficult at high (low) values of Q^2 as the contribution of G_{Mp}^2 to the reduced cross section is modulated by the factor of τ. Also, as the contribution of G_{Mp}^2 to the reduced cross section is modulated by the factor of ϵ^{-1}, a measurement of the cross section at an electron scattering angle of $\theta_{e'} = 180°$ provides a direct measure of G_{Mp}^2.

A reliable extraction of the cross section from the measured counting rates of the scattered electrons in a spectrometer requires precise knowledge of the number of incident electrons, the incident beam energy, the target density, count rate losses due to electronic and computer dead time, and background contamination from pion production and scattering from target materials other than protons; also, for extended targets (as is always the case), the acceptance of the spectrometer must be well understood as the cross section varies rapidly with the scattering angle. An accurate Rosenbluth separation of cross section data acquired in a single experiment is fairly difficult as is; therefore, Rosenbluth separation analyses attempting to combine cross section data from different experiments are, at best, somewhat tenuous as the normalizations for different experiments will, in general, differ.

In addition to the potential difficulties associated with a cross section measurement listed in the preceding paragraph, the Rosenbluth formula was derived within the tree-level approximation of one-photon exchange; however, higher-order processes, termed *radiative corrections*, contribute. Radiative corrections can, in general, be classified as *internal* or *external*; internal corrections arise from processes that occur as part of the primary electron-proton scattering vertex, while external effects are due to bremsstrahlung in the field of a nearby nucleus or ionization losses. Examples of internal radiative corrections are shown in Fig. 2-5; here, panels (a) and (b) represent two-photon exchange, panel (c) represents vacuum polarization (i.e., contributions from e^+e^-, $\mu^+\mu^-$, $q\bar{q}$, etc., loops), panels (d) and (e) represent corrections to the electron and nucleon vertex, and panels (f)–(i) represent internal bremsstrahlung by the electron or the nucleon. Although the contributions of radiative corrections are suppressed by factors of α relative to tree-level single-photon exchange, these corrections

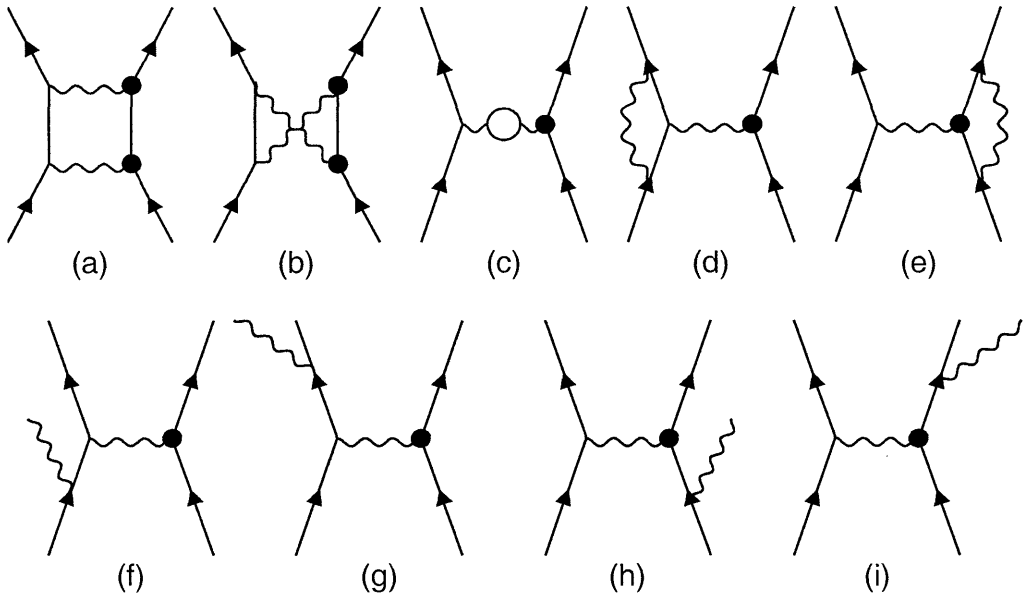

Figure 2-5: Examples of internal radiative corrections to tree-level elastic electron-nucleon scattering: two-photon exchange (a)–(b), vacuum polarization (c), electron and nucleon vertex corrections (d)–(e), and internal bremsstrahlung (f)–(i).

cannot be ignored. Complete prescriptions for the calculation of radiative corrections were developed by Mo and Tsai [21]; in this seminal paper, Mo and Tsai improved the reliability of the formalism and provided practical recipes for the calculation of radiative corrections to elastic and inelastic electron and muon scattering.

2.2.2 Unpolarized Results for G_{Ep} and G_{Mp}

The pioneering measurements of elastic electron-proton cross sections were carried out by Hofstadter and colleagues at the Stanford Mark III Accelerator in the mid-1950s (e.g., [3–5]). In an early study with a 188 MeV electron beam, Hofstadter and McAllister [3, 4] concluded that the measured elastic electron-proton cross sections did not agree with either:

- the Mott cross section (i.e., a pointlike spinless proton),
- the Dirac cross section (i.e., a pointlike spin-$\frac{1}{2}$ proton with a Dirac magnetic moment), or

- the Rosenbluth formula with $F_1(Q^2) = 1$ and $F_2(Q^2) = \kappa_p$ (i.e., a pointlike spin-$\frac{1}{2}$ proton with a Dirac magnetic moment and an anomalous Pauli magnetic moment).

Further studies with 200, 300, 400, 500, and 550 MeV electron beams [5] confirmed these findings; in fact, the cross section measured with a 550 MeV electron beam at an electron scattering angle of $\theta_{e'} = 135°$ was found to be approximately a factor of nine smaller than that predicted by the Rosenbluth formula assuming $F_1(Q^2) = 1$ and $F_2(Q^2) = \kappa_p$. On the basis of these findings, Chambers and Hofstadter [5] concluded that $F_1 < 1$ and $F_2 < \kappa_p$ for $Q^2 > 0$, thereby implying, in their own words, a "spread-out charge and spread-out Dirac moment" and a "spread-out Pauli moment".

In 1958, Hofstadter, Bumiller, and Yearian [22] demonstrated that Chambers's and Hofstadter's [5] experimental data on G_{Ep} and G_{Mp} for $Q^2 < 0.54$ $(\mathrm{GeV}/c)^2$ could be described by the following (empirical) parameterizations,

$$G_{Ep}(Q^2) = G_D(Q^2) \ , \qquad G_{Mp}(Q^2) = \mu_p G_D(Q^2) \ , \tag{2.52}$$

where

$$G_D(Q^2) = \left(1 + \frac{Q^2}{\Lambda^2}\right)^{-2} \ , \tag{2.53}$$

with $\Lambda^2 =$ constant, is known as the *dipole parameterization.* A naive inverse Fourier transformation of the dipole parameterization suggests (identical) exponential distributions of charge and magnetization in the nucleon,

$$\rho_{\mathrm{ch,mag}}(r) = \rho_0 \ \exp(-\Lambda r) \ , \tag{2.54}$$

with charge and magnetic rms radii given by

$$\langle r^2_{E,M} \rangle^{1/2} = \frac{\sqrt{12}}{\Lambda} \ . \tag{2.55}$$

Hofstadter, Bumiller, and Yearian's initial analysis suggested that $\Lambda^2 = 0.73$ $(\mathrm{GeV}/c)^2$ described the data well. A reevaluation of the existing data in 1966 by

Albrecht *et al.* [23] suggested that $\Lambda^2 = 0.71$ (GeV/c)^2 provided the best agreement with the data; hereafter, as is now standard, when we refer to the dipole parameterization, it should be assumed that $\Lambda^2 = 0.71$ (GeV/c)^2. It is important to note that Eq. (2.52) implies that G_{Ep} and G_{Mp} *scale similarly* for all values of Q^2; such scaling naively implies that the proton's charge and magnetic structure are similar.

Following Hofstadter's pioneering measurements of the proton form factors, extensive investigations of the proton's electromagnetic structure with unpolarized electron beams commenced at electron scattering facilities around the world and continued through the early 1990s. In Table 2.1, we have attempted to compile a nearly exhaustive chronological summary of proton form factor measurements conducted with unpolarized electron beams since the early 1960s; for each measurement, we list the reference, the facility at which the experiment was conducted, the kinematic reaction, the year the result was reported, the range of Q^2 accessed, and the quantities extracted from the cross section data.

The results of the measurements summarized in Table 2.1 are plotted in Fig. 2-6; here, we have, somewhat arbitrarily, only plotted those measurements reported since 1970, and we have scaled the values for G_{Ep} and G_{Mp} by G_D and $\mu_p G_D$, respectively. The results shown in this figure clearly demonstrate that the unpolarized results for G_{Ep} are consistent with the dipole parameterization for $Q^2 \lesssim 1$ (GeV/c)^2; however, the data are less precise for $Q^2 > 1$ (GeV/c)^2 and a definitive statement regarding the high Q^2 behavior of G_{Ep} cannot be made simply via visual inspection of the data. On the other hand, as G_{Mp} dominates the elastic cross section at high Q^2, relatively precise values for G_{Mp} have been extracted for Q^2 values ranging up to $\sim$31 (GeV/c)^2. Strong deviations from the dipole parameterization are seen for $Q^2 \gtrsim 10$ (GeV/c)^2; further, the dipole parameterization does not describe the intricate features of the behavior of G_{Mp} for $Q^2 \lesssim 10$ (GeV/c)^2.

Finally, unpolarized results for the proton form factor ratio, $\mu_p G_{Ep}/G_{Mp}$, are plotted versus Q^2 in Fig. 2-7. Scaling is confirmed for $Q^2 \lesssim 1$ (GeV/c)^2, but the data for $Q^2 \gtrsim 1$ (GeV/c)^2 are not as precise. Within errors, the more recent unpolarized results suggest that G_{Ep} and G_{Mp} scale similarly.

Reference(s)	Facility	Reaction	Q^2 [(GeV/c)^2]	Quantities	Note
Bumiller (1961) [24]	Mark III	^{1}H(e,e')	0.16 – 0.97	G_{Ep}, G_{Mp}	
Lehmann (1962) [25]	Orsay	^{1}H(e,e')	0.12	G_{Ep}, G_{Mp}	
Drickey (1962) [26]	Mark III	^{1}H(e,e')	0.01 – 0.09	G_{Ep}	1
Dudelzak (1963) [27]	Orsay	^{1}H(e,e')	0.01 – 0.08	G_{Ep}, G_{Mp}	
Berkelman (1963) [28]	Cornell	^{1}H$(e,e'p)$	0.97 – 1.75	G_{Ep}, G_{Mp}	
Dunning (1963) [29]	Cambridge	^{1}H(e,p)	0.23 – 0.70	G_{Ep}	2
Chen (1966) [31,32]	Cambridge	^{1}H(e,e')	1.75 – 3.88	G_{Ep}, G_{Mp}	
Frèrejacque (1966) [33]	Orsay	^{1}H(e,p)	0.03 – 0.07	G_{Ep}, G_{Mp}	
Janssens (1966) [34]	Mark III	^{1}H(e,e')	0.16 – 1.16	G_{Ep}, G_{Mp}	3
Bartel (1966) [35]	DESY	^{1}H(e,e')	0.39 – 3.88	G_{Ep}, G_{Mp}	
Albrecht (1966) [23]	DESY	^{1}H(e,e')	4.08 – 9.59	G_{Mp}	1
Behrend (1967) [36]	DESY	^{1}H(e,e')	0.39 – 4.28	G_{Ep}, G_{Mp}	1
Albrecht (1967) [37]	DESY	^{1}H(e,e')	1.94 – 9.53	G_{Ep}, G_{Mp}	
Bartel (1967) [38]	DESY	^{1}H(e,p)	2.91	G_{Ep}, G_{Mp}	
Litt (1970) [39]	SLAC	^{1}H(e,e')	1.00 – 3.75	G_{Ep}/G_{Mp}	4
Berger (1971) [40,41]	DESY	^{1}H(e,e')	0.39 – 1.94	G_{Ep}, G_{Mp}	
Price (1971) [42–44]	Cambridge	^{1}H$(e,e'p)$	0.27 – 1.75	G_{Ep}, G_{Mp}	
Ganichot (1972) [45]	Orsay	^{1}H(e,e')	0.02 – 0.19	G_{Mp}	5
Akimov (1972) [46]	Erevan	^{1}H(e,p)	0.01 – 0.02	G_{Ep}	6
Bartel (1973) [47,48]	DESY	^{1}H(e,e')	0.67 – 3.00	G_{Ep}, G_{Mp}	
Kirk (1973) [49,50]	SLAC	^{1}H(e,e')	1.00 – 25.03	G_{Mp}	1
Theissen (1974) [51]	Darmstadt	^{1}H(e,e')	0.003 — 0.01	G_{Ep}/G_{Mp}	4
Murphy (1974) [52]	Saskatchewan	^{1}H(e,p)	0.01 – 0.03	G_{Ep}	1
Borkowski (1975) [53,54]	MAMI	^{1}H(e,e')	0.01 – 0.18	G_{Ep}, G_{Mp}	
Simon (1980) [55]	MAMI	^{1}H(e,e')	0.01 – 0.05	G_{Ep}	1
Bosted (1990) [56]	SLAC	^{1}H(e,e')	0.49 – 1.75	G_{Mp}	5
Sill (1993) [57,58]	SLAC	^{1}H(e,e')	2.9 – 31.3	G_{Mp}	1
Walker (1994) [59,60]	SLAC	^{1}H(e,e')	1.00 – 3.01	G_{Ep}, G_{Mp}	
Andivahis (1994) [61,62]	SLAC	^{1}H(e,e')	1.75 – 8.83	G_{Ep}, G_{Mp}	

[1] Assumed scaling, $G_{Mp} = \mu_p G_{Ep}$, to extract the specified quantity.
[2] Used values for G_{Mp} reported in [30] to extract G_{Ep}.
[3] Neglected G_{Ep} for $Q^2 > 1.0$ (GeV/c)^2.
[4] Extracted G_{Ep}/G_{Mp} from cross section ratios.
[5] G_{Mp} extracted from cross section measurements at $\theta_{e'} = 180°$.
[6] Neglected G_{Mp}.

Table 2.1: Chronological summary of proton form factor measurements conducted with unpolarized electron beams since the early 1960s.

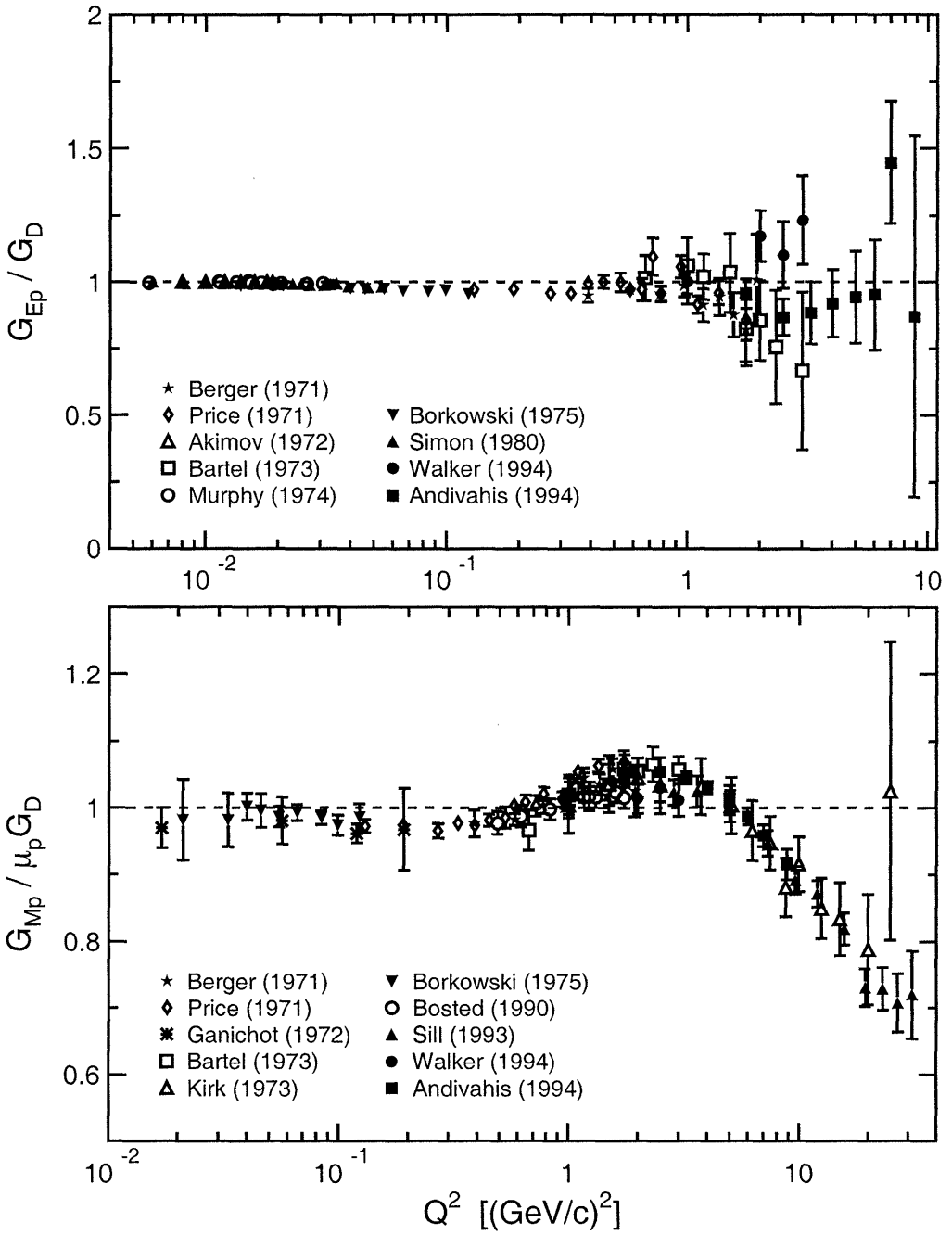

Figure 2-6: Post-1970 unpolarized results for G_{Ep}/G_D (top panel) and $G_{Mp}/\mu_p G_D$ (bottom panel) plotted versus Q^2.

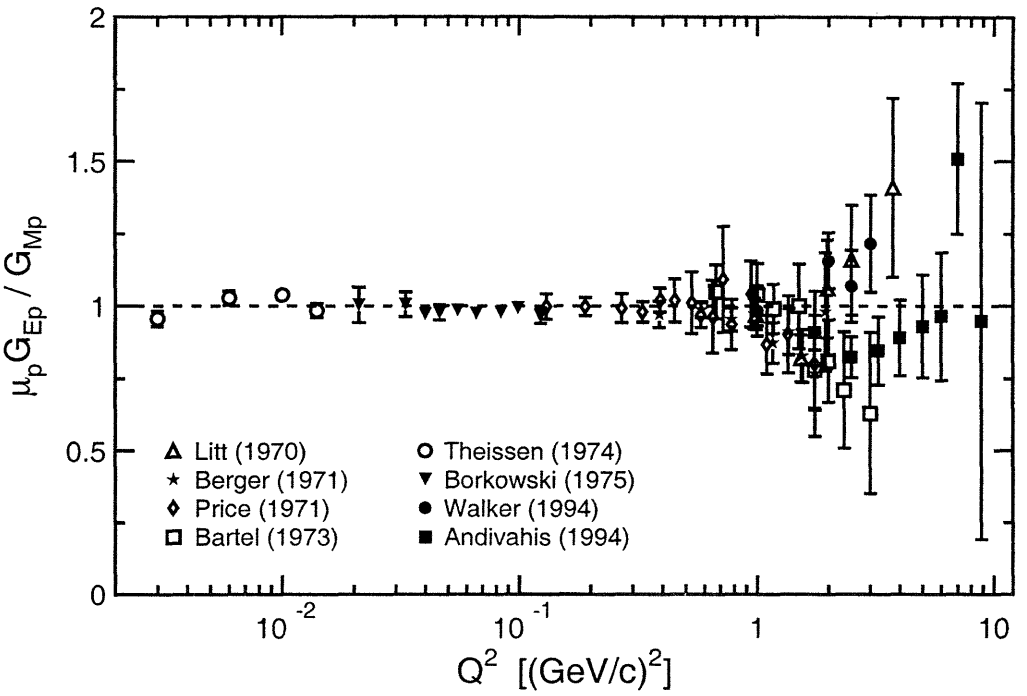

Figure 2-7: Post-1970 unpolarized results for the proton form factor ratio, $\mu_p G_{Ep}/G_{Mp}$, plotted versus Q^2.

2.2.3 Proton Charge Radius

The proton's root mean square charge radius, $\langle r_{Ep}^2 \rangle^{1/2}$, has been extracted from analyses of the slope of G_{Ep} at low Q^2. The two most precise results for $\langle r_{Ep}^2 \rangle^{1/2}$ are those reported by Hand, Miller, and Wilson [30] (dating to 1963) and Simon, Schmitt, Borkowski, and Walther [55] (dating to 1980). The result of Simon *et al.*'s analysis, yielding a value of $\langle r_{Ep}^2 \rangle^{1/2} = 0.862 \pm 0.012$ fm, has been accepted for nearly two decades by the nuclear physics community as the definitive result for this quantity; however, the Hand *et al.* result of $\langle r_{Ep}^2 \rangle^{1/2} = 0.805 \pm 0.011$ fm is still cited as an alternative by the atomic and high-energy physics communities (see, e.g., [63, 64]). Several authors have argued (see, e.g., [63, 65]) that the Hand *et al.* result is not credible as it was based on a $Q^2 \rightarrow 0$ extrapolation of the dipole form factor fitted to high Q^2 data.

Friar [65] has suggested there are, in general, several problems associated with an extraction of $\langle r_{Ep}^2 \rangle^{1/2}$ from data on G_{Ep}; for example, Friar argues that most analyses

have not fully accounted for the effect of the normalization of the cross section on the extraction of $\langle r_{Ep}^2 \rangle^{1/2}$. Another source of error is the neglect of higher-order Coulomb corrections. Indeed, Rosenfelder [63] has recently (2000) demonstrated that the inclusion of Coulomb corrections increases the value of the Simon *et al.* result to $\langle r_{Ep}^2 \rangle^{1/2} = 0.880 \pm 0.015$ fm, a value that is in good agreement with the value of $\langle r_{Ep}^2 \rangle^{1/2} = 0.883 \pm 0.014$ fm reported by Melnikov and van Ritbergen [66] in a QED analysis (at the three loop level) of the 1S Lamb shift in atomic (electronic) hydrogen; however, despite this agreement with Rosenfelder's result, the result is controversial as calculations at the two loop level seem to favor smaller values for the charge radius.

Indeed, the question of the proton's charge radius has not been resolved satisfactorily, and this issue remains open and controversial; however, several upcoming experiments, to be discussed later, should provide timely new and, hopefully, definitive data.

2.2.4 Neutron Form Factors via Unpolarized Quasielastic $^2\mathrm{H}(e,e')$ and $^2\mathrm{H}(e,e'n)$ Cross Section Measurements

We now turn to measurements of the neutron form factors via unpolarized quasielastic electron-deuteron scattering. In the *impulse approximation*, shown in Fig. 2-8, the virtual photon interacts with just the proton or the neutron (i.e., the other nucleon is treated as a "spectator"); further, following the interaction, the proton or neutron exits the nucleus without interacting with the other nucleon (e.g., no rescattering). In this approximation, the inclusive unpolarized quasielastic electron-deuteron (ed) cross section can be written as the sum of the elastic unpolarized electron-proton (ep) and electron-neutron (en) cross sections,

$$\left(\frac{\mathrm{d}\sigma}{\mathrm{d}\Omega}\right)_{ed} = \left(\frac{\mathrm{d}\sigma}{\mathrm{d}\Omega}\right)_{ep} + \left(\frac{\mathrm{d}\sigma}{\mathrm{d}\Omega}\right)_{en} , \tag{2.56}$$

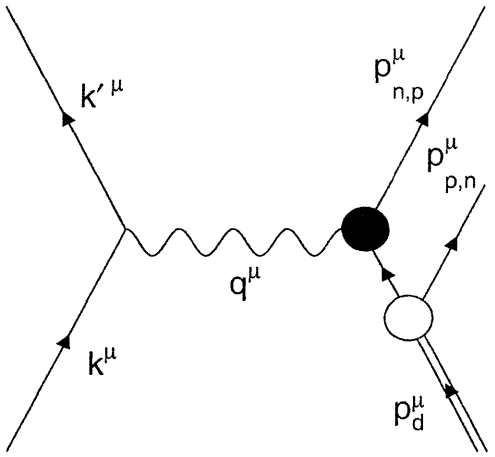

Figure 2-8: The impulse approximation in quasielastic electron-deuteron scattering.

where

$$\left(\frac{\mathrm{d}\sigma}{\mathrm{d}\Omega}\right)_{ep} = \left(\frac{\mathrm{d}\sigma}{\mathrm{d}\Omega}\right)_{\mathrm{Mott}} \left(\frac{1}{1+\tau}\right) \left[G_{Ep}^2(Q^2) + \frac{\tau}{\epsilon} G_{Mp}^2(Q^2)\right] , \tag{2.57}$$

$$\left(\frac{\mathrm{d}\sigma}{\mathrm{d}\Omega}\right)_{en} = \left(\frac{\mathrm{d}\sigma}{\mathrm{d}\Omega}\right)_{\mathrm{Mott}} \left(\frac{1}{1+\tau}\right) \left[G_{En}^2(Q^2) + \frac{\tau}{\epsilon} G_{Mn}^2(Q^2)\right] . \tag{2.58}$$

In 1956, Hofstadter [67] proposed within the framework of the impulse approximation that the neutron form factors could be extracted from a difference in a Rosenbluth separation of the inclusive unpolarized quasielastic electron-deuteron cross section and a Rosenbluth separation of the elastic unpolarized electron-proton cross section. In particular, Hofstadter noted "... the following thought occurred to the present author ... scattering electrons [quasi]elastically from deuterium and comparing such scattering with that from free protons ... should yield the neutron scattering cross section ... ".

Although seemingly simple, measurements of the neutron form factors using this technique have proven to be difficult and susceptible to large systematic errors. The subtraction of the proton contribution to the inclusive unpolarized quasielastic electron-deuteron cross section requires precise knowledge of the proton form factors, and the Rosenbluth decomposition of the inclusive cross section difference is subject to the inherent difficulties and systematic uncertainties associated with any cross

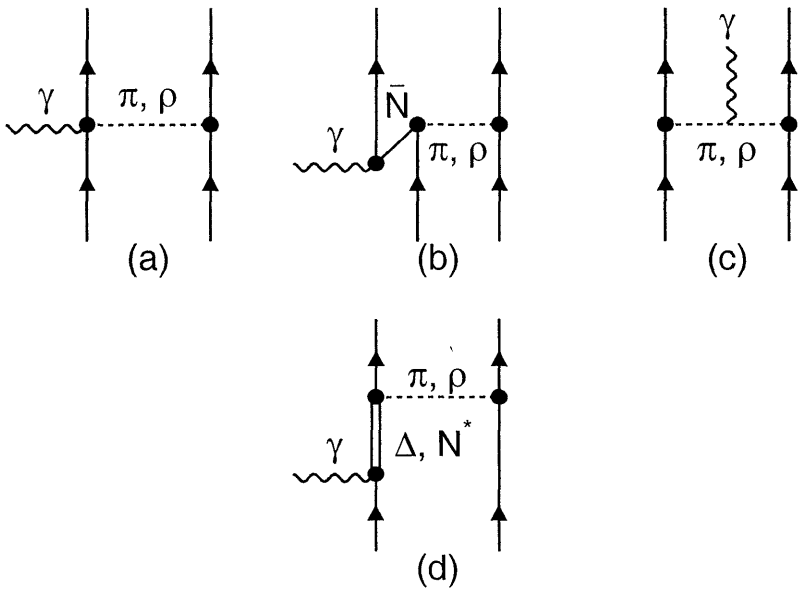

Figure 2-9: Examples of meson exchange currents (a)–(c) and isobar configurations (d) in electron-deuteron scattering.

section measurement. In addition, and perhaps most importantly, the impulse approximation does not adequately describe quasielastic electron-deuteron scattering. Although the impulse approximation is, in general, valid at the quasielastic peak, it is not capable of describing phenomena away from the quasielastic peak. In particular,

- Fermi motion in the deuteron nucleus smears the quasielastic peak;
- the nucleons may interact (e.g., rescatter) following the electrodisintegration of the deuteron (termed final-state interactions, or FSI);
- the virtual photon may couple to a virtual meson exchanged between the nucleons or to an antinucleon pair associated with the exchange of a virtual meson (termed meson exchange currents, or MEC); and
- the virtual photon may couple to an excited state of the nucleon (termed isobar configurations, or IC).

Examples of some of the lowest order MEC and IC are shown in Fig. 2-9. Panel (a) represents a contact, or "seagull", interaction. Panel (b) involves nucleon-antinucleon

pairs, and in panel (c), the virtual photon couples directly to one of the virtual mesons. Finally, panel (d) involves excited states of the nucleon (IC). These nuclear physics effects cannot be neglected, and a rigorous extraction of the neutron form factors from the difference between the inclusive quasielastic electron-deuteron cross section and the elastic electron-proton cross section must account for all of these effects.

Alternatively, if the neutron is detected in coincidence with the scattered electron, the neutron form factors can be extracted directly from the measured cross section; a coincidence experiment eliminates the difficulties associated with the subtraction of the proton contribution, but the results must still be corrected for FSI, MEC, and IC. Unfortunately, neutron coincidence experiments are difficult as a precise measurement of the cross section is possible if and only if a precise calibration of the absolute neutron detection efficiency has been achieved. Absolute calibrations of neutron detection efficiencies have, in general, been obtained via one of the following two techniques:

- The neutron detection efficiency can be calibrated *in situ* via the *associated particle technique* using either the $^1\mathrm{H}(\gamma, \pi^+ n)$ reaction or the $^2\mathrm{H}(\gamma, pn)$ reaction. In either case, the neutron detection efficiency is defined to be the ratio of the $\pi^+ n$ or pn coincidence cross section to the π^+ or p singles cross section. The result is independent of the absolute proton detection efficiency.

- The neutron detection efficiency can be calibrated via a measurement of the detection efficiency at an external facility using, for example, a tagged neutron beam produced via the $^1\mathrm{H}(n, p)$ reaction. The experimental configurations must be identical for the calibration measurement and the cross section measurements.

Due to the difficulties associated with an absolute calibration of the neutron detection efficiency, anti-coincidence quasielastic electron-deuteron cross section measurements, $^2\mathrm{H}(e, e'\overline{p})$, have been performed; here, for quasifree kinematics, the detection of a scattered electron without a coincident proton is assumed to be equivalent to the detection of a neutron. Again, a reliable extraction of the neutron form factors from

a measurement of the anti-coincidence cross section is difficult and requires a careful evaluation of all possible processes that may lead to the suppression of an otherwise coincident proton. In addition, as in the coincidence measurements, corrections for FSI, MEC, and IC must be applied to the data.

Finally, to mitigate uncertainties due to nuclear physics effects, Durand [68, 69] and Renard, Van, and Le Bellac [70, 71] suggested that the best way to extract the neutron form factors is from a measurement of the ratio of the quasielastic $^2\mathrm{H}(e, e'n)$ and $^2\mathrm{H}(e, e'p)$ cross sections. Their calculations indicated that at the quasielastic peak, the ratio of the five-fold differential coincidence cross sections,

$$R = \frac{\dfrac{\mathrm{d}^5\sigma}{\mathrm{d}E_{e'}\mathrm{d}\Omega_{e'}\mathrm{d}\Omega_n}}{\dfrac{\mathrm{d}^5\sigma}{\mathrm{d}E_{e'}\mathrm{d}\Omega_{e'}\mathrm{d}\Omega_p}} , \tag{2.59}$$

is less sensitive than the quasielastic $^2\mathrm{H}(e, e'n)$ cross section is to MEC and theoretical uncertainties in the theoretical structure of the deuteron; therefore, it was suggested that, to a good approximation,

$$R \approx \frac{G_{En}^2 + \tau G_{Mn}^2/\epsilon}{G_{Ep}^2 + \tau G_{Mp}^2/\epsilon} . \tag{2.60}$$

Although an extraction of G_{En} and G_{Mn} from measurements of the quasielastic cross section ratio promises reduced sensitivity to nuclear physics effects, precision measurements are still challenging as the neutron detection efficiency and the proton form factors must be well known.

All of the unpolarized results for G_{Mn} have been extracted from inclusive and coincidence quasielastic cross section measurements; unfortunately, an extraction of G_{En} from inclusive and coincidence quasielastic cross section measurements has proven to be nearly impossible as G_{Mn} almost completely dominates the elastic electron-neutron cross section. Almost all of the useful unpolarized information on G_{En} has been extracted from elastic electron-deuteron cross section measurements. As we discuss in what follows, although extractions of G_{En} from measurements of the unpolarized

elastic electron-deuteron cross section tend to suffer from a large model dependence, these measurements have, nevertheless, firmly established that G_{En} is non-zero for $Q^2 > 0$.

2.2.5 Neutron Electric Form Factor via Unpolarized Elastic $^2\mathrm{H}(e,e')$ Cross Section Measurements

The first relativistic calculation of the unpolarized elastic $^2\mathrm{H}(e,e')$ cross section was reported by Glaser and Jakšić [72]. Their result for the cross section, given in terms of three scalar functions of Q^2, $F_0(Q^2)$, $F_2(Q^2)$, and $G_1(Q^2)$, was

$$\begin{aligned}\frac{\mathrm{d}\sigma}{\mathrm{d}\Omega} = \left(\frac{\mathrm{d}\sigma}{\mathrm{d}\Omega}\right)_{\mathrm{Mott}} \Bigg[& F_0^2\left(1+\frac{4}{3}\tau_d+\frac{4}{3}\tau_d^2\right)+\frac{20}{9}F_0F_2\tau_d^2\left(1+\frac{2}{5}\tau_d\right) \\ & +\frac{8}{9}F_2^2\tau_d^2\left(1+\frac{2}{3}\tau_d+\frac{1}{6}\tau_d^2\right)-\frac{4}{3}F_0G_1\tau_d(1+2\tau_d)-\frac{16}{9}F_2G_1\tau_d^2\left(1+\frac{1}{2}\tau_d\right) \\ & +\frac{2}{3}G_1^2\tau_d(1+2\tau_d)+\frac{4}{3}G_1^2\tau_d(1+\tau_d)\tan^2\frac{\theta_{e'}}{2}\Bigg] , \end{aligned} \tag{2.61}$$

where $\tau_d = Q^2/4m_d^2$ and m_d denotes the deuteron mass. The scalar functions $F_0(Q^2)$, $F_2(Q^2)$, and $G_1(Q^2)$ are normalized such that they are proportional to the deuteron's charge, electric quadrupole moment, and magnetic dipole moment, respectively, at $Q^2 = 0$.

Using a method analogous to that employed by Ernst, Sachs, and Wali [17] and Sachs [18] for a physical interpretation of the nucleon form factors, Gourdin [73] showed that the following linear combinations of F_0, F_2, and G_1,

$$G_C = F_0 + \frac{2}{3}\tau_d[F_0 - G_1 + F_2(1+\tau_d)] , \tag{2.62}$$

$$G_Q = F_0 - G_1 + F_2(1+\tau_d) , \tag{2.63}$$

$$G_M = \frac{G_1}{\sqrt{1+\tau_d}} , \tag{2.64}$$

are related to the distributions of the deuteron's charge (C), quadrupole moment (Q), and magnetic moment (M) in the Breit frame. Further, Gourdin showed that

in the non-relativistic limit and the impulse approximation, G_C, G_Q, and G_M can be written in terms of the nucleon isoscalar (is) electric and magnetic form factors, $G_E^{\rm is}$ and $G_M^{\rm is}$, as

$$G_C = 2G_E^{\rm is}C_E \ , \tag{2.65}$$

$$G_Q = 2G_E^{\rm is}C_Q \ , \tag{2.66}$$

$$G_M = \frac{m_d}{m}(2G_M^{\rm is}C_S + G_E^{\rm IS}C_L) \ . \tag{2.67}$$

where m is the nucleon mass, $G_E^{\rm is}$ and $G_M^{\rm is}$ are defined in terms of the nucleon form factors as

$$G_E^{\rm is} = \frac{1}{2}(G_{En} + G_{Ep}) \ , \tag{2.68}$$

$$G_M^{\rm is} = \frac{1}{2}(G_{Mn} + G_{Mp}) \ , \tag{2.69}$$

and C_E, C_Q, C_S, and C_L describe the structure of the deuteron and can be written in terms of the deuteron S- and D-state wave functions, $u(r)$ and $w(r)$, as

$$C_E = \int_0^\infty (u^2 + w^2) j_0(Qr/2)\ {\rm d}r \ , \tag{2.70}$$

$$C_Q = \frac{3\sqrt{2}}{2\tau}\int_0^\infty \left(uw - \frac{w^2}{2\sqrt{2}}\right) j_2(Qr/2)\ {\rm d}r \ , \tag{2.71}$$

$$C_L = \frac{3}{2}\int_0^\infty w^2\left[j_0(Qr/2) + j_2(Qr/2)\right]\ {\rm d}r \ , \tag{2.72}$$

$$C_S = C_E - \frac{2}{3}\tau C_Q - C_L \ , \tag{2.73}$$

where $Q \equiv \sqrt{Q^2}$, and j_0 and j_2 are the usual spherical Bessel functions.

In terms of G_C, G_Q, and G_M, the expression for the elastic electron-deuteron cross section reduces to

$$\frac{{\rm d}\sigma}{{\rm d}\Omega} = \left(\frac{{\rm d}\sigma}{{\rm d}\Omega}\right)_{\rm Mott}\left[G_C^2 + \frac{8}{9}\tau_d^2 G_Q^2 + \frac{2}{3}\tau_d(1+\tau_d)G_M^2 + \frac{4}{3}\tau_d(1+\tau_d)^2 G_M^2 \tan^2\frac{\theta_{e'}}{2}\right] \ . \tag{2.74}$$

The form of this expression is identical to the Rosenbluth formula, Eq. (2.39); there-

fore, the deuteron structure functions, $A(Q^2)$ and $B(Q^2)$, defined to be

$$A(Q^2) = G_C^2 + \frac{8}{9}\tau_d^2 G_Q^2 + \frac{2}{3}\tau_d(1+\tau_d)G_M^2 \ , \tag{2.75}$$

$$B(Q^2) = \frac{4}{3}\tau_d(1+\tau_d)^2 G_M^2 \ , \tag{2.76}$$

can be extracted from a Rosenbluth separation of elastic electron-deuteron cross section measurements at fixed values of Q^2. While the deuteron magnetic form factor, G_M, can be extracted directly from $B(Q^2)$, G_C and G_Q cannot be separated; however, as G_C and G_Q are both proportional to $G_E^{\rm is}$, the sum of the neutron and proton electric form factors, $(G_{En} + G_{Ep})$ can be extracted from $A(Q^2)$.

The difficulties associated with an extraction of G_{En} from $A(Q^2)$ are as follows. First, $A(Q^2)$ and $B(Q^2)$ must be separated; this requires a Rosenbluth separation or prior measurements of $B(Q^2)$. Second, the separated value of $A(Q^2)$ must be corrected for nuclear physics effects, such as MEC, and for relativistic effects due to the distortion of the deuteron wave function. Third, the deuteron structure must be "unfolded"; that is, the structure integrals, Eqs. (2.70) through (2.73), must be evaluated for a particular model of the deuteron wave function. Finally, the contribution of G_{Ep} to $G_E^{\rm is}$ must be subtracted.

2.2.6 Unpolarized Results for G_{En} and G_{Mn}

In Tables 2.2 and 2.3, we have, once again, attempted to compile a nearly exhaustive chronological summary of neutron form factor measurements extracted from unpolarized quasielastic and elastic electron-deuteron cross section measurements, respectively, dating to the early 1960s. For each measurement, we list the reference, the facility at which the experiment was conducted, the measurement type, the range of Q^2 accessed, and the quantities extracted from the measured cross sections.

Results for the neutron form factors extracted from measurements of the unpolarized quasielastic cross section are plotted in Fig. 2-10; here, we have plotted only the most recent results reported since 1973. The top panel of Fig. 2-10 is a plot of the results for G_{En}^2 extracted from unpolarized quasielastic cross section measurements;

Reference(s)	Facility	Type	Q^2 [(GeV/c)^2]	Quantities	Note(s)
Littauer (1961) [74]	Cornell	inclusive	0.08 – 1.44	G_{En}, G_{Mn}	1
Stein (1962) [75]	Cornell	ratio[a]	0.19	G_{En}, G_{Mn}	1, 2
de Vries (1964) [76–79]	SLAC	inclusive	0.16 – 0.62	G_{En}, G_{Mn}	3
Akerlof (1964) [81]	Cornell	inclusive	0.43 – 1.36	G_{En}, G_{Mn}	3
Hughes (1965) [82]	SLAC	ratio[b]	0.04 – 1.17	G_{En}, G_{Mn}	3
Dunning (1966) [83,84]	Cambridge	anti-coincidence	0.39 – 1.75	G_{En}, G_{Mn}	3
Stein (1966) [85]	Cornell	coincidence	0.21 – 0.57	G_{En}, G_{Mn}	1, 2
Hughes (1966) [86]	SLAC	ratio[b]	0.06 – 0.29	G_{En}, G_{Mn}	1
Albrecht (1968) [87]	DESY	ratio[b]	0.70 – 3.89	G_{Mn}	1, 4
Budnitz (1968) [88,89]	Cambridge	anti-coincidence	0.29 – 1.75	G_{En}, G_{Mn}	1
Bartel (1973) [48,90,91]	DESY	coincidence	0.39 – 1.53	G_{En}, G_{Mn}	1, 2
Hanson (1973) [92]	Cambridge	ratio[c]	0.27 – 1.75	G_{En}, G_{Mn}	5
Rock (1982) [93]	SLAC	inclusive	2.5 – 10.0	G_{Mn}	1, 4
Esaulov (1987) [94]	Khar'kov	inclusive	0.48 – 0.83	G_{Mn}	1, 6
Arnold (1988) [95]	SLAC	inclusive	1.02 – 1.76	G_{Mn}	1, 6
Lung (1993) [96]	SLAC	inclusive	1.75 – 4.00	G_{En}, G_{Mn}	1
Markowitz (1993) [97]	MIT-Bates	coincidence	0.11 – 0.26	G_{Mn}	7, 8
Anklin (1994) [100]	NIKHEF	ratio[a]	0.09 – 0.13	G_{Mn}	8, 9, 10
Bruins (1995) [103]	ELSA	ratio[a]	0.13 – 0.61	G_{Mn}	2, 8, 10
Anklin (1998) [104]	MAMI	ratio[a]	0.24 – 0.78	G_{Mn}	8, 9
Kubon (2002) [105]	MAMI	ratio[a]	0.07 – 0.89	G_{Mn}	8, 9

[a] Ratio of quasielastic ^{2}H$(e,e'n)$ and ^{2}H$(e,e'p)$ cross section measurements.
[b] Ratio of inclusive quasielastic ^{2}H(e,e') and elastic ^{1}H(e,e') cross section measurements.
[c] Ratio of quasielastic ^{2}H$(e,e'\overline{p})$ and ^{2}H$(e,e'p)$ cross section measurements.
[1] Impulse approximation assumed.
[2] Neutron detection efficiency calibrated *in situ* via the $\gamma p \to \pi^+ n$ reaction.
[3] FSI corrections using the formalism of Nuttall and Whippman [80].
[4] Assumed $G_{En} = 0$.
[5] FSI corrections using the formalism of Renard, Van, and Le Bellac [70,71].
[6] Assumed $G_{En} = -\tau\mu_n G_D$.
[7] Neutron detection efficiency calibrated *in situ* via the $\gamma d \to pn$ reaction.
[8] FSI, MEC, and IC corrections using the unpolarized formalism of Fabian and Arenhövel [98] and Arenhövel [99].
[9] Neutron detection efficiency calibrated with tagged neutron beam at a different facility (PSI).
[10] FSI, MEC, and IC corrections using the formalism of Hummel and Tjon [101,102].

Table 2.2: Chronological summary of neutron form factor measurements extracted from unpolarized quasielastic electron-deuteron cross section measurements since the early 1960s.

Reference(s)	Facility	Type	Q^2 [(GeV/c)^2]	Quantities	Note(s)
Drickey (1962) [26]	SLAC	I	0.01 – 0.09	G_{En}	1, 2
Grossetête (1963) [106]	Orsay	I	0.04	G_{En}	1, 2
Grossetête (1966) [108–110]	Orsay	I	0.02 – 0.08	G_{En}	1, 2
Benaksas (1966) [111, 112]	Orsay	II	0.12 – 0.20	G_{En}, G_{Mn}	1, 2
Bumiller (1970) [113]	Naval, SLAC	I	0.004 – 0.031	G_{En}	3, 4
Galster (1971) [117]	DESY	I	0.24 – 0.50	G_{En}	3, 4
Berard (1973) [118]	Naval	I	0.002 – 0.011	G_{En}	3, 4
Simon (1981) [119]	MAMI	I	0.002 – 0.16	G_{En}	4, 5, 6
Platchkov (1990) [123]	Saclay	I	0.02 – 0.70	G_{En}	7, 8, 9

I: Elastic ^{2}H(e, e') cross section measurement.
II: Elastic ^{2}H(e, d) cross section measurement.
[1] Impulse approximation.
[2] Hamada-Johnston [107] wavefunction for the deuteron.
[3] Feshbach-Lomon [114] wavefunction for the deuteron.
[4] Relativistic corrections by Gross [115] and Casper and Gross [116].
[5] Reid soft core [120] wavefunction for the deuteron.
[6] MEC and IC corrections using the formalism of Fabian and Arenhövel [121, 122].
[7] Paris potential [124] for the deuteron wavefunction.
[8] Relativistic corrections by Arnold, Carlson, and Gross [125].
[9] MEC corrections by Mosconi and Ricci [126].

Table 2.3: Chronological summary of neutron form factor measurements extracted from unpolarized elastic electron-deuteron cross section measurements since the early 1960s.

it is obvious from inspection of this plot that unpolarized quasielastic cross section measurements have provided very little information about the behavior of G_{En}. Indeed, some of the results for G_{En}^2 reported by Bartel *et al.* [48, 90, 91] and Lung *et al.* [96] are negative; a result of $G_{En}^2 < 0$ is clearly an undesirable and unphysical result.

The results for G_{Mn} extracted from unpolarized quasielastic cross section measurements are shown in the bottom panel of Fig. 2-10. Data for G_{Mn} extend to Q^2 values of approximately 10 (GeV/c)^2 and are, to a rough approximation, consistent with the dipole parameterization for $Q^2 \lesssim 2-3$ (GeV/c)^2. Deviations from the dipole parameterization are seen at higher Q^2; however, the high Q^2 measurements are fairly imprecise.

There are discrepancies between recent low Q^2 [$Q^2 \lesssim 1.0$ (GeV/c)^2] experiments employing *in situ* (using the associated particle technique) and external facility (using tagged neutron beams) neutron detection efficiency calibration techniques. To

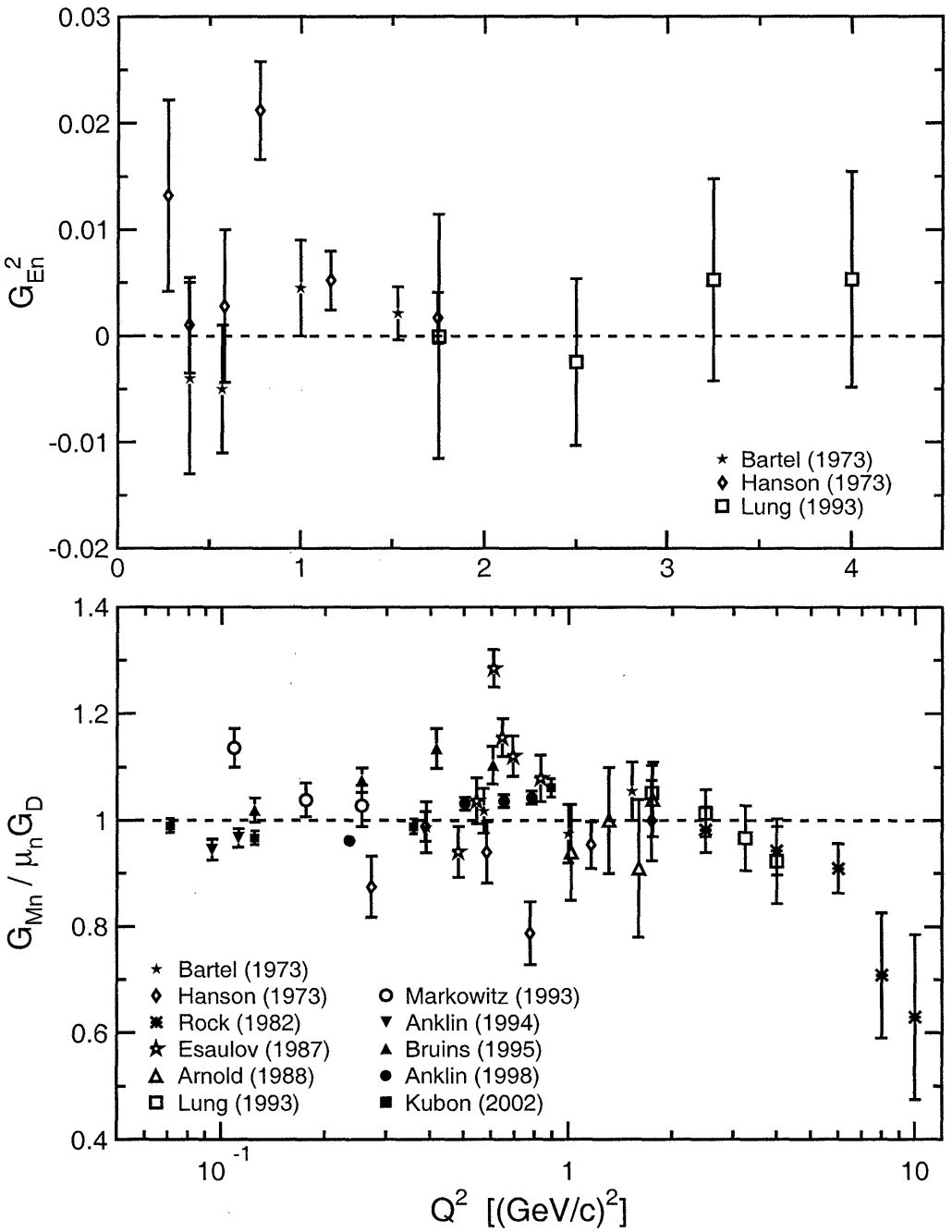

Figure 2-10: Results for G_{En}^2 (top panel) and G_{Mn} (bottom panel) extracted from unpolarized quasielastic electron-deuteron cross section measurements since 1973.

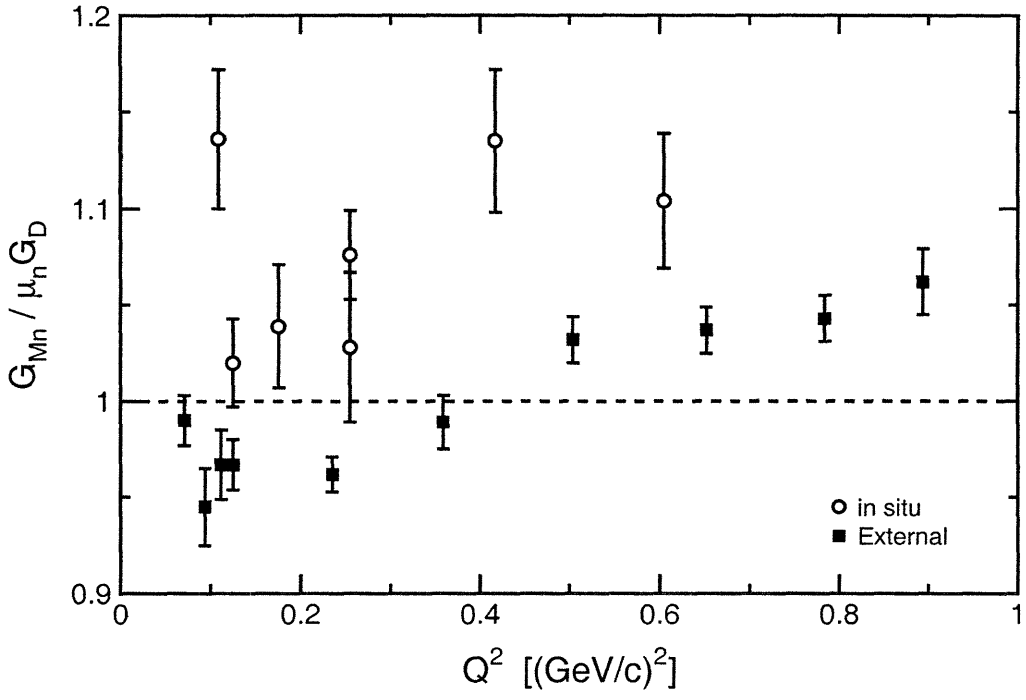

Figure 2-11: Comparison of recent unpolarized results for G_{Mn} (see text) extracted from quasielastic electron-deuteron cross section measurements using *in situ* and external neutron detection efficiency calibration techniques.

illustrate these discrepancies in more detail, we compare the most recent results for G_{Mn} obtained with *in situ* (Markowitz *et al.* [97] and Bruins *et al.* [103]) and external (Anklin *et al.* [100], Anklin *et al.* [104], and Kubon *et al.* [105]) neutron detection efficiency calibration techniques in Fig. 2-11.

It is clear that these discrepancies are significant; the *in situ* calibration technique measurements are consistently higher than the external facility calibration technique measurements. Jourdan, Sick, and Zhao [127] argued that efficiency calibrations obtained *in situ* using the $^1\mathrm{H}(\gamma, \pi^+)n$ reaction underestimate the neutron detection efficiency, thereby leading to overestimated values of the electron-neutron cross section and, consequently, the value of G_{Mn}; however, Bruins *et al.* [128] were neither able to confirm or refute the claim of Jourdan, Sick, and Zhao. Unfortunately, the discrepancy between these two types of measurements has still not, as of this writing,

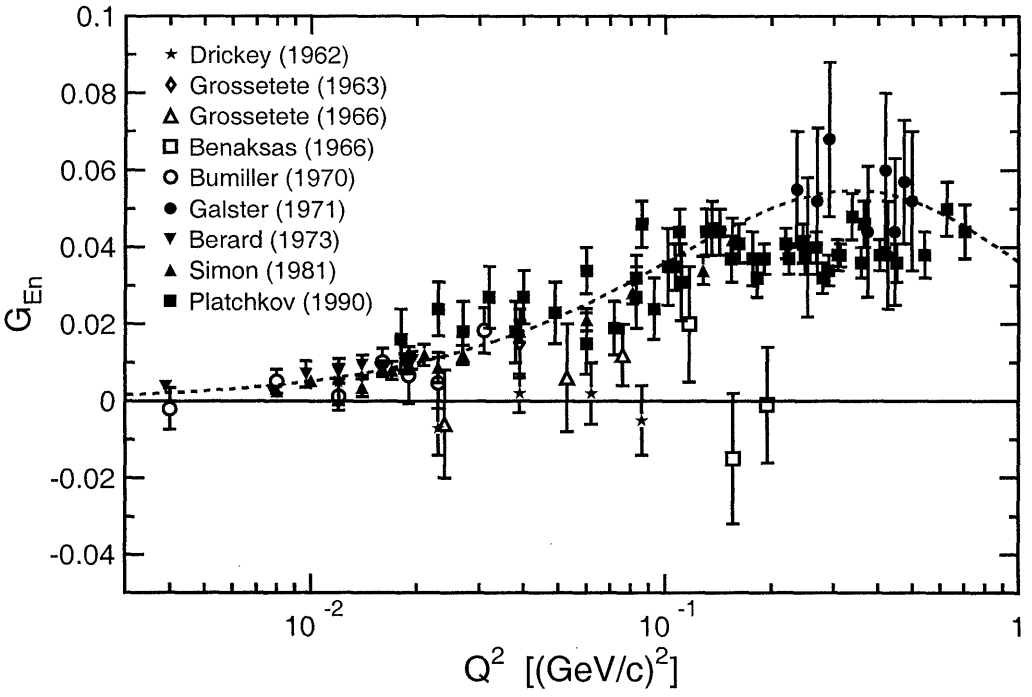

Figure 2-12: Results for G_{En} extracted from unpolarized elastic electron-deuteron cross section measurements. The Galster parameterization is plotted as the dashed line.

been resolved satisfactorily.[1]

The results for G_{En} that have been extracted from measurements of the unpolarized elastic electron-deuteron cross section are plotted in Fig. 2-12; here, the values for G_{En} that we have plotted for each experiment are the values extracted from analyses that used the deuteron wavefunction specified in Table 2.3. Unlike the results for G_{En} extracted from unpolarized quasielastic electron-deuteron cross section measurements, useful information can be extracted from these results. In particular, these results do suggest that $G_{En} > 0$ for $Q^2 > 0$.

[1] Jourdan, Sick, and Zhao [127] pointed out that *in situ* calibrations using the $^1\mathrm{H}(\gamma, \pi^+)n$ reaction do not employ pure photon beams; instead, the photons for the $^1\mathrm{H}(\gamma, \pi^+)n$ *photoproduction* reaction are produced by the incident electrons directly in the ^{1}H target; however, the detected π^+s may also be produced via the $^1\mathrm{H}(e, \pi^+)ne'$ *electroproduction* reaction. The $^1\mathrm{H}(\gamma, \pi^+)n$ reaction has a two-body final state; therefore, a measurement of the π^+ momentum and scattering angles completely determines the kinematics of the reaction. In contrast, the $^1\mathrm{H}(e, \pi^+)ne'$ reaction has a three-body final state, and a measurement of the π^+ momentum and scattering angles does not completely determine the kinematics of the reaction. Jourdan, Sick, and Zhao argued that failure to account for the competing electroproduction process leads to a non-negligible contamination of the measured cross section which overestimates the measured cross section and, consequently, the value of G_{Mn}.

One particularly noteworthy extraction of G_{En} from unpolarized measurements of $A(Q^2)$, reported by Galster *et al.* [117] in 1971, was based on the results of elastic electron-deuteron cross section measurements at DESY. Cross sections were measured at ten different values of Q^2 in the range $0.19 < Q^2 < 0.55$ $(\mathrm{GeV}/c)^2$ with two different electron beam energies of 2.5 and 2.7 GeV and scattering angles ranging from 11.2° to 15.7°. For this range of scattering angles, $B(Q^2)$ contributes less than 0.1% to the cross section; therefore, the contribution of $B(Q^2)$ to the cross section was ignored, and a Rosenbluth separation of $A(Q^2)$ and $B(Q^2)$ was not necessary.

Galster *et al.* extracted G_{En} from their experimental values for $A(Q^2)$ via the following procedure. First, relativistic corrections, calculated by Gross [115] and Casper and Gross [116], which accounted for the deformation of the deuteron's wave function in the laboratory frame were applied to the charge and quadrupole contributions to $A(Q^2)$; no corrections were applied to the magnetic contribution (the magnetic contribution to $A(Q^2)$ contributed less than 5% to the cross section for the kinematics of this experiment). Second, the deuteron structure integrals C_E and C_Q were evaluated using the Feshbach-Lomon [114], Hamada-Johnston [107], Hulthén-Sugawara [129], and McGee [130] deuteron wave functions. Third, the experimental values of $A(Q^2)$ were compared with theoretical values of $A(Q^2)$ computed using the above deuteron wave functions, the dipole parameterization for G_{Ep}, and the following functional forms for G_{En}:

$$G_{En} = 0 \ , \tag{2.77}$$

$$G_{En} = -\tau \mu_n G_D \ , \tag{2.78}$$

$$G_{En} = -\frac{\tau \mu_n}{1 + 4\tau} G_D \ , \tag{2.79}$$

$$G_{En} = -\frac{\tau \mu_n}{1 + b\tau} G_D \ . \tag{2.80}$$

Eq. (2.78) assumes the neutron Dirac form factor, F_{1n}, is equal to zero, Eq. (2.79) was an adhoc ansatz[2] for the functional form of G_{En} proposed by Budnitz *et al.* [88], and

[2]Budnitz *et al.* [88] stated that this functional form was nothing but "... a reasonable guess about the behavior of G_{En}..." which connected the behavior of G_{En} at $Q^2 = 0$ with its expected behavior at high Q^2.

Eq. (2.80) was a variant of Budnitz *et al.*'s ansatz in which b was a free parameter.

Galster *et al.* concluded that the Feshbach-Lomon wave function and Eq. (2.80) with $b = 5.6$ provided the best agreement between the experimental and theoretical values of $A(Q^2)$. Although this parameterization for G_{En}, plotted in Fig. 2-12 as the dashed line, has come to be known as the "Galster parameterization", it is important to remember that there is no underlying physical basis for this functional form for G_{En}; therefore, any agreement between the Galster parameterization and modern data for $Q^2 \gtrsim 0.7$ (GeV/c)^2 must be judged as fortuitous.

Another noteworthy extraction of G_{En} from unpolarized measurements of $A(Q^2)$, reported by Platchkov *et al.* in 1990, was based on the results of unpolarized elastic electron-deuteron cross section measurements conducted at Saclay. Cross sections were measured at 43 different values of Q^2 with electron beam energies of 200, 300, 500, and 650 MeV and scattering angles ranging from 35° to 100°; the range of Q^2 probed in this experiment was $0.04 < Q^2 < 0.70$ (GeV/c)^2. For this range of scattering angles, the contribution of $B(Q^2)$ to the cross section was non-negligible; therefore, this contribution to the cross section was subtracted using a fit to data on $B(Q^2)$ available at the time. Platchkov *et al.*'s analysis procedure for the extraction of G_{En} from their experimental values of $A(Q^2)$ was similar to that used by Galster *et al.* First, the contribution of $G_M(Q^2)$ to $A(Q^2)$ was subtracted from the experimental values of $A(Q^2)$ using a fit to the available $B(Q^2)$ measurements [119, 131–133]. Second, relativistic corrections, calculated by Arnold, Carlson, and Gross [125], and corrections for meson exchange currents, calculated by Mosconi and Ricci [126], were applied to the experimental $A(Q^2)$ values.

The deuteron structure integrals were evaluated using deuteron wave functions derived from the Argonne V14 [134], Nijmegen [135], Paris [124], and Reid soft-core (RSC) [120] potentials. After evaluation of C_E and C_Q, the value for G_{Ep}, as given by the parameterization of Simon *et al.* [55], was subtracted from G_E^{is} in order to extract G_{En}. The values of G_{En} extracted from these potentials were fitted to a modified

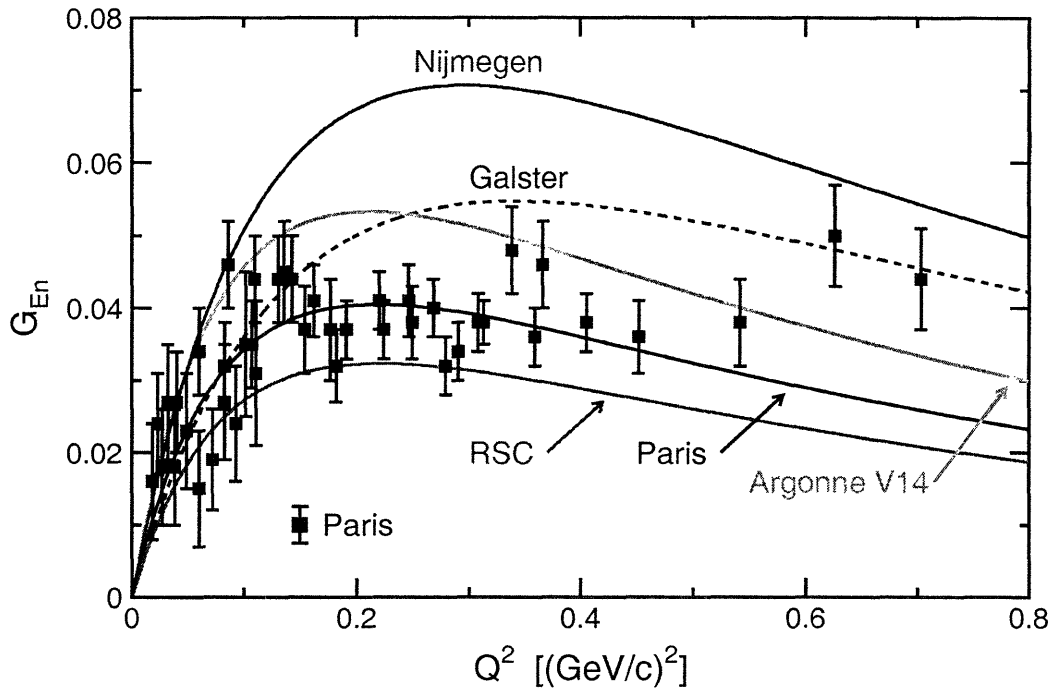

Figure 2-13: (color) Comparison of Platchkov *et al.*'s results for G_{En} extracted using the Paris potential (data points and the solid black curve) with the fits to the results for G_{En} extracted using the Argonne V14 potential (solid green curve), Nijmegen potential (solid blue curve), and the Reid soft core potential (solid red curve). The Galster parameterization is shown as the dashed curve.

form of the Galster parameterization,

$$G_{En} = -\frac{a\mu_n\tau}{1+b\tau}G_D \ , \tag{2.81}$$

where a and b are free parameters; inclusion of the parameter a enabled the slope of G_{En} to be fitted at $Q^2 = 0$. The results for G_{En} obtained with the Paris potential are plotted in Fig. 2-13 together with the two-parameter fits to the values for G_{En} obtained with the Argonne V14, Nijmegen, and RSC potentials. The two-parameter fit to the results obtained with the Paris potential, $a = 1.25 \pm 0.13$ and $b = 18.3 \pm 3.4$, is usually quoted; however, the uncertainty arising from the choice of the NN-potential was quoted by Platchkov *et al.* to be on the order of $\pm 40\%$.

2.2.7 Neutron Charge Radius

As first shown by Foldy [136], in low-energy elastic neutron-electron scattering, the observed neutron-electron scattering length, b_{ne}, is related to the neutron mean square charge radius, $\langle r_{En}^2 \rangle$, according to

$$b_{ne} = \frac{1}{3} \frac{m_n e^2}{\hbar^2} \langle r_{En}^2 \rangle \ , \tag{2.82}$$

where $\langle r_{En}^2 \rangle = -6 \, (\mathrm{d}G_{En}/\mathrm{d}Q^2)$ at $Q^2 = 0$ and m_n denotes the neutron mass. Further, Foldy showed that b_{ne} can be written as

$$b_{ne} = \frac{1}{3} \frac{m_n e^2}{\hbar^2} \left[\int \mathrm{d}^3\mathbf{r} \ r^2 \rho_{\mathrm{ch}}(\mathbf{r}) + \frac{3\kappa_n \hbar^2}{2m_n^2 c^2} \right] \ , \tag{2.83}$$

where $\rho_{\mathrm{ch}}(\mathbf{r})$ denotes the neutron's *intrinsic* charge density and $\kappa_n = -1.913$ is the neutron's anomalous magnetic moment in units of the nuclear magneton; therefore, the mean square charge radius can be written as

$$\langle r_{En}^2 \rangle = \langle r_{\mathrm{ch}}^2 \rangle + \frac{3\kappa_n \hbar^2}{2m_n^2 c^2} \ , \tag{2.84}$$

where we use $\langle r_{\mathrm{ch}}^2 \rangle$ to denote the mean square radius of the *intrinsic* charge density. The second term in the expression for $\langle r_{En}^2 \rangle$ is known as the *Foldy term* and is a relativistic correction that arises due to the phenomenon of *Zitterbewegung*.[3] It should be noted that the value of the Foldy term is -0.126 fm^2.

In general, three different experimental techniques have been employed for measurements of $\langle r_{En}^2 \rangle$. First, and most recently, given a measurement of the transmission of neutrons through a sample of heavy atoms (such as ^{208}Pb, etc.) in an energy region where the scattering is fully or partly coherent from the electron shell, b_{ne} has been extracted from the measured cross section. Second, b_{ne} has been extracted from

[3]The origin of the Foldy term is as follows. A free particle does not move with constant speed in a straight line; instead, it (and its magnetic moment) undergoes a "dancing motion" (i.e., *Zitterbewegung*) at the speed of light about a point which does move with constant speed in a straight line. The movement of the magnetic moment induces a radial separation of the charge which contributes to the neutron-electron scattering.

measurements of neutron diffraction from single crystals of ^{186}W. Third, b_{ne} has been extracted from a measurement of the angular dependence of neutron scattering from noble gases. A complete discussion of each of these techniques is beyond the scope of this thesis; therefore, we refer the reader to [137–144] for details on some of the more recent experiments employing the above-mentioned techniques.

Measurements of b_{ne} have proven to be difficult and significant discrepancies between recent measurements have complicated the extraction of a precise and definitive value for $\langle r_{En}^2 \rangle$. In general, nearly all results have clustered around two values. First, a compilation by Sears [145] of results extracted from measurements of the angular distributions of neutron scattering from noble gases at Argonne [137, 138] and transmission measurements on lead and bismuth at Garching [146, 147] gives $b_{ne} = -(1.31 \pm 0.03) \times 10^{-3}$ fm. Second, a compilation by Alexandrov [148] of neutron diffraction measurements from tungsten at Dubna [149, 150] yielded $b_{ne} = -(1.59 \pm 0.04) \times 10^{-3}$ fm. The discrepancy between these values is approximately five standard deviations. Two analyses of this discrepancy were recently reported by Leeb and Teichtmeister [140] and Alexandrov [141]; unfortunately, these analyses did not agree, and the results remain controversial. Since the publication of these analyses, two additional transmission measurements which agree with Sears' compilation were reported by Koester *et al.* [143] (^{206}Pb, ^{207}Pb, ^{208}Pb, and ^{209}Bi at Garching) and Kopecky *et al.* [142, 144] (^{208}Pb at Oak Ridge).

The value reported by Kopecky *et al.* [142, 144] is $b_{ne} = -(1.33 \pm 0.03) \times 10^{-3}$ fm; this corresponds to $\langle r_{En}^2 \rangle = -0.115 \pm 0.003$ fm^2. Indeed, this value is very close to that of the Foldy term (-0.126 fm^2). The apparent agreement between the Foldy term and Kopecky *et al.*'s result would seem to suggest that a measurement of the slope of G_{En} at $Q^2 = 0$ provides information about the Foldy term instead of the mean square radius of the neutron's intrinsic charge density; this observation has recently generated much theoretical speculation. Within a relativistic expansion of a constitutent quark model, Isgur [151] showed that the Dirac form factor F_{1n} receives a relativistic correction which cancels the Foldy term and preserves the interpretation of G_{En} in terms of the neutron's intrinsic charge density. Subsequent confirmations

of Isgur's finding were reported by Cardarelli and Simula [152, 153] and Leinweber, Thomas, and Young [154].

2.3 Nucleon Form Factor Measurements with Polarized Electrons

In this section, we discuss measurements of the nucleon form factors using polarized electron beams and polarized nuclear targets or recoil nucleon polarimeters. We discuss the formalism motivating these types of measurements, and we survey the current status of polarized results for the nucleon form factors and compare these with the previously discussed unpolarized results.

2.3.1 Historical Overview of Formalism

As previously discussed in Section 2.1, the cross section for unpolarized electron scattering from unpolarized nucleons was first calculated by Rosenbluth [14] in 1950. Soon thereafter, in 1957, Bincer [155] generalized Rosenbluth's calculation for the case of longitudinally polarized electrons, and in 1959 and 1966, Scofield [156, 157] extended Bincer's calculations and calculated the cross section for the scattering of arbitrarily polarized electrons from arbitrarily polarized charged spin-$\frac{1}{2}$ particles with anomalous magnetic moments and an extended electromagnetic structure. Scofield's work may be regarded as the original proposal for measurements of the nucleon form factors using polarization degrees of freedom; indeed, Scofield suggested [156] that the "... [s]cattering of polarized electrons on polarized nucleons at high energies could be a useful tool to investigate the charge and magnetic moment structure of nucleons ...".[4]

A more complete treatment of the scattering of longitudinally polarized electrons from polarized nucleons was given by Dombey [158] in 1969. Dombey demonstrated that, in the one-photon exchange approximation, the cross section for polarized-electron, polarized-nucleon scattering is asymmetric with respect to helicity reversal

[4] At the time, Scofield suggested that experiments be conducted using longitudinally polarized electrons arising from the beta decay of neutrons.

of the electron. Dombey showed that if the nucleons are polarized perpendicular (parallel) to the three-momentum transfer $\mathbf{q}$ in the scattering plane, the helicity asymmetry of the cross section is proportional to $G_E G_M$ (G_M^2). As pointed out by Dombey, a measurement of the asymmetry with the nucleons polarized perpendicular to $\mathbf{q}$ is of particular interest for the following reasons. First, such a measurement permits a unambiguous determination of the sign of G_E (unlike the Rosenbluth method which only determines G_E^2). Second, the contribution of G_E is enhanced by G_M (unlike cross section measurements which are dominated by G_M). In addition to considerations of polarized-electron, polarized-nucleon scattering, Dombey also stated that measurements of the final-state nucleon polarization in polarized-electron, unpolarized-nucleon scattering are equivalent to measurements of the helicity asymmetry in polarized-electron, polarized-nucleon scattering; however, details were not provided as Dombey stated that "...target polarization should become the more effective technique".

The first complete treatment of the final-state polarization of the recoil nucleon in polarized-electron, unpolarized-nucleon scattering was reported by Akhiezer and Rekalo [159] in 1974. Akhiezer and Rekalo demonstrated that, in the one-photon exchange approximation, the polarization of the recoil nucleon is confined to the scattering plane, and the component that is perpendicular (parallel) to the recoil nucleon's three-momentum (i.e., to $\mathbf{q}$) is proportional to $G_E G_M$ (G_M^2). In an extension of Akhiezer and Rekalo's initial work, in a seminal paper in 1981, Arnold, Carlson, and Gross [160] proposed that a measurement of the recoil neutron's polarization in quasielastic polarized-electron, unpolarized-deuteron scattering via a secondary, analyzing, reaction appeared to be a straightforward, albeit challenging, method for a precision measurement of the experimentally elusive neutron electric form factor.

We now begin a discussion of the underlying formalism for these "polarized target" and "recoil polarimetry" experiments; however, before beginning a detailed discussion of these types of experiments, we briefly review some of the formalism for polarized electrons. Our discussion of polarized electrons follows the pedagogical overview of this subject given by Donnelly [161].

2.3.2 Polarized Electrons

We define the contribution of the virtual photon-electron vertex to the spin averaged (i.e., unpolarized) matrix element to be the unpolarized leptonic tensor, $(\eta^{\mu\nu})^{\text{unpol}}$, which, as discussed earlier in Section 2.1, is simply equal to

$$\begin{aligned}(\eta^{\mu\nu})^{\text{unpol}} &= \text{tr}\ \left[(\not{k}' + m_e)\gamma^\mu(\not{k} + m_e)\gamma^\nu\right] \\ &= 4\left[k'^\mu k^\nu + k'^\nu k^\mu - g^{\mu\nu}\left(k \cdot k' - m_e^2\right)\right] \ . \end{aligned} \tag{2.85}$$

Now, if we consider polarized electrons, the leptonic tensor must be modified as we no longer average over the initial-state spins. Instead, we assume that the incident electrons are prepared in spin states which can be characterized by a four vector $S^\mu = (s_0, \mathbf{s})$ which must satisfy (see, e.g., [162])

$$S^2 = -1 \ , \qquad S \cdot k = 0 \ . \tag{2.86}$$

We then insert the spin projection operator,

$$\hat{P} = \frac{1}{2}\left(1 + \gamma^5 \not{S}\right) \ , \tag{2.87}$$

where, as usual, $\gamma^5 = i\gamma^0\gamma^1\gamma^2\gamma^3$, into the unpolarized leptonic tensor, with the result that

$$\begin{aligned}\eta^{\mu\nu} &= \frac{1}{2}\text{tr}\left[(\not{k}' + m_e)\gamma^\mu(1 + \gamma^5\not{S})(\not{k} + m_e)\gamma^\nu\right] \\ &= \frac{1}{2}\left[(\eta^{\mu\nu})^{\text{unpol}} + (\eta^{\mu\nu})^{\text{pol}}\right] \ , \end{aligned} \tag{2.88}$$

where

$$\begin{aligned}(\eta^{\mu\nu})^{\text{pol}} &= m_e k'_\alpha S_\beta\ \text{tr}\left[\gamma^\alpha\gamma^\mu\gamma^5\gamma^\beta\gamma^\nu\right] + m_e k_\alpha S_\beta\ \text{tr}\left[\gamma^\mu\gamma^5\gamma^\beta\gamma^\alpha\gamma^\nu\right] \\ &= 4i\epsilon^{\mu\nu\alpha\beta} q_\alpha m_e S_\beta \ . \end{aligned} \tag{2.89}$$

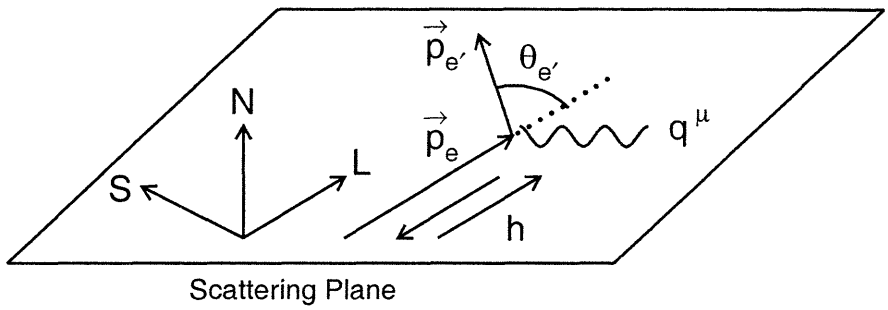

Figure 2-14: Definition of the unit vectors $\hat{\mathbf{L}}$, $\hat{\mathbf{S}}$, $\hat{\mathbf{N}}$ used to specify the direction of the initial-state electron's spin.

We specify the direction of the initial-state electron's spin according to

$$\mathbf{s} = hs\left[\cos\zeta\hat{\mathbf{L}} + \sin\zeta\cos\eta\hat{\mathbf{S}} + \sin\zeta\sin\eta\hat{\mathbf{N}}\right] , \tag{2.90}$$

where the unit vectors $\hat{\mathbf{L}}$, $\hat{\mathbf{S}}$, and $\hat{\mathbf{N}}$, shown in Fig. 2-14, denote, respectively, the "longitudinal", "sideways", and "normal" directions; here, ζ and η are the usual polar and azimuthal angles defined relative to $\hat{\mathbf{L}}$. The parameter $h(=\pm 1)$ flips the orientation of the spin, and $s = |\mathbf{s}|$ denotes the magnitude of the three-spin. The requirement that S^μ must satisfy $S^2 = -1$ and $S \cdot k = 0$ implies that

$$s_0 = hs\beta_e\cos\zeta , \tag{2.91}$$

$$s = \frac{1}{\sqrt{1-\beta_e^2\cos^2\zeta}} = \frac{\gamma_e}{\sqrt{\cos^2\zeta + \gamma_e^2\sin^2\zeta}} , \tag{2.92}$$

where $\beta_e = |\mathbf{p}_e|/E_e$ and γ_e is the usual Lorentz factor; therefore, the contribution of the four spin to the polarized leptonic tensor, $m_e S_\mu$, can be written as

$$m_e S = hE_e\left(\frac{\beta_e}{\sqrt{1+\gamma_e^2\tan^2\zeta}}, \frac{1}{\sqrt{1+\gamma_e^2\tan^2\zeta}}\hat{\mathbf{L}} + \frac{\cos\eta}{\sqrt{\cot^2\zeta+\gamma_e^2}}\hat{\mathbf{S}} + \frac{\sin\eta}{\sqrt{\cot^2\zeta+\gamma_e^2}}\hat{\mathbf{N}}\right) , \tag{2.93}$$

and it is easy to see that the effects of polarized electrons are maximized if the denominators in the above expression are minimized. Either $\zeta = 0$ (i.e., longitudinal polarization), resulting in

$$m_e S = hE_e\left(\beta_e,\ \hat{\mathbf{L}}\right) , \tag{2.94}$$

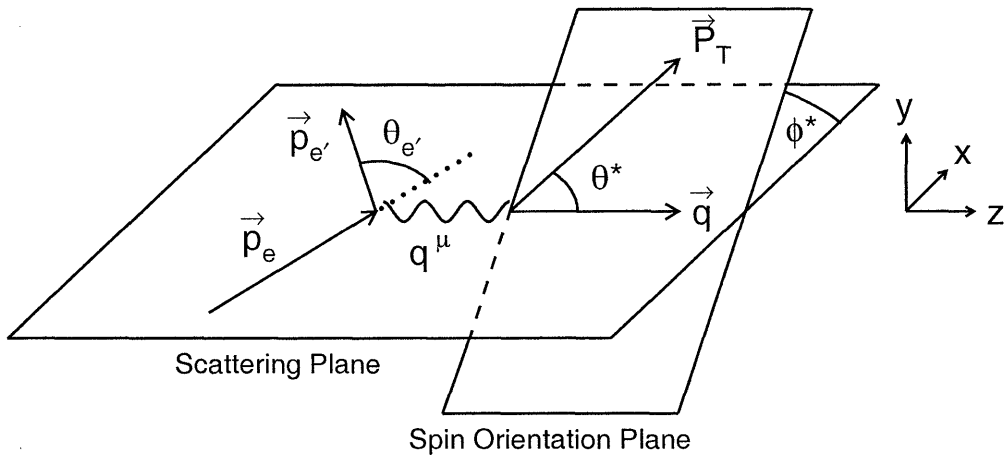

Figure 2-15: One-photon exchange approximation for elastic polarized-electron, polarized-nucleon scattering.

or $\zeta = \pi/2$ (i.e., transverse polarization), resulting in

$$m_e S = hE_e \left(0,\ \frac{\cos\eta}{\gamma_e}\hat{\mathbf{S}} + \frac{\sin\eta}{\gamma_e}\hat{\mathbf{N}}\right) , \tag{2.95}$$

minimizes the denominators; however, it is clear that the effects of transverse polarization are suppressed relative to those of longitudinal polarization by a factor of $1/\gamma_e$. As such, in all future discussions concerning polarized electrons, we will only consider longitudinally polarized electrons, and we will use P_L to denote the degree of longitudinal polarization.

2.3.3 Nucleon Form Factors via Elastic $\vec{N}(\vec{e}, e')$ Scattering

Now that we have established the relevance of longitudinally polarized electrons, we turn to the formalism for elastic polarized-electron, polarized-nucleon scattering. Authorative overviews of this subject have been given by Donnelly and Raskin [163], Raskin and Donnelly [164], and Kelly [165]; here, we follow the somewhat more pedagogical approach to this problem given by Arenhövel, Leidemann, and Tomusiak [166].

A schematic diagram of elastic polarized-electron, polarized-nucleon scattering in the one-photon exchange approximation is shown in Fig. 2-15. As before, we denote the initial (final) four-momentum of the electron and the nucleon as k^μ (k'^μ)

and p^μ (p'^μ), respectively; explicit expressions for these four-momenta were given previously in Eqs. (2.13) and (2.14). In addition to the electron kinematics, the orientation of the nucleon's polarization vector, denoted $\mathbf{P}_T$, must be specified. As is customary, we use the angles θ^* and ϕ^* to denote, respectively, the polar angle between $\mathbf{P}_T$ and $\mathbf{q}$ and the azimuthal angle between the spin orientation plane (i.e., the plane spanned by $\mathbf{P}_T$ and $\mathbf{q}$) and the scattering plane. If we define unit vectors $\hat{\mathbf{x}}$, $\hat{\mathbf{y}}$, and $\hat{\mathbf{z}}$ according to

$$\hat{\mathbf{z}} \parallel \mathbf{q} \ , \qquad \hat{\mathbf{y}} \parallel \mathbf{p}_e \times \mathbf{p}_{e'} \ , \qquad \hat{\mathbf{x}} = \hat{\mathbf{y}} \times \hat{\mathbf{z}} \ , \tag{2.96}$$

$\mathbf{P}_T$ can be written in terms of θ^* and ϕ^* as

$$\mathbf{P}_T = P_T(\sin\theta^*\cos\phi^*\hat{\mathbf{x}} + \sin\theta^*\sin\phi^*\hat{\mathbf{y}} + \cos\theta^*\hat{\mathbf{z}}) \ , \tag{2.97}$$

where we define $P_T = |\mathbf{P}_T|$.

In the one-photon exchange approximation, the differential cross section for the elastic scattering of longitudinally polarized electrons from a *stationary* nucleon is

$$\frac{\mathrm{d}\sigma}{\mathrm{d}\Omega_{e'}} = C\left[\rho_L f_L + \rho_T f_T + \rho_{LT} f_{LT} + \rho_{TT} f_{TT} + hP_L\left(\rho'_{LT} f'_{LT} + \rho'_T f'_T\right)\right] \ . \tag{2.98}$$

Here, the f_i are structure functions which, in the coordinate system just defined, are related to the components of the nucleon current operator, $\hat{J}_\mu$, according to

$$f_L = \mathrm{tr}(\hat{J}_0 \rho_N \hat{J}_0^\dagger) \ , \tag{2.99}$$

$$f_T = \mathrm{tr}(\hat{J}_x \rho_N \hat{J}_x^\dagger) + \mathrm{tr}(\hat{J}_y \rho_N \hat{J}_y^\dagger) \ , \tag{2.100}$$

$$f_{LT} = -\sqrt{2}\ \mathrm{tr}(\hat{J}_0 \rho_N \hat{J}_x^\dagger) - \sqrt{2}\ \mathrm{tr}(\hat{J}_x \rho_N \hat{J}_0^\dagger) \ , \tag{2.101}$$

$$f_{TT} = -\mathrm{tr}(\hat{J}_x \rho_N \hat{J}_x^\dagger) + \mathrm{tr}(\hat{J}_y \rho_N \hat{J}_y^\dagger) \ , \tag{2.102}$$

$$f'_{LT} = i\sqrt{2}\ \mathrm{tr}(\hat{J}_0 \rho_N \hat{J}_y^\dagger) - i\sqrt{2}\ \mathrm{tr}(\hat{J}_y \rho_N \hat{J}_0^\dagger) \ , \tag{2.103}$$

$$f'_T = -i\ \mathrm{tr}(\hat{J}_x \rho_N \hat{J}_y^\dagger) + i\ \mathrm{tr}(\hat{J}_y \rho_N \hat{J}_x^\dagger) \ , \tag{2.104}$$

where, as discussed in Section 2.1.4, the nucleon current operator can be written in

terms of G_E and G_M in the Breit frame as

$$\begin{aligned}\hat{J}_\mu &= \left(G_E, \frac{i\boldsymbol{\sigma}\times\mathbf{q}_{\rm Breit}}{2m}G_M\right) \\ &= \left(G_E,\ i\frac{|\mathbf{q}_{\rm Breit}|}{2m}\sigma_y G_M,\ -i\frac{|\mathbf{q}_{\rm Breit}|}{2m}\sigma_x G_M,\ 0\right) .\end{aligned} \tag{2.105}$$

The nucleon polarization density matrix, ρ_N, is

$$\begin{aligned}\rho_N &= \frac{1}{2}\left(1+\mathbf{P}_T\cdot\boldsymbol{\sigma}\right) \\ &= \frac{1}{2}\left(1+P_T\sin\theta^*\cos\phi^*\sigma_x + P_T\sin\theta^*\sin\phi^*\sigma_y + P_T\cos\theta^*\sigma_z\right) ,\end{aligned} \tag{2.106}$$

and the ρ_i are functions of kinematics given by

$$\rho_L = -\beta^2 Q^2\frac{\xi^2}{2\eta} , \qquad \rho_{LT} = \beta Q^2\frac{\xi}{\eta}\sqrt{\frac{\eta-\xi}{8}} , \tag{2.107}$$

$$\rho_T = -\frac{1}{2}Q^2\left(1-\frac{\xi}{2\eta}\right) , \qquad \rho_{TT} = -Q^2\frac{\xi}{4\eta} , \tag{2.108}$$

$$\rho'_{LT} = \frac{1}{2}\beta Q^2\frac{\xi}{\sqrt{2\eta}} , \qquad \rho'_T = \frac{1}{2}Q^2\sqrt{\frac{\eta-\xi}{\eta}} , \tag{2.109}$$

where

$$\xi = \frac{Q^2}{|\mathbf{q}|^2} , \qquad \eta = \tan^2\frac{\theta_{e'}}{2} , \tag{2.110}$$

and the factor β denotes the boost from the laboratory frame to the frame in which the structure functions are evaluated. As we are interested in evaluating the structure functions in terms of the Breit frame nucleon current operator components, it follows that

$$\beta = \frac{|\mathbf{q}|}{|\mathbf{q}_{\rm Breit}|} = \frac{|\mathbf{q}|}{|\mathbf{q}|/\sqrt{1+\tau}} = \sqrt{1+\tau} . \tag{2.111}$$

Finally, the constant C is given by

$$C = \frac{\alpha}{6\pi^2}\frac{|\mathbf{p}_{e'}|}{|\mathbf{p}_e|Q^4} . \tag{2.112}$$

Evaluation of the structure functions is straightforward, albeit somewhat tedious.

One-by-one, the results are

$$\begin{aligned} f_L &= G_E^2 \ \mathrm{tr}\left\{\frac{1}{2}(1+\mathbf{P}_T\cdot\boldsymbol{\sigma})\right\} \\ &= G_E^2 \ , \end{aligned} \tag{2.113}$$

$$\begin{aligned} f_T &= \frac{|\mathbf{q}_{\mathrm{Breit}}|^2}{4m^2}G_M^2\left[\mathrm{tr}\left\{\frac{1}{2}(1+\mathbf{P}_T\cdot\boldsymbol{\sigma})\sigma_x^2\right\}+\mathrm{tr}\left\{\frac{1}{2}(1+\mathbf{P}_T\cdot\boldsymbol{\sigma})\sigma_y^2\right\}\right] \\ &= \frac{|\mathbf{q}_{\mathrm{Breit}}|^2}{2m^2}G_M^2 \ , \end{aligned} \tag{2.114}$$

$$\begin{aligned} f_{LT} &= \frac{i\sqrt{2}|\mathbf{q}_{\mathrm{Breit}}|G_EG_M}{2m}\left[\mathrm{tr}\left\{\frac{1}{2}(1+\mathbf{P}_T\cdot\boldsymbol{\sigma})\sigma_y\right\}-\mathrm{tr}\left\{\frac{1}{2}\sigma_y(1+\mathbf{P}_T\cdot\boldsymbol{\sigma})\right\}\right] \\ &= 0 \ , \end{aligned} \tag{2.115}$$

$$\begin{aligned} f_{TT} &= -\frac{|\mathbf{q}_{\mathrm{Breit}}|^2G_M^2}{4m^2}\left[\mathrm{tr}\left\{\frac{1}{2}(1+\mathbf{P}_T\cdot\boldsymbol{\sigma})\sigma_y^2\right\}-\mathrm{tr}\left\{\frac{1}{2}(1+\mathbf{P}_T\cdot\boldsymbol{\sigma})\sigma_x^2\right\}\right] \\ &= 0 \ , \end{aligned} \tag{2.116}$$

$$\begin{aligned} f'_{LT} &= -\frac{|\mathbf{q}_{\mathrm{Breit}}|G_EG_M}{\sqrt{2}m}\left[\mathrm{tr}\left\{\frac{1}{2}(1+\mathbf{P}_T\cdot\boldsymbol{\sigma})\sigma_x\right\}+\mathrm{tr}\left\{\sigma_x\frac{1}{2}(1+\mathbf{P}_T\cdot\boldsymbol{\sigma})\right\}\right] \\ &= -\frac{\sqrt{2}|\mathbf{q}_{\mathrm{Breit}}|G_EG_MP_T\sin\theta^*\cos\phi^*}{m} \ , \end{aligned} \tag{2.117}$$

and

$$\begin{aligned} f'_T &= \frac{i|\mathbf{q}_{\mathrm{Breit}}|^2G_M^2}{4m^2}\left[\mathrm{tr}\left\{\sigma_y\frac{1}{2}(1+\mathbf{P}_T\cdot\boldsymbol{\sigma})\sigma_x\right\}-\mathrm{tr}\left\{\sigma_x\frac{1}{2}(1+\mathbf{P}_T\cdot\boldsymbol{\sigma})\sigma_y\right\}\right] \\ &= -\frac{|\mathbf{q}_{\mathrm{Breit}}|^2G_M^2P_T\cos\theta^*}{2m^2} \ . \end{aligned} \tag{2.118}$$

The quantity we are interested in, the polarized-electron, polarized-nucleon helic-

ity asymmetry, A_{eN}, is defined to be

$$A_{eN} \equiv \frac{\left(\frac{d\sigma}{d\Omega_{e'}}\right)^{h=+1} - \left(\frac{d\sigma}{d\Omega_{e'}}\right)^{h=-1}}{\left(\frac{d\sigma}{d\Omega_{e'}}\right)^{h=+1} + \left(\frac{d\sigma}{d\Omega_{e'}}\right)^{h=-1}} = \frac{P_L(\rho'_{LT} f'_{LT} + \rho'_T f'_T)}{\rho_L f_L + \rho_T f_T} \ . \tag{2.119}$$

As will be useful later, we see that the cross section can be written in terms of A_{eN} as

$$\frac{d\sigma}{d\Omega_{e'}} = S_0 \left(1 + h A_{eN}\right) \ , \tag{2.120}$$

where

$$S_0 \equiv C \left(\rho_L f_L + \rho_T f_T\right) \tag{2.121}$$

is the unpolarized cross section.

Following some tedious algebraic manipulations, the expression for A_{eN} can be written in terms of the nucleon form factors, the target polarization angles, and kinematics as

$$A_{eN} = -P_L P_T \frac{K_1 \sin\theta^* \cos\phi^* G_E G_M + K_2 \cos\theta^* G_M^2}{G_E^2 + K_3 G_M^2} \ , \tag{2.122}$$

where K_1, K_2, and K_3 are functions of kinematics given by

$$K_1 = 2\left[\tau(1+\tau)\right]^{1/2} \tan\frac{\theta_{e'}}{2} \ , \tag{2.123}$$

$$K_2 = 2\tau \left[(1+\tau)\left(1 + (1+\tau)\tan^2\frac{\theta_{e'}}{2}\right)\right]^{1/2} \tan\frac{\theta_{e'}}{2} \ , \tag{2.124}$$

$$K_3 = \tau + 2\tau(1+\tau)\tan^2\frac{\theta_{e'}}{2} \ . \tag{2.125}$$

As expected, if either the electron beam or the target is unpolarized, the asymmetry vanishes.

Although polarizing a target is technically challenging, beam-target asymmetry measurements offer several advantages over unpolarized cross section measurements.

In practice, what is measured is a count-rate asymmetry, ϵ, defined to be

$$\epsilon = \frac{N^+ - N^-}{N^+ + N^-} \ , \tag{2.126}$$

where N^+ (N^-) is the number of counts recorded in a detector when $h = +1$ ($h = -1$) normalized to the incident charge. If the experimental conditions are identical for measurements with $h = +1$ and $h = -1$, the results are independent of the luminosities and the detection efficiencies, and $A_{eN} = \epsilon$.

The sensitivity of A_{eN} to G_E or G_M is enhanced if $\mathbf{P}_T$ is oriented in the scattering plane (i.e., $\phi^* = 0°$ or $180°$) either parallel (i.e., $\theta^* = 0°$) or perpendicular (i.e., $\theta^* = 90°$) to $\mathbf{q}$; henceforth, for $\phi^* = 0°$ or $180°$, we shall denote the beam-target asymmetry for $\theta^* = 0°$ and $90°$ as $A_{eN,\parallel}$ and $A_{eN,\perp}$, respectively, or, simply as $A_\parallel$ and $A_\perp$. A summary of the possible measurements follows.

- If $A_\parallel$ is measured, then

$$A_\parallel = -P_L P_T \frac{K_2 G_M^2}{G_E^2 + K_3 G_M^2} \ , \tag{2.127}$$

  and the beam-target asymmetry is primarily sensitive to G_M; therefore, if G_E is assumed to be known, G_M can be extracted. Such an extraction requires knowledge of the beam polarization, P_L, and the target polarization, P_T; therefore, this technique is susceptible to non-negligible systematic errors arising from uncertainties in the values of P_L and P_T.

- If $A_\perp$ is measured, then

$$A_\perp = -P_L P_T \frac{K_1 G_E G_M}{G_E^2 + K_3 G_M^2} \ , \tag{2.128}$$

  and the beam-target asymmetry is sensitive to an interference term between G_E and G_M; this interference enhances the contribution of G_E to the asymmetry (as $G_E < G_M$ for both the proton and the neutron over the current accessible range in Q^2), and G_E (and its sign) can be extracted from measurements of $A_\perp$

provided G_M is sufficiently well known. Again, this technique requires precise knowledge of P_L and P_T.

- If both $A_{||}$ and $A_{\perp}$ are measured, then the *ratio* of the beam-target asymmetries

$$\frac{A_{\perp}}{A_{||}} = \frac{K_1}{K_2}\frac{G_E}{G_M}\,, \tag{2.129}$$

is proportional to the ratio of G_E to G_M. The polarization of the electron beam, P_L, and the polarization of the nucleon target, P_T, cancel in the ratio; therefore, if G_M is well-known, the systematic errors associated with an extraction of G_E via this "ratio technique" should be small. Again, this measurement is sensitive to the sign of G_E.

Measurements of either the proton or neutron form factors with a polarized target are very challenging due to the challenges associated with polarizing a target. In what follows, we discuss measurements of the neutron form factors using polarized ^{3}He and deuterium targets.

2.3.4 Neutron Form Factors via Quasielastic $^3\vec{\text{He}}(\vec{e},e')$ and $^3\vec{\text{He}}(\vec{e},e'n)$ Scattering

The ground state of the ^{3}He wavefunction is predominantly a spatially symmetric S-state (~89%) with small mixed symmetry S'-state (~1.5%) and D-state (~8.5%) components (see, e.g., [167–170]). In the spatially symmetric S-state component, interchanging the two protons does not affect the isospin symmetry of the wavefunction; therefore, the spin component must be antisymmetric (i.e., the protons must be coupled to spin-0 in a spin-singlet state). As such, neglecting the S'- and D-state components, the spin of the ^{3}He nucleus is carried by the neutron, and polarized ^{3}He should, in principle, serve as an "effective polarized neutron target" in quasielastic scattering. More realistic calculations by Friar *et al.* [168] which accounted for the S'- and D-state components found that the polarization of the neutron (proton) in a fully polarized ^{3}He nucleus is 87% (−2.7%).

The first calculations of cross sections and beam-target asymmetries for inclusive quasielastic ^{3}He$(\vec{e}, e')$ scattering were carried out by Blankleider and Woloshyn [167]. Blankleider and Woloshyn modeled the ^{3}He nucleus using the wave function of Afnan and Birrell [171]; this wavefunction was derived from a solution of the Faddeev equations[5] for the Reid soft core potential [120]. Neglecting FSI and MEC and using the closure approximation (i.e., using a spin-dependent momentum distribution) to sum over all possible final states, Blankleider and Woloshyn concluded that in the vicinity of the quasielastic peak, the beam-target asymmetry for inclusive quasielastic ^{3}He$(\vec{e}, e')$ scattering, denoted $A_{e(^3\mathrm{He})}$, is given approximately by

$$A_{e(^3\mathrm{He})} \approx A_{en} \left(\frac{\sigma_{en}}{\sigma_{e(^3\mathrm{He})}} \right) , \tag{2.130}$$

where A_{en} denotes the beam-target asymmetry for elastic polarized-electron, polarized-neutron scattering and σ_{en} denotes the contribution of the neutron to the total inclusive quasielastic ^{3}He$(\vec{e}, e')$ cross section, $\sigma_{e(^3\mathrm{He})}$. In other words, near the quasielastic peak, polarized ^{3}He is effectively a polarized neutron target, but the contribution from the (nearly) unpolarized protons to the inclusive quasielastic cross section dilutes the signal. Blankleider and Woloshyn also found that near the tails of the quasielastic peak, the protons contribute to the asymmetry as the probability of finding a proton with a large initial momentum and spin parallel to the ^{3}He spin is not equal to the probability of finding a proton with a large initial momentum and spin anti-parallel to the ^{3}He spin.

Subsequent calculations of the inclusive quasielastic $^3\vec{\mathrm{He}}(\vec{e}, e')$ asymmetry reported by Ciofi degli Atti, Pace, and Salme [169] which employed a spin-dependent spectral function obtained from the Reid soft core potential [120] (the use of a spin-dependent spectral function properly takes into account both the removal energy and the momentum distribution of the nucleon) found that the closure approximation provides a poor description of the asymmetry away from the top of the quasielastic peak and underestimates the contribution of the protons to the asymmetry; however, Ciofi

[5] As described succinctly in [172], in 1961, L. D. Faddeev [173] proposed the use of coupled linear integral equations with a square integrable kernel as a solution to the three-body problem.

delgi Atti, Pace, and Salme did find that if the target polarization is oriented in the scattering plane at an angle of $\sim 85^\circ$ relative to the incident electron, the proton contribution at the top of the quasielastic peak is negligible. More pessimistically, Schulze and Sauer [170], using a spin-dependent spectral function obtained with the Paris potential [124], concluded that an extraction of G_{En} from the inclusive quasielastic asymmetry would be nearly impossible given the large contribution of the protons to the asymmetry. It should be noted that none of the above mentioned calculations included FSI or MEC.

A more challenging experimental technique is detection of the recoil neutron in coincidence with the scattered electron; this eliminates the uncertainties associated with the contribution of the proton to the asymmetry. Further, for quasifree colinear kinematics (i.e., $\mathbf{p}_f \parallel \mathbf{q}$), the asymmetry is not diluted but is, instead, equal to the electron-free neutron asymmetry, A_{en}. Laget [174] studied the exclusive quasielastic $^3\vec{\mathrm{He}}(\vec{e}, e'n)$ reaction and concluded that the effects of FSI and MEC are small for $Q^2 \gtrsim 0.3$ (GeV/c)^2; indeed, Laget suggested that a measurement of the beam-target asymmetry in exclusive quasielastic $^3\vec{\mathrm{He}}(\vec{e}, e'n)$ scattering appeared to be one of the most direct ways to measure G_{En}.

2.3.5 Neutron Electric Form Factor via Quasielastic $^2\vec{\mathrm{H}}(\vec{e}, e'n)^1\mathrm{H}$ Scattering

The deuteron is a spin-1 nucleus and can be vector- and tensor-polarized simultaneously. An extraction of the neutron electric form factor, G_{En}, via beam-target asymmetry measurements using a vector-polarized deuterium target in quasielastic electron-deuteron scattering was first proposed by Cheung and Woloshyn [175] in 1983. Following Cheung and Woloshyn's initial proposal, a detailed series of studies of the inclusive $^2\vec{\mathrm{H}}(\vec{e}, e')$ and exclusive $^2\vec{\mathrm{H}}(\vec{e}, e'n)$ quasielastic reactions were reported by Tomusiak and Arenhövel [176], Arenhövel, Leidemann, and Tomusiak [166, 177, 178], Leidemann, Tomusiak, and Arenhövel [179], and Laget [174]; below, we outline the formalism for the exclusive reaction that was developed in these references.

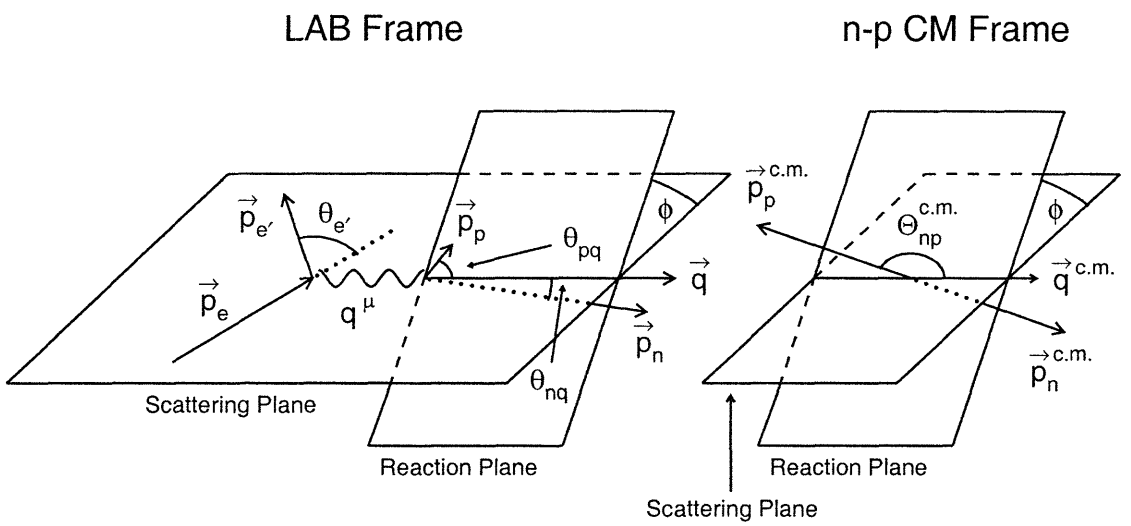

Figure 2-16: Schematic diagram of the kinematics for the electrodisintegration of the deuteron.

Before we discuss this formalism, it is necessary to define a certain amount of kinematic notation. For simplicity of notation, all kinematic quantities in the center-of-mass frame of the recoiling neutron-proton (n-p) system will carry a $^{\text{c.m.}}$ superscript; however, kinematic quantities in the laboratory frame will not be adorned with a $^{\text{lab}}$ superscript.

A schematic diagram of the kinematics for the electrodisintegration of the deuteron in the one-photon exchange approximation is shown in Fig. 2-16. We assume an electron, with initial four-momentum $k = (E_e, \mathbf{p}_e)$, scatters from a deuteron with initial four-momentum $d = (m_d, \mathbf{0})$, where m_d denotes the deuteron mass. The scattered electron, with four-momentum $k' = (E_{e'}, \mathbf{p}_{e'})$, is detected at an angle $\theta_{e'}$ relative to $\mathbf{p}_e$. The electron couples with the deuteron via the exchange of a virtual photon carrying four-momentum $q = (\omega, \mathbf{q})$, where $\omega = E_e - E_{e'}$ and $\mathbf{q} = \mathbf{p}_e - \mathbf{p}_{e'}$. Following the electrodisintegration of the deuteron, the proton and neutron exit with three-momentum $\mathbf{p}_p$ and $\mathbf{p}_n$, respectively. As is customary, we denote the angle between $\mathbf{p}_p$ ($\mathbf{p}_n$) and $\mathbf{q}$ in the laboratory frame as θ_{pq} (θ_{nq}). The scattering plane is defined by $\mathbf{p}_e$ and $\mathbf{p}_{e'}$; similarly, the reaction plane is defined by $\mathbf{q}$, $\mathbf{p}_p$, and $\mathbf{p}_n$. As indicated in Fig. 2-16, the reaction plane is tilted at a dihedral angle ϕ with respect to the scattering plane. It should be noted that in the n-p CM frame, the dihedral angle, $\phi_{np}^{\text{c.m.}}$, is, obviously,

just equal to ϕ; below, we will use ϕ and $\phi_{np}^{\text{c.m.}}$ interchangeably.

The n-p CM frame is reached via a Lorentz boost along $\mathbf{q}$. In the laboratory frame, the final n-p state has an invariant mass, W_{np}, given by

$$W_{np}^2 = E_{np}^2 - |\mathbf{q}|^2 \ , \tag{2.131}$$

where the relative n-p energy in the laboratory frame is

$$E_{np} = m_d + \omega \ ; \tag{2.132}$$

therefore, the Lorentz factor for the boost from the laboratory frame to the n-p CM frame, γ, is

$$\gamma = \frac{E_{np}}{W_{np}} = \frac{\omega + m_d}{\sqrt{(\omega + m_d)^2 - |\mathbf{q}|^2}} \ , \tag{2.133}$$

and the boost parameter, β, is, as always,

$$\beta = \sqrt{1 - 1/\gamma^2} = \frac{|\mathbf{q}|}{\omega + m_d} \ . \tag{2.134}$$

We denote the polar angle between the relative n-p motion in the CM frame, $\mathbf{p}_{np}^{\text{c.m.}} = \frac{1}{2}(\mathbf{p}_p^{\text{c.m.}} - \mathbf{p}_n^{\text{c.m.}}) = \mathbf{p}_p^{\text{c.m.}}$ (assuming equal nucleon masses), and $\mathbf{q}^{\text{c.m.}}$ as $\Theta_{np}^{\text{c.m.}}$, where

$$\cos\Theta_{np}^{\text{c.m.}} = \frac{\mathbf{p}_p^{\text{c.m.}} \cdot \mathbf{q}^{\text{c.m.}}}{|\mathbf{p}_p^{\text{c.m.}}| \ |\mathbf{q}^{\text{c.m.}}|} \ . \tag{2.135}$$

A straightforward evaluation of the three-momenta in the n-p CM frame shows that $\Theta_{np}^{\text{c.m.}}$ can be written solely in terms of the laboratory frame observables $E_n = (|\mathbf{p}_n|^2 + m_n^2)^{1/2}$, $|\mathbf{p}_n|$, θ_{nq}, and ω as

$$\cos\Theta_{np}^{\text{c.m.}} = -\frac{|\mathbf{p}_n|\cos\theta_{nq} - \dfrac{|\mathbf{q}|E_n}{\omega + m_d}}{\left[|\mathbf{p}_n|^2\sin^2\theta_{nq}\left(1 - \dfrac{|\mathbf{q}|^2}{(\omega + m_d)^2}\right) + \left(|\mathbf{p}_n|\cos\theta_{nq} - \dfrac{|\mathbf{q}|E_n}{\omega + m_d}\right)^2\right]^{1/2}} \ . \tag{2.136}$$

Clearly, $\Theta_{np}^{\text{c.m.}} = 0^\circ$ (180°) corresponds to perfect quasifree emission of the proton (neu-

tron); however, it should be noted that there is no phase space for perfect quasifree emission (as either $\mathbf{p}_p$ or $\mathbf{p}_n$ would have to be perfectly aligned with $\mathbf{q}$).

Now that we have finished our discussion of the kinematics of deuteron electrodisintegration, we turn to possible measurements using polarized electrons and a polarized deuteron target. Following the notation of [166, 177–179], the five-fold differential coincidence cross section, including beam and (vector and tensor) target polarizations, for the $^2\vec{\mathrm{H}}(\vec{e},e'N)$ reaction is

$$\begin{aligned}
\frac{\mathrm{d}^5\sigma}{\mathrm{d}E_{e'}\mathrm{d}\Omega_{e'}\mathrm{d}\Omega_{np}^{\mathrm{c.m.}}} = C\Bigg\{ & \rho_L f_L + \rho_T f_T + \rho_{LT} f_{LT}\cos\phi + \rho_{TT} f_{TT}\cos 2\phi + hP_L\rho'_{LT} f'_{LT}\sin\phi \\
& + P_1^d\Big[\left(\rho_L f_L^{11} + \rho_T f_T^{11}\right) d^1_{10}(\theta^*)\sin(\phi-\phi^*) \\
& \quad + \sum_{M=-1}^{1} \left(\rho_{LT} f_{LT}^{1M}\sin\xi_M + \rho_{TT} f_{TT}^{1M}\sin\psi_M\right) d^1_{M0}(\theta^*)\Big] \\
& + P_2^d\Big[\sum_{M=0}^{2} \left(\rho_L f_L^{2M} + \rho_T f_T^{2M}\right) d^2_{M0}(\theta^*)\cos[M(\phi-\phi^*)] \\
& \quad + \sum_{M=-2}^{2} \left(\rho_{LT} f_{LT}^{2M}\cos\xi_M + \rho_{TT} f_{TT}^{2M}\cos\psi_M\right) d^2_{M0}(\theta^*)\Big] \\
& + hP_L P_1^d\Big[\rho'_T \sum_{M=0}^{1} f_T^{\prime 1M}\cos[M(\phi-\phi^*)] d^1_{M0}(\theta^*) \\
& \quad + \rho'_{LT} \sum_{M=-1}^{1} f_{LT}^{\prime 1M}\cos\xi_M d^1_{M0}(\theta^*)\Big] \\
& + hP_L P_2^d\Big[\rho'_T \sum_{M=0}^{1} f_T^{\prime 2M}\sin[M(\phi-\phi^*)] d^2_{M0}(\theta^*) \\
& \quad + \rho'_{LT} \sum_{M=-2}^{2} f_{LT}^{\prime 2M}\sin\xi_M d^2_{M0}(\theta^*)\Big]\Bigg\} \\
\equiv\ & S(h, P_1^d, P_2^d)\ . \qquad (2.137)
\end{aligned}$$

Here, as always, $h = \pm 1$ and P_L denote the helicity and polarization, respectively, of the incident electron beam; P_1^d and P_2^d denote, respectively, the vector- and tensor-polarization of the deuteron target; θ^* and ϕ^* define, as before, the orientation of the target polarization relative to $\mathbf{q}$; the factor C is the same as that given in Eq. (2.112);

the angles ξ_M and ψ_M are defined by

$$\xi_M = M(\phi - \phi^*) + \phi \ , \qquad \psi_M = M(\phi - \phi^*) + 2\phi \ ; \tag{2.138}$$

and the d^i_{M0} are the standard rotation matrices given by

$$d^1_{00}(\theta^*) = \cos\theta^* \ , \qquad d^1_{10}(\theta^*) = -\frac{\sin\theta^*}{\sqrt{2}} \ , \qquad d^2_{00}(\theta^*) = \frac{3}{2}\cos^2\theta^* - \frac{1}{2} \ , \tag{2.139}$$

$$d^2_{10}(\theta^*) = -\frac{\sqrt{3}}{\sqrt{2}}\sin\theta^*\cos\theta^* \ , \qquad d^2_{20}(\theta^*) = \frac{\sqrt{6}}{4}\sin^2\theta^* \ . \tag{2.140}$$

In all of the above listed references, the structure functions, f_i, are evaluated in the n-p CM frame; therefore, the factor of β in the expressions for the kinematic functions, ρ_i, given in Eqs. (2.108) and (2.109), is as given in Eq. (2.134).

Finally, before turning to our discussion of the possible measurements, we note that the expression for the five-fold differential coincidence cross section, as given in Eq. (2.137), is differential in $E_{e'}$, $\Omega_{e'}$, and $\Omega^{\text{c.m.}}_{np}$. The Jacobian, $\mathcal{J}$, which transforms $\Omega^{\text{c.m.}}_{np} \to \Omega_n$ is given by [98]

$$\mathcal{J} = \frac{\partial\Omega^{\text{c.m.}}_{np}}{\partial\Omega_n} = \frac{1}{\gamma}\left(\frac{\beta_n\gamma_n}{\beta^{\text{c.m.}}_n\gamma^{\text{c.m.}}_n}\right)^3\left(1 + \frac{\beta}{\beta^{\text{c.m.}}_n}\cos(\pi - \Theta^{\text{c.m.}}_{np})\right)^{-1} \ . \tag{2.141}$$

Here, γ and β are as given in Eq. (2.133) and Eq. (2.134), respectively; $\gamma^{\text{c.m.}}_n$ is the Lorentz factor for the boost which takes the neutron from its rest frame to the n-p CM frame,

$$\gamma^{\text{c.m.}}_n = \frac{W_{np}}{2m_n} \ , \tag{2.142}$$

and γ_n is the Lorentz factor for the boost which takes the neutron from its rest frame to the laboratory frame,

$$\gamma_n = \gamma\gamma^{\text{c.m.}}_n\left[1 + \beta\beta^{\text{c.m.}}_n\cos(\pi - \Theta^{\text{c.m.}}_{np})\right] \ , \tag{2.143}$$

where $\beta^{\text{c.m.}}_n = \sqrt{1 - 1/(\gamma^{\text{c.m.}}_n)^2}$.

Similar to Eq. (2.120), the full expression for the five-fold differential coincidence

cross section, Eq. (2.137), can be rewritten in terms of electron, A_e, (vector and tensor) target A_d^V and A_d^T, and (vector and tensor) beam-target, A_{ed}^V and A_{ed}^T, asymmetries as

$$S(h, P_1^d, P_2^d) = S_0 \left[1 + P_1^d A_d^V + P_2^d A_d^T + h P_L \left(A_e + P_1^d A_{ed}^V + P_2^d A_{ed}^T\right)\right] \ , \qquad (2.144)$$

where $S_0 \equiv S(0,0,0)$ is, again, the unpolarized cross section. Here, the electron asymmetry, A_e, defined by

$$\begin{aligned} A_e &\equiv \frac{1}{2hP_L S_0}\left[S(h,0,0) - S(-h,0,0)\right] \\ &= \frac{C}{S_0}\rho'_{LT} f'_{LT} \sin\phi_{np} \ , \end{aligned} \qquad (2.145)$$

is proportional to f'_{LT}, the *fifth structure function*, and vanishes in the scattering plane; therefore, A_e can only be determined via an out-of-(scattering)plane measurement. Leidemann and Arenhövel [180] found that f'_{LT} is very sensitive to G_{En}; however, the model dependence arising from the choice of an NN potential was found to be of the same size as the sensitivity to G_{En}. [An out-of-plane measurement necessitates a departure from strict quasifree kinematics. Away from the quasielastic peak, the effects of FSI become more important; therefore, a reliable interpretation of the experimental results would require a good model for the NN interaction.]

Similarly, the (unpolarized electron) vector and tensor target helicity asymmetries, A_d^V and A_d^T, respectively, are defined by

$$A_d^V = \frac{1}{2S_0 P_1^d}\left[S(0, P_1^d, P_2^d) - S(0, -P_1^d, P_2^d)\right] \ , \qquad (2.146)$$

$$A_d^T = \frac{1}{2S_0 P_2^d}\left[S(0, P_1^d, P_2^d) + S(0, -P_1^d, P_2^d) - 2S_0\right] \ . \qquad (2.147)$$

Arenhövel, Leidemann, and Tomusiak [166] found that A_d^V and A_d^T are relatively insensitive to G_{En} for quasifree emission. A_d^T was found to be sensitive to G_{En} for $130° < \Theta_{np}^{\text{c.m.}} < 150°$; however, FSI, MEC, and IC are expected to be important in this kinematic region.

Finally, the (polarized electron) vector and tensor beam-target asymmetries, A_{ed}^V and A_{ed}^T, respectively, are defined by

$$A_{ed}^V = \frac{1}{4S_0 h P_L P_1^d}\Big[\big(S(h,P_1^d,P_2^d) - S(-h,P_1^d,P_2^d)\big) - \big(S(h,-P_1^d,P_2^d) - S(-h,-P_1^d,P_2^d)\big)\Big], \tag{2.148}$$

$$A_{ed}^T = \frac{1}{4S_0 h P_L P_2^d}\Big[\big(S(h,P_1^d,P_2^d) - S(-h,P_1^d,P_2^d)\big) + \big(S(h,-P_1^d,P_2^d) - S(-h,-P_1^d,P_2^d)\big)\Big]. \tag{2.149}$$

Cheung and Woloshyn [175] found that A_{ed}^V was very sensitive to G_{En}; however, their analysis neglected the effects of FSI, MEC, and IC. The first calculation of A_{ed}^V that included FSI, MEC, and IC was reported by Tomusiak and Arenhövel [176] in 1988, and, as noted earlier, following this initial work, an extensive series of investigations concerning the role of G_{En} in $^2\vec{\mathrm{H}}(\vec{e},e'n)$ were reported [166,174,177–179]. All of these studies found that near the quasielastic peak, A_{ed}^V is strongly sensitive to G_{En}, is insensitive to FSI, MEC, and IC, and is insensitive to the choice of the NN potential.

To illustrate the sensitivity of A_{ed}^V to G_{En} and the insensitivity of A_{ed}^V to FSI, MEC, IC, and the choice of the NN potential, we will, shortly, present several illustrative examples of Arenhövel's calculations [181] of A_{ed}^V; however, first, some explanation is necessary. As described in detail in [166, 177–179], these calculations model the deuteron as a nonrelativistic n-p system and employ an NN potential for the deuteron wavefunction and the inclusion of FSI; further, leading order relativistic contributions to the wavefunctions are added via inclusion of the most important kinematic part of the wavefunction boost. In the current operator, explicit meson exchange contributions beyond the Siegert operators[6] (essentially from π- and ρ-exchange) and isobar configurations are included. The treatment of IC includes relativistic contributions to one-body currents, as discussed in [184], and permits consideration of kinematic

[6]The Siegert theorem, first formulated by Siegert [182] in 1937, follows from current conservation and states that at very low energies, there are no $E\lambda$ MEC contributions. At higher energies, such as in electron scattering, there are exchange contributions from $E\lambda$ processes; the use of the Siegert operator permits an evaluation of nearly all $E\lambda$ MEC contributions (see, e.g., [183]) without specific knowledge of the current. $M\lambda$ contributions to MEC are due to the exchange of virtual charged mesons and must be explicitly included in the current.

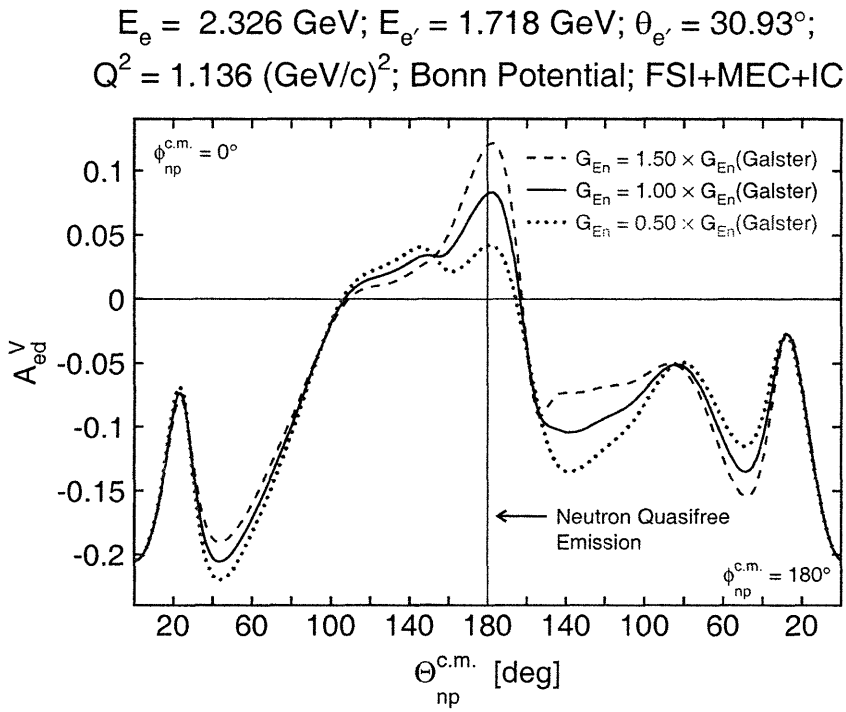

Figure 2-17: (color) Sensitivity of Arenhövel's FSI+MEC+IC calculations of A_{ed}^V to the value of G_{En}.

regions away from the quasielastic ridge and excitations up to the Δ region.

Henceforth, we will use the following notational scheme to categorize Arenhövel's calculations:

- "PWBA" will denote Arenhövel's calculations in the Born approximation (i.e., neglect of FSI, MEC, and IC).
- "FSI+MEC+IC" will denote Arenhövel's calculations which include FSI, MEC, and IC (i.e., the full calculation).
- Unless otherwise noted, it should be assumed that Arenhövel's calculations employed the Bonn r-space NN potential [185]; however, other possibilities include the Argonne V18 [186], Nijmegen [135], and Paris [124] NN potentials.

Each of the above also includes the leading order relativistic contributions.

All of the results for A_{ed}^V which follow were calculated for the following electron kinematics and orientation of the target polarization:

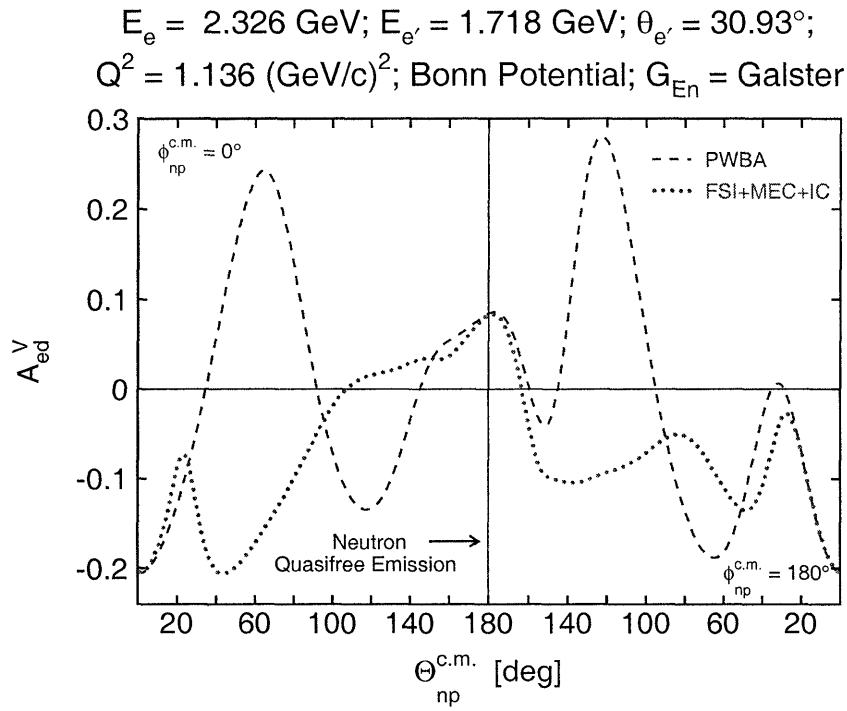

Figure 2-18: (color) Comparison of Arenhövel's PWBA and FSI+MEC+IC calculations of A_{ed}^V.

- $E_e = 2.326$ GeV, $E_{e'} = 1.718$ GeV, $\theta_{e'} = 30.93°$, $\phi_{np}^{\text{c.m.}} = 0°$
  $\Longrightarrow Q^2 = 1.136$ (GeV/c)^2
- $\theta^* = 90°$, $\phi^* = 0°$

The strong sensitivity of A_{ed}^V to the value of G_{En} is shown in Fig. 2-17; here, Arenhövel's FSI+MEC+IC calculations of A_{ed}^V are plotted as a function of $\Theta_{np}^{\text{c.m.}}$ for three values of G_{En} scaled by the value of the Galster parameterization at $Q^2 = 1.136$ (GeV/c)^2: 0.50, 1.00, and 1.50. It is readily apparent that A_{ed}^V is very sensitive to the value of G_{En} near the quasielastic peak. The insensitivity of A_{ed}^V to FSI, MEC, and IC for quasifree emission of the neutron is demonstrated in Fig. 2-18; here, we compare Arenhövel's PWBA and FSI+MEC+IC calculations of A_{ed}^V. Near the quasielastic peak, there is little difference between the PWBA results and the FSI+MEC+IC results. Finally, in Fig. 2-19, we compare Arenhövel's FSI+MEC+IC calculations of A_{ed}^V for the Argonne V18 [186], Bonn [185], Nijmegen [135], and Paris [124] NN potentials. Again, near the quasielastic peak, the differences between these calculations

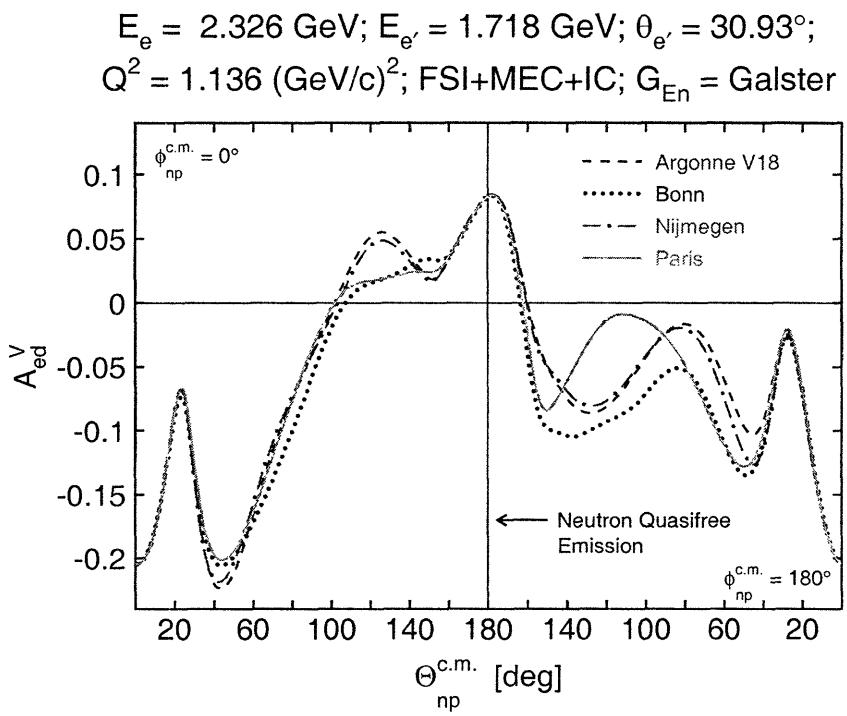

Figure 2-19: (color) Comparison of Arenhövel's FSI+MEC+IC calculations of A_{ed}^V for the Argonne V18, Bonn, Nijmegen, and Paris potentials.

are negligible.

Despite the technical challenges associated with polarizing a deuterium target, it is clear that a measurement of A_{ed}^V in quasifree kinematics permits an extraction of G_{En} that is relatively insensitive to FSI, MEC, and IC and suffers from little model dependence.

2.3.6 Nucleon Form Factors via Elastic $N(\vec{e}, e'\vec{N})$ Scattering

Now, we present an overview of the formalism for measurements of the nucleon form factors via measurements of the final-state nucleon polarization (i.e., the recoil polarization) in elastic polarized-electron, unpolarized-nucleon $N(\vec{e}, e'\vec{N})$ scattering. As noted earlier, Dombey [158] stated that the formalism for recoil polarization was identical to that for target polarization; however, details were not provided. The first detailed results were reported by Akhiezer and Rekalo [159] and Arnold, Carlson, and Gross [160]. Below, we follow the pedagogical overview of the recoil polarimetry

technique given by Arenhövel, Leidemann, and Tomusiak [166].

Again, in the one-photon exchange approximation, the differential cross section for the elastic scattering of longitudinally polarized electrons from a *stationary* nucleon is

$$\frac{\mathrm{d}\sigma}{\mathrm{d}\Omega_{e'}} = C\left[\rho_L f_L + \rho_T f_T + \rho_{LT} f_{LT} + \rho_{TT} f_{TT} + hP_L\left(\rho'_{LT} f'_{LT} + \rho'_T f'_T\right)\right] , \qquad (2.150)$$

where the factor C is as given in Eq. (2.112), the f_i structure functions are as given in Eqs. (2.113) through (2.118), the ρ_i kinematic factors are as given in Eqs. (2.107) through (2.109), and $h = \pm 1$ and P_L denote, respectively, the helicity and polarization of the incident electron beam. If the nucleon is unpolarized, the recoil polarization that results, denoted $\mathbf{P}$, is given by

$$\frac{\mathrm{d}\sigma}{\mathrm{d}\Omega_{e'}}\mathbf{P} = C\left[\rho_L \mathbf{g}_L + \rho_T \mathbf{g}_T + \rho_{LT} \mathbf{g}_{LT} + \rho_{TT} \mathbf{g}_{TT} + hP_L\left(\rho'_{LT} \mathbf{g}'_{LT} + \rho'_T \mathbf{g}'_T\right)\right] , \qquad (2.151)$$

where the $\mathbf{g}_i$ structure functions are related to the components of the nucleon current operator, $\hat{J}_\mu$, according to

$$\mathbf{g}_L = \frac{1}{2}\mathrm{tr}(\hat{J}_0 \hat{J}_0^\dagger \boldsymbol{\sigma}) , \qquad (2.152)$$

$$\mathbf{g}_T = \frac{1}{2}\mathrm{tr}(\hat{J}_x \hat{J}_x^\dagger \boldsymbol{\sigma}) + \frac{1}{2}\mathrm{tr}(\hat{J}_y \hat{J}_y^\dagger \boldsymbol{\sigma}) , \qquad (2.153)$$

$$\mathbf{g}_{LT} = -\frac{1}{\sqrt{2}}\mathrm{tr}(\hat{J}_0 \hat{J}_x^\dagger \boldsymbol{\sigma}) - \frac{1}{\sqrt{2}}\mathrm{tr}(\hat{J}_x \hat{J}_0^\dagger \boldsymbol{\sigma}) , \qquad (2.154)$$

$$\mathbf{g}_{TT} = -\frac{1}{2}\mathrm{tr}(\hat{J}_x \hat{J}_x^\dagger \boldsymbol{\sigma}) + \frac{1}{2}\mathrm{tr}(\hat{J}_y \hat{J}_y^\dagger \boldsymbol{\sigma}) , \qquad (2.155)$$

$$\mathbf{g}'_{LT} = \frac{i}{\sqrt{2}}\mathrm{tr}(\hat{J}_0 \hat{J}_y^\dagger \boldsymbol{\sigma}) - \frac{i}{\sqrt{2}}\mathrm{tr}(\hat{J}_y \hat{J}_0^\dagger \boldsymbol{\sigma}) , \qquad (2.156)$$

$$\mathbf{g}'_T = -\frac{i}{2}\mathrm{tr}(\hat{J}_x \hat{J}_y^\dagger \boldsymbol{\sigma}) + \frac{i}{2}\mathrm{tr}(\hat{J}_y \hat{J}_x^\dagger \boldsymbol{\sigma}) . \qquad (2.157)$$

Here, we have again adopted a coordinate system in which $\hat{\mathbf{z}}$ is parallel to $\mathbf{q}$ (i.e., parallel to the nucleon's momentum), $\hat{\mathbf{y}}$ is perpendicular to the scattering plane, and $\hat{\mathbf{x}} = \hat{\mathbf{y}} \times \hat{\mathbf{z}}$. As before, the evaluation of the traces is easiest in the Breit frame where $\hat{J}_\mu$ is as given in Eq. (2.43). As we are interested in evaluating the structure functions

in terms of the Breit frame current operator components, the factor of β in the ρ_i is, again, as given in Eq. (2.111).

Again, the evaluation of the structure functions in the Breit frame is straightforward, albeit somewhat tedious. One-by-one, the results are

$$\begin{aligned} \mathbf{g}_L &= \frac{1}{2} G_E^2 \mathrm{tr}(\boldsymbol{\sigma}) \\ &= \mathbf{0} \,, \end{aligned} \tag{2.158}$$

$$\begin{aligned} \mathbf{g}_T &= \frac{|\mathbf{q}_{\mathrm{Breit}}|^2 G_M^2}{8m^2} \mathrm{tr}(\sigma_y^2 \boldsymbol{\sigma}) + \frac{|\mathbf{q}_{\mathrm{Breit}}|^2 G_M^2}{8m^2} \mathrm{tr}(\sigma_x^2 \boldsymbol{\sigma}) \\ &= \mathbf{0} \,, \end{aligned} \tag{2.159}$$

$$\begin{aligned} \mathbf{g}_{LT} &= \frac{i|\mathbf{q}_{\mathrm{Breit}}| G_E G_M}{2\sqrt{2}m} \mathrm{tr}(\sigma_y \boldsymbol{\sigma}) - \frac{i|\mathbf{q}_{\mathrm{Breit}}| G_E G_M}{2\sqrt{2}m} \mathrm{tr}(\sigma_y \boldsymbol{\sigma}) \\ &= \mathbf{0} \,, \end{aligned} \tag{2.160}$$

$$\begin{aligned} \mathbf{g}_{TT} &= -\frac{|\mathbf{q}_{\mathrm{Breit}}|^2 G_M^2}{8m^2} \mathrm{tr}(\sigma_y^2 \boldsymbol{\sigma}) + \frac{|\mathbf{q}_{\mathrm{Breit}}|^2 G_M^2}{8m^2} \mathrm{tr}(\sigma_x^2 \boldsymbol{\sigma}) \\ &= \mathbf{0} \,, \end{aligned} \tag{2.161}$$

$$\begin{aligned} \mathbf{g}'_{LT} &= -\frac{|\mathbf{q}_{\mathrm{Breit}}| G_E G_M}{2\sqrt{2}m} \mathrm{tr}(\sigma_x \boldsymbol{\sigma}) - \frac{|\mathbf{q}_{\mathrm{Breit}}| G_E G_M}{2\sqrt{2}m} \mathrm{tr}(\sigma_x \boldsymbol{\sigma}) \\ &= -\frac{\sqrt{2}|\mathbf{q}_{\mathrm{Breit}}| G_E G_M}{m} \hat{\mathbf{x}} \,, \end{aligned} \tag{2.162}$$

and

$$\begin{aligned} \mathbf{g}'_T &= -\frac{i|\mathbf{q}_{\mathrm{Breit}}|^2 G_M^2}{8m^2} \mathrm{tr}(\sigma_y \sigma_x \boldsymbol{\sigma}) - \frac{i|\mathbf{q}_{\mathrm{Breit}}|^2 G_M^2}{8m^2} \mathrm{tr}(\sigma_x \sigma_y \boldsymbol{\sigma}) \\ &= \frac{|\mathbf{q}_{\mathrm{Breit}}|^2 G_M^2}{2m^2} \hat{\mathbf{z}} \,. \end{aligned} \tag{2.163}$$

After substituting these results into Eq. (2.151), it follows that the recoil polarization

is given by

$$\frac{\mathrm{d}\sigma}{\mathrm{d}\Omega_{e'}}\mathbf{P} = ChP_L\left[-\frac{\sqrt{2}\rho'_{LT}|\mathbf{q}_{\mathrm{Breit}}|G_E G_M}{m}\hat{\mathbf{x}} + \frac{\rho'_T|\mathbf{q}_{\mathrm{Breit}}|^2 G_M^2}{2m^2}\hat{\mathbf{z}}\right] . \tag{2.164}$$

As will be useful later, the above expression can be rewritten as

$$\frac{\mathrm{d}\sigma}{\mathrm{d}\Omega_{e'}}\mathbf{P} = S_0\left(\mathbf{P}^0 + h\mathbf{P}^h\right) , \tag{2.165}$$

where it is clear that the *helicity-independent* recoil polarization, denoted $\mathbf{P}^0$, is

$$\mathbf{P}^0 = \mathbf{0} , \tag{2.166}$$

and the *helicity-dependent* recoil polarization, denoted $\mathbf{P}^h$, is

$$\mathbf{P}^h = \frac{P_L}{(\rho_L f_L + \rho_T f_T)}\left[-\frac{\sqrt{2}\rho'_{LT}|\mathbf{q}_{\mathrm{Breit}}|G_E G_M}{m}\hat{\mathbf{x}} + \frac{\rho'_T|\mathbf{q}_{\mathrm{Breit}}|^2 G_M^2}{2m^2}\hat{\mathbf{z}}\right] . \tag{2.167}$$

Finally, after some tedious algebraic manipulations, the components of $\mathbf{P}^h$ can be written in terms of the nucleon form factors and kinematics as

$$P_x^h = -P_L\frac{2G_E G_M\left[\tau(1+\tau)\right]^{1/2}\tan\frac{\theta_{e'}}{2}}{G_E^2 + \left[\tau + 2\tau(1+\tau)\tan^2\frac{\theta_{e'}}{2}\right]G_M^2} , \tag{2.168}$$

$$P_y^h = 0 , \tag{2.169}$$

$$P_z^h = P_L\frac{2G_M^2\,\tau(1+\tau)^{1/2}\left[1+\tau\sin^2\frac{\theta_{e'}}{2}\right]^{1/2}\sec\frac{\theta_{e'}}{2}\tan\frac{\theta_{e'}}{2}}{G_E^2 + \left[\tau + 2\tau(1+\tau)\tan^2\frac{\theta_{e'}}{2}\right]G_M^2} . \tag{2.170}$$

We immediately deduce that in the one-photon exchange approximation for elastic scattering from a stationary nucleon, the helicity-independent polarization is identically zero and the helicity-dependent polarization vanishes if $P_L = 0$. Also, we see that the x-component of the helicity-dependent polarization is proportional to an interference term between G_E and G_M, the y-component is zero (i.e., the recoil po-

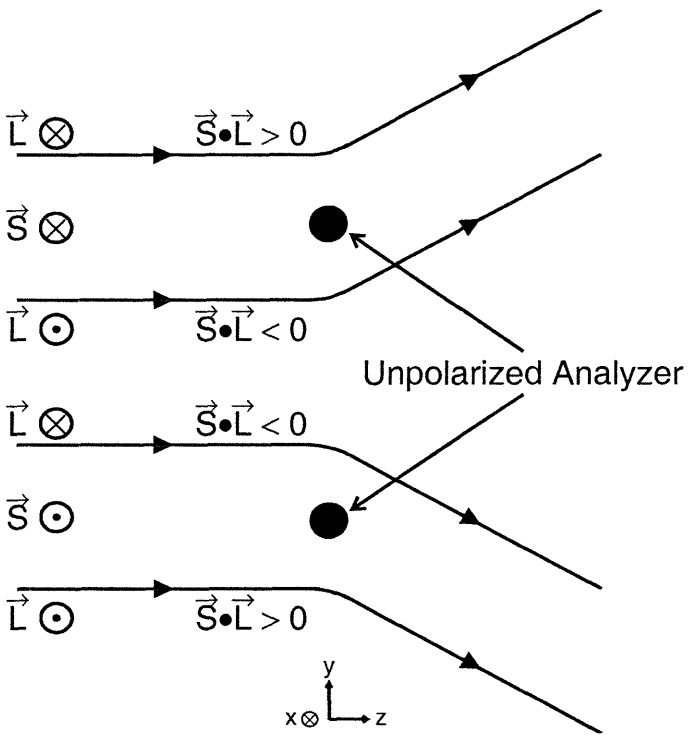

Figure 2-20: Schematic of polarimetry. If the nucleons incident along the $\hat{\mathbf{z}}$ axis are polarized in the $+\hat{\mathbf{x}}$ $(-\hat{\mathbf{x}})$ and the stationary target nucleons are unpolarized, the incident nucleons will scatter preferentially in the $+\hat{\mathbf{y}}$ $(-\hat{\mathbf{y}})$ direction.

larization is restricted to the scattering plane), and the z-component is proportional to G_M^2. It is clear that these results for P_x^h and P_z^h are completely analogous to the beam-target asymmetries $A_\perp$ and $A_{||}$, respectively, in elastic polarized-electron, polarized-nucleon scattering.

These polarization components can be analyzed via a secondary (nuclear) scattering. As is well known (see, e.g., [187]), the nucleon-nucleon potential contains a two-body spin-orbit operator term, $\mathbf{L} \cdot \mathbf{S}$, where (assuming the target nucleon is at rest) $\mathbf{L}$ denotes the angular momentum of the incident nucleon with respect to the target nucleon and $\mathbf{S}$ denotes its spin; therefore, for one event, if $\mathbf{L} \cdot \mathbf{S} > 0$ (< 0), the nuclear force is repulsive (attractive). Suppose, as shown schematically in Fig. 2-20, the incoming nucleons are incident in the $\hat{\mathbf{z}}$ direction and the target nucleons are stationary. Averaged over many events, if the incoming nucleons are polarized in the $+\hat{\mathbf{x}}$ $(-\hat{\mathbf{x}})$ direction and the target nucleons are unpolarized, the incident nucleons will

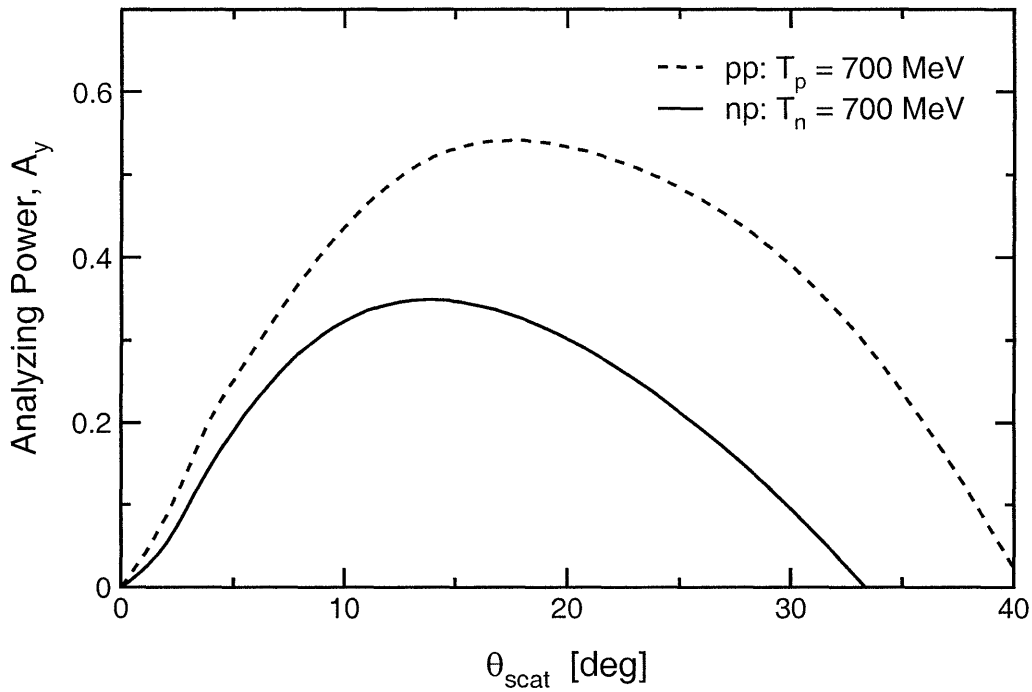

Figure 2-21: Analyzing powers for 700 MeV *pp* and *np* scattering computed as a function of the scattering angle by the SAID [188] code.

scatter preferentially in the $+\hat{\mathbf{y}}$ $(-\hat{\mathbf{y}})$ direction. If we denote the number of nucleons that scatter in the $+\hat{\mathbf{y}}$ $(-\hat{\mathbf{y}})$ direction as N^U (N^D) respectively, the observed up-down scattering asymmetry,

$$\xi = \frac{N^U - N^D}{N^U + N^D} \,, \tag{2.171}$$

should be proportional to the projection of the polarization on the $\hat{\mathbf{x}}$ axis, $\mathbf{P} \cdot \hat{\mathbf{x}}$. The proportionality constant is known as the *analyzing power*, A_y, and is defined to be

$$A_y = \frac{\xi}{\mathbf{P} \cdot \hat{\mathbf{x}}} \,; \tag{2.172}$$

therefore, it is clear that $\mathbf{P} \cdot \hat{\mathbf{x}}$ can be extracted from a measurement of ξ provided A_y is well known and non-zero.

Indeed, Arnold, Carlson, and Gross [160] specifically suggested that a secondary scattering from unpolarized protons should be employed as the analyzing reaction as the analyzing powers for *pp* and *np* scattering are large and well known. To illustrate

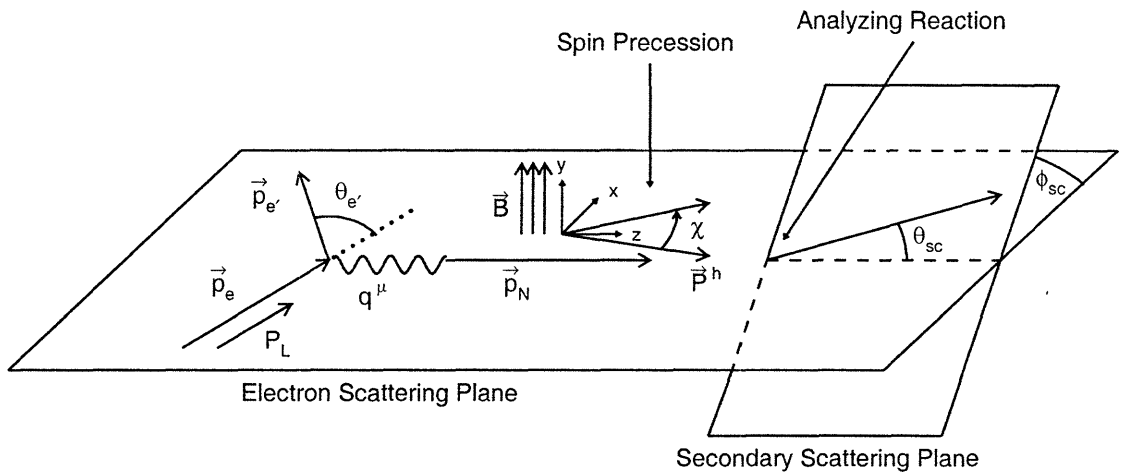

Figure 2-22: Schematic of the recoil polarimetry experiment suggested by Arnold, Carlson, and Gross [160].

this point, the analyzing powers for 700 MeV protons and neutrons as computed by the code SAID [188] are plotted in Fig. 2-21 as a function of the scattering angle. A schematic diagram of Arnold, Carlson, and Gross's proposal is shown in Fig. 2-22, and a description of their proposal is as follows. A beam of longitudinally polarized electrons scatters elastically (quasielastically) from an unpolarized proton (neutron in a deuteron). The electron is detected in a spectrometer, and the polarization of the recoiling proton or neutron is analyzed in coincidence via a secondary elastic scattering from an unpolarized proton (or nucleus) in a polarimeter configured to measure the up-down (i.e., $\hat{\mathbf{y}}$ direction) scattering asymmetry, henceforth, denoted ξ, from the projection of the polarization on the x-axis, $\mathbf{P} \cdot \hat{\mathbf{x}}$. Further, Arnold, Carlson, and Gross suggested that a vertical magnetic field placed ahead of the polarimeter would permit measurements of the up-down scattering asymmetry from different projections of the recoil polarization on the x-axis.

Without such a magnetic field, the up-down scattering asymmetry is only sensitive to P_x^h,

$$\xi = A_y P_x^h = -A_y P_L \frac{2G_E G_M \left[\tau(1+\tau)\right]^{1/2} \tan\frac{\theta_{e'}}{2}}{G_E^2 + \left[\tau + 2\tau(1+\tau)\tan^2\frac{\theta_{e'}}{2}\right] G_M^2}\ ; \qquad (2.173)$$

therefore, given knowledge of A_y, P_L, and G_M, G_E can be extracted from ξ. If,

instead, such a magnetic field is available and the polarization is precessed in the $\hat{\mathbf{x}}$-$\hat{\mathbf{z}}$ plane through an angle χ (as indicated schematically in Fig. 2-22), the measured asymmetry, $\xi(\chi)$, will be sensitive to a combination of P_x^h and P_z^h,

$$\begin{aligned}\xi(\chi) &= A_y \left[P_x^h \cos\chi + P_z^h \sin\chi\right] \ , \\ &= A_y |\mathbf{P}^h| \ \sin(\chi + \delta) \ , \end{aligned} \tag{2.174}$$

where $|\mathbf{P}^h| = \sqrt{(P_x^h)^2 + (P_z^h)^2}$ and

$$\begin{aligned}\tan\delta &\equiv \frac{P_x^h}{P_z^h} \\ &= -\frac{G_E}{G_M} \cos\frac{\theta_{e'}}{2} \left[\tau\left(1 + \tau \sin^2\frac{\theta_{e'}}{2}\right)\right]^{-1/2} \ . \end{aligned} \tag{2.175}$$

If asymmetry measurements are conducted at three or more precession angles and the asymmetries are fitted to Eq. (2.174) with $A_y|\mathbf{P}^h|$ and δ as free parameters, the form factor ratio G_E/G_M can be extracted from the fit result for δ. Alternatively, if asymmetry measurements are only conducted at two different precession angles, χ_1 and χ_2, it can easily be shown that the form factor ratio can be written as

$$\frac{G_E}{G_M} = -\left[\tau\left(1 + \tau \sin^2\frac{\theta_{e'}}{2}\right)\right]^{1/2} \sec\frac{\theta_{e'}}{2} \left[\frac{\sin\chi_1 - \eta \ \sin\chi_2}{\eta \ \cos\chi_2 - \cos\chi_1}\right] \ , \tag{2.176}$$

where $\eta \equiv \xi(\chi_1)/\xi(\chi_2)$ denotes the ratio of the scattering asymmetries for the two spin precession angles. The advantage of measuring the scattering asymmetries at two or more spin precession angles is that the analyzing power and the beam polarization cancel in the G_E/G_M ratio; therefore, systematic uncertainties should be small if the spin precession technique is employed.

To illustrate the spin precession technique for the extraction of the neutron form factors, $\xi(\chi)/A_y$ is plotted as a function of χ in the top panel of Fig. 2-23, and δ is plotted as a function of G_{En} in the bottom panel. These calculations assumed $Q^2 = 1.0$ (GeV/c)^2 and $\theta_{e'} = 25°$; also, for simplicity, we assumed G_{En} is given by the Galster parameterization and G_{Mn} is given by the dipole parameterization.

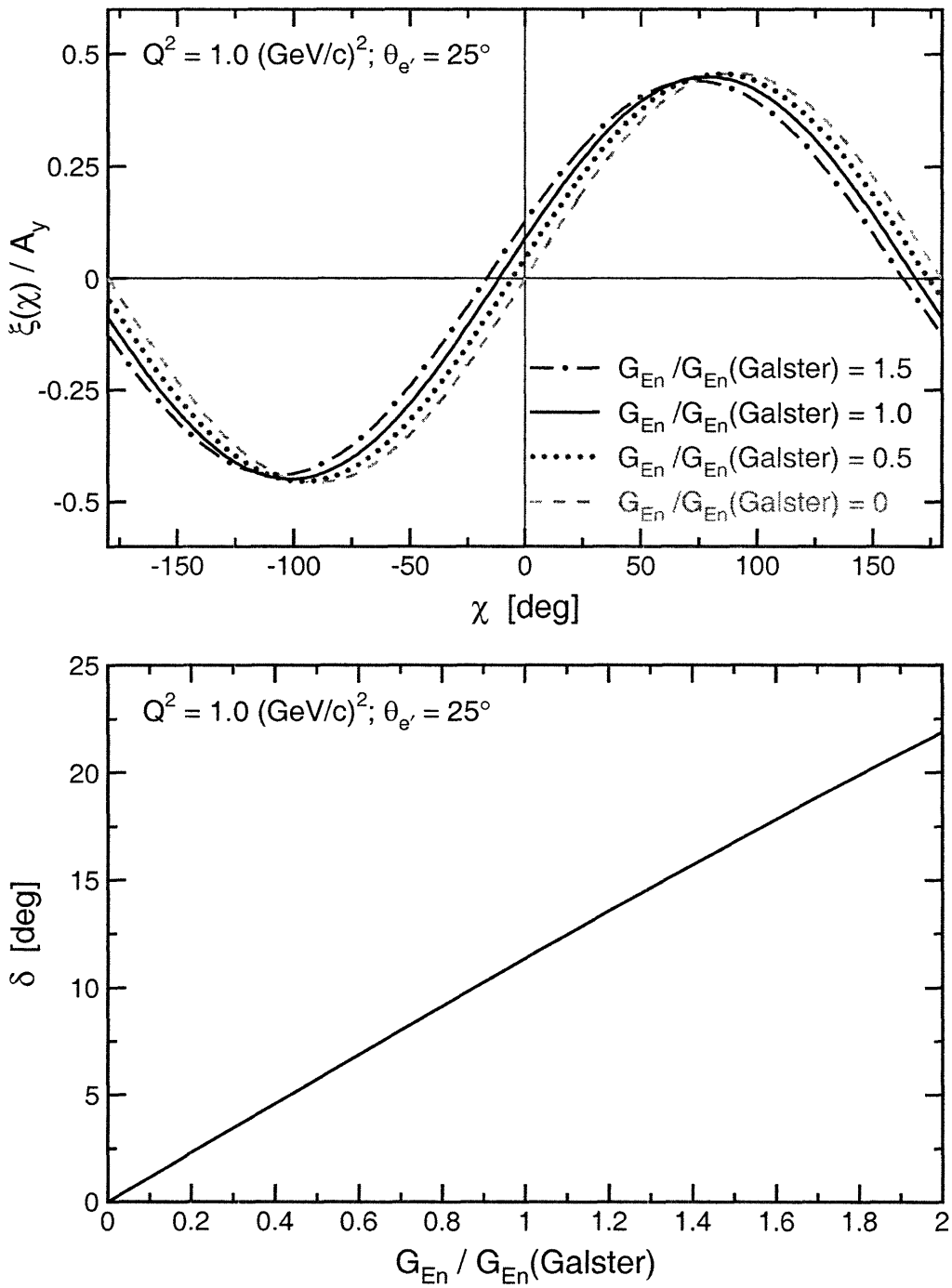

Figure 2-23: (color) $\xi(\chi)/A_y$ plotted as a function of χ (top panel) and δ plotted as a function of G_{En} (bottom panel) for $Q^2 = 1.0$ (GeV/c)^2 and $\theta_{e'} = 25°$.

Measurements of the nucleon form factors via recoil polarimetry are challenging as the second scattering greatly reduces the efficiency of these types of experiments. A precise extraction of the proton form factor ratio from measurements of the scattering asymmetries requires precise knowledge of the proton's deflection and precession in the magnetic field. For the neutron, a precise extraction of the neutron form factor ratio is complicated by the small size of G_{En} relative to G_{Mn} and, as always, the lack of a free neutron target. In what follows, we discuss measurements of the neutron form factor ratio via recoil polarimetry from the quasielastic $^2\mathrm{H}(\vec{e}, e'\vec{n})$ reaction.

2.3.7 Neutron Electric Form Factor via Quasielastic $^2\mathrm{H}(\vec{e},e'\vec{n})^1\mathrm{H}$ Scattering

Following Arnold, Carlson, and Gross's [160] specific proposal for a measurement of G_{En} via recoil polarimetry from the quasielastic $^2\mathrm{H}(\vec{e}, e'\vec{n})^1\mathrm{H}$ reaction, detailed studies of this reaction and its sensitivity to G_{En} were undertaken and reported by Arenhövel [189], Arenhövel, Leidemann, and Tomusiak [166], Rekalo, Gakh, and Rekalo [190], and Laget [174]. In what follows, we briefly outline the formalism that was developed in these references.

For the purposes of this discussion, our notational scheme for kinematics is identical to that employed during our discussion of an extraction of G_{En} from measurements of the beam-target asymmetry A_{ed}^V in quasielastic $^2\vec{\mathrm{H}}(\vec{e}, e'n)$ scattering. For an unpolarized deuteron target, the expression for the five-fold differential coincidence cross section, as given in Eq. (2.137), reduces to

$$\begin{aligned}\frac{\mathrm{d}^5\sigma}{\mathrm{d}E_{e'}\mathrm{d}\Omega_{e'}\mathrm{d}\Omega_{np}^{\mathrm{c.m.}}} &= C[\rho_L f_L + \rho_T f_T + \rho_{LT} f_{LT}\cos\phi + \rho_{TT} f_{TT}\cos 2\phi \\ &\qquad + hP_L\rho'_{LT} f'_{LT}\sin\phi] \\ &\equiv S(h,0,0)\ , \end{aligned} \tag{2.177}$$

where the factor C is, as usual, given in Eq. (2.112), $h = \pm 1$ and P_L denote, respectively, the helicity and polarization of the electron beam, the ρ_i are as previously

given in Eqs. (2.107) through (2.109), and the f_i structure functions are evaluated in the n-p CM frame. For an unpolarized target, the separation of the cross section into an unpolarized and a polarized component is simple,

$$S(h,0,0) = S_0\left[1 + hP_L A_e\right] \ , \tag{2.178}$$

as the electron asymmetry, A_e, is the only polarized contribution to the cross section.

The recoil polarization in the n-p CM frame can be written as

$$\frac{\mathrm{d}^5\sigma}{\mathrm{d}E_{e'}\mathrm{d}\Omega_{e'}\mathrm{d}\Omega_{np}^{\mathrm{c.m.}}}\mathbf{P} = S_0\left(\mathbf{P}^0 + hP_L\mathbf{P}^h\right) \ , \tag{2.179}$$

where, as before, $\mathbf{P}^0$ and $\mathbf{P}^h$ denote, respectively, the helicity-independent and helicity-dependent recoil polarization.

Written in terms of structure functions, the helicity-independent polarization components are

$$P_x^0 = \frac{C}{S_0}\left(\rho_{LT}g_{LT}^x\mathrm{sin}\phi + \rho_{TT}g_{TT}^x\mathrm{sin}2\phi\right) \ , \tag{2.180}$$

$$P_y^0 = \frac{C}{S_0}\left(\rho_L g_L^y + \rho_T g_T^y + \rho_{LT}g_{LT}^y\mathrm{cos}\phi + \rho_{TT}g_{TT}^y\mathrm{cos}2\phi\right) \ , \tag{2.181}$$

$$P_z^0 = \frac{C}{S_0}\left(\rho_{LT}g_{LT}^z\mathrm{sin}\phi + \rho_{TT}g_{TT}^z\mathrm{sin}2\phi\right) \ , \tag{2.182}$$

and the helicity-dependent polarization components are

$$P_x^h = \frac{C}{S_0}\left(\rho'_{LT}g_{LT}^{\prime x,z}\mathrm{cos}\phi + \rho'_T g_T^{\prime x,z}\right) \ , \tag{2.183}$$

$$P_y^h = \frac{C}{S_0}\rho'_{LT}g_{LT}^{\prime y}\mathrm{sin}\phi \ . \tag{2.184}$$

$$P_z^h = \frac{C}{S_0}\left(\rho'_{LT}g_{LT}^{\prime z}\mathrm{cos}\phi + \rho'_T g_T^{\prime z}\right) \ , \tag{2.185}$$

Here, the coordinate system to which the polarization components (of the neutron) are referred in the n-p CM system is defined by

$$\hat{\mathbf{z}} \ \| \ \mathbf{p}_n^{\mathrm{c.m.}} \ , \tag{2.186}$$

$$\hat{\mathbf{y}} \parallel \mathbf{q}^{\text{c.m.}} \times \mathbf{p}_n^{\text{c.m.}} , \tag{2.187}$$

$$\hat{\mathbf{x}} \parallel \hat{\mathbf{y}} \times \hat{\mathbf{z}} . \tag{2.188}$$

Often, this choice of a coordinate system is referred to as the Madison convention [191] for recoil polarization; however, in this thesis, we shall henceforth refer to this coordinate system as the *reaction basis*. It should be noted that the (x, y, z) labels we have employed above for the reaction basis are frequently interchanged with (t, n, ℓ) labels; however, we prefer the (x, y, z) labels as these are the labels employed by Arenhövel. We note that if $\langle \sin\phi \rangle = \langle \sin 2\phi \rangle = 0$, $P_x^0 = P_z^0 = P_y^h = 0$ as we saw for elastic scattering from a nucleon; however, if $\rho_L g_L^y$ or $\rho_T g_T^y$ are non-zero, unlike elastic scattering, P_y^0 will be non-zero.

It is important to realize that the polarization components written above in terms of the structure functions are evaluated in the n-p CM frame; however, experimentalists tend to be interested in the polarization components in the laboratory frame. Assuming non-relativistic kinematics, the spin eigentates (defined relative to the above-defined reaction basis coordinate system) for the neutron in the n-p CM frame and the laboratory frame are simply related by a *rotation* through an angle $(\theta_n^{\text{c.m.}} - \theta_n)$ about the y-axis, where $\theta_n^{\text{c.m.}} = \pi - \Theta_{np}^{\text{c.m.}}$ and θ_n denote, respectively, the neutron's polar angle relative to $\mathbf{q}$ in the n-p CM frame and the laboratory frame, respectively; however, for *relativistic kinematics*, there is a correction such that the actual angle of rotation, the Wigner angle θ_n^W (for the neutron), is given by [192]

$$\theta_n^W = \sin^{-1}\left[\frac{1+\gamma}{\gamma_n^{\text{c.m.}} + \gamma_n} \sin\left(\theta_n^{\text{c.m.}} - \theta_n\right)\right] , \tag{2.189}$$

where γ is as given in Eq. (2.133), $\gamma_n^{\text{c.m.}}$ is as given in Eq. (2.142), and γ_n is as given in Eq. (2.143). From this, it is easy to see that for nonrelativistic boosts (i.e., $\gamma,\ \gamma_n^{\text{c.m.}},\ \gamma_n \sim 1$), we recover the non-relativistic case. As the rotation is about the y-axis, the y-components undergo no change, but the x- and z-components mix according to

$$P_k = \mathcal{R}_{kl}(\theta_n^W) P_l^{\text{c.m.}} , \tag{2.190}$$

where the Wigner rotation matrix is given by

$$\mathcal{R}(\theta_n^W) = \begin{pmatrix} \cos\theta_n^W & 0 & \sin\theta_n^W \\ 0 & 1 & 0 \\ -\sin\theta_n^W & 0 & \cos\theta_n^W \end{pmatrix} . \tag{2.191}$$

An alternative formulation for relativistic spin rotation is presented in Appendix A.

The pioneering study of the influence of G_{En} on the neutron's recoil polarization in $^2\mathrm{H}(\vec{e}, e'\vec{n})^1\mathrm{H}$ was reported by Arenhövel [189] in 1987. Arenhövel concluded that for quasifree emission of the neutron, P_x^h is proportional to G_{En} and is insensitive to FSI, MEC, IC, and the choice of the NN potential. A more detailed study of the $^2\mathrm{H}(\vec{e}, e'\vec{n})^1\mathrm{H}$ reaction reported by Arenhövel, Leidemann, and Tomusiak [166] in 1988 also found that these results apply to P_z^h. Later, these results were independently verified by Rekalo, Gakh, and Rekalo [190] and Laget [174].

To demonstrate the sensitivity of P_x^h to the value of G_{En} and the insensitivity of P_x^h and P_z^h to FSI, MEC, IC, and the choice of the NN-potential, we present several examples of Arenhövel's $^2\mathrm{H}(\vec{e}, e'\vec{n})^1\mathrm{H}$ recoil polarization calculations [181] in Figs. 2-24 through 2-26. The electron kinematics for these calculations are identical to the electron kinematics for the A_{ed}^V calculations we showed previously [i.e., $E_e = 2.326$ GeV, $E_{e'} = 1.718$ GeV, $\theta_{e'} = 23.55^\circ \Longrightarrow Q^2 = 1.136$ (GeV/c)^2].

First, Arenhövel's FSI+MEC+IC calculations of P_x^h for $\phi_{np}^{\mathrm{c.m.}} = 0^\circ$ and 180° are plotted in Fig. 2-24 as a function of $\Theta_{np}^{\mathrm{c.m.}}$ for three values of G_{En} scaled by the Galster parameterization: 0.50, 1.00, and 1.50. Here, just as with A_{ed}^V, we see the strong (nearly linear) sensitivity of P_x^h to the value of G_{En} for quasifree emission of the neutron. The insensitivity of the recoil polarization to FSI, MEC, and IC for quasifree emission is shown in Fig. 2-25; here, we compare Arenhövel's PWBA and FSI+MEC+IC calculations of P_x^h and P_z^h for $\phi_{np}^{\mathrm{c.m.}} = 0^\circ$ and 180°. Again, for quasifree emission, there is little difference between the PWBA and the FSI+MEC+IC calculations. Next, in Fig. 2-26, we compare Arenhövel's FSI+MEC+IC calculations of P_x^h and P_z^h for the Argonne V18 [186], Bonn [185], Nijmegen [135], and Paris [124] NN potentials. Again, for quasifree emission, we see little model dependence. Fi-

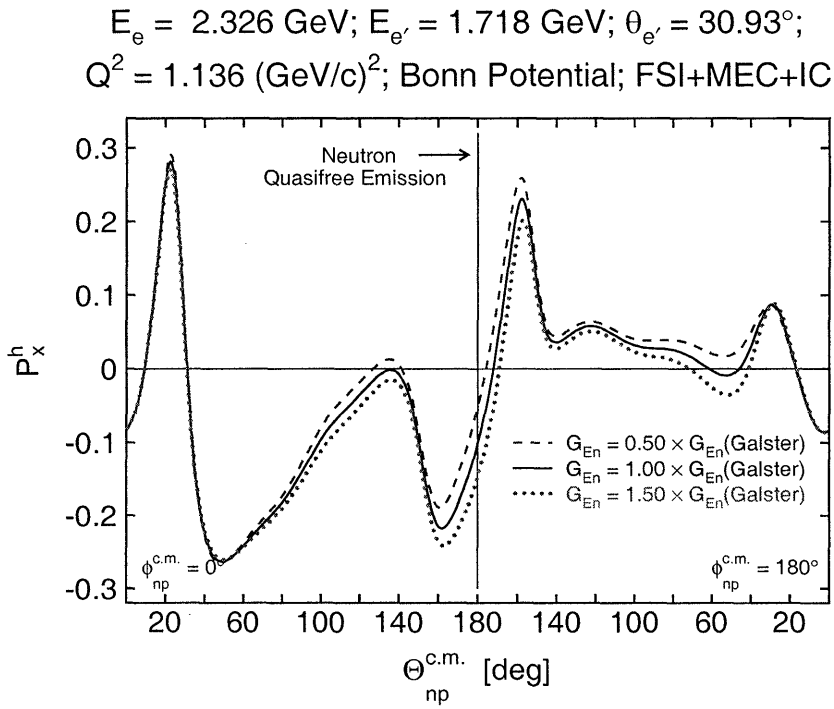

Figure 2-24: (color) Sensitivity of Arenhövel's FSI+MEC+IC calculations of P_x^h to the value of G_{En}.

nally, in Fig. 2-27, we compare Arenhövel's PWBA and FSI+MEC+IC calculations of P_y^0 for $\phi_{np}^{\text{c.m.}} = 0°$ and 180°; here, we see that FSI+MEC+IC induces a non-zero helicity-independent polarization component in the $\hat{\mathbf{y}}$ direction.

The strong sensitivity of P_x^h to the value of G_{En} and the minimal model dependence in quasifree emission led Arenhövel [189] to conclude that "...this process looks very promising for the extraction of G_{En}, even though it will be a difficult experiment due to the necessary polarization analysis of the outgoing neutron". Laget's calculations [174] indicated that the corrections due to FSI, MEC, and IC would be negligible above $Q^2 = 0.3$ (GeV/c)^2 and, on this basis, concluded that "... ^{2}H$(\vec{e}, e'\vec{n})$ [and $^3\vec{\text{He}}(\vec{e}, e'n)$] appeared to be the most direct way to determine the neutron electric form factor".

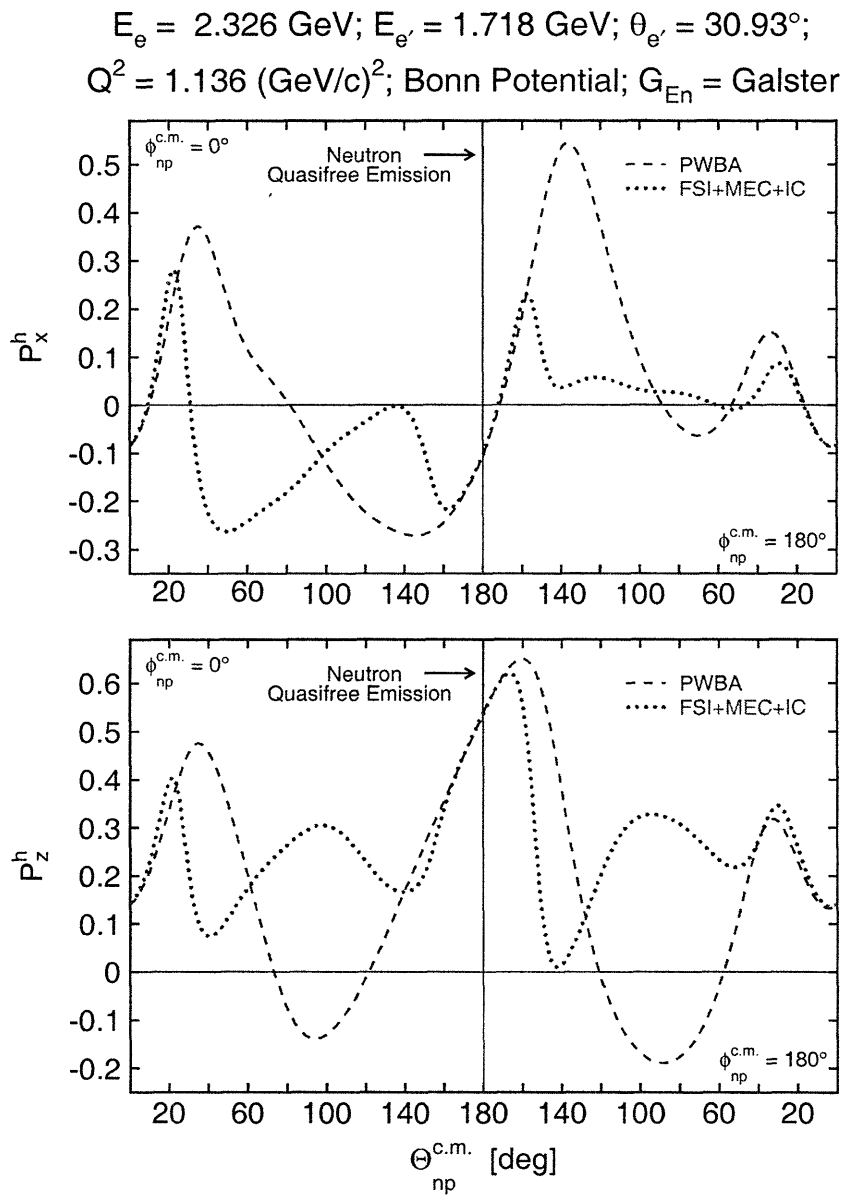

Figure 2-25: (color) Comparison of Arenhövel's PWBA and FSI+MEC+IC calculations of P_x^h and P_z^h.

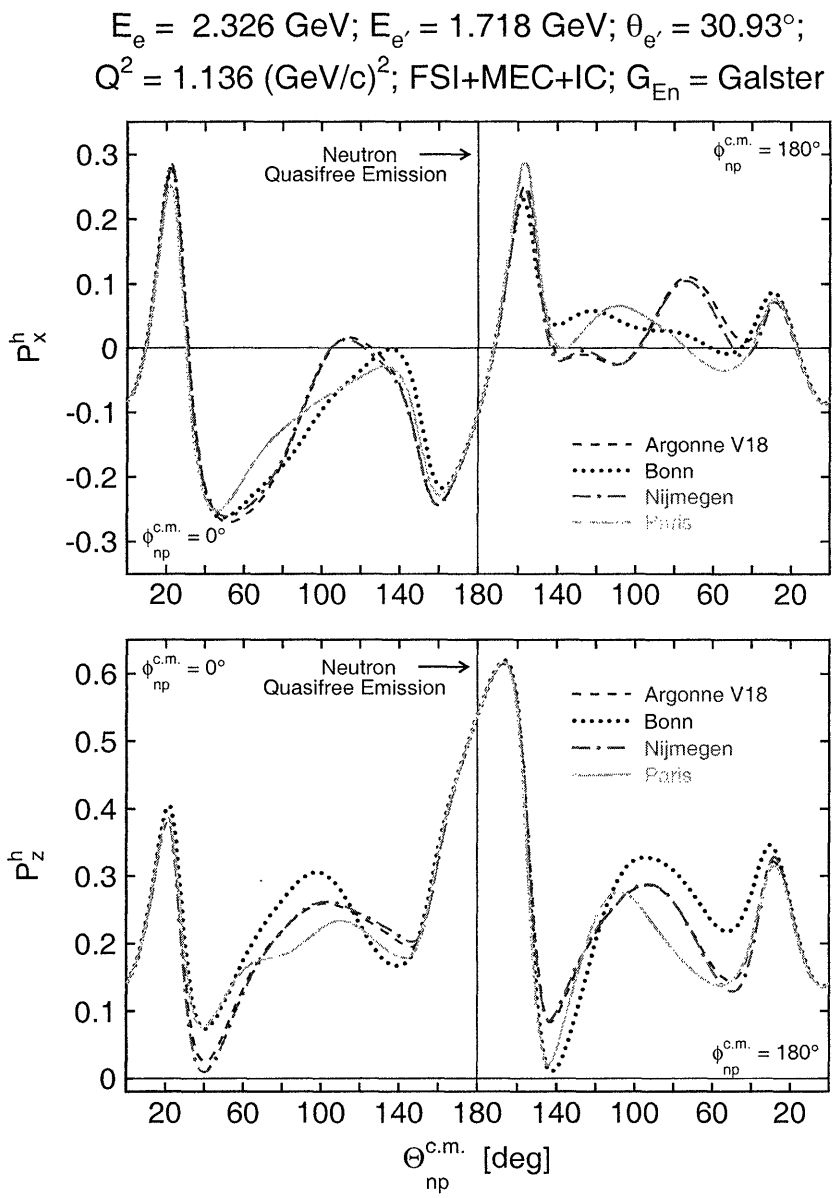

Figure 2-26: (color) Comparison of Arenhövel's FSI+MEC+IC calculations of P_x^h and P_z^h for the Argonne V18, Bonn, Nijmegen, and Paris potentials.

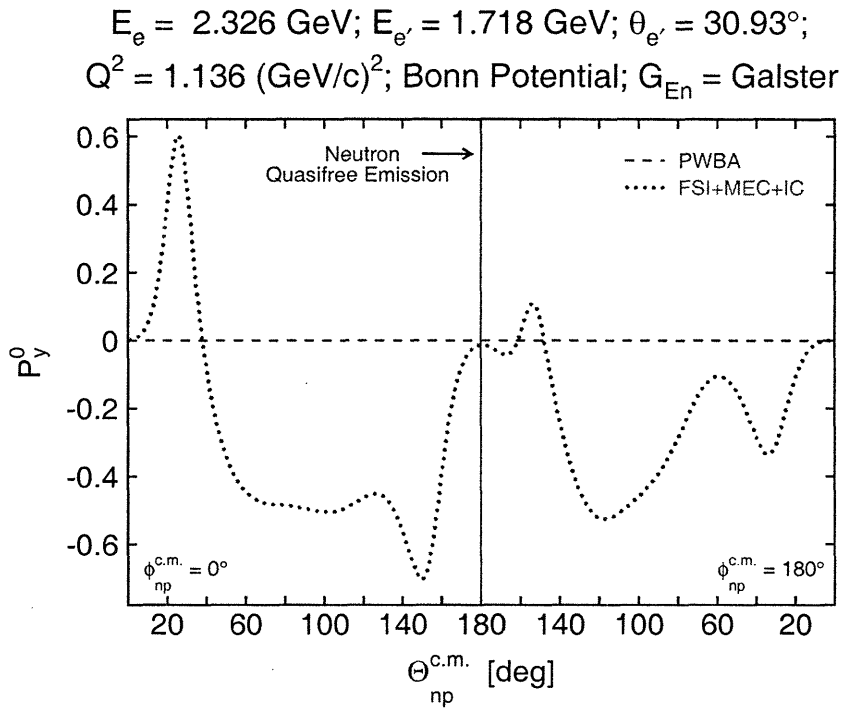

Figure 2-27: (color) Comparison of Arenhövel's PWBA and FSI+MEC+IC calculations of P_y^0.

2.3.8 Neutron Electric Form Factor from Deuteron G_Q Data

As discussed previously, the unpolarized elastic electron-deuteron cross section can be written as

$$\frac{\mathrm{d}\sigma}{\mathrm{d}\Omega_{e'}} = \left(\frac{\mathrm{d}\sigma}{\mathrm{d}\Omega_{e'}}\right)_{\mathrm{Mott}} \left[A(Q^2) + B(Q^2)\tan^2\frac{\theta_{e'}}{2}\right] , \tag{2.192}$$

where $A(Q^2)$ and $B(Q^2)$ can be written in terms of the deuteron's charge, G_C, quadrupole, G_Q, and magnetic, G_M, form factors as

$$A(Q^2) = G_C^2 + \frac{8}{9}\tau_d^2 G_Q^2 + \frac{2}{3}\tau_d(1+\tau_d)G_M^2 , \tag{2.193}$$

$$B(Q^2) = \frac{4}{3}\tau_d(1+\tau_d)^2 G_M^2 . \tag{2.194}$$

Also, as noted previously, G_C and G_Q cannot be separately extracted from a Rosenbluth separation of the unpolarized cross section; an unambiguous separation of all three form factors requires a third observable. The tensor moments, t_{2j}

$(j = 0, 1, 2)$, extracted from recoil polarization measurements in elastic unpolarized-electron, unpolarized-deuteron scattering, are of particular interest as these can be written in terms of G_C, G_Q, and G_M as (see, e.g., [193])

$$t_{20} = -\frac{1}{\sqrt{2}I_0}\left[\frac{8}{3}\tau_d G_C G_Q + \frac{8}{9}\tau_d^2 G_Q^2 + \frac{1}{3}\tau_d\left(1 + 2(1+\tau_d)\tan^2\frac{\theta_{e'}}{2}\right)G_M^2\right] \quad (2.195)$$

$$t_{21} = \frac{2\tau_d}{\sqrt{3}I_0}\sec\frac{\theta_{e'}}{2}\left[\tau_d + \tau_d^2\sin^2\frac{\theta_{e'}}{2}\right]^{1/2} G_M G_Q \ , \quad (2.196)$$

$$t_{22} = -\frac{\tau_d}{2\sqrt{3}I_0}G_M^2 \ , \quad (2.197)$$

where $I_0 \equiv A(Q^2) + B(Q^2)\tan^2\frac{\theta_{e'}}{2}$. Alternatively, the tensor analyzing powers, T_{2j} $(j = 0, 1, 2)$, as measured in elastic unpolarized-electron, polarized-deuteron scattering are also of interest as they, too, can be written in terms of G_C, G_Q, and G_M as[7] (see, e.g., [194])

$$T_{20} = -\frac{1}{\sqrt{2}I_0}\left[\frac{8}{3}\tau_d G_C G_Q + \frac{8}{9}\tau_d^2 G_Q^2 + \frac{1}{3}\tau_d\left(1 + 2(1+\tau_d)\tan^2\frac{\theta_{e'}}{2}\right)G_M^2\right] \quad (2.198)$$

$$T_{21} = \frac{2\tau_d}{\sqrt{3}I_0}\sec\frac{\theta_{e'}}{2}\left[\tau_d + \tau_d^2\sin^2\frac{\theta_{e'}}{2}\right]^{1/2} G_M G_Q \ , \quad (2.199)$$

$$T_{22} = -\frac{\tau_d}{2\sqrt{3}I_0}G_M^2 \ , \quad (2.200)$$

After G_C, G_Q, and G_M have been been separated from $A(Q^2)$, $B(Q^2)$, and $t_{20}(Q^2)$ or $T_{20}(Q^2)$, G_{En} can be extracted from either G_C or G_Q; however, recent theoretical calculations by Schiavilla and Sick [195] demonstrated that the contributions of theoretical uncertainties associated with short-range two-body exchange operators (such as ρ-exchange, etc.) to G_Q are relatively small. As such, Schiavilla and Sick's analysis suggested that an extraction of G_{En} from G_Q should be relatively insensitive to theoretical uncertainties.

[7] Note that the expressions for the t_{2j} are equivalent to those for the T_{2j}.

2.3.9 Historical Overview of Experiments

In this subsection, we present a historical overview of nucleon form factor experiments conducted with polarized electron beams and polarized targets or recoil nucleon polarimeters.

Historical Overview of Polarized Target Experiments

The first polarized measurement of a nucleon form factor with a polarized electron beam was an extraction of G_{En} from a measurement of the beam-target asymmetry $A_\perp$ in inclusive quasielastic $^3\vec{\text{He}}(\vec{e}, e')$ scattering at $Q^2 = 0.16$ (GeV/c)^2; this experiment was conducted at the MIT-Bates Linear Accelerator Center, and the results were reported by Jones-Woodward *et al.* [196] in 1991. Although the significance of this measurement was severely limited by statistics, this experiment did, nevertheless, demonstrate the technical feasibility of using polarized ^{3}He for nucleon form factor measurements. Following this initial study, two additional measurements employing the inclusive quasielastic $^3\vec{\text{He}}(\vec{e}, e')$ reaction were carried out at MIT-Bates: a measurement of G_{En} at $Q^2 = 0.2$ (GeV/c)^2 was reported by Thompson *et al.* [197] in 1992, and the first polarized measurement of G_{Mn} was reported by Gao *et al.* [198] in 1994 at $Q^2 = 0.19$ (GeV/c)^2. Further measurements of G_{Mn} employing the inclusive quasielastic $^3\vec{\text{He}}(\vec{e}, e')$ reaction were conducted at Jefferson Laboratory at Q^2 values ranging from 0.1 to 0.6 (GeV/c)^2 and reported by Xu *et al.* [199, 200] in 2000 and 2003. It should be noted that in all of the above mentioned experiments, G_{En} or G_{Mn} was extracted from an impulse approximation analysis of the appropriate beam-target asymmetry; corrections for FSI, MEC, and IC were not applied to any of these results.

The first extraction of G_{En} from measurements of $A_\perp$ and $A_{||}$ in exclusive quasielastic $^3\vec{\text{He}}(\vec{e}, e'n)$ scattering was conducted at MAMI; this pilot experiment was conducted at $Q^2 = 0.31$ (GeV/c)^2, and the results were reported by Meyerhoff *et al.* [201] in 1994. Again, these results were not corrected for FSI, MEC, and IC; however, this proof-of-principle experiment demonstrated the technical feasibility of a coincidence

experiment with a polarized target. Further extractions of G_{En} from measurements of $A_\perp$ and $A_\parallel$ in exclusive quasielastic $^3\vec{\mathrm{He}}(\vec{e}, e'n)$ scattering were conducted at MAMI at Q^2 values of 0.40 and 0.67 $(\mathrm{GeV}/c)^2$. The measurement reported by Becker *et al.* [202] at $Q^2 = 0.40$ $(\mathrm{GeV}/c)^2$ was extracted from an impulse approximation analysis of $A_\perp$ and $A_\parallel$. Becker *et al.*'s result was corrected for FSI and MEC by Golak *et al.* [203] within a calculational framework that employed Faddeev solutions for the three-nucleon continuum and bound state. First results from the measurement at $Q^2 = 0.67$ $(\mathrm{GeV}/c)^2$ were reported by Rohe *et al.* [204] and recently updated by Bermuth *et al.* [205]. The final result reported by Bermuth *et al.* includes corrections for FSI; however, these corrections were not calculated specifically for the kinematics of this experiment. Instead, Bermuth *et al.* argued the Faddeev calculation by Golak *et al.* [206] at $Q^2 = 0.37$ $(\mathrm{GeV}/c)^2$ could be scaled to their kinematics by comparing the ratio of the elastic *e-p* and *e-n* cross sections at $Q^2 = 0.37$ and 0.67 $(\mathrm{GeV}/c)^2$.

The first measurement of G_{En} using a vector-polarized deuterium target was conducted at NIKHEF at a Q^2 value of 0.21 $(\mathrm{GeV}/c)^2$ and reported by Passchier *et al.* [207] in 1999. To extract G_{En}, A_{ed}^V was measured in quasifree $^2\vec{\mathrm{H}}(\vec{e}, e'n)$ kinematics, and the results were corrected for FSI, MEC, and IC using Arenhövel's formalism that we have already described. The second measurement of G_{En} using a vector-polarized solid deuterated ammonia ($^{15}\mathrm{ND}_3$) external target was conducted at the Jefferson Laboratory at a Q^2 value of 0.495 $(\mathrm{GeV}/c)^2$ and reported by Zhu *et al.* [208] in 2002. Again, G_{En} was extracted from measurements of A_{ed}^V in quasifree $^2\vec{\mathrm{H}}(\vec{e}, e'n)$ kinematics, and these results were, too, corrected for FSI, MEC, and IC using Arenhövel's formalism. Additional measurements at Q^2 values of 0.5 and 1.0 $(\mathrm{GeV}/c)^2$ employing the same experimental arrangement were very recently reported by Warren *et al.* [209]; as with the results reported by Zhu *et al.*, the Warren *et al.* results were corrected for FSI, MEC, and IC using Arenhövel's formalism. Before proceeding to discuss recoil polarimetry experiments, we note that, as of this writing, there have been no polarized target measurements of the proton form factors.

Historical Overview of Recoil Polarimetry Experiments

The pioneering recoil polarimetry experiment, conducted at MIT-Bates, was a measurement of G_{En} in quasifree $^2\mathrm{H}(\vec{e}, e'\vec{n})$ kinematics at $Q^2 = 0.255$ (GeV/c)^2 that was reported by Eden *et al.* [210] in 1994. The x-component of the recoil neutron's polarization was analyzed via np scattering in a stand-alone neutron polarimeter that was designed and installed specifically for this experiment [211]. Although the significance of this measurement was limited due to low statistics, this experiment demonstrated the technical feasibility of the recoil polarimetry technique. The first recoil polarimetry measurement of the proton form factors was also conducted at MIT-Bates; here, the polarization of the recoil proton in elastic $^1\mathrm{H}(\vec{e}, e'\vec{p})$ scattering was analyzed via scattering from carbon in a polarimeter that was installed in the focal plane of a magnetic spectrometer. The results from this experiment at Q^2 values of 0.38 and 0.50 (GeV/c)^2 were reported by Milbrath *et al.* [212] in 1998.

Measurements of G_{En} via recoil polarimetry from the quasielastic $^2\mathrm{H}(\vec{e}, e'\vec{n})$ reaction were conducted at MAMI at Q^2 values of 0.15 and 0.34 (GeV/c)^2 and reported, respectively, by Ostrick *et al.* [213] and Herberg *et al.* [214] in 1999. Here, as at MIT-Bates, the polarization of the recoil neutron was analyzed via np scattering in a polarimeter; further, in this experiment, a vertical dipole field placed ahead of the polarimeter permitted, as first suggested by Arnold, Carlson, and Gross [160], measurements of P_x^h and, for the first time (for the neutron), of P_z^h. The first high Q^2 recoil polarimetry measurements of the proton form form factors were conducted at the Jefferson Laboratory at Q^2 values ranging from 0.5 to 3.5 (GeV/c)^2 and reported by Jones *et al.* [215] in 2000. As in the experiment at MIT-Bates, the recoil proton's polarization was analyzed via scattering from carbon in a polarimeter installed in the focal plane of a magnetic spectrometer. In a subsequent experiment at the Jefferson Laboratory employing essentially the same experimental configuration, the proton form factor ratio measurements were extended to $Q^2 = 5.6$ (GeV/c)^2 and reported by Gayou *et al.* [216] in 2002. An additional low Q^2 recoil polarimetry measurement of the proton form factor ratio at $Q^2 = 0.4$ (GeV/c)^2 was conducted at MAMI and

reported in 2001 by Pospischil *et al.* [217]; as in the experiments at MIT-Bates and the Jefferson Laboratory, the recoil proton's polarization was analyzed via scattering from carbon in a polarimeter installed in the focal plane of a magnetic spectrometer.

The highest Q^2 experimental polarized results for G_{En} to date were obtained via recoil polarimetry from the quasielastic $^2\mathrm{H}(\vec{e}, e'\vec{n})^1\mathrm{H}$ reaction at three Q^2 values of 0.45, 1.13, and 1.45 $(\mathrm{GeV}/c)^2$; these measurements, conducted at the Jefferson Laboratory by the E93-038 collaboration and reported by Madey *et al.* [218], were recently published, and the description of this experiment and the analysis of the data will constitute the remainder of this thesis.

G_{En} from Deuteron G_Q Data

Finally, for the first time, Schiavilla and Sick [195] extracted G_{En} from a theoretical analysis of deuteron quadrupole form factor, G_Q, data. The world's data on $A(Q^2)$, $B(Q^2)$, $t_{20}(Q^2)$, and $T_{20}(Q^2)$ were analyzed; data for $A(Q^2)$ and $B(Q^2)$ exist for Q^2 values extending to $Q^2 \sim 2.5$ $(\mathrm{GeV}/c)^2$, but the current range of t_{20} and T_{20} data restricted the analysis to $Q^2 = 1.64$ $(\mathrm{GeV}/c)^2$. In order to determine G_{En}, the results obtained with different NN potentials were averaged, and the theoretical uncertainties associated with the choice of the NN potential were combined with the experimental uncertainties on $A(Q^2)$, $B(Q^2)$, $t_{20}(Q^2)$, and $T_{20}(Q^2)$.

Chronological Summary

A complete chronological summary of polarized nucleon form factor measurements may be found in Table 2.4. There, for each measurement, we list the reference, the facility at which the experiment was conducted, the kinematic reaction, the range of Q^2, and the extracted quantities.

Reference(s)	Facility	Reaction	Q^2 [(GeV/c)^2]	Extracted Quantities			Note(s)
Jones-Woodward (1991) [196]	MIT-Bates	$^3\vec{\mathrm{He}}(\vec{e},e')$	0.16	$A_\perp$	$\rightarrow$	G_{En}	1, 2
Thompson (1992) [197]	MIT-Bates	$^3\vec{\mathrm{He}}(\vec{e},e')$	0.2	$A_\perp$, $A_\parallel$	$\rightarrow$	G_{En}	1, 2
Meyerhoff (1994) [201]	MAMI	$^3\vec{\mathrm{He}}(\vec{e},e'n)$	0.31	$A_\perp$, $A_\parallel$	$\rightarrow$	G_{En}	1, 2
Gao (1994) [198]	MIT-Bates	$^3\vec{\mathrm{He}}(\vec{e},e')$	0.20	$A_\parallel$	$\rightarrow$	G_{Mn}	1
Eden (1994) [210]	MIT-Bates	$^2\mathrm{H}(\vec{e},e'\vec{n})$	0.255	P_x^h	$\rightarrow$	G_{En}	3, 4
Milbrath (1998) [212]	MIT-Bates	$^1\mathrm{H}(\vec{e},e'\vec{p})$	0.38, 0.50	P_x^h/P_z^h	$\rightarrow$	G_{Ep}/G_{Mp}	
Ostrick (1999), Herberg (1999) [213,214]	MAMI	$^2\mathrm{H}(\vec{e},e'\vec{n})$	0.15, 0.34	P_x^h, P_z^h	$\rightarrow$	G_{En}	2, 3
Becker (1999) [202]	MAMI	$^3\vec{\mathrm{He}}(\vec{e},e'n)$	0.40	$A_\perp$, $A_\parallel$	$\rightarrow$	G_{En}	2, 5
Passchier (1999) [207]	NIKHEF	$^2\vec{\mathrm{H}}(\vec{e},e'n)$	0.21	$A^V_{ed,\perp}$	$\rightarrow$	G_{En}	2, 3
Rohe (1999) [204], Bermuth (2003) [205]	MAMI	$^3\vec{\mathrm{He}}(\vec{e},e'n)$	0.67	$A_\perp$, $A_\parallel$	$\rightarrow$	G_{En}	6, 7
Jones (2000) [215]	JLab	$^1\mathrm{H}(\vec{e},e'\vec{p})$	0.5 – 3.5	P_x^h/P_z^h	$\rightarrow$	G_{Ep}/G_{Mp}	
Xu (2000) [199], Xu (2003) [200]	JLab	$^3\vec{\mathrm{He}}(\vec{e},e')$	0.1 – 0.6	$A_\parallel$	$\rightarrow$	G_{Mn}	1
Zhu (2001) [208]	JLab	$^2\vec{\mathrm{H}}(\vec{e},e'n)$	0.495	A^V_{ed}	$\rightarrow$	G_{En}	2, 3
Pospischil (2001) [217]	MAMI	$^1\mathrm{H}(\vec{e},e'\vec{p})$	0.4	P_x^h/P_z^h	$\rightarrow$	G_{Ep}/G_{Mp}	
Schiavilla and Sick (2001) [195]	—	—	0.00 – 1.65	G_Q, t_{20}	$\rightarrow$	G_{En}	8
Gayou (2002) [216]	JLab	$^1\mathrm{H}(\vec{e},e'\vec{p})$	3.5 – 5.6	P_x^h/P_z^h	$\rightarrow$	G_{Ep}/G_{Mp}	
Madey (2003) [218]	JLab	$^2\mathrm{H}(\vec{e},e'\vec{n})$	0.45, 1.13, 1.45	P_x^h, P_z^h	$\rightarrow$	G_{En}	**this thesis**
Warren (2003) [209]	JLab	$^2\vec{\mathrm{H}}(\vec{e},e'n)$	0.5, 1.0	A^V_{ed}	$\rightarrow$	G_{En}	3, 9

[1] Assumed the impulse approximation.
[2] Assumed the dipole parameterization for G_{Mn}.
[3] Corrected for FSI, MEC, and IC by averaging Arenhövel *et al.*'s [166,177–179] FSI+MEC+IC calculations over the acceptance.
[4] Assumed $G_{Mn}/\mu_n G_D = 1.03 \pm 0.04$ at $Q^2 = 0.255$ (GeV/c)^2 [97].
[5] Corrections for FSI and MEC calculated by Golak *et al.* [203].
[6] Assumed $G_{Mn}/\mu_n G_D = 1.04 \pm 0.01$ at $Q^2 = 0.67$ (GeV/c)^2 [105].
[7] Corrections for FSI estimated by scaling the calculations of Golak *et al.* [206] at $Q^2 = 0.37$ (GeV/c)^2 to 0.67 (GeV/c)^2.
[8] Theoretical analysis of deuteron quadrupole form factor, G_Q, data and tensor polarization, t_{20}, data.
[9] Assumed $G_{Mn}/\mu_n G_D = 1.007 \pm 0.005$ and 1.072 ± 0.014 at $Q^2 = 0.5$ and 1.0 (GeV/c)^2, respectively [105].

Table 2.4: Chronological summary of published polarized nucleon form factor measurements.

2.3.10 Comparison of Unpolarized and Polarized Results for Nucleon Form Factors

Proton Form Factors

In Fig. 2-28, we compare polarized results for the proton form factor ratio, $\mu_p G_{Ep}/G_{Mp}$, [212, 215–217] with the unpolarized results [39, 41, 44, 48, 51, 54, 60, 62] shown previously in Fig. 2-7; clearly, there are large discrepancies between the polarized and unpolarized results. Whereas the older unpolarized results (although somewhat imprecise) suggested G_{Ep} and G_{Mp} scale similarly over the range of accessed Q^2 values, the recent polarized results have revealed that the proton form factor ratio decreases nearly linearly with Q^2 for $Q^2 \gtrsim 1$ (GeV/c)^2. [It should be noted that the unpolarized results reported by Bartel *et al.* [48] in 1973 suggested a decrease in the ratio, but later unpolarized results in this Q^2 range contradicted these results.]

The (strong) deviation of the polarized results from unity shocked the nuclear physics community as these results implied that the previously held notion that the proton's charge and magnetization distributions are similar was no longer a valid assumption. This discrepancy has generated an enormous amount of recent experimental and theoretical interest. In terms of the experimental results, the older unpolarized results extracted from cross section measurements have recently been reexamined by Arrington [219, 220]. Arrington performed a global reanalysis of the results extracted from cross section measurements. The existing data were scrutinized for the inclusion of bad data points and/or improper constraints on the relative normalization of data sets, radiative corrections were updated for some of the older measurements, some normalization uncertainties were updated, and several results were updated to include the final published values for the cross sections. On the basis of this global analysis, Arrington concluded that the unpolarized results are all internally consistent, but are still in significant discrepancy with the polarized results. The results of this global analysis are plotted in Fig. 2-28, and the disagreement with the polarized results is obvious.

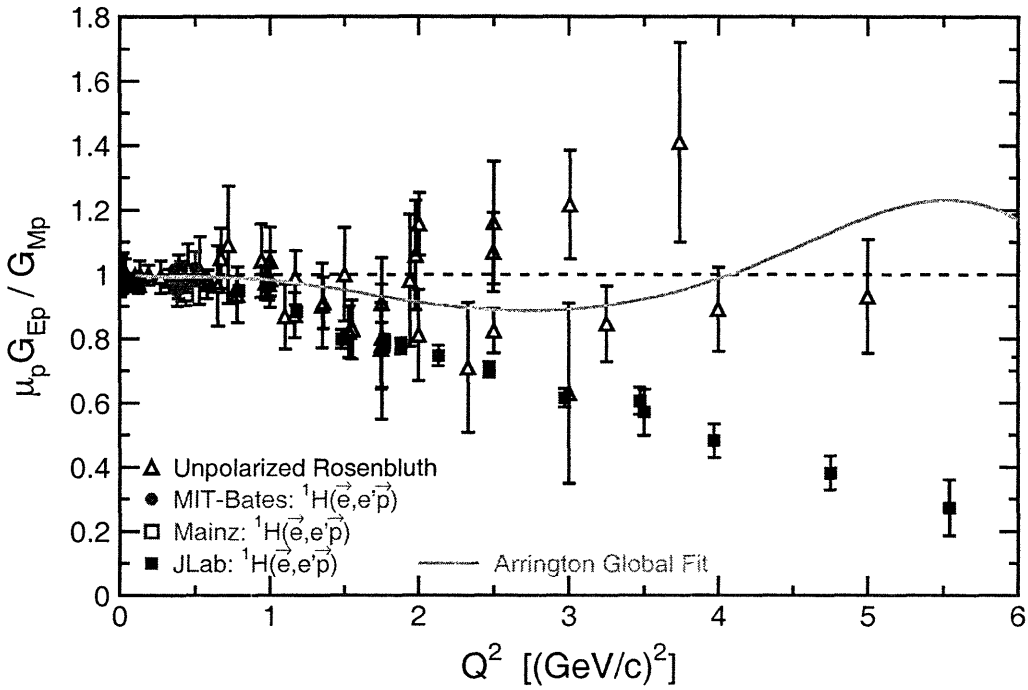

Figure 2-28: (color) Comparison of polarized results for the proton form factor ratio, $\mu_p G_{Ep}/G_{Mp}$, with the unpolarized results. The result of Arrington's [219, 220] global analysis of the unpolarized results extracted from cross section measurements is shown as the solid green curve.

Theoretically, higher-order two-photon exchange[8] and its effect on elastic electron-proton scattering has been considered recently by number of different authors (see, e.g., Afanasev, Akushevich, and Merenkov [221]; Guichon and Vanderhaeghen [222]; and Blunden, Melnitchouk, and Tjon [223]) in an attempt to understand this discrepancy from a theoretical point of view. Afanasev, Akushevich, and Merenkov calculated the effects of two-photon exchange for elastic electron-proton scattering at Q^2 values comparable to those where the discrepancy becomes significant and outlined a number of different experimental approaches for testing the importance of two-photon exchange [i.e., (i) measurement of a single-spin beam asymmetry, and (ii) measurement of a single-spin target asymmetry or recoil polarization induced by an unpolarized electron beam]. Guichon and Vanderhaeghen went so far as to claim that the discrepancy can be explained by a two-photon exchange correction which does

[8]Two-photon exchange in this context does not refer to radiative corrections, but, instead, to the geniune exchange of two hard photons between the electron and the nucleon.

not destroy the linearity of the Rosenbluth method. Such a reconciliation was also reported by Blunden, Melnitchouk, and Tjon; they found that the corrections are small in magnitude but are subject to a strong angular dependence at a fixed value of Q^2.

Other than questions regarding experimental error in either the cross section or recoil polarization measurements, two-photon exchange is currently the best hypothesis for an explanation of this discrepancy, and it is important that experiments designed to search for two-photon effects, such as those proposed by Afanasev, Akushevich, and Merenkov, are conducted. To date, both the experimental results and theoretical hypotheses remain highly controversial and of great interest to the nuclear physics community.

Neutron Form Factors

Turning to the neutron form factors, Fig. 2-29 compares the polarized and the most recent unpolarized results for G_{Mn}; here, we show only results in the $Q^2 < 1$ $(\mathrm{GeV}/c)^2$ region as measurements of G_{Mn} that have been conducted with polarized electron beams are currently limited to Q^2 values below 0.6 $(\mathrm{GeV}/c)^2$. The polarized results appear to agree better with the unpolarized results extracted from cross section measurements employing external neutron detection efficiency calibrations than with those employing *in situ* calibration techniques.

Finally, the status of polarized results for G_{En} is shown in Fig. 2-30. Due to the poor quality of the results for G_{En} extracted from unpolarized quasielastic cross section measurements and the large model dependence associated with the results extracted from elastic cross section measurements, we do not compare the unpolarized and polarized results for G_{En}. Also, due to their large error bars, we have omitted the early polarized results reported by Jones-Woodward *et al.* [196] and Thompson *et al.* [197]; in addition, the results of Meyerhoff *et al.* [201] are omitted as these were not corrected for nuclear physics effects. It is readily apparent that, relative to our knowledge of the other nucleon form factors, G_{En} remains poorly determined. Prior to the release of the new data reported by Madey *et al.* [218] and Warren *et al.* [209],

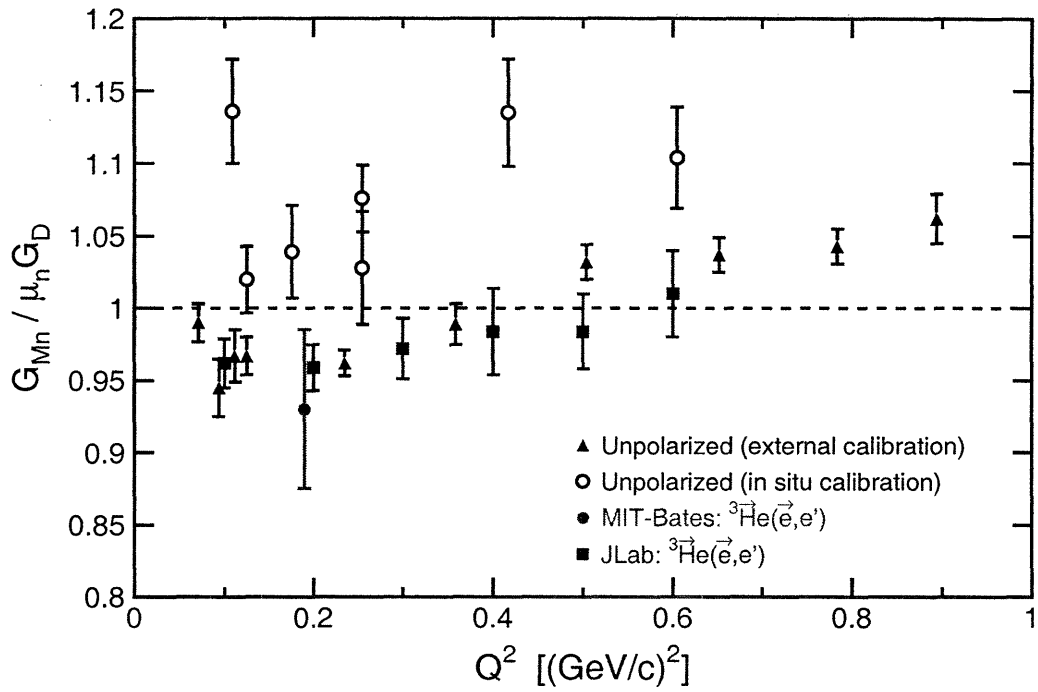

Figure 2-29: (color) Comparison of polarized results for $G_{Mn}/\mu_n G_D$ with the most recent unpolarized results extracted from quasielastic electron-deuteron cross section measurements using *in situ* and external neutron detection efficiency calibration techniques.

experimental polarized measurements of G_{En} were limited to $Q^2 = 0.67$ (GeV/c)^2; these new data will be presented later in this thesis. Schiavilla and Sick's [195] extraction of G_{En} from a theoretical analysis of the deuteron G_Q and t_{20} data is limited by the available range of t_{20} and T_{20} data to $Q^2 = 1.64$ (GeV/c)^2. These data are plotted versus the Galster parameterization; as we stated previously, the agreement between the modern data and the Galster parameterization is certaintly fortuitous and, indeed, somewhat remarkable.

2.3.11 Expected and Future Unpolarized and Polarized Results for Nucleon Form Factors

The dramatic decrease observed in the proton form factor ratio remains controversial and of interest. Further measurements of G_{Ep}/G_{Mp} via recoil polarimetry at the Jefferson Laboratory [224] are planned to extend the range of polarized measurements

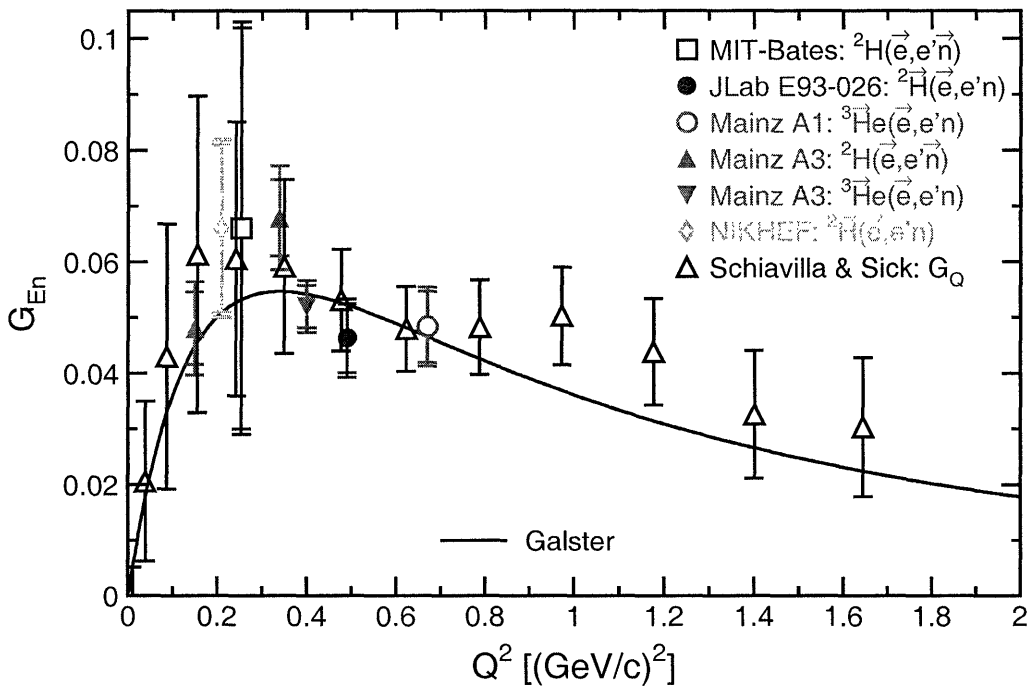

Figure 2-30: (color) Current status of polarized results for G_{En}. The Galster parameterization is shown as the solid line. The higher Q^2 results recently reported by Madey *et al.* [218] and Warren *et al.* [209] will be presented later in this thesis.

to $Q^2 = 9$ (GeV/c)^2; this experiment expects to take data in 2006. An unpolarized "super-Rosenbluth" measurement of the proton form factors [225] was recently completed (2002) at Jefferson Laboratory. In this experiment (elastic unpolarized-electron, unpolarized-proton scattering), recoil protons were detected simultaneously in two magnetic spectrometers centered at different Q^2 values for a fixed value of the beam energy. Simultaneous measurements of the cross section at two values of Q^2 permits an extraction of the form factors from cross section ratios; the advantage of this technique is that the results are independent of target thickness and beam intensity (i.e., luminosity) and are relatively insensitive to beam energy uncertainties. Also, detection of the recoil proton instead of the scattered electron reduces the size of the radiative corrections. Nevertheless, despite these advantages, the difficulties inherent to a cross section measurement are still present, and the experimental acceptance must be modeled very carefully.

The first polarized target measurement of the proton form factor ratio [226] will

soon be conducted at MIT-Bates following commissioning of the BLAST (Bates Large Acceptance Spectrometer Toroid) detector; the large acceptance of the BLAST detector will permit measurements of the form factor ratio for a range of Q^2 values below approximately 1 $(\mathrm{GeV}/c)^2$. Also, a separate low Q^2, $0.005 < Q^2 < 0.088$ $(\mathrm{GeV}/c)^2$, measurement of the proton form factor ratio using a laser-driven polarized hydrogen target [227] will permit a precise extraction of the proton charge radius; the goal of this experiment is to provide timely new data for the still controversial value of the proton's root mean square charge radius. Also, an experiment at PSI (see, e.g., [228]) is underway to measure the Lamb shift in muonic hydrogen. We hope that careful analyses of the data from both of these experiments will yield agreeing and definitive results for this fundamental property of the proton.

An extensive series of polarized measurements of G_{En} has recently been completed at Jefferson Laboratory and Mainz. At MAMI, recoil polarimetry measurements by the A1 collaboration at $Q^2 = 0.3$, 0.6, and 0.8 $(\mathrm{GeV}/c)^2$ using the same experimental arrangement as Ostrick *et al.* [213] and Herberg *et al.* [214] were completed recently, and results are expected soon. Finally, new measurements of G_{En} using polarized targets will soon be conducted at MIT-Bates and at the Jefferson Laboratory. The BLAST collaboration will measure G_{En} with a polarized deuterium target, and data taking will soon commence. Finally, the Jefferson Laboratory E02-013 collaboration [229] will use a polarized ^{3}He target to extend the range of polarized measurements of G_{En} to $Q^2 = 3.4$ $(\mathrm{GeV}/c)^2$; this experiment is expected to take data in 2005.

Last, an experiment designed to extract G_{Mn} from measurements of the unpolarized quasielastic $^2\mathrm{H}(e, e'n)$ and $^2\mathrm{H}(e, e'p)$ cross section ratio was recently conducted with the CLAS detector at the Jefferson Laboratory [230]. The results from this experiment will span a wide range of Q^2 values from 0.4 to 4.8 $(\mathrm{GeV}/c)^2$ and promise to greatly increase our understanding of this form factor.

A listing of completed (but unpublished) and future approved measurements of the measurements of the nucleon form factors is summarized in Table 2.5. There, for each experiment, we list the facility at which the experiment was/will be conducted, the

Experiment	Reaction	Q^2 [(GeV/c)^2]	Quantities	Year/Status
JLab E94-017	^{2}H$(e,e'n)/^2$H$(e,e'p)$	0.4 – 4.8	G_{Mn}	2000/Preliminary
JLab E01-001	^{1}H(e,p)	1.45, 3.20, 4.90	G_{Ep}, G_{Mp}	2002/Preliminary
MAMI A1	^{2}H$(\vec{e},e'\vec{n})$	0.3, 0.6, 0.8	G_{En}	2002/Preliminary
MIT-Bates BLAST	$^1\vec{\text{H}}(\vec{e},e'p)$	< 1.0	G_{Ep}/G_{Mp}	2003, 2004
MIT-Bates BLAST	$^2\vec{\text{H}}(\vec{e},e'n)$	< 1.0	G_{En}	2003, 2004
JLab E02-013	$^3\vec{\text{He}}(\vec{e},e'n)$	1.3, 2.4, 3.5	G_{En}	2005
JLab E01-109	^{1}H$(\vec{e},e'\vec{p})$	4.2, 7.5, 9.0	G_{Ep}/G_{Mp}	2006

Table 2.5: Summary of completed (but as of yet unpublished) and future approved measurements of the nucleon form factors.

kinematic reaction, the range of Q^2, the quantities that have been/will be extracted, and the status of the experiment.

2.4 Theoretical Calculations of Nucleon Form Factors

In this section, we provide brief overviews of a number of different recent approaches for theoretical calculations of the nucleon form factors. A complete comprehensive survey of all techniques that have been employed over the past several decades for such calculations is beyond the scope of this thesis; therefore, we will mostly restrict our discussion to those recent calculations that tend to agree well with the existing experimental data. We discuss the essential ingredients for each type of calculation and then compare the results of these calculations with the existing experimental data; the theoretical calculations discussed below are presented in no particular order. We note that excellent overviews of this subject have been given by Gao [64] and Petratos [231]; some of our discussion below follows those given in these references.

2.4.1 High Q^2 Scaling and Perturbative QCD Predictions

As stated in Chapter 1, at very large values of Q^2, the strong coupling constant $\alpha_s \rightarrow 0$, and QCD can be solved using perturbative techniques as the theory becomes asymptotically free; such an approach is, appropriately, termed perturbative Quantum

Chromodynamics (pQCD).

High Q^2 Predictions from Dimensional Scaling Laws

In a seminal analysis reported in 1975, Brodsky and Farrar [232] employed dimensional scaling laws to derive predictions for the behavior of the form factors in the asymptotic limit. According to the dimensional scaling law, the asymptotic behavior for fixed angle scattering will satisfy the rule [232]

$$\frac{\mathrm{d}\sigma}{\mathrm{d}\Omega}(AB \to CD) \sim s^{-n+2}\, f(Q^2/s)\ , \tag{2.201}$$

where s is the usual Mandelstam variable and the integer n denotes the number of lepton, photon, and elementary quark fields carrying a finite fraction of the momentum of particles A, B, C, and D. As argued by Brodsky and Farrar, this rule leads to the following prediction for the (helicity-conserving) Dirac form factor in elastic electron-hadron scattering,

$$F_1 \sim (Q^2)^{1-n_h}\ , \tag{2.202}$$

where n_h denotes the number of fields in the hadron; therefore, in the quark model, $F_1 \sim Q^{-2}$ for mesons and $F_1 \sim Q^{-4}$ for baryons. The (helicity-flipping) Pauli form factor F_2 was predicted to scale as Q^{-6} instead of Q^{-4} as a consequence of *hadron helicity conservation.*[9]

It then immediately follows that these scaling laws predict

$$Q^2 \frac{F_2}{F_1} = Q^2\, \frac{1 - G_E/G_M}{\tau + G_E/G_M} \ \to\ \text{constant} \tag{2.203}$$

in the high Q^2 limit.

[9]Hadron helicity conservation arises from the vector (helicity-conserving) nature of the quark-gluon interaction, the assumption of quark helicity conservation at high energies, and the neglect of non-zero orbital angular momentum quark states [64].

Perturbative QCD Predictions

The scaling law for Q^2F_2/F_1 given above was not derived from a true pQCD calculation; however, this scaling law was confirmed by Lepage and Brodsky [233, 234] in 1979 and 1980 in a pQCD analysis of high Q^2 exclusive processes.

Their theoretical analysis of the nucleon's magnetic form factor at high Q^2 was conducted within the following physical picture in the Breit frame. A nucleon, pictured as a composite system of three valence quarks, each carrying some fraction x_i of the nucleon's momentum (i.e., $\sum x_i = 1$), was assumed to interact with a highly virtual photon; the amplitude for the nucleon to absorb the virtual photon and emerge as a final-state nucleon is the form factor. This form factor is then the product of three amplitudes: (i) the amplitude for finding the three-quark valence state in the nucleon, (ii) the amplitude for this quark state to scatter with the photon producing three quarks in the final state with approximately co-linear momenta, and (iii) the amplitude for the final three-quark valence state to reform a nucleon. The contributions of the more complicated Fock states in the nucleon (e.g., $qqqq\bar{q}$, $qqqg$, ... , states) were found to be unimportant at high Q^2. Within this picture, Lepage and Brodsky then found that at very large Q^2 the magnetic form factor can be written as

$$G_M \rightarrow \frac{32\pi^2}{9} C^2 \frac{\alpha_s^2(Q^2)}{Q^4} \left(\log \frac{Q^2}{\Lambda^2} \right)^{4/3\beta} (e_{\parallel} - e_{-\parallel}) \, , \tag{2.204}$$

where C is a generally unknown constant, Λ is the QCD momentum scale parameter, $\beta = 11 - \frac{2}{3} n_{\text{flavor}}$, and $e_{\parallel}$ ($e_{-\parallel}$) is the mean total charge of quarks with helicity parallel (antiparallel) to the nucleon's helicity.[10] A similar result was found for the electric form factor G_E; therefore, this more careful pQCD calculation verified the earlier prediction based solely on dimensional scaling laws.

[10] For protons and neutrons, $e^p_{\parallel} = 1$, $e^p_{-\parallel} = 0$, and $e^n_{\parallel} = e^n_{-\parallel} = -\frac{1}{3}$. Assuming isospin symmetry ($C_p = C_n$) pQCD predicts that $G_{Mn}/G_{Mp} = -\frac{2}{3}$ at high Q^2. This prediction is rather remarkable because if it is assumed G_{Mn} and G_{Mp} are described by the dipole parameterization (which is not, of course, valid at large Q^2), the ratio of the form factors is then $\mu_n/\mu_p = -0.686$.

Comparison With Data

The most recent polarized results for $\mu_p G_{Ep}/G_{Mp}$ [215, 216] are plotted in the top panel of Fig. 2-31 as $Q^2 F_{2p}/F_{1p}$ versus Q^2. Assuming the validity of the pQCD predictions described above, these data would appear to suggest that the asymptotic limit has not yet been reached at the highest available Q^2 point of 5.6 $(\mathrm{GeV}/c)^2$.

In contrast, the ratio QF_{2p}/F_{1p} is plotted in the bottom panel of this same figure; here, we see that the data now plateau in the $2 < Q^2 < 6$ $(\mathrm{GeV}/c)^2$ region. The observation that QF_{2p}/F_{1p} plateaus, first reported by Gayou *et al.* [216], has generated an enormous amount of theoretical interest. Ralston and Jain [235] have argued that there is no reason hadron helicity conservation should hold and that consideration of quark states with non-zero orbital angular momentum may explain the plateau observed in QF_{2p}/F_{1p}. Similarly, Miller and Frank [236] argued that imposing Poincaré invariance[11] leads to a substantial violation of hadron helicity conservation. On the other hand, Belitsky, Ji, and Yuan [238] found in a pQCD analysis of F_2 that, to leading order, F_2 has the expected Q^{-6} behavior; however, they found that F_2 has a coefficient which depends on leading-order (twist-three) and next-to-leading order (twist-four) contributions [the lowest order QCD operators are twist-two], and that inclusion of these higher-twist contributions leads to an asymptotic scaling relation of the form

$$Q^2 \frac{F_2}{F_1} \sim \log^2 \frac{Q^2}{\Lambda^2} \,. \tag{2.206}$$

As such a form was found to describe the data well, Belitsky, Ji, and Yuan argued that asymptotic pQCD is unlikely to be the dominant contribution to F_2 at $2 < Q^2 < 6$ $(\mathrm{GeV}/c)^2$ as higher-order corrections and higher-twist effects contribute and must be accounted for.

[11] As discussed in detail by Goldstein [237], the most general transformation in Minkowski space that preserves the velocity of light is of the form

$$\mathbf{x}' = \mathbf{L}\mathbf{x} + \mathbf{a} \,, \tag{2.205}$$

where $\mathbf{a}$ is an arbitrary translation vector and $\mathbf{L}$ is an orthogonal matrix; such a transformation is known as a Poincaré transformation. Poincaré invariance requires that a theory must satisfy the commutation relations for the generators of Poincaré transformations.

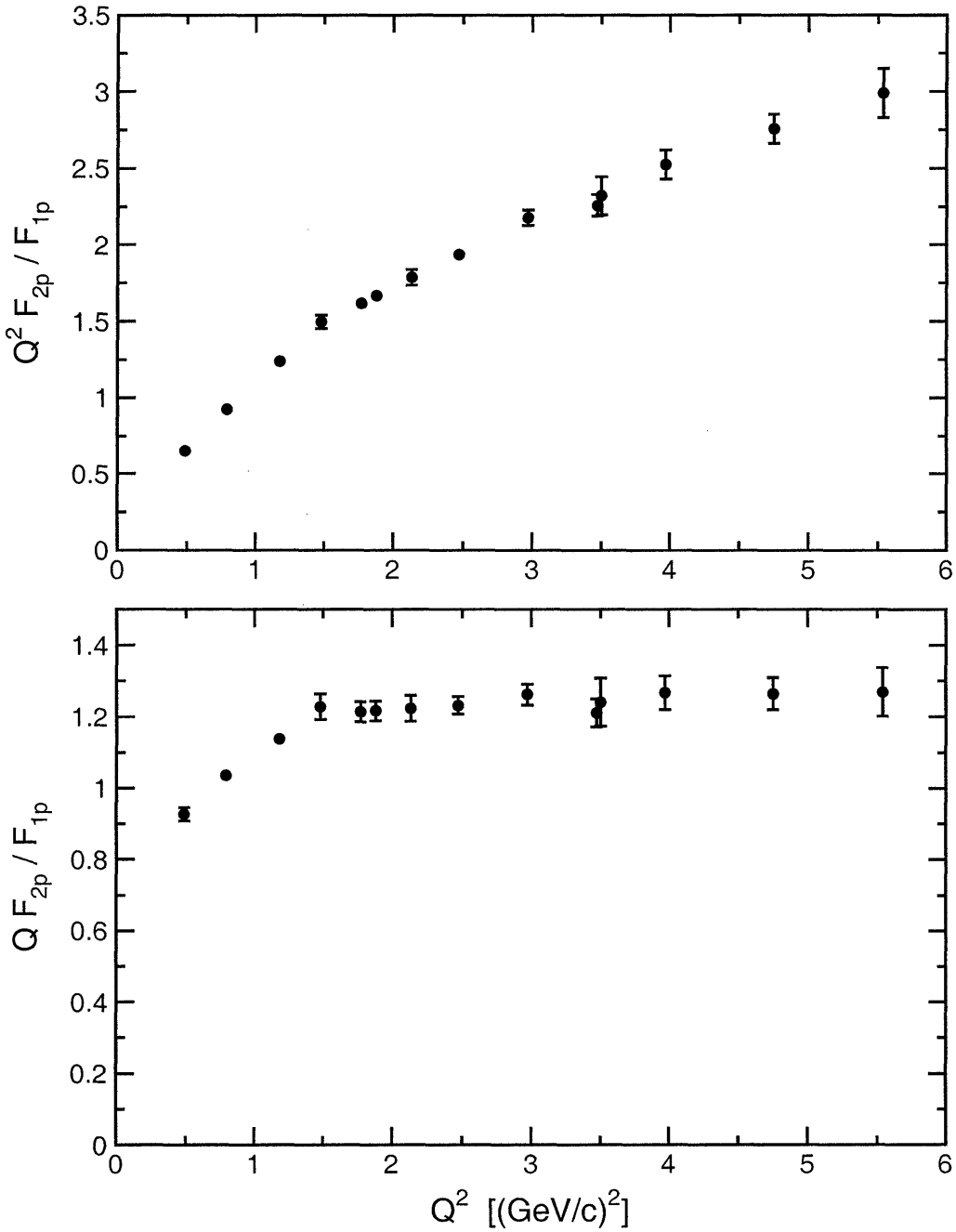

Figure 2-31: Polarized results for $\mu_p G_{Ep}/G_{Mp}$ [215, 216] plotted as $Q^2 F_{2p}/F_{1p}$ (top panel) and QF_{2p}/F_{1p} (bottom panel).

Indeed, this issue remains controversial; the question of whether the data imply that the pQCD asymptotic limit has not yet been reached or that the assumption of hadron helicity conservation is not valid remains open. Data for the neutron were not shown here as the present data are too limited in Q^2 to address the issue of asymptotic scaling.

2.4.2 Vector Meson Dominance

Overview

Some of the earliest theoretical attempts (dating to the 1960s) to calculate the nucleon form factors were performed within the framework of the *vector meson dominance* (VMD) model, a technique pioneered largely by Sakurai (see, e.g., [239]); also, an enlightening discussion of VMD was given by Feynman [240].

In this model, the virtual photon is assumed to couple to the nucleon via vector mesons. The isoscalar and isovector Pauli and Dirac form factors, $F_{1,2}^{\mathrm{is,iv}}$, can then be written in terms of a photon-meson coupling strength, $C_{\gamma V}$, and meson-nucleon vertex form factors, F_{VN}, as

$$F_{1,2}^{\mathrm{is,iv}}(Q^2) = \sum_{i \text{ mesons}} \frac{m_i^2 C_{\gamma V_i}}{Q^2 + m_i^2} F_{V_i N}(Q^2) \ , \tag{2.207}$$

where the sum is taken over the different vector mesons i included in the calculation and m_i denotes the meson mass. The electric and magnetic form factors are then expressed in the usual way as

$$G_E = \frac{1}{2}\left(F_1^{\mathrm{is}} \pm F_1^{\mathrm{iv}}\right) - \tau\frac{1}{2}\left(F_2^{\mathrm{is}} \pm F_2^{\mathrm{iv}}\right) \ , \tag{2.208}$$

$$G_M = \frac{1}{2}\left(F_1^{\mathrm{is}} \pm F_1^{\mathrm{iv}}\right) + \frac{1}{2}\left(F_2^{\mathrm{is}} \pm F_2^{\mathrm{iv}}\right) \ , \tag{2.209}$$

where the $+$ $(-)$ sign is for the proton (neutron) form factors.

Calculation of the nucleon form factors then requires specification of a functional form for the meson-nucleon vertex form factor; however, it is clear that this form

factor cancels in the ratio of the electromagnetic form factors (e.g., G_E/G_M). Also, it should be noted that the above formulation neglects the widths of the vector mesons.

Early Work

Some of the earliest attempts to model the nucleon form factors using the VMD model were those reported by Iachello, Jackson, and Lande [241] in 1973. These early calculations included the ρ, ω, and ϕ mesons, and the width of the ρ, Γ_ρ, was included by making the replacement

$$\frac{m_\rho^2}{Q^2+m_\rho^2} \rightarrow \frac{m_\rho^2+8\Gamma_\rho m_\pi/\pi}{(Q^2+m_\rho^2)+(Q^2+4m_\pi^2)\Gamma_\rho\ \alpha(Q^2)/m_\pi} \tag{2.210}$$

in Eq. (2.207) where

$$\alpha(Q^2)=\frac{2}{\pi}\left[\frac{Q^2+4m_\pi^2}{Q^2}\right]^{1/2}\log\left[\frac{(Q^2+4m_\pi^2)^{1/2}+\sqrt{Q^2}}{2m_\pi}\right]. \tag{2.211}$$

(The widths of the ω and ϕ were not included as these states are much narrower than the ρ.) Various forms for the meson-nucleon vertex form factor were employed (i.e., monopole, dipole, and eikonal), and the remaining parameters were obtained via fits to the data. Good agreement between their calculations and the then-existing data was observed.

In 1985, Gari and Krümpelmann [242] extended Iachello, Jackson, and Lande's early version of the VMD model to include the high Q^2 predictions of pQCD; this was done by interpolating the expected behavior of the meson-nucleon vertex form factors at low and high values of Q^2 to intermediate values of Q^2. Their calculations included the ρ and ω; however, the ϕ was not included as the Zweig rule tends to decouple the ϕ (essentially a pure $s\bar{s}$ state in the quark model) and the nucleon. Again, these fits achieved reasonable agreement with the then-existing data.

Then, in 1992, Gari and Krümpelmann [243] reanalyzed the existing nucleon form factor data within their "VMD + pQCD" model with a special emphasis on the neutron electric form factor. The goal of their analysis was to investigate the (at the

time) unknown importance of the strange quark content in the nucleon by considering the coupling of the ϕ to the nucleon via a two-step intermediate process. Their analysis showed that strange quark contributions can reduce the value of G_{En} at low Q^2 while having little effect on the other nucleon form factors.

Recent Work

Recently, in 2001 and 2002, Lomon [244,245] extended the Gari-Krümpelmann VMD + pQCD model by including the width of the ρ and adding the ρ' and the ω'. Fits to the current data were performed with a number of different forms for the meson-nucleon vertex form factors, and relatively good agreement with the data was found for fits that included 12 free fit parameters. Although the results of these fits (shown later after we have concluded our discussion of the various theoretical approaches) achieve reasonable agreement with the data, they have little absolute predictive power for Q^2 ranges in which data do not already exist.

2.4.3 Dispersion Relation Calculations

Overview

Other early attempts to model the nucleon form factors employed dispersion relations. For an excellent overview of the utility of dispersion relations in physics calculations, we refer the reader to Arfken and Weber [246], and a brief synopsis of their discussion is as follows.

Suppose we have a complex function $f(z)$ [where, as usual, $z = x + iy$] that is analytic in the upper half plane and on the real axis and satisfies

$$\lim_{|z| \to \infty} |f(z)| = 0 \ , \qquad 0 \leq \arg z \leq \pi \ , \tag{2.212}$$

such that the integral over an infinite semicircle vaishes. Given these conditions, $f(z)$

may be rewritten using the Cauchy integral formula as

$$f(z_0) = \frac{1}{2\pi i} \oint \frac{f(z)}{z - z_0} \, \mathrm{d}z \ . \tag{2.213}$$

The integral over the upper semicircle vanishes, and if the value of z_0 approaches the real axis from above (i.e., if we let $z_0 \to x_0$), the contour integral reduces to

$$f(x_0) = \frac{1}{\pi i} \, \mathrm{p.v.} \int_{-\infty}^{\infty} \frac{f(x)}{x - x_0} \, \mathrm{d}x \ . \tag{2.214}$$

Then, if $f(x_0)$ is written in terms of real and imaginary parts as $f(x_0) = u(x_0) + iv(x_0)$, it follows that the real and imaginary parts are related according to the following *dispersion relations*

$$u(x_0) = \frac{1}{\pi} \, \mathrm{p.v.} \int_{-\infty}^{\infty} \frac{v(x)}{x - x_0} \, \mathrm{d}x \ , \qquad v(x_0) = -\frac{1}{\pi} \, \mathrm{p.v.} \int_{-\infty}^{\infty} \frac{u(x)}{x - x_0} \, \mathrm{d}x \ ; \tag{2.215}$$

that is, the real and imaginary parts are Hilbert transforms of each other. From a physical point of view, $u(x)$ and/or $v(x)$ could represent experimental data at some values of x; the function $f(z)$ is then an analytic continuation over the upper half plane with the values on the real-axis serving as boundary conditions.

Calculations of the nucleon form factors using dispersion relations assign $t = -Q^2$ to the real axis, and in the dispersion *ansatz*, it is assumed that the Dirac and Pauli isoscalar and isovector form factors can be written in terms of a dispersion integral from threshold to a value well above resonance (ideally, infinity) according to

$$F_{1,2}^{\mathrm{is,iv}} = \frac{1}{\pi} \int_{4m_\pi^2, \ 9m_\pi^2}^{\infty} \frac{\Im F(t')}{t' - t} \, \mathrm{d}t' \ , \tag{2.216}$$

where the lower integration limit of $4m_\pi^2$ ($9m_\pi^2$) is for the isoscalar (isovector) case and $F(t)$ is a *spectral function.* The integration is performed over the timelike region; therefore, $F(t)$ characterizes the electromagnetic structure of the nucleon in the timelike region. As such, an extraction of the electromagnetic form factors in the desired spacelike region requires a parameterization for the spectral function in the timelike

region.

The simplest approach to a parameterization of the spectral function is the VMD approach in which the spectral functions are approximated by a few vector meson poles in the isoscalar and isovector channels. In this case, the pole terms contribute to the spectral function in terms of δ-functions, and the form factors take the form

$$F_{1,2}^{\mathrm{is,iv}} = \sum_{i \text{ mesons}} \frac{a_{1,2}^{\mathrm{is,iv}}}{m_i^2 - t} \,, \tag{2.217}$$

where the sum is taken over all vector mesons i included in the calculation. Here, the $a_{1,2}^{\mathrm{is,iv}}$ are the (scalar and vector) strength parameters (which include the various vector-meson-nucleon coupling constants) and are generally fitted to data; the m_i mass parameters are usually taken to be the known meson masses.

Early Work

The classic work performed in dispersion theory calculations of the nucleon form factors was that conducted by Höhler *et al.* [247] in 1976. The simple VMD approach described above was employed (with contributions from the ρ, ω, ϕ, ρ', and ω'), and the strength parameters $a_{1,2}^{\mathrm{is,iv}}$ were taken to be free fit parameters. Good agreement was achieved with the then-available data. As an added benefit, the fits permitted an extraction of the vector-meson-nucleon coupling constants. Space does not permit a complete discussion of their analysis, and so we refer the reader to the original reference for details.

Recent Work

More recently (mid-1990s), the original Höhler *et al.* dispersion theory calculations were extended by Mergell, Meissner, and Drechsel [248] and Hammer, Meissner, and Drechsel [249]. Using constraints from unitarity[12] and the high Q^2 predictions from

[12]On a very technical note, Mergell, Meissner, and Drechsel [248] pointed out that the VMD approach for the approximation of the spectral functions it at odds with the requirements of unitarity; we refer the reader to this reference and those found therein for a complete discussion of this theoretical issue.

pQCD (by requiring the spectral functions to scale properly at high Q^2), Mergell, Meissner, and Drechsel were available to achieve reasonable agreement with the then-available data (i.e., before the release of the polarized results for $\mu_p G_{Ep}/G_{Mp}$ [215, 216]). These calculations were then further extended by Hammer, Meissner, and Drechsel to include nucleon form factor data obtained in the timelike region.[13]

In what follows later, we do not compare the results from either of the above calculations with the current available data because these calculations tend to substantially overpredict the recent polarized results for the proton form factor ratio.

2.4.4 Skyrme/Soliton Model Calculations

Overview

The standard Skyrme model is a field theory that was developed in the early 1960s by Skyrme [251, 252] as a theory of the strong interaction; the traveling wave solutions were interpreted as pion waves, and the solitons[14] (or Skyrmions) were identified as baryons.

Early Work

As discussed in detail by Braaten, Tse, and Willcox [253, 254], interest in Skyrme's original (two-parameter) model was revived in the early 1980s after it was suggested by Witten [255, 256] that such a model would arise as the low-energy effective Lagrangian in the $1/N_c$ expansion of QCD. The Lagrangian of the Skyrme model was then coupled to electromagnetism, and the first phenomenological application of this model was a calculation in 1983 by Adkins, Nappi, and Witten [257] of the static

[13] In this thesis, we have, and will continue, to only consider nucleon form factor data in the spacelike region; however, the form factors have also been measured in the timelike region either in $\overline{p}p$ annihilation or $e^+e^- \to \overline{p}p$, $\overline{n}n$ collisions. For a fairly recent review of the status of nucleon form factor measurements conducted in the timelike region, we refer the reader to [250]. Some interesting results have been found; for example, the data suggest that the cross section for $e^+e^- \to \overline{n}n$ is greater than that for $e^+e^- \to \overline{p}p$.

[14] Within the context of field theory, fields can contain particle states that are not simply related to the original fields [8]; such new states can appear as solutions of the *classical* field equations. Such solutions, and the corresponding particle states, are known as solitons. This more specialized term is borrowed from the theory of partial differential equations in which solitons are nonlinear wave solutions.

properties of the nucleon such as the magnetic moments for the proton, neutron, and the N-Δ transition. These results agreed with the accepted values to within 30%, and the Q^2 dependence of the form factors was subsequently considered by Braaten, Tse, and Willcox. The results from these initial calculations for the Q^2 evolution of the form factors was somewhat unsatisfying; although the calculations reproduced the overall shape of the experimental data, they did not achieve good quantitative agreement with the data (e.g., G_{En} was predicted to be nearly a factor of four too large).

Recent Work

In 1996, Holzwarth [258] demonstrated that better agreement was obtained following the inclusion of three ingredients: (i) a purely pionic soliton created through the standard Skyrme term (representing an extended object with a spatial structure), (ii) minimal coupling to the electromagnetic field partly mediated through vector mesons, and (iii) relativistic boost factors to the Breit frame to account for kinematic corrections. One interesting result of Holzwarth's original calculations (from 1996) was the prediction that the proton form factor ratio $\mu_p G_{Ep}/G_{Mp}$ should decrease nearly linearly with Q^2, *a result that was at odds with the then-existing Rosenbluth data.*

In light of the recent polarized results for $\mu_p G_{Ep}/G_{Mp}$ [215, 216] that revealed the proton form factor ratio *does* decrease with Q^2, Holzwarth updated this model calculation in 2002 [259]. Two different models were considered, "Model A" and "Model B"; a brief overview of these two different models is as follows. In Model A, the pionic Skyrme model for the chiral SU(2)-field U[15] is

$$\mathcal{L}^{\pi} = \mathcal{L}^{(2)} + \mathcal{L}^{(4)} \ , \tag{2.219}$$

[15]The Skryme model is a field theory of an SU(2)-valued matrix $U(x)$ called the chiral field with a Lagrangian that is invariant under the chiral transformations

$$U(x) \rightarrow V_L U(x) V_R \ , \tag{2.218}$$

where V_L and V_R are constant SU(2) matrices [254].

where

$$\mathcal{L}^{(2)} = \frac{f_\pi^2}{4}\int \mathrm{d}^3x \ \left[-\mathrm{tr}(L_\mu L^\mu) + m_\pi^2 \ \mathrm{tr}\ (U + U^\dagger - 2)\right] \ , \tag{2.220}$$

$$\mathcal{L}^{(4)} = \frac{1}{32e^2}\int \mathrm{d}^3x \ \mathrm{tr}\ \left([L_\mu, L_\nu]^2\right) \ . \tag{2.221}$$

Here, $L_\mu = U^\dagger \partial_\mu U$ is the chiral gradient, f_π is the pion decay constant, m_π is the pion mass, and $e = 4.25$ is a standard Skyrme parameter. To incorporate vector meson effects, the form factors derived from this model were multiplied by factors

$$\Lambda_{0,1}(Q^2) = \lambda_{0,1}\left(\frac{m_{0,1}^2}{m_{0,1}^2 + Q^2}\right) + (1 - \lambda_{0,1}) \ , \tag{2.222}$$

where the 0 (1) subscript is for isoscalar (isovector) form factors, m_0 (m_1) is the mass of the ω (ρ), and the λ_0 and λ_1 are parameters which allow for admixture of the vector meson poles to purely pionic formfactors; therefore, Model A only contains two free parameters (as e is kept fixed to its standard Skyrme value).

In Model B, the vector mesons are instead included explicitly as dynamical degrees of freedom in the Lagrangian. As discussed in detail by Holzwarth, the axial vector mesons are eliminated in a chirally invariant way which leaves two coupling constants, g_ρ and g_ω, for the ρ and ω mesons, respectively. The Lagrangian is then of the form

$$\mathcal{L} = \mathcal{L}^{(\pi)} + \mathcal{L}^{(\rho)} + \mathcal{L}^{(\omega)} \ , \tag{2.223}$$

where

$$\mathcal{L}^{(\rho)} = \int \mathrm{d}^3x \ \left[-\frac{1}{8}\ \mathrm{tr}\ (\rho_{\mu\nu}\rho^{\mu\nu}) + \frac{m_\rho^2}{4}\ \mathrm{tr}\left(\rho_\mu - \frac{i}{2g_\rho}(l_\mu - r_\mu)\right)^2\right] \ , \tag{2.224}$$

$$\mathcal{L}^{(\omega)} = \int \mathrm{d}^3x \ \left[-\frac{1}{4}\omega_{\mu\nu}\omega^{\mu\nu} + \frac{m_\omega^2}{2}\omega_\mu\omega^\mu + 3g_\omega\omega_\mu B^\mu\right] \ , \tag{2.225}$$

where the baryon current is $B_\mu = \frac{1}{24\pi^2}\epsilon_{\mu\nu\rho\sigma}\mathrm{tr}(L^\nu L^\rho L^\sigma)$, $l_\mu = \xi^\dagger\partial_\mu\xi$, $r_\mu = \partial_\mu\xi\xi^\dagger$, and $\xi^2 = U$. Finally, as explained by Holzwarth, in Model B, the parameter e is considered as an additional fit parameter because as the Skyrme term $\mathcal{L}^{(4)}$ already

partly accounts for statis ρ-meson effects, its strength in Model B must be reduced.

Again, we will compare the results of Holzwarth's calculations with experimental data later; henceforth, it should be noted that whenever we discuss Holzwarth's calculations we are referring to the results from "Model B2".[16]

2.4.5 Constituent Quark Model Calculations

Nonrelativistic Constituent Quark Model Predictions

The highly successful non-relativistic constituent quark model has a long and storied history to which we cannot possibly do justice here. Within the framework of this model, the nucleon is, of course, assumed to consist of three quarks each with a mass of $\sim$300 MeV that can described in terms of a symmetric spin-flavor SU(6) wavefunction. Predictions can be made for the nucleon form factors within the framework of this model, and such a calculation was first reported by Barnes, Carruthers, and von Hippel [260] in 1965. Assuming that SU(6) symmetry is exact (which, as we know, is not), Barnes, Carruthers, and von Hippel showed that the ratios of the form factors are, at all values of Q^2, equal to their values in the static limit:

$$G_{Mn}(Q^2)/G_{Mp}(Q^2) = -2/3 \ , \qquad G_{En}(Q^2)/G_{Ep}(Q^2) = 0 \ . \tag{2.226}$$

Indeed, the magnetic form factors do not scale (exactly) according to this prediction, and we know that G_{En}, although small, is not zero for $Q^2 > 0$; however, the fact that these predictions are not accurate is not surprising — SU(6) is not an exact symmetry, the calculation was not relativistic, and interactions between the quarks were not considered.

In what was perhaps one of the first serious attempts to calculate values for the nucleon form factors within the framework of the nonrelativistic constituent quark model, in 1981, Isgur, Karl, and Sprung [261] extended the idea that the (non-zero) charge radius of the neutron is due to color hyperfine interactions which mix non-

[16]Two different fits for Model B were conducted with different values for the gauge coupling constants. Model B2 provided the best agreement with the data.

symmetric components into the nucleon spatial wavefunction to a calculation of G_{En} and G_{Ep} assuming a harmonic oscillator potential for the interaction between the quarks. The results they derived were

$$G_{En}(Q^2) = -\frac{1}{6}\langle r_{En}^2 \rangle \; Q^2 \; \exp\left(-Q^2/6\alpha^2\right) \; , \tag{2.227}$$

$$G_{Ep}(Q^2) = \exp\left(-Q^2/6\alpha^2\right) \; . \tag{2.228}$$

Although the above calculation for G_{En} agrees somewhat with the Galster parameterization, the authors noted that their results were not, in general, valid for values of Q^2 greater than the square of the (constituent) quark mass.

Relativistic Quantum Dynamics

Before proceeding to a discussion of a number of recent relativistic constitutent quark model calculations of the nucleon form factors, it is instructive to recall that relativistic constituent quark models are based on relativistic quantum mechanics, not relativistic quantum field theory (as is QCD). As first formulated by Dirac [262], three forms of relativistic quantum mechanics can be defined: the instant form, the light-front form, and the point-form; our discussion below primarily follows that given originally by Dirac.

- *instant form*: this formulation was strongly motivated by nonrelativistic dynamics and is the most intuitive. The dynamical variables refer to physical conditions at some instant of time, and a particle's state is defined by its three spatial coordinates. Also, the usual relation between the momentum and energy holds

  $$p^0 = \pm\sqrt{|\mathbf{p}|^2 + m^2} \; . \tag{2.229}$$

  In the instant form, the interaction is present in p^0, and the two solutions for p^0 admitted within this formulation tend to complicate calculations.

- *light-front form*: this form is less intuitive (but see the discussion given by Miller [263] for a useful explanation of light-front dynamics). A *front* is de-

fined to be a three-dimensional surface in space-time formed by a plane-wave advancing at the speed of light. In the light-front formalism, fields are then quantized at a "time" $\tau = x^0 + x^3 \equiv x^+$, and the τ-development operator is given by $p^0 - p^3 \equiv p^-$. Accordingly, any four-vector V^μ is then expressed as $V^\pm \equiv V^0 \pm V^3$. A canonical spatial variable must then be orthogonal to the τ time variable, and is defined to be $x^- = x^0 - x^3$; the canonical momentum is then given by $p^+ = p^0 + p^3$. The other spatial and momentum coordinates are written as $\mathbf{x}_\perp$ and $\mathbf{p}_\perp$. The most important consequence of the light-front formulation is that the usual relation between momentum and energy,

$$p^\mu p_\mu = m^2 = p^+ p^- - p_\perp^2 \ , \tag{2.230}$$

becomes

$$p^+ = \frac{p_\perp^2 + m^2}{p^-} \ ; \tag{2.231}$$

that is, the relativistic kinetic energy does not contain a square root which greatly simplifies calculations. Also, this permits a separation of center-of-mass and relative coordinates such that the resulting wave functions are frame-independent. Last, it is worth noting that if p^- is viewed as a mass parameter, p^+ is analogous in form to the non-relativisitic Hamiltonian for a particle in two dimensions.

- *point form*: a dynamical theory can be constructed in terms of variables that refer to physical conditions on some three-dimensional surface other than an instant. The surface must then satisfy the condition that the world-line of every particle must meet it; otherwise, the particle could not be described by variables on the surface. A simple form of this theory can be obtained if the surface is taken to be one that is left invariant by some subgroup of the Lorentz transformation. An example is a rotation about the origin; the surface is then given by a three-dimensional hyperboloid defined according to

$$x_0^2 - |\mathbf{x}|^2 = a^2 \ , \tag{2.232}$$

where a is a constant. A new form of dynamics is then obtained that is characterized via association with the group of Lorentz transformations which leave a point invariant.

We now proceed to a general overview of a number of recent calculations of the nucleon form factors that have been performed within relativistic constituent quark models employing light-front form and point form dynamics; for a more complete historical survey of early calculations, we refer the reader to that given by Gao [64].

Recent Relativistic Constitutent Quark Model Calculations

A very large number of calculations within the light-front formalism have been performed recently by Cardarelli, Pace, Salmè, and Simula [264], Cardarelli and Simula [152,153], and Simula [265]. Cardarelli, Pace, Salmè, and Simula [264] began, in 1995, by evaluating the nucleon form factors within the light-front formalism using Gaussian wave functions for the description of the pointlike constituent quarks within the nucleon. In their initial calculation they considered: (i) hadron wave functions which were eigenvectors of a light-front mass operator constructed from the effective $q\bar{q}$- and qq-interaction of Godfrey and Isgur [266] and Capstick and Isgur [267]; (ii) a one-gluon-exchange (OGE) mechanism for the interaction between the constituent quarks leading to high momentum components and SU(6) breaking effects in the hadron wave function; and (iii) Dirac and Pauli form factors for the constituent quarks. These initial calculations were refined by Cardarelli and Simula [152, 153] in 1999 and 2000 where it was argued that the kinematical SU(6) breaking caused by the Melosh rotations of the quark spins[17] as well as the dynamical SU(6) breaking due to a mixed-symmetry component generated in the nucleon wave function by spin-dependent terms in the quark-quark interaction due to OGE leads to a good description of G_{En} and an explanation for the decrease observed in the $\mu_p G_{Ep}/G_{Mp}$ ratio with Q^2. Finally, the effects of a finite constituent quark size were again considered by Simula [265] in 2001 via the introduction of constituent quark form factors

[17]Dynamics within the light-front formalism can essentially be viewed as a Lorentz transformation to a frame boosted along the z axis moving close to the speed of light. As shown by Melosh [268], under such a transformation, the spins undergo a relativistic rotation that mixes different spin states.

fixed using $Q^2 < 1$ (GeV/c)^2 data; accordingly, the predictions for $Q^2 > 1$ (GeV/c)^2 were argued to be parameter-free. As we shall see shortly, these calculations achieve reasonable agreement with the experimental data.

Miller [269] has recently used light-front dynamics to model the nucleon as a system of three bound relativistic constituent quarks surrounded by a cloud of pions. The three-quark model that was used for this calculation was originally constructed by Berestetskii and Terent'ev [270] and Chung and Coester [271]. The wave function for this model is antisymmetric, a function of relative momenta, independent of reference frame, and an eigenstate of the canonical spin operator. The calculation of the form factors was simplified via the use of completeness to express the wave function in terms of light-cone spinors (related to Dirac spinors by a Melosh rotation). Finally, the effects of the pion cloud were computed relativistically in order to confront experimental data at high Q^2. This component of the calculation involved using photon-bare nucleon form factors and a relativistic π-nucleon form factor; the resulting model was termed the "light-front cloudy bag model (LFCBM)". As discussed by Miller, inclusion of the pion cloud was necessary to reproduce the data on the neutron form factors; the effect of the pion cloud on the proton form factors at large values of Q^2 was shown to be of less importance.

A calculation of the nucleon form factors within the point form approach was recently reported by Wagenbrunn *et al.* [272] and Boffi *et al.* [273]. Their calculations employed the constituent quark model proposed by Glozman *et al.* [274]; this constituent quark model relies on constituent quarks and a Goldstone boson exchange interaction and was shown to provide a unified description of the ground state and low-energy excited spectra of the baryons and mesons. A relativistic kinetic energy operator was used along with an instantaneous pairwise linear confinement potential; the hyperfine interaction of the constituent quarks was derived from pseudoscalar Goldstone boson exchange. As a final necessary ingredient, the calculation assumed

the point-form spectator approximation (PFSA).[18]

Finally, Kaskulov and Grabmayr [275] have very recently considered the effects of OGE pair currents on the proton form factor ratio $\mu_p G_{Ep}/G_{Mp}$ within a nonrelativistic constituent quark model with relativistic corrections for the Lorentz boost of the wavefunction. Within the framework of this calculation, Kaskulov and Grabmayr concluded that gluonic corrections were needed in order to reproduce the decrease in $\mu_p G_{Ep}/G_{Mp}$ with Q^2. These calculations were further extended to a consideration of the neutron form factors [276, 277]. The neutron was modeled as a system of confined valence quarks surrounded by pions, and it was found that inclusion of the pion cloud was necessary for reproduction of the neutron form factors; in fact, Kaskulov and Grabmayr even argued in [276] that the functional form of the Galster parameterization can be linked to properties of the pion cloud. As we will see, their calculations achieve very good agreement with the data.

2.4.6 Quark Spectator-Diquark Model Calculations

A relativistic quark spectator-diquark model formulated in the light-cone frame was originally proposed by Close [278] and Field and Feynman [279] in the mid-1970s in order to study deep inelastic scattering.[19] More recently, Ma [280] demonstrated that after the effects of Melosh rotations were properly accounted for, this model provided good agreement with experimental data from polarized deep inelastic scattering. This work was then very recently extended by Ma, Qing, and Schmidt [281] to investigate elastic electron-nucleon scattering processes in an attempt to calculate the nucleon electromagnetic form factors.

A brief overview of their calculation is as follows. First, the wave function of the quark-diquark system was written in the instant form assuming SU(6) symmetry.

[18]The current operator was assumed to be a single-particle current operator for pointlike constituent quarks. Such an assumption corresponds to a relativistic impulse approximation formulated within the point form formalism. The approximation is termed the point-form spectator approximation because the impulse delivered to the nucleon is different than that delivered to the struck constituent quark.

[19]The impulse approximation to deep inelastic scattering assumes the incident lepton scatters off a single quark in the nucleon with the remaining constituents treated as a quasiparticle (diquark) spectator; hence, the quark spectator-diquark model.

Second, the spin portion of the light-cone wave function was obtained by transforming the instant states into light-cone states via Melosh rotations applied to both the quark and the vector diquark. Last, the nucleon form factors were calculated with the transformed wave functions, and the effects of SU(6) breaking were introduced by employing different parameters for the scalar (spin-0) and vector (spin-1) diquarks of the model (e.g., variations in the mass of the scalar diquark and vector diquark); Ma, Qing, and Schmidt found that such symmetry breaking was necessary in order to reproduce the experimental data.

The results of these calculations will be compared with the current data later.

2.4.7 Lattice QCD Calculations

The most rigorous test of our theoretical understanding of the nucleon's electromangetic structure will be the ultimate confrontation between experimental data and the results from lattice gauge theory QCD calculations, currently the only means available for *ab initio* QCD calculations.

In lattice QCD, space-time is discretized into a four-dimensional grid of points, and observables are calculated via Monte Carlo simulations of path integrals. As discussed pedagogically by Richards [282], lattice QCD calculations are subject to both statistical and systematic uncertainties. First, because the observables are calculated within a Monte Carlo framework, the results have statistical uncertainties. Second, and more importantly, the calculations are subject to systematic uncertainties that can arise from a number of different sources. These include possible errors associated with the finite space-time volume that is discretized and errors associated with the (non-zero) spacing between the lattice points.

Despite these difficulties, lattice QCD has evolved rapidly due to improvements both in computing power and computational algorithms, and one of the great successes of lattice QCD has been the reproduction of the light quark hadron spectrum [282]; however, precise calculations of the nucleon form factors are still several years away. A number of first-principle calculations of the nucleon form factors have been carried out (see, e.g., [283–285]), but these calculations were conducted in the

quenched approximation in which the contributions from closed quark loops (i.e., contributions from sea quarks) are neglected. Also, due to current limitations in computer speed, lattice calculations of the nucleon form factors are currently restricted to quark masses that are a factor of 5 to 10 larger than those of the physical masses; this then requires an extrapolation of the results from the large mass region down to the physical mass region. Within this extrapolation scheme, some very recent results [285] achieve qualitative agreement with experimental data at low values of Q^2.

2.4.8 Comparison of Calculations with Data

We conclude our discussion of these various theoretical calculations in this subsection by comparing the results of a number of the model calculations discussed above with the existing experimental data; lattice data are not shown here as those results are still preliminary and restricted to fairly small Q^2 values.

First, various predictions for the proton form factor ratio $\mu_p G_{Ep}/G_{Mp}$ are compared with the recent polarized results for this quantity in the top panel of Fig. 2-32. A glossary of our notation for the various calculations shown there is as follows:

- "VMD + pQCD" denotes Lomon's [244,245] extension of the Gari-Krümpelmann VMD + pQCD model
- "Chiral Soliton" denotes Holzwarth's [258,259] chiral soliton calculation; recall, Model B2 is shown
- "OGE CQM" denotes Cardarelli and Simula's [153] and Simula's [265] light-front calculation employing the OGE mechanism and constituent quark form factors
- "LFCBM" denotes Miller's [269] light-front cloudy bag model calculation including the pion cloud
- "GBE CQM" denotes Wagenbrunn *et al.*'s [272] and Boffi *et al.*'s [273] calculations employing the point-form spectator approximation and a Goldstone boson exchange interaction

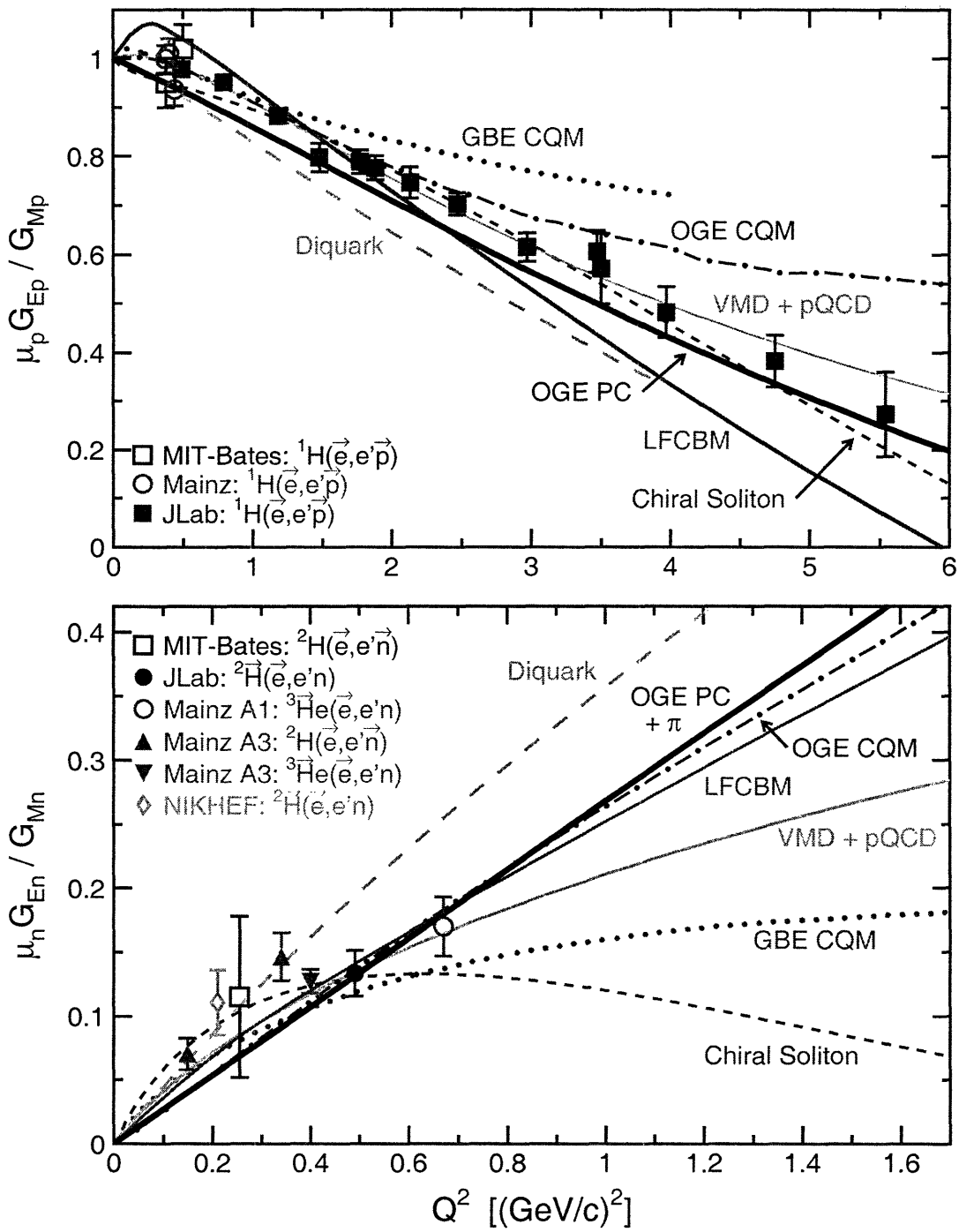

Figure 2-32: (color) Comparison of predictions from selected models (see text for glossary and references) with experimental data for $\mu_p G_{Ep}/G_{Mp}$ (top panel) and $\mu_n G_{En}/G_{Mn}$ (bottom panel). The data shown for $\mu_p G_{Ep}/G_{Mp}$ are from [212,215–217], and those for $\mu_n G_{En}/G_{Mn}$ are from [202–205, 207, 210, 213, 214]. The recent results reported by Madey *et al.* [218] and Warren *et al.* [209] are not shown here but will be presented later.

- "OGE PC" and "OGE PC + π" denotes Kaskulov and Grabmayr's [275–277] calculations including the effects of OGE pair currents and OGE pair currents plus the pion cloud, respectively

- "Diquark" denotes Ma, Qing, and Schmidt's [281] relativistic light-cone quark spectator-diquark calculation

Here, we see that all of the model predictions for the proton form factor ratio achieve reasonable qualitative agreement with the data. In contrast, the results of these model predictions for the neutron form factor ratio, $\mu_n G_{En}/G_{Mn}$, are compared with the existing data in the bottom panel of this same figure; the recent high Q^2 results reported recently by Madey *et al.* [218] and Warren *et al.* [209] will be added to this plot at the conclusion of this thesis. The predictions of these various models diverge rapidly for $Q^2 \gtrsim 0.6$ (GeV/c)^2, and the data plotted there do not, by any means, provide useful constraints on any of these calculations. Indeed, a statement that all of these model calculations (except for the light-cone quark spectator-diquark model) achieve agreement with the existing neutron data is not inaccurate.

2.5 Summary of Motivations for Measurements of Nucleon Form Factors

By now, the motivations for precise measurements of the nucleon form factors should be clear; however, we believe it is useful to summarize our claims in this section.

1. First, the electric and magnetic form factors are fundamental observables that are of intellectual interest due to their relation to the basic notion of an extended charge and magnetization distribution within the nucleon. Precise data over a wide range of Q^2 values are needed for an understanding of this basic property of the nucleon.

2. Second, precise measurements of all four nucleon form factors are needed over a wide range of Q^2 for stringent tests of our understanding of the structure of

the nucleon as formulated in nonperturbative QCD either in model or lattice calculations; a successful theory of confinement must be able to predict all four form factors simultaneously. The data shown in Fig. 2-32 do not sufficiently constrain any of the theoretical calculations shown there. Also, it is important that measurements of all four nucleon form factors be extended to Q^2 values as large as possible in order to determine where the asymptotic scaling predicted by pQCD becomes valid.

3. Third, the nucleon form factors are needed as input for the interpretation of many other quantities in nuclear physics. Examples include, but are certainly not limited to:

   (a) The interpretation of results from parity-violating electron scattering experiments designed to probe the strange content of the nucleon requires precise values for the electromagnetic form factors. In the results from one such experiment [286], the assumed uncertainties in the nucleon form factors (in particular, the uncertainty in G_{En}) were by far the largest systematic uncertainties.

   (b) The interpretation of electron scattering experiments from nuclei and the determination of the charge and magnetization radii of nuclei require precise values for the nucleon form factors; for example, in a classic analysis dating to 1972, Bertozzi, Friar, Heisenberg, and Negele [287] demonstrated that previously ignored contributions from G_{En} could partly explain the otherwise anomalous decrease observed in the rms charge radii of ^{40}Ca to ^{48}Ca.

   (c) In an exciting new area of nuclear physics, the recently discovered Generalized Parton Distributions (GPDs) (see [288–292] for the original work) provide model-independent relations between inclusive and exclusive observables. The first moments of the GPDs are related to the Dirac and Pauli form factors; therefore, precise data on the nucleon form factors over a wide range of Q^2 will provide important constraints on this new formal-

ism.

Unfortunately, as we have seen, the neutron electric form factor remains poorly determined relative to the three other nucleon form factors. The remainder of this thesis is devoted to a detailed discussion of an experiment designed to remedy this situation by providing the first precise data for G_{En} in the $Q^2 > 1$ $(\mathrm{GeV}/c)^2$ region.

Chapter 3

Accelerator and Hall C

In this chapter and the next, we provide a detailed description of the experimental arrangement for the Jefferson Laboratory experiment 93-038. As stated in the previous chapter, E93-038 was designed to extract the ratio of the neutron's electric to magnetic form factors, G_{En}/G_{Mn}, from measurements of the recoil neutron's polarization in quasielastic $^2\mathrm{H}(\vec{e}, e'\vec{n})^1\mathrm{H}$ kinematics.

3.1 Overview of the Experiment

E93-038 was conducted in Hall C of the Jefferson Laboratory (JLab) from September 2000 to April 2001. A brief overview of this experiment is as follows.

Longitudinally polarized electrons provided by the JLab accelerator scattered from a liquid deuterium target mounted in Hall C. The scattered electrons were detected in the Hall C High Momentum Spectrometer (HMS) in coincidence with the recoil neutrons. A neutron polarimeter (NPOL), installed in Hall C specifically for this experiment, measured the up-down scattering asymmetry from the projection of the recoil neutrons' polarization on an axis perpendicular to the three-momentum and parallel to the floor of Hall C. A dipole magnet (with a vertical magnetic field) located ahead of the polarimeter was used to precess the recoil neutrons' polarization vectors through an angle χ in a plane parallel to the Hall C floor. Precession of the polarization vectors with a vertical dipole field permitted measurements of the up-down

Q^2 [(GeV/c)^2]	E_e [GeV]	$E_{e'}$ [GeV]	$\theta_{e'}$	$\lvert\mathbf{p}_n\rvert$ [MeV/c]	T_n [MeV]	χ
0.447	0.884	0.643	52.65°	711	239	±40°
1.136	2.326	1.718	30.93°	1227	606	0°, ±90°
1.169	2.415	1.789	30.15°	1249	624	±40°
1.474	3.395	2.606	23.55°	1448	786	0°, ±40°, ±90°

Table 3.1: The nominal (central) values of the electron and neutron kinematics and the neutron spin precession angles.

scattering asymmetry from different projections of the recoil neutrons' polarization vector on this axis. Also, the vertical dipole field reduced the background levels by sweeping the incoming flux of charged particles from the polarimeter's acceptance.

Data were taken at four central Q^2 values of 0.447, 1.136, 1.169, and 1.474 (GeV/c)^2 with associated electron beam energies of 0.884, 2.326, 2.415, and 3.395 GeV, respectively. The central values of the electron and neutron kinematics and the neutron spin precession angles χ for each of these central Q^2 points are summarized in Table 3.1. The neutron polarimeter was fixed at a scattering angle of 46° relative to the incident electron beam line for the duration of the experiment.

In the remainder of this chapter, we provide an overview of the JLab accelerator and the equipment in Hall C; this includes the polarized electron source and the accelerator, the Hall C beamline (including the Møller polarimeter and the scattering chamber and cryotarget), and the HMS. The following chapter provides a detailed description of the neutron polarimeter.

3.2 Jefferson Laboratory Accelerator

3.2.1 Overview of CEBAF

The JLab accelerator, formally known as the Continuous Electron Beam Accelerator Facility (CEBAF) at the Thomas Jefferson National Accelerator Facility (TJNAF), is a continuous-wave, superconducting radiofrequency (rf) accelerator that operates at a fundamental frequency of 1497 MHz. Until LEP II became operational, JLab was the world's largest implementation of superconducting rf technology [293]. A

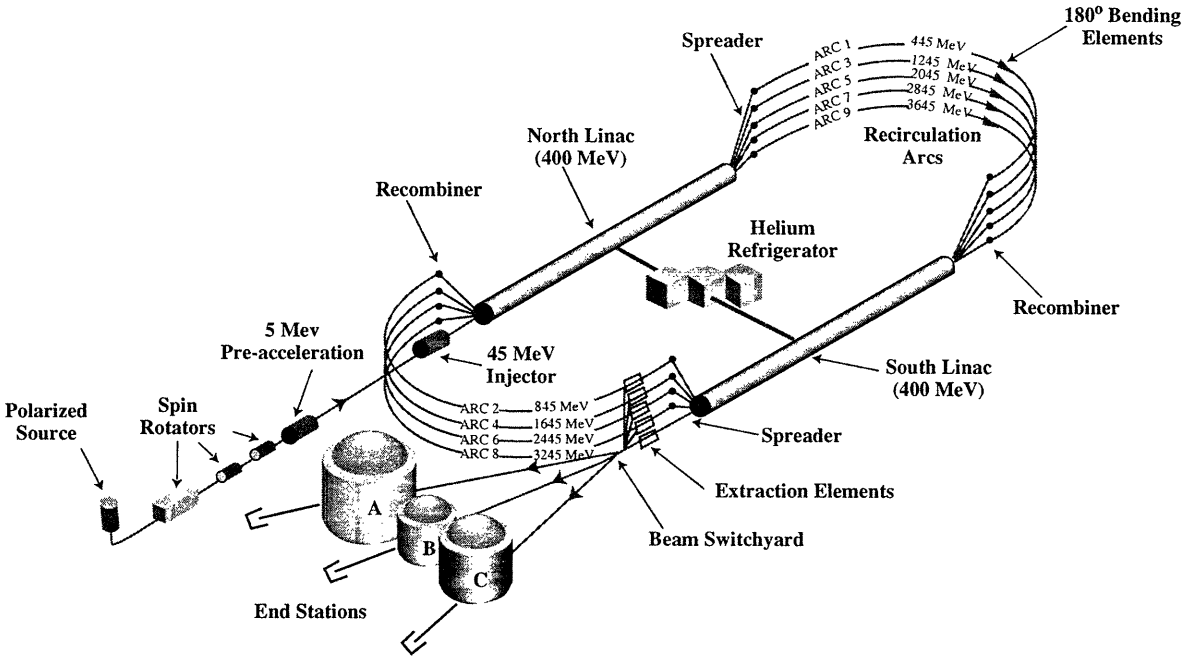

Figure 3-1: (color) A schematic diagram of the Jefferson Laboratory accelerator.

schematic diagram of the accelerator's "racetrack" layout is shown in Fig. 3-1, and a brief overview of accelerator operations is as follows.

Three interlaced 499 MHz beams of polarized electrons separated by 120° of rf phase are produced at the polarized source via optical illumination of a strained crystal of gallium arsenide (GaAs) and accelerated to a nominal energy of 45 MeV in the injector. The electrons are then directed to the North Linac, a nominal 400 MeV superconducting rf linear accelerator, where they are accelerated to an energy of 445 MeV. After traversing the North Linac, the electrons are steered through a 180° turn in the East Recirculation Arc and then enter the South Linac, identical to the North Linac. At the end of the South Linac, the one-pass nominal 845 MeV beam can be either extracted and transported at the Beam Switchyard for redirection to the experimental end stations (Halls A, B, and C) or steered through a second 180° turn in the West Recirculation Arc for further acceleration in the North and South Linacs. A maximum of five passes, corresponding to a maximum nominal beam energy of 4045 MeV, is possible, and each hall can receive either a one-, two-, three-, four-, or five-pass 499 MHz beam.

Polarized electrons beams with polarizations exceeding 75% and currents ranging from 1–100 μA (1–100 nA) can be simultaneously delivered to Halls A and C (B). The North and South Linacs are now capable of accelerating the beam by approximately 600 MeV [293]. The injector energy scales by the same ratio to 67.5 MeV (i.e., the ratio of the injector energy to the linac energy is fixed at 0.1125 [294]); therefore, at present, the maximum beam energy is approximately 6067.5 MeV.

In order to minimize exposure to radiation, the concrete accelerator tunnel is located approximately 25 feet underground, and the experimental halls are located within concrete dome-like structures with diameters ranging from 98 to 172 feet that are surrounded by several feet of dirt.

3.2.2 Polarized Electron Source

During E93-038, polarized electrons were produced at the polarized source via optical illumination of a strained GaAs photocathode (GaAs on GaAsP [295]) with circularly polarized laser light from a high-power Ti-sapphire laser. Before proceeding to a more technical discussion of the JLab polarized source, we provide a brief overview of the physics of electron photoemission from strained GaAs crystals.

Electron Photoemission from Bulk and Strained GaAs Crystals

The first polarized electron source that was used in an accelerator environment produced polarized electrons via Stern-Gerlach separation of an electron beam produced by photoionization of atomic lithium [296]; this source was developed at SLAC and became operational in 1974. Some of the earliest experiments that employed this polarized source were the pioneering proton spin structure experiments conducted at SLAC in the late 1970s (E80 [297, 298] and E130 [299, 300]). Polarizations in excess of 80% and peak currents up to 25 mA (but very low duty-factor) were achieved with this source. Despite these high values of the polarization and current, this source possessed several undesirable features [296]. First, the helicity of the electron beam could only be reversed (over long time scales) by reversing the direction of the

Stern-Gerlach magnetic field. Second, this source was difficult to operate, and the operational efficiency was, at best, ~50%.

As described by Clendenin [296], a breakthrough for accelerator-based polarized electron sources came in 1974 and 1975 when Garwin [301] and Lampel and Weisleuch [302], respectively, proposed that bulk GaAs, a type III-V semiconductor, might prove to be a good source of polarized electrons. Photoemission from GaAs treated to have a negative electron affinity was found to be an efficient process, and studies had demonstrated that if the incident light was circularly polarized and monoenergetic with wavelengths corresponding to the GaAs band-gap energy, the electrons promoted from the conduction band to the valence band would be polarized at or slightly below 50%. Despite this lower value of the polarization, the advantages of employing photoemission from bulk GaAs were quickly realized. First, the intensity would be limited only by the intensity of the light source. Second, the helicity of the electron beam could be reversed quickly with optical elements. Finally, a solid-state source promised a higher degree of reliability than the atomic lithium source. Soon thereafter, a GaAs source was developed, installed, and successfully operated at SLAC in 1978 for the famous Prescott experiment.[1]

A schematic diagram of the energy levels and possible transitions in bulk GaAs is shown in Fig. 3-2. In bulk GaAs, the electrons in the valence band are in a P-state (i.e., orbital angular momentum of $L = 1$); therefore, according to the rules for angular momentum addition, the electrons in the valence band are coupled to a total angular momentum, J, of either $J = \frac{3}{2}$ (i.e., a $P_{3/2}$ state) or $J = \frac{1}{2}$ (i.e., a $P_{1/2}$

[1]The Prescott experiment [303,304] measured the parity-violating asymmetry (due to interference between γ- and Z^0-exchange) in deep-inelastic $^2\mathrm{H}(\vec{e}, e')$ scattering. The non-zero parity-violating asymmetry measured in this experiment provided what is generally considered to be the first experimental observation of weak neutral currents in electron-nucleon interactions and permitted an extraction of the electroweak mixing angle, $\sin^2\theta_W$. Parity-violation experiments remain at the forefront of electron scattering. Historical examples include extractions of $\sin^2\theta_W$ from quasielastic $^9\mathrm{Be}(\vec{e}, e')$ scattering at MAMI [305] and elastic $^{12}\mathrm{C}(\vec{e}, e')$ scattering at MIT-Bates [306]. More recently, measurements of the parity-violating asymmetry in elastic $^1\mathrm{H}(\vec{e}, e')$ and quasielastic $^2\mathrm{H}(\vec{e}, e')$ scattering at MIT-Bates [307–310] and JLab [286,311] have attempted to measure the strange quark content of the nucleon. Similar experiments at JLab [312–315] and MAMI [316] are either underway or have been approved for future running. In addition, a high-precision parity-violating Møller scattering experiment designed to provide a challenging test for the Standard Model's prediction for the "running" of $\sin^2\theta_W$ with Q^2 was recently completed at SLAC [317], and a $^1\mathrm{H}(\vec{e}, e')$ parity-violation experiment soon to be conducted at JLab [318] has similar goals.

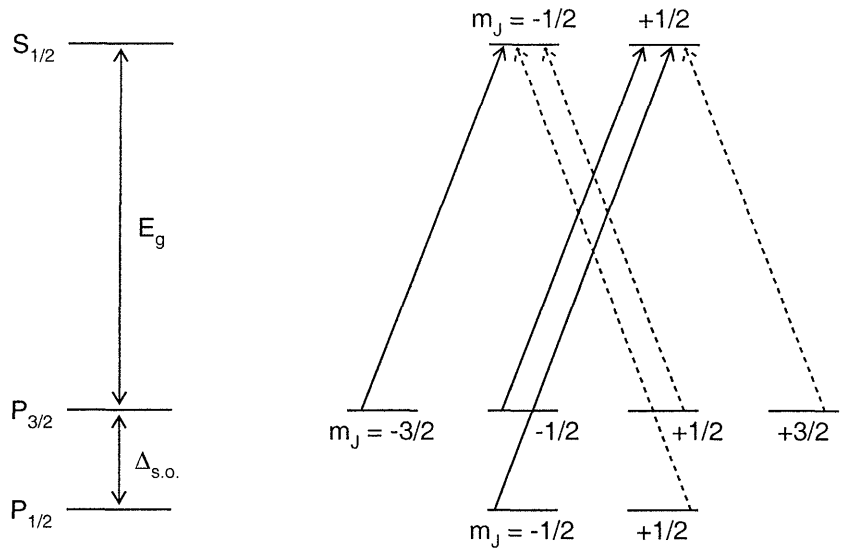

Figure 3-2: Energy levels and possible transitions for bulk GaAs. The transitions that can be excited by right- (left-) circularly polarized laser light are shown as the solid (dashed) arrows.

state). Due to the $\mathbf{L} \cdot \mathbf{S}$ spin-orbit interaction, the otherwise six-fold degenerate P-state splits such that the "heavy-hole" ($m_J = \pm 3/2$) and "light-hole" ($m_J = \pm 1/2$) states are separated by an energy difference denoted $\Delta_{\text{s.o.}}$. The conduction band lies approximately 1.54 eV above the heavy-hole states (this energy gap is usually denoted E_g); therefore, if the photon energy, E_γ, satisfies $E_g \leq E_\gamma < E_g + \Delta_{\text{s.o.}}$, electrons can be optically pumped from the $P_{3/2}$ valence band to the $S_{1/2}$ conduction band. Photons are spin-1 particles; therefore, the possible $P_{3/2} \rightarrow S_{1/2}$ transitions that can be induced by left-circularly polarized photons are $|\frac{3}{2}, \frac{3}{2}\rangle \rightarrow |\frac{1}{2}, \frac{1}{2}\rangle$ and $|\frac{3}{2}, \frac{1}{2}\rangle \rightarrow |\frac{1}{2}, -\frac{1}{2}\rangle$ transitions. Symmetric results hold for right-circularly polarized photons.

The relatively probabilities for these transitittions are governed by the rules for angular momentum addition. To illustrate this, we consider $E_g \leq E_\gamma < E_g + \Delta_{\text{s.o.}}$ left-circularly polarized photons, $|1, -1\rangle$, incident on bulk GaAs. If the photons couple with the $|\frac{3}{2}, \frac{3}{2}\rangle$ electrons in the $P_{3/2}$ valence band, we can use the standard Clebsch-Gordan coefficients to deduce the following possibilities for the coupled value of the

angular momenta

$$\left|\frac{3}{2},+\frac{3}{2}\right\rangle\left|1,-1\right\rangle = \frac{1}{\sqrt{10}}\left|\frac{5}{2},\frac{1}{2}\right\rangle + \sqrt{\frac{2}{5}}\left|\frac{3}{2},\frac{1}{2}\right\rangle + \underbrace{\frac{1}{\sqrt{2}}\left|\frac{1}{2},\frac{1}{2}\right\rangle}_{S_{1/2}} \; ; \tag{3.1}$$

therefore, we see that the probability for an excitation from the $|\frac{3}{2},\frac{3}{2}\rangle$ state to the $|\frac{1}{2},\frac{1}{2}\rangle$ state is $\frac{1}{2}$. Similarly, if the photons couple with the $|\frac{3}{2},\frac{1}{2}\rangle$ electrons in the $P_{3/2}$ valence band, we can again use the standard Clebsch-Gordan coefficients to deduce the following possibilities for the coupled value of the angular momenta

$$\left|\frac{3}{2},+\frac{1}{2}\right\rangle\left|1,-1\right\rangle = \sqrt{\frac{3}{10}}\left|\frac{5}{2},-\frac{1}{2}\right\rangle - \sqrt{\frac{8}{15}}\left|\frac{3}{2},-\frac{1}{2}\right\rangle + \underbrace{\frac{1}{\sqrt{6}}\left|\frac{1}{2},-\frac{1}{2}\right\rangle}_{S_{1/2}} \; ; \tag{3.2}$$

here, we see that the probability for an excitation from the $|\frac{3}{2},\frac{1}{2}\rangle$ state to the $|\frac{1}{2},-\frac{1}{2}\rangle$ state is $\frac{1}{6}$. Assuming a photon is equally likely to couple with an electron in a $|\frac{3}{2},\frac{3}{2}\rangle$ state or a $|\frac{3}{2},\frac{1}{2}\rangle$ state, it is clear that left-circularly polarized photons are three times more likely to induce a $|\frac{3}{2},\frac{3}{2}\rangle \rightarrow |\frac{1}{2},\frac{1}{2}\rangle$ transition than a $|\frac{3}{2},\frac{1}{2}\rangle \rightarrow |\frac{1}{2},-\frac{1}{2}\rangle$ transition; therefore, the maximum theoretical polarization for bulk GaAs is 50%.[2] In general, the polarization of the emitted electrons is less than the initial polarization (50%) of the electrons promoted from the valence band to the conduction band due to depolarization effects during the photoemission process [319].

Soon after the successful installation and operation of bulk GaAs photocathodes

[2]If $E_\gamma \geq E_g + \Delta_{\text{s.o.}}$, the photons can also excite transitions from the $P_{1/2}$ valence band to the $S_{1/2}$ conduction band; however, this is undesirable as can be seen from the Clebsch-Gordan couplings. Again, if left-circularly polarized photons, $|1,-1\rangle$, couple with the $|\frac{1}{2},\frac{1}{2}\rangle$ electrons in the $P_{1/2}$ valence band, the following possibilities for the coupled value of the angular momenta are

$$\left|\frac{1}{2},\frac{1}{2}\right\rangle\left|1,-1\right\rangle = \frac{1}{\sqrt{3}}\left|\frac{3}{2},-\frac{1}{2}\right\rangle + \underbrace{\sqrt{\frac{2}{3}}\left|\frac{1}{2},-\frac{1}{2}\right\rangle}_{S_{1/2}} \; . \tag{3.3}$$

From this, it follows that the polarization will (in theory) be

$$\frac{\frac{1}{2}-\frac{1}{6}-\frac{2}{3}}{\frac{1}{2}+\frac{1}{6}+\frac{2}{3}} = -25\% \; . \tag{3.4}$$

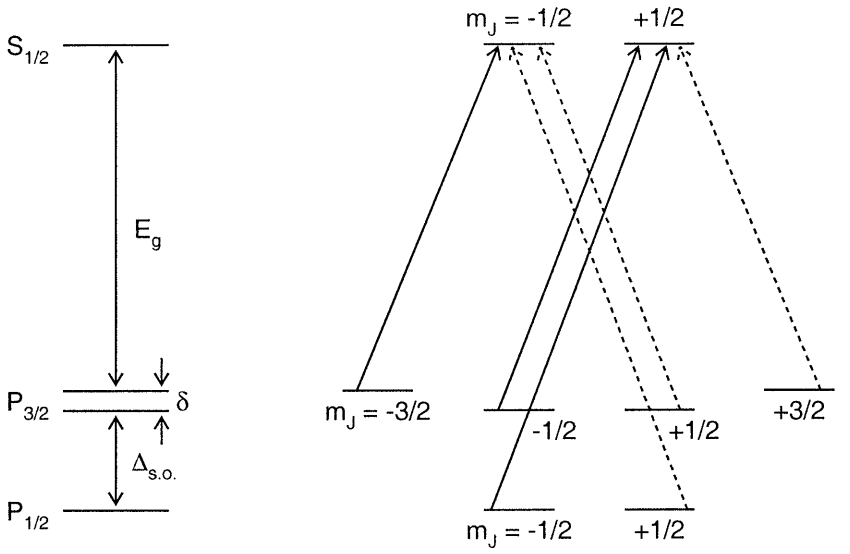

Figure 3-3: The energy levels and possible transitions for strained GaAs grown on GaAsP. The transitions that can be excited by right- (left-) circularly polarized laser light are shown as the solid (dashed) arrows.

at SLAC, MIT-Bates, Bonn, and MAMI, much effort was devoted to achieving higher polarizations. Theoretically, it was well known (see, e.g., [320, 321]) that the application of a uniaxial stress to a semiconductor induces a strain which reduces the symmetry of the material and results in significant changes in the electronic energy bands; in particular, it was found that the heavy- and light-hole states in strained GaAs are not degenerate. The first observation of polarizations (significantly) in excess of 50% was reported by Maruyama *et al.* [322] in 1991; Maruyama *et al.* observed polarizations in excess of 70% in photoemission from a sample of InGaAs grown on a GaAs substrate under conditions that induced strain in the InGaAs sample due to lattice mismatches between the two crystals. A similar polarization enhancement (of $\sim$80%) using photoemission from a strained crystal of GaAs grown on a thick GaAsP buffer was subsequently reported by Maruyama *et al.* [323] in 1992.

The band structure of strained GaAs grown on GaAsP is shown in Fig. 3-3. If the strain is induced in the growth direction of the crystal, the $|\frac{3}{2}, \pm\frac{3}{2}\rangle$ substates will be higher in energy than the $|\frac{3}{2}, \pm\frac{1}{2}\rangle$ substates (see, e.g., [296]); as is customary, this energy difference is denoted δ. If the energy of the photons satisfy $E_g \leq E_\gamma < E_g + \delta$, left- (right-) circularly polarized photons will only induce

$|\frac{3}{2},\frac{3}{2}\rangle \rightarrow |\frac{1}{2},\frac{1}{2}\rangle$ ($|\frac{3}{2},-\frac{3}{2}\rangle \rightarrow |\frac{1}{2},-\frac{1}{2}\rangle$) transitions; therefore, in theory, optical emission from a strained GaAs crystal should yield a polarization of 100%. Again, as with bulk GaAs, polarizations of 100% are not achievable due to depolarization effects during the photoemission process.

Laser System

As described in detail by Leemann, Douglas, and Krafft [293], the polarized source consists of two horizontally mounted "polarized guns". Each gun is mounted at a 15° angle relative to the injector axis and consists of three lasers; each laser pulses at the third subharmonic of the accelerator's fundamental 1497 MHz frequency (i.e., at 499 MHz) and produces "bunches" of polarized electrons at a repetition rate of 499 MHz for one of the experimental halls. One gun is used during normal production operations; the other serves as a spare and can, if needed, be interchanged remotely.

Prior to E93-038, only diode laser systems were used. These diode laser systems, composed of gain-switched diode seed lasers and diode optical amplifiers, produced optical pulsewidths of ~50 ps with an average power of ~100 mW at a repetition rate of 499 MHz [295]. As described by Poelker *et al.* [295], there were many appealing features associated with the diode laser systems. First, they were low cost systems that required very little maintenance. Second, the laser output from these systems was "clean" (i.e., low amplitude noise and pulse-to-pulse jitter). Last, each laser's 499 MHz optical pulse train could easily be phase locked to the third subharmonic of the accelerator's fundamental frequency. Unfortunately, the main disadvantage of the diode laser systems, their relatively low power output, led, ultimately, to the development of a novel high power Ti-sapphire laser system.

A schematic diagram of the polarized source laser system (including the Ti-sapphire and diode laser systems) and associated optics is shown in Fig. 3-4; the Ti-sapphire laser system is shown on the left side of the figure. A complete description of the Ti-sapphire laser system is beyond the scope of this thesis; therefore, we describe only the salient features and refer the reader to [295, 324] for a complete description. The Ti-sapphire laser system emits 50 ps pulses at a repetition rate of

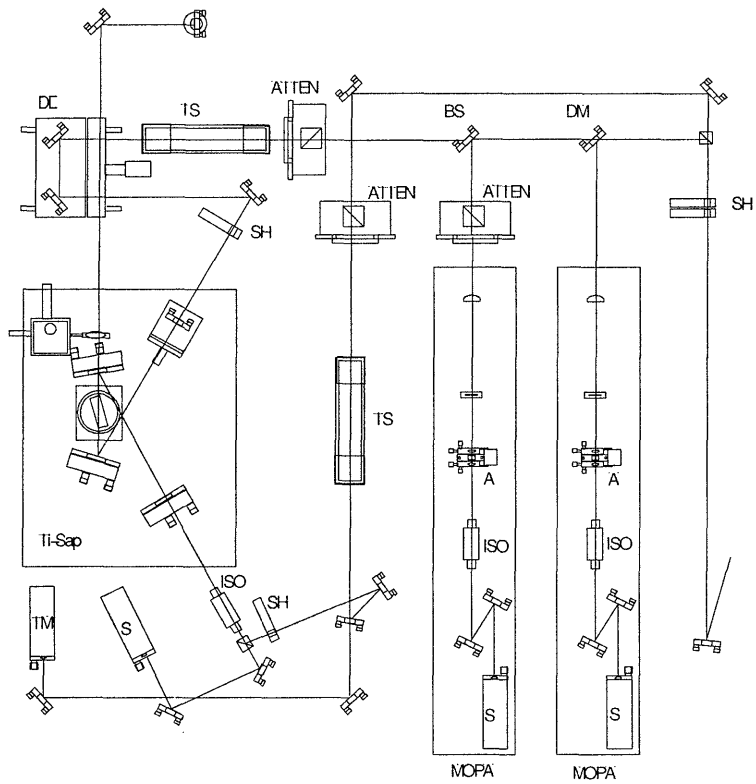

Figure 3-4: A schematic diagram of the polarized source laser system and associated optics. Ti-Sap denotes the Ti-Sapphire laser system; MOPA, the diode laser systems; S, gain-switched diode lasers; A, diode amplifiers; ISO, optical isolators; ATTEN, optical attenuators; TS, telescope; SH, shutter; DM, dichroic mirror; BS, beam splitter; DL, optical delay line; and TM, tune-mode diode laser.

499 MHz and produces on the order of 500 mW of power with ~30 nm wavelength tunability centered at ~850 nm; further, the Ti-sapphire laser can be configured with one or two output mirrors (for delivery of high beam currents to one or two experimental halls). The Ti-sapphire laser cavity is pumped with light from a gain-switched diode laser; the cavity length is 60.1 cm (corresponding to a frequency of 249.5 MHz — the sixth subharmonic of the fundamental 1497 MHz frequency). The phase of the Ti-sapphire optical pulse train is set by the rf signal used to drive the diode laser; this locks the phase of the laser's optical pulse train to the accelerator's frequency.

Due to the high-power capability of the Ti-sapphire laser, the source can be operated for several days before steps are required to restore the photocathode quantum

efficiency [324]. A number of minor adjustments, such as realignment of the laser mirrors, adjustments to the cavity length, and changes to the laser spot on the photocathode can be accomplished remotely.

Pockels Cells and Half-Wave Plate

Before impinging on the GaAs photocathode, the laser light is circularly polarized with a Pockels cell. A Pockels cell is a birefringent crystal (i.e., a crystal with different indices of refraction along its three principal axes, i.e., $n_x \neq n_y \neq n_z$). The indices of refraction are proportional to the magnitude of the electric field (or the voltage) that is applied to the crystal; therefore, if we take the z-axis to be the direction of propagation, the phase difference between the x- and y-components of the transmitted light will be proportional to the magnitude of the electric field. If the magnitude of the electric field is adjusted such that the phase difference is 90°, the Pockels cell acts as a $\lambda/4$ wave plate, and the linearly polarized laser light is transformed into circularly polarized laser light. If, instead, the field is tuned such that the induced phase difference is 180°, the Pockels cell acts as a $\lambda/2$ wave plate, and the helicity of the linearly polarized laser light is flipped. A $\lambda/2$ Pockels cell is located upstream of the $\lambda/4$ Pockels cell in the optics path. During this experiment, the helicity of the $\lambda/2$ Pockels cell (and, hence, the circular helicity of the laser light incident on the photocathode) was flipped pseudorandomly at a frequency of 30 Hz. The pseudorandom scheme that was employed generated a random helicity for one 33.3 ms window and then required the next 33.3 ms window to have the complementary helicity; for example, a sequence of "helicity pairs" could possibly have been: $+-$, $-+$, $-+$, $+-$, $-+$, etc.

In addition, a $\lambda/2$ wave plate can be manually (remotely) inserted in the optics path upstream of the Pockels cells. This $\lambda/2$ wave plate reverses the helicity of the electron beam that would otherwise be induced by the $\lambda/2$ Pockels cell. Data were taken during E93-038 with the $\lambda/2$ wave plate both "in" and "out"; this provides a useful systematic check for any possible helicity correlated differences associated with the polarized source.

Crystals

Polarized source operations at JLab began in 1997 with bulk GaAs crystals. In 1998, operations were switched from bulk GaAs crystals to strained GaAs on GaAsP crystals; strained GaAs on GaAsP photocathodes have been employed ever since [325]. All crystals have been purchased from Bandwidth Semiconductor (formerly known as the Spire Corporation).

The crystals are enclosed in vacuum (at the level of 10^{-12} Torr [295]). In order to achieve the highest possible quantum efficiencies, the surfaces of the photocathodes are cleaned via exposure to atomic hydrogen prior to activation with cesium [326].[3]

3.2.3 Injector

After the laser light impinges on the photocathode, the electrons are "bunched" and "chopped" in the injector and then accelerated to a nominal energy of 45 MeV prior to injection into the North Linac.[4] At 45 MeV, the beam is sufficiently relativistic ($\gamma = 88.1$) to match an 845 MeV recirculated beam. The majority of our discussion of the injector follows that given by Diamond [328].

100 keV Line

The first element in the injector is the 100 keV line. As its name implies, the 100 keV line accelerates the electron beam to 100 keV and is used to prepare the chopped and bunched beam that is accelerated further in the capture section of the injector. Transmissions as high as 75% from the photocathode to the experimental end stations have been achieved at beam currents as high as 110 μA [326].

[3]The application of cesium to a clean GaAs surface decreases the work function and thereby lowering the vacuum level below the conduction band; this leads to the negative electron affinity that is necessary for photoemission (see, e.g., [327]).

[4]It should be noted that because the laser systems already operate in a pulsed mode (instead of a continuous mode), losses associated with bunching and chopping are small; this increases the effective lifetime of the photocathodes as the majority of the electrons produced at the source are delivered to the experimental halls.

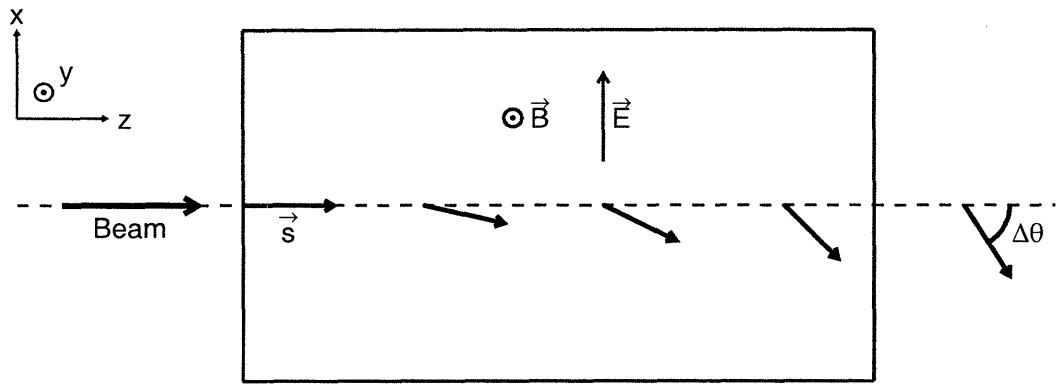

Figure 3-5: Schematic diagram of a Wein filter.

Wein Filter

The electron's anomalous magnetic moment induces the well-known phenomenon of $g-2$ longitudinal spin precession (see, e.g., [329]) in the magnetic fields in the East and West Recirculation Arcs. As discussed in detail by Sinclair [294], if the beam energy for each experimental hall, E_i, is

$$E_i = (2n_i + r)E_\ell \ , \qquad i \in \{\mathrm{A}, \mathrm{B}, \mathrm{C}\} \tag{3.5}$$

where E_ℓ is the energy of each linac, n_i is the number of passes for hall i, and r is the ratio of the injector to linac energy (0.1125), then the total spin precession angle, θ_i, for electrons delivered to each hall is

$$\theta_\mathrm{A} = \frac{E_\ell}{m_e}\left(\frac{g-2}{2}\right)\left[2n_\mathrm{A}^2 - n_\mathrm{A}(1-2r-C_1) - r(1-C_2)\right]\pi \ , \tag{3.6}$$

$$\theta_\mathrm{B} = \frac{E_\ell}{m_e}\left(\frac{g-2}{2}\right)\left[2n_\mathrm{B}^2 - n_\mathrm{B}(1-2r) - r\right]\pi \ , \tag{3.7}$$

$$\theta_\mathrm{C} = \frac{E_\ell}{m_e}\left(\frac{g-2}{2}\right)\left[2n_\mathrm{C}^2 - n_\mathrm{C}(1-2r+C_1) - r(1+C_2)\right]\pi \ , \tag{3.8}$$

where, $C_1 = 1/2.4$ and $C_2 = 1/4.8$.

As discussed previously in Section 2.3.2, the effects of transverse polarization are suppressed relative to those of longitudinal polarization by a factor of $1/\gamma_e$; therefore, in order to restore longitudinal polarization in the halls, a Wein filter is located in

the injector following the 100 keV line (see, e.g., [330]). As shown schematically in Fig. 3-5, a Wein filter is essentially a region of crossed electric, $\mathbf{E}$, and magnetic, $\mathbf{B}$, fields that are perpendicular to the direction of the electrons' motion. Here, for simplicity, we define the $\hat{\mathbf{z}}$ axis to be parallel to the direction of the electrons' motion, and we assume the $\mathbf{E}$ and $\mathbf{B}$ fields are parallel to the $\hat{\mathbf{x}}$ and $\hat{\mathbf{y}}$ axes, respectively. If the magnitudes of the fields are adjusted such that

$$\mathbf{E} + \beta\hat{\mathbf{z}} \times \mathbf{B} = \mathbf{0} \quad \Longrightarrow \quad |\mathbf{E}| = \beta|\mathbf{B}| \;, \tag{3.9}$$

the spins will precess, but the velocities will be unchanged.

Assuming static homogenous fields, the rate of change of the component of the spin parallel to the velocity, $\mathbf{s} \cdot \hat{\mathbf{z}}$, is [329]

$$\frac{\mathrm{d}}{\mathrm{d}t}(\hat{\mathbf{s}} \cdot \mathbf{z}) = -\frac{e}{m_e c}\, \mathbf{s}_\perp \cdot \left[\left(\frac{g-2}{2}\right)\hat{\mathbf{z}} \times \mathbf{B} + \left(\frac{g\beta}{2} - \frac{1}{\beta}\right)\mathbf{E}\right] \;, \tag{3.10}$$

where $\mathbf{s}_\perp$ denotes the component of $\mathbf{s}$ that is perpendicular to the velocity. From this, it can easily be shown that the total spin precession angle, $\Delta\theta$ (defined relative to the electrons' motion), can be written in terms of field integrals as

$$\begin{aligned} \Delta\theta &= \frac{e}{m_e\beta c}\left(\frac{g-2}{2}\right)\int |\mathbf{B}|\;\mathrm{d}\ell + \frac{e}{m_e\beta c}\left(\frac{g}{2}\beta - \frac{1}{\beta}\right)\int |\mathbf{E}|\;\mathrm{d}\ell \\ &= \frac{e}{m_e\beta c}\left[\frac{g}{2}(1+\beta^2) - 2\right]\int |\mathbf{B}|\;\mathrm{d}\ell \;; \end{aligned} \tag{3.11}$$

therefore, the spin can be manipulated in the Wein filter to any desired angle with appropriate adjustments to $|\mathbf{B}|$ (and $|\mathbf{E}|$). [Spin precession in electromagnetic fields is discussed in more detail in Section 4.2.1.]

Certain values of the linac energy, referred to as "magic linac settings", permit simulataneous delivery of longitudinal polarization to all three halls. These are well documented and may be found in [331].

Capture Section

After extraction from the 100 keV line and the Wein filter, the beam is directed to the capture section. The capture section consists of five room-temperature rf accelerator cavities powered, in parallel, by two klystrons.[5] The electrons gain 440 keV in the capture section; therefore, the energy of the beam is 0.540 MeV after traversing the capture section.

Pre-Accelerator Section and Two 1/4 Cryomodules

The beam is then directed to the pre-accelerator section of the injector. The pre-accelerator section consists of two superconducting rf cavities (referred to as a "quarter-cryomodule") that accelerate the beam to an energy of 5.15 MeV.[6] After the beam has traversed the pre-accelerator section, it is directed through an approximately 6-m long diagnotistic and tuning area that is shielded by a 5-foot-thick wall. The beam is then injected into two successive crymodules where it is accelerated to the nominal injector energy of 45 MeV.

3.2.4 Central Helium Liquifier

The Central Helium Liquifier (CHL), located at the center of the accelerator's race-track layout (see Fig. 3-1), provides the refrigeration that cools the cryomodules in the injector and the North and South Linacs to the accelerator's operating temperature of 2.08 K. The CHL consists of three pairs of compressors, a "main cold box" that produces 45 K and 4.5 K refrigeration, and a "subatmospheric cold box" that cools the 4.5 K refrigerant to 2.0 K. In addition to supplying the compressors with

[5]The Jefferson Laboratory klystrons are continuous-wave, water-cooled microwave amplifiers that operate at the accelerator's fundamental 1497 MHz frequency and can produce a maximum power output of 5 kW.

[6]As discussed in detail by Leemann, Douglas, and Krafft [293], a standard JLab "cryomodule" consists of four "cryounits". Each cryounit consists of a pair of niobium superconducting rf cavities; the cryounits maintain the cavities at the acclerator's operating temperature of 2.08 K (well below niobium's superconducting transition temperature of 9 K) and shield the cavities from magnetic fields. A 5 kW klystron provides the rf power for each cavity. The klystrons are arranged in groups of eight and are located in service buildings directly above the injector and the North and South Linacs.

liquid helium, the CHL also supplies the Test Lab's Cryogenic Test Facility and the End Station Refrigerator with liquid helium; the End Station Refrigerator supplies the refrigeration for the cryogenic targets and the magnetic spectrometers in the experimental halls.

The CHL can store a total of 113,550 liters of liquid helium (including 67,600 liters in the cryomodules) and 40,000 gallons of liquid nitrogen.

3.2.5 Linacs and Recirculation Arcs

The North and South linacs are identical, and each consist of 20 cryomodules; the original design goal for the North and South Linacs was 400 MeV acceleration. Each cavity is phase locked to within 1° and the gradient of the rf field is regulated to within 10^{-4} [293]. After the beam has traversed the North Linac, the beam is spread vertically, according to energy (i.e., number of passes) into the separate East Recirculation Arc lines shown in Fig. 3-1. The recirculation arcs were designed to minimize degradation of beam quality due to, for example, synchrotron radiation or optical aberrations. At the end of the East Recirculation Arc, a recombiner, essentially a mirror image of the spreader, phase matches the individual beam lines to the South Linac.

At the end of the South Linac, a 499 MHz separator system either extracts the beam and directs it to the beam switchyard or steers the beam to the West Recirculation Arc for further acceleration in the North and South Linacs. The beam energy for each experimental hall can be any of the five-pass multiples. As described by Leemann, Douglas, and Krafft [293], if each hall requests the full (five-pass) energy, one of the bunch trains is phased with the zero crossing of the deflecting field in the rf separator. This bunch train is then, of course, not deflected and propagates forward through the field-free central aperture of a three-aperture Lambertson septum magnet. The other two bunch trains are then deflected through equal angles in opposite directions by the deflecting field in the separator into conventional septum magnets and subsequently steered into the two high-field apertures of the Lambertson septum; the bunch trains are then directed into the appropriate experimental hall.

Maximum Energy	6067.5 MeV
Beam Polarization	$> 75\%$
Currents (Halls A and C)	1–100 μA
Current (Hall B)	1–100 nA
Hall Repetition Rate	499 MHz
Bunch Charge	< 0.3 pC
Beam Size (rms transverse)	$\sim$80 μm
Bunch Length (rms)	300 fs, 90 μm
Energy Spread	2.5×10^{-5}
Beam Loss	< 1 μA
Number of rf Cavities	338
rf Power	< 3.5 kW/cavity
Amplitude Control	10^{-4} rms
Phase Control	0.1° rms

Table 3.2: Some of the principal accelerator parameters as given in [293].

If, instead, multiple-energy delivery to the halls is requested, a "two-beam" split is performed. In the extraction region, rf separators are phased to provide the maximum deflection to the desired bunch train. This bunch train is then steered through a number of septa magnets and then directed to the appropriate experimental hall. The other bunch trains are, of course, 120° out of phase with the maximum (in the rf separation field) and, as a result, are deflected in the opposite direction into the West Recirculation Arcs.

To conclude our discussion of the polarized source and the accelerator, we summarize, in Table 3.2, some of the principal accelerator parameters as given in [293].

3.3 Hall C Arc and Beamline

3.3.1 Overview

After the beam of the desired energy has been extracted from the accelerator, it is directed to the Hall C arc and beamline. The Hall C arc and beamline consists of the following general list of elements:

- A series of magnets which focus and steer the beam from the beam switch yard to the cryotarget (the arc).
- Several devices along the Hall C beamline that monitor the beam's energy, position, and current.
- A fast raster system, designed to prevent damage to solid targets and mimimize local boiling in cryogenic targets.
- A Møller polarimeter used to measure the polarization of the electron beam.
- The scattering chamber which houses the cryotargets.
- The exit beamline which leads from the cryotarget to the beam dump tunnel.

In what follows, we provide an overview of each of these components. Unless otherwise noted, much of our discussion follows that given by Arrington [332], Gustafsson [333], Tireman [334], and Zhu [335].

3.3.2 Hall C Beam Diagnostics

A schematic diagram of the instrumentation along the Hall C arc and beamline is shown in Fig. 3-6. In what follows, we provide a brief overview of the superharps, the beam position monitors, and the beam current monitors.

Superharps and Beam Energy Measurements

A number of superharps, located along the Hall C arc and beamline, are used to monitor the beam profile. The original harps, as their name suggests, consisted of a movable frame with two vertically oriented wires and one horizontally oriented wire. During a "harp scan", the harp is moved across the beam; as the wires intercept the beam, an analog-to-digital converter (ADC) records the signals that are measured on each wire, and a position encoder determines the positions of the wires as they pass through the beam. The beam position and profile can then be extracted from the ADC and position information.

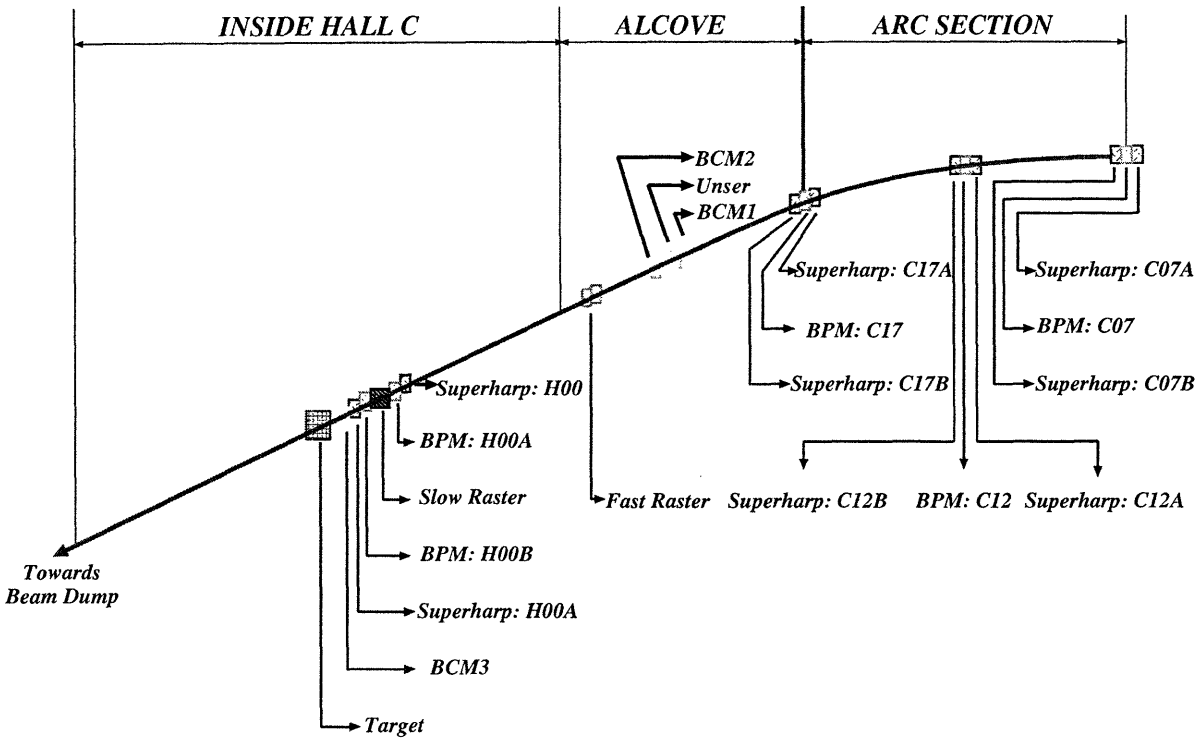

Figure 3-6: (color) Schematic diagram of the instrumentation along the Hall C arc and beamline.

The superharps are essentially an upgraded version of the original harps; the superharps include absolute position readout electronics, a dual beam profile detection system with two analog signal pick-up channels (direct current pick-up by the wires and bremsstrahlung detection), and a vibration-free support system. During a "superharp scan", all non-dipole magnets along the Hall C arc beamline are turned off, and the currents in the dipole magnets are adjusted such that the beam is centered at the end of the arc. The positions and directions of the beam are recorded by the three superharps along the arc section of the beamline (shown in Fig. 3-6), and from these measurements, the bend angle, Θ, can be determined. If the total field integral, $\int |\mathbf{B}|\, d\ell$, is well-known, the momentum of the beam, $|\mathbf{p}_e|$, can be determined according to

$$|\mathbf{p}_e| = \frac{e}{\Theta} \int |\mathbf{B}|\, d\ell \,. \tag{3.12}$$

The position accuracy of a superharp scan is better than 20 μm, and the energy

can be measured to an accuracy of 10^{-3}. We refer the reader to [336] for a complete technical discussion of the harps, superharps, and energy measurements.

Beam Position Monitors

As shown in Fig. 3-6, there are four beam position monitors (BPMs) located along the Hall C beamline. Each BPM is a cavity with four antennae oriented at an angle of $\pm 45°$ relative to the horizontal and vertical directions. When the beam passes through the BPM cavities, the antennas detect the beam's 499 MHz frequency and digitize the amplitude of the signal. The amplitude of this signal is proportional to the distance of the beam from the antenna; therefore, provided the signals from two separate antennas are properly normalized, the position can be determined from the difference between the amplitudes of two antennae located on opposite sides of the beam.

Beam Current Monitors

There are two different types of beam current monitors that have been installed in the Hall C beamline. The first is a resonant cavity type, and the second is an Unser monitor (see, e.g., [337]); the Unser monitor is a parametric DC current transformer that is used to calibrate the resonant cavities.

The Unser monitor consists of a toroidal sensor which fits over the beam pipe. The signal from the Unser monitor is very sensitive to stray rf fields, magnetic fields, temperature changes, and mechanical vibrations; therefore, the Unser monitor is shielded with a copper rf shield and a magnetic shield and is thermally insulated at a temperature of 43.3° C. The Unser monitor has excellent linearity and has a very stable and well measured gain; however, it suffers from a poor signal-to-noise ratio and large drifts in its offsets. Because the gain is stable, the Unser can be used to calibrate the gain of the cavity BCMs.

The three cavity BCMs located along the Hall C beamline, shown in Fig. 3-6 as BCM1, BCM2, and BCM3, are cylindrical wave guides that contain wire loop antennas that couple to resonant modes of the cavity; the signal is proportional

to the beam current for all resonant modes. Further, if the cavity length is chosen appropriately, the 499 MHz beam will excite the 1497 MHz TM_{010} mode of the cavity; this mode is insensitive to the beam position. These BCM cavity monitors have a good signal-to-noise ratio, and their gain and offsets are reasonably stable. During E93-038, BCM1 and BCM2 were operational, but BCM3 was not. BCM1 and BCM2 were calibrated prior to the start of the experiment; however, as E93-038 measured asymmetries instead of cross sections, the details of the analysis do not require precise measurements of the beam current.

3.3.3 Fast Raster System

The electron beam has a very small transverse size ($\sim$80 μm rms width [293]), and the average energy deposition in a cryogenic target is on the order of 5 MeV cm^2 g^{-1} [338]. This large value of the energy deposition can lead to local density fluctuations (i.e., local boiling) in a cryotarget if the energy deposition is not distributed uniformly over the cryotarget volume.

To distribute the energy deposition in a more uniform manner over the cryotarget volume, a fast raster system was developed and installed 21 m upstream of the cryotarget along the Hall C beamline [338, 339]. As described by Wojcik and Yan [338], the present raster system consists of two 250 W power amplifiers that drive two raster magnets at different frequencies (24 and 17 kHz); one magnet rasters the beam vertically while the other rasters the beam horizontally. Such a frequency ratio in the vertical and horizontal directions generates a non-standing Lissajous pattern. During E93-038, the fast raster was configured to raster the beam over a 2 mm $\times$ 2 mm spot on the cryotarget.

3.3.4 Hall C Møller Polarimeter

The beam polarization was measured with the Møller polarimeter located in the alcove section of the Hall C beamline (see Fig. 3-6). Before proceeding to a technical discussion of the Hall C Møller polarimeter, we provide a brief overview of the two primary

techniques that have been developed for electron beam polarization measurements: Møller polarimetry and Compton polarimetry.

Overview of Møller Polarimetry

Møller scattering [340] (i.e., polarized-electron, polarized-electron scattering) is purely a QED process; therefore, the cross section can be calculated to very high precision. To lowest order, the cross section in the center-of-mass frame (CM) is

$$\frac{\mathrm{d}\sigma}{\mathrm{d}\Omega} = \frac{\mathrm{d}\sigma_0}{\mathrm{d}\Omega}\left[1 + \sum_{i,j\ =\ x,y,z} A_{ij} P_i^{\mathrm{beam}} P_j^{\mathrm{target}}\right] , \tag{3.13}$$

where

$$\frac{\mathrm{d}\sigma_0}{\mathrm{d}\Omega} = \frac{\alpha^2(4-\sin^2\theta)}{4E_e^2\sin^4\theta} \tag{3.14}$$

is the unpolarized cross section, θ denotes the scattering angle in the CM frame, the A_{ij} are analyzing powers, and P_i^{beam} and P_i^{target} denote, respectively, components of the beam and target polarization.

For a longitudinally polarized beam and target (here, we define the z-axis to be parallel to the beam axis, and we denote the magnitudes of the beam and target polarizations as P_L and P_T, respectively), the cross section reduces to (see, e.g., [341])

$$\frac{\mathrm{d}\sigma}{\mathrm{d}\Omega} = \frac{\mathrm{d}\sigma_0}{\mathrm{d}\Omega}\left[1 + A_{zz}(\theta) P_L P_T\right] , \tag{3.15}$$

where the analyzing power is given by

$$A_{zz}(\theta) = -\frac{\sin^2\theta(8-\sin^2\theta)}{(4-\sin^2\theta)^2} . \tag{3.16}$$

A straightforward calculation shows that A_{zz} achieves its maximum value, $A_{zz} = -\frac{7}{9}$, at $\theta = 90°$.

It is clear that the cross section is asymmetric with respect to helicity reversal of the electron beam (provided the orientation of the target polarization remains fixed).

This helicity asymmetry, denoted ϵ, can be written as

$$\epsilon = \frac{(\mathrm{d}\sigma^{\uparrow\uparrow}/\mathrm{d}\Omega) - (\mathrm{d}\sigma^{\uparrow\downarrow}/\mathrm{d}\Omega)}{(\mathrm{d}\sigma^{\uparrow\uparrow}/\mathrm{d}\Omega) + (\mathrm{d}\sigma^{\uparrow\downarrow}/\mathrm{d}\Omega)} = A_{zz}(\theta) P_L P_T \ , \tag{3.17}$$

where $\uparrow\uparrow$ ($\uparrow\downarrow$) denotes aligned (anti-aligned) beam and target spins; therefore, it is clear that the beam polarization can be extracted from the helicity asymmetry if the scattering angle and the target polarization are well known. These expressions are only strictly valid to lowest order; however, DeRaad and Ng [342] found that radiative corrections (calculated to order α^4) have negligible effect on A_{zz}.

Although the analyzing power is large for scattering angles near 90° in the CM frame, the exploitation of Møller scattering for electron beam polarization measurements has proven to be difficult [341]. In a typical ferromagnetic material, such as iron, only 2 of the 26 electrons can be polarized; this leads to an effective target polarization of only ~7.7%. The precision achieved by early polarimeters installed at MAMI [343] and MIT-Bates [344] was limited by three factors: the statistics that could be acquired within a reasonable period of time, uncertainties due to background contributions (e.g., Mott scattering from nuclei), and uncertainties in the target polarization. Further, these early designs neglected the influence of the non-zero initial momentum of the atomic electrons on the analyzing power; this effect, known as the Levchuk [345] effect, was identified only recently in 1994.

As described in detail by Hauger *et al.* [341], the Møller polarimeter installed in Hall C was designed to significantly reduce the uncertainties from the three sources listed above. First, the large acceptance of the polarimeter reduces the amount of time required to collect sufficient statistics; in addition, the large acceptance mitigates the influence of the Levchuk effect on the instrument's effective analyzing power. Second, the polarimeter was designed to operate in coincidence mode; detection of both the incident electron and the scattered electron reduces background contamination from Mott scattered electrons. Last, as proposed by deBever *et al.* [346], the polarimeter's target foils are composed of pure iron that are magnitized to saturation using a 4 T

field; the polarization of pure iron in saturation is known with great accuracy [347].[7]

Overview of Compton Polarimetry

Compton scattering, as relevant for electron beam polarimetry studies, is polarized-electron, circularly-polarized-photon scattering.

In a "head-on" collision between high-energy electrons and low-energy photons, the photons will backscatter into a narrow cone centered around the collision axis. As usual, we use P_L to denote the longitudinal polarization of the electrons. The polarization of the photons is specified by the Stokes vector [348], $\mathbf{S}$, denoted

$$\mathbf{S} = (S_0, S_1, S_2, S_3) \ , \tag{3.18}$$

where the degree of linear polarization is given by $\sqrt{S_1^2 + S_2^2}$, the degree of circular polarization is given by $|S_3|$ [$S_3 > 0$ ($S_3 < 0$) for left- (right-) handed circular polarization], and S_0 is unity. The cross section differential in the scattered photon's energy, E_γ, for longitudinally polarized electrons and circularly polarized photons is

$$\frac{\mathrm{d}\sigma}{\mathrm{d}E_\gamma} = \frac{\mathrm{d}\sigma_0}{\mathrm{d}E_\gamma}\left[1 + S_3 P_L \alpha_{3z}\right] \ , \tag{3.19}$$

where $\mathrm{d}\sigma_0/\mathrm{d}E_\gamma$ is the differential cross section for unpolarized electrons and photons and α_{3z} is known as the circular-longitudinal spin correlation function (see, e.g., [349]).

Again, it is clear that the cross section is asymmetric with respect to helicity reversal of the electron beam; therefore, a measurement of the helicity asymmetry,

$$\epsilon = \frac{(\mathrm{d}\sigma/\mathrm{d}E_\gamma)^{h=+1} - (\mathrm{d}\sigma/\mathrm{d}E_\gamma)^{h=-1}}{(\mathrm{d}\sigma/\mathrm{d}E_\gamma)^{h=+1} + (\mathrm{d}\sigma/\mathrm{d}E_\gamma)^{h=-1}} = S_3 P_L \alpha_{3z} \ , \tag{3.20}$$

where $h = \pm 1$ denotes the helicity of the electron beam, is sensitive to the beam polarization. Provided the circular polarization of the photons is well known (α_{3z} can

[7] As discussed in detail by deBever *et al.* [346], in saturation, the magnetic properties of an isolated iron atom and atoms in a foil are essentially identical. In particular, as shown by Reck and Fry [347], the contribution from orbital motion to the total magnetization of an iron target is on the order of ~4%; the remaining contribution is due entirely to the spin of the electrons and is known to an accuracy of 0.25%.

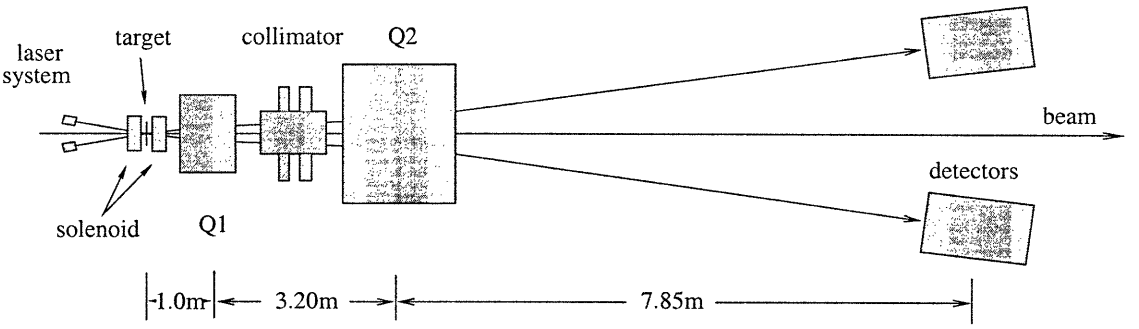

Figure 3-7: Schematic diagram of the layout of the Hall C Møller polarimeter.

be calculated very precisely in QED), P_L can be extracted from ϵ.

In a typical arrangement, electrons, deflected from the incident electron beam using a magnetic chicane, scatter from circularly polarized laser light. Following the scattering, the chicane is used to separate the electrons and the backscattered photons. The backscattered photons are then, typically, detected in a calorimeter, and the helicity asymmetry is extracted from the rates measured in the calorimeter for the different beam helicities. Compton polarimeters have been developed and installed at HERA [350], NIKHEF [349], and JLab Hall A [351]; we refer the reader to these references for a more complete technical description of Compton polarimetry.

Møller Polarimeter Setup in Hall C

The Møller polarimeter is located in the alcove in the Hall C beamline (see Fig. 3-6) approximately 30 m upstream of the scattering chamber; a schematic diagram of the polarimeter layout is shown in Fig. 3-7. A detailed description of the polarimeter has been given by Hauger *et al.* [341]; below, we summarize the most important features and parameters.

The incoming electrons impinge on a thin (few μm) foil of pure iron mounted on a target ladder that can be remotely inserted into the beam.[8] The foil is saturated with a superconducting split-coil solenoid that can produce a maximum field of 4 T;

[8]Moller polarimetry, unlike typical Compton polarimetry setups, is destructive to the incident electron beam; therefore, in general, Møller measurements are conducted at the expense of experimental production measurements.

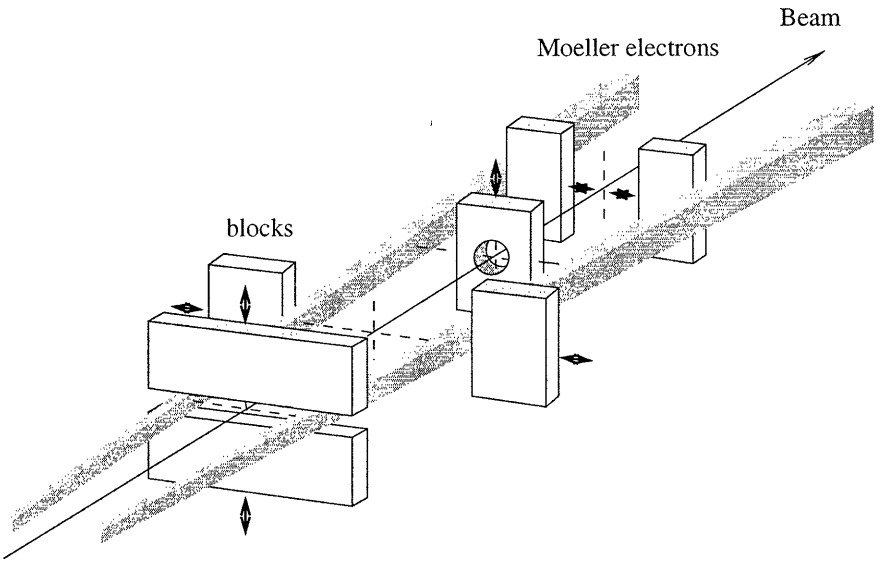

Figure 3-8: Schematic diagram of the collimator system for the Hall C Møller polarimeter. Shown are the movable "jaws" and the centrally located collimator with a fixed acceptance.

the solenoid's longitudinal magnetic field has little effect on the trajectories of the incoming and scattered electrons.

After scattering in the foil, a two-quadrupole system (denoted Q1 and Q2 in Fig. 3-7) deflects the scattered electron and the recoil target electron; this increase in the scattered and recoil target electrons' scattering angles reduces the distance the detectors must be placed from the target foil. At low incident electron energies, Møller-scattered electrons at 90° CM angles emerge at relatively large scattering angles in the laboratory frame; Q1 then focuses these electrons into the acceptance of Q2. At high incident electron energy, the laboratory scattering angles are small and Q1 has little effect on the trajectories. The advantage of this two-quadrupole setup is that Q2 can be located at a greater distance from the target foil; this maximizes the overall deflection of Møller scattered electrons.

Møller scattering does, of course, yield a spectrum of scattering angles; however, only CM scattering angles near 90° are of interest. Further, Mott scattered electrons emerge at small scattering angles; therefore, the collimator system, shown in detail in Fig. 3-8, was designed to suppress small scattering angles as much as possible. The

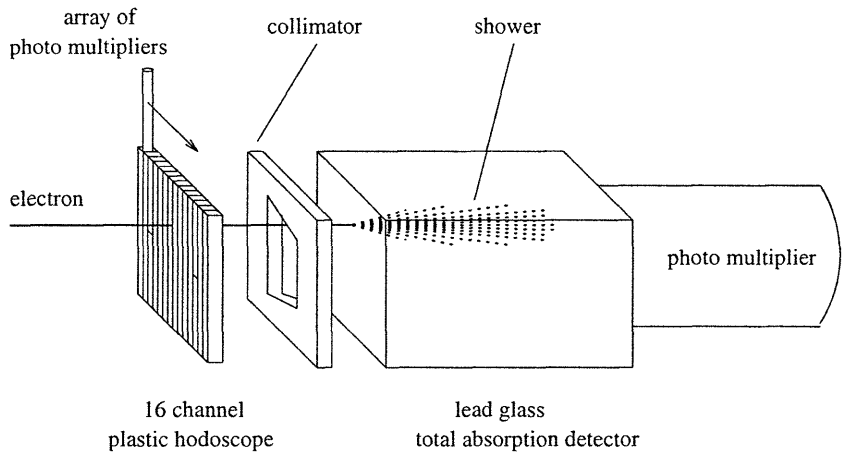

Figure 3-9: Detector package for the Hall C Møller polarimeter. Shown are the hodoscope, the slits, the lead-glass shower counter, and the photomultiplier tube.

collimator system consists of six moveable "jaws" designed to eliminate both small and large (i.e., much greater than 90° CM angles) scattering angles and a centrally located seventh collimator with a fixed acceptance designed to suppress electrons originating from the the small-angle side of the inner horizontal collimator; the collimator system can be inserted and removed remotely. The "jaws" were constructed of densimet (an alloy with a high tungsten content) and are 8-cm thick (approximately 22 radiation lengths).

The scattering angle selection applied by the collimators is less rigorous than that applied by two slits located in front of each detector. These slits define the actual angular acceptance of the polarimeter and are 12-cm wide in the horizontal direction with a 2-3 cm tapered opening in the vertical direction. This geometrical configuration for the slits, optimized by Hauger *et al.* via simulation, minimizes uncertainties due to the Levchuk effect. The slits are composed of 9 radiation lengths of lead.

The detector package consists, primarily, of lead-glass total absorption shower counters (lead-glass shower counters will be discussed in greater detail during our discussion of the HMS detector package); a schematic of the detector package is shown in Fig. 3-9. The shower counters, composed of SF2 lead-glass, are 20 cm $\times$ 14 cm $\times$ 23 cm in size and are coupled to 5-inch photomultiplier tubes. The signal recorded in the photomultipliers is used to select electrons of the appropriate energy;

this energy selection, combined with the coincidence requirement, eliminates most of the background.

Two hodoscopes are located ahead of each lead-glass shower counter; the hodoscopes provide position information for the electrons entering the shower counters. Each hodosope consists of 14 channels, and each channel consists of a scintillator bar, 8 mm $\times$ 12 mm in width and 80 mm high, coupled to an 8-mm photomultiplier. The hodoscopes were used during the commissioning phase of the polarimeter; at present, the hodosope position information is not, in general, recorded during polarization measurements. Finally, a 1-cm thick lead curtain, located ahead of the hodoscopes, serves to attenuate low-energy background.

The entire Møller polarimeter is controlled with two Graphical User Interfaces (GUIs) which employ the standard Experimental Physics and Industrial Control Systems (EPICS) software tools. The primary information provided by the polarimeter is the counting rate of the two lead-glass detectors (as measured by their photomultipliers). Prompt and delayed coincidences are registered with VME scalers, and the scalers are read out when the helicity of the electron beam is flipped at the polarized source.

Polarimeter Performance

At present, the polarimeter operates reliably and a <1% statistical uncertainty can be achieved after approximately 15–20 minutes of data taking. Also, the systematic uncertainty quoted by Hauger *et al.* is on the order of 0.5%. Although a 1% (or better) measurement can be achieved in a reasonable amount of time, the polarimeter does possess one slightly undesirable feature. During E93-038, production data were taken with beam currents as high as 70 μA; however, the Møller polarimeter was only designed for currents up to $\sim$8 μA (due to beam heating and, subsequently, depolarization of the target foil). During E93-038, most of the Møller measurements were conducted with $\sim$1–2 μA beam currents; therefore, it was necessary to assume that the values of the beam polarization extracted from the Møller measurements at low beam currents were valid for the high beam currents at which the production

data were taken.[9]

Møller Measurements During E93-038

During E93-038, the beam polarization was measured approximately every one to two days. Also, the polarization was usually measured after the $\lambda/2$ plate was either inserted or removed at the polarized source or after major accelerator changes (e.g., energy changes, laser spot moves on the photocathode, reactivation of the photocathode, etc.) Details of the results of the beam polarization measurements will be provided later. Also, as will be discussed later, the details of the analysis are largely insensitive to exact knowledge of the beam polarization; instead, the polarization information was primarily used to assess the systematic uncertainty associated with temporal fluctuations in the beam polarization.

3.3.5 Scattering Chamber and Cryotargets

Scattering Chamber

The Hall C scattering chamber is a large vertically standing cylindrical chamber (height of 136.5 cm) mounted atop the pivot located at the center of the hall. The chamber is composed of a single ring of aluminum (outer diameter of 135.9 cm and a wall thickness of 6.35 cm) that houses and thermally insulates the cryotargets from the room temperature air in the hall. The beam connects directly (in vacuum) to the scattering chamber; therefore, the beam does not need to pass through any entrance windows en route to the target. In addition, the chamber has two exit windows. For this experiment, the two exit windows and the beam exit port were made of beryllium; one faced the HMS while the other faced the neutron polarimeter. The interior of the chamber is maintained in a vacuum at the level of $\sim 10^{-6}$ Torr; the

[9]The validity of this assumption has been verified in JLab Hall A with the Møller and Compton polarimeters installed there [352]. The beam polarizations measured with the Møller polarimeter at low currents ($\sim$0.5 μA) and the Compton polarimeter at high currents ($\sim$40 μA) have been found to agree to within $\sim$3%, well within the quoted systematic errors for the two different techniques. In Hall C, efforts are currently underway to develop a Compton polarimeter, and a high-current upgrade of the Møller polarimeter has been discussed [353].

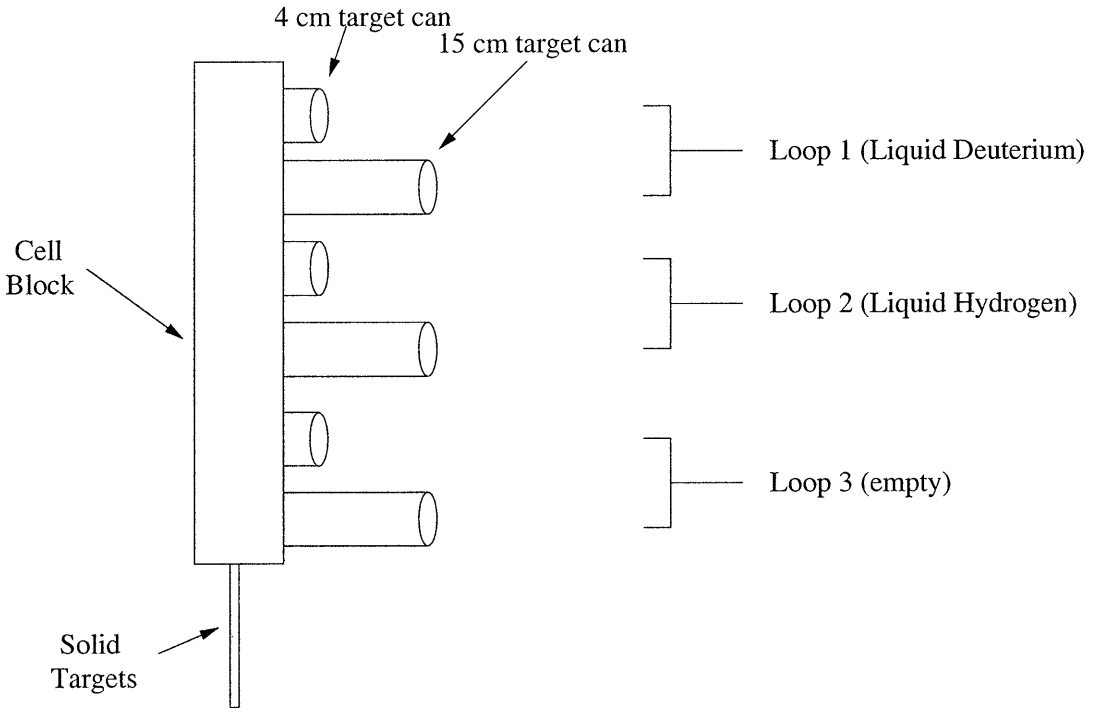

Figure 3-10: Schematic sideview of the target ladder showing the Loop 1 (liquid deuterium), Loop 2 (liquid hydrogen), and Loop 3 (empty/reserve) cryotarget loops mounted on the cell block and the solid targets mounted below the cell block.

vacuum minimizes the conductive heat load on the cryotargets and the probability for multiple scattering processes between the cryotarget and the exit windows.

Cryotargets

The scattering chamber can, in general, house two target ladders: one for solid (foil) targets and the other for cryogenic targets. E93-038 devoted very little time to measurements with solid targets; therefore, the solid target ladder was removed, and the solid targets were attached to the bottom of the cryogenic target ladder.

A simplified schematic diagram of the target ladder is shown in Fig. 3-10. The cryogenic portion of the ladder consisted of three cryogenic target loops mounted on a common cell block. Each loop consisted of a 4-cm and 15-cm long target "cans" made of aluminum. As indicated in this figure, liquid deuterium flowed through Loop 1, and liquid hydrogen flowed through Loop 2. Loop 3 was filled with gaseous helium

Cell Window	Thickness [mils]
Loop 1, 4-cm, Entrance	4.43
Loop 1, 4-cm, Exit	5.48
Loop 1, 15-cm, Entrance	4.41
Loop 1, 15-cm, Exit	5.95
Loop 2, 4-cm, Entrance	5.72
Loop 2, 4-cm, Exit	6.32
Loop 2, 15-cm, Entrance	5.00
Loop 2, 15-cm, Exit	5.86
Dummy, 4-cm, Entrance	37.04
Dummy, 4-cm, Exit	36.92
Dummy, 15-cm, Entrance	37.12
Dummy, 15-cm, Exit	36.96

Table 3.3: Summary of the cryogenic target cell window thicknesses during E93-038. The cell window thicknesses reported for each cell windown are the average of six thickness measurements conducted at a radius of 1 mm at 60° intervals [354]. [1 mil $= \frac{1}{1000}$ inch]

and functioned as a reserve. The solid targets (carbon, etc.) and 4-cm and 15-cm aluminum "dummy targets" were mounted below the cryogenic cell block; these dummy targets consisted solely of two aluminum foils spaced either 4 cm or 15 cm apart.[10] The target cell window thicknesses for Loops 1 and 2 and the dummy cells are summarized in Table 3.3 [354].

Each cryogenic target loop consisted of the target cells, a heat exchanger, high- and low-powered heaters, and a number of different sensors. The heat exchanger is a stainless steel cylinder surrounding 6.35-mm copper tubing. Helium (14 K) extracted from the End Station Refrigerator flows through the copper tubing, and the cryogen in the target is forced to flow past the heat exchanger. The heat exchanger can dissipate on the order of several hundred Watts of power deposited by the electron beam. The high-power heater (2 Ω resistance and a maximum power output of $\sim$800 Watts) is used to maintain a constant heat load on the system, while the low-power heater (24 Ω resistance and a maximum power output of $\sim$80 Watts) is used to maintain the cryotargets at their specified operating temperatures and to correct for small

[10]During the experiment, data were taken with the dummy targets in order to assess the level of contamination due to scattering from the target cell windows.

fluctuations in the power deposited by the electron beam (i.e., due to fluctuations in the beam current). The nominal operating temperatures for the liquid deuterium and liquid hydrogen targets were 22.0 K and 19.0 K, respectively.

Production data were taken with the Loop 1 15-cm liquid deuterium target. Target conditions were continuously monitored and regulated using the standard Hall C cryotarget control system. The primary control system includes an Input-Output-Controller (IOC), a single board VME computer, connected to a workstation. The target control system uses EPICS as its operating software, and the target conditions were monitored and regulated with a GUI that was an EPICS client.

The above is certainly not intended to serve as a comprehensive overview of the Hall C cryotarget system. For that, we refer the reader to theses written on Hall C experiments which measured cross sections (see, e.g., [332]).

3.3.6 Downstream Beamline

Unscattered electrons exited the scattering chamber and proceeded to the downstream beam line. The downstream beam line consists of an aluminum pipe that is filled with gaseous helium and separated from the scattering chamber vacuum by the beam exit port beryllium oxide window. This aluminum pipe is 2 inches in diameter at the scattering chamber and slowly grows to a 36 inch diameter 25 meters from the target (as there are no magnets along the downstream beamline); there, the downstream beam line connects to a 33-meter long tunnel leading to the beam dump. The beam dump itself consists of a heat exchanger that is cooled with deionized water.

3.4 High Momentum Spectrometer

Two magnetic spectrometers were constructed for Hall C operations: the High Momentum Spectrometer (HMS) and the Short Orbit Spectrometer (SOS). The HMS is a superconducting three-quadrupole single-dipole spectrometer with a large solid angle acceptance, a maximum central momentum of 7.5 GeV/c, a $\pm$18% momentum acceptance, and a $\sim$27-m flight path from the target to the end of the detector pack-

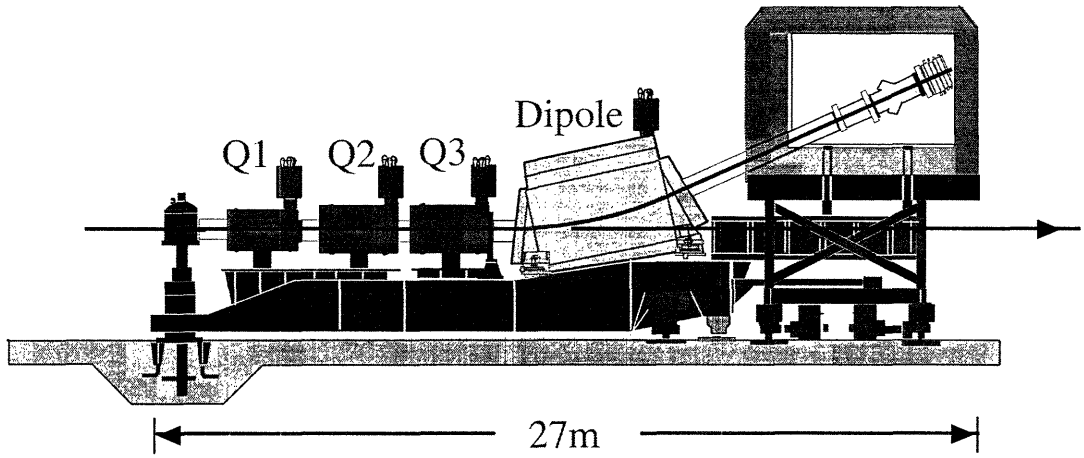

Figure 3-11: (color) Schematic sideview of the HMS showing the three quadrupoles (Q1, Q2, and Q3), the dipole, and the concrete shielding hut for the detector package.

age. In contrast, the SOS is a water-cooled non-superconducting single-quadrupole two-dipole spectrometer with a large solid angle acceptance, a maximum central momentum of 1.8 GeV/c, a $\pm 40\%$ momentum acceptance, and a short $\sim$9-m flight path from the target to the end of the detector package. The SOS flight path is much shorter than the HMS flight path because the SOS was designed to detect hadrons (such as short-lived kaons and pions) in coincidence with electrons in the HMS.

During E93-038, the scattered electrons were detected in the HMS. A schematic figure of the HMS is shown in Fig. 3-11. In what follows, we describe the HMS in greater detail; we discuss the properties of the collimator, the three quadrupole magnets and the dipole magnet, and the detector package. The SOS was not used for this experiment; therefore, we do not discuss this spectrometer in any further detail and instead refer the reader to [332] for details. Again, much of our discussion of the HMS properties follows that given by Arrington [332], Gustafsson [333], and Zhu [335].

3.4.1 Collimator

The HMS collimator was designed to limit the solid angle acceptance of the HMS and is located between the scattering chamber and the first quadrupole (Q1). The

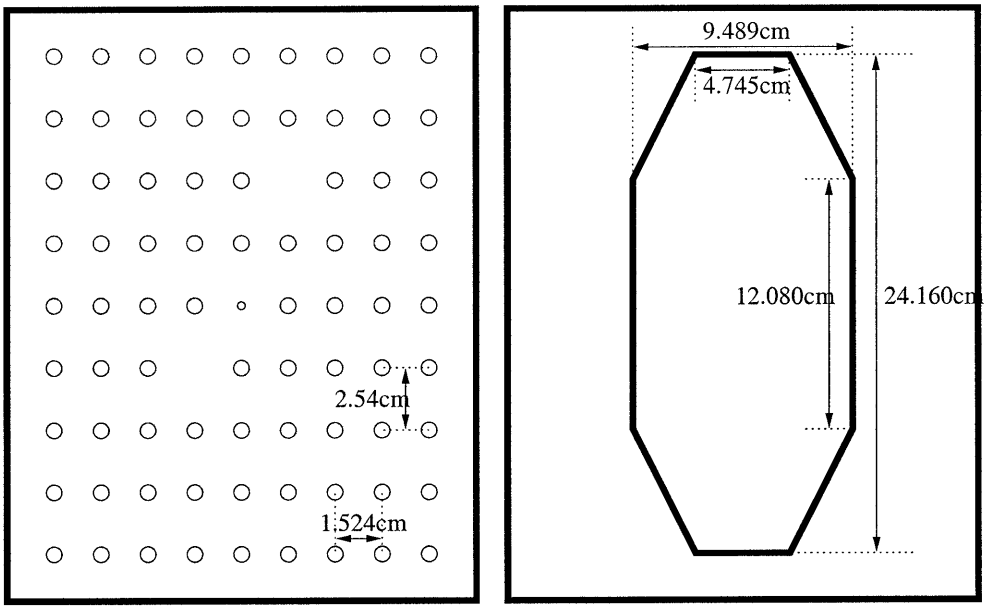

Figure 3-12: Schematic diagram of the HMS collimator. The sieve slit is shown on the left, and the pion collimator is shown on the right.

collimator consists of two sets of slits, a "sieve slit" and a "pion collimator", both of which are shown in Fig. 3-12. The sieve slit, shown on the left-hand side of Fig. 3-12, is a 3.175-cm thick Tungsten-CuNi plate composed of an array of small holes (0.508-cm diameter) that is used during HMS optics studies. The two holes that are missing are used to verify the orientation of the reconstructed pattern. The central hole is smaller than the other holes because the central hole is used to determine the angular resolution of the reconstruction. Optics studies using the sieve slit were not conducted (successfully) during E93-038; therefore, we will not discuss the sieve slit in any further detail in the remainder of this thesis.

The octogonally-shaped pion collimator, shown on the right-hand side of Fig. 3-12, consists of 6.35-cm of heavimet (a tungsten alloy). The pion collimator is flared in order to match the spectrometer's geometrical acceptance; the dimensions that are shown are the exit dimensions. The angular acceptance of the HMS with the pion collimator in place is $\sim$6 msr.

3.4.2 Quadrupole and Dipole Magnets

The three quadrupole magnets and the dipole magnet are mounted on a common carriage that rotates on a rail system about the target pivot. The magnets are superconducting and are cooled with liquid helium drawn from the End Station Refrigerator.

The quadrupoles are 20-ton (Q1) and 30-ton (Q2 and Q3) cold iron superconducting magnets; the soft iron surrounding the superconducting coils enhances the central field and minimizes stray fields. Q2 and Q3 are identical, and the magnetic length of Q1 (Q2/Q3) is 1.89 m (2.10 m). The current for the quadrupoles is provided by three water-cooled Danfysik System 8000 power supplies that can supply up to 1250 A of current at 5 V. In addition to the quadrupole coils, each quadrupole has multipole windings; these correction coils are powered by three Hewlett Packard power supplies that can supply up to 100 A of current at 5 V.

The dipole is a 470-ton superconducting magnet with a magnetic length of 5.26-m that bends the central ray (momentum) vertically through 25° (12.06-m bend radius). The current for the dipole is provided by a Danfysik System 8000 power supply that can supply up to 3000 A of current at 10 V.

The HMS was operated in its standard point-to-point optics tune in both the dispersive and non-dispersive directions for the duration of E93-038. Q1 and Q3 focus in the dispersive direction, and Q2 focuses in the transverse direction. This tune yields a large momentum acceptance, a large solid angle, and can accommodate an extended target. A summary of the quoted performance parameters for the point-to-point tune [355] may be found in Table 3.4. [The HMS may also be operated in a parallel-point tune; this tune is optimal for thin (instead of extended) targets.]

3.4.3 Detector Package

The HMS detector package is shielded by a concrete shield house (shown as the gray frame in Fig. 3-11). The support frame for the detector package is mounted on the same carriage as the magnets; therefore, the detector frame is fixed relative to the

Parameter	Value
Momentum Range	0.5 – 7.5 GeV/c
Momentum Bite	$\pm 18\%$
Momentum Resolution	$< 0.1\%$
Acceptance with Pion Collimator	6 msr
Scattering Angle Range	12.5° – ~90°
Vertex Reconstruction Accuracy	~1 mm
In-Plane Angle Reconstruction Precision	0.8 mr
Out-of-Plane Angle Reconstruction Precision	0.8 mr
Luminosity	$> 10^{38}$ cm^{-2} sec^{-1}

Table 3.4: Summary of the quoted HMS performance parameters for a point-to-point tune [355].

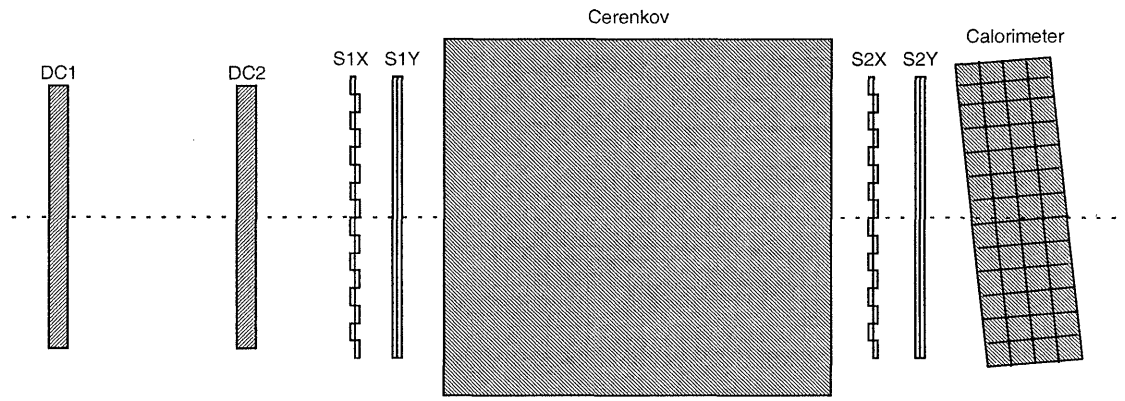

Figure 3-13: Schematic diagram of the HMS detector package. Shown are the two drift chambers (DC1 and DC2), the two x-y hodoscopes (S1X/S1Y and S2X/S2Y), the gas Čerenkov counter, and the lead-glass calorimeter.

spectrometer's optical axis. The concrete shielding hut is mounted on a separate carriage. The detector package includes two drift chambers that provide tracking information, two sets of x-y hodosopes that form the trigger, and a gas Čerenkov detector and lead-glass calorimeter that are used for particle identification. A schematic diagram of the detector package is shown in Fig. 3-13.

Drift Chambers

As shown in Fig. 3-14, each drift chamber in the HMS consists of six planes: the X and X' planes (measuring x; the dispersive direction), the Y and Y' planes (measuring

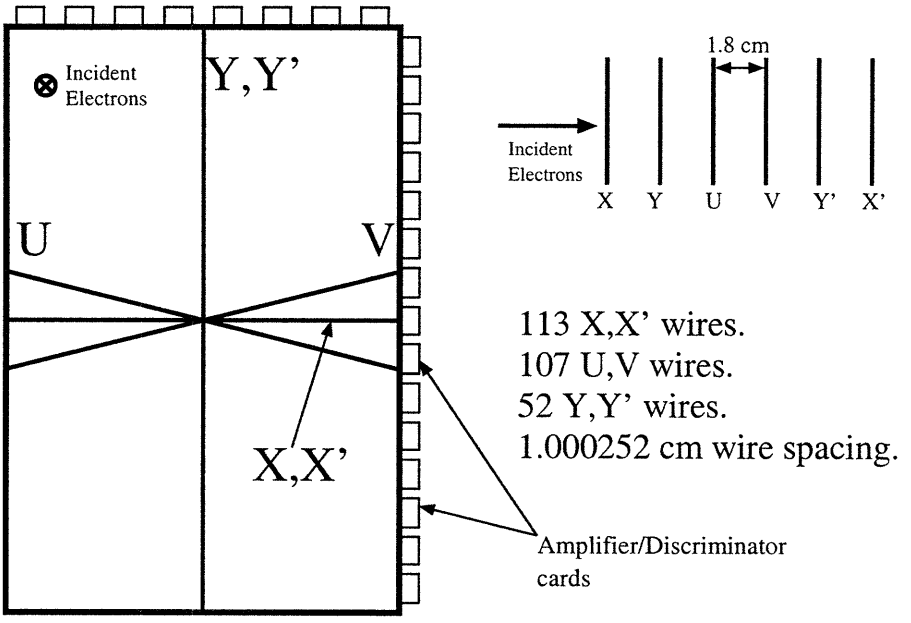

Figure 3-14: Schematic front view of the HMS drift chambers. Shown are the X, X', Y, Y', U and V planes.

y; the non-dispersive direction), and the U and V planes (rotated by $\pm 15°$ relative to the X and X' planes). As seen by incoming particles, the ordering of the planes is X, Y, U, V, Y', and X'. The planes are each separated by 1.8 cm, and the two drift chambers are separated by 81.2 cm. The drift chambers are filled with argon and ethane (equal by weight) together with $\sim$1% isopropyl alcohol and are maintained at a pressure slightly above atmospheric pressure.

Each plane consists of an alternating sequence of field and sense wires. The active area of each plane is approximately 113 cm (x) $\times$ 52 cm (y), and the sense wire spacing is $\sim$1 cm. The field wires (cathodes) are 150 μm gold-plated copper-beryllium wires. The sense wires (anodes), 25 μm gold-plated tungsten wires, detect the ionization generated by charged particles passing through the drift chamber. The signals from each individual sense wire are amplified and digitized in either a Nanometric or LeCroy 2735DC drift chamber card. These signals are read out in groups of 16 and then sent to multi-hit LeCroy 1879 Time-to-Digital Converters (TDCs) located at the rear of the detector hut; these multi-hit TDCs can store all hits (up to 16 per wire) that arrive within a 32 μs window. The fast signals from the TDCs in the hodosopes (to

be described shortly) form the TDC start, while the delayed signals from the wire chamber TDCs form the TDC stop. Relative to the trigger formed by the hodoscope TDC signals, the hodoscope TDC signals are used to determine the time the particle passed through the wire chamber, and the wire chamber TDC signals determine the time the sense wires detected the ionization. With this information, the drift time (of the ionization) can be inferred. The position of the event can then be extracted from the drift time, and the particle's trajectory can be reconstructed from the position information provided by the six planes.

We refer the reader to [356] for a more complete technical discussion of the HMS drift chambers.

Hodoscopes

The HMS detector package includes two sets of x-y hodoscopes (denoted S1X/S1Y and S2X/S2Y). Each x (y) plane consists of 16 (10) 75.5-cm (120.5-cm) long Bicron BC404 plastic scintillators that are 1.0-cm thick and 8.0-cm wide. UVT lucite light guides and Philips XP2282B photomultiplier tubes (PMTs) are coupled to both ends of each scintillator. The S1X/S1Y and S2X/S2Y planes are separated by approximately 2.2 m.

The signals from each PMT were first sent to a patch panel in the detector hut through approximately 30 feet of RG-58 cable and then to the counting house through approximately 450 feet of RG-8 cable. Upon arrival in the counting house, the signals were split. A smaller signal ($\frac{1}{3}$ the amplitude of the original signal) was delayed by approximately 400 ns with RG-58 delay cable and then directed to an Analog-to-Digital Converter (ADC) that measured the integral of the signal. The larger signals ($\frac{2}{3}$ the amplitude of the original signal) were sent to Philips PS7106 leading edge discriminators. One set of outputs from the discriminators was sent to custom logic delay modules and then to FASTBUS TDCs and VME scalers. Another set of outputs was sent to a LeCroy 4654 logic module; this logic module generated the OR for all PMTs on one side (+ or −) of a given plane (e.g., S1X+). The outputs that were later used for the HMS trigger logic are the AND of the sets of PMTs on each side

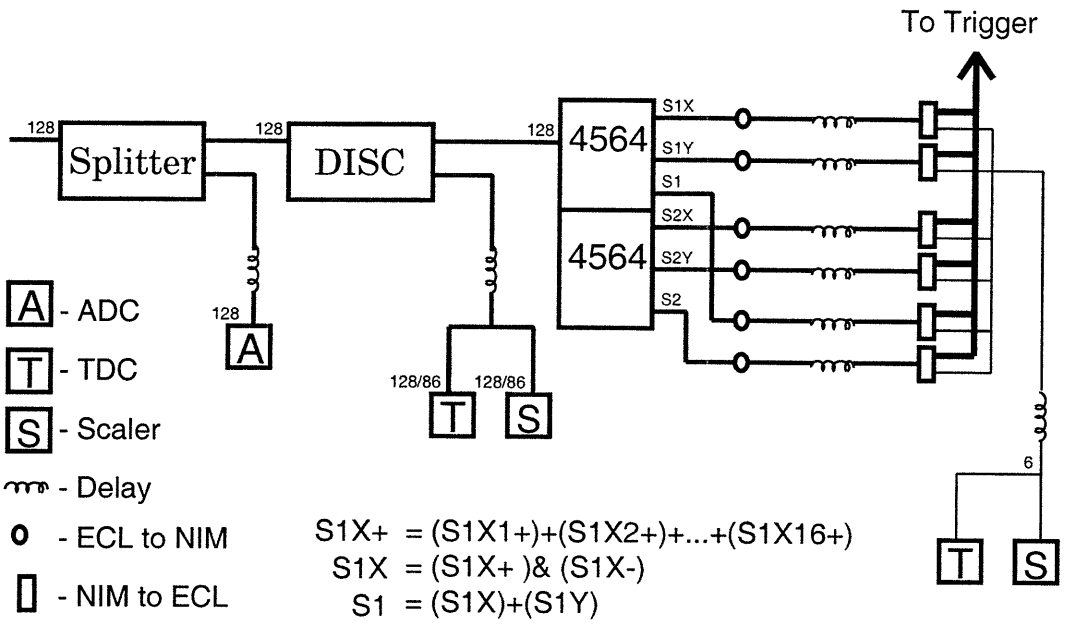

Figure 3-15: Hodoscope trigger and readout electronics. Here, & denotes AND, and + denotes OR.

of a plane (e.g., S1X $\equiv$ S1X+ AND S1X-) as well as the OR of the front (and back) pairs of hodoscope planes (e.g., S1 $\equiv$ S1X OR S1Y). A schematic diagram of the hodosope trigger and readout electronics is shown in Fig. 3-15.

Čerenkov Detector

As is well known (see, e.g., [357–359]), when a high-energy charged particle traverses a medium, part of the light emitted by excited atoms appears in the form of a coherent wave-front emitted at a fixed angle with respect to the particle's trajectory. This radiation, known as Čerenkov radiation, is produced whenever the particle's velocity, β, exceeds c/n, where n denotes the medium's index of refraction. The wavefront is conical in shape, and the radiation is emitted at an angle of $\cos^{-1}(1/\beta n)$ relative to the charged particle's trajectory. If the material's index of refraction is chosen appropriately, the presence (or absence) of Čerenkov radiation can be used to distinguish between charged particles of equal momentum but different velocities.

The HMS Čerenkov detector is a cylindrical tank (165-cm length and 150-cm inner diameter) filled with Perfluorobutane (C_4F_{10}, $n = 1.00143$ at 1 atm, 300 K). During

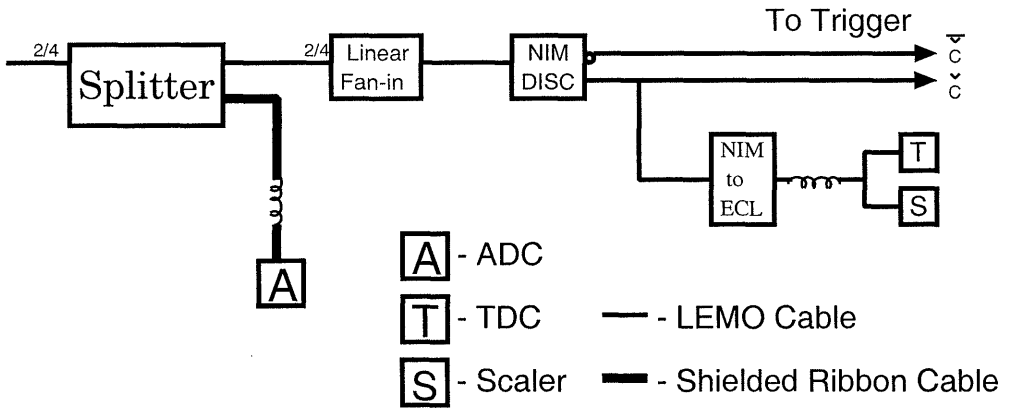

Figure 3-16: Schematic of the electronics for the Čerenkov detector.

E93-038, the pressure and temperature in the tank were monitored on a nearly daily basis; the pressure and temperature were found to be very stable. The pressure was typically ~5.9 – 6.1 psi (0.401 – 0.415 atm). At STP, the index of refraction for C_4F_{10} is 1.00143. The index of refraction varies linearly with pressure; therefore, during E93-038, the index of refraction was typically ~1.00057 – 1.00059. A straightforward calculation shows that these indices of refraction correspond to an energy threshold of 21.0 – 21.4 MeV (5.56 – 5.67 GeV) for electrons (charged pions).

Two mirrors located at the rear of the tank focused the Čerenkov light into two 5-inch Burle 8854 PMTs. The signals from the PMTs were sent to the counting house through ~10 m of RG-58 cable and ~150 m of RG-8 cable. Upon arrival in the counting house, the signals were split. One set was routed through 360 ns of RG-58 delay cable and then sent to a LeCroy 1881M ADC; these ADC values were then used to deduce the number of detected Čerenkov photoelectrons. The second set was summed in a Phillips 740 linear fan-in module and sent to a discriminator that can, in general, produce signals for the HMS trigger logic and additional outputs for TDCs and scalers. A diagram of the Čerenkov detector electronics is shown in Fig. 3-16.

Lead-Glass Calorimeter

The HMS lead-glass calorimeter is an electromagnetic calorimeter that measures the energy deposition of charged particles. Again, as is well known (see, e.g., [357–359]), a

high-energy electron traversing a dense absorber radiates photons via bremsstrahlung in the field of nuclei. These photons will, in turn, convert into electron/positron pairs via pair production, and these electron/positron pairs will then radiate additional photons, etc., leading to an electromagnetic shower. In general, high Z materials with a small radiation length, such as lead-loaded glass, are preferable, as the lateral spread of a shower (due to Coulomb scattering) is proportional to the material's radiation length; therefore, electrons will deposit nearly all of their energy in a calorimeter of sufficient length and width. In contrast, a hadronic shower results when a hadron suffers an inelastic nuclear collision leading to further hadron generation, etc. In general, the length scale for a hadronic shower is determined by the material's nuclear absorption length. As nuclear absorption lengths are, in general, large compared with radiation lengths, hadrons will deposit only a fraction of their energy in a calorimeter; therefore, a comparison of a particle's energy deposition in a calorimeter to the momentum measured in a magnetic spectrometer can be used to discriminate between electrons and hadrons.

The calorimeter in the HMS consists, as shown in Fig. 3-13, of a four-layer-deep stack of TF1 lead-glass blocks. Each layer contains 13 blocks, and the dimension of each block is 70 cm $\times$ 10 cm $\times$ 10 cm; therefore, the active area of the (52-block) calorimeter is 70 cm $\times$ 130 cm. Also, as shown in Fig. 3-13, the calorimeter is tilted at a 5° angle relative to the central axis of the detector package; this eliminates losses due to gaps between the blocks. The radiation length for TF1 lead-glass is 2.54 cm; therefore, the depth of the calorimeter is approximately 16 radiation lengths.

A Philips XP3462B 3-inch PMT is coupled to one end of each block. The signals from the PMTs are sent through $\sim$30 feet of RG-58 cable and $\sim$450 feet of RG-8 cable to the counting house. Upon arrival, they are split. One set of output is routed through 400 ns of RG-58 delay cable and then sent to a LeCroy 1881M ADC; the raw values recorded by the calorimeter ADCs are corrected for both attenutation in the blocks and variations in gain. The other set of outputs is sent to a Philips 740 linear fan-in module where it is summed. The sum in the first layer of the calorimeter (denoted PRSUM) and the sum of the entire calorimeter (denoted SHSUM) are dis-

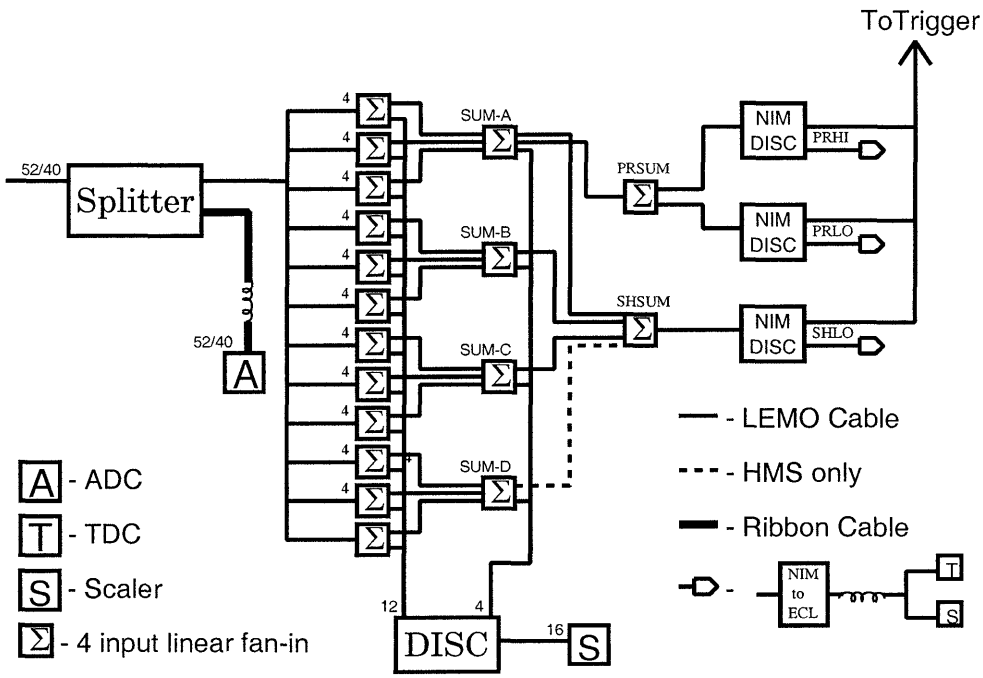

Figure 3-17: Electronics for the lead-glass calorimeter.

criminated according to high (denoted PRHI) and low (denoted PRLO) thresholds on the energy deposited in the first layer and an overall threshold (denoted SHLO) on the entire energy deposited in the calorimeter; this discrimination can, in general, generate three logic signals for the HMS trigger. A schematic diagram of the lead-glass calorimeter electrons is shown in Fig. 3-17.

3.4.4 HMS Trigger

During E93-038, the HMS trigger was defined to be coincident hits in three of the four scintillator planes in the S1X/S1Y and S2X/S2Y hodocopes; this trigger indicated that a charged particle was detected in the HMS. For this experiment, the HMS trigger did not require positive logic signals from either the Čerenkov detector or the lead-glass calorimeter. We discuss the logic and various types of triggers in more detail at the end of the next chapter.

3.5 Summary

In this chapter, we attempted to provide an overview of the JLab accelerator and the experimental equipment located in Hall C that was relevant for E93-038. In the next chapter, we turn to a detailed description of the neutron polarimeter, and we also provide an overview of the different types of triggers/event types that were recorded by the data acquisition system (DAQ).

Chapter 4

Neutron Polarimeter

In this chapter, we provide a detailed description of the neutron polarimeter (NPOL) that was designed and installed in Hall C specifically for E93-038. In addition, we provide an overview of the data acquisition system that was employed for this experiment.

4.1 Overview

A schematic diagram of the experimental arrangement with an isometric view of the neutron polarimeter is shown in Fig. 4-1, and a brief overview of the different NPOL components is as follows.

For the duration of the experiment, the central axis of the polarimeter was oriented at a scattering angle of 46° relative to the incident beam line. The first element in the NPOL flight path was the Charybdis[1] dipole magnet. Charybdis's vertical dipole field was used to precess the neutron's spin through an angle χ in a plane parallel to the Hall C floor. Also, as a by-product, the Charybdis field swept protons from the acceptance of the polarimeter during asymmetry measurements with the magnet turned on. The next item in the flight path was a 10.16-cm thick lead curtain; the lead curtain, located directly in front of a steel collimator (not shown in Fig. 4-1), suppressed the

[1]In ancient Greek mythology, Charybdis was the daughter of Poseidon and Gaia. She flooded lands for her father's underwater kingdom until Zeus turned her into a monster.

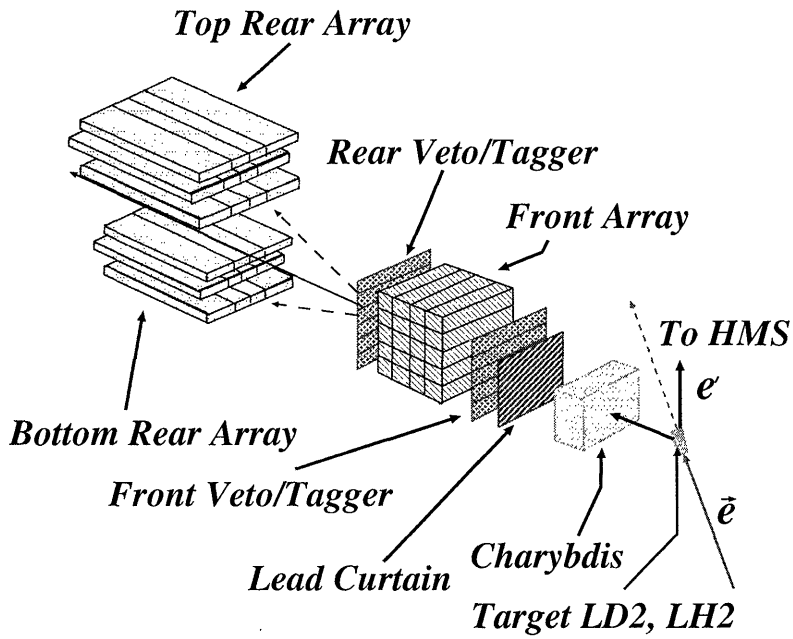

Figure 4-1: (color) Isometric view of NPOL showing the Charybdis dipole magnet, the lead curtain, the front veto/tagger array, the front array, the rear veto/tagger array, and the top and bottom rear arrays.

flux of electromagnetic radiation and degraded in energy charged particles entering the polarimeter during measurements conducted with the Charybdis field off.

The polarimeter itself consisted of 44 plastic scintillation detectors; all of the detectors were enclosed within a steel and concrete shielding hut. The front array of the polarimeter served as the "polarization analyzer" (via spin-dependent elastic scattering from unpolarized protons in hydrogen nuclei in the scintillators) and was segmented into 20 100 cm $\times$ 10 cm $\times$ 10 cm detectors; the segmentation permitted data taking with luminosities as high as 3×10^{38} cm^{-2} s^{-1} [15-cm liquid deuterium target and beam currents up to 70 μA]. The top and bottom rear arrays, shielded from the direct path of target particles by the collimator, detected the up-down scattering asymmetry from the projection of the polarization on the sideways axis; each rear array (i.e., top and bottom) consisted of six "20-inch" detectors [101.6 cm $\times$ 50.8 cm $\times$ 10.16 cm] and six "10-inch" detectors [101.6 cm $\times$ 25.4 cm $\times$ 10.16 cm]. A double layer of thin "veto/tagger" detectors (each 0.64-cm thick) located directly ahead of and behind the front array identified incoming and scattered charged particles. The

flight path from the center of the target to the center of the front array was 7.0 m, and the distance from the center of the front array to the center of the rear array along the central axis of the polarimeter was 2.5 m.

In the remainder of this chapter, we discuss each of these components in more detail; however, before doing so, we briefly review the concept of polarimetry, and we provide a brief historical overview of the development of this specific neutron polarimeter.

4.1.1 Review of Polarimetry

Coordinate Systems

Throughout the remainder of this thesis, we will employ a number of different coordinate systems when discussing recoil polarizations and the geometric configuration of the polarimeter; therefore, to avoid confusion later, we define these coordinate systems now. First, as is customary (and previously discussed in Section 2.3.7) calculations of recoil polarizations are, in general, referred to an (x, y, z) [or, as noted in Section 2.3.7, equivalently labeled (t, n, ℓ)] *reaction basis* defined according to

$$\hat{\mathbf{z}} \parallel \mathbf{p}_n \,, \tag{4.1}$$

$$\hat{\mathbf{y}} \parallel \mathbf{q} \times \mathbf{p}_n \,, \tag{4.2}$$

$$\hat{\mathbf{x}} \parallel \hat{\mathbf{y}} \times \hat{\mathbf{z}} \,, \tag{4.3}$$

where $\mathbf{p}_n$ denotes the neutron's three-momentum and $\mathbf{q}$ denotes the three-momentum transfer. Second, we define an $(\hat{\mathbf{x}}_{\rm NPOL}, \hat{\mathbf{y}}_{\rm NPOL}, \hat{\mathbf{z}}_{\rm NPOL})$ *polarimeter basis* according to

$$\hat{\mathbf{z}}_{\rm NPOL} \parallel \text{NPOL central axis} \,, \tag{4.4}$$

$$\hat{\mathbf{y}}_{\rm NPOL} \perp \text{Hall C floor} \,, \tag{4.5}$$

$$\hat{\mathbf{x}}_{\rm NPOL} \parallel \hat{\mathbf{y}}_{\rm NPOL} \times \hat{\mathbf{z}}_{\rm NPOL} \,, \tag{4.6}$$

with the origin of this coordinate system, $(0,0,0)$, defined to be at the center of the target. Last, the symmetric geometrical configuration of the polarimeter's top/bottom rear arrays suggests the definition of an $(\hat{\mathbf{S}},\hat{\mathbf{N}},\hat{\mathbf{L}})$ *polarimeter momentum basis* which we define according to

$$\hat{\mathbf{L}} \parallel \hat{\mathbf{p}}_n \ , \tag{4.7}$$

$$\hat{\mathbf{S}} \parallel \hat{\mathbf{y}}_{\mathrm{NPOL}} \times \mathbf{p}_n \ , \tag{4.8}$$

$$\hat{\mathbf{N}} \parallel \hat{\mathbf{L}} \times \hat{\mathbf{S}} \ . \tag{4.9}$$

We shall henceforth refer to the $\hat{\mathbf{S}}$ and $\hat{\mathbf{L}}$ axes as the "sideways" and "longitudinal" axes, respectively. We note that $\hat{\mathbf{S}}$ points "to the left" for an observer facing the polarimeter with her back to the target.

Finally, it should be noted that we employed an identical $(\hat{\mathbf{S}},\hat{\mathbf{N}},\hat{\mathbf{L}})$ notation when we discussed polarized electrons in Section 2.3.2; however, because we concluded there that only longitudinally polarized electrons are relevant, whenever we employ this notation in the future, it should be obvious that we are referring to the polarimeter momentum basis.

Asymmetry Measured in the Polarimeter

We define polar and azimuthal scattering angles, θ and ϕ, respectively, in the polarimeter according to

$$\sin\theta = |\hat{\mathbf{p}}_n \times \hat{\mathbf{p}}'_n| \ , \qquad \cos\phi = \hat{\mathbf{S}} \cdot \hat{\mathbf{n}} \ , \tag{4.10}$$

where $\hat{\mathbf{p}}_n$ ($\hat{\mathbf{p}}'_n$) is a unit vector along the incident (scattered) neutron's three-momentum, and the unit vector $\hat{\mathbf{n}}$, defined according to

$$\hat{\mathbf{n}} = \frac{\hat{\mathbf{p}}_n \times \hat{\mathbf{p}}'_n}{|\hat{\mathbf{p}}_n \times \hat{\mathbf{p}}'_n|} \ , \tag{4.11}$$

is perpendicular to the plane spanned by $\mathbf{p}_n$ and $\mathbf{p}'_n$. We write the recoil polarization in terms of the polarimeter momentum basis as

$$\mathbf{P} = P_S\hat{\mathbf{S}} + P_N\hat{\mathbf{N}} + P_L\hat{\mathbf{L}} \ . \tag{4.12}$$

The differential cross section for elastic polarized-nucleon, unpolarized-nucleon scattering, denoted $\sigma(\theta,\phi)$ for short, can be written as [360, 361]

$$\begin{aligned}
\sigma(\theta,\phi) &= \sigma_0(\theta)\left[1 + A_y(\theta)\mathbf{P}\cdot\hat{\mathbf{n}}\right] \\
&= \sigma_0(\theta)\left[1 + A_y(\theta)(P_S\hat{\mathbf{S}} + P_L\hat{\mathbf{L}} + P_N\hat{\mathbf{N}})\cdot\hat{\mathbf{n}}\right] \\
&= \sigma_0(\theta)\left[1 + A_y(\theta)P_S\cos\phi + A_y(\theta)P_N\hat{\mathbf{N}}\cdot\hat{\mathbf{n}}\right] \\
&= \sigma_0(\theta)\left[1 + A_y(\theta)P_S\cos\phi\right] \ ,
\end{aligned} \tag{4.13}$$

where $\sigma_0(\theta)$ is the unpolarized cross section and $A_y(\theta)$ is the analyzing power; to simplify the above expression, we used the the facts that $\hat{\mathbf{L}}\cdot\hat{\mathbf{n}} = 0$ and P_N should be small. From this, we see that with our above definition for ϕ (i.e., $\phi = 0°$, $180°$ for scattering in the vertical direction), the cross section is sensitive only to P_S; therefore, the scattering asymmetry, $\xi(\theta,\phi)$, between scattering "up" ($\hat{\mathbf{S}}\cdot\hat{\mathbf{n}} < 0 \Longrightarrow \cos\phi < 0$) and scattering "down" ($\hat{\mathbf{S}}\cdot\hat{\mathbf{n}} > 0 \Longrightarrow \cos\phi > 0$) into infinitesimal solid angles (θ,ϕ) and $(\theta,\phi+180°)$, respectively, for a particular value of P_S is

$$\begin{aligned}
\xi(\theta,\phi) &= \frac{\sigma(\theta,\phi) - \sigma(\theta,\phi+\pi)}{\sigma(\theta,\phi) + \sigma(\theta,\phi+\pi)} \\
&= \frac{[1 + A_y(\theta)P_S\cos\phi] - [1 + A_y(\theta)P_S\cos(\phi+\pi)]}{[1 + A_y(\theta)P_S\cos\phi] + [1 + A_y(\theta)P_S\cos(\phi+\pi)]} \\
&= A_y(\theta)P_S\cos\phi \ .
\end{aligned} \tag{4.14}$$

In reality, a single value of P_S is not presented to the polarimeter as the recoil polarization varies with kinematics. Also, the top and bottom rear arrays have a finite geometry; therefore, if the polarimeter is geometrically symmetric in ϕ (or, equivalently, if the top/bottom rear arrays are geometrically symmetric), the asymmetry that is actually measured by the polarimeter (i.e., averaged over kinematics

and geometry), $\langle \xi \rangle$, is

$$\langle \xi \rangle = \langle P_S \rangle A_y^{\text{eff}} \ , \tag{4.15}$$

where $\langle P_S \rangle$ and A_y^{eff} denote, respectively, the acceptance-averaged values of the sideways component of the polarization and the effective analyzing power of the polarimeter. Henceforth, when we refer to the analyzing power of the polarimeter, it should be assumed that we are referring to the effective analyzing power.

4.1.2 Historical Overview of NPOL

The evolution of the E93-038 neutron polarimeter is a storied history that reflects nearly three decades of dedication and effort. Although we cannot do justice to a detailed discussion of this effort, we have attempted to provide a brief historical overview below.

Time-of-flight spectrometers for neutrons with energies up to ~500 MeV were first developed in the mid-1970s by Madey and Waterman [362] and Madey, Waterman, and Baldwin [363]. These spectrometers consisted, essentially, of two organic scintillation detectors, and the operating principle of these spectrometers was simple. Incident neutrons scattered elastically from protons in the first scintillator and then traveled over a fixed flight path to the second scintillator; the time interval between the scintillation pulses in the two detectors defined the scattered neutron's time-of-flight. Active organic scintillation detectors were employed instead of passive hydrogen scatterers because the requirement of a coincidence between the scintillation pulses in the two detectors eliminated a large portion of the background.

These time-of-flight spectrometers evolved in the 1980s into polarimeters consisting of large-volume, mean-timed NE-102 plastic scintillation and BC517L mineral-oil scintillation detectors arranged in a "V-shape" [364–366]. The double-scattering efficiencies[2] and analyzing powers of these polarimeters were calibrated in a series of experiments at the Indiana University Cyclotron Facility (IUCF) and subsequently used to extract polarization transfer coefficients in the the $^{40,48}\text{Ca}(\vec{p},\vec{n})$ reaction at

[2]The efficiency of a neutron polarimeter is defined to be the probability that a neutron incident on the front analyzing detectors generates an event that satisfies all analysis thresholds and cuts.

135 MeV [367–370].

These polarimeters then evolved into the neutron polarimeter that was eventually used for the pioneering recoil polarimetry measurement of G_{En} at MIT-Bates reported by Eden *et al.* [210] in 1994. This neutron polarimeter consisted of a total of twelve scintillation detectors (four BC517L mineral-oil scintillators in the front array and top/bottom rear arrays of four NE-102 plastic scintillators each), and the analyzing power was calibrated as experiment E326 at IUCF in 1989 [371]. We refer the reader to Appendix D of [372] for a very interesting account of the history behind this neutron polarimeter. Also, we note that the polarimeter's detector configuration was subsequently used for the measurement of G_{Mn} at MIT-Bates reported by Markowitz *et al.* [97].

Following the successful completion of the experiment at MIT-Bates, a new configuration for the neutron polarimeter to be used at JLab for E93-038 (originally LOI-88-22 and E89-005) was conceived by Madey [373] while at a hotel outside of Saclay, France in 1994 and described by Madey, Lai, and Eden [374] in 1995. This new design doubled the height of the front array, thereby doubling the acceptance of the polarimeter, while still shielding the top/bottom rear arrays from the direct flux of particles from the target. Prototype versions of this polarimeter (with a smaller number of larger-sized detectors in the front and rear arrays) were calibrated and tested at IUCF as experiment E377 [375] using a flux of 120, 160, and 195 MeV neutrons of known polarization from the $0^+ \rightarrow 0^+$ transition in the $^{14}C(\vec{p},\vec{n})$ reaction at 0° scattering angle and at Saclay [376] with polarized neutron beams (produced by the breakup of polarized deuteron beams on aluminum and beryllium targets) of various energies ranging from 261 to 1057 MeV.

In order to take data during E93-038 with higher beam currents, in 1999, Madey and Eden [377] proposed to use (smaller) 100 cm × 10 cm × 10 cm detectors in the front array. These detectors were tested during a parasitic run in Hall C during the summer of 1999 [378]. Installation of the final version of NPOL and its components in Hall C began in June 2000 and continued through August 2000. We now proceed to a detailed discussion of NPOL and its components.

4.2 Charybdis Dipole Magnet

The Charybdis magnet is a water-cooled 38-ton iron dipole magnet that is approximately 1.5-m tall, 2.3-m wide, and 1.7-m long. The magnet's two coils each have a resistance of $\sim$0.5 Ω, and the magnet can be configured with a gap between the pole pieces that can be adjusted between approximately 8 and 10 inches.

As with the other NPOL components, Charybdis was installed in Hall C specifically for this experiment. The power supply for Charybdis was an Inverpower unipolar series linear pass transistor rated for 1000 A at 160 V [379]; during the experiment, the two poles were wired in parallel. The geometric center of the magnet was located at a distance of 2.107 m from the center of the target, and the magnetic field length (for a central path along the polarimeter axis) was approximately 1.7 m. The gap between the pole pieces was 8.25 inches, and 2-inch thick iron field clamps with apertures that matched the 8.25-inch pole gap were placed at the entrance and exit apertures of the magnet to reduce the range of the fringe fields. Before discussing the Charybdis field in more detail, we present a brief overview of spin precession in electromagnetic fields.

4.2.1 Spin Precession in Electromagnetic Fields

[Note: As is customary in discussions involving relativistic electrodynamics, we employ Gaussian units (and $\hbar = 1$) in all subsequent discussions concerning spin precession in electromagnetic fields.]

As is well known (see, e.g., [380]), the *rest-frame* equation of motion for a particle's spin is

$$\frac{\mathrm{d}\mathbf{s}}{\mathrm{d}t'} = g\frac{e}{2mc}\,\mathbf{s}\times\mathbf{B}'\,, \tag{4.16}$$

where $\mathbf{s}$ denotes the rest-frame spin, g denotes the particle's Lande g factor, and the primes denote quantities measured in the rest frame. Although this equation is classical in origin, it is completely equivalent to the quantum-mechanical Heisenberg equation of motion for the spin operator. This equation of motion, as written above, is valid only in the particle's rest frame; however, this result can be generalized to any

inertial reference frame. In what follows, we outline the relativistic generalization of this problem given by Jackson [329].

The four-spin, $S^\mu = (S_0, \mathbf{S})$, valid in any inertial reference frame, is defined according to

$$S^0 = \gamma\boldsymbol{\beta} \cdot \mathbf{s} \ , \qquad \mathbf{S} = \mathbf{s} + \frac{\gamma^2}{\gamma + 1}(\boldsymbol{\beta} \cdot \boldsymbol{s})\boldsymbol{\beta} \ , \tag{4.17}$$

where $c\boldsymbol{\beta}$ is the particle's velocity in this inertial frame and γ is the usual Lorentz factor. Also, the four-velocity, $U^\mu = (U^0, \mathbf{U})$, is, as usual, defined according to

$$U^0 = \gamma c \ , \qquad \mathbf{U} = \gamma c\boldsymbol{\beta} \ . \tag{4.18}$$

U^μ and S^μ must satisfy $U_\mu S^\mu = 0$ at all times.

The relativistic generalization of $\mathrm{d}\mathbf{s}/\mathrm{d}t$ is $\mathrm{d}S^\mu/\mathrm{d}\tau$, where τ denotes the proper time in the inertial frame. As argued in detail by Jackson, because the left-hand side of Eq. (4.16) has been generalized from a three-vector to a four-vector, so, too, must the right-hand side. Further, Jackson argues that if the equation of motion is linear in S^μ and the electromagnetic field tensor $[F^{\mu\nu} = \partial^\mu A^\nu - \partial^\nu A^\mu]$ and involves only U^μ and $\mathrm{d}U^\mu/\mathrm{d}\tau$, the latter linear in $F^{\mu\nu}$ itself, the only possible form for the equation of motion is

$$\frac{\mathrm{d}S^\alpha}{\mathrm{d}\tau} = A_1 F^{\alpha\beta} S_\beta + \frac{A_2}{c^2}\left(S_\lambda F^{\lambda\mu} U_\mu\right) U^\alpha + \frac{A_3}{c^2}\left(S_\beta \frac{\mathrm{d}U^\beta}{\mathrm{d}\tau}\right) U^\alpha \ , \tag{4.19}$$

where A_1, A_2, and A_3 are constants. Imposing the constraint $U_\alpha S^\alpha = 0$ gives us

$$\frac{\mathrm{d}}{\mathrm{d}\tau}\left(U_\alpha S^\alpha\right) = S^\alpha \frac{\mathrm{d}U_\alpha}{\mathrm{d}\tau} + U_\alpha \frac{\mathrm{d}S^\alpha}{\mathrm{d}\tau} = 0 \ , \tag{4.20}$$

from which it is straightforward to show that

$$(A_1 - A_2) U_\alpha F^{\alpha\beta} S_\beta + (1 + A_3) S_\beta \frac{\mathrm{d}U^\beta}{\mathrm{d}\tau} = 0 \ . \tag{4.21}$$

This is satisfied, most generally, by $A_1 = A_2$ and $A_3 = -1$. Further, demanding that we recover Eq. (4.16) in the rest frame yields $A_1 = ge/2mc$; therefore, the equation

of motion reduces to

$$\frac{\mathrm{d}S^\alpha}{\mathrm{d}\tau} = g\frac{e}{2mc}\left[F^{\alpha\beta}S_\beta + \frac{1}{c^2}U^\alpha\left(S_\lambda F^{\lambda\mu}U_\mu\right)\right] - \frac{1}{c^2}U^\alpha\left(S_\lambda\frac{\mathrm{d}U^\lambda}{\mathrm{d}\tau}\right) . \tag{4.22}$$

Finally, if we assume that the electromagnetic fields are uniform and that there are no other forces acting on the particle, it follows that

$$\frac{\mathrm{d}U^\alpha}{\mathrm{d}\tau} = \begin{cases} \dfrac{e}{mc}F^{\alpha\beta}U_\beta & \text{charged particles ,} \\ 0 & \text{neutral particles .} \end{cases} \tag{4.23}$$

The final result, known as the *BMT equation*,[3] is

$$\frac{\mathrm{d}S^\alpha}{\mathrm{d}\tau} = \begin{cases} \dfrac{e}{mc}\left[\dfrac{g}{2}F^{\alpha\beta}S_\beta + \dfrac{1}{c^2}\left(\dfrac{g-2}{2}\right)U^\alpha\left(S_\lambda F^{\lambda\mu}U_\mu\right)\right] & \text{charged particles ,} \\ \dfrac{e}{mc}\left[\dfrac{g}{2}F^{\alpha\beta}S_\beta + \dfrac{1}{c^2}\dfrac{g}{2}U^\alpha\left(S_\lambda F^{\lambda\mu}U_\mu\right)\right] & \text{neutral particles .} \end{cases} \tag{4.24}$$

Now, it is useful to separate the BMT equation for charged particles into time and spatial components as

$$\frac{\mathrm{d}S^0}{\mathrm{d}\tau} = F^0 + \gamma^2\left(\mathbf{S}\cdot\frac{\mathrm{d}\boldsymbol{\beta}}{\mathrm{d}\tau}\right) , \tag{4.25}$$

$$\frac{\mathrm{d}\mathbf{S}}{\mathrm{d}\tau} = \mathbf{F} + \gamma^2\boldsymbol{\beta}\left(\mathbf{S}\cdot\frac{\mathrm{d}\boldsymbol{\beta}}{\mathrm{d}\tau}\right) , \tag{4.26}$$

and that for neutral particles as

$$\frac{\mathrm{d}S^0}{\mathrm{d}\tau} = F^0 , \tag{4.27}$$

$$\frac{\mathrm{d}\mathbf{S}}{\mathrm{d}\tau} = \mathbf{F} , \tag{4.28}$$

[3]The BMT equation so bears its name for the authors, Bargmann, Michel, and Telegdi [381], who, in 1959, considered the precession of the polarization of particles moving in a homogenous electromagnetic field; however, as pointed out by Jackson, many other authors contributed to the development of this theory dating to the late 1920s.

where we define F_0 and $\mathbf{F}$ to be, respectively, the time and spatial components of

$$g\frac{e}{2mc}\left[F^{\alpha\beta}S_\beta + \frac{1}{c^2}U^\alpha\left(S_\lambda F^{\lambda\mu}U_\mu\right)\right] . \tag{4.29}$$

Also, we have used the fact that

$$S_\lambda\frac{\mathrm{d}U^\lambda}{\mathrm{d}\tau} = -\gamma c\left(\mathbf{S}\cdot\frac{\mathrm{d}\boldsymbol{\beta}}{\mathrm{d}\tau}\right); \tag{4.30}$$

this result is a straightforward consequence of the constraint $U_\alpha S^\alpha = 0$. Now, using Eq. (4.17), after some tedious algebraic manipulations, we can write an expression for $\mathrm{d}\mathbf{s}/\mathrm{d}t$ as

$$\frac{\mathrm{d}\mathbf{s}}{\mathrm{d}t} = \begin{cases} \dfrac{1}{\gamma}\mathbf{F} - \dfrac{\boldsymbol{\beta}}{\gamma+1}F^0 - \dfrac{\gamma}{\gamma+1}\left[\mathbf{s}\times\left(\boldsymbol{\beta}\times\dfrac{\mathrm{d}\boldsymbol{\beta}}{\mathrm{d}\tau}\right)\right] & \text{charged particles ,} \\ \dfrac{1}{\gamma}\mathbf{F} - \dfrac{\boldsymbol{\beta}}{\gamma+1}F^0 & \text{neutral particles .} \end{cases} \tag{4.31}$$

The extra term in the above expression for charged particles is due to the phenomenon of *Thomas precession*. Thomas precession is purely kinematic in origin and is a consequence of the non-commutativity of the Lorentz transformations. A rigorous discussion of Thomas precession would not be complete without a derivation of the result; although such a discussion is not beyond the scope of this thesis, for purposes of brevity, we do not present such a discussion here. Instead, we refer the reader to Jackson [329] for a detailed discussion of the underlying mathematics.

For charged particles, the expression for $\mathrm{d}\mathbf{s}/\mathrm{d}t$ is customarily rewritten in terms of the Thomas precession frequency, $\boldsymbol{\omega}_T$, defined according to

$$\boldsymbol{\omega}_T = \frac{1}{c^2}\frac{\gamma^2}{\gamma+1}\left(\frac{\mathrm{d}\boldsymbol{\beta}}{\mathrm{d}t}\times\boldsymbol{\beta}\right) . \tag{4.32}$$

Here, we see explicity that $\boldsymbol{\omega}_T = 0$ for neutral particles as $\mathrm{d}\boldsymbol{\beta}/\mathrm{d}t = 0$ for neutral particles in uniform, static electromagnetic fields.

Next, it is also well known (see, e.g., [380]) that the time rate of change of an

arbitrary vector, $\mathbf{V}$, in a coordinate system rotating at an angular velocity $\boldsymbol{\omega}$ with respect to a non-rotating coordinate system is related to the time rate of change of the vector in the non-rotating coordinate system according to

$$\left(\frac{\mathrm{d}\mathbf{V}}{\mathrm{d}t}\right)_{\mathrm{non-rot}} = \left(\frac{\mathrm{d}\mathbf{V}}{\mathrm{d}t}\right)_{\mathrm{rot}} + \boldsymbol{\omega} \times \mathbf{V} \; ; \tag{4.33}$$

therefore, in the rest frame (where $\mathrm{d}\boldsymbol{\beta}/\mathrm{d}\tau = 0$), the spin must satisfy

$$\frac{\mathrm{d}\mathbf{s}}{\mathrm{d}t} = \frac{1}{\gamma}\mathbf{F} - \frac{\boldsymbol{\beta}}{\gamma+1}F^0 = g\frac{e}{2mc}\,\mathbf{s} \times \mathbf{B}' \; , \tag{4.34}$$

The Lorentz transformation for the magnetic field $\mathbf{B}$ is

$$\mathbf{B}' = \gamma(\mathbf{B} - \boldsymbol{\beta} \times \mathbf{E}) - \frac{\gamma^2}{\gamma+1}\boldsymbol{\beta}(\boldsymbol{\beta} \cdot \mathbf{B}) \; , \tag{4.35}$$

and the relativistic equation of motion is

$$\frac{\mathrm{d}\boldsymbol{\beta}}{\mathrm{d}t} = \frac{e}{\gamma mc}\left[\mathbf{E} + \boldsymbol{\beta} \times \mathbf{B} - \boldsymbol{\beta}(\boldsymbol{\beta} \cdot \mathbf{E})\right] \; . \tag{4.36}$$

After combining all of the above, we find that

$$\frac{\mathrm{d}\mathbf{s}}{\mathrm{d}t} = \begin{cases} \dfrac{e}{mc}\,\mathbf{s} \times \left[\left(\dfrac{g-2}{2} + \dfrac{1}{\gamma}\right)\mathbf{B} - \left(\dfrac{g-2}{2}\right)\dfrac{\gamma}{\gamma+1}(\mathbf{B} \cdot \boldsymbol{\beta})\boldsymbol{\beta} \right. \\ \qquad\qquad \left. - \left(\dfrac{g}{2} - \dfrac{\gamma}{\gamma+1}\right)\boldsymbol{\beta} \times \mathbf{E}\right] & \text{charged particles} \\ \dfrac{e}{mc}\,\mathbf{s} \times \left[\dfrac{g}{2}\mathbf{B} - \dfrac{g}{2}\dfrac{\gamma}{\gamma+1}(\boldsymbol{\beta} \cdot \mathbf{B})\boldsymbol{\beta} - \dfrac{g}{2}\boldsymbol{\beta} \times \mathbf{E}\right] & \text{neutral particles} \end{cases} \tag{4.37}$$

This form of the equation of motion is known as Thomas' equation.

Finally, for the case $\mathbf{E} = \mathbf{0}$, it can be shown that the rate of change of the

projection of the spin on the velocity (i.e., the longtudinal polarization) is

$$\frac{\mathrm{d}}{\mathrm{d}t}(\mathbf{s}\cdot\hat{\boldsymbol{\beta}}) = \begin{cases} -\dfrac{e}{mc}\,\mathbf{s}_{\perp}\cdot\left[\left(\dfrac{g-2}{2}\right)\hat{\boldsymbol{\beta}}\times\mathbf{B}\right] & \text{charged particles}\,, \\ \\ -\dfrac{e}{mc}\,\mathbf{s}_{\perp}\cdot\left[\dfrac{g}{2}\hat{\boldsymbol{\beta}}\times\mathbf{B}\right] & \text{neutral particles}\,, \end{cases} \tag{4.38}$$

Now, if we denote the instantaneous angle between $\hat{\mathbf{s}}$ and $\hat{\boldsymbol{\beta}}$ as $\theta(t)$, and if we assume that $\mathbf{B}$ and $\boldsymbol{\beta}$ are perpendicular, we can rewrite the above equation for neutral particles as

$$\frac{\mathrm{d}}{\mathrm{d}t}(\mathbf{s}\cdot\hat{\boldsymbol{\beta}}) = \frac{\mathrm{d}}{\mathrm{d}t}\left(\cos\theta(t)\right) = -\sin\theta(t)\frac{\mathrm{d}\theta(t)}{\mathrm{d}t} = \left(-\frac{e}{mc}\sin\theta(t)\right)\left(\frac{g}{2}|\mathbf{B}|\right)\,; \tag{4.39}$$

therefore, we find that the total spin precession angle, χ, can be written in terms of a path field integral, $\int|\mathbf{B}|\,\mathrm{d}\ell$, as

$$\chi \equiv \Delta\theta = \int\frac{\mathrm{d}\theta(t)}{\mathrm{d}t}\,\mathrm{d}t = \frac{eg}{2mc}\int|\mathbf{B}|\,\mathrm{d}t = \frac{eg}{2mc}\frac{1}{\beta}\int|\mathbf{B}|\,\mathrm{d}\ell\,, \tag{4.40}$$

where β denotes the magnitude of the neutral particle's velocity.

A similar simple closed-form expression in terms of a field integral cannot be written for the total spin precession angle of a charged particle due to the deflection of the charged particle's trajectory by the magnetic field.

4.2.2 Charybdis Field Profile and Field Integrals

TOSCA Calculations

In Fig. 4-2, TOSCA calculations[4] of the magnitude of the vertical component of the Charybdis field, B_y, are shown for power supply currents of 200, 500, and 600 A.

[4] All TOSCA calculations of the Charybdis field for the 8.25-inch gap and 2-inch field clamp configuration were performed by Lassiter and communicated to Taylor [382,383]. The calculations that we show for power supply currents of 200, 500, and 600 A were performed for the t_{20} experiment [193] conducted prior to E93-038 in Hall C. Three calculations were performed specifically for this experiment at power supply currents of 373.9, 542.1, and 593.3 A. Unfortunately, these calculations were not performed over a sufficiently dense grid in y; therefore, we employed the t_{20} TOSCA calculations for all analyses related to spin precession in the Charybdis field.

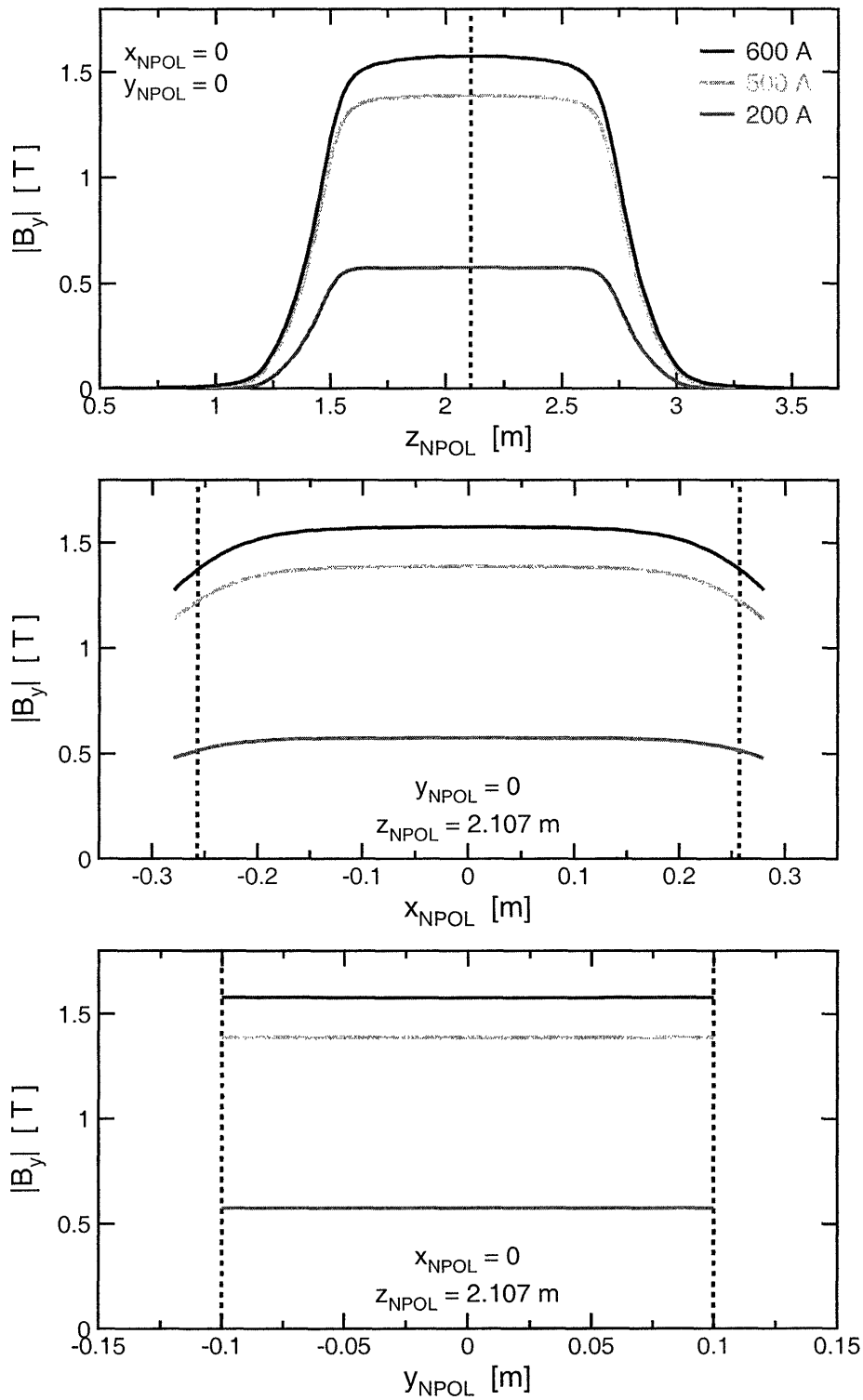

Figure 4-2: (color) TOSCA calculations of the magnitude of the vertical component of the Charybdis field, $|B_y|$. The dashed line in the top panel denotes the geometric center of the magnet, and the dashed lines in the middle and bottom panels denote the physical edges of the magnet.

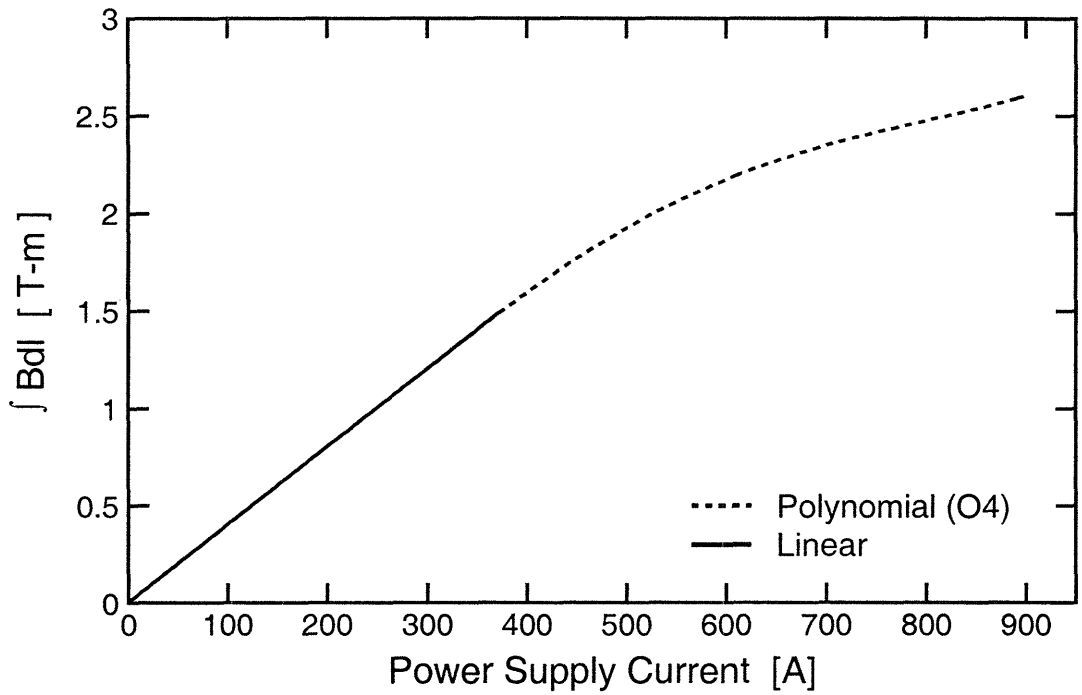

Figure 4-3: The field integral plotted as a function of the power supply current. The solid (dashed) line represents the results of a linear (fourth-order polynomial) fit to the low (high) power supply current settings [383, 384].

In the top panel, B_y is plotted as a function of z_{NPOL} for $x_{\mathrm{NPOL}} = y_{\mathrm{NPOL}} = 0$ (i.e., along the central axis of the polarimeter); in the middle panel, B_y is plotted as a function of x_{NPOL} for $y_{\mathrm{NPOL}} = 0$ and $z_{\mathrm{NPOL}} = 2.107$ m (i.e., the horizontal profile at the center of the magnet); and in the bottom panel, B_y is plotted as a function of y_{NPOL} for $x_{\mathrm{NPOL}} = 0$ and $z_{\mathrm{NPOL}} = 2.107$ m (i.e., the vertical profile at the center of the magnet). We see that the vertical component of the field is fairly uniform along the central path and in the horizontal and vertical directions.

Field Integrals

The values of the field integrals, $\int B\ \mathrm{d}\ell$, along the central path were derived from a set of TOSCA calculations at various power supply currents. At lower power supply currents ($\lesssim 300$ A), the relation between the current and the field integral was found

to be approximately linear, and a linear fit by Taylor [384] to

$$\int B \, \mathrm{d}\ell = p_0 + p_1 I \ , \tag{4.41}$$

where I denotes the power supply current in Amperes, gave $p_0 = 0.0058$ T-m, and $p_1 = 0.00401$ T-m-A^{-1}. At higher currents, this linearity was found to no longer hold; therefore, Taylor [383] fitted these to a fourth-order polynomial,

$$\int B \, \mathrm{d}\ell = p_0 + p_1 I + p_2 I^2 + p_3 I^3 + p_4 I^4 \ , \tag{4.42}$$

and he found $p_0 = 0.2422$ T-m, $p_1 = 1.085 \times 10^{-3}$ T-m-A^{-1}, $p_2 = 1.249 \times 10^{-5}$ T-m-A^{-2}, $p_3 = -2.070 \times 10^{-8}$ T-m-A^{-3}, and $p_4 = 9.692 \times 10^{-12}$ T-m-A^{-4}. To illustrate the relationship between the power supply current and the resulting value of the field integral, these fits are plotted in Fig. 4-3 over the range of their validity.

The nominal values of the field integrals for the various precession angles can be calculated according to

$$\int B \, \mathrm{d}\ell = \frac{\chi \beta_n}{\mu_N g} \ , \tag{4.43}$$

where the magnitude of the neutron's velocity, β_n, can be written in terms of Q^2 as

$$\beta_n = \frac{\sqrt{Q^4 + 4m_n^2 Q^2}}{Q^2 + 2m_n^2} \ . \tag{4.44}$$

Here, $\mu_N = e/2m_p c = 3.152451 \times 10^{-14}$ MeV-T^{-1} is the nuclear magneton, and $g/2 = -1.913$. The resulting field integrals and the nominal values of the power supply currents for the various precession angles at the different Q^2 points are tabulated in Table 4.1.

Mapping Results

The Charybdis field was mapped at the conclusion of the experiment [384]. Unfortunately, due to time constraints and equipment failure, the field was only mapped along the central axis for the three power supply currents employed for $\chi = \pm 40°$

Central Q^2 [(GeV/c)^2]	Precession Angle χ	Nominal $\int B\ \mathrm{d}\ell$ [T-m]	Nominal Charybdis I [A]
0.447	$\pm 40°$	0.6884	∓ 170.5
1.136	$\pm 90°$	2.0394	∓ 538.2
1.169	$\pm 40°$	0.9123	∓ 226.5
1.474	$\pm 40°$	0.9576	∓ 237.6
1.474	$\pm 90°$	2.1547	∓ 592.2

Table 4.1: Summary of the nominal values of the field integrals and Charybdis power supply currents for the precession angles at each of the Q^2 points.

Central Q^2 [(GeV/c)^2]	Precession Angle χ	Mapping $\int B\ \mathrm{d}\ell$ [T-m]	TOSCA $\int B\ \mathrm{d}\ell$ [T-m]
0.447	$\pm 40°$	0.6831	0.6884
1.169	$\pm 40°$	0.9111	0.9123
1.474	$\pm 40°$	0.9556	0.9576

Table 4.2: Comparison of the $\int B\ \mathrm{d}\ell$ field integrals (for the central path) extracted by Taylor [384] from the measured field maps and the TOSCA calculations.

precession at the central Q^2 values of 0.447, 1.169, and 1.474 (GeV/c)^2. The results of this exercise are plotted in Fig. 4-4.

Taylor [384] extracted the values of the $\int B\ \mathrm{d}\ell$ field integrals from the measured field maps, and the results were compared with the field integrals extracted from the TOSCA calculations. As can be seen in Table 4.2, the values for the field integrals derived from the mapping results and the TOSCA calculations agreed to better than 0.77%.

4.3 Neutron Polarimeter Shielding

4.3.1 Lead Curtain and Steel Collimator

The physical acceptance of the polarimeter was defined by a tapered steel collimator. A schematic diagram of the steel collimator including the center coordinates (i.e., $x_{\mathrm{NPOL}} = y_{\mathrm{NPOL}} = 0$) and dimensions of the collimator entrance and exit is shown in Fig. 4-5.

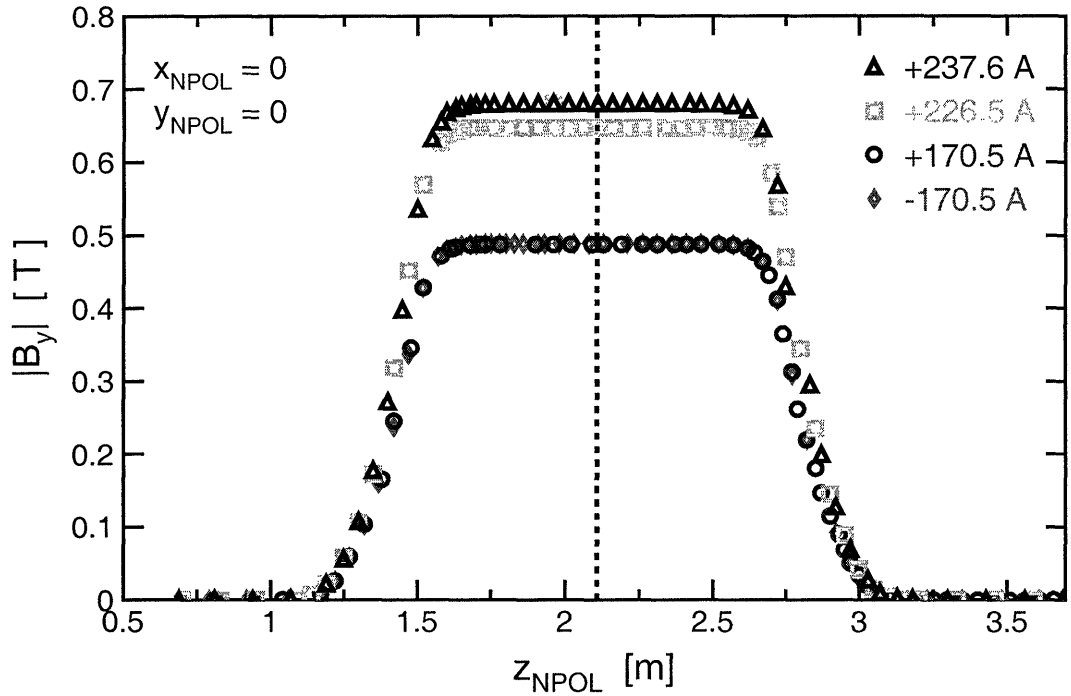

Figure 4-4: (color) Measurements of the magnitude of the vertical component of the Charybdis field along the central path. The dashed line denotes the geometric center of the magnet.

The lead curtain consisted of 40 0.254-cm thick lead sheets giving a total thickness of 10.16-cm.[5] The lead curtain attenuated the flux of electromagnetic radiation from the target and degraded the energy of protons incident on the polarimeter. The entrance to the collimator was located a distance of 483.92 cm from the target; therefore, the front face of the lead curtain was 473.76 cm from the target.

4.3.2 Shielding Hut

In order to suppress accidental coincidences between the front and rear detector arrays as much as possible, the polarimeter was enclosed within a steel and concrete shielding hut.

As already shown in Fig. 4-5, the front wall consisted of steel blocks that were

[5]It should be noted that during the early part of the experiment, 12 sheets (3.048 cm) of lead shielded the entrance to the collimator while the remaining 28 sheets (7.112 cm) of lead were placed ahead of the entrance aperture to Charybdis. On December 13, 2000, the lead sheets were rearranged such that all 40 sheets shielded the entrance to the collimator.

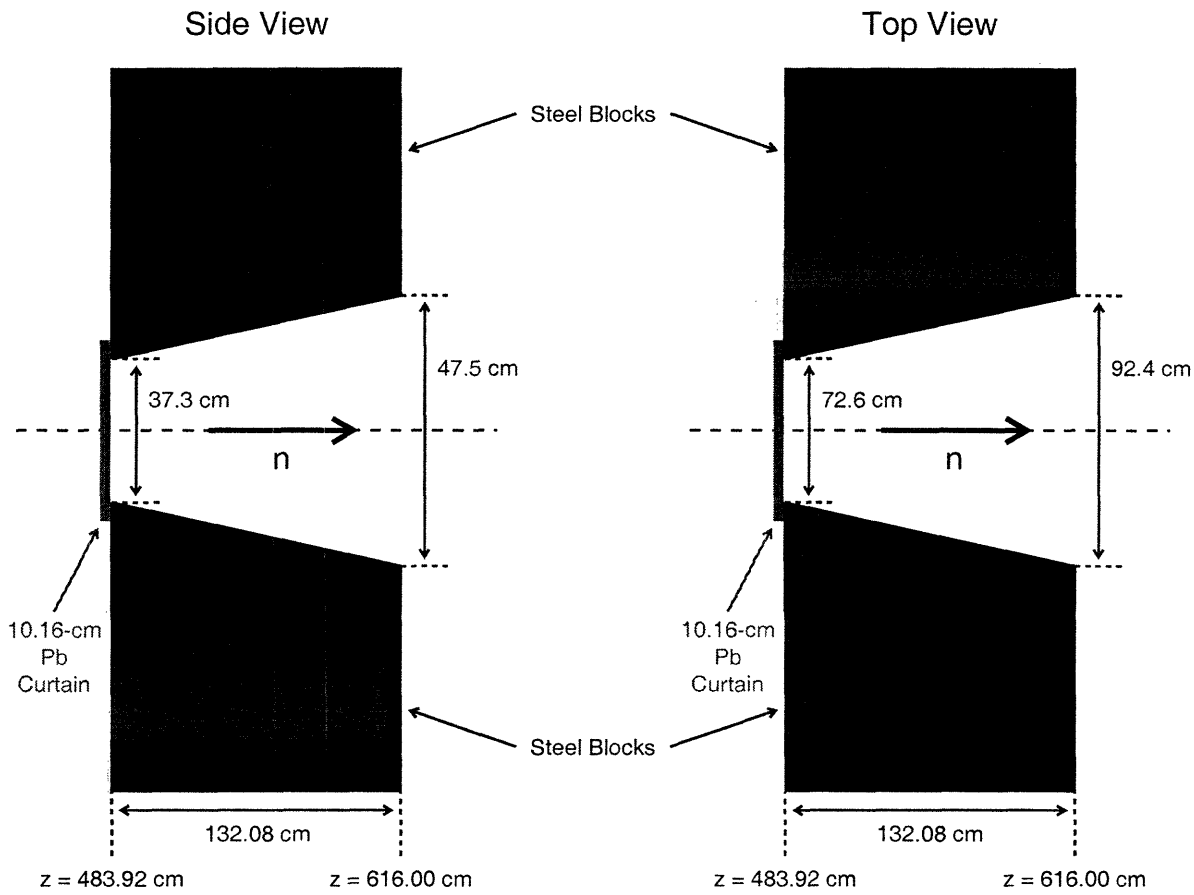

Figure 4-5: (color) Side and top views of the lead curtain and the tapered steel collimator. The z-coordinates shown refer to the polarimeter basis (i.e., the distance from the center of the target).

132.08-cm thick; the only opening in the front wall was the lead-curtain-shielded collimator. Steel blocks, 132.08-cm thick, were used also for the rear wall of the shielding hut. The side walls were composed of 48-inch thick reinforced concrete blocks stacked two layers deep. Finally, the roof of the shielding hut consisted of 21-inch thick reinforced concrete beams. These beams were stacked two layers deep directly above the detectors, and one layer of roof beams was used to shield the remainder of the hut. A schematic diagram of the polarimeter and the shielding hut is shown in Fig. 4-6.

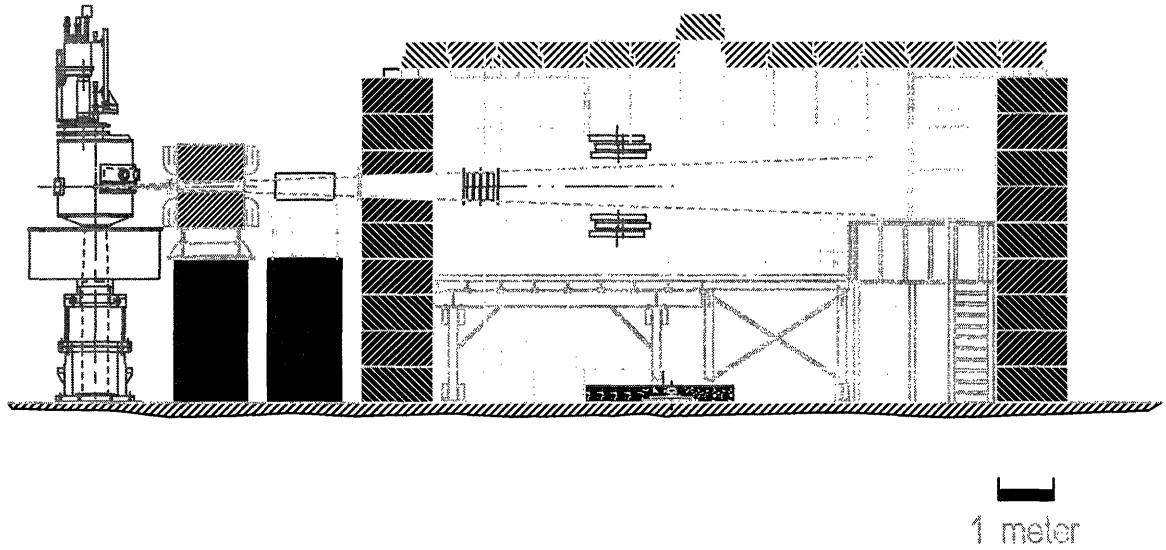

Figure 4-6: (color) Sideview of the NPOL shielding hut and the detector platform.

4.4 Neutron Polarimeter Detectors

4.4.1 Overview

The neutron polarimeter consisted of a total of 70 mean-timed plastic scintillation detectors of various sizes. The detectors were supported by a frame that was designed specifically for this experiment; this frame was mounted on a platform enclosed within the shielding hut. A schematic diagram of the detector configuration geometry is shown in Fig. 4-7.

All of the detectors were made of BICRON-400 fast plastic scintillation material (the BICRON equivalent of NE-102A). As described in detail by Leo [357], the principal application of BICRON-400/NE-102A plastic scintillation material is for the detection of γ rays, α particles, β particles, and fast neutrons (i.e., neutrons with energies greater than a few hundred keV).[6] Some of the primary physical features of BICRON-400, as listed in [385], are the following: (a) 65% light output of an-

[6]Neutron detection in plastic scintillators relies on the detection of the ionization created in the scintillator volume by a recoil proton following an np interaction, or by the products of a n-C interaction.

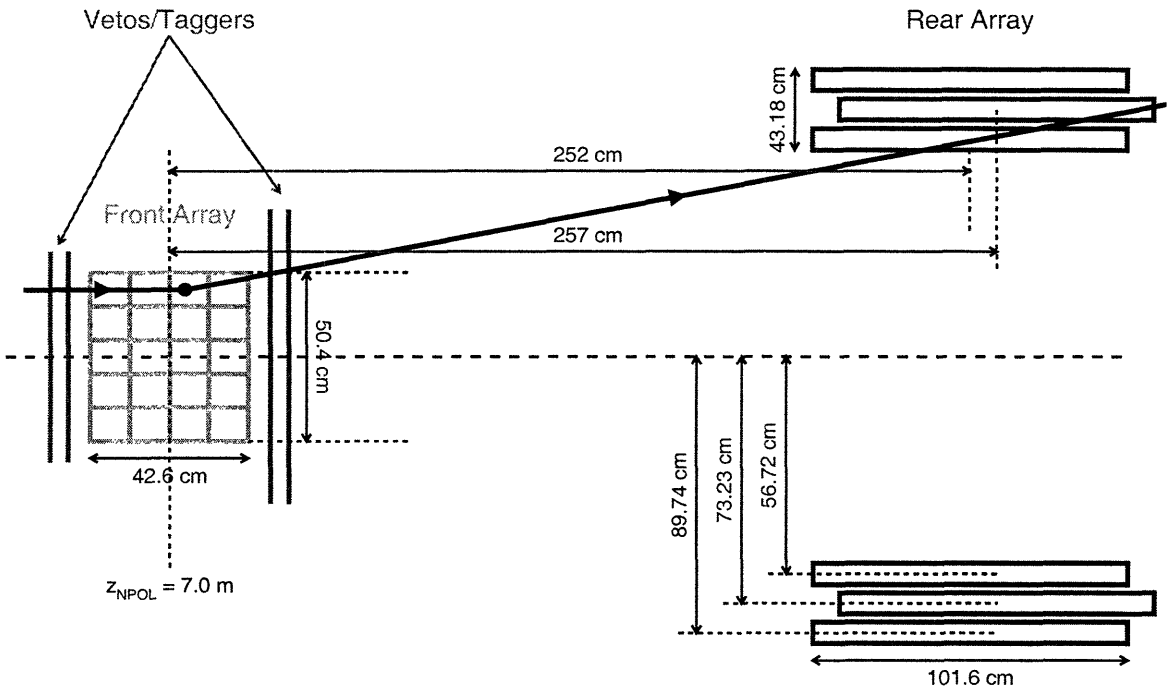

Figure 4-7: (color) Geometry for the NPOL detector configuration.

thracene,[7] (b) wavelength of maximum emission of 423 nm, (c) index of refraction of 1.581, (d) attenuation length (in bulk) of 250 cm, (e) hydrogen-to-carbon ratio of 1.103, and (f) decay constant (main component) of 2.4 ns.

Light guides made of Plexiglas were attached via optical cement to the long ends of every scintillator; these light guides were designed such that the majority of the light incident on the light guides would reflect off of the Plexiglas and continue down the guide into the photomultiplier tube. Plexiglas was the material chosen for the light guides because its index of refraction, 1.51, is very close to that of BICRON-400 plastic. Each light guide was coupled to a photomultiplier tube (PMT) via a Plexiglas coupling plate that was attached via optical cement to the face of the PMT; this coupling plate permitted a PMT to be changed during the experiment (e.g., in the event of a failure) without compromising the optical cement joint.

In order to minimize exposure to ambient light, each detector was wrapped with

[7]Anthracene, $C_{14}H_{10}$, has the highest light output of any organic scintillator; therefore, anthracene is customarily chosen as the reference to which the light output of all other scintillator materials is compared [357].

at least one layer of white paper and two or more layers of black electrical tape prior to installation. Also, in order to shield the PMTs from the earth's magnetic field (and other possible stray magnetic fields such as fringe fields from Charybdis), each PMT was enclosed within a cylindrical magnetic shield. Magnetic shields for PMTs are necessary because if a PMT is exposed to a magnetic field, the electron cascade in the dynode string may be deflected which, in general, tends to reduce the efficiency of the PMT.

4.4.2 Front Veto/Tagger Detectors

The first series of detectors in the flight path, the front veto/tagger array, consisted of 10 thin BICRON-400 plastic scintillation detectors stacked in two layers; this array of detectors vetoed/tagged charged particles incident on the polarimeter. Each layer consisted of five 160.0 cm $\times$ 11.0 cm $\times$ 0.635 cm detectors. The detectors were stacked with the long (160.0 cm) dimension oriented horizontally and perpendicular to the central axis of the polarimeter, the 11.0 cm dimension oriented vertically, and the 0.635 cm dimension oriented along the flight path; therefore, particles incident on the polarimeter traversed the thinnest dimension of these detectors. As a result, the front veto/tagger array was sensitive, primarily, only to the ionization created by charged particles traversing the scintillator volume; the probability for an np interaction in either layer of the front veto/tagger array was small. The spacing between the detectors in each layer was 1.0 cm; therefore, in order to eliminate the possibility of charged particle leakage, the two layers were slightly offset from each other other in the vertical direction by 1.0 cm.

Each detector in the front veto/tagger array was coupled to two Phillips XP2262 51-mm (2-inch) diameter PMTs. The Phillips XP2262 PMTs are twelve-stage (i.e., twelve dynodes), bi-alkali, head-on PMTs with a wavelength of maximum sensitivity of 400 nm and a stated gain on the order of 3×10^7 [386]. These PMTs were rated for a maximum voltage of 2500 Vdc and were powered by standard Phillips voltage dividers.

The University of Virginia provided all of the detectors for the front veto/tagger

array.

4.4.3 Front Array Detectors

The front array of the polarimeter consisted of 20 100 cm × 10 cm × 10 cm BICRON-400 plastic scintillation detectors. The long (100-cm) dimensions of the detectors were oriented horizontally and perpendicular to the central axis of the polarimeter, and the detectors were stacked into four layers of five detectors each. The distance from the center of the target to the center of the front array was 7.0 m, and the frame supporting the detectors was configured such that the centers of the four layers were at the incoming beam height of 3.96 m (defined relative to the floor of the hall).

The light guides attached to each end of the scintillators funneled the 10 cm × 10 cm detector cross section into a circular 51-mm diameter cross section. Each light guide was coupled to a 51-mm Hamamatsu R1828-01 twelve-stage, bi-alkali, head-on PMT specifically chosen for the front array detector geometry. The spectral response of Hamamatsu R1828-01 PMTs is 300 – 650 nm, the wavelength of maximum response is 420 nm, and the stated gain is on the order of 2×10^7 [387]. [It should be noted that the Hamamatsu R1828-01 420 nm wavelength of maximum response coincidences nicely with the BICRON-400 423 nm wavelength of maximum emission.] The Hamamatsu R1828-01 PMTs were rated for a maximum voltage of 3000 Vdc.

Jefferson Laboratory and Hampton University each provided one-half of the detectors for the front array; in addition, the front array PMTs were powered by "bases" that were designed and configured specifically for this experiment by Baldwin of Kent State University. These bases were designed to generate a high gain and were capable of handling high rates while remaining highly linear in the output signal.

As previously discussed, the front array analyzed the polarization of the incoming neutrons via spin-dependent scattering from unpolarized protons in hydrogen or carbon nuclei in the scintillators. In addition to functioning as the polarization analyzer, the output from the front array PMTs provided information about the interaction between the incoming neutrons and the protons in the scintillators (e.g., time of the "hit", location of the "hit", and pulse height information). As will be discussed

in greater detail in the next chapter, this information was used to reconstruct the track of the incoming particles and to calculate various kinematic quantities (e.g., energy/momentum of incoming particles, time-of-flight, etc.).

4.4.4 Rear Veto/Tagger Detectors

A second double layer[8] of 16 thin BICRON-400 plastic scintillation detectors was located immediately behind the front array; this array of detectors tagged charged particles (e.g., the recoil protons from the *np* interaction in the front array) exiting the front array of the polarimeter. The detectors in the rear veto/tagger array were identical to those in the front veto/tagger array and were stacked in an identical fashion. Each layer consisted of eight detectors, and the two layers were offset vertically by 0.95 cm.

As in the front veto/tagger array, each detector in the rear veto/tagger array was coupled to two 51-mm Phillips XP2262 PMTs. Again, the University of Virginia provided all of the detectors for the rear veto/tagger array.

4.4.5 Rear Array Detectors

The rear array of the polarimeter consisted of 24 BICRON-400 plastic scintillation detectors subdivided into top and bottom rear arrays; the twelve detectors in the top and bottom rear arrays were stacked into three layers of four detectors each. Each layer contained two "20-inch" 50.8 cm $\times$ 10.16 cm $\times$ 101.6 cm detectors and two "10-inch" 25.4 cm $\times$ 10.16 cm $\times$ 101.6 cm detectors.

The detectors were oriented with their long (101.6 cm) axes parallel to the central axis of the polarimeter and the 50.8 cm and 25.4 cm dimensions oriented horizontally; in each layer, the two smaller 25.4 cm detectors were sandwiched in between the two larger 50.8 cm detectors. The centers of the "inner", "middle", and "outer" layers were located a vertical distance of 56.72 cm, 73.23 cm, and 89.74 cm, respectively, either above or below the beam height (or, equivalently, the center of the front array).

[8]From September 2000 to December 2000, the rear veto/tagger array consisted only of one layer of eight scintillators. The second layer was installed in early January 2001.

The centers of the "inner" and "outer" layers were located a (horizontal) distance of 252 cm from the center of the front array, while the center of the "middle" layers were located a (horizontal) distance of 257 cm from the center of the front array; simulations performed prior to the start of the experiment suggested that this staggered configuration would maximize the front-to-rear coincidence counting rate.

Similar to the light guides in the front array, the rear array light guides funneled the 50.8-cm $\times$ 10.16-cm or 25.4-cm $\times$ 10.16 cm cross sections into a circular 127-mm diameter cross section. The light guides (for both the "10-inch" and "20-inch" detectors) were coupled to 127-mm Hamamatsu R1250, 14-stage, bi-alkali, head-on PMTs that were also chosen specifically for these detector geometries. The spectral response of Hamamatsu R1250 PMTs is 300 – 650 nm, the wavelength of maximum response is 420 nm, and the stated gain is on the order of 1.4×10^7 [387]; these PMTs were rated for a maximum voltage of 3000 Vdc. The rear array PMTs were powered by the same bases as the front array PMTs.

Kent State University provided all of the detectors for the rear array.

4.4.6 Detector Geometry

For reference, we provide a complete summary of the detector geometry for the front and rear array detectors and the front and rear veto/tagger array detectors in Table B.1 and Table B.2, respectively, which may be found in Appendix B. There, we list each detector's center position and dimensions as referred to the polarimeter basis coordinate system.

4.5 Neutron Polarimeter Electronics

4.5.1 Overview

The signals from the 140 NPOL PMTs were processed with E93-038-specific electronics sited in two different locations: (1) one set of electronics was located in the hall inside the shielding hut, and (2) a second set of electronics was located in the counting

house electronics room. Experience with neutron time-of-flight experiments acquired during the evolution of the neutron polarimeter revealed that the best time resolution was obtained when the discriminators were placed as close to the PMTs as practical; therefore, the electronics in Hall C were located in the shielding hut underneath the detector platform (the electronics received a minimal amount of radiation there). In what follows, we describe the E93-038-specific electronics in more detail; here, some of our discussion follows that given by Howell [388, 389] and Tireman [334].

4.5.2 NPOL Shielding Hut Electronics

The electronics located in the shielding hut underneath the detector platform were mounted on three large racks and included four NIM power crates and other NIM modules. The primary purpose of the electronics in the shielding hut was to form the timing logic signal for each PMT.

Schematic diagrams of the shielding hut electronics for the front and rear array detectors and the front and rear veto/tagger array detectors are shown in Figs. 4-8 and 4-9, respectively. Each PMT was powered remotely by an EPICS-controlled 64-channel high-voltage CAEN mainframe crate that was located on the second floor of the counting house. The particle interaction time and the energy deposition (referred to as the pulse height) in each scintillator were obtained from the anode signal of the PMT on each end of the scintillator. The anode signal from each PMT in the front array was first amplified by a fast preamplifier with a gain of eight. The purpose of these preamplifiers, which were custom designed by Baldwin of Kent State University, was to enable a low threshold setting while operating the PMTs at a modest high-voltage level. We made the compromise of obtaining gain directly from the PMT with keeping the current in each PMT at a level such that the gain of each PMT did not deteriorate substantially over the duration of the experiment. The anode signals from the PMTs in the rear array detectors were not preamplified.

The anode signal from the preamplifier was then directed to an LED driver and pulse height monitor (PHM). When desired, this device was used to assess the pulse height response of each PMT to a flashing blue LED mounted on the light guide of

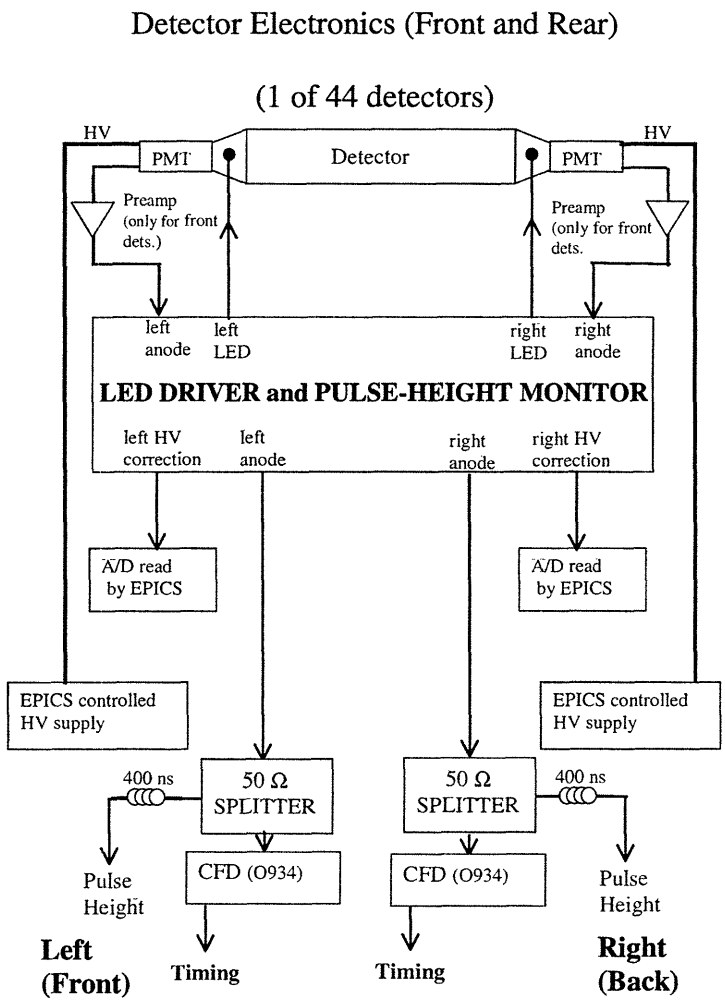

Figure 4-8: Schematic diagram of the shielding hut electronics configuration for the front and rear array detectors.

each detector. The response of the PMTs to these flashes of light were integrated by the PHM and plotted on a 1024-channel analyzer. The pulse-height response of the PMT to the LED was Gaussian, and the centroid channel was extracted from a fit to the spectra produced by the multi-channel analyzer. All of this was done internal to the PHM, and the value of the centroid for each PMT could be requested from the PHM via an RS-222 serial link to the PHM. A specific response to energy was not required; instead, the PHM was used to monitor the response of each PMT to its LED over time. The centroid channels of the LED spectra were monitored periodically throughout the course of the experiment (typically after the detectors

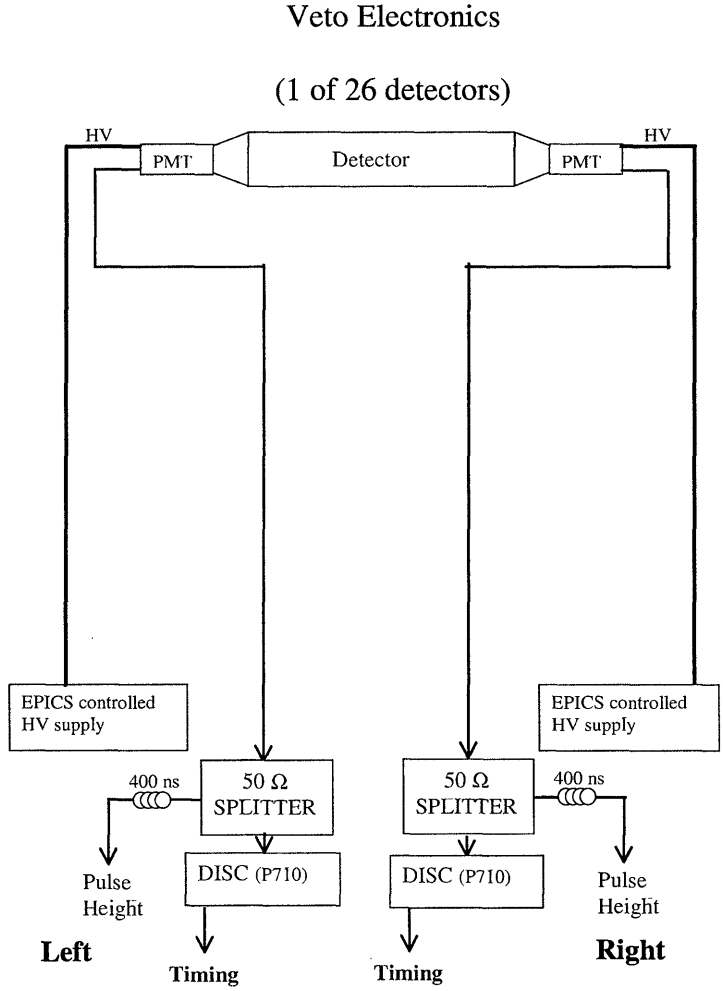

Figure 4-9: Schematic diagram of the shielding hut electronics configuration for the front and rear veto/tagger array detectors.

had been exposed to a particle flux for a period of time). If the centroid channel for a particular PMT was found to be lower than its previously recorded value (i.e., if the gain for a PMT had decreased), the high voltage applied to that PMT was increased appropriately. Changes to the high voltages were performed remotely using software that communicated with the PHM and the CAEN mainframe crate.

After leaving the PHM, the anode signals were sent to the two branches of the polarimeter electronics via a 50-ohm 50/50 resistive splitter. One signal was used for the pulse-height measurement and the other was used to form the event trigger and the timing measurements. The signal used for the pulse-height measurements

was directed through 400 ns of RG-58 delay cable located underneath the detector platform in the shielding hut; after traversing the delay cable, these signals were sent to the counting house via a patch panel (located along the wall of the hall near the polarimeter) through 250 feet of low-loss RG-213 cable. The other signal from the splitter was directed to either an ORTEC 934 constant-fraction-discriminator (for the front and rear array PMTs) or a LeCroy P710 leading-edge discriminator (for the front and rear veto/tagger array PMTs); the timing signals (NIM logic) generated by these discriminators were then sent to the counting house via the same patch panel through the same length of RG-213 cable.

As can be seen from a comparison of Figs. 4-8 and 4-9, the electronics configuration for the front and rear veto/tagger detectors differed slightly from that for the front and rear arrays. First, the gains of the PMTs were not monitored using LEDs; therefore, the veto/tagger circuit did not require the PHM. Second, neither the front or rear veto/tagger anode signals were preamplified. Last, as mentioned above, constant-fraction-discimination (CFD) was employed for the formation of the timing signals for the front and rear array detectors, whereas leading-edge-discrimination was employed for the front and rear veto/tagger array detectors. There are two reasons why CFD was not necessary for the veto/tagger detectors. First, the dynamic range of the energy deposition in the veto/tagger detectors was small for events of interest, so the time-walk was tolerable. Second, the time measurements from these detectors were not used for determination of the particle's energy and so a timing resolution of a few nanoseconds was sufficient for tagging charged particles in each event. Other than these differences, the configuration of the electronics in the hall for the veto/tagger detectors was identical to that for the front/rear array detectors.

4.5.3 NPOL Counting House Electronics

Detailed schematic diagrams of the counting house electronics for the front array, rear array, front veto/tagger, and rear veto/tagger detector trigger logic are shown in Figs. 4-10 through 4-13, and a brief overview is as follows.

Upon arrival in the counting house, both the analog and timing signals were di-

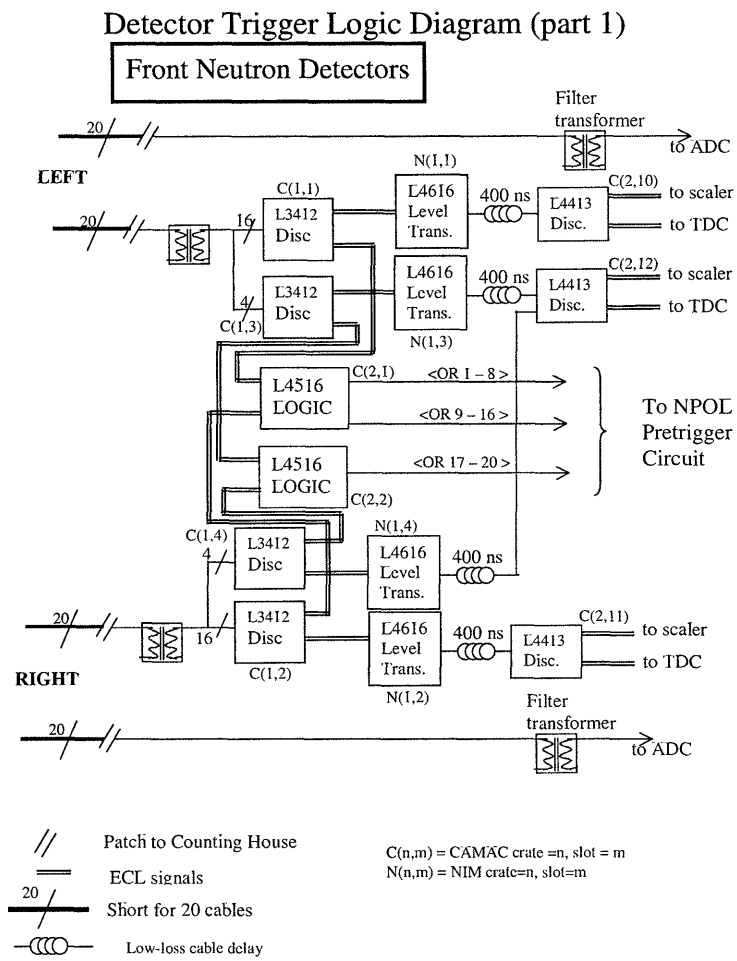

Figure 4-10: Schematic diagram of the counting house electronics for the NPOL front array detector logic.

rected through filters/transformers designed to eliminate low-frequency ground noise. As shown in these figures, the analog signals were then sent directly to FASTBUS crate ADC channels. After passing through the filter/transformer, the timing signals (NIM logic) were first sent to a LeCroy 3412 discriminator; here, the timing signals were converted from NIM logic to ECL (emitter-coupled logic)[9] and sent to two branches of the timing circuit. In one branch, the signals formed the stop signals for the TDCs and were sent to the scalers in order to measure the counting rates in each PMT. In this branch, the output from the LeCroy 3412 discriminator was directed to a LeCroy 4616 level translator (ECL-to-NIM convertor). After passing through

[9]The emitter-coupled logic family is currently the fastest form of digital logic available [357].

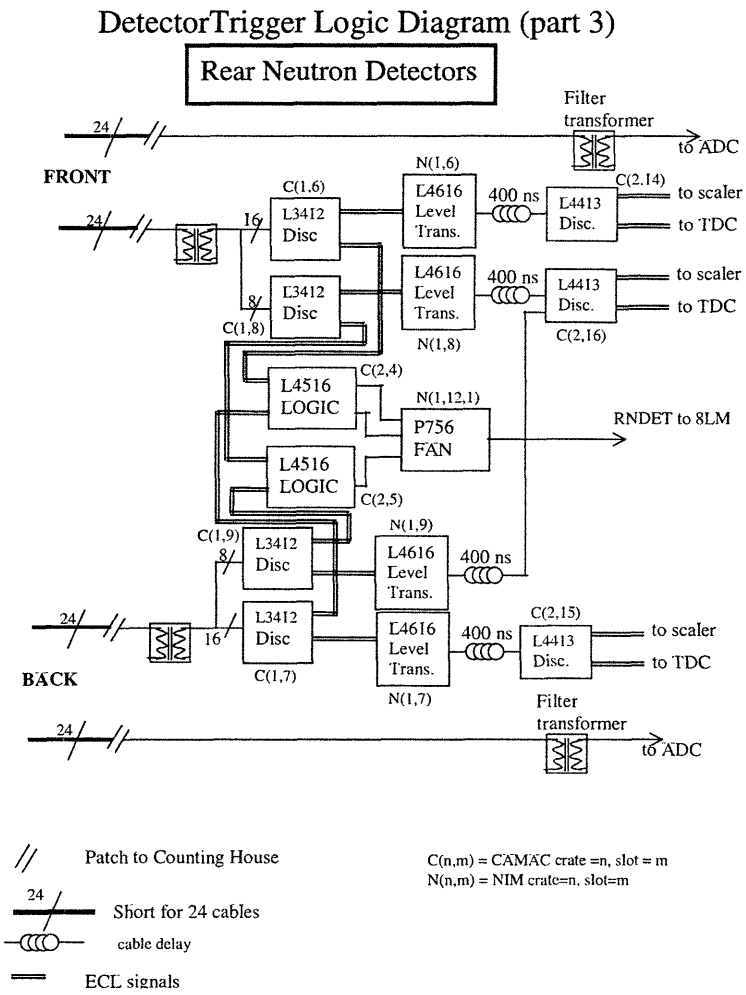

Figure 4-11: Schematic diagram of the counting house electronics for the NPOL rear array detector logic.

the LeCroy 4616, this set of signals was then directed to a LeCroy 4413 discriminator where it was further split into two signals directed to CAMAC crate scaler channels and FASTBUS crate TDC channels. In the other branch, the PMT timing signals were used to form the event triggers, the common signals for the TDCs, and the gate signals for the ADCs. In this branch, the output from the LeCroy 3412 discriminator was directed to a LeCroy 4516 logic module; this unit generated timing logic signals for coincidences between the timing signals for the left and right PMTs of each detector. The LeCroy 4516 logic modules were configured to output the logical OR of the two-PMT coincidences for eight detectors. The first unit generated the logical

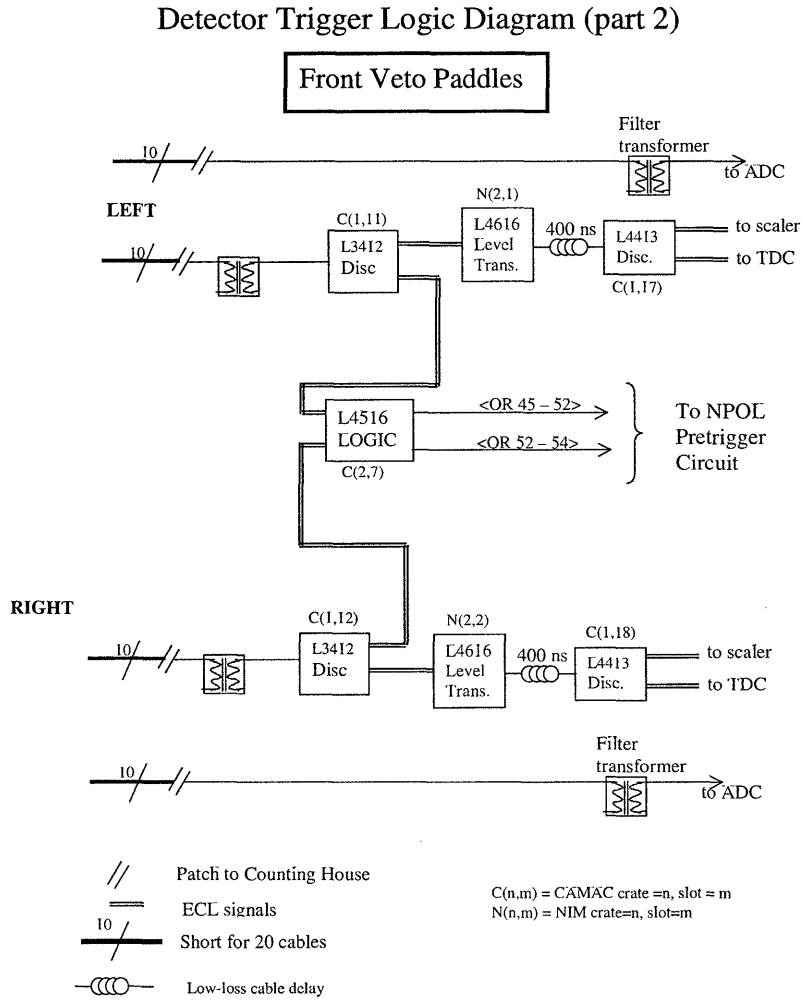

Figure 4-12: Schematic diagram of the counting house electronics for the NPOL front veto/tagger array detector logic.

OR of detectors 1 through 8 and of detectors 9 through 16, and the second unit gave the logical OR of detectors 17 through 20. The output from the LeCroy 4516 logic modules was then directed either to the NPOL pretrigger circuit (for the front array detectors and the front veto/tagger detectors) or a Phillips 756 fan-in module (for the rear array detectors — the summed signal from the P756 was then sent to a LeCroy 8LM 2365 Octal Logic Matrix module, to be discussed in more detail later). For the rear veto/tagger detectors, the output from the LeCroy 3412 was sent directly to CAMAC crate scaler channels and FASTBUS crate TDC channels; they were not used to form the trigger.

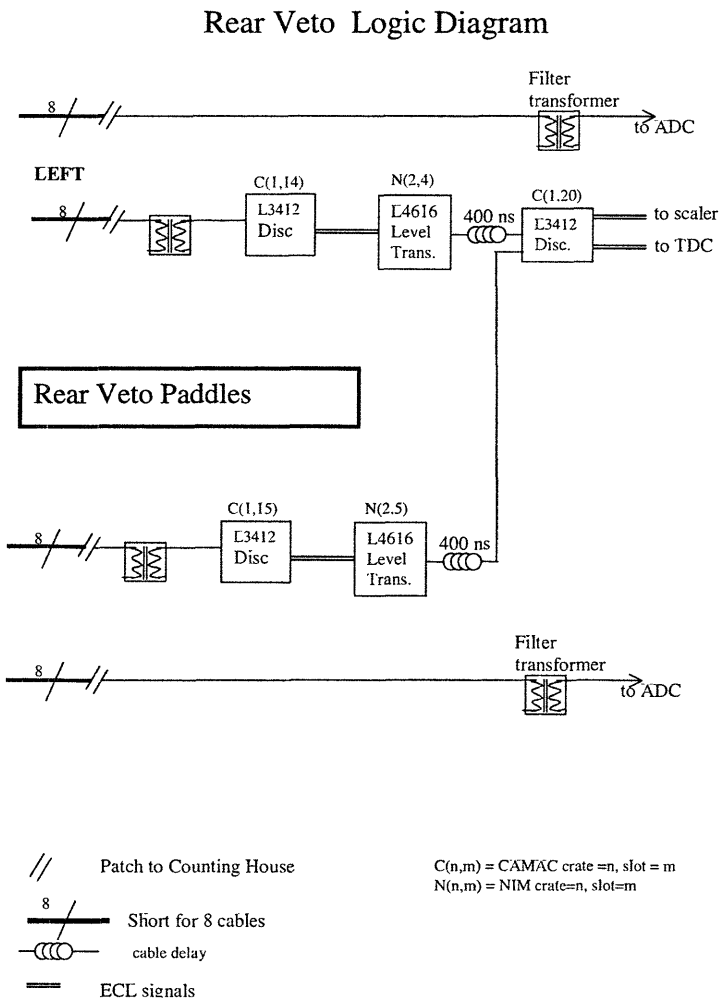

Figure 4-13: Schematic diagram of the counting house electronics for the NPOL rear veto/tagger array detector logic. Note that the electronics for only one of the two rear veto/tagger planes is shown. The logic diagram for the second plane was identical.

4.5.4 NPOL Pretrigger Circuit

A schematic diagram of the NPOL pretrigger circuit is shown in Fig. 4-14. This circuit is fairly complicated and was configured to process both the incoming timing signals from the front and rear array detector logic circuits, the front veto/tagger array detector logic circuit, and the L1 trigger accept from the trigger supervisor module. The conditions under which the L1 accept signal is logically TRUE are described in Section 4.6.2. The function of the NPOL pretrigger circuit was to generate the TDC common signals and the ADC gate signals for each valid trigger, which was indicated

E93-038 NPOL Pretrigger Circuit

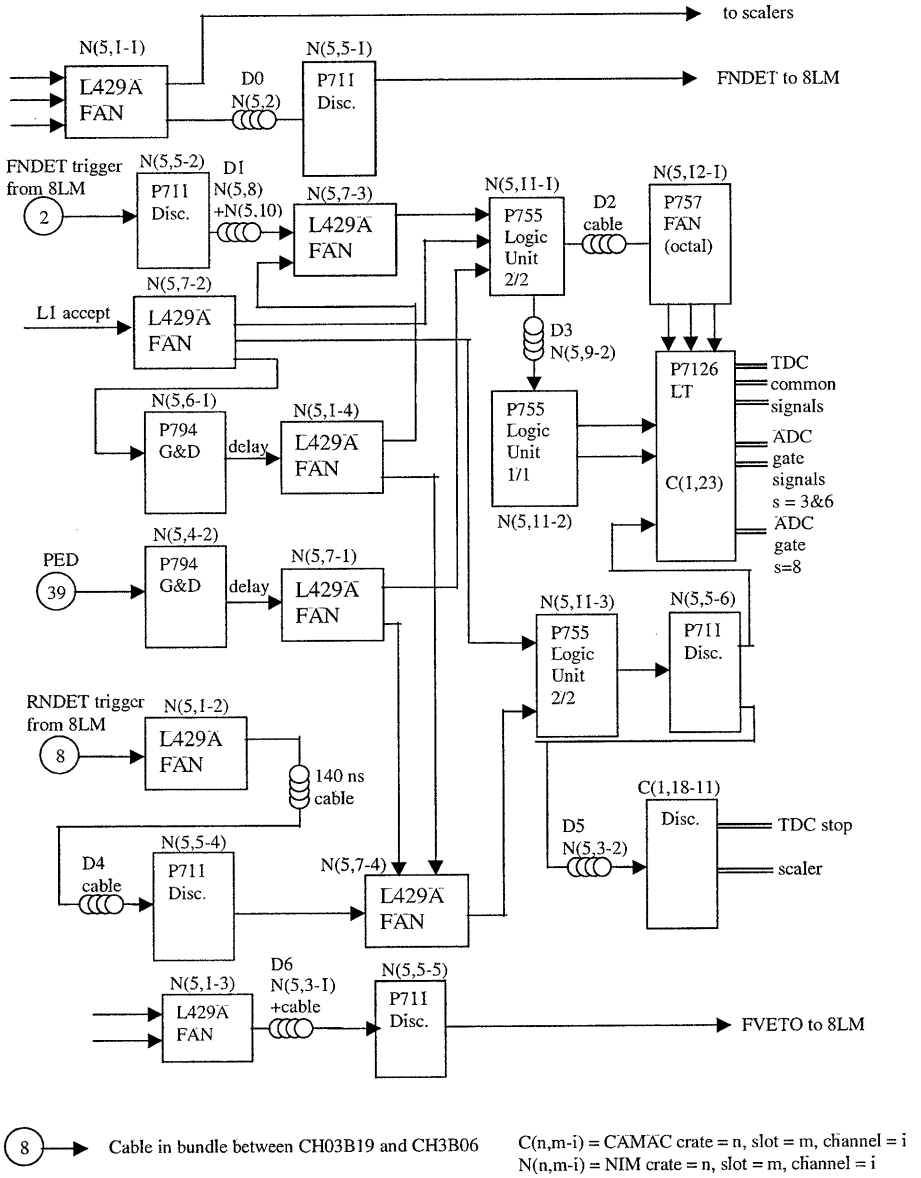

Figure 4-14: Schematic diagram of the NPOL pretrigger circuit.

by the state of the L1 accept signal. It should be noted that a narrow pulse is generated at the transition of the L1 accept from FALSE to TRUE. This pulse was delayed and used to form a logical OR with both the front array and rear array trigger signals. This circuit feature was added to ensure that all ADCs (TDCs) were gated (started) for all events, independent of the type.

First, as shown in this figure, the timing signals from the front array detector logic circuit were directed to a LeCroy 429A fan-in module. One set of output was sent to scalers, and the other set of output was directed to a Phillips 711 discriminator and then to the LeCroy 8LM. Second, the timing signals from the front veto/tagger array detector logic circuit were directed to a LeCroy 429A fan-in module; the single output from this module was then directed to a Phillips 711 discriminator and then to the LeCroy 8LM.

The remaining portion of the figure diagrams how the NPOL pretrigger circuit processed the triggers generated by the LeCroy 8LM. We defer our discussion of this portion of the circuit until after we have discussed the LeCroy 8LM, the trigger supervisor, and the various event types in more detail in the next section.

4.6 Triggers, Event Types, and Data Acquisition

4.6.1 Overview

The Hall C trigger electronics can generate either a single spectrometer trigger or a multi-detector coincidence trigger. All trigger logic was performed by two LeCroy 8LM 2365 Octal Logic Matrix modules. The interface between the trigger logic hardware modules and the data acquisition system (to be described shortly) is an electronic module known as the Trigger Supervisor (TS); the TS generates the control signals that synchronize all the major hardware components (i.e., VME crates, FASTBUS crates, and the LeCroy 8LM modules) in the data acquisition system.

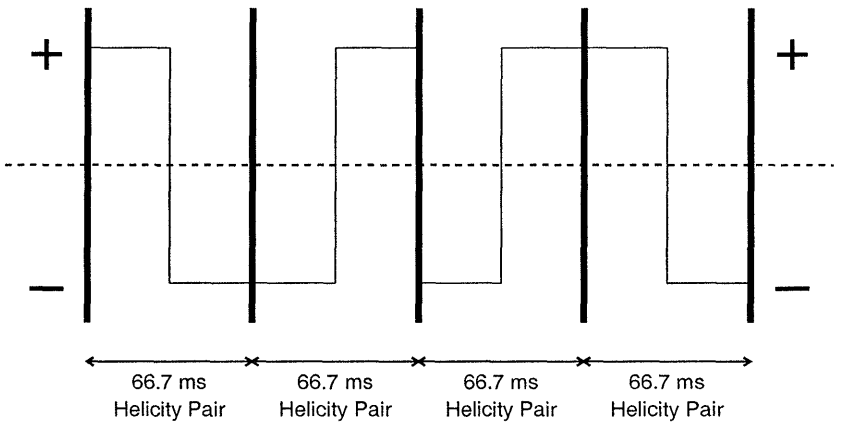

Figure 4-15: Schematic diagram of the 30 Hz pseudorandom beam helicity scheme.

4.6.2 Beam Helicity, Trigger Supervisor, and Event Types

Beam Helicity

As discussed previously in Section 3.2.2, the helicity of the electron beam was flipped pseudorandomly at a rate of 30 Hz with the helicity chosen according to the "helicity pairs" method (i.e., after the helicity for one 33.3 ms window was chosen pseudorandomly, the helicity for the next 33.3 ms window was required to be of the opposite helicity). For each (potential) helicity flip every 33.3 ms, the electronics at the polarized source generated an HGS pretrigger (i.e., a pretrigger for readout of the helicity-gated scalers); also, the electronics were configured to generate a PHT pretrigger (i.e., a period of helicity transition pretrigger) during transitions at the polarized source from one helicity state to another. As will be discussed shortly, the PHT pretrigger was used to veto otherwise valid data triggers generated during periods when the helicity state of the electron beam was assumed to be unknown.

A schematic diagram of the 30 Hz pseudorandom "helicity-pairs" scheme with the 66.7 ms helicity-pair windows is shown in Fig. 4-15. During this experiment, the duration of the PHT pretrigger was $\sim$600 μs; therefore, each effective helicity window was $\sim$32.7 ms.

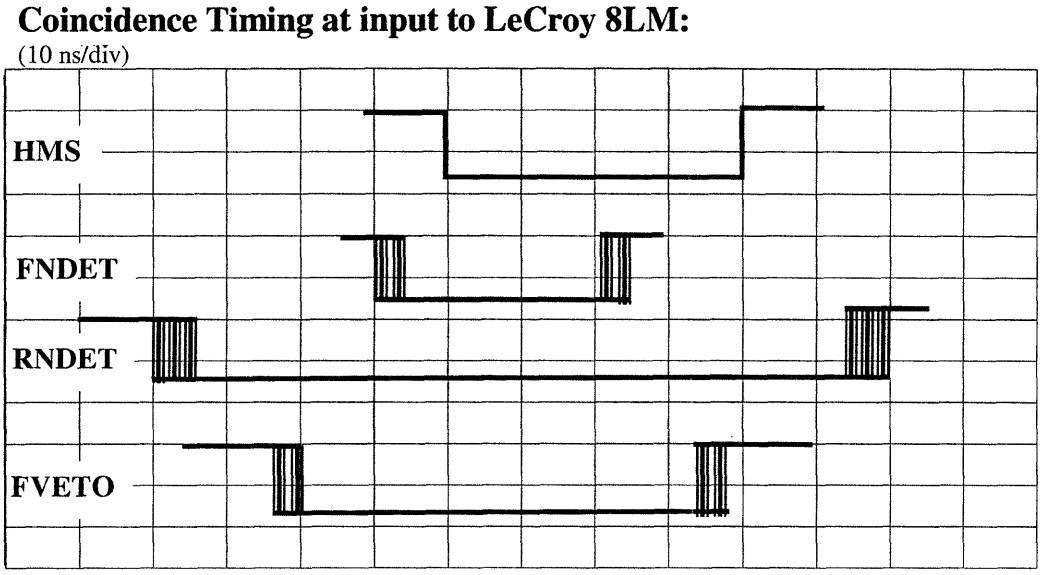

Figure 4-16: The relative coincidence timing of the HMS pretrigger, the FNDET pretrigger, the RNDET pretrigger, and the VETO trigger at the input to the LeCroy 8LM modules.

Trigger Supervisor and Event Types

The TS determined how events were processed. During active data acquisition, the TS generated three different signal outputs:

- GO: This signal was active at all times during data acquisition.
- EN1: This signal indicated that normal physics data acquisition was in progress (EN1 was FALSE when pedestal data for the HMS ADCs were being taken; this will be discussed in slightly more detail later).
- BUSY: This signal indicated that the TS was already busy processing an event; the LeCroy 8LM could not generate new triggers when the TS was BUSY.

The HMS pretrigger (charged particle in the HMS), the FNDET pretrigger (particle in the NPOL front array), the RNDET pretrigger (particle in the NPOL rear array, and the FVETO trigger (particle in the NPOL front veto/tagger array) arrived at the LeCroy 8LM modules with the relative coincidence timing shown in Fig. 4-16. These triggers [viz., a PED trigger (HMS pedestal data acquisition), the three TS signals

(GO, EN1, and BUSY), the HGS pretrigger, and the PHT trigger] were input to the two LeCroy 8LM modules. The two logic modules then determined whether the logic for any of the sixteen different coincidence pretriggers and triggers listed in Table 4.3 was satisifed. The logic for the pretriggers and triggers was identical except for the fact that the triggers required a .not.BUSY signal from the TS.[10] As can be seen there, all physics pretriggers required the absence of a positive PHT pretrigger as knowledge of the beam helicity was absolutely essential for this experiment.

A summary of the various E93-038 event types and their prescale factors are summarized in Table 4.4.[11] If the logic requirement for a pretrigger was satisified but the TS was BUSY, the incoming pretriggers were rejected and an event trigger was not generated. Similarly, if the logic requirement for a trigger was satisfied but the trigger prescale factor was not satisfied, an event trigger was not generated. Finally, if both the logic requirement and the trigger prescale factor were satisfied for events in the HMS and/or NPOL, the TS generated an L1 accept signal, and the appropriate ADC gates and the TDC common signals were generated in the HMS and/or NPOL pretrigger electronics.[12] The values of the ADC and TDC channels and the scalers processed by the FASTBUS, CAMAC, and VME crates were then read out with processors known as "Read Out Controllers" (ROCs); the ROCs are real-time UNIX-based processors which function as front-end interfaces to the FASTBUS, CAMAC, and VME crates. Alternatively, if the logic for a helicity scalers trigger was satisfied, beam helicity scalers were read out, and the resulting helicity (+ or −) was assigned to all subsequent events within the 33.3 ms helicity window; beam helicity scaler events were not, of course, prescaled.

[10]The ratio of the number of pretriggers to triggers generated by the TS is a measure of the data acquisition system live time.

[11]It should be noted that events with a charged particle incident on the polarimeter were not vetoed in hardware. Instead, charged particles were vetoed in software; a complete discussion of this follows in the next chapter.

[12]During E93-038, both the HMS and NPOL ADCs and TDCs were read out in what is referred to as "sparsified mode". In sparsified mode, an event is recorded for a particular TDC channel only if that channel receives a stop signal after the common start signal; similarly, an event is recorded for a particular ADC channel only if the analog signal satisfies a certain threshold (the thresholds are generally set a few channels above the expected value of the pedestal).

LeCroy 8LM #1			
Output	Logic	TS Input	Trigger Label
0	(HMS).and.(EN1).and.(.not.PHT)	—	HMS Singles pretrigger
1	(SOS).and.(EN1).and.(.not.PHT)	—	—
2	(HMS).and.(FNDET).and.(RNDET).and.(EN1).and.(.not.PHT)	—	HMS-NPOL GEN pretrigger
3	(PED).and.(GO).and.(.not.EN1)	—	Pedestals pretrigger
4	(HMS).and.(EN1).and.(.not.PHT).and.(.not.BUSY)	1	HMS Singles trigger
5	(SOS).and.(EN1).and.(.not.PHT).and.(.not.BUSY)	2	SOS Singles trigger
6	(HMS).and.(FNDET).and.(RNDET).and.(EN1).and.(.not.PHT).and.(.not.BUSY)	5	HMS-NPOL GEN trigger
7	(PED).and.(GO).and.(.not.EN1).and.(.not.BUSY)	8	Pedestals trigger
LeCroy 8LM #2			
Output	Logic	TS Input	Label
0	(HMS).and.(FNDET).and.(EN1).and.(.not.PHT)	—	HMS-NPOL GMN pretrigger
1	(FNDET).and.(RNDET).and.(EN1).and.(.not.BUSY)	—	NPOL Front-Rear pretrigger
2	(RNDET).and.(EN1).and.(.not.PHT).and.(.not.BUSY)	4	NPOL Cosmics pretrigger
3	(HMS).and.(FNDET).and.(RNDET).and.(.not.FVETO).and.(EN1).and.(.not.PHT)	—	—
4	(HMS).and.(FNDET).and.(EN1).and.(.not.PHT).and.(.not.BUSY)	6	HMS-NPOL GMN trigger
5	(FNDET).and.(RNDET).and.(EN1).and.(.not.PHT).and.(.not.BUSY)	3	NPOL Front-Rear trigger
6	(HGS).and.(EN1).and.(PHT).and.(.not.BUSY)	7	Helicity Scalers trigger
7	(FNDET).and.(EN1).and.(.not.PHT).and.(.not.BUSY)	4	NPOL Cosmics trigger

Table 4.3: The logic and trigger labels for the sixteen coincidence pretriggers and triggers generated by the LeCroy 8LM modules. The SOS pretrigger was not active during E93-038; however, it is listed here for completeness.

TS Input	Event Type	Prescale Factor
1	1: HMS Singles	1000
2	2: SOS Singles	9999999
3	6: NPOL Front-Rear Coincidences	9999999[1]
4	6: NPOL Cosmics	9999999[1]
5	3: HMS-NPOL GEN Coincidences	1
6	3: HMS-NPOL GMN Coincidences	400[1]
7	5: Beam Helicity Scalers	1
8	4: HMS Pedestals	1

[1] Was 999999 during early stages of the experiment.

Table 4.4: Summary of the E93-038 event types and prescale factors during normal data acquisition.

4.6.3 Data Acquisition System

Overview

The Data Acquisition System (DAQ) in Hall C is controlled by the CEBAF Online Data Acquisition System (CODA) [390,391]. CODA manages the DAQ and includes an Event Builder subsystem that receives the ADC, TDC, and scaler data from each ROC and assembles these individual data fragments into an "event". After the Event Builder has constructed an event, another subsystem, the Event Recorder, writes the data for the event directly to disk.

Run Control and Data Taking

In addition to directing the DAQ, CODA also includes a graphical user interface (GUI), the RunControl, that allows the user to start and stop data acquisition (i.e., to start and stop runs).

After the user directed the DAQ to start a run, the first few events that were recorded were "status events"; status events included prestart/start events and a user defined event (e.g., comments concerning the run conditions the user could enter into the RunControl). After these first few events were taken and recorded, 1000 random triggers were generated in order to determine the pedestals for the HMS ADCs (the DAQ disables sparsification of the HMS ADCs during pedestal data acquisition). Fol-

lowing acquisition of the HMS pedestal events, physics data production commenced and continued until the end of the run (typically, one, two, or three million events) or until the user stopped the DAQ for any number of different reasons. In addition to physics events, scalers were read out and recorded every two seconds, and beam helicity scalers were read out for each (potential) beam helicity flip at the rate of 30 Hz. Finally, certain slow control (i.e., detector and beamline controls not directly associated with data acquisition such as HMS magnet settings, target variables, etc.) parameters for the accelerator and Hall C equipment were read out every 30 seconds through EPICS; accordingly, these are, in general, referred to as "EPICS events".

During E93-038, one million events could typically be acquired in $\sim$0.5 hours ($\sim$1.0 hour) with the Charybdis magnet off (on). Typically, $\sim$80–85% of these events were those events of interest: Type 3 HMS-NPOL GEN Coincidences (see Table 4.3). The raw events encoded in the CODA data format were written to what is generally known as a ".log" file. During the course of data production, the .log files were written to a local disk and then automatically copied to the JLab Mass Storage System (a robotic tape server). The .log files required approximately 1.8 gigabytes of storage space for one million events; therefore, the data rate in this experiment was on the order of $\sim$1.0 ($\sim$0.5) megabytes/second with Charybdis off (on). This experiment took on the order of $\sim$5 *terabytes* of data.

4.7 Summary

In this chapter, we described the neutron polarimeter in detail, and we also provided an overview of the various event types and the data acquisition system. This concludes our description of the E93-038 experimental arrangement. In the remainder of this thesis, we discuss the analysis of the data that were taken during E93-038.

Chapter 5

Reconstuction to Asymmetry Extraction

In this and the next two chapters, we detail the E93-038 analysis procedures. We begin, in this chapter, with an overview of the E93-038 modified version of the standard Hall C analysis package, `ENGINE`, that was used for the analysis of the raw data.[1] Following a brief overview of this analysis package, we discuss tracking and event reconstruction for the scattered electrons in the HMS. Second, we discuss the calibration of the neutron polarimeter; this includes the pulse height and timing calibrations for each NPOL detector. Third, we present an overview of the E93-038 `Analyzer`; this E93-038-specific code was used for tracking and event reconstruction in the polarimeter. Next, we discuss another E93-038-specific code, the `casym` asymmetry program, that was used to extract the scattering asymmetries in the polarimeter. Following an overview of this code, we conclude this chapter by presenting the final asymmetry data for each of the Q^2 points; in addition, we extract the values of G_{En}/G_{Mn} from the asymmetry data assuming infinitesimal pointlike HMS and NPOL acceptances and neglecting nuclear physics corrections for FSI, MEC, and IC.

[1] Here, raw data refers to ADC/TDC channels and scaler information.

5.1 HMS Reconstruction and Tracking

5.1.1 Overview of E93-038 ENGINE

For Hall C experiments, the decoding of the raw data encoded in the .log files in the CODA data format and the subsequent reconstruction and tracking in the HMS and SOS is, in general, conducted with the Hall C analysis ENGINE; ENGINE is a robust general-purpose analysis code, written almost entirely in FORTRAN, that can accommodate either single-arm or coincidence experiments solely employing standard Hall C equipment (i.e., the HMS and SOS) or, with appropriate modifications, "third-arm" experiments employing standard Hall C equipment and an additional detector/spectrometer (such as NPOL). Major modifications to the standard ENGINE were made for E93-038 in order to decode the NPOL-specific detector data that was also encoded in the CODA data format in the raw .log data files. These changes were implemented by Tajima and are described in detail in [392, 393]. Hereafter, when discussing specific features of the E93-038-modified version of ENGINE, we shall specifically refer to this version of the standard ENGINE as the "E93-038 ENGINE".

A schematic flowchart for the E93-038 ENGINE analysis code is shown in Fig. 5-1. As indicated in this figure, the E93-038 ENGINE began with a series of initialization routines configured to read detector parameters and calibration constants from various input files. Following the execution of the initialization routines, the code proceeded to read the raw data from the .log files for the different event types (i.e., start-of-run status events, physics events, scaler events, and EPICS events); each event type was then processed with a different set of routines. For physics events, the E93-038 ENGINE decoded the raw HMS detector data, generated tracks, reconstructed various target quantities, and calculated a number of physics quantities for the scattered electron. Also, for coincidence events, the E93-038 ENGINE decoded the raw NPOL detector data and returned a small amount of NPOL tracking information (e.g., number of detectors recording hits, etc.). Following the analysis of an entire run, the E93-038 ENGINE wrote two different types of output to disk:

- ASCII text files containing scaler information (e.g., total charge, beam current,

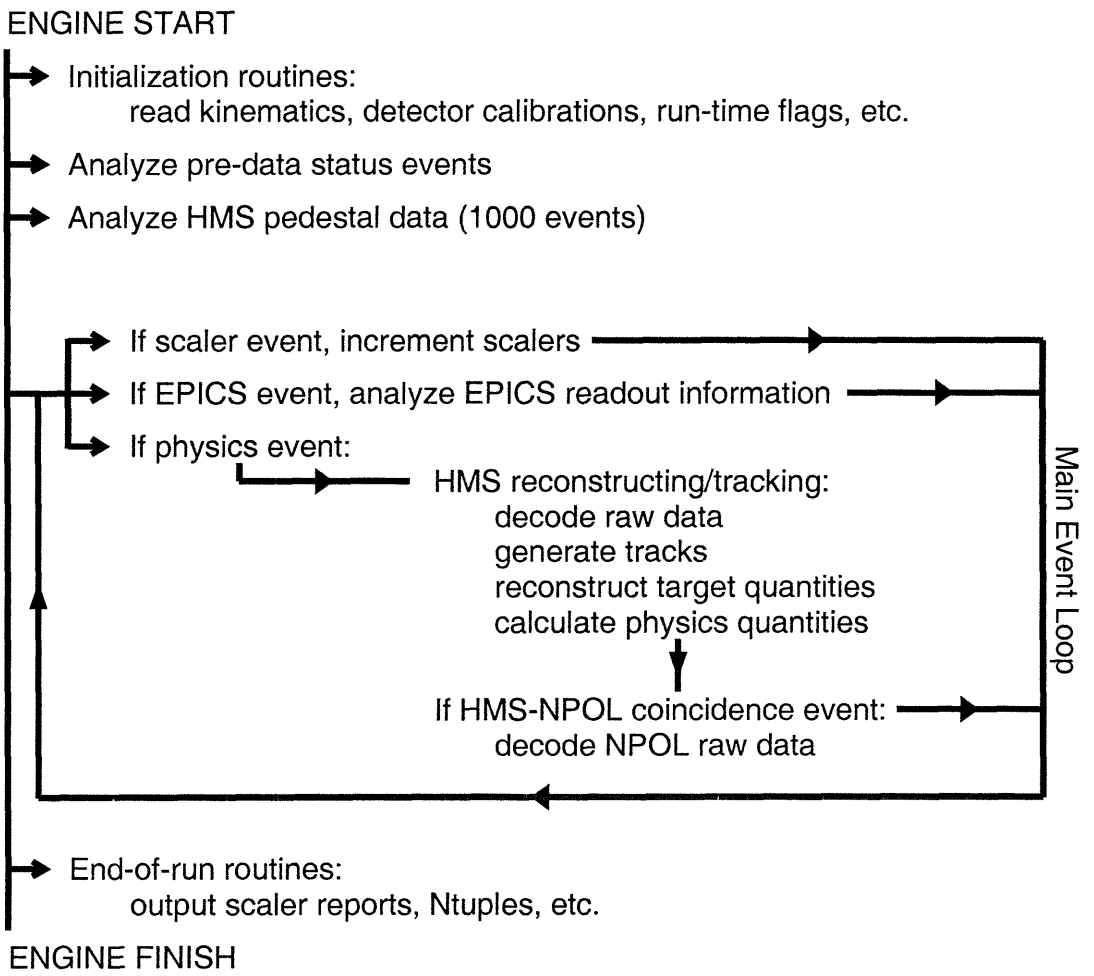

Figure 5-1: Schematic flowchart for the E93-038 `ENGINE` analysis code.

detector counting rates, etc.) and information derived from EPICS; and

- `.rzdat` Ntuple files (created with standard CERNLIB [394] routines) containing the event-by-event reconstructed kinematics for the scattered electron, raw time-of-flight spectra, and raw ADC and TDC spectra for NPOL detectors recording hits.

Detailed descriptions of the HMS- and SOS-specific sections of the general `ENGINE` code may be found in early Hall C theses (see, e.g., [332, 395, 396]). In what follows below, we describe the salient features of this code; however, before proceeding to an overview of the code, we provide a brief overview of an essential element of the standard `ENGINE`, the CEBAF Test Package.

5.1.2 CEBAF Test Package

ENGINE's input and output are streamlined with the use of Wood's CEBAF Test Package (CTP) [397]. CTP is a set of analysis tools for nuclear physics data acquisition systems written in C and based loosely on the LAMPF Q [398] test, histogram, and dynamic parameter packages. CTP permits an analysis code to receive parameter settings, definitions for cuts, and definitions for histograms either through external ASCII files loaded at execution time or through a remote procedure call interface. The user is then permitted to change various data analysis parameters without recompiling the entire data acquisition system. Also, in CTP, parameter settings, definitions for cuts, and definitions for histograms defined in external files all refer to data elements by the same variable names as used in the source code for the analyzer. This reduces the amount of necessary "bookkeeping" within the source code and is accomplished by requiring the analyzer to "register" each variable that CTP will access. Each registered variable, in addition to the parameter settings, definitions for cuts, and definitions for histograms, can then be dynamically read and modified by tasks that communicate via remote procedure calls.

As described by Arrington [332], ENGINE is configured such that all variables stored in COMMON blocks are defined in .cmn files. When the source code for ENGINE is compiled, the .cmn files are parsed, and all of the variables are automatically registered with CTP. Following registration, these variables can then either be examined or modified without recompiling the source code. Also, additional variables that are not part of the source code can be defined in input files and used to define various tests or histograms. All of these shared variables can then be accessed via remote procedure calls.

ENGINE primarily uses CTP to input various parameters, kinematics, and flags that dictate the flow of the analysis and to define the histograms and scalers that will be output to the Ntuples and ASCII files, respectively, at the conclusion of the analysis. As discussed next, these CTP input parameters are read from ASCII files by a series of initialization routines.

5.1.3 Initialization Routines

As shown in Fig. 5-1, the E93-038 ENGINE began with a series of initialization routines. First, the main configuration file, usually named "REPLAY.PARM", was read; this file contained a number of different run flags and the filenames for a number of different important files (e.g., the name of the raw .log data file, the name of a separate file which itself contained the filenames for different kinematics parameter files and decoding maps for the HMS detectors, filenames for output, etc.). Second, after all of the run parameters were defined, the output data files (i.e., the output ASCII files and Ntuple .rzdat files) were initialized. Last, the raw .log data file was opened, and the E93-038 ENGINE processed the first few events in the data file (i.e., the "status events").

5.1.4 Main Event Loop

In the main event loop, again, shown schematically in Fig. 5-1, each event was read and subsequently analyzed according to its event type. In general, the standard ENGINE recognizes three different types of events: scaler, EPICS, and physics events (previously discussed in Section 4.6.3).

If an event was recognized as a scaler event, the total number of counts recorded by the scaler was incremented (in software). Similarly, if an event was recognized as an EPICS event, the appropriate EPICS values were read from the raw data file and stored. In general, the standard ENGINE recognizes four different types of physics events: HMS pedestal, HMS singles, SOS singles, and user-defined coincidence (COIN) events; recognition of SOS events was disabled in the E93-038 ENGINE.

As previously discussed, the first 1000 physics events were HMS pedestal events. These events were analyzed by the E93-038 ENGINE, and the value of the pedestal (in channels) for each ADC in the HMS was extracted from the data; thereafter, in all subsequent analyses, the raw ADC spectra were corrected for the pedestals. The two other types of physics events, HMS and COIN events, were events generated by singles events in the HMS and HMS-NPOL coincidences, respectively. The raw detector data

from the HMS and NPOL were read from the raw `.log` data file and then passed to HMS and NPOL reconstruction algorithms. For the scattered electron, the track of the electron through the HMS was reconstructed, and various kinematic quantities (e.g., momentum, energy, target variables, etc.) were computed and subsequently written to the `.rzdat` file. For the NPOL detectors, the E93-038 `ENGINE` decoded the raw detector data from the `.log` files and subsequently wrote the values of the ADC and TDC channels for NPOL detectors recording hits for that event to the `.rzdat` file. A new `.rzdat` file was written to disk every 20000 events (or at the conclusion of a run), and after all events were analyzed, the `ASCII` scaler files containing scaler and EPICS information were written to disk.

5.1.5 Extraction of HMS Information

Here, we provide a general overview of tracking and event reconstruction in the HMS. The E93-038 `ENGINE` employed the standard `ENGINE` algorithms for the extraction of HMS information; no modifications were made to these routines. Again, for a detailed description of these algorithms we refer the reader to [332, 395, 396].

Tracking

First, for each event, the E93-038 `ENGINE` translated the raw HMS ADC and TDC values (i.e., channels) for scintillators recording hits in the hodoscopes into pulse heights and times, respectively. After timing corrections for variations in pulse height, cable length offsets, and signal propagation through the scintillators were applied to the raw values, the timing signals were used to calculate the particle's velocity and, subsequently, the times the particle traversed the drift chamber planes; these times were then used as the reference start time for each plane in the drift chambers.

Second, after the ADC and TDC data from the hodoscopes were decoded, the hits in the drift chambers and track-independent information, such as the number of photoelectrons detected by the Čerenkov detector and the energy deposition in the lead-glass calorimeter, were decoded.

Next, after all of the detector information was decoded, the E93-038 ENGINE attempted to reconstruct the track of the particle through the HMS. The overall strategy of the tracking algorithm was to use the drift chamber information and the reference start time provided by the hodoscopes to reconstruct the trajectories of the particles that traversed the drift chambers. As previously discussed in Section 3.4.3, the difference between the reference start time and the time recorded by the drift chamber TDCs determines the time the sense wires detected the ionization; the drift time and the position of the event (given knowledge of the drift velocity) were then extracted from this information. Unfortunately, this information does not uniquely identify the spatial location of a hit in a particular drift chamber plane as it is ambiguous whether the particle passed to the left or to the right of any given wire; appropriately, this ambiguity is usually referred to as a "left-right ambiguity". In order to resolve this left-right ambiguity, a track was fit to each left-right combination in the six planes of each drift chamber (clearly, there are on the order of $\sim 2^6 = 64$ combinations in each drift chamber to fit). The track was then reconstructed by fitting a straight line (as there are no electric or magnetic fields in the drift chambers) to each of these combinations. For each combination in the first and second drift chamber, a full track through both drift chambers was fit if the two separate tracks were consistent (e.g., in slope, etc.). The full track with the overall smallest χ^2 (calculated for the deviations between the predicted and recorded hit positions in the drift chamber planes) was then selected as the final track through the drift chambers. We refer the reader to the above-mentioned references for a more sophisticated technical discussion of the tracking algorithm.

Reconstruction

After the E93-038 ENGINE constructed the particle's track between the two wire chambers, the next step was to relate the positions and angles at the focal plane to similar quantities at the target.

A schematic diagram of transport through the HMS is shown in Fig. 5-2. As described by Arrington [332], the *true focal plane* is, in general, the surface defined

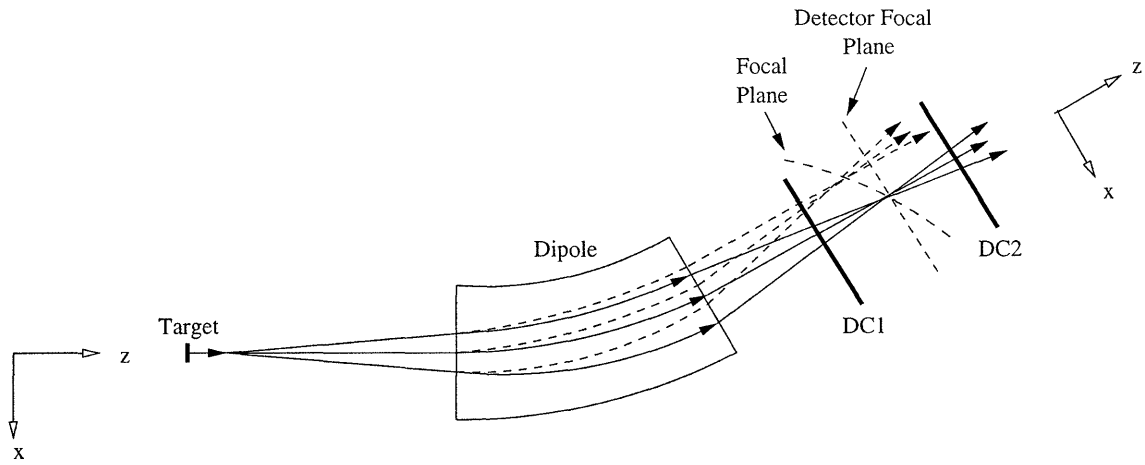

Figure 5-2: Schematic diagram of transport through the HMS.

by the focal points of a magnetic system for rays of different momentum. As shown in this figure, the true focal plane of the HMS is actually a curved surface (and is not, as a result, parallel to the drift chamber planes); therefore, when analyzing data, HMS quantities are referred to the *detector focal plane*, defined to be perpendicular to the central momentum ray (i.e., parallel to the drift chamber planes) and located where the central momentum ray intersects the true focal plane (half-way between the two drift chambers). Hereafter, it should be assumed that we are referring to the detector focal plane whenever we discuss focal plane quantities.

The coordinate system for transport through the HMS shown in Fig. 5-2 is defined according to the standard TRANSPORT [399] convention; here, $\hat{\mathbf{z}}$ points along the central ray of the spectrometer, $\hat{\mathbf{x}}$ points in the dispersive direction, and $\hat{\mathbf{y}} = \hat{\mathbf{z}} \times \hat{\mathbf{x}}$ points in the non-dispersive direction. By convention, for a vertical-bend spectrometer, $\hat{\mathbf{x}}$ points "downward"; therefore, for an observor facing the HMS with her back to the target, $\hat{\mathbf{y}}$ points "to the left". The origin of the coordinate system for the standard TRANSPORT focal plane variables $(x_{\rm fp}, y_{\rm fp})$ is defined to be where the central momentum ray intersects the focal plane; therefore, $x_{\rm fp}$ and $y_{\rm fp}$ provide a measure of the position in the dispersive and non-dispersive directions, respectively, at the focal plane. Two other TRANSPORT variables, $x'_{\rm fp}$ and $y'_{\rm fp}$, are defined to be the slopes of the rays in the dispersive and non-dispersive directions, respectively, at the focal plane; that is,

$x'_{\rm fp} \equiv {\rm d}x_{\rm fp}/{\rm d}z$ and $y'_{\rm fp} \equiv {\rm d}y_{\rm fp}/{\rm d}z$.

The goal of the reconstruction algorithm was to convert the quantities measured at the focal plane into the target quantities $x'_{\rm tar} \equiv {\rm d}x_{\rm tar}/{\rm d}z$, $y_{\rm tar}$, $y'_{\rm tar} \equiv {\rm d}y_{\rm tar}/{\rm d}z$, and $\delta \equiv (|\mathbf{p}_{e'}| - |\overline{\mathbf{p}_{e'}}|)/|\overline{\mathbf{p}_{e'}}|$, where $|\overline{\mathbf{p}_{e'}}|$ denotes the central value of the momentum. With this choice of target quantities, $x_{\rm tar}$ could not be reconstructed by the E93-038 `ENGINE` and was instead defined to be $x_{\rm tar} = 0$ for all events.

Assuming the validity of a Taylor expansion for the solutions to the equations of motion for charged particles in a spectrometer, transport from the focal plane to the target can be expressed in terms of Penner's [400] matrix formalism as

$$q^i_{\rm tar} = \sum_{j,k,\ell,m} \mathcal{M}^i_{jk\ell m}\; x^j_{\rm fp}\; x'^k_{\rm fp}\; y^\ell_{\rm fp}\; y'^m_{\rm fp}\;, \tag{5.1}$$

where $q^i_{\rm tar}$ denotes $x'_{\rm tar}$, $y_{\rm tar}$, $y'_{\rm tar}$ and δ for $i = 1$, 2, 3, and 4, respectively, and $\mathcal{M}^i_{jk\ell m}$ is a transport matrix element written symbolically as

$$\mathcal{M}^i_{jk\ell m} = \langle q^i_{\rm tar} | x^j_{\rm fp}\; x'^k_{\rm fp}\; y^\ell_{\rm fp}\; y'^m_{\rm fp} \rangle\;. \tag{5.2}$$

As discussed in detail by Dutta [396], the symmetry about the center of the focal plane imposes certain restrictions on the $\mathcal{M}^i_{jk\ell m}$ matrix elements. First, the exponents for the dispersive target coordinates, $x'_{\rm tar}$ and δ, are restricted such that $\ell + m$ must be even. Second, the exponents for the non-dispersive target coordinates, $x_{\rm fp}$ and $x'_{\rm fp}$, are similarly restricted such that $j + k$ must be even. All other combinations are said to be "forbidden", and the matrix elements for these combinations are, in general, identically zero.

The reconstructed target quantities, a number of other event-wise physics quantities (e.g., $\beta_{e'}$, $\mathbf{p}_{e'}$, $\mathbf{q}$, etc.) computed by the E93-038 `ENGINE`, and the track-independent quantities (e.g., energy deposition in the calorimeter, number of Čerenkov photoelectrons, etc.) were written to the `.rzdat` file.

Matrix Element Optimization

Given a sufficiently precise model for the magnetic fields in the spectrometer, the matrix elements could, in principle, be calculated with a standard particle optics code such as COSY [401]; however, the precision of such a calculation is limited by the precision of the model for the spectrometer's magnetic fields. Alternatively, Loffler *et al.* [402] demonstrated that a spectrometer's optics could best be determined via experiments with particle rays traced over the acceptance of the spectrometer; hence, we see the motivation for the sieve slit discussed previously in Section 3.4.1. The optical properties of the HMS were studied extensively during experiments conducted prior to E93-038; we especially refer the reader to [396] for an excellent overview of the matrix element extraction and optimization procedure.

During E93-038, a short running period during April 2001 was devoted to HMS optics studies. First, an attempt was made to conduct a "$y_{\rm tar}$-scan" with the sieve slit; unfortunately, this effort had to be aborted due to a water leak in the HMS dipole. Second, a "δ-scan" was successfully performed with a ^{12}C target and a 0.884 GeV beam. In order to extract new optimized values for the "delta matrix elements" (i.e., the $\mathcal{M}^{\delta}_{jk\ell m}$), elastic ^{12}C$(e,e')$ data were taken for seven different settings of the HMS dipole field. The Hall C CMOP software package (see, e.g., [396]) was used to center the elastic peaks about their appropriate locations at the focal plane, and the delta matrix elements were extracted from the parameters needed to correct the elastic peaks. We refer the reader to [403] for a complete description of the E93-038 delta matrix element optimization procedure.

HMS Detector Calibrations

A number of extensive HMS detector calibrations (i.e., timing calibrations for the hodoscope scintillators, gain calibrations for the Čerenkov and lead-glass calorimeter PMTs, and TDC-to-drift distance calibrations for the drift chambers) were performed for experiments conducted prior to E93-038. No new HMS detector calibrations were performed for E93-038; therefore, instead of discussing these calibrations, we refer

the reader to [332] for an excellent overview of the HMS calibration procedures.

5.1.6 Minimal Extraction of NPOL Information

In addition to tracking and event reconstruction in the HMS, the E93-038 `ENGINE` was configured to write a minimal number of NPOL variables to the output `.rzdat` files. The raw ADC and TDC spectra (i.e., neither pedestal-subtracted nor time-calibrated) were decoded and saved as were a number of other variables which indexed the detectors recording hits. The E93-038 `ENGINE` did not perform physics reconstruction for NPOL; instead, all NPOL tracking and reconstruction (energy, momentum, scattering angles, time-of-flight information, etc.) was performed by the `Analyzer` code. Before proceeding to a discussion of the `Analyzer`, we discuss the pulse-height and timing calibration of the polarimeter in the next two sections.

5.1.7 Sample HMS Reconstruction and Tracking Results

We now present some sample HMS reconstruction and tracking results computed by the E93-038 `ENGINE` for each of the Q^2 points. In order to illustrate the full range of the HMS acceptance, the only cut that was applied to these spectra was the requirement that the event be a Type 3 HMS-NPOL coincidence event.

Kinematic Distributions

Histograms of the δ-distribution for the particles detected in the HMS at each of the Q^2 points are shown in Fig. 5-3; hereafter, we will change our notation slightly and refer to the δ-distribution as the "$\Delta p/p$-distribution". The quasielastic peak is clearly visible in each of these spectra. In addition, inelastic peaks, corresponding to the following pion-production reactions in the target,

$$n(e,e'n)\pi^0 \ , \qquad p(e,e'n)\pi^+ \ , \tag{5.3}$$

$$n(e,e'p)\pi^- \ , \qquad p(e,e'p)\pi^0 \ , \tag{5.4}$$

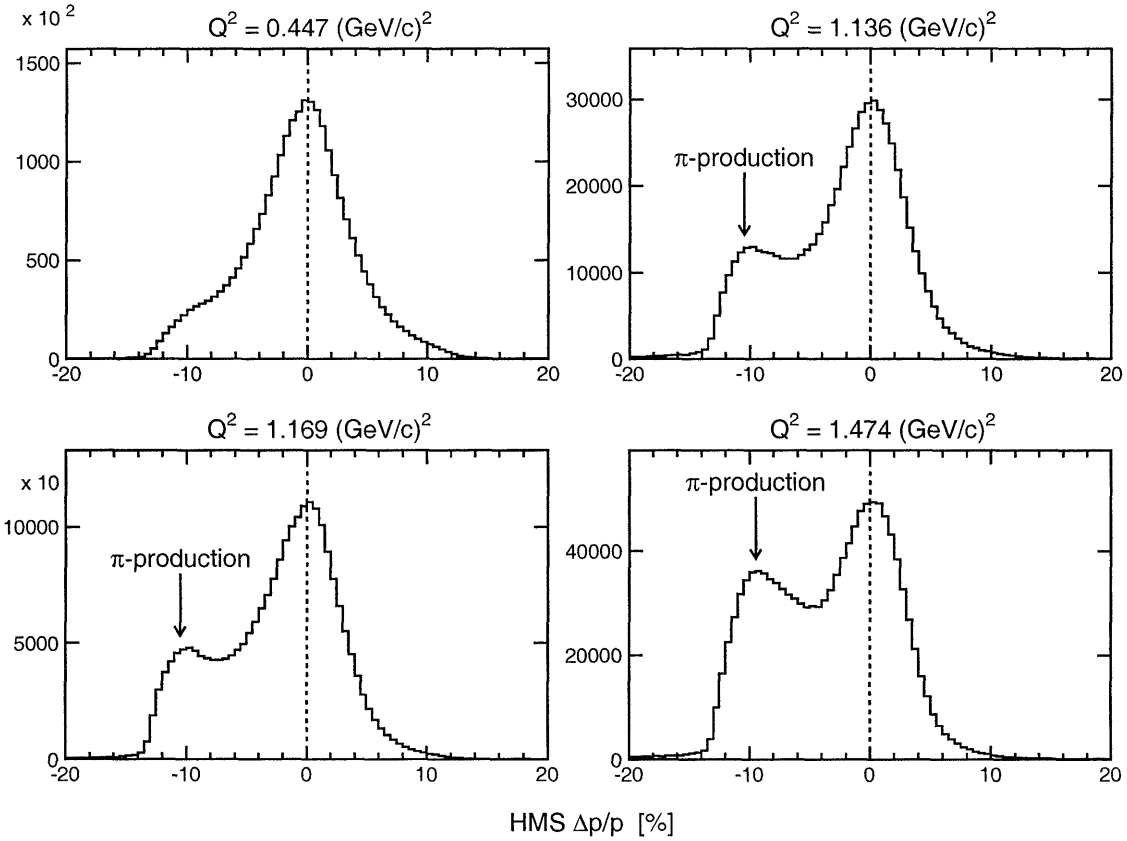

Figure 5-3: HMS $\Delta p/p$ distributions without cuts. The dashed lines at $\Delta p/p = 0$ denote the quasielastic peaks. Pion-production peaks are present in the $Q^2 = 1.136$, 1.169, and 1.474 $(\mathrm{GeV}/c)^2$ spectra.

are clearly visible in the $Q^2 = 1.136$, 1.169, and 1.474 $(\mathrm{GeV}/c)^2$ $\Delta p/p$-spectra. A pion-production peak is not seen in the $Q^2 = 0.447$ $(\mathrm{GeV}/c)^2$ $\Delta p/p$ spectrum because the smallest value of $\Delta p/p$ observed in our data for coincidence events, $\sim -14\%$ (see Fig. 5-3), corresponding to a maximum energy transfer of $\omega = 331$ MeV, lies below the neutral pion-production threshold[2] of 383 MeV; the thresholds at the other Q^2 points are 750, 767, and 930 MeV at $Q^2 = 1.136$, 1.169, and 1.474 $(\mathrm{GeV}/c)^2$, respectively.

[2]At threshold, pion electroproduction proceeds via a number of different $\gamma^* + N \rightarrow \pi + N$ (non-resonant) Born terms (e.g., pion-pole, nucleon-pole, "seagull", etc.). Assuming the initial nucleon is at rest, the initial-state four-momentum in the laboratory frame is

$$p^\mu = (\omega' + m_N,\ \omega') \ , \tag{5.5}$$

where ω' denotes the energy transfer above the quasielastic peak; here, the x- and y-components of the three-momentum are assumed to be spurious. At threshold, the final-state four-momentum in the center-of-mass frame is

$$p'^\mu = (m_N + m_\pi,\ 0) \ . \tag{5.6}$$

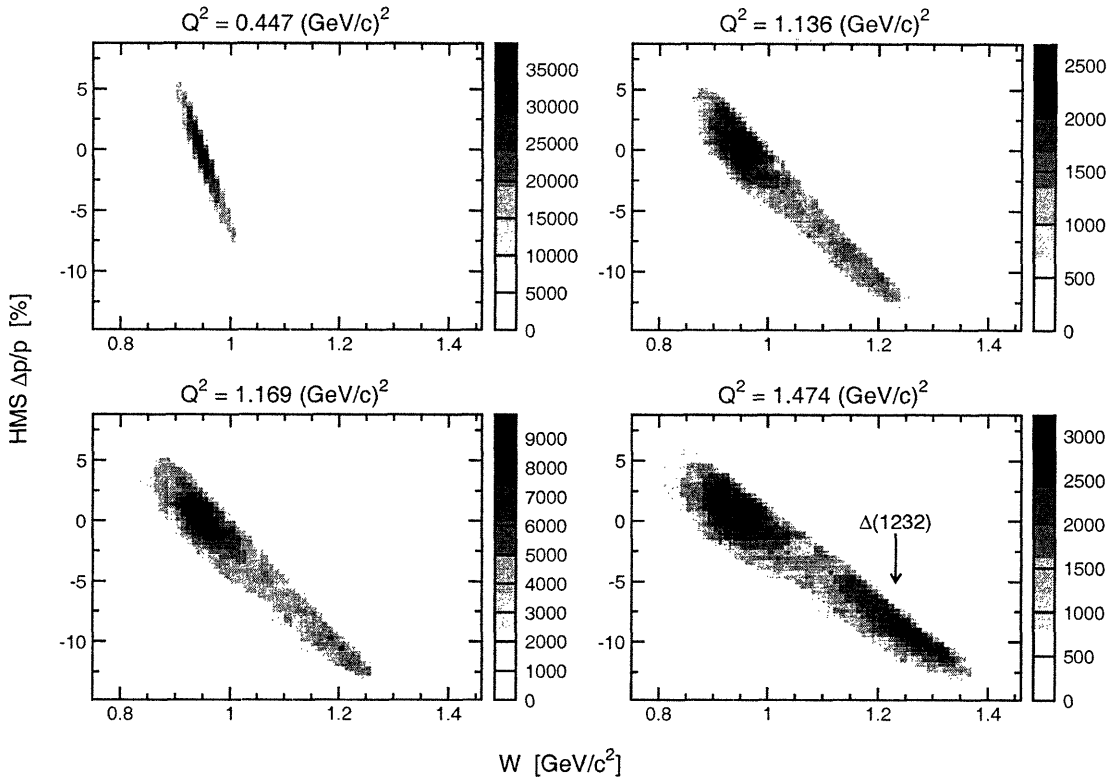

Figure 5-4: (color) HMS $\Delta p/p$ versus W distributions without cuts. The $\Delta(1232)$ resonance is prominent in the $Q^2 = 1.474$ (GeV/c)^2 distribution.

Two-dimensional histograms of $\Delta p/p$ versus the invariant mass

$$W = \sqrt{(\omega + m_N)^2 - |\mathbf{q}|^2} \tag{5.9}$$

are presented in Fig. 5-4. Here, we see in the $Q^2 = 1.474$ (GeV/c)^2 spectrum a prominent pion-production peak associated with the electroexcitation and subsequent decay of the $\Delta(1232)$ resonance at an invariant mass of 1232 MeV/c^2.

Next, in Figs. 5-5 and 5-6, we show, respectively, the range of accepted electron

Using the Lorentz invariant, $p^2 = p'^2$, it is easy to show that, at threshold,

$$\omega' = m_\pi + \frac{1}{2}\frac{m_\pi^2}{m_N} \approx 145 \text{ MeV} ; \tag{5.7}$$

therefore, the threshold laboratory frame energy transfer is

$$\omega_{\text{thr}} \approx \frac{Q^2}{2m_N} + 145 \text{ MeV} , \tag{5.8}$$

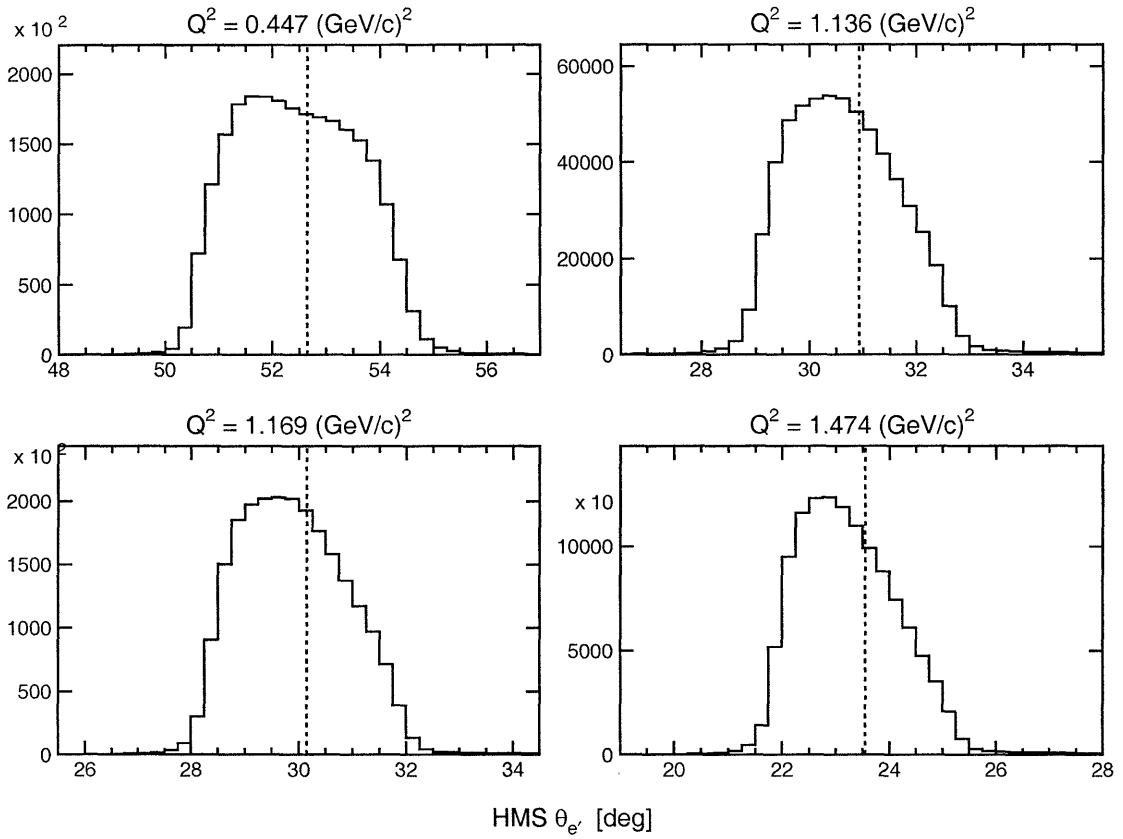

Figure 5-5: HMS scattering angle $\theta_{e'}$ distributions without cuts. The dashed lines indicate the (nominal) central scattering angles of $\theta_{e'} = 52.65°$, $30.93°$, $30.15°$, and $23.55°$ at $Q^2 = 0.447$, 1.136, 1.169, and 1.474 $(\mathrm{GeV}/c)^2$, respectively.

scattering angles, $\theta_{e'}$ and $\phi_{e'}$, for the four Q^2 points. Finally, we conclude our discussion of the HMS kinematic distributions by showing, in Figs. 5-7 and Figs. 5-8, $\beta_{e'}$ and Q^2 distributions, respectively.

Focal Plane Distributions

Two-dimensional histograms of x_{fp} versus y_{fp} for each of the Q^2 points are shown in Fig. 5-9. Here, we see, as expected, a higher concentration of events at negative values of x_{fp} (i.e., electrons bent through a larger angle by the dipole) at the higher Q^2 points due to pion-production. For completeness, we also show two-dimensional histograms of x'_{fp} versus y'_{fp} in Fig. 5-10.

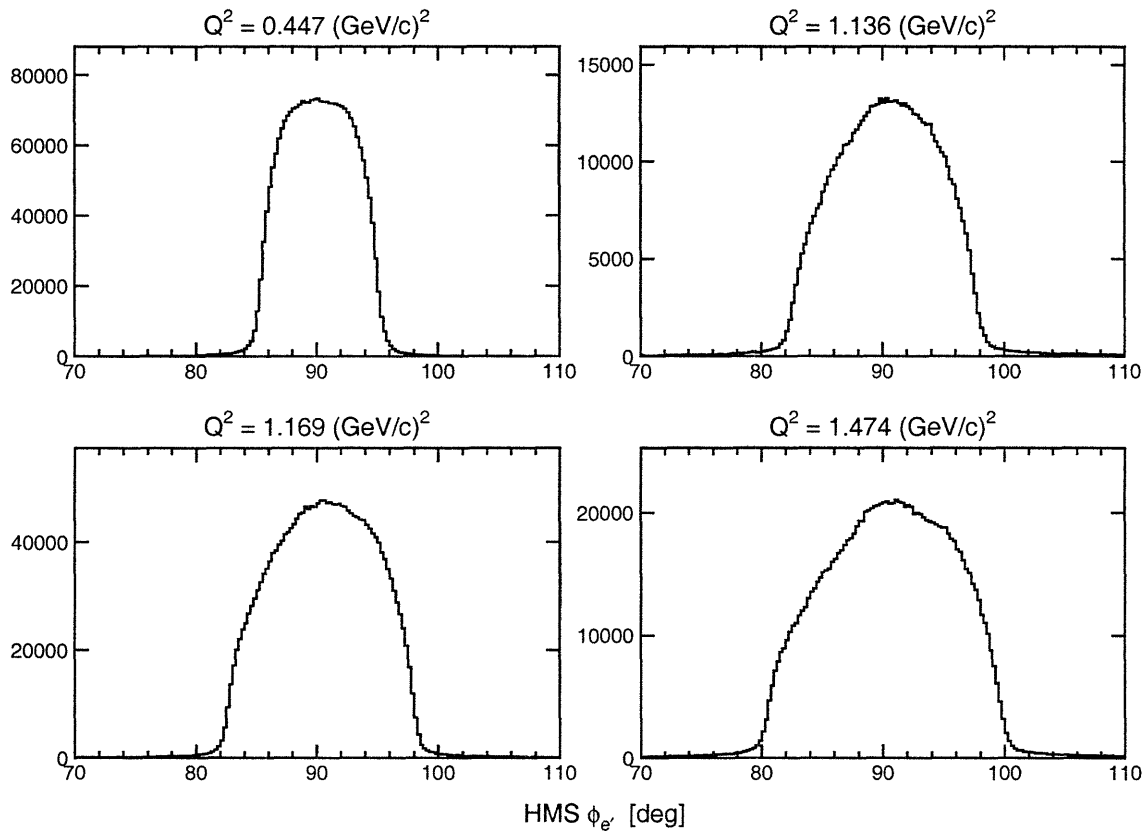

Figure 5-6: HMS scattering angle $\phi_{e'}$ distributions without cuts.

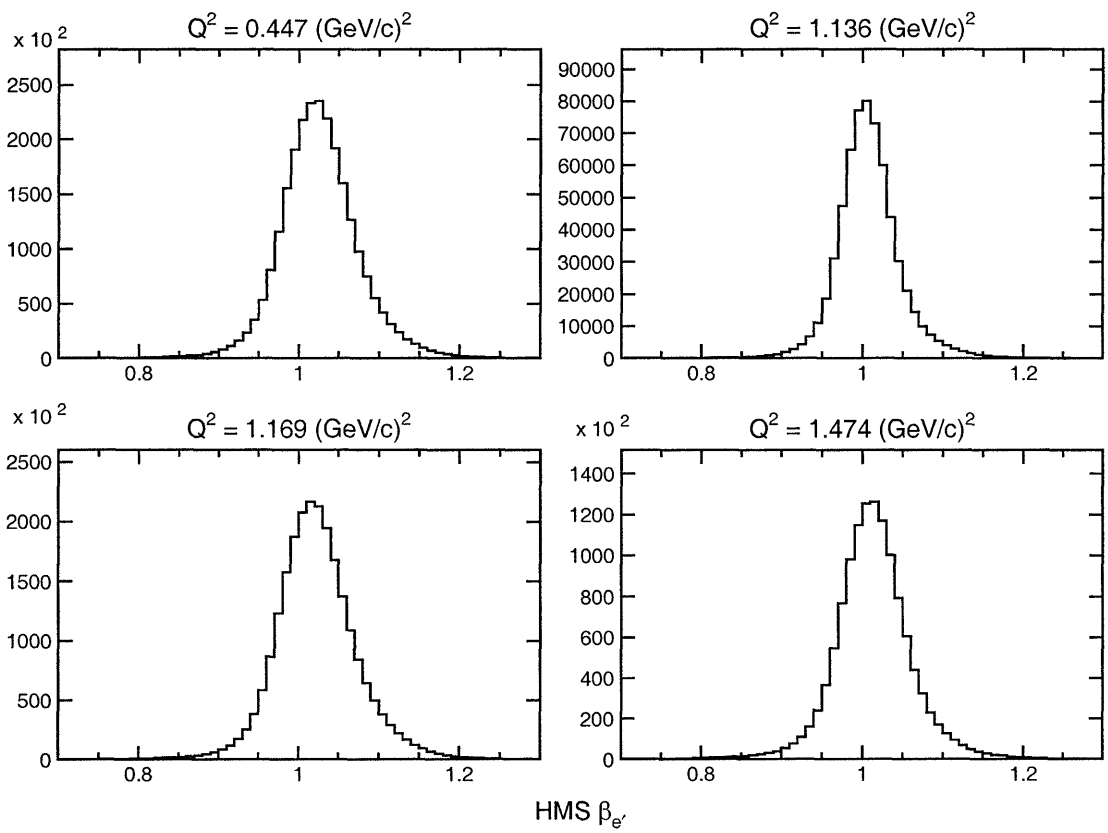

Figure 5-7: HMS $\beta_{e'}$ distributions without cuts.

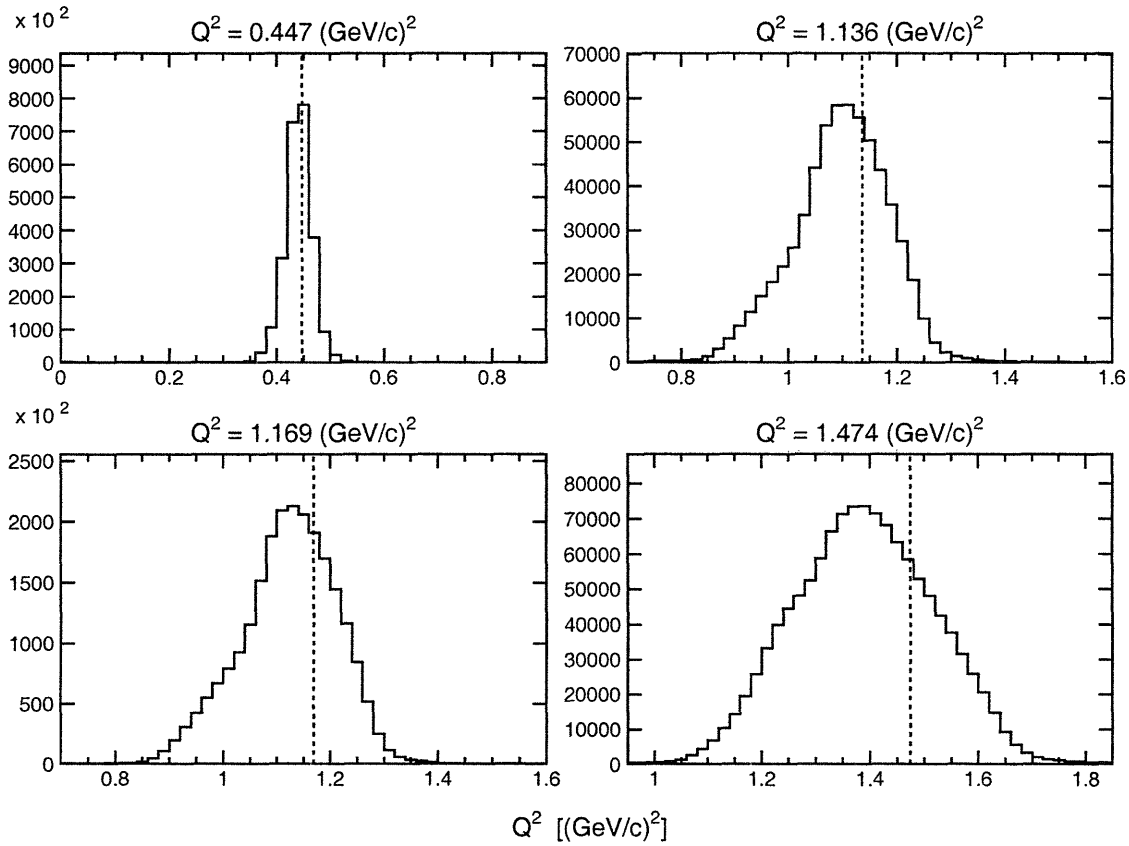

Figure 5-8: Q^2 distributions without cuts. The dashed lines are located at the (nominal) central Q^2 values.

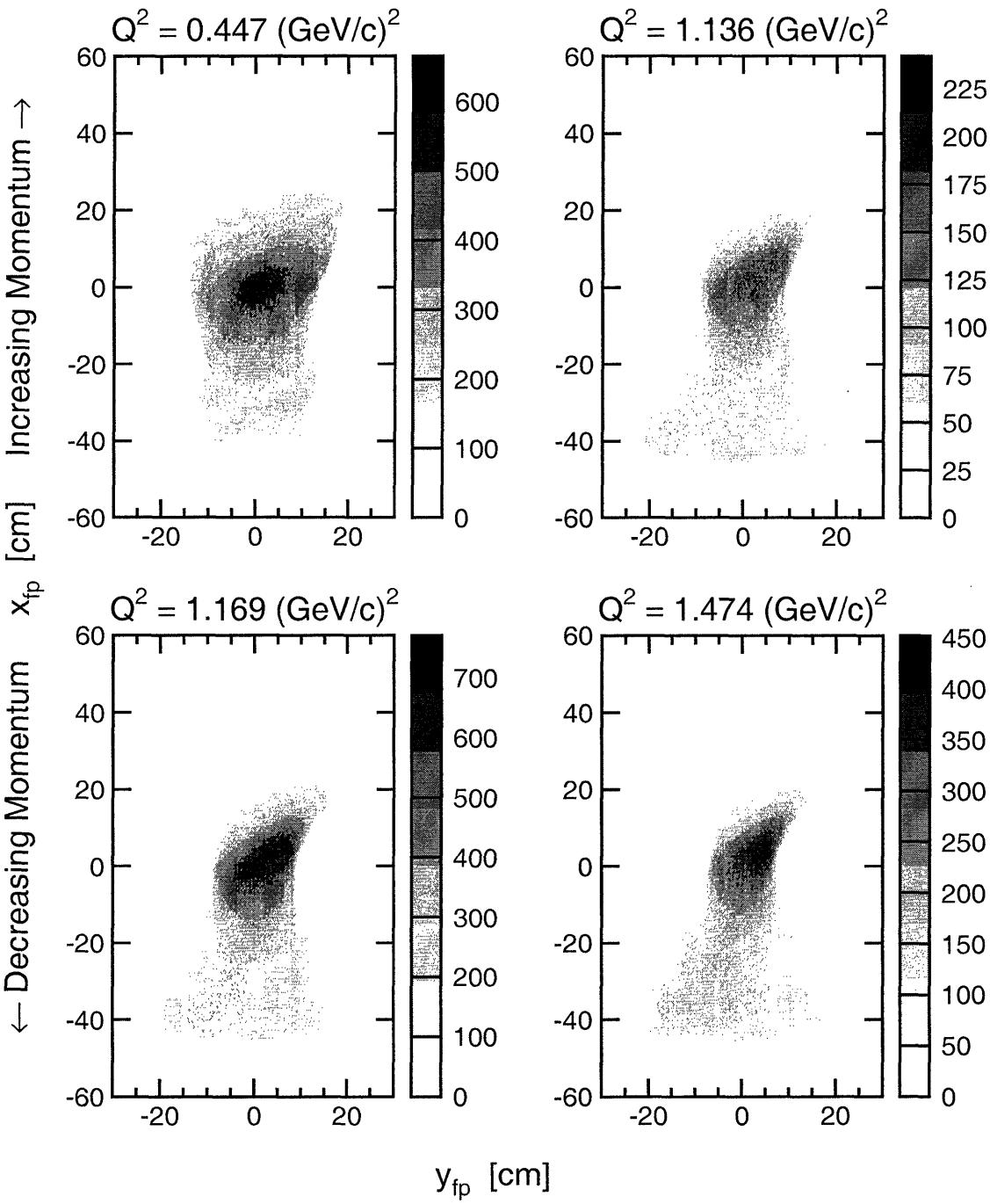

Figure 5-9: (color) $x_{\rm fp}$ versus $y_{\rm fp}$ distributions without cuts.

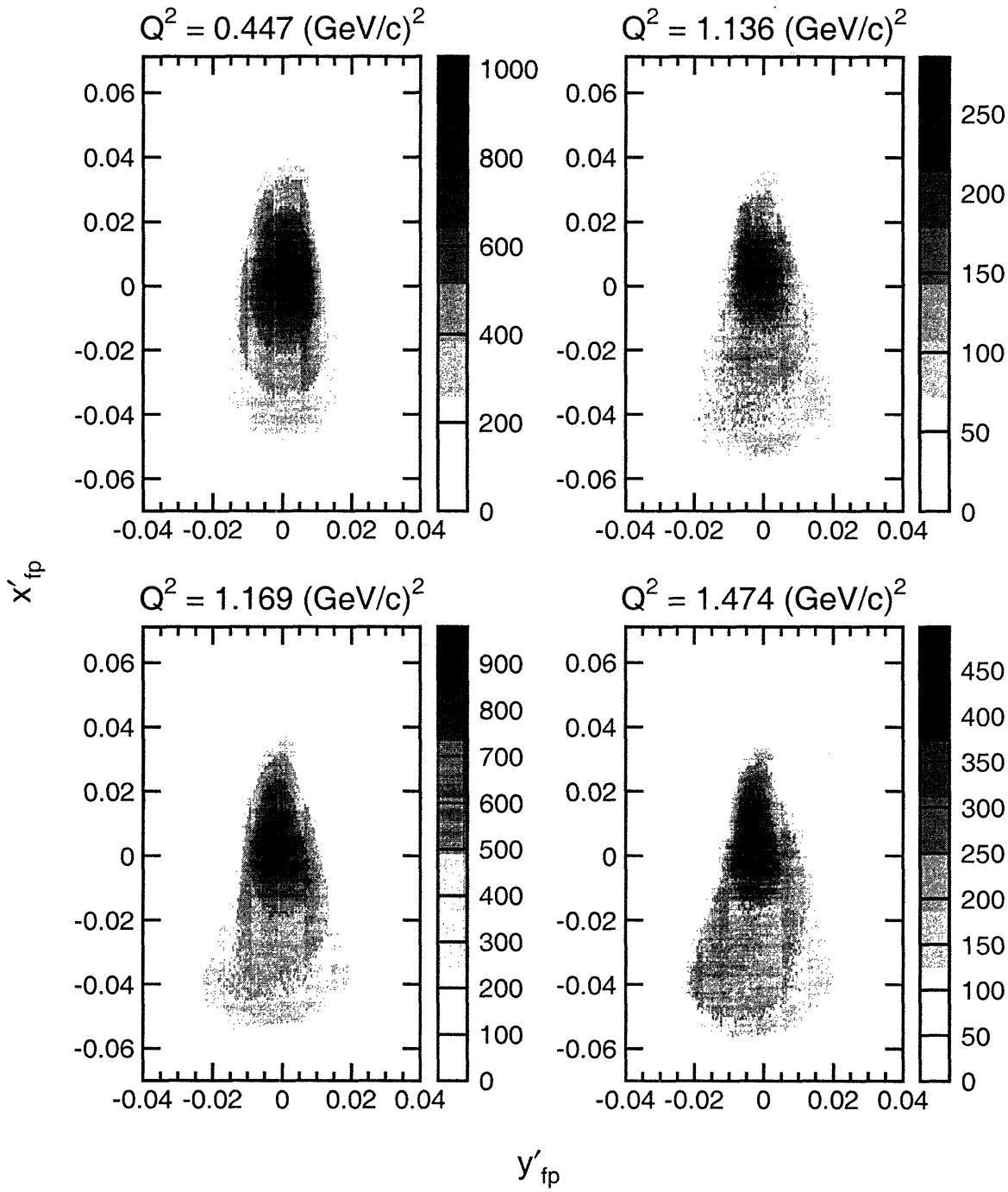

Figure 5-10: (color) $x'_{\rm fp}$ versus $y'_{\rm fp}$ distributions without cuts.

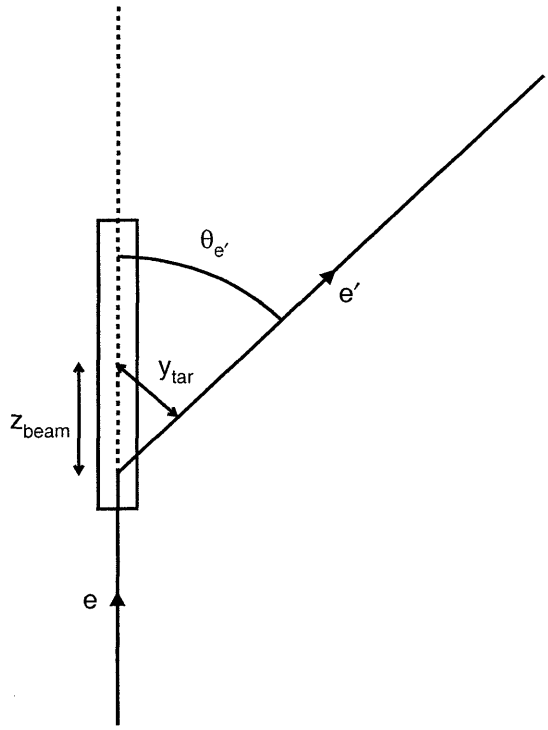

Figure 5-11: A schematic diagram of the target variables $y_{\rm tar}$ and $z_{\rm beam}$.

Target and Collimator Distributions

As previously discussed, $x_{\rm tar}$ was reconstructed to $x_{\rm tar} = 0$ for all events. Although $y_{\rm tar}$ was reconstructed for each event, a more useful quantity is a non-TRANSPORT variable we shall henceforth refer to as "$z_{\rm beam}$". This variable, defined to be

$$z_{\rm beam} = \frac{y_{\rm tar}}{\sin\theta_{e'}} \ , \tag{5.10}$$

represents the location of the reconstructed vertex along the long axis of the target ($z_{\rm beam} = 0$ at the center of the target); a schematic diagram of $y_{\rm tar}$ and $z_{\rm beam}$ is shown in Fig. 5-11. Histograms of $z_{\rm beam}$ distributions for the four Q^2 points are shown in Fig. 5-12; here, we see that a non-negligible number of events were reconstructed to positions outside of the physical dimensions of the target.

Again, for completeness, we show two-dimensional histograms of $x'_{\rm tar}$ versus $y'_{\rm tar}$ distributions in Fig. 5-13. Finally, in Fig. 5-14, we present two-dimensional histograms of the x versus y distributions at the collimator; these were calculated from the

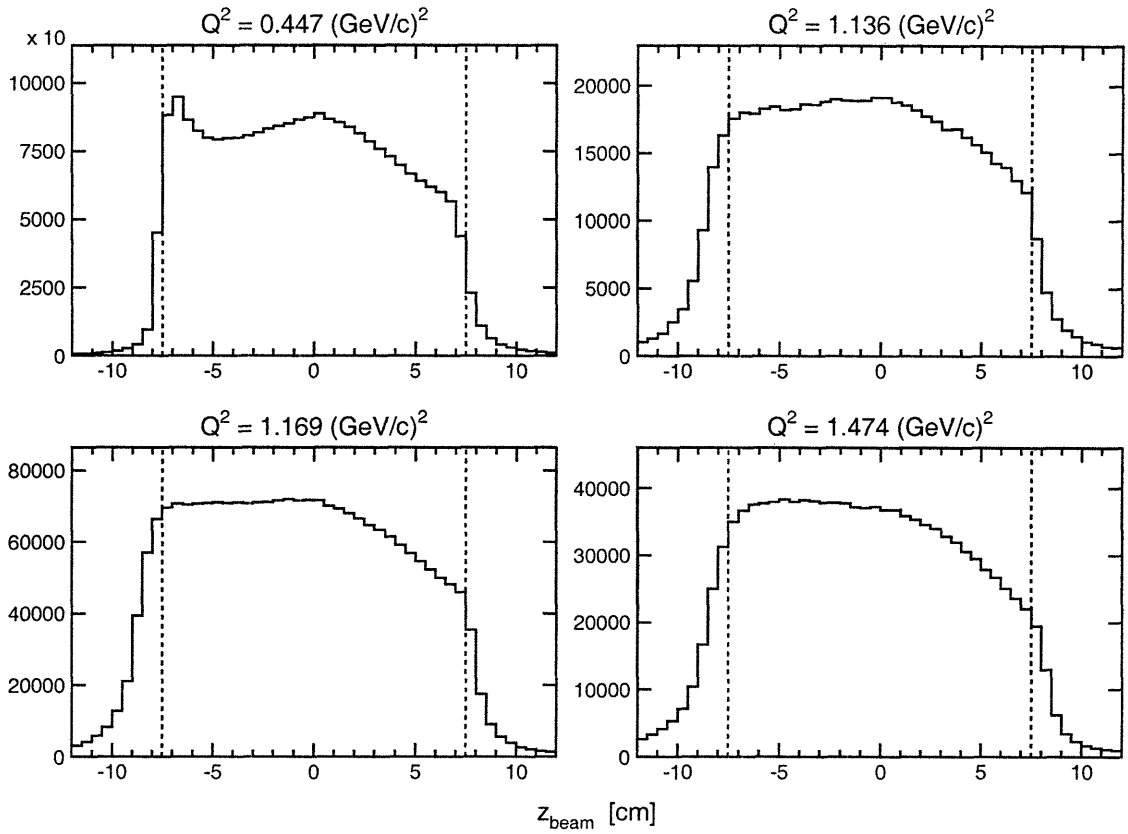

Figure 5-12: $z_{\rm beam}$ distributions without cuts. The dashed lines represent the physical edges of the 15-cm target.

reconstructed target quantities according to

$$x_{\rm coll} = x_{\rm tar} + x'_{\rm tar}\ d\ , \tag{5.11}$$

$$y_{\rm coll} = y_{\rm tar} + y'_{\rm tar}\ d\ , \tag{5.12}$$

where $d = 166$ cm denotes the distance from the target to the pion collimator exit (see the discussion in Section 3.4.1).

Electron-Hadron Separation and Track Diagnostics

We conclude our presentation of sample HMS reconstruction and tracking results by presenting in Figs. 5-15 and 5-16 histograms of the HMS Čerenkov photoelectron distribution and the ratio of the calorimeter energy to the measured momentum,

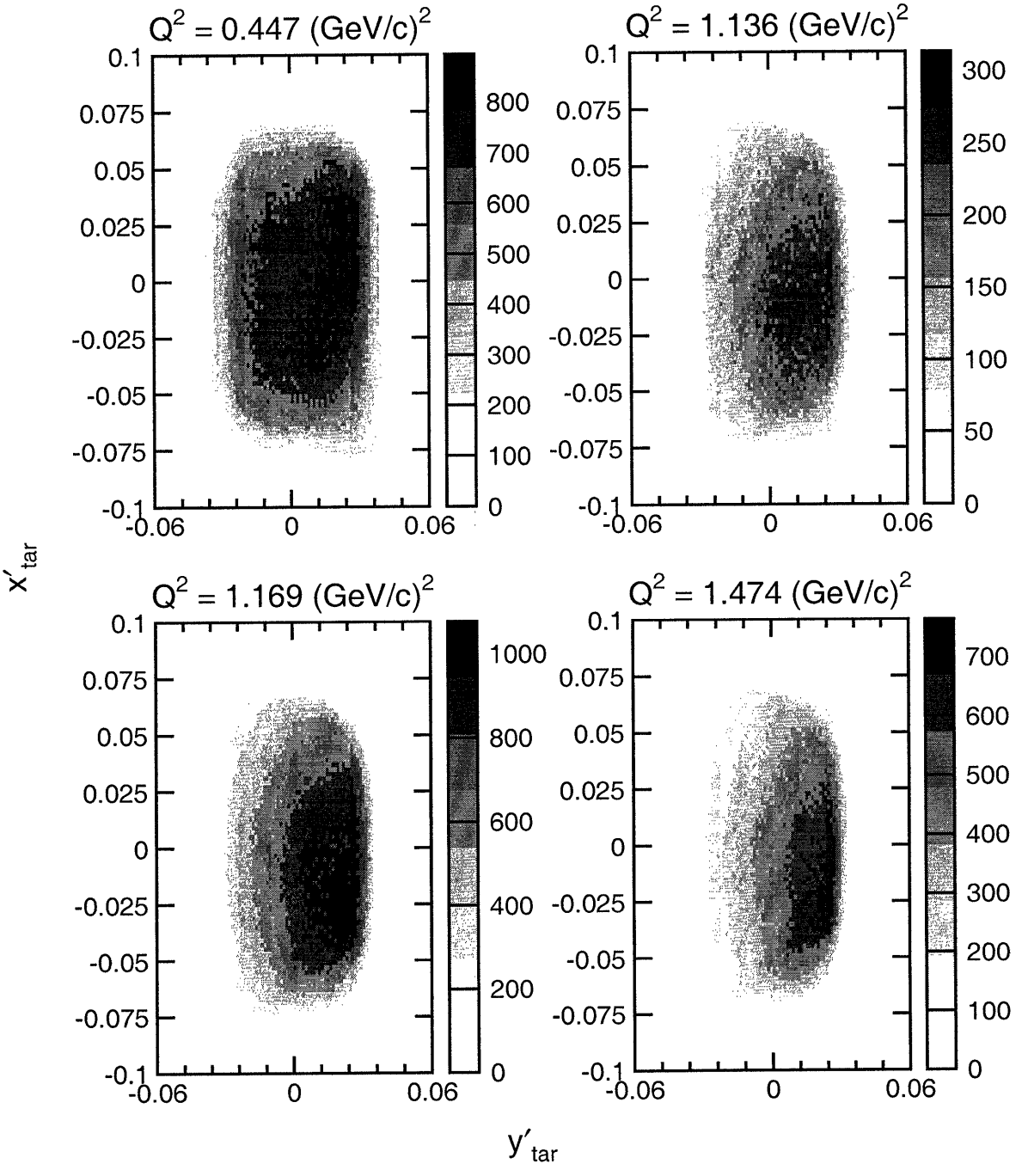

Figure 5-13: (color) $x'_{\rm tar}$ versus $y'_{\rm tar}$ distributions without cuts.

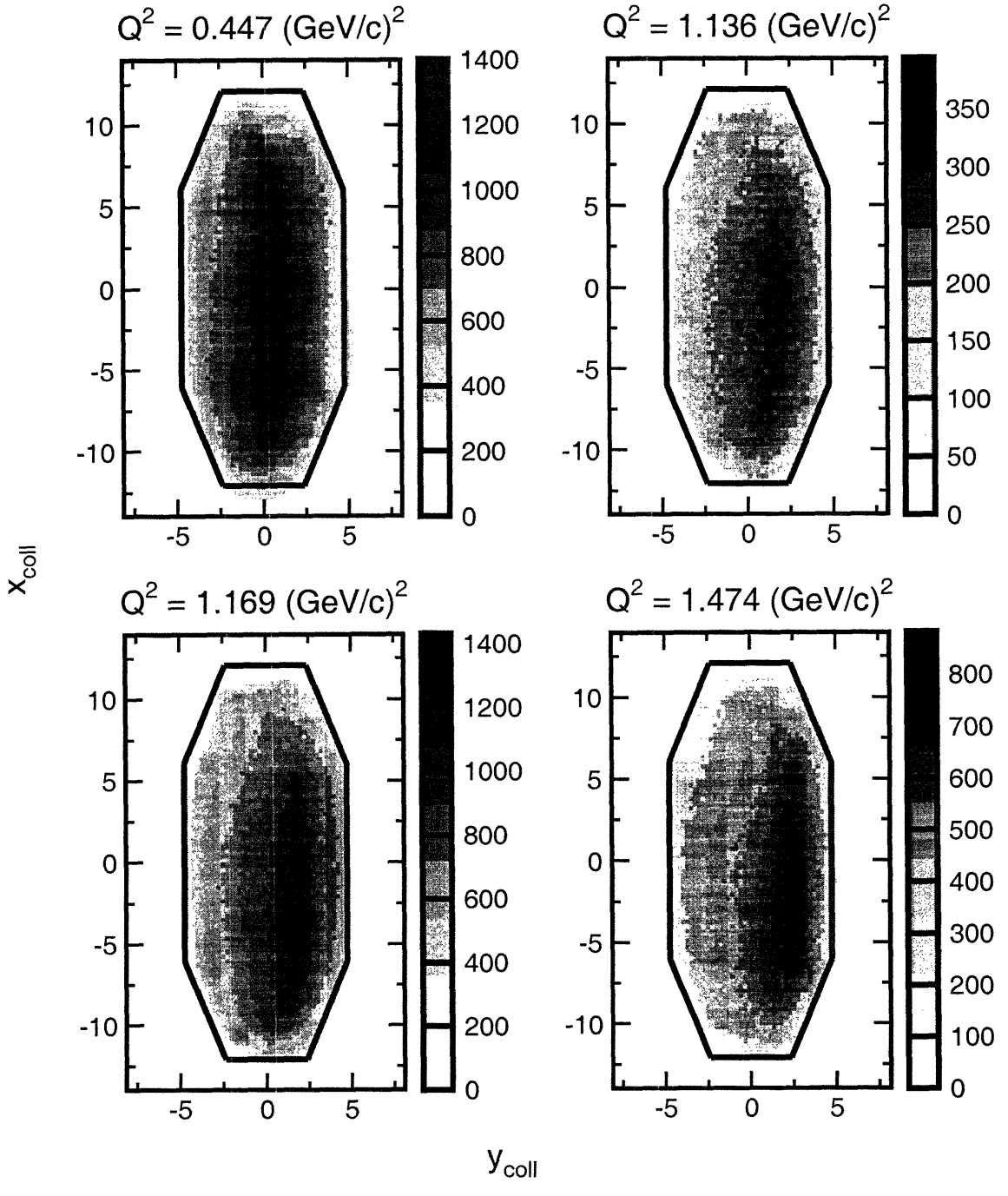

Figure 5-14: (color) $x_{\rm coll}$ versus $y_{\rm coll}$ distributions at the HMS collimator exit without cuts. The solid lines indicate the physical dimensions of the octogonal collimator.

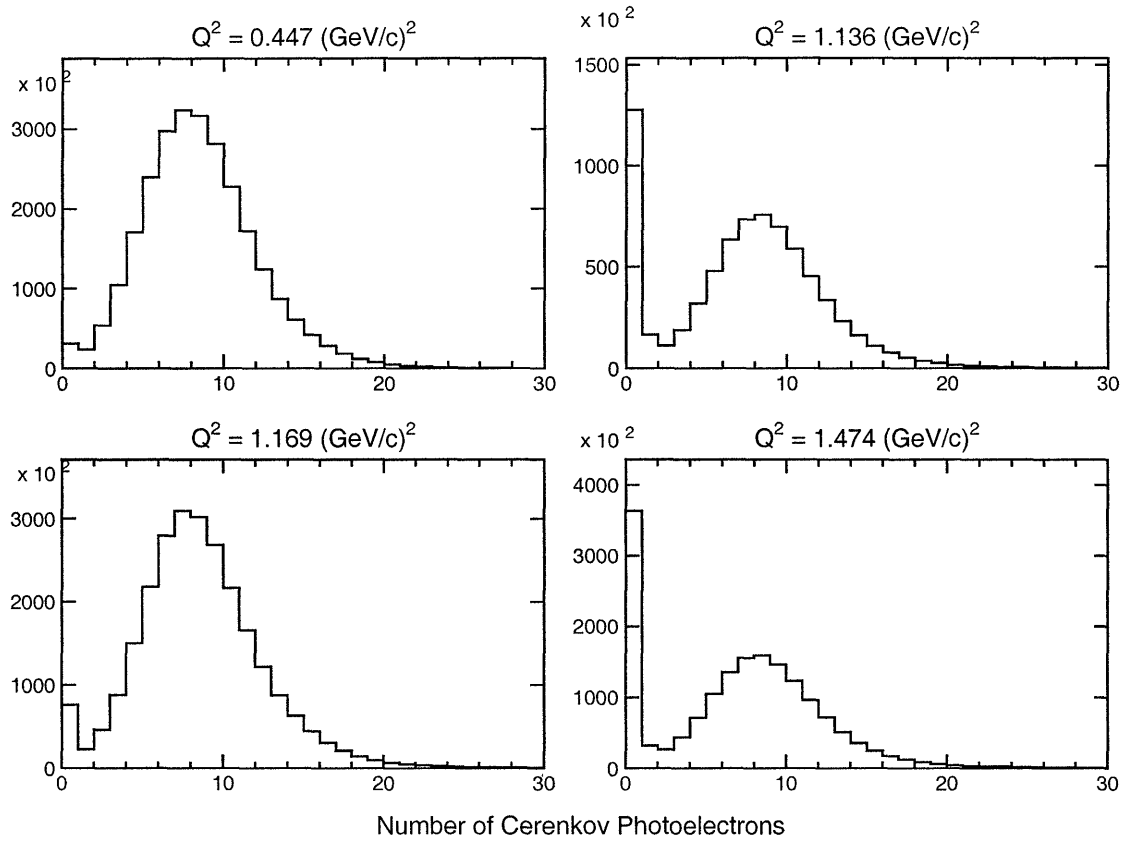

Figure 5-15: HMS Čerenkov photoelectron distributions without cuts.

respectively. In the Čerenkov photoelectron distribution, we see a hadron peak at 0 in the $Q^2 = 1.136$, 1.169, and 1.474 $(\mathrm{GeV}/c)^2$ spectra; similarly, in the histograms of the ratio of the energy deposition in the calorimeter to the measured momentum, we see hadron peaks at 0. Finally, we show in Fig. 5-17 χ^2 distributions for the reconstructed tracks through the HMS drift chambers. The majority of the events are clustered near small values of χ^2; however, long tails extending to large values of χ^2 are visible.

5.2 Neutron Polarimeter Pulse Height Calibrations

In this section, we provide a detailed description of the procedures that were employed for the pulse height calibrations of the NPOL detectors.

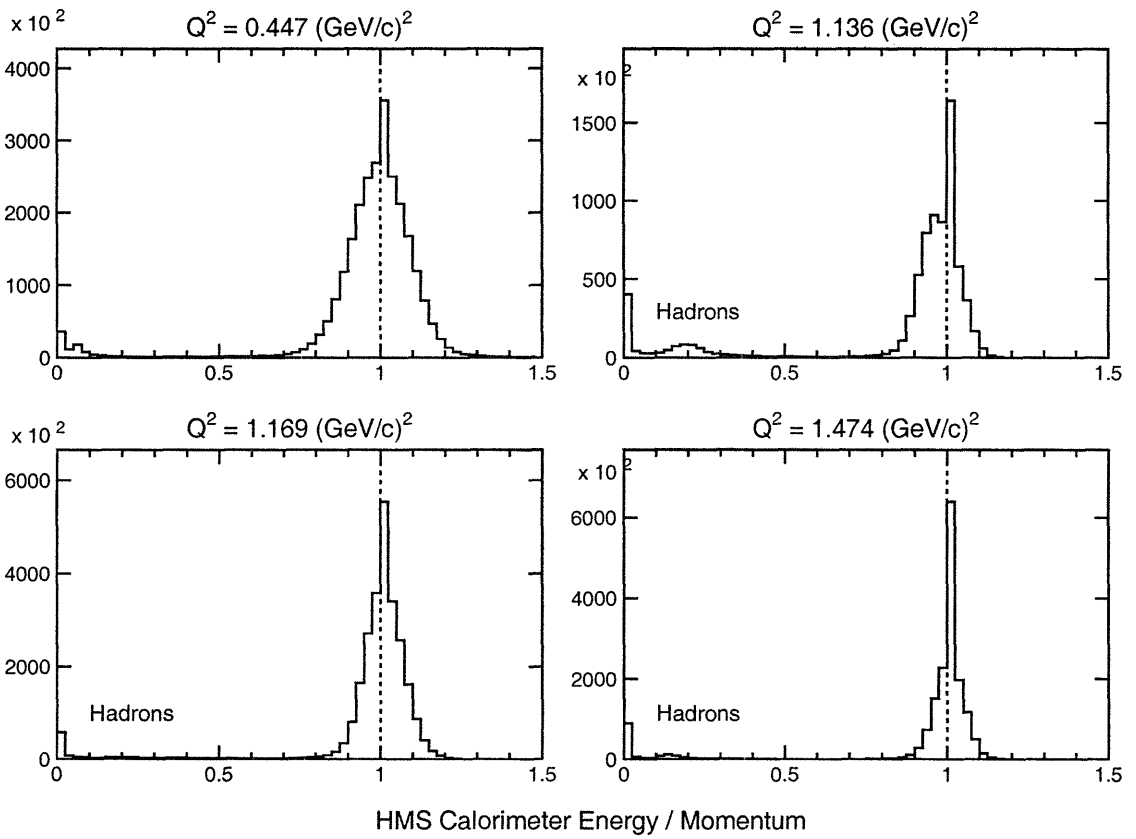

Figure 5-16: Distributions of the ratio of the energy deposition in the calorimeter to the measured momentum without cuts.

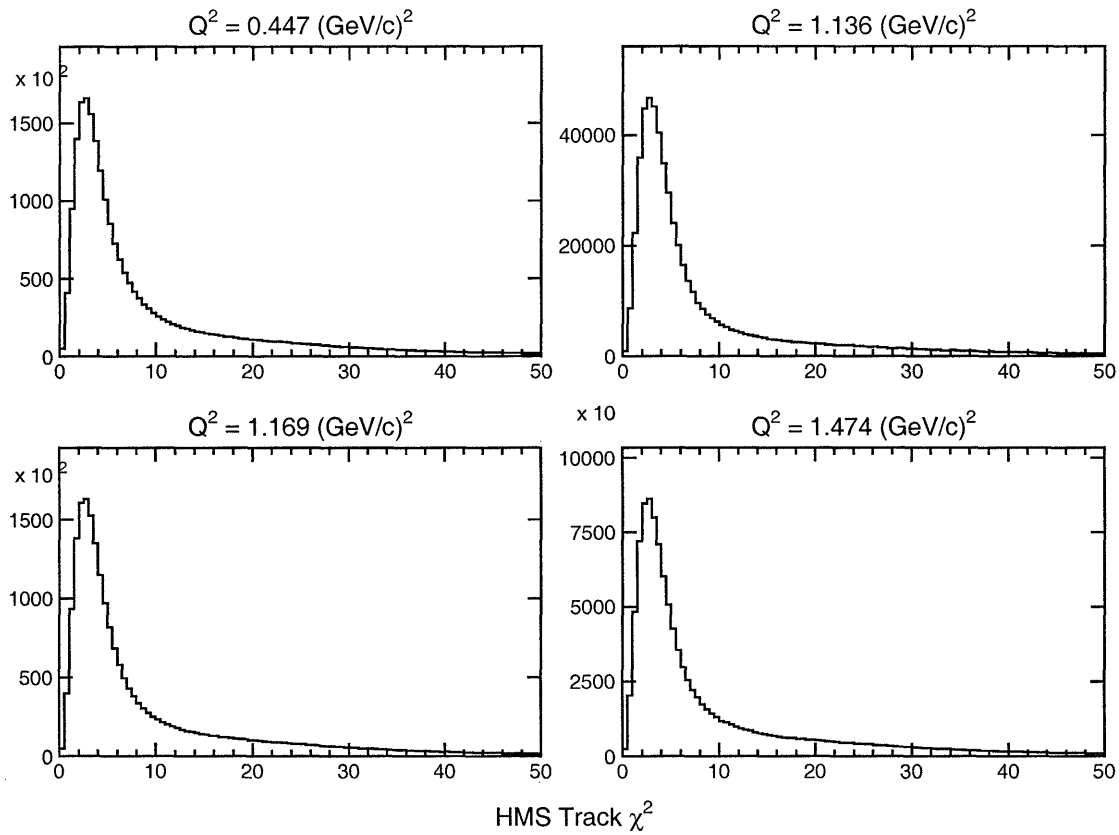

Figure 5-17: χ^2 distributions for the reconstructed tracks through the HMS drift chambers without cuts.

5.2.1 Overview

The ADCs for the pulse height signals from the NPOL PMTs were charge sensitive ADCs (i.e., sensitive to the total integrated current) with a full range of 4096 channels. The total charge integrated by the ADCs was assigned a channel number; this channel number can be converted into energy units if the appropriate channel-to-energy conversion factor is known and assumed to hold over the full operating range of the ADC. In what follows below, we outline the procedure for the pulse height/energy calibration of the NPOL ADCs, and we present some sample results.

5.2.2 Method

The pulse height calibration of an ADC requires, in general, at least two peaks of known energy deposition (see, e.g., [334, 372]); for example, an ADC may be energy

calibrated if the response of the ADC to a source of known energy deposition is measured and the pedestal is well known. Such a calibration with only two data points assumes the ADC is linear over its entire operating range. As discussed previously, the ADC modules that were used for the NPOL detectors were designed to be highly linear over a large operating range.

The source of known energy deposition that was employed for the energy calibration of the NPOL detectors was the Compton spectra for 2.61 MeV gamma rays from a ^{228}Th source. As described in detail by Madey *et al.* [404], the light output/pulse height of an organic scintillator is a linear function of the energy deposited by an *electron* at energies greater than ~100 keV; however, as the light output of an organic scintillator for a more heavy-ionizing particle (e.g., a proton) is not linear in the energy deposition, it is customary to state the response of a scintillator to a charged particle in terms of an *equivalent electron energy*, denoted "eVee".[3] In a series of measurements at the Ohio University Tandem Van de Graaff accelerator with monoenergetic neutrons, Madey *et al.* [404] found that the relation between the light output of recoil protons in organic scintillator material to that of Compton scattered electrons from various gamma ray sources could be described well by

$$T_e = a_1 \left[1 - \exp(-a_2 T_p^{a_3})\right] + a_4 T_p \ , \tag{5.13}$$

where T_p is the energy deposition of the recoil proton in MeV, T_e is the electron energy in MeV that yields the same light output (i.e., the equivalent electron energy), and the a_i are empirically determined parameters. For NE-102, it was found that $a_1 = -8.0$, $a_2 = 0.10$, $a_3 = 0.90$, and $a_4 = 0.95$.

As can easily be shown using four-momentum conservation, the energy of a Compton scattered electron, T_e, is

$$T_e = h\nu \frac{\gamma(1 - \cos\theta)}{1 + \gamma(1 - \cos\theta)} \ , \tag{5.14}$$

[3]The electron energy equivalent to a charged particle is defined to be the electron energy that induces the same light output/pulse height as the charged particle.

where $h\nu$ is the energy of the incident photon (i.e., 2.61 MeV for the ^{228}Th source), θ is the photon scattering angle, and $\gamma \equiv h\nu/m_e c^2$. It is straightforward to show that T_e attains its maximum value of

$$(T_e)_{\max} = h\nu \left(\frac{2\gamma}{1+2\gamma} \right) \tag{5.15}$$

for $\theta = \pi$ (i.e., backscattering of the photon); for $h\nu = 2.61$ MeV, $(T_e)_{\max} = 2.38$ MeV. The cross section (differential in the scattered photon's solid angle) for Compton scattering, first calculated in QED by Klein and Nishina [405], is (to lowest order)

$$\frac{\mathrm{d}\sigma}{\mathrm{d}\Omega} = \frac{\alpha^2}{2m_e^2} \frac{1}{[1+\gamma(1-\cos\theta)]^2} \left[1 + \cos^2\theta + \frac{\gamma^2(1-\cos\theta)^2}{1+\gamma(1-\cos\theta)} \right] . \tag{5.16}$$

As shown by Leo [357], the above expression for the cross section can be rewritten such that it is differential in the Compton electron energy as

$$\frac{\mathrm{d}\sigma}{\mathrm{d}T_e} = \frac{\pi\alpha^2}{m_e^3\gamma^2} \left[2 + \frac{s^2}{\gamma^2(1-s)^2} + \frac{s}{1-s} \left(s - \frac{2}{\gamma} \right) \right] , \tag{5.17}$$

where $s = T_e/h\nu$. The distributions of Compton electron energies for a number of different values of $h\nu$ are plotted in Fig. 5-18; there, for each value of $h\nu$, the *Compton edge* is clearly visible at $(T_e)_{\max}$.

Unfortunately, as we now show, the range of available Compton electron energies for the ^{228}Th source ($T_e < 2.38$ MeV) is too restricted for the range of recoil proton deposition energies associated with the E93-038 kinematics. As shown in Table 3.1, the central quasielastic neutron kinetic energies for the $Q^2 = 0.447$, 1.136, 1.169, and 1.474 $(\mathrm{GeV}/c)^2$ data points were $T_n = 239$, 606, 624, and 786 MeV, respectively. Assuming elastic np scattering in the front array of the polarimeter, it can easily be shown that the kinetic energy of the scattered neutron, denoted T_{np}, is

$$T_{np} = \frac{2T_n\cos^2\theta}{(\gamma_n+1) - (\gamma_n-1)\cos^2\theta} , \tag{5.18}$$

where T_n denotes the incident neutron kinetic energy, θ is the neutron scattering

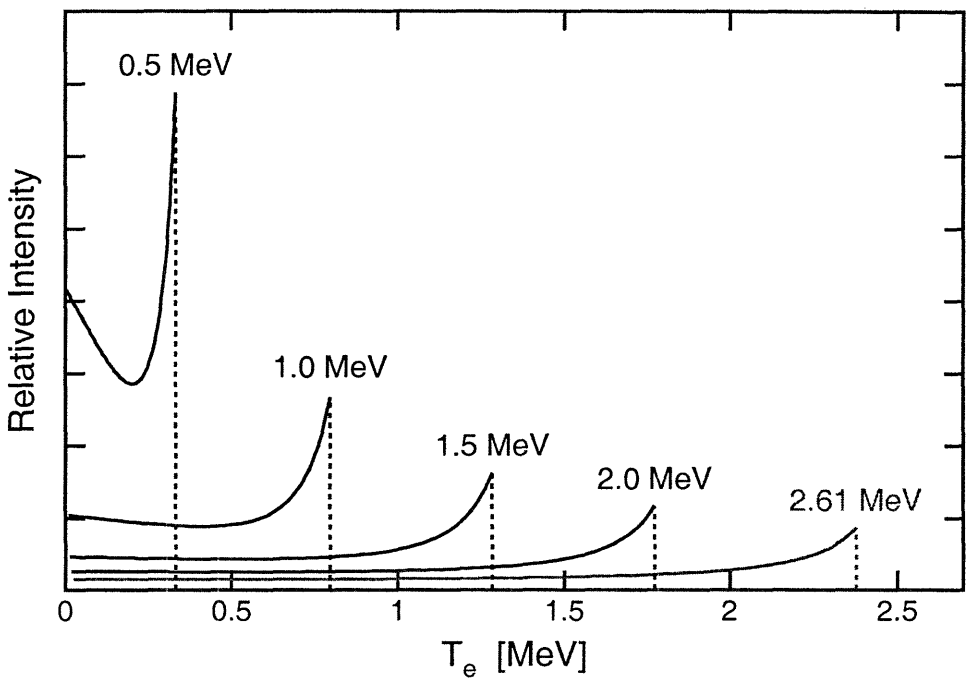

Figure 5-18: Energy distribution of Compton scattered electron energies for various values of $h\nu$. The Compton edge for each energy is shown as the dashed line. The units of the ordinate are arbitrary.

angle, and $\gamma_n = 1 + T_n/m_n$ is the usual Lorentz factor for the incident neutron. In order to obtain a rough "back of the envelope" estimation of the energy deposition by the recoil proton in the scintillators, we will assume a neutron scattering angle of 18° (as will be shown later, the distributions of scattering angles for neutron scattered from the front array into the rear array of the polarimeter peak around ~18°). For this choice of scattering angle, T_{np} = 214, 532, 547, and 672 MeV, from which it follows that T_p, the kinetic energy of the recoil protons, is 25, 74, 77, and 114 MeV, respectively, at Q^2 = 0.447, 1.136, 1.169, and 1.474 (GeV/c)^2. Next, using Cecil, Anderson, and Madey's [406] empirical formulas for the range-energy curves for recoil protons in plastic scintillators,

$$\begin{aligned} \log R(T) &= -3.8103 + 1.6171 \log T + 0.08193 \log^2 T - 0.020364 \log^3 T \\ &\quad + 0.003147 \log^4 T - 0.0002321 \log^5 T \,, \qquad (5.19) \\ \log T(R) &= 2.1964 + 0.56148 \log R + 0.0010055 \log^2 R - 0.00008885 \log^3 R \end{aligned}$$

$$- 0.0001821 \log^4 R + 0.00002742 \log^5 R \ , \tag{5.20}$$

where R denotes the range in mm and T denotes the energy in MeV, we find that $R =$ 0.62, 4.39, 4.71, and 9.49 cm for 25, 74, 77, and 114 MeV protons, respectively. Again, as a rough approximation, if we assume that the recoil protons traverse approximately 5 cm of scintillator material in the detector the *np* interaction occurred, the energy of the recoil proton after it leaves the detector, T_{exit}, will be

$$\log T_{\text{exit}} = \begin{cases} \log T(R - 5 \text{ cm}) & \text{if } R > 5 \text{ cm} \ , \\ -\infty & \text{else} \ . \end{cases} \tag{5.21}$$

From this, we see that, in our rough approximation, the 25, 74, and 77 MeV protons will be stopped in the scintillator, but the 114 MeV protons will escape the scintillator with an energy of 75.6 MeV; therefore, in this simple approximation, the energy deposition of the recoil protons in the scintillators will be ~25–77 MeV (~17–65 MeVee).

The above exercise was not intended to be rigorous; instead, the intent was to demonstrate that the ^{228}Th source by itself did not provide a sufficient range of energies for the energy calibration of the neutron detectors. Further, the $0 < T_e <$ 2.38 MeV Compton electron energies were below the 4 (10) MeVee hardware thresholds on the constant-fraction discriminators for the front (rear) array detectors in the timing logic circuit[4]; therefore, the ^{228}Th source by itself would not have triggered any NPOL singles events. In order to remedy these deficiencies, a linear amplifier, custom designed and constructed by Baldwin of Kent State University, with a gain of ten and a precision attenuator with four different settings (0.1×, 0.2×, 0.5×, and 1.0×) was placed in the timing circuit after the pulse height monitor and before the 50-ohm 50/50 resistive splitter in the shielding hut electronics circuit. With the attenuator set at 1.0×, the effective maximum calibration signal was 23.8 MeVee; although proton energy depositions in the scintillators routinely exceeded 23.8 MeVee,

[4]The hardware thresholds (and, as will be discussed later, the software thresholds) were higher for the rear array detectors than the front array detectors because the long axis for the rear array detectors was oriented parallel to the central axis of the polarimeter whereas the long axis for the front array detectors was oriented perpendicular to the central axis of the polarimeter.

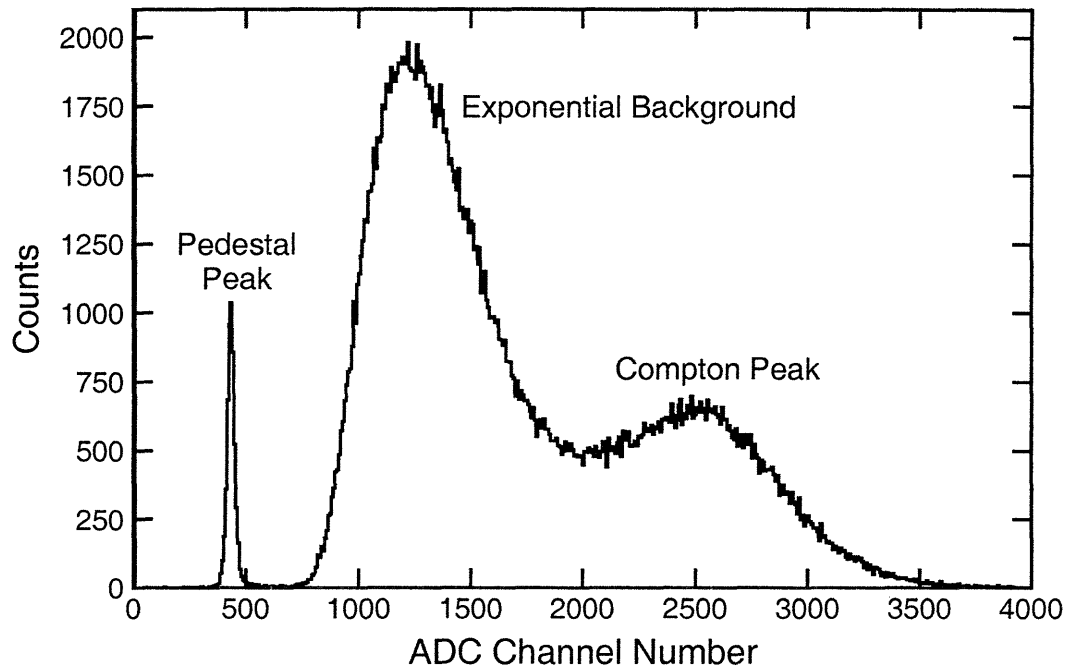

Figure 5-19: Raw ADC spectrum from the left PMT of detector #1 for pulse height calibration run #38245. The pedestal peak, exponential background, and Compton peak are clearly visible.

this calibration point (unlike the 2.38 MeVee datum) was at least of the same order of magnitude as the expected energy deposition.

With the linear amplifier in place, the procedure for the calibration of the 44 primary NPOL detectors[5] using the 2.61 MeV gamma rays from the ^{228}Th source was straightforward. The ^{228}Th source was placed at the external geometric center of each detector, and data were taken with the attenuator in the linear amplifier set at 1.0× and the DAQ configured to record NPOL singles events (this trigger setting, not discussed previously, simply required a coincidence between the timing signals from the PMTs from any one of the 44 primary detectors). The data were written to disk and later analyzed with a simpler version of the E93-038 `ENGINE`.

An example of a raw ADC spectrum taken from the pulse height calibration data set (from the left PMT of detector #1) is plotted in Fig. 5-19. There, we see that the

[5]The front and rear array detectors were energy calibrated; however, the front veto/tagger and rear veto/tagger detectors were not energy calibrated. As will be discussed later, ADC information was not used for the identification of charged particles entering/leaving the front array of the polarimeter.

theoretical sharp Compton edge is smeared by the finite resolution of the detector. Also, the pedestal is clearly visible as is a sharp decaying exponential background. In order to extract the desired quantity, the ADC channel-to-energy conversion factor, first, the value of the pedestal (in channels) was extracted from the raw ADC spectra by fitting the pedestal peak to a Gaussian. Second, the pedestal-subtracted ADC spectra were fitted to the sum of a Klein-Nishina distribution smeared by a Gaussian resolution function (i.e., the convolution of a Gaussian with the Klein-Nishina distribution) and an exponential background tail; this fitting function can be written symbolically as

$$f(x) = |P_3| \int_0^{(T_e)_{\max}} \mathrm{d}T' \exp\left[-\left(\frac{T'-t}{2\sigma}\right)^2\right] \left.\frac{\mathrm{d}\sigma}{\mathrm{d}T}\right|_{T=T'} + |P_4| \exp(P_5 t) \ , \qquad (5.22)$$

where $t = P_1(x - \text{pedestal})$, $\sigma = \frac{1}{2}P_2\sqrt{t}$, x is the (non pedestal-subtracted) ADC channel number, and the P_i are fit parameters; the desired quantity, the ADC channel-to-energy conversion factor, is P_1.

5.2.3 Data Collection and Results

Pulse height calibration data were taken with the ^{228}Th source during experimental downtime in October 2000, January 2001, and April 2001. The pedestals and ADC channel-to-energy conversion factors were extracted from the raw ADC spectra by Tireman, and a detailed report and discussion of these calibrations may be found in [407, 408]. Minor differences (i.e., $\sim$10–15% variation in the pedestal channels and the channel-to-energy conversion factors) in the results of the three calibrations were found; however, as we will see later, these differences are fairly unimportant as the selection of quasielastic ^{2}H$(e, e'n)$ events did not rely heavily on pulse height information.

5.3 Neutron Polarimeter Timing Calibrations

We continue our discussion of the neutron polarimeter calibrations in this section by providing a detailed overview of the timing calibrations of the NPOL detectors.

5.3.1 Overview

To optimize track reconstruction and background rejection in the neutron polarimeter, the relative timing relationships between the NPOL detectors and between the neutron polarimeter and the HMS were carefully calibrated with a series of algorithms designed to: (1) generate position calibrations for each detector, (2) generate relative timing calibrations for each detector in the front array, (3) discern the relationship between the trigger mean time and the mean time for each front array detector, (4) calibrate the timing between the HMS and the front array, (5) generate relative timing calibrations for each detector in the rear array and calibrate the time-of-flight between the front array and the rear array, and (6) generate position and timing calibrations for the front and rear veto/tagger detectors.

A schematic flowchart for these algorithms, collectively referred to as the NPOL time calibration program, is shown in Fig. 5-20. In what follows below, we describe each of the individual algorithms, (1)–(6), in detail, and we present examples of the calibration results; all of the sample calibration results we present are from a calibration that was performed for the central $Q^2 = 1.169$ $(\mathrm{GeV}/c)^2$ data set. A detailed description of an earlier version of the timing calibration algorithms was given by Kelly [409] (the primary author of these timing calibration algorithms); here, we provide a detailed overview of the version that was employed for the final production analysis.

5.3.2 Input

The NPOL time calibration program began by reading a number of different `ASCII` input files; these included an input file containing a user-specified list of run numbers to be used by each step, (1)–(6), of the timing calibration algorithms, an input file

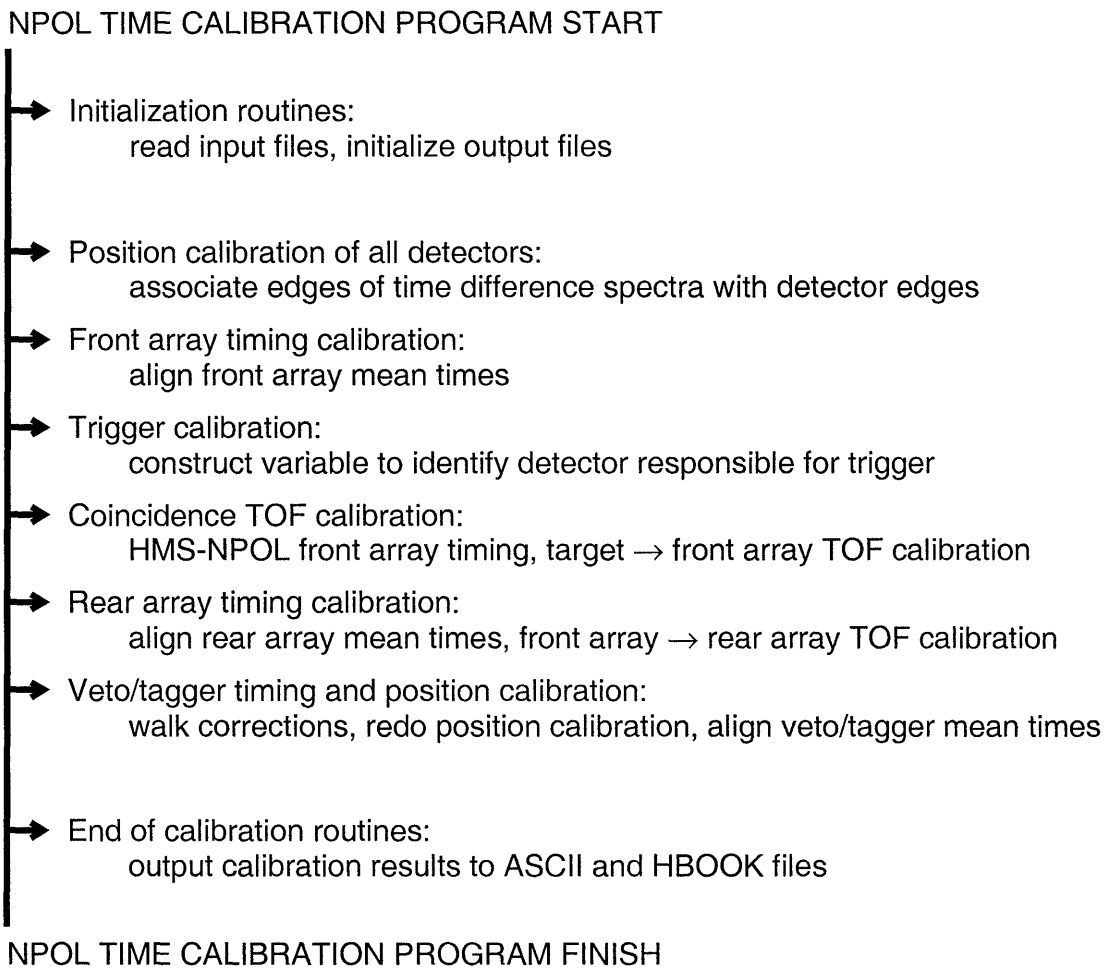

Figure 5-20: A schematic flowchart for the NPOL timing calibration program.

containing the NPOL detector geometry, and an input file containing a minimal listing of event selection criteria for use by the calibration algorithms. Next, an `ASCII` output file for the calibration results and an `HBOOK` file for histograms of the calibration results were initialized.

It should be noted that the NPOL time calibration program processed the event-by-event NPOL data stored in the `.rzdat` files.

5.3.3 Position Calibration

The difference between the TDC signals from the left (L) and right (R) PMTs[6] was used to determine the hit position along the long axis of the scintillator; here, and throughout our description of the calibration algorithms, we will label the long axis of the scintillator as the x-axis. Assuming this relationship is linear, the hit position along the long axis of detector id, xd(id), where id $\in \{1, 2, \ldots, 70\}$, can be written as

$$\texttt{xd(id)} = \texttt{x\_slope(id)}\,[\texttt{TDCR(id)} - \texttt{TDCL(id)}] + \texttt{x\_offset(id)}\ , \tag{5.23}$$

where TDCR(id) and TDCL(id) denote, respectively, the TDC signals (in channels) from the right and left PMTs. The sign convention for xd is such that xd > 0 (xd < 0) is associated with the left (right) halves of the front array detectors, the left (right) halves of the front and rear veto/tagger detectors, and the front (rear) halves of the rear array detectors. The position slope parameter for each detector, x_slope, is related to the velocity and pathlength of the light in the scintillator, and the position offset for each detector, x_offset, is related to delays in the PMTs, cables, and electronics.

In general, the position calibration algorithm was performed with data acquired when the Charybdis magnet was off; this guaranteed that charged particles illuminated the front array and the front and rear veto/tagger arrays as uniformly as possible. Histograms of [TDCR(id) − TDCL(id)] for Type 3 events (i.e., HMS-NPOL coincidences) were constructed for each detector recording a hit. After these histograms were filled, the histograms were boxcar-smoothed over ± 2 channels.[7] Following the

[6]For the front array, front veto/tagger array, and rear veto/tagger array detectors, the direction "left" is defined to be that observed by a person facing the polarimeter with her back to the target. For the rear array detectors, the front (closest to the target) and rear (farthest from the target) PMTs correspond to left and right PMTs, respectively.

[7]Boxcar-smoothing is defined as follows. Suppose an unsmoothed histogram consisting of N channels, labeled $i = 1, 2, \ldots, N$, each with content $C_{\rm un}(i)$, is to be boxcar-smoothed over $\pm n$ channels. The resulting boxcar-smoothed histogram consists of $N + 2n$ channels, labeled $j = 1 - n, \ldots, N + n$, with the content of channel j, $C_{\rm sm}(j)$, defined to be

$$C_{\rm sm}(j) = \frac{1}{2n+1} \sum_{i=j-n}^{j+n} C_{\rm un}(i)\ . \tag{5.24}$$

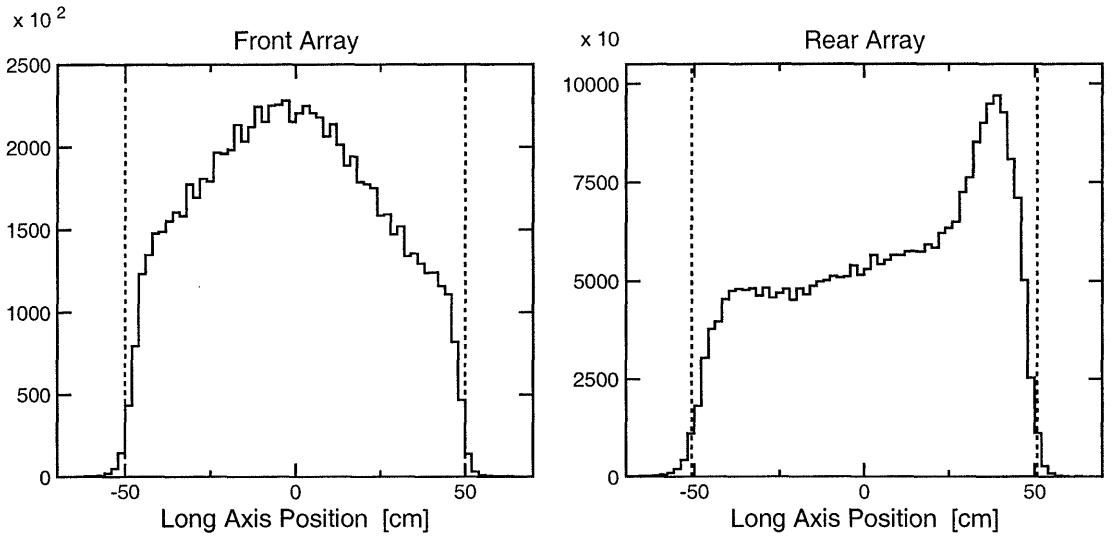

Figure 5-21: Summed calibrated position spectra for the front array and rear array detectors. The dashed lines represent the physical edges of the detectors.

boxcar-smoothing, the algorithm identified the channel with the maximum content, and the edges were identified by scanning away from the maximum content channel in both directions until channels were found with a content 10% that of the maximum content channel. Finally, the slope and offset parameters, `x_slope` and `x_offset`, were chosen such that edges of the `xd` spectra were aligned with the physical edges of the detectors.

This algorithm was employed for the position calibration of all 70 NPOL detectors; however, the position calibration of the front and rear veto/tagger detectors was revised in a later step because the collimator limited the illumination of some of the detectors in the front veto/tagger array and the outer detectors in the rear veto/tagger array (i.e., detectors 55, 62, 63, and 70; see Table B.2) were not well illuminated by front-to-rear charged particle tracks. Accordingly, we defer our discussion of the results from the front and rear veto/tagger array position calibration until after we have discussed the veto/tagger-specific calibration algorithm in detail.

Position spectra summed over all detectors in the front and rear arrays are shown in the left and right panels, respectively, of Fig. 5-21. Here, we see that the position spectra display sharp edges near the physical edges of the detectors due to the good

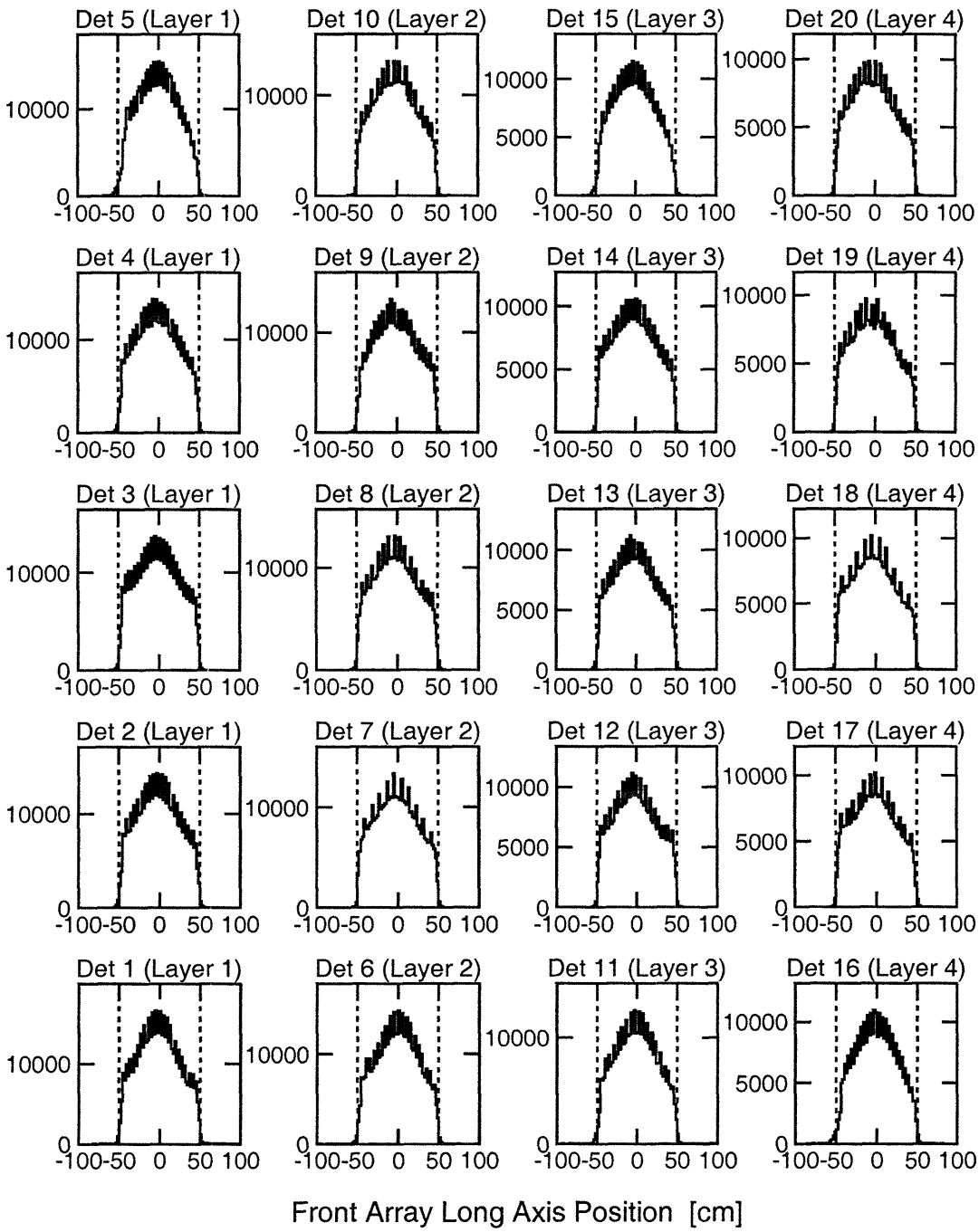

Figure 5-22: Calibrated position spectra for the front array detectors. The dashed lines represent the physical edges of the detectors.

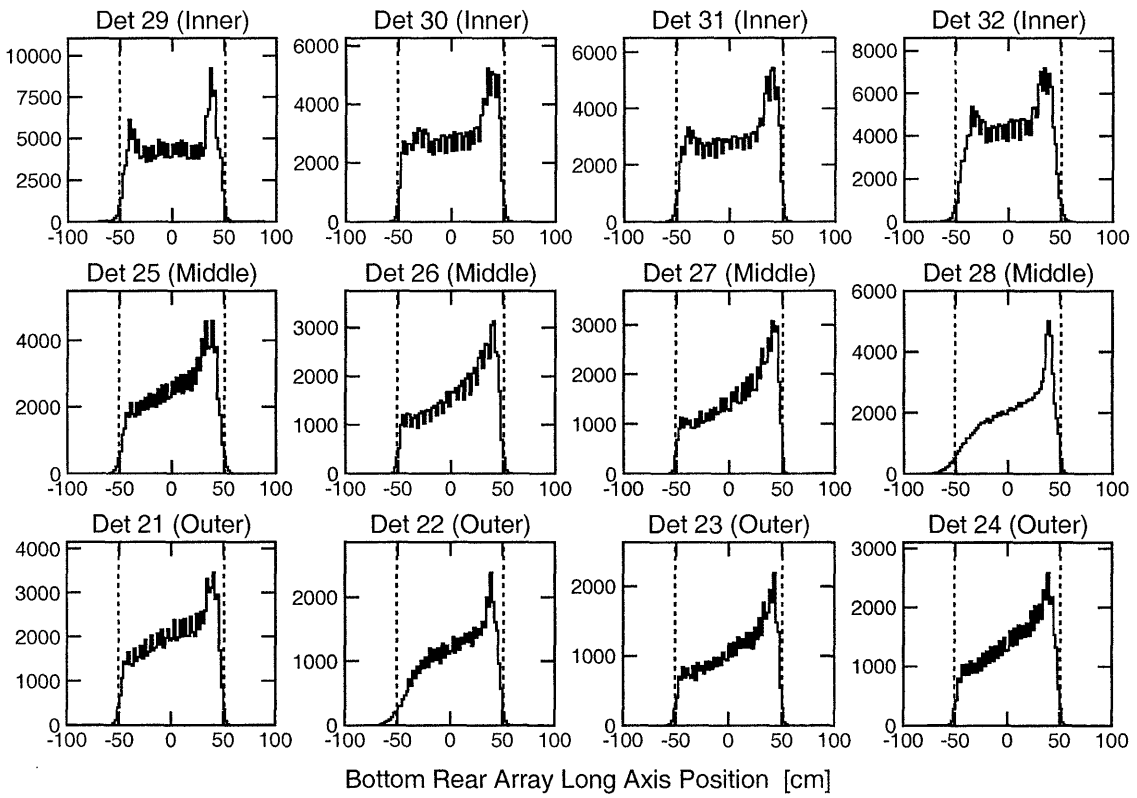

Figure 5-23: Calibrated position spectra for the bottom rear array detectors. The dashed lines represent the physical edges of the detectors.

time resolution afforded by the constant-fraction discriminators; the sharp peak at the positive edge of the rear array is due primarily to protons scattering from the front array to the rear array.

In more detail, position spectra for each detector in the front array, the bottom rear array, and the top rear array are shown in Figs. 5-22, 5-23, and 5-24 respectively; the nonstatistical fluctuations in these spectra are an artifact of the histogram binning and should be disregarded. Each of the individual position spectra for the front array detectors are well aligned and display good uniformity. On the other hand, the spectra for some of the rear array detectors are not as sharp as the position spectra for the front array detectors.

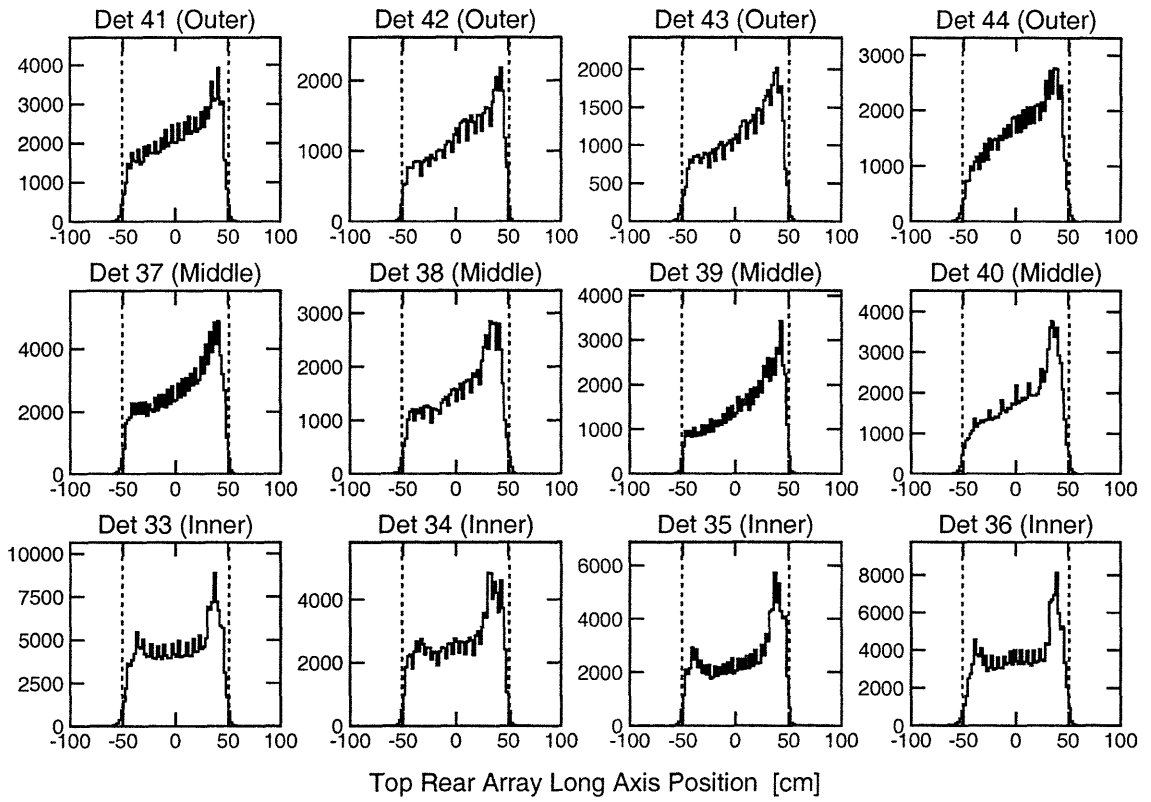

Figure 5-24: Calibrated position spectra for the top rear array detectors. The dashed lines represent the physical edges of the detectors.

5.3.4 Front Array Timing Calibration

Similar to the definition of the hit position in terms of the difference between the TDC signals from the left and right PMTs, the mean time for the hit in detector `id`, `td(id)`, relative to the NPOL trigger, can be written as

$$\texttt{td(id)} = \texttt{t\_slope(id)}[\texttt{TDCR(id)} + \texttt{TDCR(id)}]/2 + \texttt{t\_offset(id)} \ , \qquad (5.25)$$

where `t_slope`, the TDC slope parameter, was 0.05 ns/channel for each detector and `t_offset` is an offset parameter.

The goal of the front array timing calibration was to align the mean times for all the detectors in the front array. For this step of the calibration, the algorithm selected Type 3 events with a single hit in the front array and no hits in any of the front veto/tagger array detectors. Also, this step of the calibration was conducted

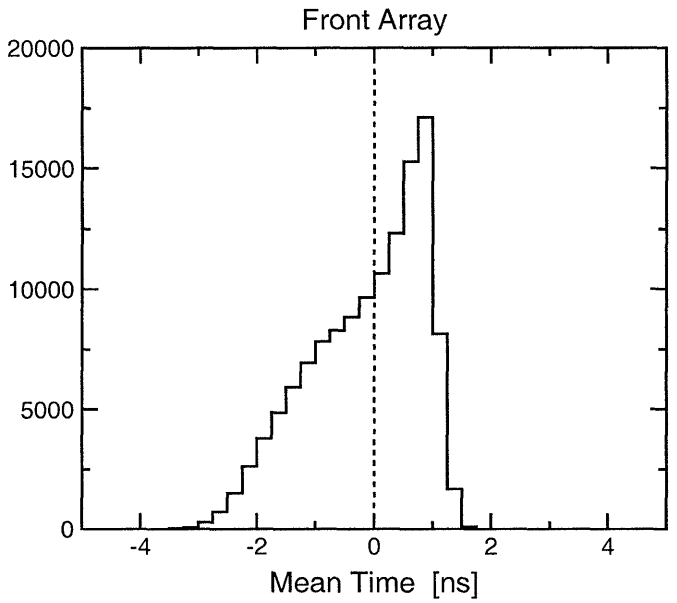

Figure 5-25: Summed calibrated mean time spectrum for the front array detectors.

with data acquired with the Charybdis magnet on (to ensure the data were as clean and free from background processes as possible). Histograms of the mean times with a 0.25 ns bin size were constructed for each detector in the front array. The algorithm identified the channel of maximum content and then computed the mean value of `td` using only the data from channels within a ± 5 ns interval surrounding the channel of maximum content. The offset parameter, `t_offset`, was then chosen for each detector such that the mean value of `td` for that detector within the ± 5 ns interval was aligned on zero.

A mean time spectrum summed over all detectors in the front array is shown in Fig. 5-25, and individual mean time spectra for each detector in the front array are shown in Fig. 5-26. The origin of the asymmetric feature on the right side will become apparent very shortly when we discuss the trigger calibration.

5.3.5 Trigger Calibration

The trigger circuit did not identify which hit in the front array generated the common TDC start when more than one detector in the front array recorded a hit; therefore,

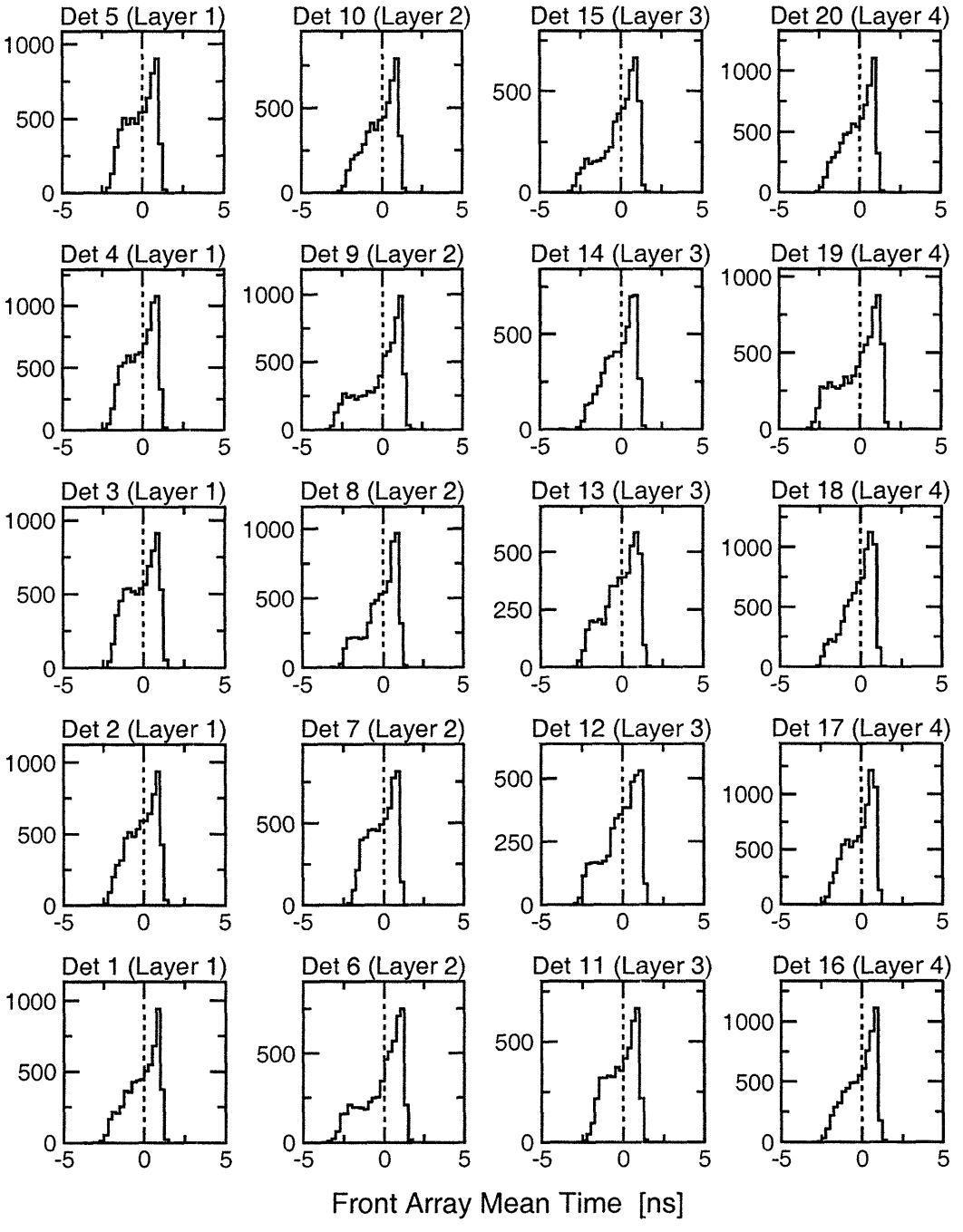

Figure 5-26: Calibrated mean time spectra for the front array detectors.

the trigger calibration algorithm was designed to construct a variable which could be used to identify the hit that generated the trigger. For this step of the calibration, the algorithm employed Type 3 events with a single hit in the front array (so as to correctly identify the detector in the front array that generated the trigger) and no hits in the front veto/tagger array detectors. Again, this step of the calibration employed data acquired with the Charybdis magnet on.

Scatter plots of TDCL versus TDCR for each detector in the front array are presented in Fig. 5-27; here, we see that these scatter plots consist of horizontal and vertical bands connected by a curved transition region. When the timing signal from the left PMT arrived at the trigger module first, the TDCL channel number was determined by the delay between the TDC start and its own timing signal; therefore, for each detector, the horizontal band represents the TDCL self-timing peak for events in which the signal from that particular left PMT generated the trigger (as this step of the calibration only selected events with a single hit in the front array). Similarly, the vertical band represents the TDCR self-timing peak for events in which the signal from the right PMT generated the trigger.

Ideally, if the delays within the left and right PMTs and their respective cables to the trigger module were perfectly equal, the horizontal and vertical bands for a particular detector would be the same length, and the transition region would correspond to the physical center of the detector; however, as is evident in Fig. 5-27, the horizontal and vertical bands for a particular detector are not, in general, of the same length. The differences in the lengths are most likely attributable to differences in the performance or the voltage applied to the left and right PMTs for each detector. Also, in the ideal case, the transition region would form a sharp 90° angle. The curvature that is seen in the transition region for each detector is most likely the result of variations in the effective signal velocity within the detectors due to reflections or may be the result of a correlation between time and pulse height (i.e.,

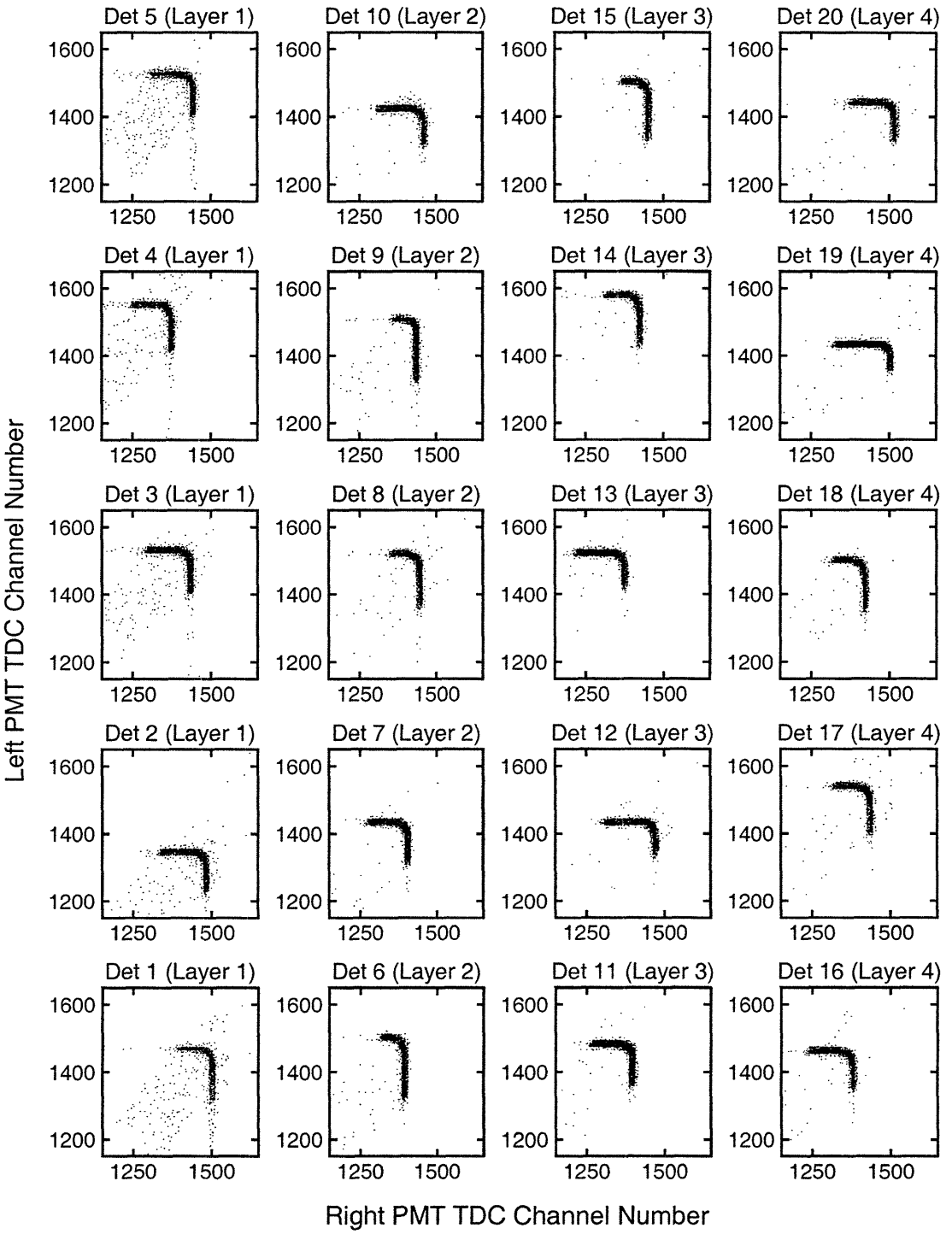

Figure 5-27: Correlation between the left and right PMT TDC values for the front array detectors.

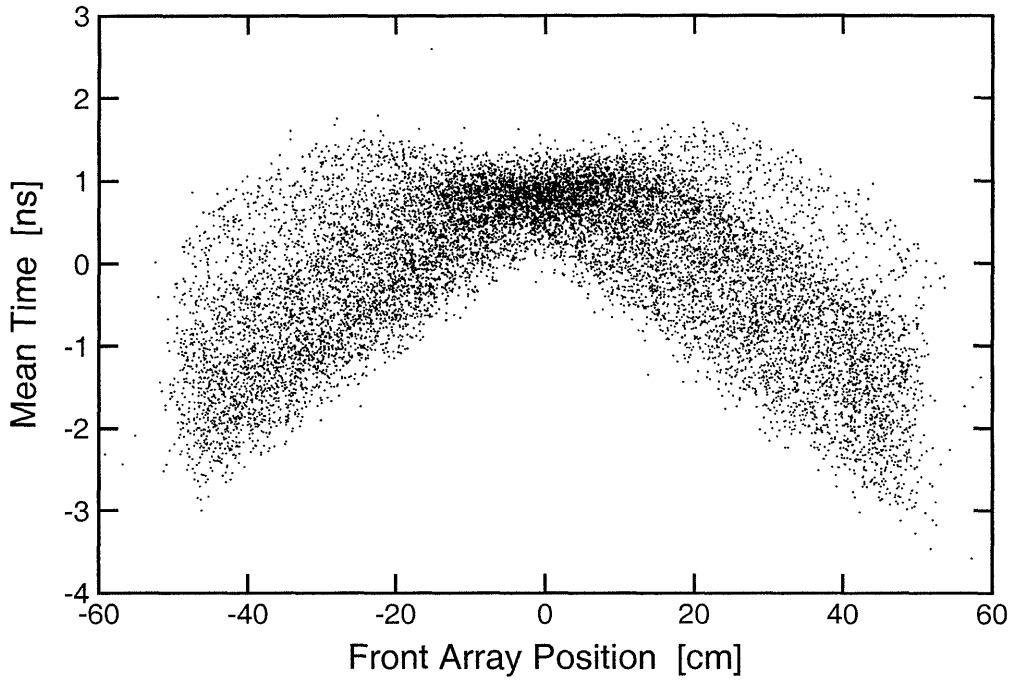

Figure 5-28: Correlation between td and xd for the front array detectors.

walk[8]).

Instead of analyzing the exact correlations between the raw TDCL and TDCR channels, the algorithm examined the position dependence of the mean times for each detector via a comparison of td with xd. Ideally, a scatter plot of td versus xd would be perfectly triangular in shape with a sharp vertex at xd = 0 (i.e., at the center of the detector)[9]; however, as shown in Fig. 5-28, this vertex is rounded as a result of the curvature in the transition region in the TDCL versus TDCR scatter plot. Also, we see that a disproportionately large number of events are clustered near xd = 0; this is expected as attenuation in the scintillators favors events with hits near the center of

[8]In general, there are, potentially, two different sources of walk [357]. First, in leading-edge discrimination (employed for the front and rear veto/tagger detectors), coincident signals of different amplitudes will trigger a discriminator at different times. Second, a certain amount of charge must be integrated before reaching the threshold on a discriminator; due to variations in the risetime and/or amplitude differences, a walk effect may also result.

[9]This is best illustrated with an example. Suppose the timing signal from the left PMT arrives at the trigger module first. In this case, the value of TDCL is constant (within the resolution of that detector's left PMT self-timing peak), but the value of TDCR increases as the location of the hit moves away from the left end towards the center of the detector. This increase is expected to be linear; therefore, the mean time is expected to increase linearly as the hit moves away from the left end towards the center of the detector.

each scintillator. Hits near the center of the scintillator correspond to the transition region in the TDCL versus TDCR plot. In the transition region, the sum of TDCL and TDCR is maximized; therefore, we now see why the front array mean time spectra are asymmetric with the pronounced feature on the right edge.

In order to account for the variation of the mean time with the position of the hit, the td versus xd curve was parameterized with a piecewise function f (to account for the linear regions and the curved transition region) according to

$$f(\mathtt{xd(id)}) = \begin{cases} t_0(\mathtt{id}) - \dfrac{|\mathtt{xd(id)} - x_0(\mathtt{id})|}{v} & |\mathtt{xd(id)} - x_0(\mathtt{id})| \geq a \ , \\ \\ t_0(\mathtt{id}) - \dfrac{a}{2v} - \dfrac{|\mathtt{xd(id)} - x_0(\mathtt{id})|^2}{2av} & |\mathtt{xd(id)} - x_0(\mathtt{id})| < a \ , \end{cases} \tag{5.26}$$

where v = 2*x_slope/t_slope is the signal propagation speed in the scintillators (x_slope was determined by the position calibration and t_slope = 0.05 ns) and a = 15 cm was deemed an appropriate choice via inspection of a td versus xd plot (see Fig. 5-28). The remaining (unknown) parameters, x_0 and t_0, were determined for each detector via an iterative procedure. For each detector recording a hit, the following sums

$$x_1(\mathtt{id}) = \frac{\sum_i w_1 \ \mathtt{xd(id)}_i}{\sum_i w_1} \ , \qquad t_1(\mathtt{id}) = \frac{\sum_i w_1 \ \mathtt{td(id)}_i}{\sum_i w_1} \ , \tag{5.27}$$

$$x_2(\mathtt{id}) = \frac{\sum_i w_2 \ \mathtt{xd(id)}_i}{\sum_i w_2} \ , \qquad t_2(\mathtt{id}) = \frac{\sum_i w_2 \ \mathtt{td(id)}_i}{\sum_i w_2} \ , \tag{5.28}$$

were evaluated; here,

$$w_1 = \Theta\left(\mathtt{xd} > x_0 \ \ \mathtt{.and.} \ \ x_{\min} < |\mathtt{xd}| < 60 \text{ cm}\right) \ , \tag{5.29}$$

$$w_2 = \Theta\left(\mathtt{xd} < x_0 \ \ \mathtt{.and.} \ \ x_{\min} < |\mathtt{xd}| < 60 \text{ cm}\right) \ , \tag{5.30}$$

are tests expressed using the truth function Θ [i.e., Θ = 1 (0) if the argument is .true. (.false.)].

As x_0 was an unknown parameter, the algorithm began by assuming $x_0 = 0$ and

$x_{\min} = 40$ cm; then, in subsequent iterations, $x_{\min}$ was reduced in 10 cm steps to 30 cm and then to 20 cm. At the conclusion of each iteration, x_0 and t_0 were estimated, using Eq. (5.26), according to

$$x_0 = v\frac{t_1 - t_2}{2} + \frac{x_1 + x_2}{2} , \tag{5.31}$$

$$t_0 = \frac{t_1 + t_2}{2} + \frac{x_1 - x_2}{2v} . \tag{5.32}$$

After three iterations, the values of x_0 and t_0 computed by the algorithm tended to converge rapidly; therefore, the algorithm did not employ a greater number of iterations and/or smaller step sizes. The quality of the trigger calibration was verified by computing

$$\texttt{tc(id)} = \texttt{td(id)} - \texttt{trigger\_correction(id, xd)} , \tag{5.33}$$

where

$$\texttt{trigger\_correction(id, xd)} = \begin{cases} t_0(\texttt{id}) - \dfrac{x}{v} & |x| \geq a , \\ \\ t_0(\texttt{id}) - \dfrac{a}{2v} - \dfrac{x^2}{2av} & |x| < a , \end{cases} \tag{5.34}$$

and $x = \texttt{xd(id)} - x_0(\texttt{id})$. The parameters x_0 and t_0 were then stored and recorded as the variables `trigger_x0` and `trigger_t0`, respectively.

The results of the trigger calibration are shown in Fig. 5-29; here, we see that the above described corrections for correlations between the left PMT TDC and the right PMT TDC permitted a reconstruction of the self-timing peaks for single hit events with a FWHM of ~0.3–0.4 ns (the bin size in these histograms is 0.1 ns).

As will be discussed in greater detail later, during the data analysis, `tc` was computed for each detector in the front array recording a hit; the detector with the smallest value of |`tc`| was then identified as the location of the triggering hit.

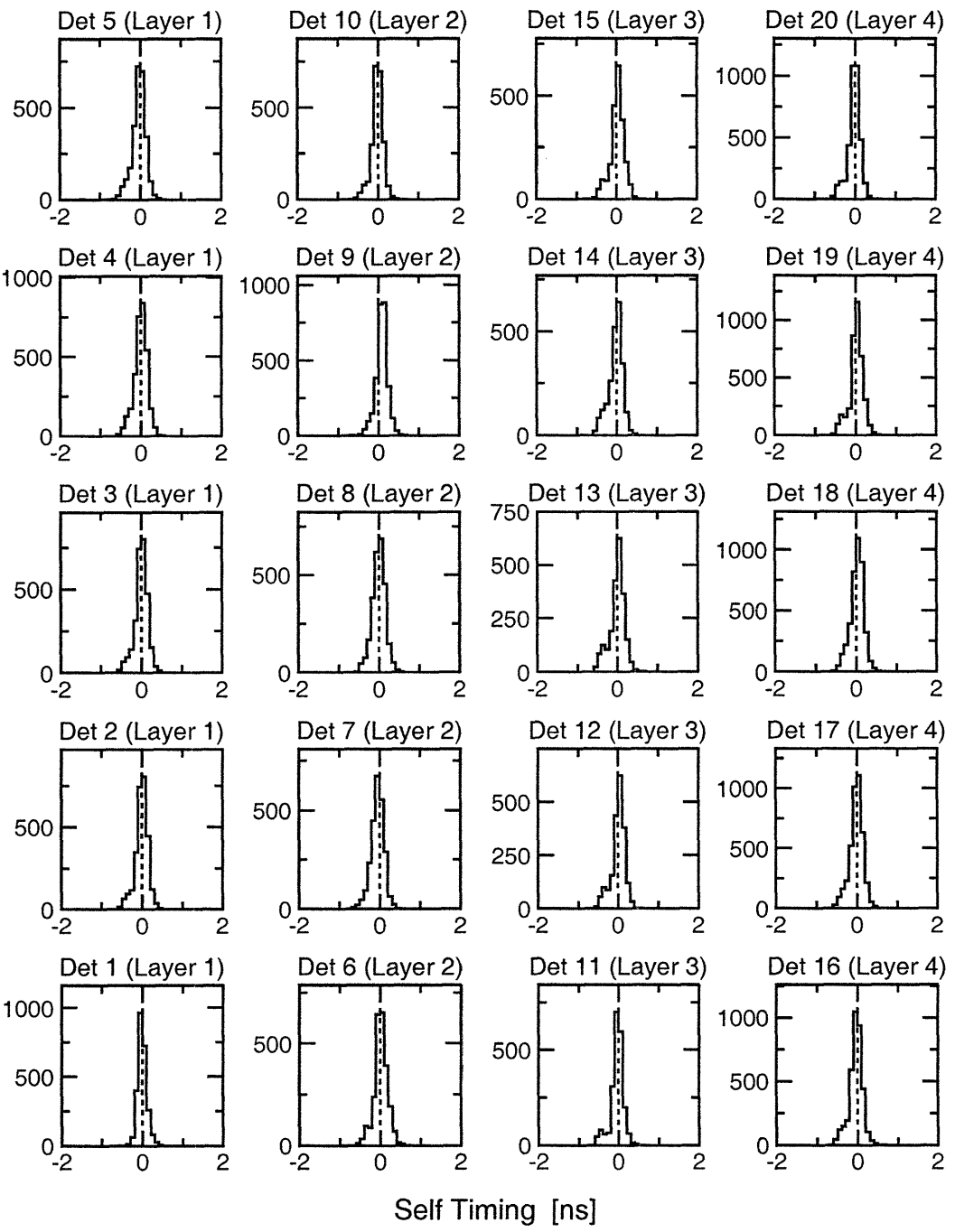

Figure 5-29: Self timing spectra `tc` for the front array detectors.

Variable	Cut for Central Q^2 [(GeV/c)^2] 0.447	1.136	1.169	1.474
Čerenkov Photoelectrons	> 2	> 2	> 2	> 2
Calorimeter Energy [GeV]	> 0.3	> 1.1	> 1.1	> 1.6
Scattered Electron $\beta_{e'}$	$\in [0.7, 1.3]$	$\in [0.7, 1.3]$	$\in [0.7, 1.3]$	$\in [0.7, 1.3]$
Momentum Bite $\Delta p_{e'}/\overline{p}_{e'}$ [%]	$\in [-10, 10]$	$\in [-5, 10]$	$\in [-5, 10]$	$\in [-3, 10]$
Target Position $\lvert z_{\rm tar}\rvert$ [cm]	< 7	< 7	< 7	< 7
HMS Track χ^2	< 50	< 50	< 50	< 50
`ph_start`	$\in [2280, 2630]$	$\in [2400, 2900]$	$\in [2400, 2900]$	$\in [2460, 2830]$

Table 5.1: Minimal set of cuts for the cTOF calibration.

5.3.6 Coincidence Time-of-Flight Calibration

To maximize the signal-to-noise ratio, the NPOL time calibration program constructed a coincidence time-of-flight spectrum that accounted for the ^{2}H$(e, e'n)$ reaction kinematics, pathlength variations in the HMS and NPOL, and variations in the delay between an interaction in a detector and the arrival of its timing signal at the TDC. For the coincidence time-of-flight (cTOF) calibration, the algorithm used data acquired with the Charybdis magnet on and Type 3 events with one hit in the front array and no hits in the front veto/tagger array. Further, a minimal set of cuts, summarized in Table 5.1, were applied to the data in order to (loosely) select quasielastic ^{2}H$(e, e'n)$ events. With the exception of the variable `ph_start`, all of these variables were previously discussed in Section 5.1; the variable `ph_start` represents the output (in channels) of a TDC started by a signal generated by the NPOL trigger and stopped by a signal generated by the HMS trigger (slower nucleons yielded smaller values of `ph_start`). A sample `ph_start` spectrum is shown in Fig. 5-30.

For those events satisfying the cuts listed in Table 5.1, the algorithm first predicted the neutron time-of-flight from the target to the front array using only position information (i.e., the reconstructed vertex for the ^{2}H$(e, e'n)$ scattering event in the target and the detection position for the hit in the front array) and electron kinematics (i.e., $\mathbf{q}$). Assuming quasifree ^{2}H$(e, e'n)$ kinematics, four-momentum conservation demands

$$m_d + \omega = \sqrt{|\mathbf{p}_n|^2 + m_n^2} + \sqrt{|\mathbf{p}_p|^2 + m_p^2}\ , \tag{5.35}$$

$$\mathbf{q} = \mathbf{p}_n + \mathbf{p}_p\ . \tag{5.36}$$

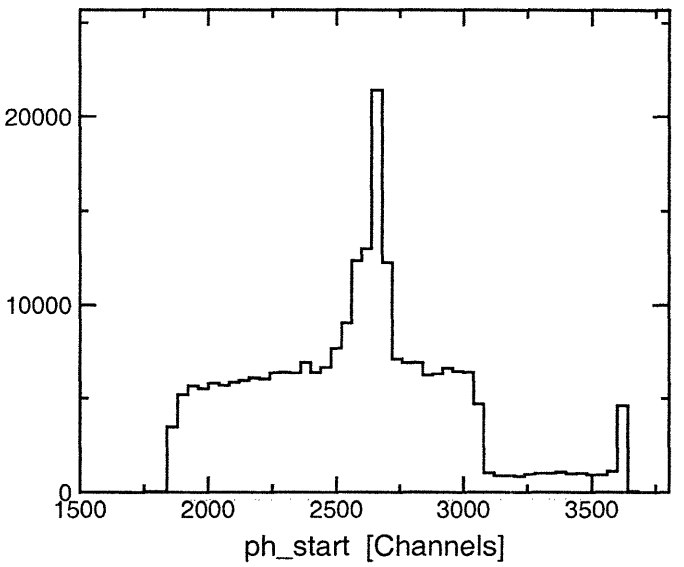

Figure 5-30: Sample `ph_start` spectrum.

From this, it can easily be shown in a few lines of algebra that the magnitude of the neutron's three-momentum, $|\mathbf{p}_n|$, is given by the solution to the quadratic equation

$$A|\mathbf{p}_n|^2 + B|\mathbf{p}_n| + C = 0 \ , \tag{5.37}$$

where

$$A = (m_d + \omega)^2 - (\mathbf{q} \cdot \hat{\mathbf{p}}_n)^2 \ , \tag{5.38}$$

$$B = -2(\mathbf{q} \cdot \hat{\mathbf{p}}_n)D \ , \tag{5.39}$$

$$C = m_n^2(m_d + \omega)^2 - D^2 \ , \tag{5.40}$$

$$D = \frac{1}{2}\left(m_d^2 + m_n^2 - m_p^2 - Q^2 + 2m_d\omega\right) \ . \tag{5.41}$$

Here, our notation is such that $\hat{\mathbf{p}}_n$ denotes the unit vector between the reconstructed vertex in the target and the detection position in the front array. After computation of $|\mathbf{p}_n|$, the predicted time-of-flight, denoted `ntof`, was computed very simply using $|\mathbf{p}_n|$ and the calculated distance between the reconstructed vertex and the detection position in the front array.

Next, the actual time-of-flight from the target to the front array was estimated

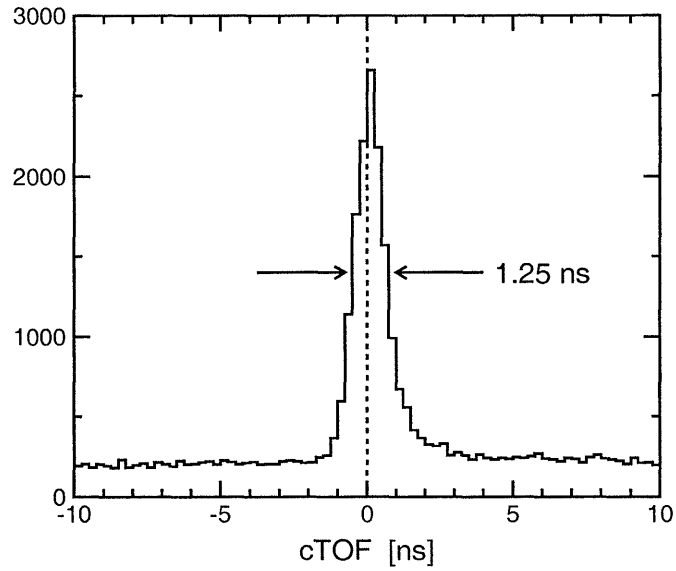

Figure 5-31: Calibrated cTOF spectrum summed over all detectors in the front array.

with the variable `t_front`, defined by

$$\texttt{t\_front} = -\texttt{ph\_start} * \texttt{dt} + \texttt{hs\_tof} + \texttt{t\_slope(id)} * [\texttt{TDCL(id)} + \texttt{TDCR(id)}]/2 \ , \tag{5.42}$$

where `ph_start` is as described above, `dt` = 0.05 ns/channel is the usual TDC channel-to-time-conversion factor, and `hs_tof` is a correction for pathlength variations and for delays between interactions and signals in the HMS computed by the E93-038 `ENGINE`.

After computation of `t_front`, the coincidence time-of-flight (cTOF), defined by

$$\text{cTOF} = \texttt{t\_front} - \texttt{ntof} \ , \tag{5.43}$$

was computed for each event. cTOF spectra (with a 0.25 ns bin size) were accumulated for each detector, and the algorithm determined the mode (peak channel) for each detector. An offset parameter, `ctof_offset`, was then chosen for each detector such that the peak channel was centered on zero.

A sample cTOF spectrum summed over all detectors in the front array is shown in Fig. 5-31, and individual cTOF spectra for each detector in the front array are

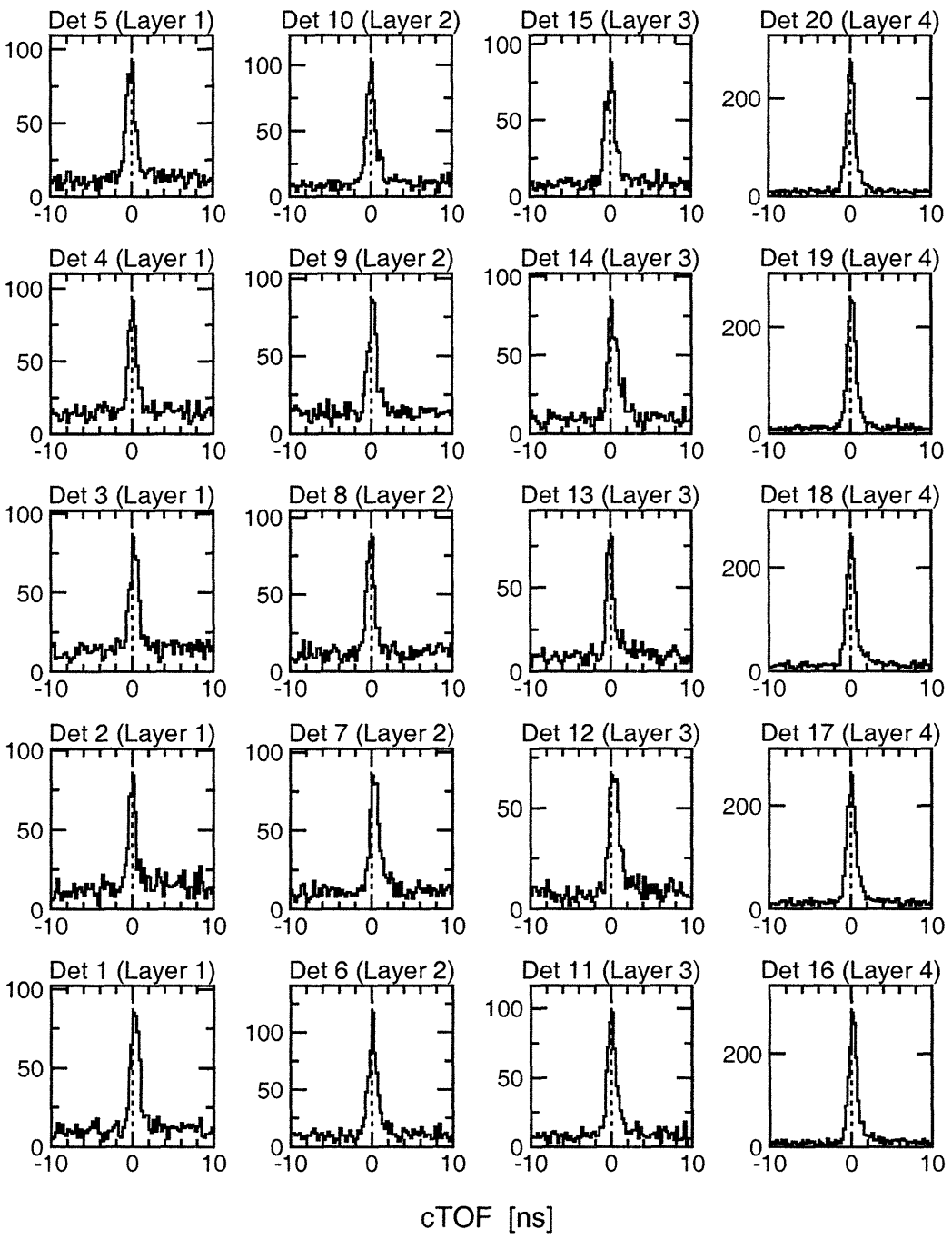

Figure 5-32: Calibrated cTOF spectra for each detector in the front array.

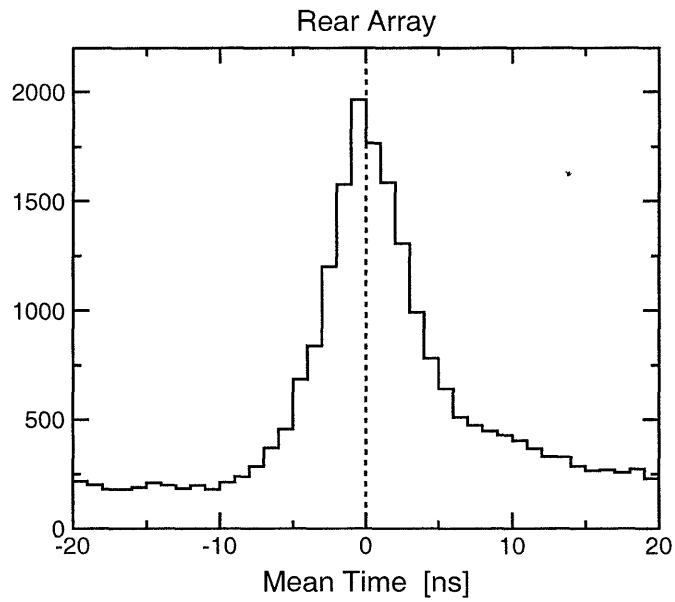

Figure 5-33: Calibrated mean time spectrum summed over all of the rear array detectors.

shown in Fig. 5-32. Although the cTOF peaks are fairly sharp (with a FWHM of $\sim$1.5 ns), there is, as seen most clearly in the summed spectrum, a tail on the slow side (i.e., the right-hand side); we will return to a discussion of this tail in Chapter 7.

5.3.7 Rear Array Timing Calibration

Similar to the cTOF calibration, the timing calibration of the rear array detectors employed data acquired with the Charybdis magnet on and Type 3 events with a single hit in the front array and the rear array and no hits in the front or rear veto/tagger array detectors. The same set of cuts summarized in Table 5.1 were applied to the data for this step of the timing calibration; in addition, a $|\text{cTOF}| \leq 2$ ns cut was applied to the data for this step of the calibration.

First, the algorithm aligned the mean-time spectra of the rear array detectors relative to each other. Histograms of mean times, `td`, with a 0.5 ns bin size were constructed for each detector in the rear array. As with the relative time alignment of the front array detectors, the channel of maximum content was identified, and the mean value of `td` within a $\pm$2.5 ns interval surrounding the channel of maximum

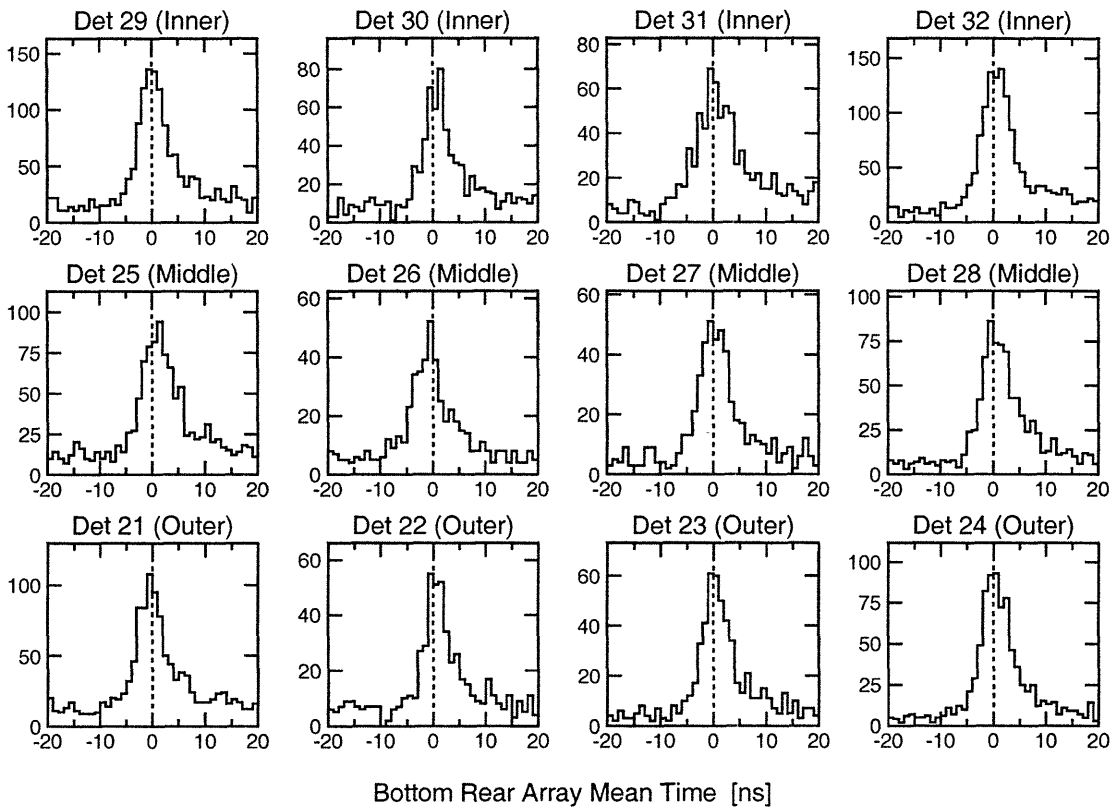

Figure 5-34: Calibrated mean-time spectra for the bottom rear array detectors.

content was computed; however, unlike the procedure for the alignment of the front array mean times, the time offset parameter for each rear array detector, `t_offset`, was chosen such that the peak channel (as opposed to the mean value) was aligned on zero. A mean time spectrum summed over all detectors in the rear array is shown in Fig. 5-33, and individual mean time spectra for each detector in the bottom and top rear array are shown in Figs. 5-34 and 5-35, respectively. Here, we see that the mean-time spectra for each detector are all aligned well relative to each other.

Second, the algorithm performed an absolute time calibration of the rear array detectors relative to the front array detectors via a front-to-rear velocity calibration. The scattering angle for the front-to-rear track was computed using the incident neutron three-momentum and the position information for the hits in the front and rear array, and then the algorithm predicted the front-to-rear velocity, denoted v_{np}, for elastic np scattering using the kinetic energy calculation given in Eq. (5.18). The

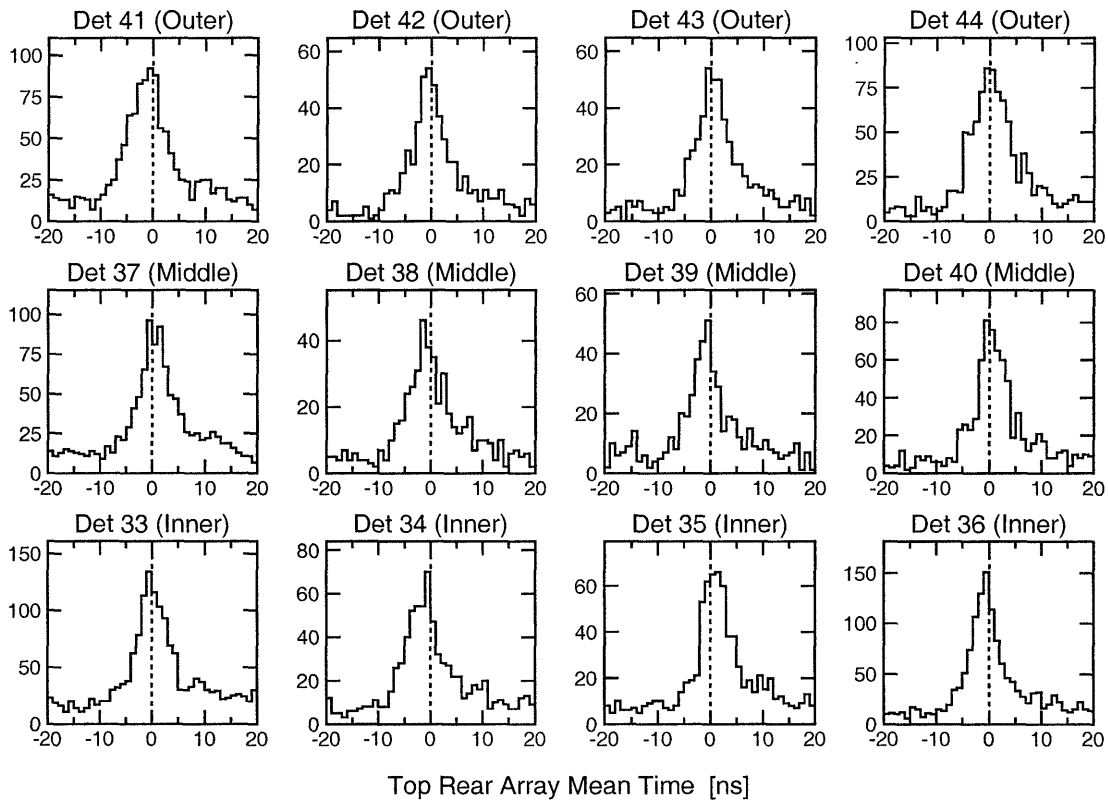

Figure 5-35: Calibrated mean-time spectra for the top rear array detectors.

algorithm then computed the predicted time-of-flight for elastic np scattering using the hit positions in the front and rear array and the computed value of v_{np}; this predicted time-of-flight was then compared with an estimate of the actual front-to-rear time-of-flight, `t_rear` − `t_front`, where the definition of `t_rear` is identical to that for `t_front` given in Eq. (5.42). Following the computation of `t_rear` − `t_front`, histograms of a relative time-of-flight, rTOF, defined to be

$$\text{rTOF} = (\texttt{t\_rear} - \texttt{t\_front}) - d/v_{np} \ , \tag{5.44}$$

where d denotes the distance between the hits in the front array and the rear array, were constructed for each detector in the rear array. The algorithm then identified the peak channel, and offsets, labeled `ctof_offset` (instead of `rtof_offset` for internal consistency with the cTOF calibration), were chosen for each detector such that the peak channels were aligned on zero.

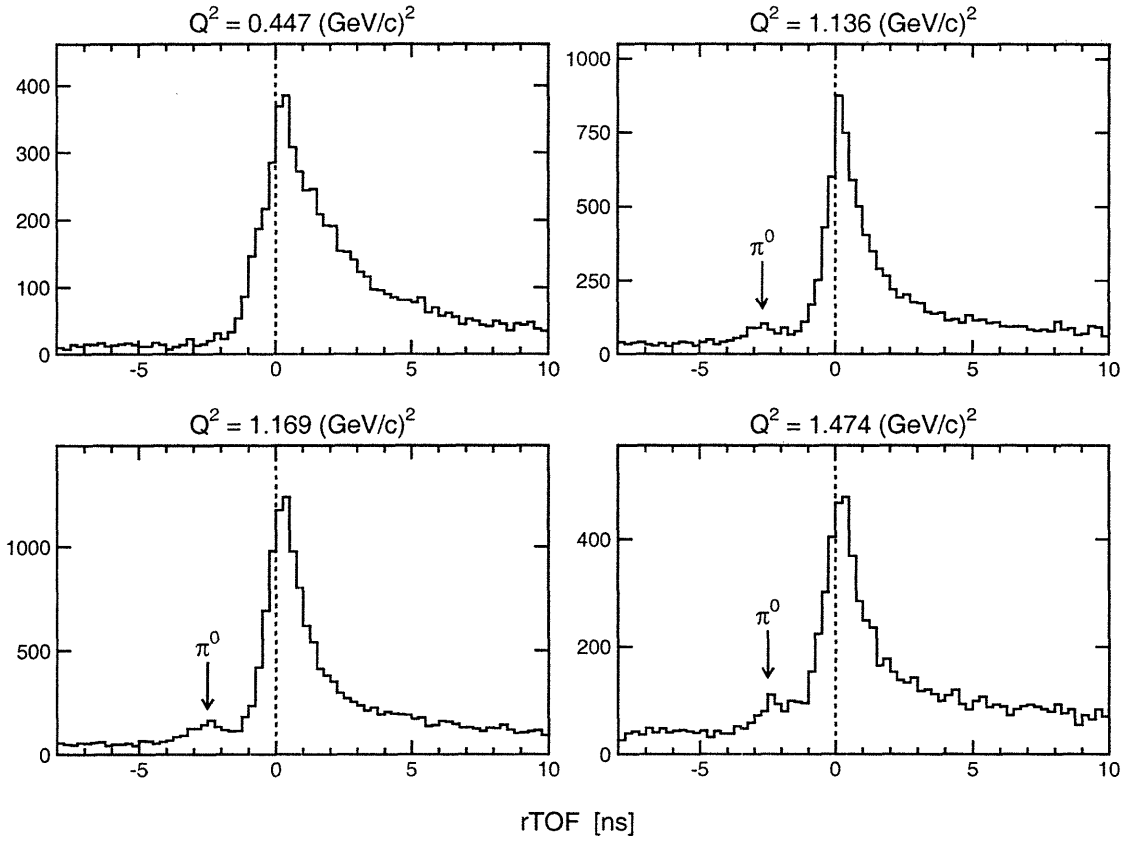

Figure 5-36: Calibrated $Q^2 = 0.447$, 1.136, 1.169, and 1.474 $(\mathrm{GeV}/c)^2$ rTOF spectra.

Sample rTOF spectra summed over all detectors in the front array and the rear array for all Q^2 points (instead of just the $Q^2 = 1.169$ $(\mathrm{GeV}/c)^2$ point) are shown in Fig. 5-36; we do not show individual rTOF spectra for tracks from specific detectors in the front array to specific detectors in the rear array as the combinations are too numerous. Several features of these spectra are worth mentioning. First, the calibrated rTOF spectrum is well aligned and centered on zero. Second, the asymmetric tail on the slow side is due to scattering from protons bound in carbon nuclei (i.e., Fermi motion) and other nuclear reactions. Last, the small secondary peak located on the fast side of the $Q^2 = 1.136$, 1.169, and 1.474 $(\mathrm{GeV}/c)^2$ spectra at ~ -2.5 ns is, as will be discussed in more detail later, attributed to quasifree π^0-production in the scintillators via the reaction

$$n + p \rightarrow n + p + \pi^0 \ , \qquad \pi^0 \rightarrow \gamma\gamma \ . \tag{5.45}$$

As we will see later, this peak is more visible after the final sets of analysis cuts are applied to the data. For now, we see that the π^0-production peak is visible in the $Q^2 = 1.136$, 1.169, and 1.474 $(\mathrm{GeV}/c)^2$ rTOF spectra, with corresponding central neutron kinetic energies of $T_n = 606$, 624, and 786 MeV, respectively; however, it it absent in the $Q^2 = 0.447$ $(\mathrm{GeV}/c)^2$ rTOF spectrum, with a corresponding central neutron kinetic energy of $T_n = 239$ MeV. As can easily be shown, the threshold kinetic energy for π^0-production assuming neutron bombardment on stationary protons is 280 MeV[10]; therefore, this result is not unexpected (neutron kinetic energy spectra will be shown in the next section of this chapter).

5.3.8 Front and Rear Veto/Tagger Calibration

The position and timing calibration of the front and rear veto/tagger detectors consisted of three steps. First, as previously discussed, leading-edge discrimination was employed for these detectors; therefore, corrections for walk were computed during the first step of this algorithm. Second, after corrections for walk were applied to the TDC values from the front and rear veto/tagger PMTs, the position calibration of the rear veto/tagger detectors was repeated using a different algorithm than that employed for the position calibration of the front and rear array detectors. Last, the algorithm aligned the mean times of the front and rear veto/tagger detectors. In what follows below, we describe each of these algorithms in greater detail and then present the results of this calibration.

First, to correct for walk effects, the relationship between the observed TDC

[10] Assuming a neutron is incident on a stationary proton, the initial-state four-momentum in the laboratory frame is

$$p^\mu = (T_n + m_n + m_p \ , \ \sqrt{(T_n + m_n)^2 - m_n^2}) \ , \tag{5.46}$$

where the x- and y-components of the three-momentum are spurious. At threshold, the final-state four-momentum in the center-of-mass frame is

$$p'^\mu = (m_n + m_p + m_{\pi^0} \ , \ 0) \ . \tag{5.47}$$

Using the Lorentz invariant, $p^2 = p'^2$, after a small amount of algebraic maniuplation, we find, at threshold, that

$$T_n = \frac{2m_n m_{\pi^0} + 2m_p m_{\pi^0} + m_{\pi^0}^2}{2m_p} = 279.848 \text{ MeV} \tag{5.48}$$

channel, $\texttt{TDC}_{\text{obs}}$, and the observed ADC channel, $\texttt{ADC}_{\text{obs}}$, for the left or right PMT was parameterized as

$$\texttt{TDC}_{\text{obs}} = \texttt{TDC} + \gamma \log \frac{\texttt{ADC}_{\text{obs}}}{\texttt{ADC}_{\text{peak}}} , \tag{5.49}$$

where TDC denotes the TDC channel in the absence of walk effects, γ is an unknown parameter, and $\texttt{ADC}_{\text{peak}}$ denotes the peak ADC channel. [This parameterization assumes corrections for walk vanish at the peak of the ADC spectrum.] After the algorithm determined the peak ADC channel, γ was determined via the method of least squares. If the desired linear relationship given in Eq. (5.49) is parameterized in the usual form as

$$y = ax + b , \tag{5.50}$$

where $y \leftrightarrow \texttt{TDC}$, $a \leftrightarrow \gamma$, $x \leftrightarrow \texttt{ADC}$, and $b \leftrightarrow \texttt{TDC} - \gamma \log \texttt{ADC}_{\text{peak}}$, a can be uniquely determined via a minimization of

$$\chi^2 = \frac{1}{N} \sum_{i=1}^{N} (y_i - ax_i - b)^2 , \tag{5.51}$$

where y_i $(ax_i + b)$ denotes the observed (predicted) value of y for the i^{th} event. As can easily be shown (see, e.g., [410]), χ^2 is minimized if

$$a = \frac{N \sum_i x_i y_i - \sum_i x_i \sum_i y_i}{N \sum_i x_i^2 - \left(\sum_i x_i\right)^2} , \qquad b = \frac{\sum_i x_i^2 \sum_i y_i - \sum_i x_i \sum_i y_i}{N \sum_i x_i^2 - \left(\sum_i x_i\right)^2} . \tag{5.52}$$

After computation of γ according to this scheme, the desired quantity, the walk-corrected TDC value, was determined according to

$$\texttt{TDC} = \texttt{TDC}_{\text{obs}} - \gamma \log \frac{\texttt{ADC}_{\text{obs}}}{\texttt{ADC}_{\text{peak}}} . \tag{5.53}$$

The values of γ and $\gamma \log \texttt{ADC}_{\text{peak}}$ for each PMT were then stored as the calibration constants `walk_slope` and `walk_offset`, respectively.

Second, as already discussed, the algorithm for the position calibration of the front and rear array detectors associated the edges of the $\texttt{TDCR} - \texttt{TDCL}$ difference spectrum with the physical edges of the detector. Although this method worked well for the

front array and rear array detectors, it did not work well for the front and rear/veto tagger detectors for two primary reasons: (1) the collimator partly obscured the edges of the front veto/tagger detectors, and (2) the outer rear veto/tagger detectors did not receive adequate illumination from front-to-rear charged particle tracks. [The front and rear/veto tagger arrays were designed to provide more than adequate coverage of the front array and front-to-rear tracks, respectively.] As a result, the veto/tagger position calibration algorithm instead deduced position calibration parameters by comparing the hit position in a veto/tagger detector with the corresponding hit position in the nearest element in the front array. This position calibration scheme consisted of two steps which we now describe in detail.

In the first step of the veto/tagger position calibration algorithm, events with one hit in both layers of the front array, one hit in each layer of the front array, and one hit in both layers of the rear veto/tagger array (if both layers existed) were selected (i.e., a hit in all layers was taken to signal the detection of an incoming proton). The TDC values from the detectors recording hits were corrected for walk, and the hit positions in the front and rear veto/tagger detectors were then predicted using the track in the front array assuming normal incidence (e.g., the vertical and horizontal hit position predicted for both layers of the front veto/tagger array was the vertical and horizontal hit position of the hit in the first layer of the front array). The algorithm assumed the hit position in the veto/tagger detectors, x, was related (linearly) to the difference of the walk-corrected TDC values according to

$$x = a\tau + b \ , \tag{5.54}$$

where $\tau = \texttt{TDCR} - \texttt{TDCL}$. The offset, b, was then determined via a minimization of

$$\chi^2 = \frac{1}{N}\sum_{i=1}^{N} (a\tau_i + b - \overline{x}_i) \ , \tag{5.55}$$

where $\overline{x}_i$ denotes the predicted hit position and N denotes the number of events satisfying the selection criteria. A straightforward calculation shows that χ^2 is minimized

if

$$b = \frac{1}{N}\sum_{i=1}^{N} \overline{x}_i - a\frac{1}{N}\sum_{i=1}^{N} \tau_i \ . \tag{5.56}$$

Here, the parameter a was not uniquely determined as the procedure was not stable (probably due to the inadequate time resolution of the leading-edge discriminators); therefore, a was assigned a value typical of that for the front and rear array detectors (as all of the detectors were composed of the same material), and b was then computed according to the above formula. The algorithm then replaced the previously determined values of `x_slope` and `x_offset` for the front and rear veto/tagger detectors with a and b, respectively.

In the second step of the veto/tagger position calibration algorithm, the algorithm attempted to improve the statistics for the position calibration of the outer rear veto/tagger detectors by selecting (n, p) charge-exchange events in the front array of the polarimeter; for the purposes of the rear veto/tagger position calibration, an (n, p) charge-exchange event was defined to be an event with no hits in the front veto/tagger array, one or more hits in the front array (it should be noted that the algorithm required, e.g., successive hits in the third and fourth layer if a hit occurred in the second layer), one hit in each layer of the rear veto/tagger array (if both layers existed), and at least one hit in the rear array (events with hits in both the top and bottom rear array were rejected). The location of the charge-exchange event was defined to be the location of the first hit; this hit position, together with the first hit position in the rear array, was used to predict the hit positions in the rear veto/tagger array (assuming a straight track from the front array to the rear array). The position offsets for the rear veto/tagger detectors were then determined in exactly the same manner as described above (i.e., via a χ^2 minimization of the difference between the recorded and predicted hit positions). The statistics from the charge-exchange position calibration were combined with those from the first step of the veto/tagger position calibration, and the weighted average of `x_offset` for each rear veto/tagger detector was computed and stored.

Last, the algorithm aligned the mean times for each of the detectors in the front

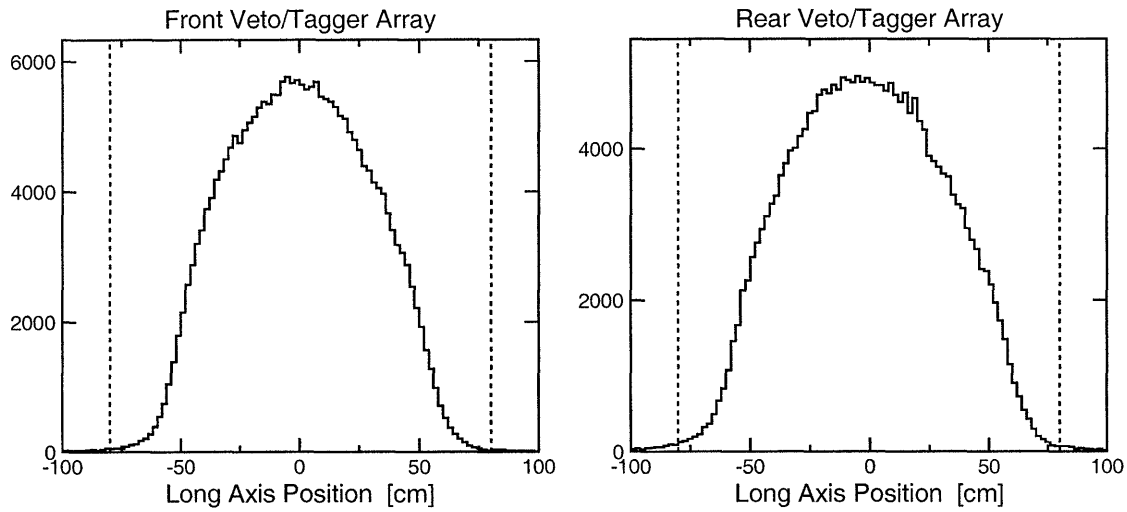

Figure 5-37: Summed calibrated position spectra for the front and rear veto/tagger array detectors. The dashed lines represent the physical edges of the detectors.

and rear veto/tagger arrays; for this step of the calibration, events with one hit in both layers of the front veto/tagger array, one hit in each layer of the front array, and one hit in both layers of the rear veto/tagger array (if both layers existed) were used. As with all of the relative time calibrations, histograms of the mean times, `td`, with a 0.5 ns bin size were constructed for each detector in the front and rear veto/tagger arrays. The algorithm identified the channel of maximum content and then computed the mean value of `td` within a ± 5 ns interval surrounding the peak channel. Offset parameters for each veto/tagger detector, `t_offset`, were then chosen such that the mean values of `td` for the veto/tagger detectors were aligned on zero.

Position spectra summed over all detectors in the front and rear veto/tagger arrays are shown in the left and right panels, respectively, of Fig. 5-37. Here, we see that the veto/tagger position spectra are more rounded than the front and rear array position spectra; this is primarily due to the fact that the resolution of the leading-edge discriminators was not as good as the resolution of the constant-fraction discriminators. Also, although the front and rear veto/tagger detectors were longer than the front array detectors (160 cm versus 100 cm), the range of hit positions in these spectra is similar to those seen in the front array spectra; this is simply a result of the fact that the position calibration of the veto/tagger detectors only used events with a hit in

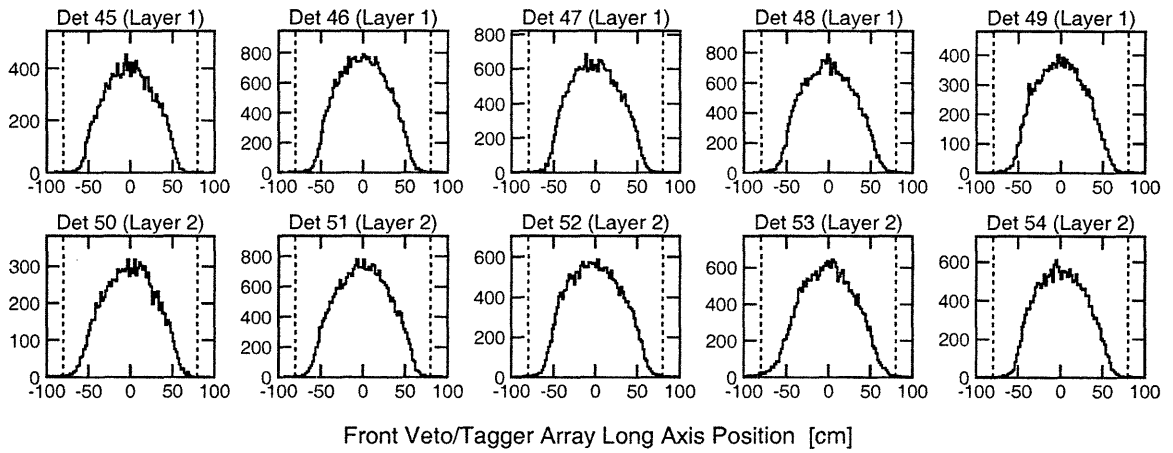

Figure 5-38: Calibrated position spectra for the front veto/tagger array detectors. The dashed lines represent the physical edges of the detectors.

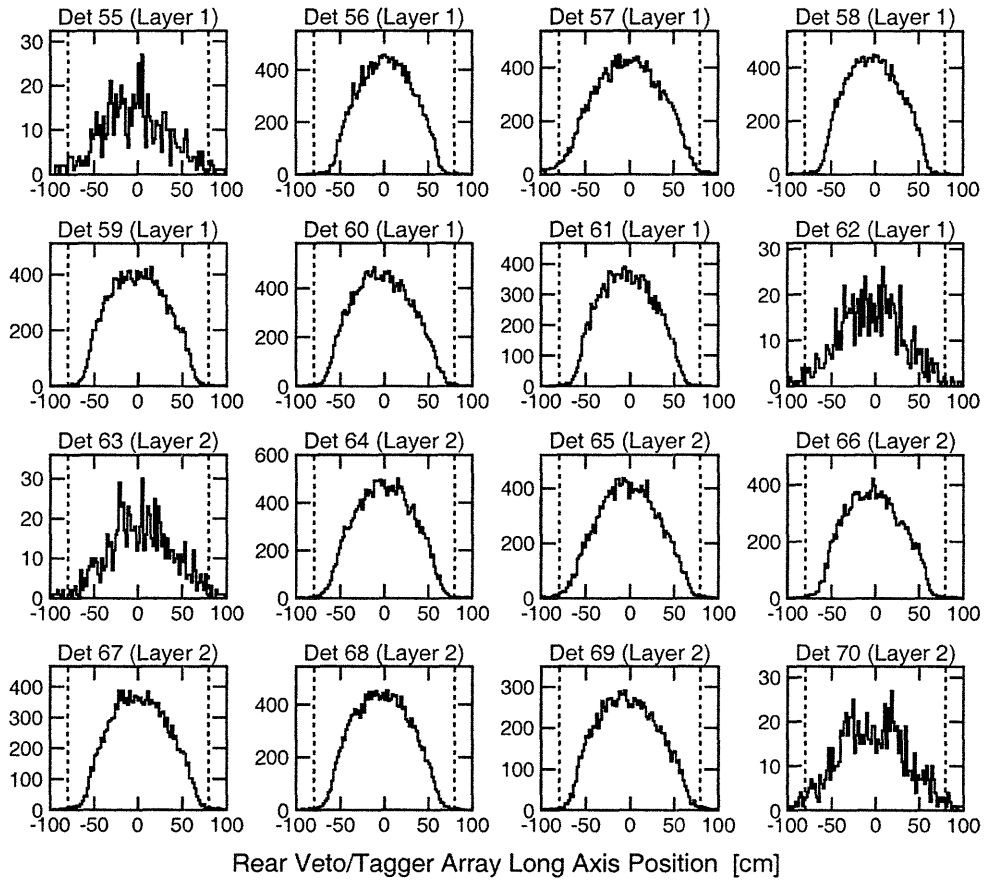

Figure 5-39: Calibrated position spectra for the rear veto/tagger array detectors. The dashed lines represent the physical edges of the detectors.

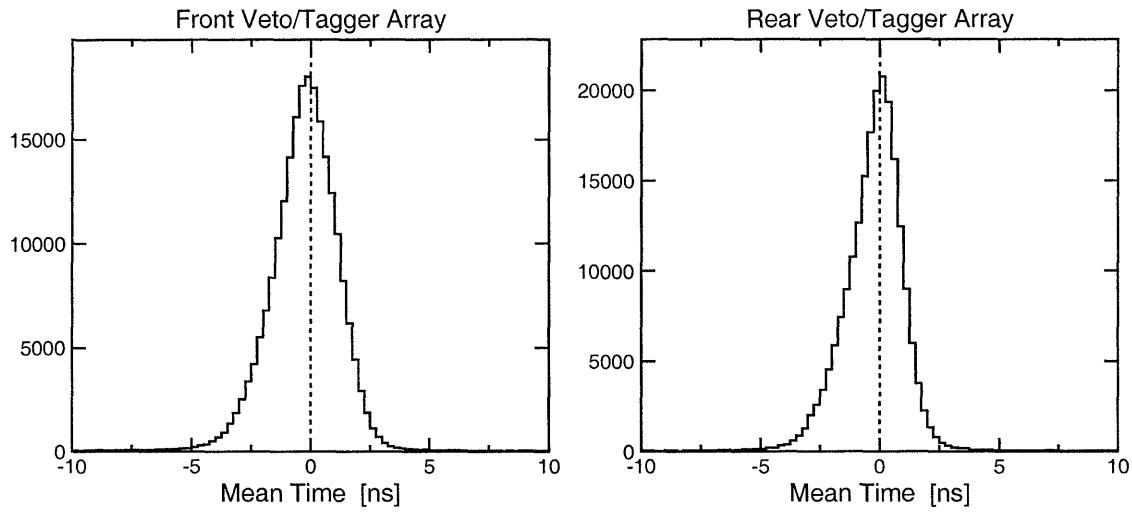

Figure 5-40: Summed calibrated mean-time spectra for the front and rear veto/tagger array detectors.

each layer of the front array. Again, in more detail, position spectra for each detector in the front and rear veto/tagger arrays are shown in Figs. 5-38 and 5-39, respectively; here, the low statistics for the outer rear veto/tagger detectors (i.e., detectors 55, 62, 63, and 70) are clearly visible.

Mean time spectra summed over all detectors in the front and rear veto/tagger arrays are presented in the left and right panels, respectively, of Fig. 5-40, and individual mean-time spectra for each detector in the front and rear veto/tagger arrays are shown in Figs. 5-41 and 5-42, respectively. These are all well aligned on zero.

We conclude our discussion of the calibration of the front and rear veto/tagger detectors by noting that an absolute time calibration of the veto/tagger detectors relative to the trigger time was complicated (and, as a result, not performed) due to a lack of reliable discrimination between protons and pions (as the timing calibration algorithms did not compute the necessary kinematic quantities needed to discriminate between pions and protons); therefore, as described above, the mean times of the veto/tagger detectors were aligned relative to each other, but an absolute time calibration of the veto/tagger detectors was not conducted.

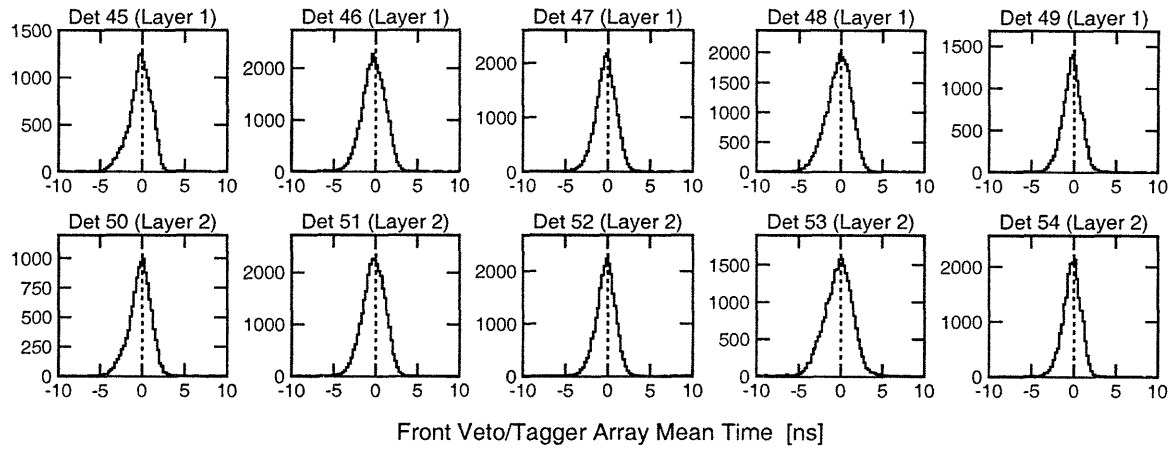

Figure 5-41: Calibrated mean-time spectra for the front veto/tagger array detectors.

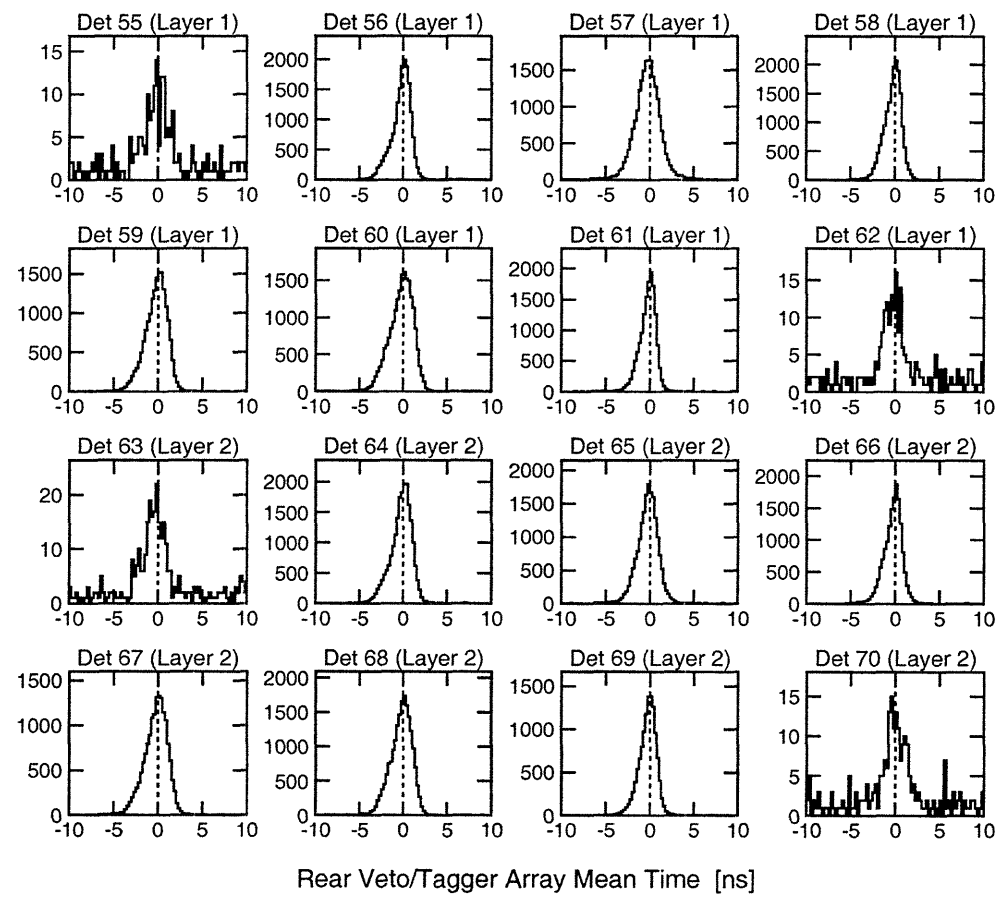

Figure 5-42: Calibrated mean-time spectra for the rear veto/tagger array detectors.

5.3.9 Output

At the conclusion of the NPOL time calibration program, the various calibration parameters for each detector were written to an `ASCII` file and histograms of the calibration results (i.e., such as those shown during our discussion of the various calibration algorithms) were written to an `HBOOK` file.

5.4 Neutron Polarimeter Tracking and Event Reconstruction

In this section, we begin with a detailed description of an E93-038-specific code, the `Analyzer`, that was developed for tracking and event reconstruction in the neutron polarimeter. Following an overview of these algorithms, we present examples of the results from the analysis at each of the Q^2 points.

5.4.1 Overview of the `Analyzer`

The E93-038 `Analyzer` code was written entirely in `FORTRAN` under the leadership of Kelly [411].

A schematic flowchart for the `Analyzer` is shown in Fig. 5-43. As shown in this figure, the `Analyzer` began with a series of initialization routines designed to read NPOL detector geometry parameters and the pulse-height and time-calibration parameters from various input files. Following the execution of these initialization routines, the code proceeded, in the main event loop, to read the raw NPOL data for each event from the `.rzdat` files produced by the E93-038 `ENGINE`. After computation of the positions and times for each hit, the `Analyzer` then attempted to determine which hit in the front array generated the trigger; following this, all hits were filtered according to a number of different selection criteria. Next, those hits that survived the filtering were grouped into recognizable patterns, and the `Analyzer` attempted to determine the primary hits in the front array and the rear array and the charge of the incident particle and the particle detected in the rear. Finally, a number of kinematic

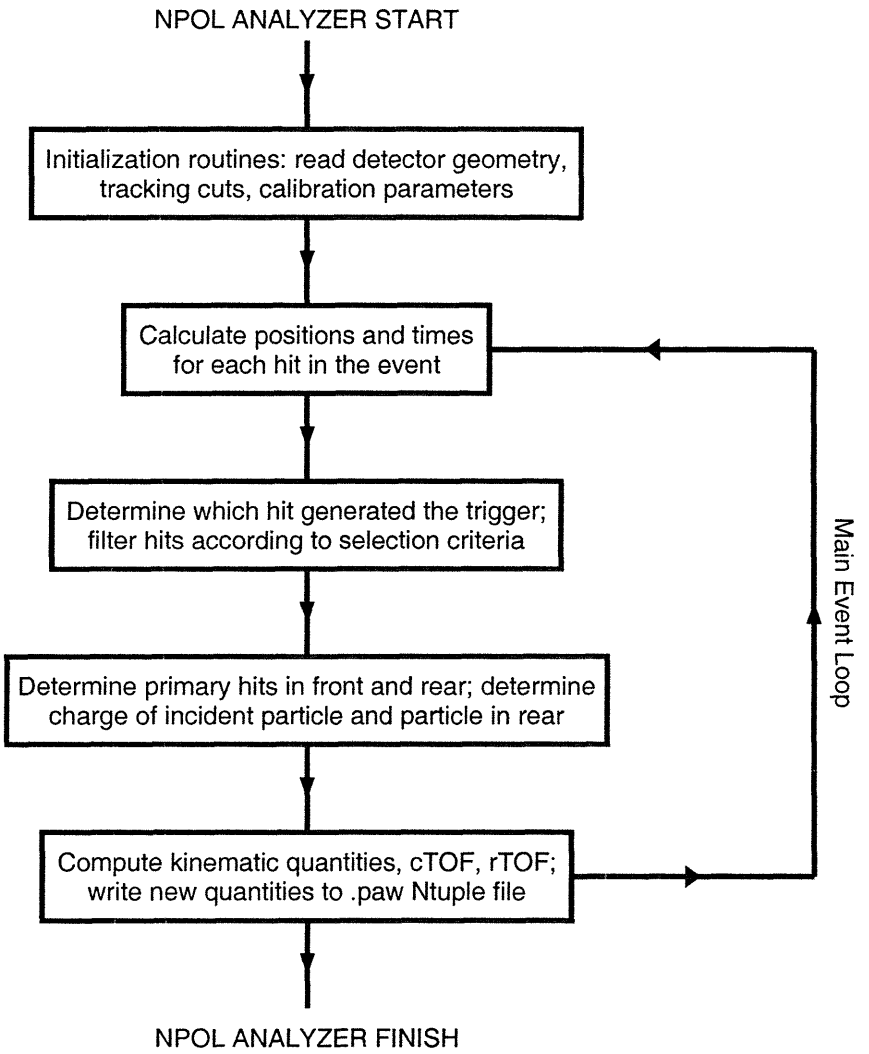

Figure 5-43: A schematic flowchart for the E93-038 `Analyzer` code.

quantities and time-of-flight variables (e.g., cTOF, rTOF, etc.) were computed for those events satisfying the track reconstruction selection criteria.

Following the complete analysis of an event, the original event-wise information contained in the `.rzdat` file plus the newly-computed event-wise tracking, reconstruction, and kinematic information for the NPOL data were written to an expanded Ntuple, hereafter referred to as a "`.paw` file". In what follows below, we describe each of the steps of the `Analyzer` shown in Fig. 5-43 in greater detail.

Variable	Selection Criteria
Front/Rear Array Position `xd`	$\|\texttt{xd}\| \leq 60$ cm
Front/Rear Veto/Tagger Array Position `xd`	$\|\texttt{xd}\| \leq 100$ cm
Front Array Mean Time `td`	$\texttt{td} \in [-5, 10]$ ns
Rear Array Mean Time `td`	$\texttt{td} \in [-10, 25]$ ns
Front Veto/Tagger Array Mean Time `td`	$\texttt{td} \in [-12, 5]$ ns
Rear Veto/Tagger Array Mean Time `td`	$\texttt{td} \in [-12, 5]$ ns

Table 5.2: Selection criteria used to filter the hits in the polarimeter.

5.4.2 Initialization Routines

The `Analyzer` began with a sequence of initialization routines. These routines read `ASCII` files containing the coordinates and geometry for each NPOL detector, the pulse height calibration parameters, the time calibration parameters, and a number of different reconstruction and tracking cuts. Also, the output `.paw` file was initialized, and the first `.rzdat` file was opened. Following the completion of these initialization routines, the `Analyzer` entered the main event loop.

5.4.3 Hit Positions and Times

For each event, the Analyzer computed the hit positions, `xd`, and mean times, `td`, for each detector recording a hit according to Eqs. (5.23) and (5.25), respectively. The absolute time-of-flight, `t_front` or `t_rear`, was computed for each hit in the front and rear array according to Eq. (5.42), and the trigger variable `tc` was computed for each hit in the front array according to Eq. (5.33).

5.4.4 Trigger Selection and Hit Filtering

The hit with the smallest value of $|\texttt{tc}|$ was identified as the hit responsible for the NPOL trigger.

Following the identification of the hit responsible for the trigger, each hit was filtered according to the selection criteria listed in Table 5.2. The motivation for the position selection criteria is obvious; however, the motivation for the mean time

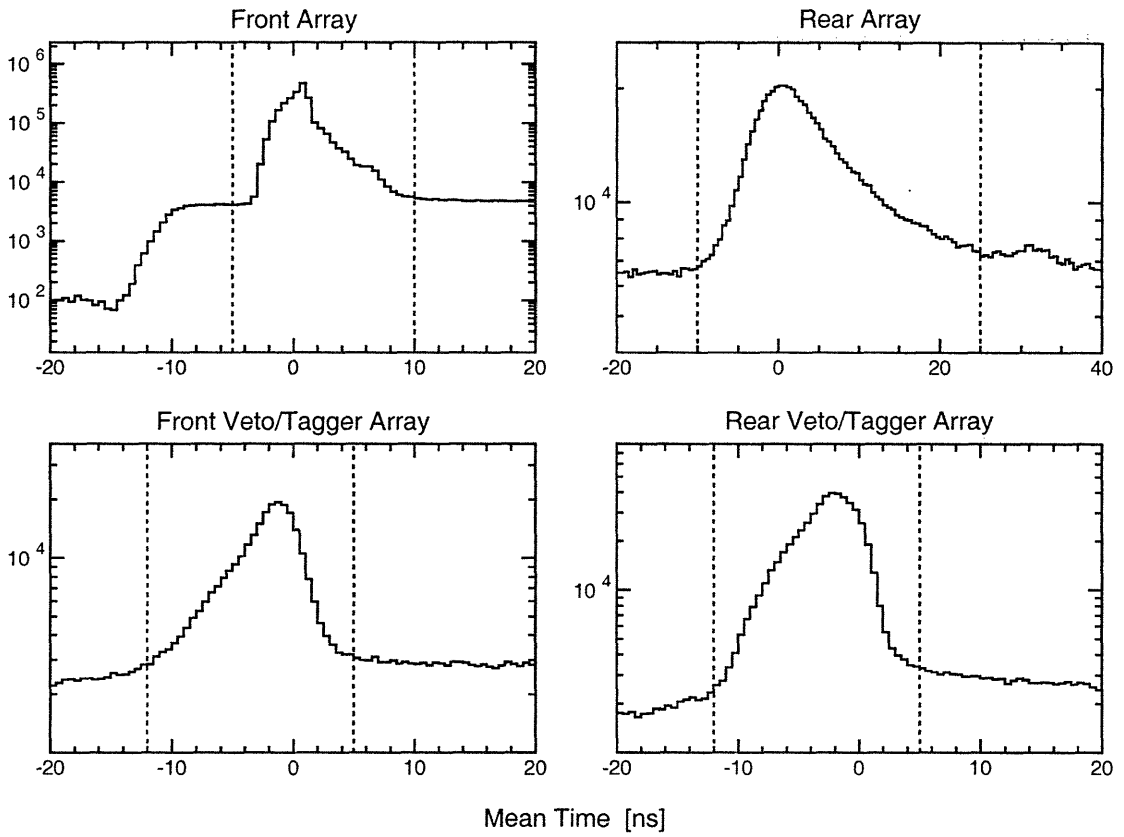

Figure 5-44: Mean-time spectra for all Type 3 HMS-NPOL coincidence events. The dashed lines correspond to the mean time windows used by the `Analyzer` to filter hits in the polarimeter.

windows requires explanation.

Semi-logarithmic plots of mean-time spectra for all Type 3 HMS-NPOL coincidence events (i.e., not just single-hit front array events as shown during the discussion of the time-calibration results) without cuts are shown for the four detector arrays in Fig. 5-44. The mean-time spectrum for the front array detectors contains a prominent peak centered at zero due to the primary scattering event in the front array. In addition, evidence of a secondary peak is seen at $\sim +6$ ns; this is due to secondary scattering of the recoil proton. It is clear that hits with front array mean times falling outside of the chosen $[-5, 10]$ ns window may be safely disregarded; in fact, this window may have been chosen to be somewhat tighter. The peak in the rear array mean-time spectrum corresponds to elastic/quasielastic scattering from the front array to the rear array; here, we see that the chosen $[-10, 25]$ ns window safely

eliminates early hits in the rear array. Finally, the front and rear veto/tagger array mean-time spectra contain peaks centered approximately at zero; these, of course, correspond to protons entering and exiting the front array. Here, we see that the chosen $[-12, 5]$ ns mean-time window safely identifies entering and exiting protons, and hits outside of this window can be discarded.

It should be noted that pulse height information was not used to filter hits in the polarimeter.

5.4.5 Hit Selection and Track Reconstruction

After the hits were filtered according to the selection criteria discussed in the previous subsection, the `Analyzer` attempted to group the remaining hits into recognizable patterns in an attempt to reconstruct the track through the polarimeter.

The hit selection and track reconstruction algorithm began by identifying incomplete and simple events. First, events with either (1) no surviving hits in the front and/or rear array or (2) hits in both the top and bottom rear array were discarded; a track-reconstruction error condition was assigned to these events, and they were not processed in any further detail. Second, simple events with one hit in the front array, one hit in the rear array, and no hits in the front and rear veto/tagger arrays were identified; for such events, the incident particle and the particle detected in the rear were, of course, designated neutral particles, and the event was not processed in any further detail by the track reconstruction algorithm.

The majority of the events were more complicated than the simple events with a single hit in the front and the rear array.[11] For these more complicated events, the `Analyzer` began by identifying the first layer (i.e., first, second, third, or fourth) in the front array to record a hit; henceforth, we shall refer to the hit(s) in this layer as the "first cluster". If the first cluster contained more than one hit, the highest and lowest hits were identified; such hit patterns were, in all likelihood, the result of an *np*

[11] Single hits in the front and the rear array imply than an incident neutron scattered from the front array to the rear array with the recoil protons stopped in the scintillator where the *np* interaction occurred.

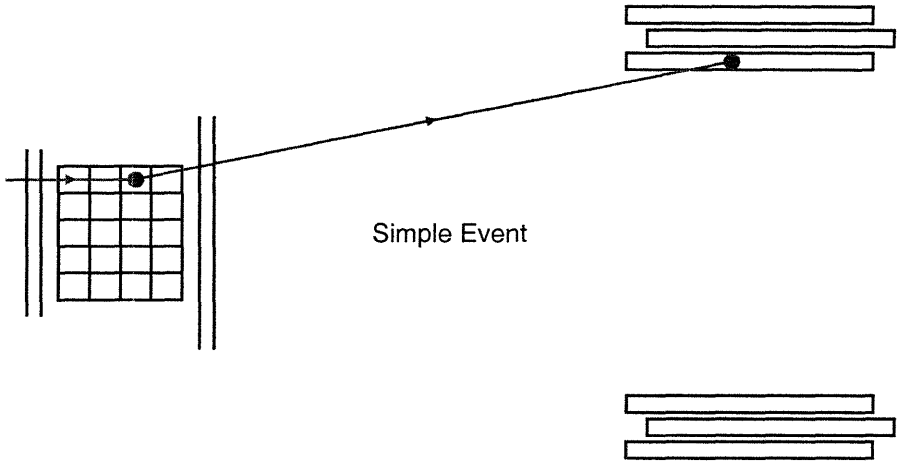

Figure 5-45: (color) Example of a reconstructed track for a simple event in the polarimeter.

or *pp* interaction in one detector followed by the penetration of the recoil proton into the detector located either directly above or below the detector where the primary *np* or *pp* interaction occurred. Accordingly, if the hits occurred in non-contiguous detectors within a layer (i.e., if there was a detector "gap" between the detectors recording hits), a track-reconstruction error condition was assigned to the event.

Next, the `Analyzer` looked for evidence of one or more "missing layers" in the front array (e.g., an event with hits in the first layer and the fourth layer, but no hits in the second or third layers); a missing layer was taken to be evidence for multiple scattering of the incident neutron. If a "second cluster" of hits was not found, the location of the front array scattering vertex was assigned to the highest (lowest) hit in the first cluster if the top (bottom) rear array was hit. If, instead, a second cluster of hits was identified, the `Analyzer` again determined whether the second cluster contained a gap; if a gap was identified, as before, a track-reconstruction error was assigned to the event. The algorithm then attempted to discern whether the second cluster was located either above or below the first cluster; if the second cluster was above (below) the first cluster, the location of the first cluster scattering vertex was assigned to the highest (lowest) hit in the first cluster. Then, if the top (bottom) rear array was hit, the location of the second cluster scattering vertex was assigned to the highest (lowest) hit in the second cluster. Finally, if more than one hit was

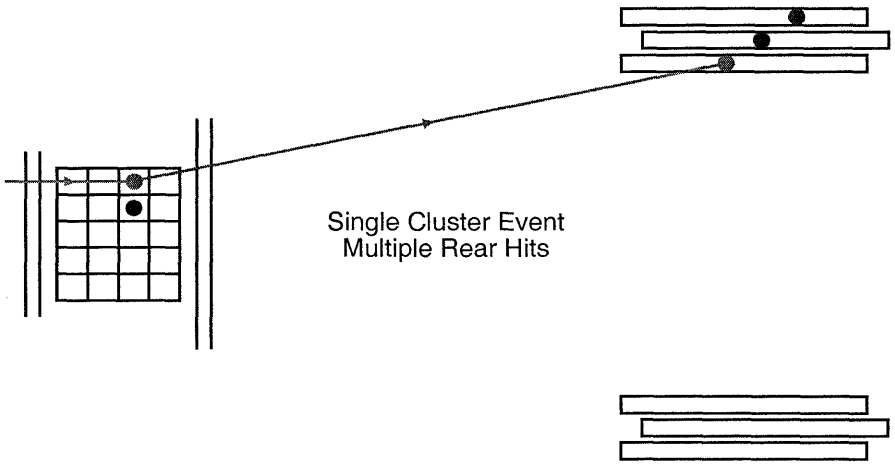

Figure 5-46: (color) Example of a reconstructed track for an event with a single cluster in the front array and multiple hits in the top rear array.

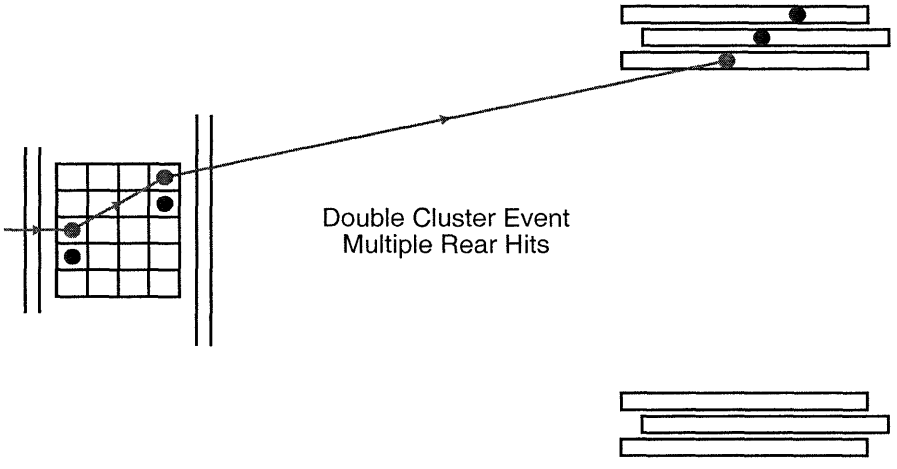

Figure 5-47: (color) Example of a reconstructed track for an event with two clusters in the front array and multiple hits in the top rear array.

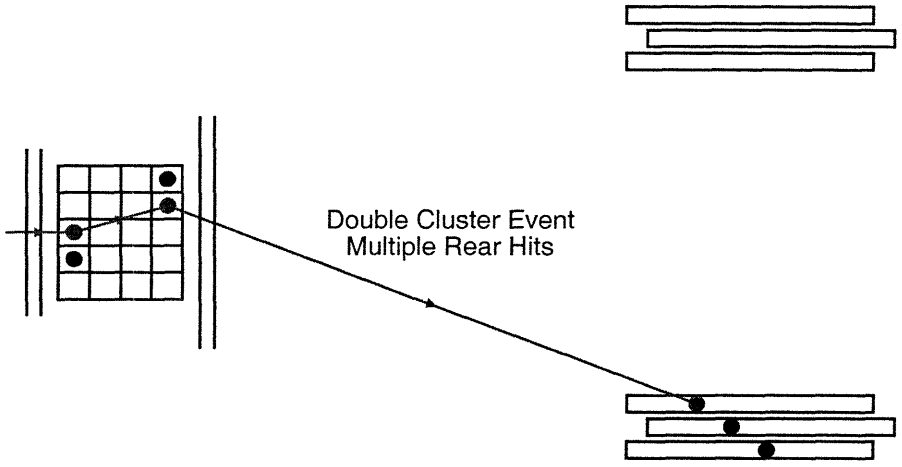

Figure 5-48: (color) Example of a reconstructed track for an event with two clusters in the front array and multiple hits in the bottom rear array.

recorded in either the top or bottom rear array, the hit in the rear array closest in distance to the final scattering vertex in the front array was chosen as the location of the rear array scattering vertex. Several illustrative examples of scattering vertex selection and track reconstruction through the polarimeter are shown in Figs. 5-45 through 5-48.

After the `Analyzer` reconstructed the track through the front array and the rear array, the algorithm checked for hits in the front veto/tagger array that were close to the track of the incident particle. The charge of the incident particle was determined as follows:

- If there were no hits in any of the front veto/tagger detectors, the particle was designated a *neutral particle.*

- If there were hits in the front veto/tagger detectors, the radial distance between the location of the veto/tagger hit and the location of the first scattering vertex in the front array, d, was computed for each veto/tagger hit according to

$$d = \sqrt{(x_{\rm vt} - x_{\rm fr})^2 + (y_{\rm vt} - y_{\rm fr})^2}\ , \tag{5.57}$$

where the x- and y-coordinates refer to the polarimeter basis.

- If a hit in each veto/tagger layer satisfied $d \leq 30$ cm, the particle was designated a *charged particle.*

- If no hits in either veto/tagger layer satisfied $d \leq 30$ cm, the particle was designated a *neutral particle.*

- If a hit in one of the veto/tagger layers satisifed $d \leq 30$ cm but no hits in the other layer satisified this condition, the charge of the particle was declared to be *ambiguous.*

We note that a more rigorous test for the identification of the incident particle's charge was employed during the extraction of the asymmetries from the `.paw` Ntuples created by the `Analyzer`; this test will be discussed in detail later.

Similarly, the charge of the particle detected in the rear array was determined as follows:

- If there were no hits in any of the rear veto/tagger detectors, the particle was tagged a *neutral particle.*

- If there were hits in the rear/veto tagger detectors, the `Analyzer` predicted where hits in the two rear veto/tagger arrays (if both layers existed) should have occurred assuming a straight-line trajectory from the final front array scattering vertex to the rear array scattering vertex. The radial distance between the location of the actual hit and the predicted hit, d, was then computed according to

$$d = \sqrt{(x_{\rm vt} - x_{\rm pred})^2 + (y_{\rm vt} - y_{\rm pred})^2} \ , \tag{5.58}$$

  where, again, the x- and y-coordinates refer to the polarimeter basis.

  - If only one rear veto/tagger layer existed, the particle was tagged a *charged (neutral) particle* if $d \leq 30$ cm ($d > 30$ cm).

  - If both rear veto/tagger layers existed, the particle was tagged a *charged* particle if hits in both layers satisfied $d \leq 30$ cm or a *neutral* particle if no hits in either rear veto/tagger layer satisifed $d \leq 30$ cm. As with the

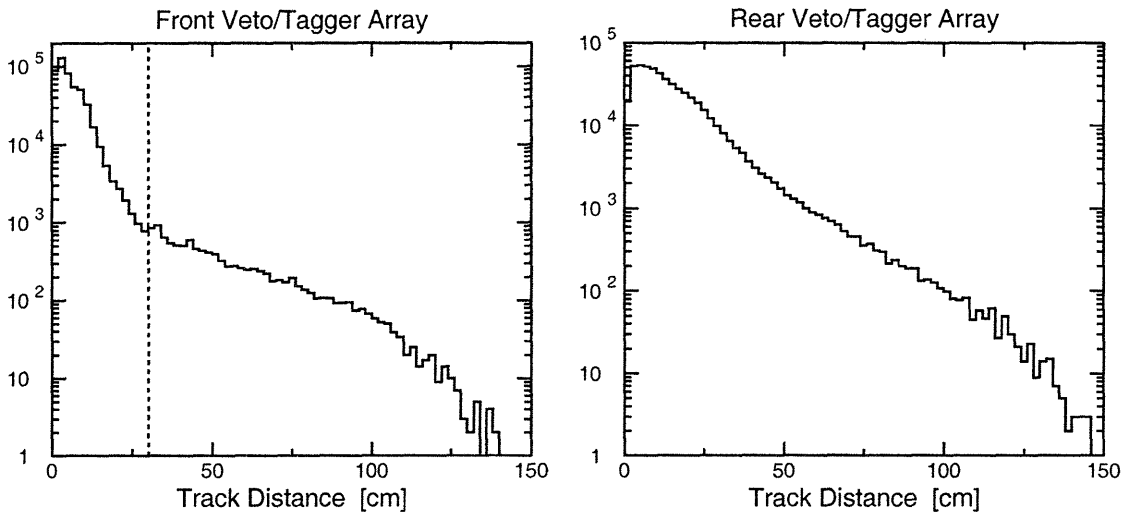

Figure 5-49: Track distance spectra for the front and rear veto/tagger arrays.

front veto/tagger layer, the charge of the particle detected in the rear array was declared to be *ambiguous* if a hit in one of the rear veto/tagger layers satisfied $d \leq 30$ cm but no hits in the other layer satisfied this condition.

The motivation for the choice of 30 cm as the threshold for the identification of a charged particle is illustrated in sample histograms of d for the front and rear veto/tagger arrays shown in Fig. 5-49. Here, we see for the front veto/tagger array a relatively narrow distribution with a significant change in slope around 30 cm; this abrupt change in slope is related to the position resolution in these scintillators. The histogram for the rear veto/tagger array does not contain the same feature (or, at least, is not as visible) as the recoil protons arising from interactions in the front array are widely distributed in angle and can originate anywhere along the track; however, the same 30-cm condition was employed for the rear veto/tagger array as the position resolution for these detectors should have been similar to that for the front veto/tagger array.

5.4.6 Computation of Kinematic and Time-of-Flight Variables

After the tracks through the polarimeter were reconstructed, kinematic and time-of-flight quantities were computed for those events without a track-reconstruction error condition. These calculations can be roughly grouped into three different categories and are described below.

First, the incident particle's momentum and kinetic energy was computed using the position information for the reconstructed vertex in the target, the position information for the first scattering vertex in the front array, and the four-momentum transfer $(\omega, \mathbf{q})$ according to Eq. (5.37). The reconstructed momentum was used to predict the time-of-flight; this predicted value was then compared with the actual time-of-flight, `t_front`, and the difference was stored in the variable cTOF. Then, the scattering angles θ_{nq} and ϕ_{nq}[12], the polar and azimuthal angles of $\mathbf{p}_n$ relative to $\mathbf{q}$ (with ϕ_{nq} defined relative to a horizontal plane) were computed according to

$$\theta_{nq} = \cos^{-1}\left(\hat{\mathbf{q}} \cdot \hat{\mathbf{u}}\right) \ , \qquad \phi_{nq} = \tan^{-1}\left[\frac{\hat{\mathbf{u}} \cdot \hat{\mathbf{q}} \times \left(\hat{\mathbf{y}}_{\mathrm{NPOL}} \times \hat{\mathbf{q}}\right)}{\hat{\mathbf{u}} \cdot \hat{\mathbf{y}}_{\mathrm{NPOL}} \times \hat{\mathbf{q}}}\right] \ , \tag{5.59}$$

where $\hat{\mathbf{q}}$ denotes a unit vector along $\mathbf{q}$, $\hat{\mathbf{u}}$ denotes a unit vector pointing from the reconstructed target vertex to the front array scattering vertex, and $\hat{\mathbf{y}}_{\mathrm{NPOL}}$ is the previously defined polarimeter basis unit vector that is perpendicular to the floor of Hall C.

Second, after computation of the target-to-front array variables described above, the time-of-flight from the front array to the rear array was predicted using the position information for the front array scattering vertex, the rear array scattering vertex, the reconstructed momentum, and the velocity for elastic np scattering, v_{np}, calculated from the equation for T_{np} given in Eq. (5.18). The front-to-rear time-of-flight predicted using v_{np} was compared with the actual front-to-rear time-of-flight,

[12]Here, we use the subscripts nq which specifically imply the scattering angles relative to $\mathbf{q}$ for a neutron. The `Analyzer` was not designed to compute θ_{pq} and ϕ_{pq} as a proper determination of these variables would require a precise model for the deflection of the proton in the Charybdis field.

t_rear − t_front, and the difference was stored as the variable rTOF.[13] Another quantity of interest, the ratio of the reconstructed front-to-rear velocity (computed using the front/rear position information and the actual front-to-rear time of flight) to v_{np} was stored as the variable v_{ratio}. Then, the front-to-rear scattering angles defined relative to the incident neutron's momentum, θ_{scat} and ϕ_{scat}, (with ϕ_{scat} defined relative to the horizontal) were computed using Eq. (5.59) with $\mathbf{q} \rightarrow \hat{\mathbf{p}}_n$ and $\hat{\mathbf{u}}$ now denoting a unit vector pointing from the front array scattering vertex to the rear array scattering vertex.

Last, the missing momentum, $\mathbf{p}_{\text{miss}}$, missing energy, E_{miss}, and missing mass, m_{mass}, were computed according to

$$\mathbf{p}_{\text{miss}} = \mathbf{q} - \mathbf{p}_n \ , \tag{5.60}$$

$$E_{\text{miss}} = (m_d + \omega) - (T_n + m_n) \ , \tag{5.61}$$

$$m_{\text{miss}} = \sqrt{E_{\text{miss}}^2 - |\mathbf{p}_{\text{miss}}|^2} \ , \tag{5.62}$$

and stored.

5.4.7 Sample NPOL Reconstruction and Tracking Results

We now present a number of sample NPOL reconstruction and tracking results computed by the E93-038 Analyzer. A minimal set of cuts designed to eliminate hadrons in the HMS, scattering from the target end cell walls, protons incident on the polarimeter (for physics distributions), and events with track-reconstruction error conditions in the polarimeter were applied to the spectra shown in this subsection. We do not present any time-of-flight spectra (i.e., cTOF and rTOF spectra) in this subsection; these will be discussed in extensive detail in later sections of this chapter.

[13] It should be noted that the rTOF calculation described here was conducted for events without a second cluster. For those events with a second cluster, rTOF was computed using the position and time information for the two clusters in the front array. Such a calculation avoids depolarization (due to the second scattering), but sacrifices resolution; however, as will be discussed very shortly, asymmetries were only extracted from events with a single cluster in the front array.

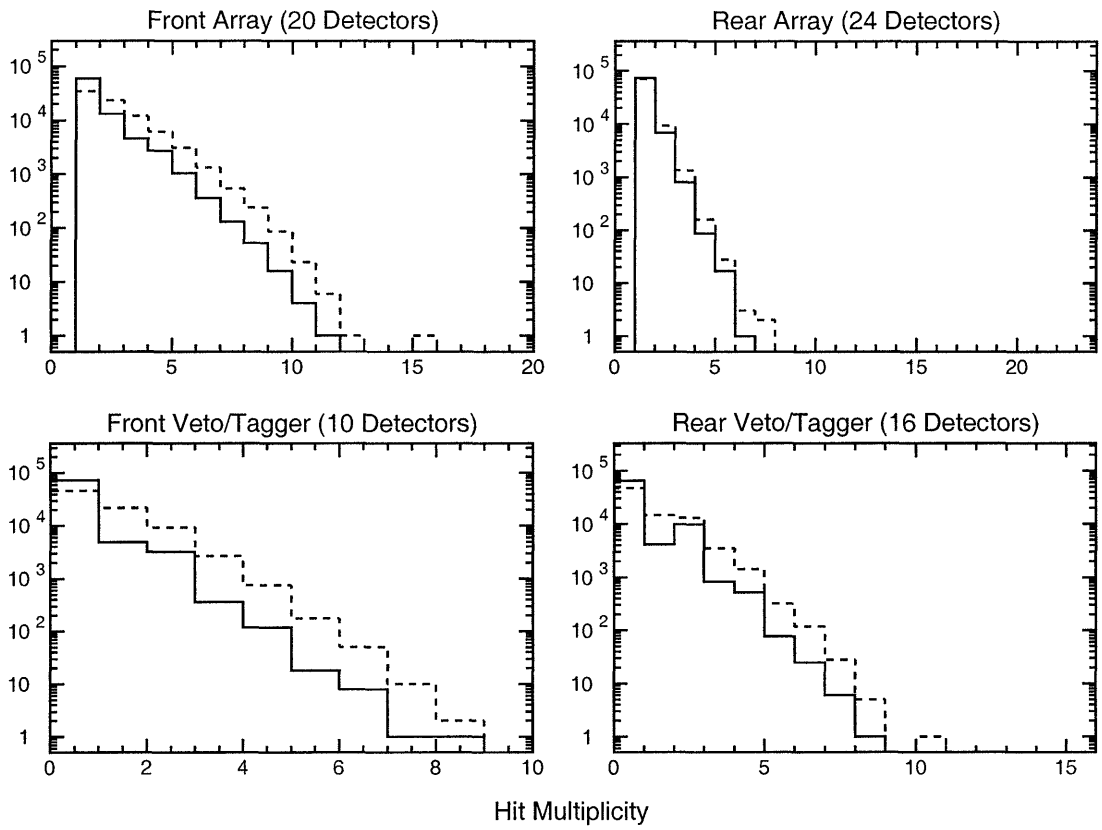

Figure 5-50: Hit multiplicities in the polarimeter for the front and rear array detectors and the front and rear veto/tagger array detectors. The multiplicities before (after) the position and mean-time filtering are presented as the histograms with dashed (solid) borders.

Hit Multiplicities and Pulse Height Distributions

We begin by showing in Fig. 5-50 sample histograms of hit multiplicities (i.e., the number of detectors recording a hit) for the front and rear array detectors and front and rear veto/tagger array detectors. Here, the hit multiplicities before and after the position and mean-time filtering are presented as the histograms with dashed and solid borders, respectively; we see that the position and mean-time filtering eliminated a substantial number of the hits.

Next, pulse height spectra for the front and rear array detectors at each of the Q^2 points are shown in Figs. 5-51 and 5-52. The hardware thresholds of 4 (10) MeVee for the front (rear) array detectors are shown as the dashed lines; a small amount of leakage through the constant-fraction discriminators can be seen. The abnormal

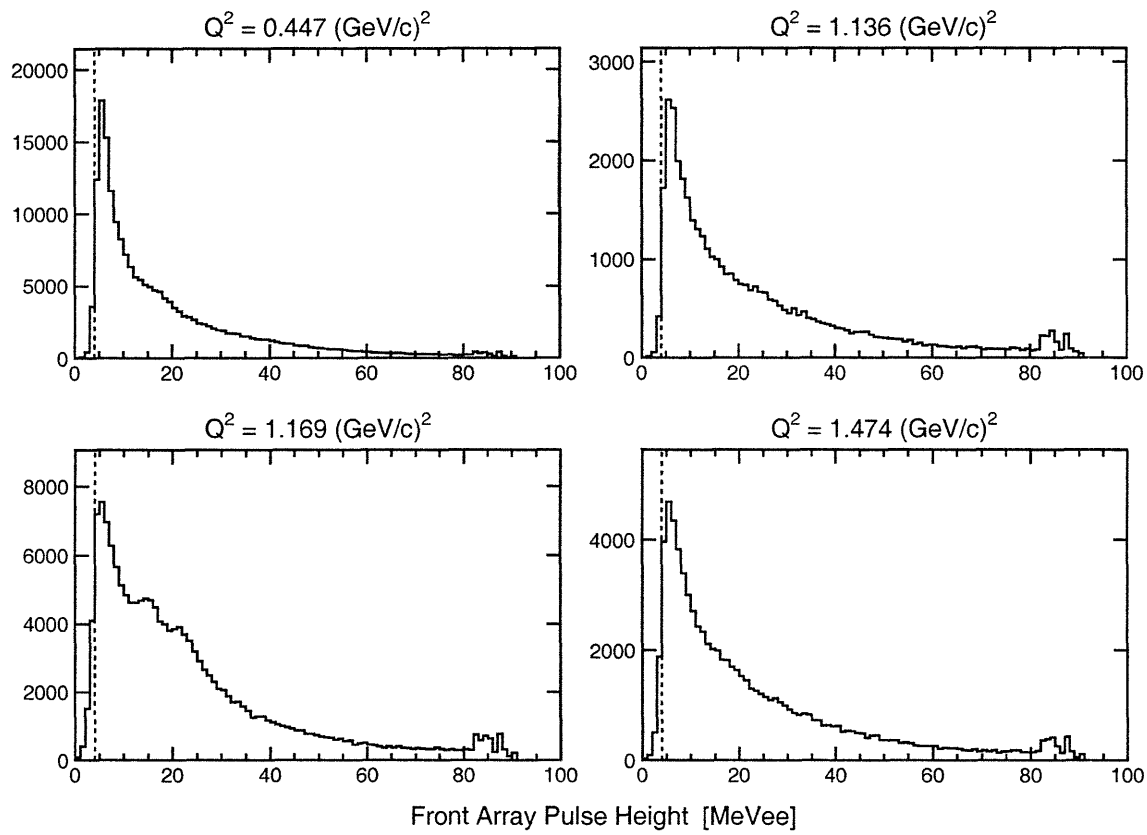

Figure 5-51: Pulse height spectra for the front array detectors with a minimal set of cuts. The dashed lines denote the hardware thresholds of 4 MeVee.

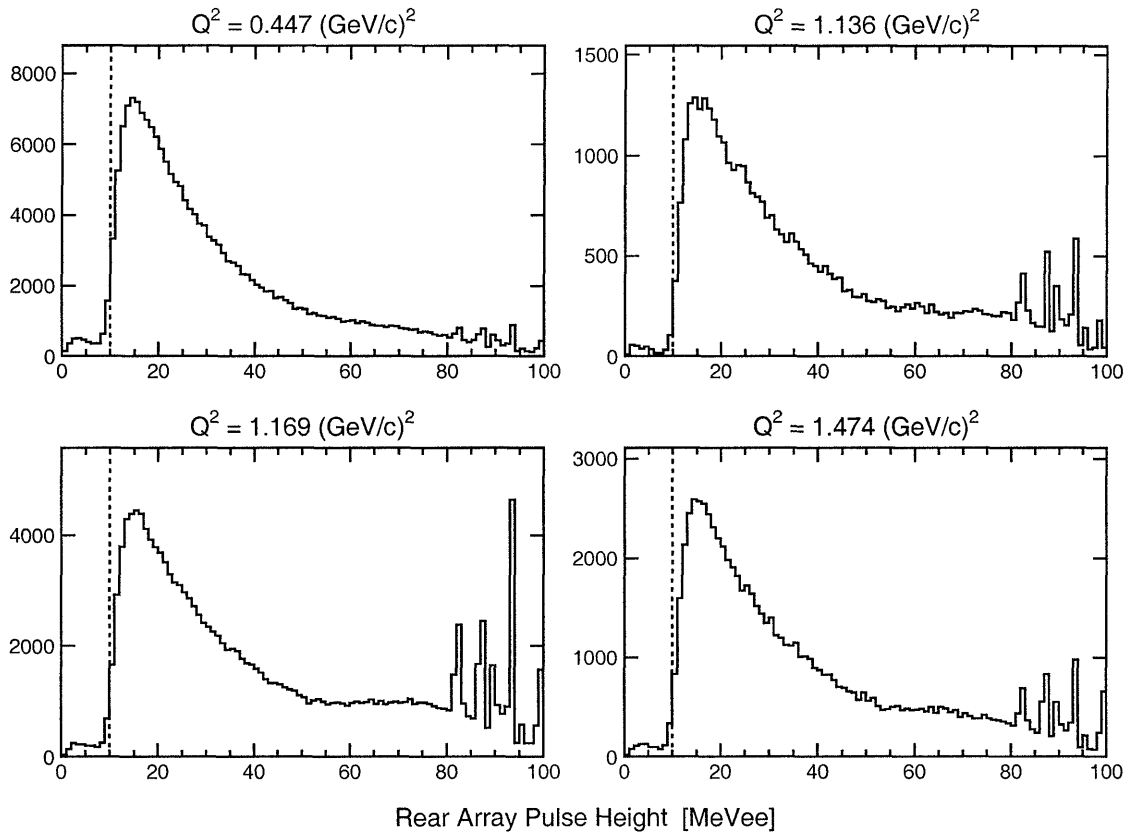

Figure 5-52: Pulse height spectra for the rear array detectors with a minimal set of cuts. The dashed lines denote the hardware thresholds of 10 MeVee.

structure (i.e., the spikes and shoulders) seen in the spectra at large pulse height values, $\gtrsim$ 60 MeVee, is due to overflow in the ADCs.

Incident Kinematic Distributions

Neutron kinetic energy distributions for each of the Q^2 points are shown in Fig. 5-53; the secondary peaks at values of T_n greater than the (nominal) central values (indicated by the dashed lines) are due to the inelastic excitations seen in the HMS $\Delta p/p$ spectra.

Next, in Figs. 5-54 through 5-56, we show a decomposition of the three-momentum into polarimeter basis x-, y- and z-components. Here, in the histograms of the x-component, we see a (fairly) uniform distribution with abrupt edges due to the polarimeter's limited horizontal acceptance; as expected, the widths of these distri-

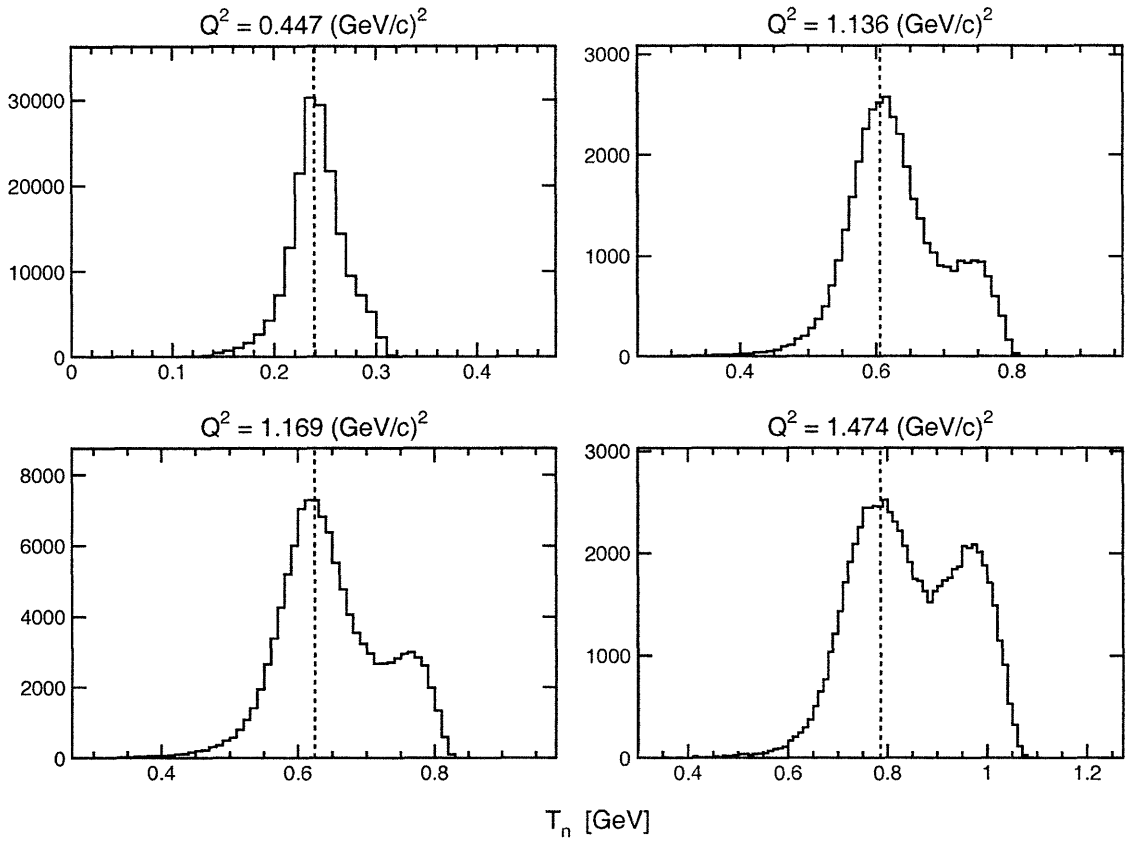

Figure 5-53: NPOL T_n distributions with a minimal set of cuts. The dashed lines indicate the central values of the kinetic energy (239 MeV, 606 MeV, 624 MeV, and 786 MeV).

butions increase with decreasing time-of-flight. In the histograms of the y-component, the segmentation of the front array is readily apparent (as the three-momentum is calculated using only position information and electron kinematics), and in the histograms of the z-component, we see the same secondary peaks that are present in the T_n spectra.

Histograms of θ_{nq} and ϕ_{nq} for the four Q^2 points are shown in Figs. 5-57 and 5-58, respectively. Here, we see that the range of accepted θ_{nq} values increases with Q^2 (i.e., with T_n); also, as expected, we see that there are, within the resolution of the reconstruction, no events at $\theta_{nq} = 0°$ (i.e., perfect quasifree emission). The ϕ_{nq} values, of course, span the entire $[-180°, 180°]$ range.

Finally, we show histograms of $|\mathbf{p}_{\rm miss}|$ distributions in Fig. 5-59 and two-dimensional histograms of $|\mathbf{p}_{\rm miss}|$ versus the invariant mass, W, in Fig. 5-60. Here, we see the ac-

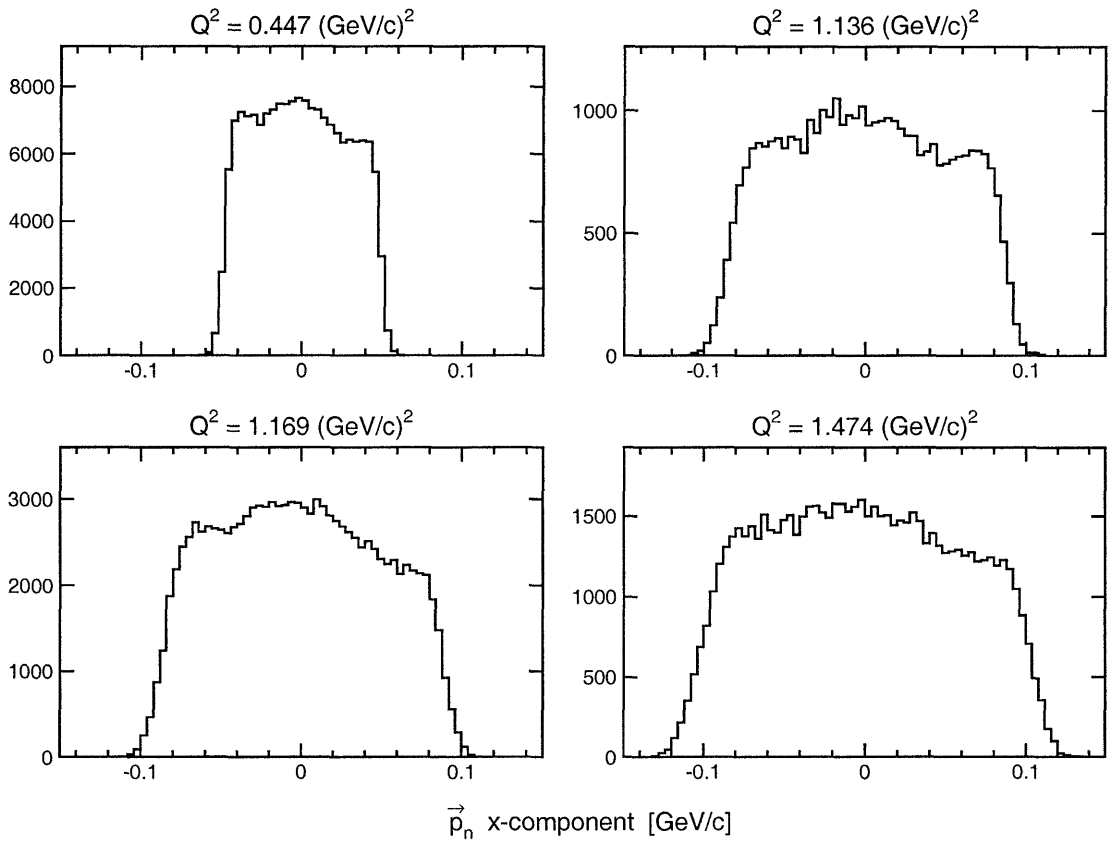

Figure 5-54: NPOL $\mathbf{p}_n$ x-component distributions with a minimal set of cuts.

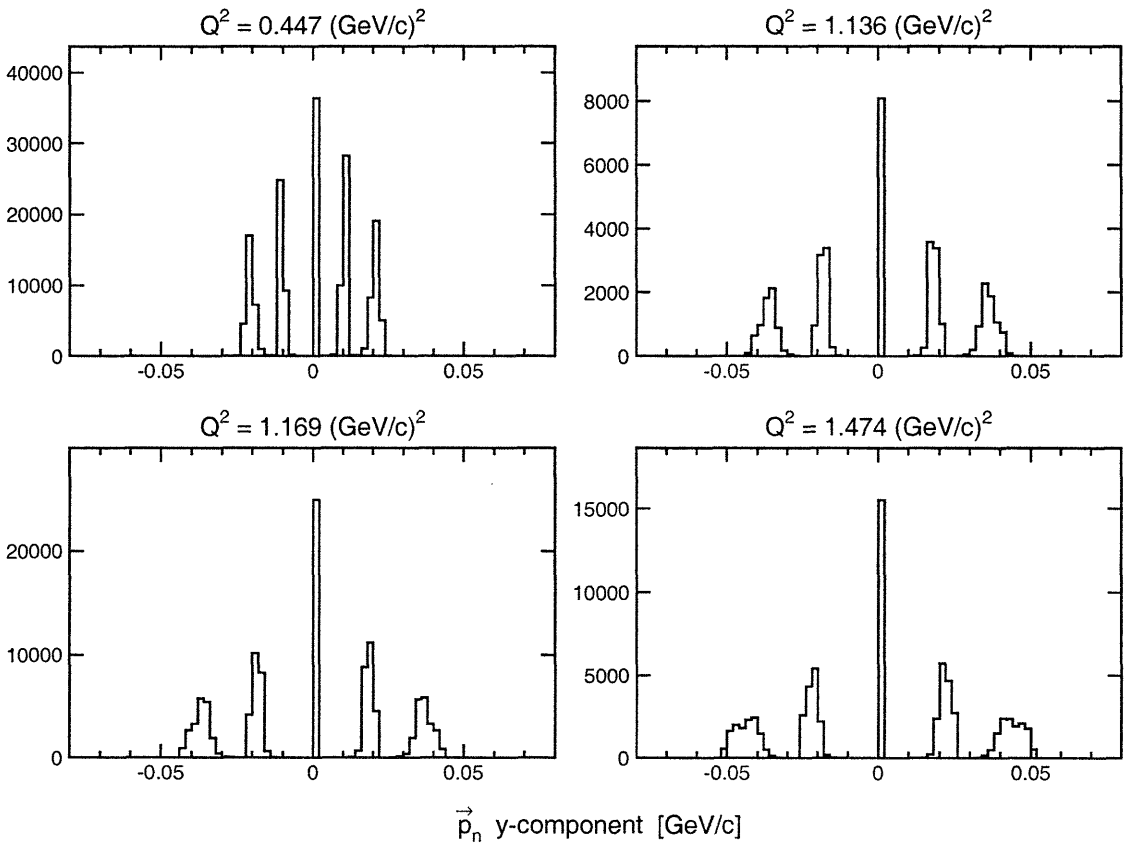

Figure 5-55: NPOL $\mathbf{p}_n$ y-component distributions with a minimal set of cuts.

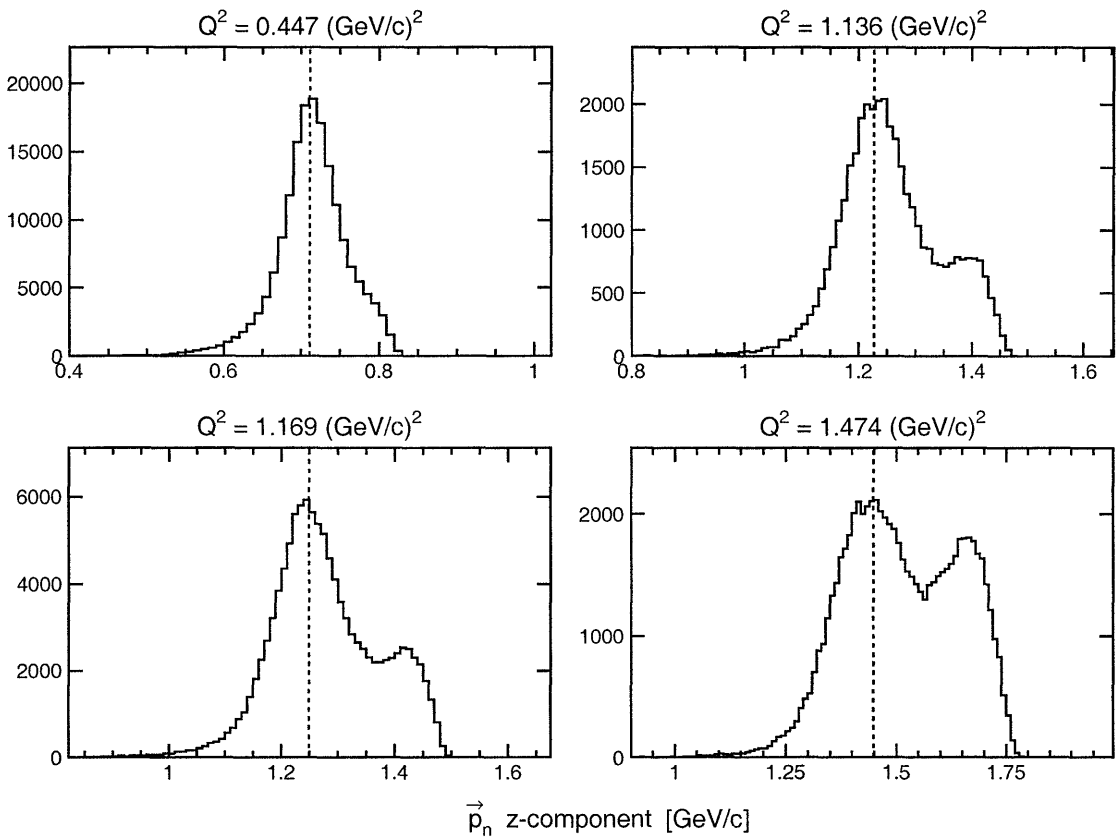

Figure 5-56: NPOL $\mathbf{p}_n$ z-component distributions with a minimal set of cuts. The dashed lines indicate the central value of $|\mathbf{p}_n|$.

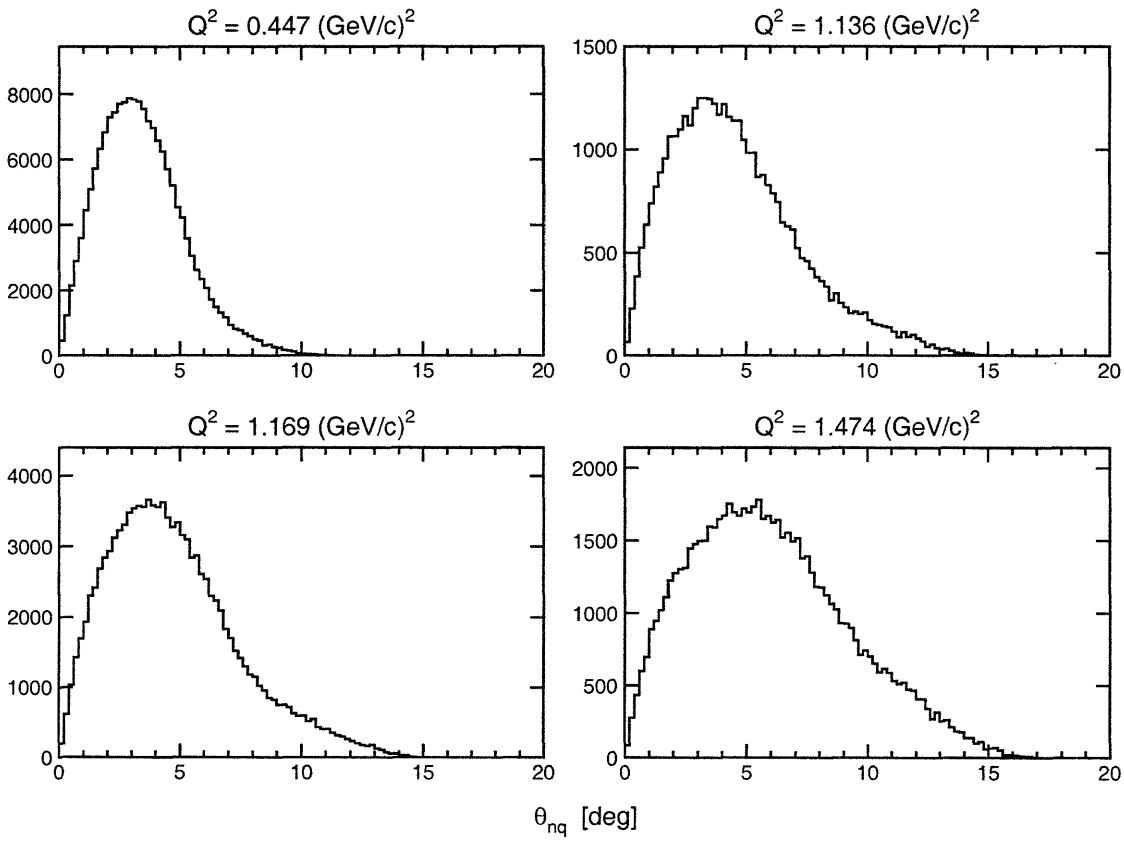

Figure 5-57: NPOL θ_{nq} distributions with a minimal set of cuts.

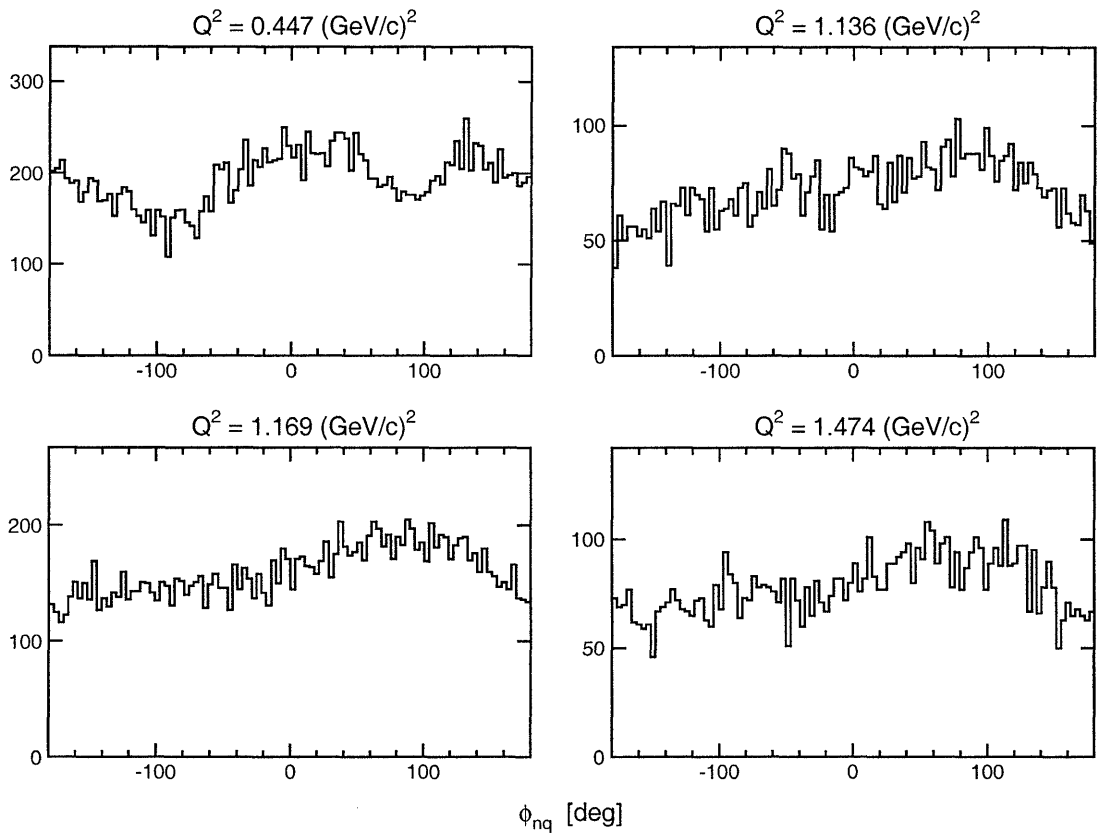

Figure 5-58: NPOL ϕ_{nq} distributions with a minimal set of cuts.

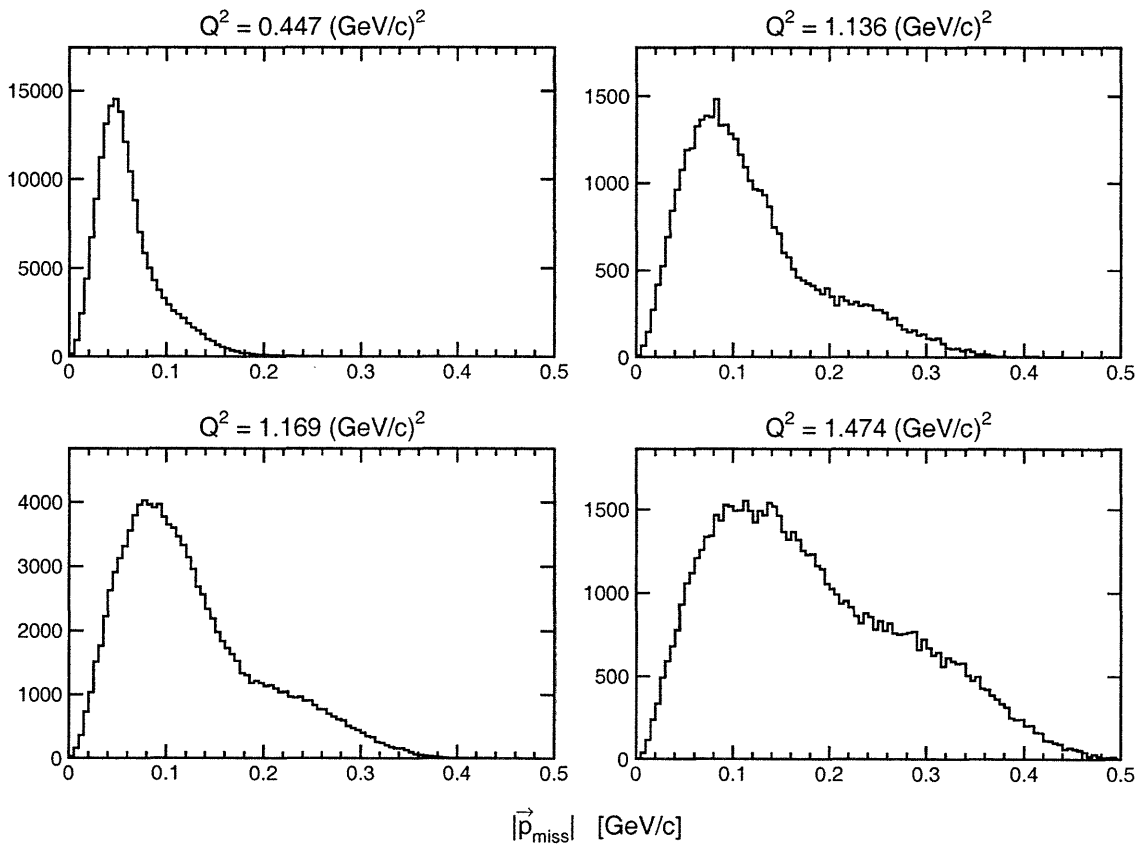

Figure 5-59: $|\mathbf{p}_{\mathrm{miss}}|$ distributions with a minimal set of cuts.

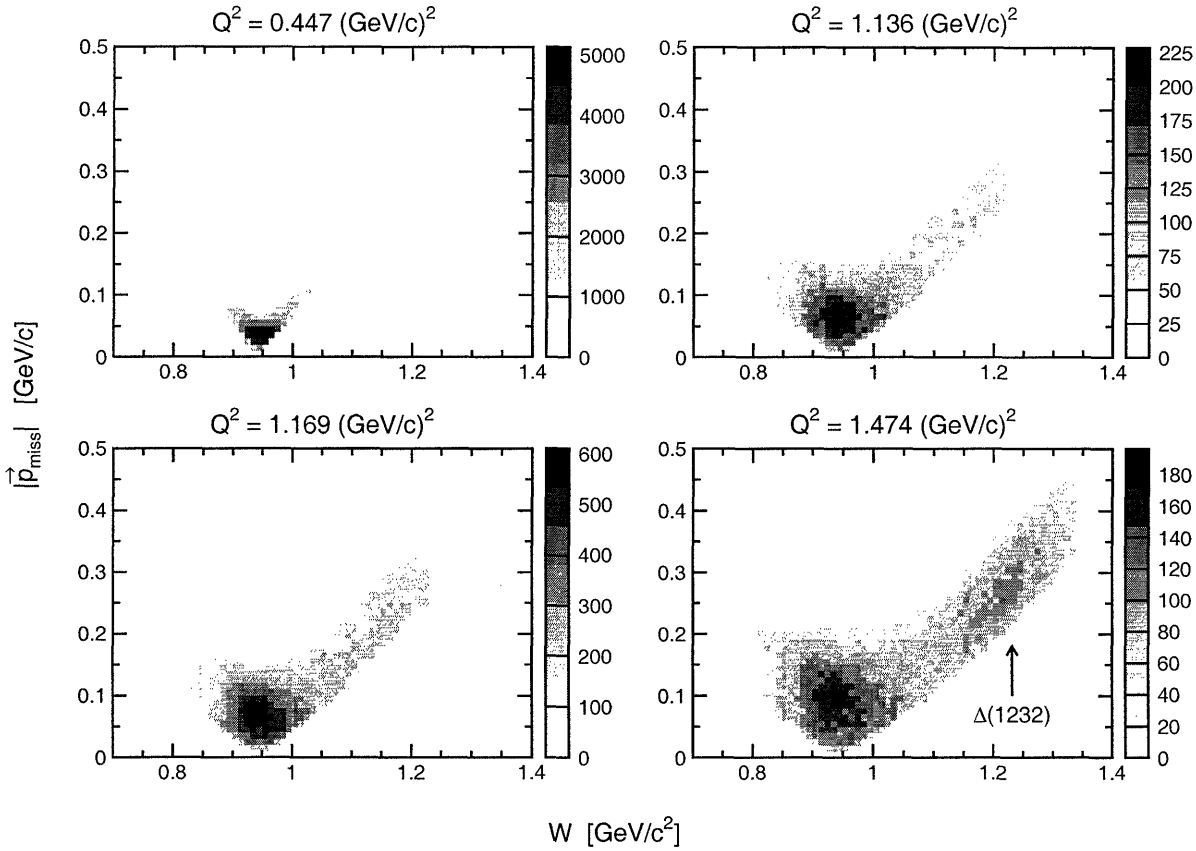

Figure 5-60: (color) $|\mathbf{p}_{\rm miss}|$ versus W distributions with a minimal set of cuts. The $\Delta(1232)$ resonance is prominent at large missing momenta in the $Q^2 = 1.474$ (GeV/c)^2 distribution.

ceptance was sensitive to missing momenta ranging up to ~500 MeV/c at $Q^2 = 1.474$ (GeV/c)^2. As can clearly be seen in the two-dimensional histograms, the events of interest, the quasielastic events, are restricted to $|\mathbf{p}_{\rm miss}| \lesssim$ 100–150 MeV/c; in general, events with larger values of $|\mathbf{p}_{\rm miss}|$ are associated with pion-production. For $W \gtrsim 1$ GeV/c^2, we see an almost linear relation between $|\mathbf{p}_{\rm miss}|$ and W.

NPOL Scattering Distributions

In Figs. 5-61 and 5-62, we show distributions of $\theta_{\rm scat}$ and $\phi_{\rm scat}$, respectively. The $\theta_{\rm scat}$ distributions peak at ~18° (roughly the scattering angle from the center of the front array to the center of either the top or bottom rear array). $\phi_{\rm scat} < 0$ (> 0) corresponds to detection of a particle in the bottom (top) rear array. The small number of events

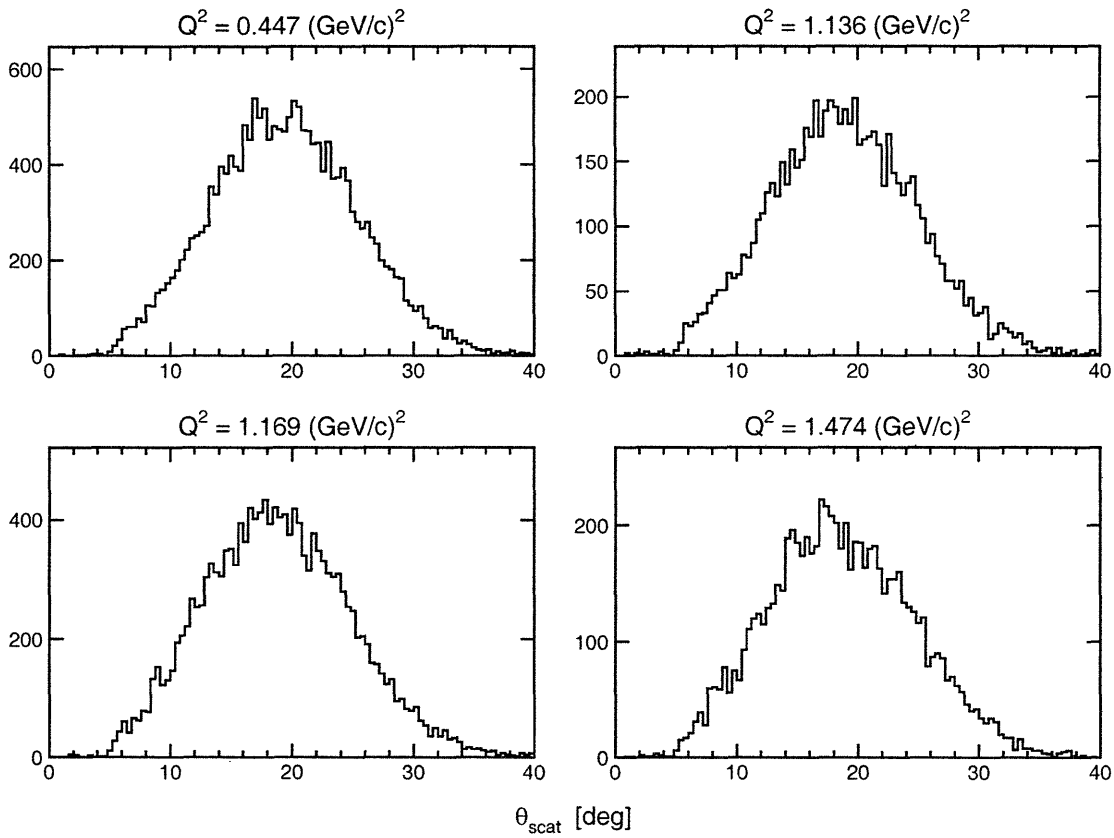

Figure 5-61: NPOL $\theta_{\rm scat}$ distributions with a minimal set of cuts.

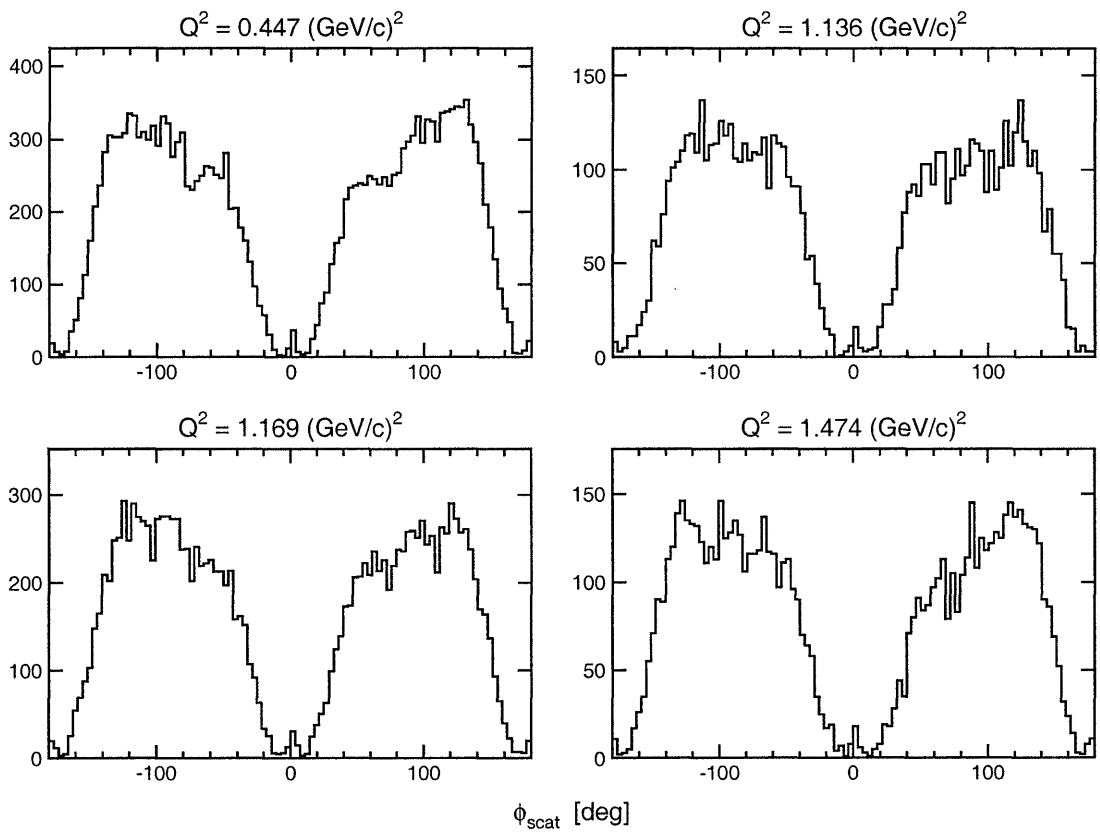

Figure 5-62: NPOL ϕ_{scat} distributions with a minimal set of cuts.

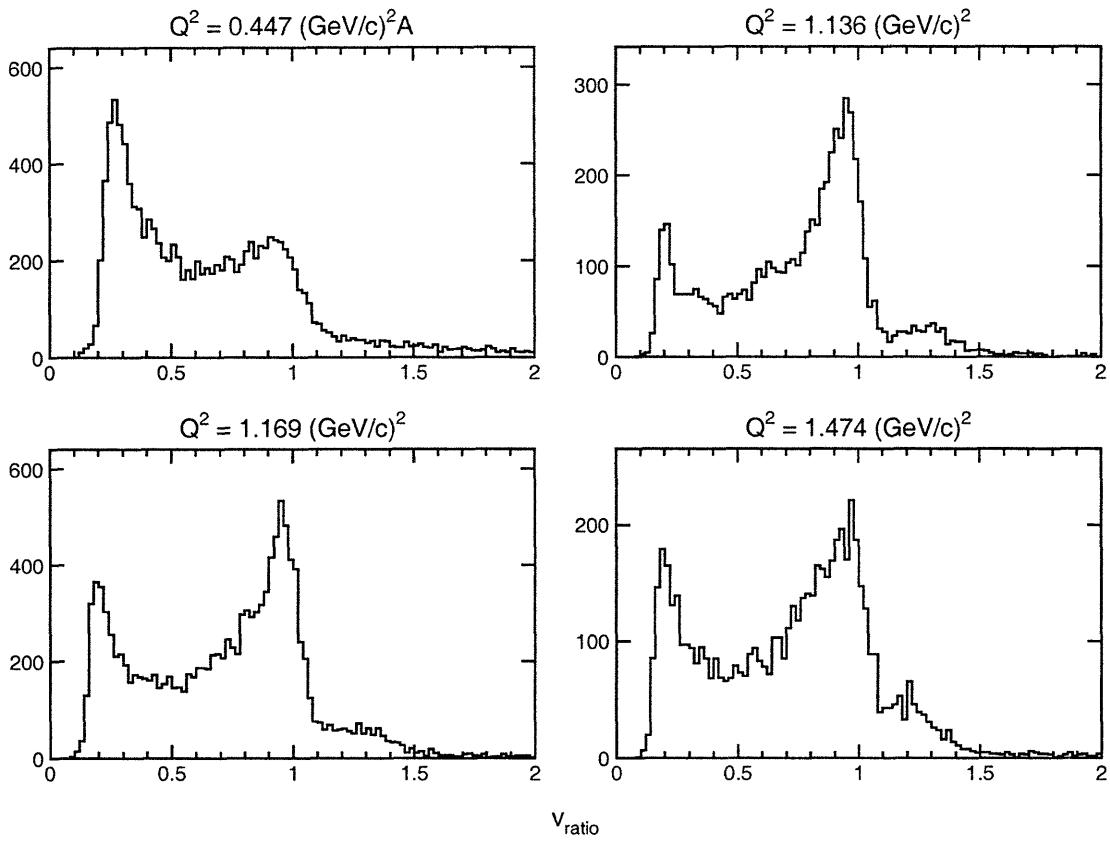

Figure 5-63: NPOL v_{ratio} distributions with a minimal set of cuts.

at $\phi_{\text{scat}} \sim 0°$ are, of course, unphysical and were eliminated with later cuts.

Distributions of v_{ratio} are shown in Fig. 5-63; here, we see a sharp quasifree peak at $v_{\text{ratio}} \sim 1$ in addition to a substantial inelastic background.

5.5 Data Selection Criteria, Processing, and Cuts

In this section, we discuss the criteria that were established for the selection of quality data (i.e., "good runs"), we identify the individuals who were responsible for the data processing, and we present the complete list of cuts that were applied to the data for the final extraction of the time-of-flight spectra and the scattering asymmetries in the polarimeter.

5.5.1 Selection Criteria

Only those runs that satisfied the following criteria were employed for the production analysis:

- No problems with the HMS equipment (i.e., magnet trips, detector failures, etc.) during the course of a run.
- No problems with the delivery of the electron beam (i.e., accelerator trips, unstable beam parameters, etc.) during the course of a run.
- No problems with the data acquisition system (i.e., DAQ or ROC failures, etc.).
- No problems with the cryogenic target (i.e., monitoring system failures, large temperature fluctuations, etc.).
- No problems with the NPOL detectors or the Charybdis magnet (i.e., detector trips, fluctuating currents in Charybdis, etc.).
- High statistics (i.e., greater than 500,000 events).[14]

This listing of criteria is not, of course, exhaustive; additional problems may have have resulted in the designation of a run as unsuitable for the production analysis.

5.5.2 Data Sets

The quantity of data which passed the above selection criteria at each of the Q^2 points are summarized in Table 5.3; there, we list the number of "good runs" and accumulated charge for each of the Q^2 points and precession angles. In addition, we list the quantity of available data with the $\lambda/2$-plate either "in" or "out".

[14]The threshold of 500,000 events was somewhat arbitrary but well motivated. In general, a typical run consisted of either one, two, or three million events; therefore, early termination was usually indicative of some type of problem. The quality of the documentation concerning the running conditions was not uniform; therefore, this threshold functioned as a "safety net".

Central Q^2 $[(\mathrm{GeV}/c)^2]$	χ	Total Data	$\lambda/2$ Out Data	$\lambda/2$ In Data
0.447	$-40°$	77 [25.122]	45 [13.736]	32 [11.386]
0.447	$+40°$	47 [14.569]	36 [10.371]	11 [4.198]
0.447	Total	124 [39.691]	81 [24.107]	43 [15.584]
1.136	$0°$	450 [27.587]	291 [18.014]	159 [9.573]
1.136	$-90°$	41 [4.701]	23 [2.687]	18 [2.014]
1.136	$+90°$	38 [4.158]	24 [2.618]	14 [1.540]
1.136	Total	529 [36.446]	338 [23.319]	191 [13.127]
1.169	$-40°$	25 [7.006]	25 [7.006]	0 [0]
1.169	$+40°$	16 [6.321]	16 [6.321]	0 [0]
1.169	Total	41 [13.327]	41 [13.327]	0 [0]
1.474	$0°$	209 [26.239]	126 [15.563]	83 [10.676]
1.474	$-90°$	21 [4.097]	14 [2.756]	7 [1.341]
1.474	$+90°$	17 [4.098]	12 [2.688]	5 [1.410]
1.474	Total	247 [34.434]	152 [21.007]	95 [13.427]
1.474	$-40°$	91 [20.803]	53 [13.150]	38 [7.653]
1.474	$+40°$	86 [16.762]	43 [8.163]	43 [8.599]
1.474	Total	177 [37.565]	96 [21.313]	81 [16.252]
ALL	TOTAL	1118 [161.463]	708 [103.073]	410 [58.390]

Table 5.3: Quantity of data employed for the production analysis. The number of runs [accumulated charge in Coulombs] is listed outside [inside] the brackets.

5.5.3 Data Processing

The data listed in Table 5.3 were processed within a collaborative effort involving thesis students, postdoctoral research associates, and other research associates. Those individuals responsible for the data selection (i.e., determination of "good runs"), calibrations, creation of the `.rzdat` files (E93-038 `ENGINE` output), creation of the `.paw` files (`Analyzer` output), and the final extraction of the scattering asymmetries in the polarimeter (`casym` asymmetry program output; to be discussed later) are listed in Table 5.4.

Those responsible for the production of the "official results" (i.e., those reported in this thesis) are listed in this table; in addition, an independent analysis of the $Q^2 = 0.447$ $(\mathrm{GeV}/c)^2$ and 1.136 $(\mathrm{GeV}/c)^2$ data sets with alternative analysis codes

Central Q^2 $[(\mathrm{GeV}/c)^2]$	χ	Data Selection	Time Calibration	E93-038 ENGINE Output	Analyzer Output	Asymmetry Extraction
0.447	$\pm 40°$	E. Crouse[1]	E. Crouse	E. Crouse	E. Crouse	I. Semenova[2]
1.136	$0°$, $\pm 90°$	B. Plaster	B. Plaster	B. Plaster	B. Plaster	B. Plaster
1.169	$\pm 40°$	B. Plaster	B. Plaster	B. Plaster	B. Plaster	B. Plaster
1.474	$0°$, $\pm 90°$	W. Tireman[3]	W. Tireman	W. Tireman	W. Tireman	A. Semenov[4]
1.474	$\pm 40°$	E. Crouse	E. Crouse	E. Crouse	E. Crouse	A. Semenov

[1] Erick Crouse was a thesis student at The College of William and Mary.
[2] Irina Semenova was a research associate at Kent State University.
[3] William Tireman was a thesis student at Kent State University.
[4] Andrei Semenov was a postdoctoral research associate at Kent State University.
Note: All pulse height calibrations were performed by William Tireman.

Table 5.4: Individuals responsible for the various steps of the final analysis reported in this thesis.

was conducted by Tajima[15] [412, 413]. We refer the reader to [413] for a complete description of this alternative analysis procedure.

5.5.4 Cuts for Extraction of Time-of-Flight Spectra

A complete listing of the final cuts that were applied to the data for the final extraction of the time-of-flight spectra, cTOF and rTOF, are listed in Table 5.5. Only Type 3 HMS-NPOL coincidence events were, of course, employed for the final production analysis; the remaining cuts can be roughly grouped into four different categories: target variable cuts, HMS variable cuts, NPOL variable cuts, and $^2\mathrm{H}(e,e'n)$ reaction cuts.

First, for the target variables, z_{beam} was required to satisfy $|z_{\mathrm{beam}}| \leq 7$ cm in order to suppress scattering events from the target end cell walls. Also, events with unreasonable reconstructed values of x'_{tar} and y'_{tar} were eliminated. The motivation for these cuts should be apparent via inspection of Figs. 5-12 and 5-13.

Second, for the HMS variables, the values of x_{coll} and y_{coll} computed according to Eqs. (5.12) and (5.12) were required to fall within the collimator acceptance, and events with large track reconstruction χ^2 values were eliminated. Hadrons in the HMS were suppressed via cuts on the number of photoelectrons detected in the Čerenkov

[15] Shigeyuki Tajima was a thesis student at Duke University.

Variable	Cut	Comment
General		
Event Type	$= 3$	select HMS-NPOL coincidence events
Target Variables		
$\lvert z_{\text{beam}}\rvert$	≤ 7 cm	suppress scattering from target end cell walls
$\lvert x'_{\text{tar}}\rvert$	≤ 0.07	suppress unreasonable reconstructed values of x'_{tar}
$\lvert y'_{\text{tar}}\rvert$	≤ 0.03	suppress unreasonable reconstructed values of y'_{tar}
HMS Variables		
$(x_{\text{coll}}, y_{\text{coll}})$	within collimator	suppress unreasonable reconstructed values of $(x_{\text{coll}}, y_{\text{coll}})$
Track Reconstruction χ^2	≤ 50	select reasonable tracks through the HMS drift chambers
Čerenkov Photoelectrons	≥ 2	suppress hadrons in the HMS
$E_{\text{shower}}/\lvert\mathbf{p}_{\text{HMS}}\rvert$	$\in [0.7, 1.4]$	suppress hadrons in the HMS
β_{HMS}	$\in [0.7, 1.3]$	eliminate unreasonable velocities in the HMS
$\Delta p/p$	$\in [-3\%, 5\%]$	select events near the quasielastic peak
NPOL Variables		
Track Reconstruction	no errors	eliminate bad tracks through the polarimeter
Front Array Pulse Height	≥ 8 MeVee	suppress low-energy background events in the front array
Rear Array Pulse Height	≥ 20 MeVee	suppress low-energy background events in the rear array
|Mean Time| for Front Array Hit	≤ 5 ns	suppress neutrons originating from charge-exchange processes in the lead curtain[1]
θ_{scat}	$\in [5°, 35°]$ or $[5°, 30°]$	$35°$ for $Q^2 = 0.447$ (GeV/c)^2, $30°$ for other Q^2 points; see text for motivation
^{2}H$(e, e'n)$ Reaction Variables		
$\lvert\mathbf{p}_{\text{miss}}\rvert$	≤ 100 MeV/c	suppress pion-production events
W	≤ 1.04 GeV/c^2	suppress pion-production events

[1] As will be discussed in more detail later, incident protons may convert into neutrons via a two-step $^2\text{H}(\vec{e}, e'\vec{p})$+Pb$(\vec{p}, \vec{n})$ charge-exchange reaction in the lead curtain ahead of the steel collimator. The protons will, in general, degrade in energy before the charge-exchange reaction; therefore, the mean times for such events will, in general, fall outside of the $[-5, 5]$ ns mean-time window for normal $^2\text{H}(\vec{e}, e'\vec{n})$ events.

Table 5.5: Cuts for the final extraction of the cTOF and rTOF time-of-flight spectra.

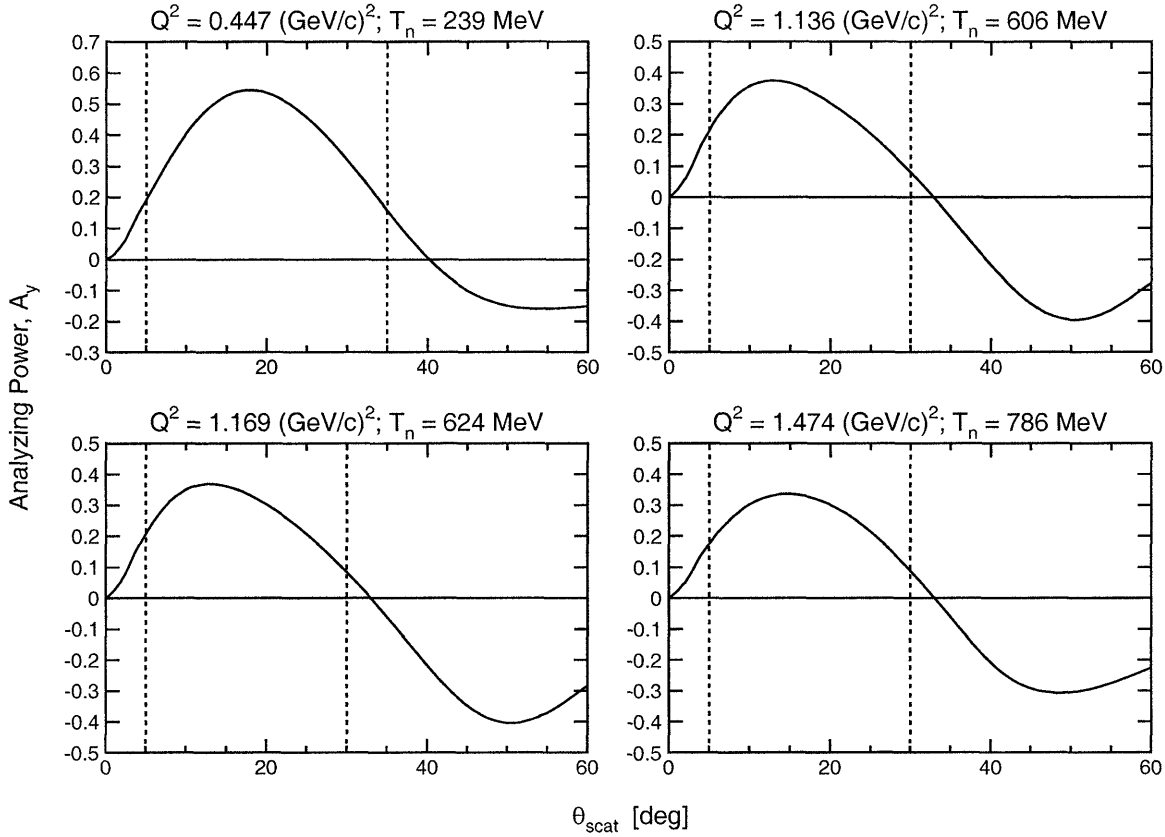

Figure 5-64: Analyzing powers for 239, 606, 624, and 786 MeV np scattering computed as a function of the scattering angle by the SAID [188] code. The dashed lines denote the cut on $\theta_{\rm scat}$.

detector and on the ratio of the calorimeter energy to the measured momentum, $E_{\rm shower}/|\mathbf{p}_{\rm HMS}|$. Finally, low velocity $\beta_{\rm HMS}$ events were eliminated, and events away from the quasielastic peak were eliminated via a cut on $\Delta p/p$.

Third, for the NPOL variables, events with track reconstruction error conditions were eliminated. Software thresholds of 8 (20) MeVee designed to eliminate low-energy background were applied to the front (rear) array pulse heights. Also, to suppress lower-energy neutrons originating from charge-exchange reactions in the lead curtain ahead of the collimator (see the footnote in the table), the mean time for the primary hit in the front array was required to satisfy $|\texttt{td}| \leq 5$ ns.

Last, the front-to-rear scattering angle, $\theta_{\rm scat}$ was required to satisfy $\theta_{\rm scat} \in [5°, 35°]$ at $Q^2 = 0.447$ (GeV/c)^2 and $\theta_{\rm scat} \in [5°, 30°]$ at the other Q^2 points. The motivation

for the lower value of the cut, 5°, can clearly be seen via inspection of Fig. 5-61. The motivation for the upper value of the cut, 30° or 35°, is not as obvious. In Fig. 5-64, the analyzing powers, A_y, for np scattering computed by the code SAID [188] as a function of $\theta_{\rm scat}$ are plotted for the central values of T_n at each of the Q^2 points. Here, we see that A_y becomes zero or even negative beyond the upper threshold of 30° or 35°. Inclusion of such events would dilute the measured scattering asymmetry; therefore, these events were eliminated.

Last, two ^{2}H$(e,e'n)$ reaction-specific variables, $|\mathbf{p}_{\rm miss}|$ and W, were required to satisfy $|\mathbf{p}_{\rm miss}| \leq 100$ MeV/c and $W \leq 1.04$ GeV/c^2; these cuts were intended to suppress pion-production events and the motivation for the choice of thresholds is readily apparent via inspection of Fig. 5-60. We will re-address the choice of these cuts in Section 6.3.4.

Finally, we note that no cuts were placed on Q^2; instead, as will be discussed in extensive detail later, the acceptance-averaging procedure accounted for the finite Q^2 acceptance.

5.6 Time-of-Flight Spectra, Event Types, and Extraction of Asymmetries

We begin this section with a description of another E93-038 specific code, the casym asymmetry program, that was developed to extract the scattering asymmetries in the polarimeter from the time-of-flight spectra. We present sample time-of-flight spectra for those events satisfying the cuts listed in the previous section, we discuss the various event types seen in our data, and we discuss the extraction of the asymmetries from the time-of-flight data. We then conclude this section by presenting the final asymmetry data for each of the Q^2 points.

5.6.1 Overview of the casym Asymmetry Program

The casym asymmetry program code was written entirely in FORTRAN by Semenov [414].

The `casym` program began with a series of initialization routines that read user-specified cuts for various kinematic variables from an `ASCII` input file and initialized an output `HBOOK` file for various kinematic distributions and time-of-flight spectra. After the cuts were read and histograms were initialized, `casym` began processing the event-by-event data written to the `.paw` files by the `Analyzer`. Each event was then subjected to the cuts listed in the previous section of this chapter and to a stringent test for the determination of the incident particle's charge; a description of this incident charged particle test is as follows:

- The (polarimeter basis) y-coordinate for the front array scattering vertex, $y_{\rm fr}$, was determined and compared with the y-coordinate for each hit (if any existed) in the front veto/tagger array, $y_{\rm vt}$.

- If the vertical distance between the front array scattering vertex and any hit in the front veto/tagger array satisified $|y_{\rm fr} - y_{\rm vt}| < 16$ cm and if the mean time, `td`, for the front/veto tagger hit satisifed `td` < 7 ns (note, no absolute value condition here), a charged particle flag was set.[16]

  - If the `Analyzer` had tagged the incident particle as a charged particle, this tag was not modified.

  - If the `Analyzer` had tagged the incident particle as a neutral particle or had declared the charge to be ambiguous, the particle was tagged a charged particle if the `casym` charged particle flag was true; otherwise, the `Analyzer` tag was not modified.

Histograms of cTOF for those events surviving the cuts and charged particle tests were accumulated for both (n,n) and (n,p) events in the front array of the

[16]The logic for this test is best illustrated with an example. Suppose there was a very early accidental hit in a veto/tagger detector. This accidental would then *block* that TDC from recording any later hits in that particular veto/tagger detector (the TDCs for the NPOL detectors were single-hit TDCs); therefore, if a "real" proton hit occurred in the front array at a y-position corresponding to the veto/tagger detector with the blocked TDC, the proton would be identified as a neutron! The test described in the text safely accounts for such scenarios.

polarimeter.[17] To compensate for variations in the flight path between the front array and the rear array, histograms of rTOF values normalized to a nominal 250-cm flight path according to

$$\text{rTOF} \rightarrow \text{rTOF}\left(\frac{250}{d}\right) , \tag{5.63}$$

where d denotes the actual flight path distance (in cm), were accumulated for those events falling within a user-specified cut on the cTOF spectra. [Henceforth, we shall refer to these path-normalized rTOF values simply as rTOF.] In addition to accumulation of rTOF spectra for all events falling within the user-specified cTOF window, histograms of decomposed rTOF spectra were accumulated for:

- "RU events" (positive beam helicity, R, and scattering from the front array to the top rear array, U),

- "LU events" (negative beam helicity, L, and scattering from the front array to the top rear array, U),

- "RD events" (positive beam helicity, R, and scattering from the front array to the bottom rear array, D), and

- "LD events" (negative beam helicity, L, and scattering from the front array to the bottom rear array, D).

After accumulation of the decomposed rTOF spectra, `casym` extracted the scattering asymmetries from the yields in the four (background-subtracted) rTOF spectra. The procedure for the extraction of the asymmetries will be discussed in detail shortly; however, first, we turn to a discussion of the various event types (i.e., true coincidence events, accidentals, etc.) observed in the cTOF and rTOF spectra.

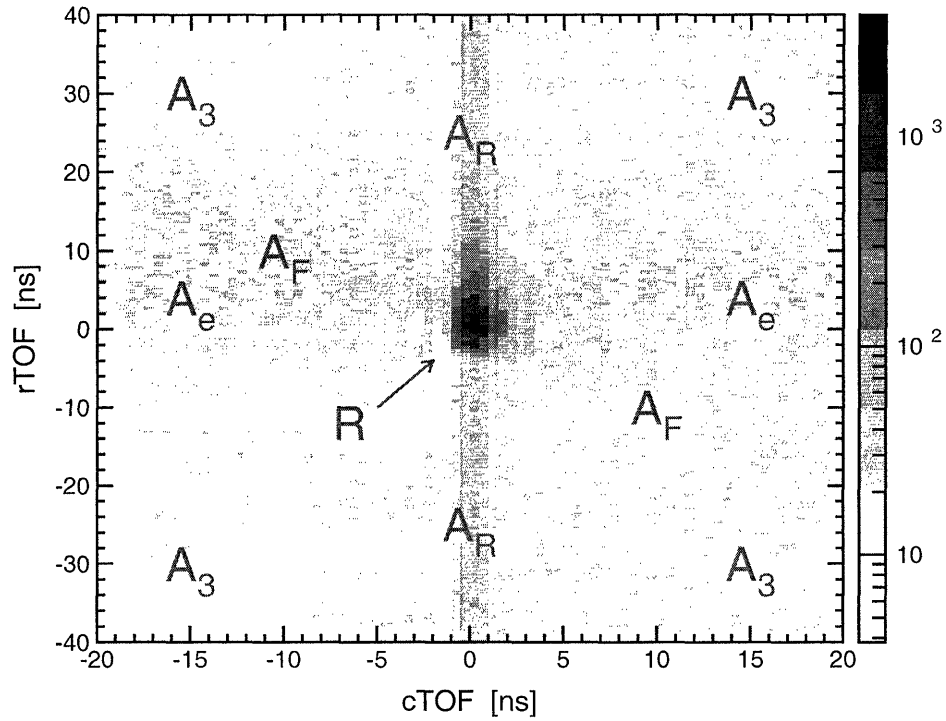

Figure 5-65: (color) Correlation between rTOF and cTOF at $Q^2 = 1.474$ (GeV/c)^2 with the various event types (see text) identified.

5.6.2 Event Types

A two-dimensional histogram of the correlation between rTOF and cTOF for all events [i.e., the sum of (n,n) and (n,p) events] passing cuts and the incident charged-particle test at $Q^2 = 1.474$ (GeV/c)^2 is shown in Fig. 5-65; for aesthetic purposes, an alternative view of this correlation plot is shown in Fig. 5-66. An early discussion of the various event types seen in these rTOF-cTOF correlation plots was given by Madey and Semenov [415]; here, much of our discussion follows that given in this reference.

In general, five different types of HMS-NPOL coincidence events can be identified in these correlation plots. First, a *real three-fold coincidence event*, denoted R, arises

[17] An (n,n) [(n,p)] event in the front array of the polarimeter was defined to be the detection of a neutral particle in the front array and a neutral [charged] particle in the rear array. In an (n,n) event, the neutron scattered from the front array to the rear array, whereas in an (n,p) event, the recoil proton from the np interaction in the front array was scattered forward with sufficient energy to penetrate the front array.

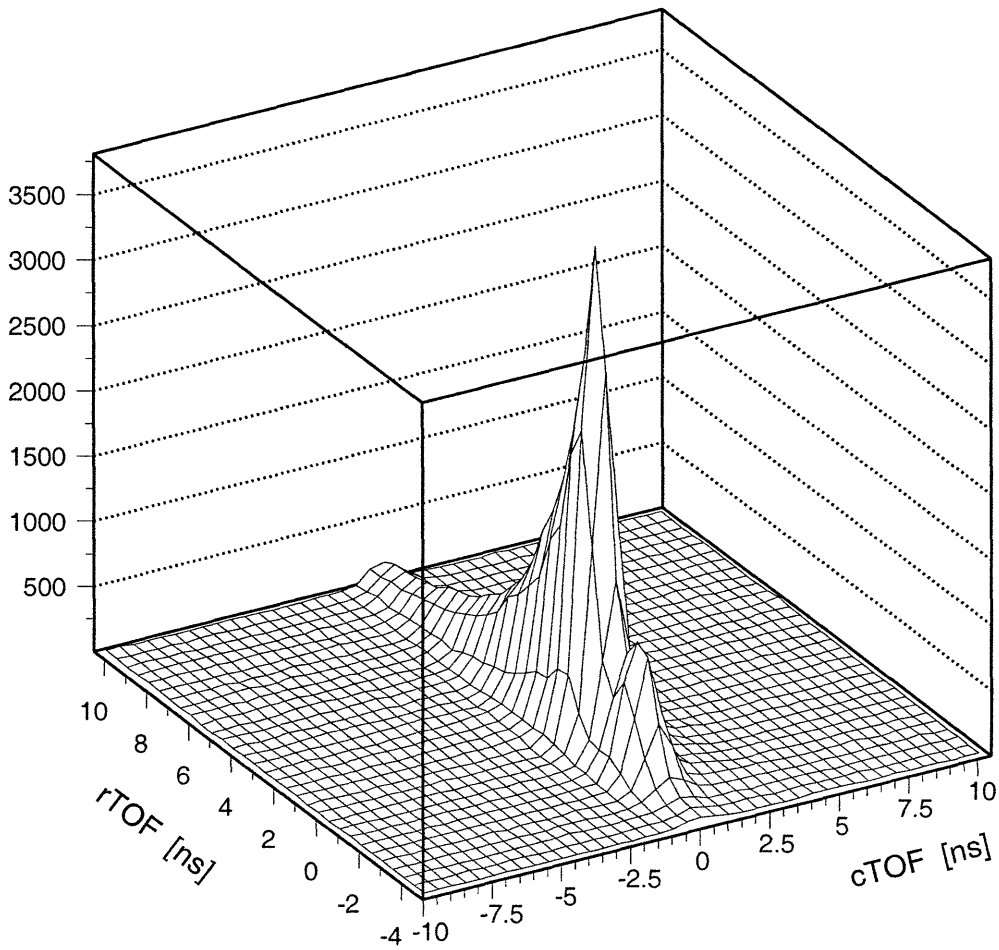

Figure 5-66: Alternative view of the correlation between rTOF and cTOF at $Q^2 = 1.474$ (GeV/c)^2.

from an electron in the HMS in coincidence with a neutron that scatters from the front array to the rear array of NPOL. Second, a *three-fold accidental coincidence event*, denoted A_3, requires a random electron in the HMS, a random neutral particle in the front array, and a random particle in the rear array. Last, three types of *double coincidence events*, each accompanied by either an accidental electron, a neutral particle in the front array, or a particle in the rear array, can occur; these are denoted

- A_e: real front array-rear array coincidence in NPOL with an accidental electron in the HMS
- A_R: real electron-front array coincidence with an accidental particle in the NPOL rear array

- A_F: real electron-rear array coincidence with an accidental particle in the NPOL front array

With these definitions, we can now proceed to a discussion of the rTOF-cTOF correlation plot shown in Fig. 5-65. A_e-type events are easily identified as the "horizontal band" (i.e., defined by rTOF = 0 ns); here, the time-of-flight from the front array to the rear array is correct, but the time-of-flight from the target to the front array is incorrect. Similarly, A_R-type events are easily identified as the "vertical band" (i.e., defined by cTOF = 0 ns); here, the time-of-flight from the target to the front array is correct, but the time-of-flight from the front array to the rear array is incorrect. A_3-type events are distributed uniformly over the entire range of the plot, and the events of interest, R-type events, form the peak at cTOF = rTOF = 0 ns.

Finally, A_F events comprise the "diagonal band" that can be faintly distinguished in Fig. 5-65; the origin of the diagonal band can be understood as follows [415]. As discussed in Chapter 4, the rear array was shielded from the direct path of particles originating in the target by the steel collimator. As a result, a particle originating in the target could not have reached the rear array without interacting in the front array; therefore, A_F events are presumably due to the corruption of a real three-fold coincidence event by an accidental hit in the front array that occurred before the true interaction. The timing signal from the front array is then, of course, generated by the accidental hit, and the cTOF and rTOF times are distorted. This distortion could also occur, for example, if the true interaction generated a pulse-height signal that fell below threshold but an accidental hit above threshold occurred either before or after the true interaction.

The fact that these events are clustered along a (linear) diagonal band can be explained quantitatively as follows. Suppose the accidental hit occurred a time Δt_A before or after the true interaction. If we denote the uncorrupted values of cTOF and rTOF as $\mathrm{cTOF}_{\mathrm{uncorr}}$ and $\mathrm{rTOF}_{\mathrm{uncorr}}$, respectively, the values of cTOF and rTOF extracted from the data by the analysis codes will be

$$\mathrm{cTOF} = \mathrm{cTOF}_{\mathrm{uncorr}} - \Delta t_A \ , \tag{5.64}$$

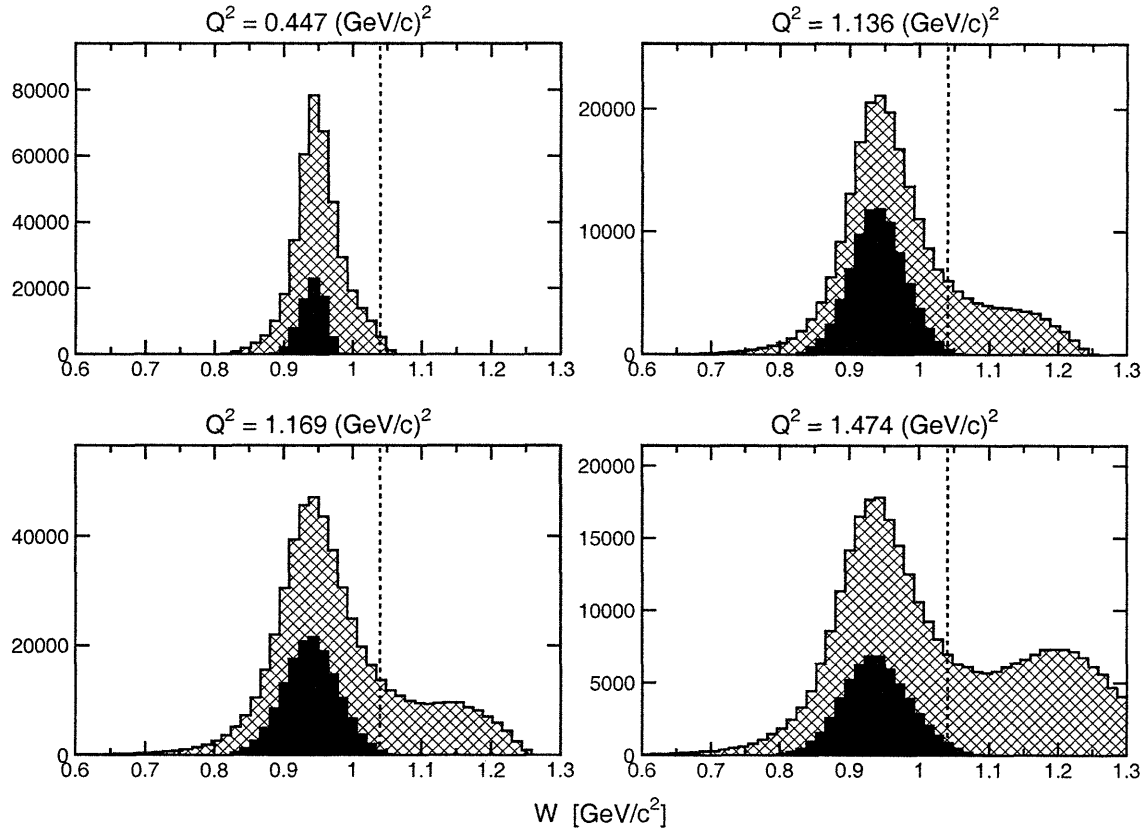

Figure 5-67: Invariant mass, W, spectra before (light cross-hatched) and after (solid) all cuts except for the $\Delta p/p$, $|\mathbf{p}_{\rm miss}|$, and cTOF cuts. The final $W < 1.04$ (GeV/c)^2 cut is indicated by the dashed line.

$$\text{rTOF} = \text{rTOF}_{\text{uncorr}} + \Delta t_A \ ; \tag{5.65}$$

therefore, we see that if $\text{cTOF}_{\text{uncorr}} = \text{rTOF}_{\text{uncorr}} = 0$ ns, then cTOF $= -$rTOF. Indeed, the negative slope of the diagonal band with a slope parameter of ~ -1 supports this hypothesis.

5.6.3 Kinematic Distributions After Cuts

Real R-type coincidence events were selected via a tight $[-1, 1]$ ns cut on cTOF and a $[-1, 8]$ ns cut on rTOF.

As evidence our cuts primarily selected real quasielastic ^{2}H$(e, e'n)$ events, distributions after cuts for two relevant kinematic variables are shown in Figs. 5-67 and

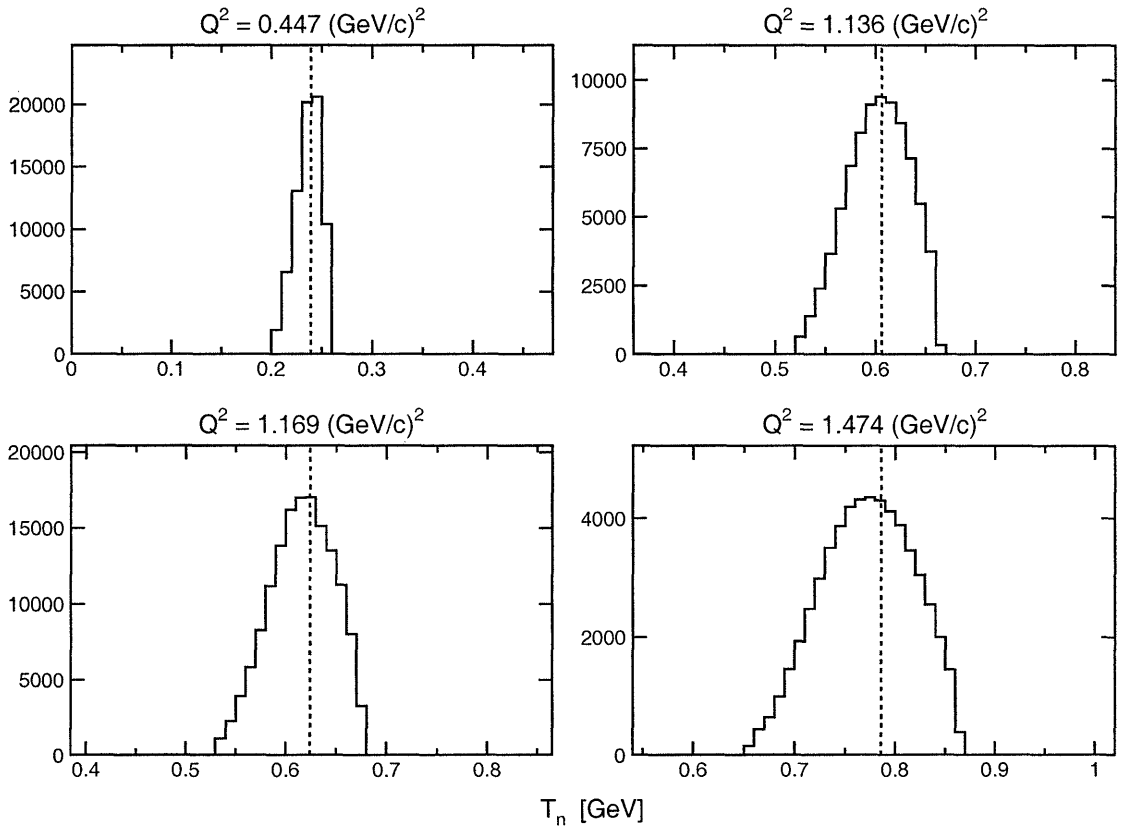

Figure 5-68: Incident neutron kinetic energy, T_n, spectra after all cuts. The dashed lines denote the value for quasifree kinematics at the (nominal) central values of the electron kinematics.

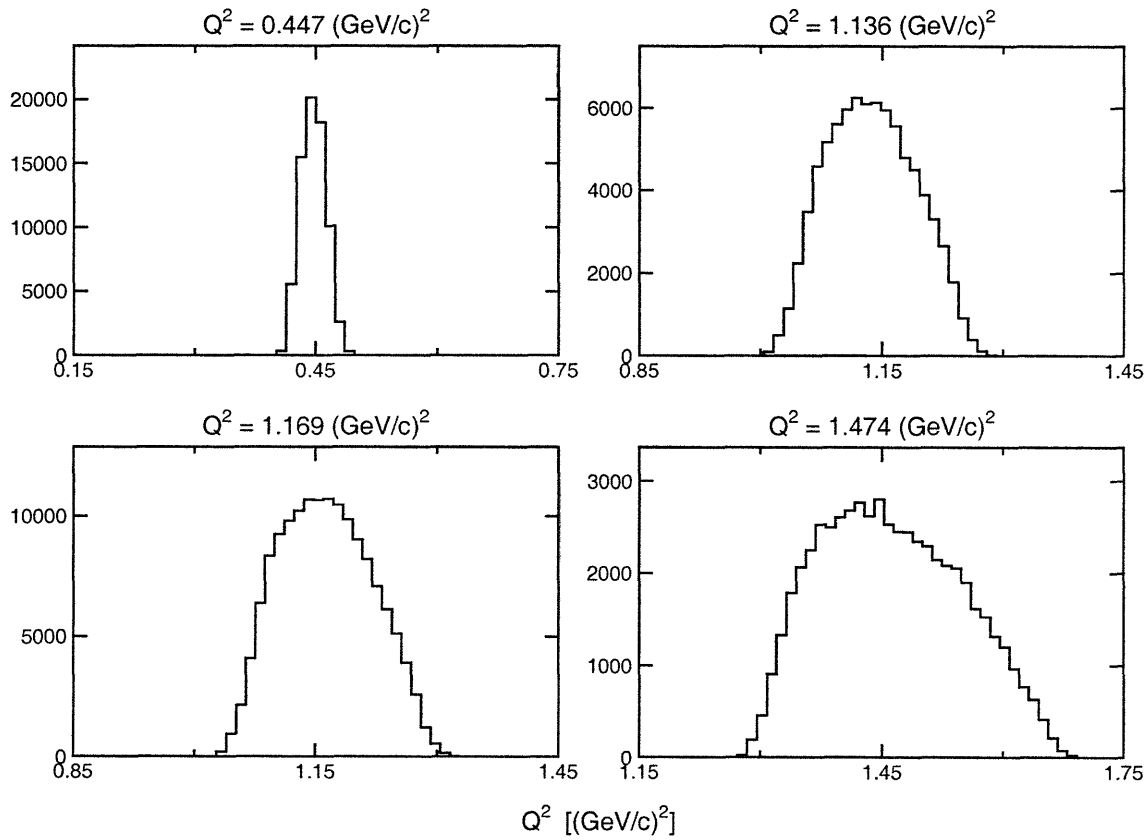

Figure 5-69: Q^2 spectra after all cuts.

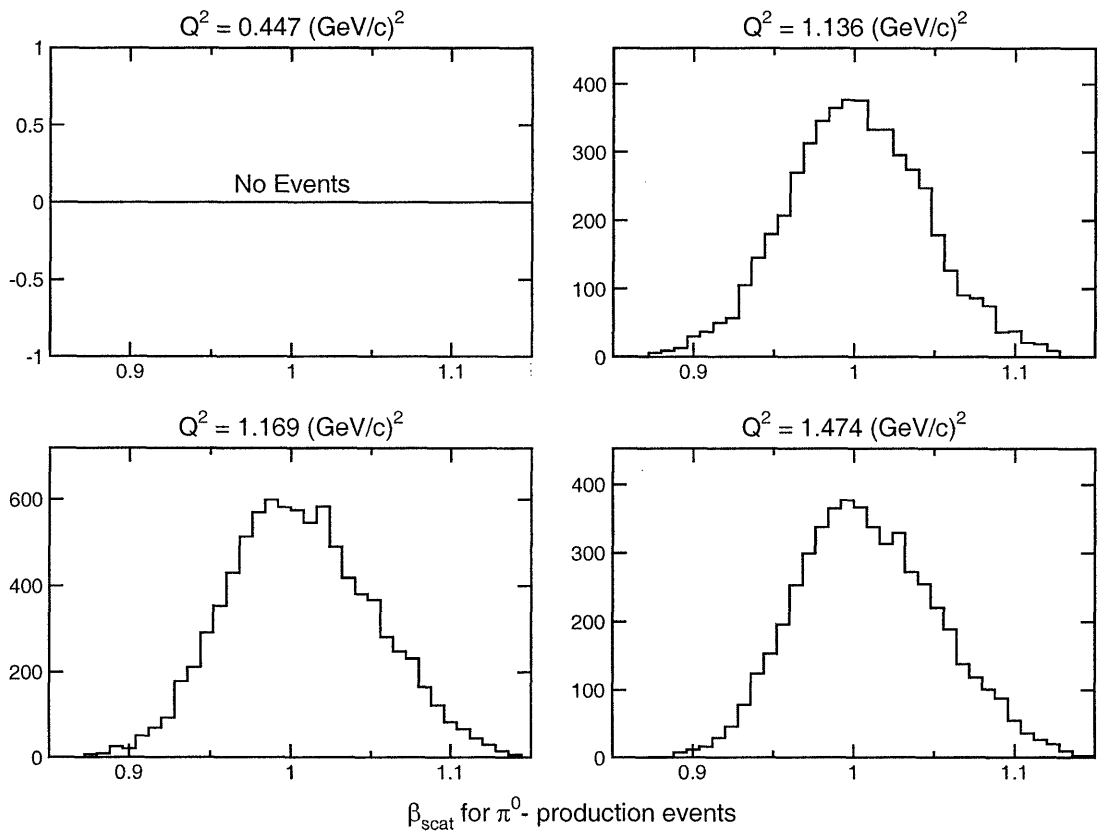

Figure 5-70: β_{scat} spectra after all cuts for those events within the π^0-production peak region in the rTOF spectra.

5-68. First, we compare distributions of W before and after cuts on $\Delta p/p$, $|\mathbf{p}_{\rm miss}|$, cTOF, and rTOF in Fig. 5-67; after all cuts (except for the cut on W itself), these distributions converge to fairly narrow peaks centered on the neutron mass. Second, final distributions for the incident neutron kinetic energy are presented in Fig. 5-68; here, again, we see that these distributions are centered reasonably well around the value expected for quasifree emission at the nominal values for the electron kinematics. Finally, to illustrate the range of acceptance in Q^2, final distributions for this variable are shown in Fig. 5-69. Also, we have claimed numerous times in the past that the secondary peak in the rTOF spectra centered at ~ -2.5 ns is due to π^0-production in the front array. The best evidence for this claim can be seen in Fig. 5-70 where we have plotted $\beta_{\rm scat}$ for those events within the π^0-production peak region in the rTOF spectra. Here, we see no evidence of $\beta_{\rm scat} \sim 1$ particles in the $Q^2 = 0.447$ (GeV/c)^2 spectrum; however, the $\beta_{\rm scat}$ distributions are clearly centered around $\beta_{\rm scat} \sim 1$ at the higher Q^2 points.

5.6.4 Extraction of Asymmetries from Time-of-Flight Spectra

The scattering asymmetries in the polarimeter were extracted from the yields in the rTOF spectra for R-type events. Specifically, rTOF spectra were accumulated for events falling within the $[-1, 1]$ ns cTOF window, and, as we describe in detail below, the asymmetries were extracted from the yields in the rTOF spectra for events within a $[-1, 8]$ ns rTOF window.

One-dimensional projections of cTOF for the four Q^2 points after cuts are shown in Fig. 5-71; here, the peak $[-1, 1]$ ns windows are indicated by the dark shaded regions.[18] In addition to the accumulation of rTOF spectra for events within the peak window, `casym` permitted the user to either enable or disable cTOF background subtraction. If the user elected to conduct the analysis with the former option, histograms of rTOF

[18]The background levels as $Q^2 = 0.447$ (GeV/c)^2 are somewhat higher than those at the other Q^2 points; this is partially due to the high radiation levels that contaminated the hall at the low beam energy of 884 MeV [416].

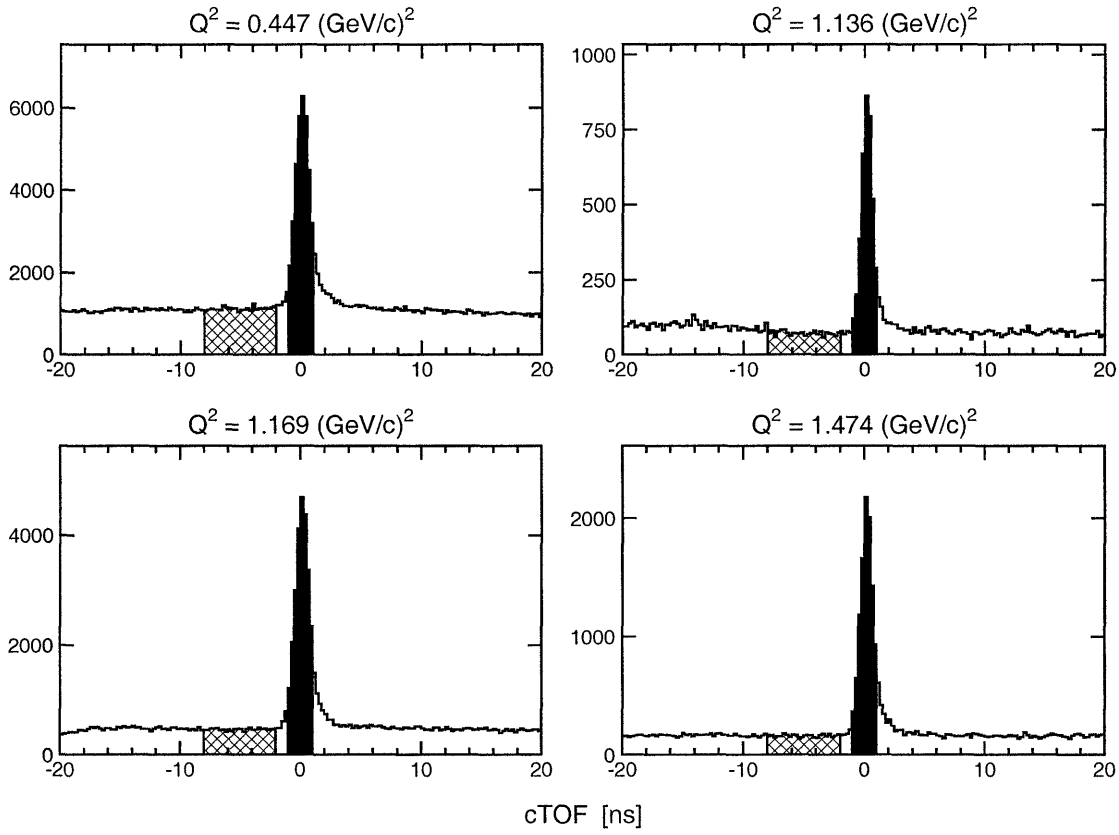

Figure 5-71: cTOF spectra after the final set of cuts. The dark shaded regions indicate the peak window, and the light cross-hatched regions indicate the sampled background window.

spectra were accumulated for background events within a user-specified background window; the nominal choice, as indicated by the light cross-hatched regions in Fig. 5-71, was $[-8, -2]$ ns.[19] Conversely, if the user elected to perform the analysis with the cTOF background subtraction feature disabled, histograms of background rTOF spectra were not accumulated.

Sample summed rTOF spectra at each of the Q^2 points for cTOF peak events are shown in Fig. 5-72; for completeness, we also present sample decomposed rTOF spectra (i.e., for RU, LU, RD, and LD events) for cTOF peak events at $Q^2 = 1.169$ $(\mathrm{GeV}/c)^2$ in Fig. 5-73. After accumulation, the rTOF spectra were fitted with the

[19]Technically, histograms of rTOF spectra for background events were accumulated with each background event contributing a weight of $w_{\mathrm{peak}}/w_{\mathrm{bkgd}}$, where w_{peak} (w_{bkgd}) denotes the width of the peak (background) cTOF window.

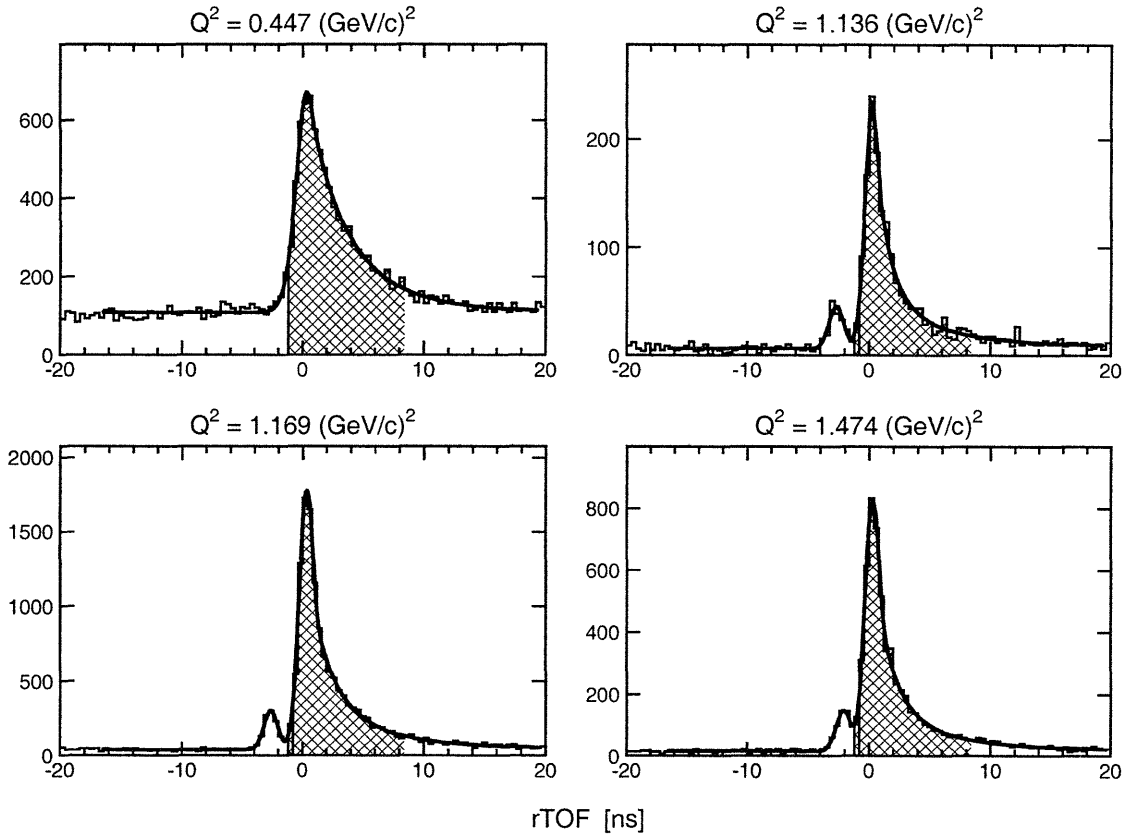

Figure 5-72: rTOF spectra for cTOF peak events. The cross-hatched regions indicate the accepted window, and the solid curves are the results of the fits to Eq. (5.66). The gamma (π^0-production) peak is clearly visible in the three higher Q^2 spectra.

CERNLIB MINUIT fitting tool [394][20] to an 11-parameter fit-function, $f(x)$, given by

$$f(x) = P_6 + P_9 \exp\left[-\frac{1}{2}\left(\frac{x - P_{10}}{P_{11}}\right)^2\right] + \begin{cases} P_1 \exp\left[-\frac{1}{2}\left(\frac{x - P_2}{P_3 + x/20}\right)^{P_7}\right] & \text{if } x \le P_2 + |P_4| \,, \\ \left(\frac{|P_5|}{|x - (P_2 + |P_4| - |P_5|)|}\right)^{P_8} |P_1| \exp\left[-\frac{1}{2}\left(\frac{|P_4|}{P_3 + x/20}\right)^{P_7}\right] & \text{if } x > P_2 + |P_4| \,. \end{cases} \tag{5.66}$$

Here, the first term, P_6, is a fit parameter for the background level in the rTOF

[20] MINUIT is a commonly used CERNLIB tool that can be used to fit data to complex multi-parameter functions either via a search for a minimum in χ^2-space or via the method of maximum log likelihood. MINUIT can compute the best-fit parameter values, the statistical uncertainties in the parameters, and the correlation matrix.

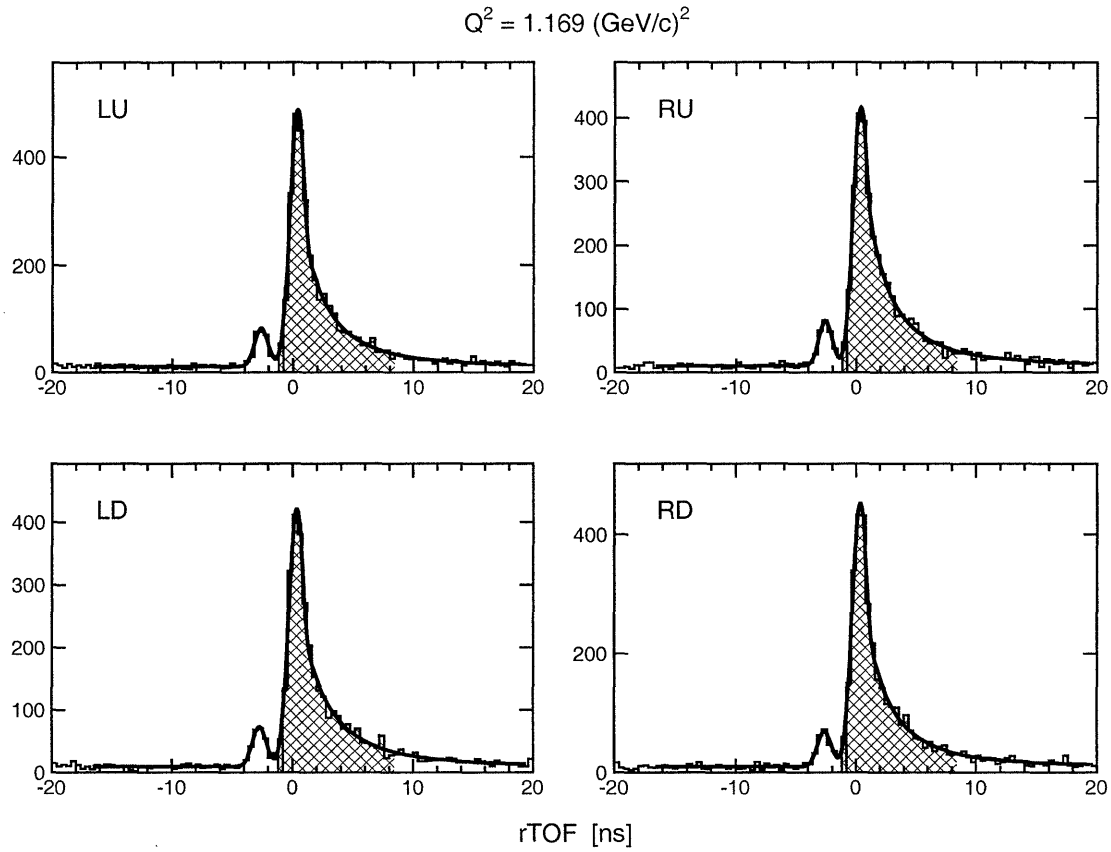

Figure 5-73: Decomposition of the rTOF spectra for cTOF peak events at $Q^2 = 1.169$ $(\mathrm{GeV}/c)^2$.

spectra, the second term is a Gaussian fit for the gamma (π^0-production) peak, and the last term includes a generalized Gaussian (long tail) for the left (right) side of the primary peak.

The fit results for the rTOF spectra shown in Figs. 5-72 and 5-73 are plotted as the solid curves. The yields for events within the $[-1, 8]$ ns peak rTOF window were extracted from a numerical evaluation of the fit-function excluding contributions from the background (i.e., fit-parameter P_6) and the Gaussian fit to the π^0-production peak along a dense set of grid points.[21] As an alternative to extracting the content of the

[21]The content was evaluated according to the following algorithm. Suppose the content of a histogram with T bins each of width Δw is fitted to a fit-function $f(x)$, and suppose an algorithm evaluates the value of $f(x)$ at M different points within each bin. The fitted content of bin j, N_j, is then

$$N_j = \frac{1}{\Delta w} \sum_{i=1}^{M} f(x_i) \Delta x_i \ , \tag{5.67}$$

peak rTOF spectra from the fit-function, `casym` also permitted the user to extract N_{peak} via counting.

If the user elected to perform the asymmetry analysis with cTOF background subtraction enabled, the content of the rTOF spectra for the cTOF background window, N_{bkgd}, was determined via counting (as opposed to fitting); the final content, N, for each histogram was then computed as

$$N = N_{\text{peak}} - N_{\text{bkgd}} \ , \tag{5.69}$$

and the statistical error in N, ΔN, was computed according to

$$\Delta N = \sqrt{(\Delta N_{\text{bkdg}})^2 + (\Delta N_{\text{peak}})^2} \ , \tag{5.70}$$

where ΔN_{bkgd} and ΔN_{peak} denote the (Poisson) statistical errors for their respective quantities. It should be noted that if N_{peak} was extracted from numerical evaluation of the fit-function, ΔN_{peak} was increased, as is customary (see, e.g., [359]), by $\sqrt{\chi^2}$ if the χ^2 for the fit was greater than 1.

Finally, the desired quantities, the physical scattering asymmetries, were extracted from the yields in the four decomposed rTOF spectra via the *cross-ratio technique* of Ohlsen and Keaton [417]. The cross ratio, r, is defined to be the ratio of two geometric means,

$$r = \sqrt{\frac{N_{RU} N_{LD}}{N_{RD} N_{LU}}} \ , \tag{5.71}$$

where the notation for the yields is obvious, and the statistical error in r is given simply by

$$\Delta r = \frac{1}{2} \, r \left[\left(\frac{\Delta N_{RU}}{N_{RU}} \right)^2 + \left(\frac{\Delta N_{LD}}{N_{LD}} \right)^2 + \left(\frac{\Delta N_{RD}}{N_{RD}} \right)^2 + \left(\frac{\Delta N_{LU}}{N_{LU}} \right)^2 \right] \ . \tag{5.72}$$

---

where $\Delta x_i \equiv x_i - x_{i-1}$. The total fitted content, N, is then, of course, just

$$N = \sum_{j=1}^{T} C_j \ . \tag{5.68}$$

After `casym` computed the cross ratio, the physical scattering asymmetry ξ, given by

$$\xi = \frac{r-1}{r+1} = \frac{\sqrt{N_{RU}N_{LD}} - \sqrt{N_{RD}N_{LU}}}{\sqrt{N_{RU}N_{LD}} + \sqrt{N_{RD}N_{LU}}} , \tag{5.73}$$

and its statistical error,

$$\Delta\xi = \frac{2\ \Delta r}{(r+1)^2} , \tag{5.74}$$

were computed. The merit of the cross-ratio technique is that ξ is insensitive to the number of particles incident on the polarimeter (i.e., target luminosities) for the different beam helicity states and the relative efficiencies and acceptances of the top and bottom rear arrays of the polarimeter; we prove these claims in Appendix C.

5.6.5 Asymmetry Results

Electron Beam Polarization Normalization

The magnitude of the scattering asymmetry measured by a polarimeter is proportional to the electron beam polarization [recall Eqs. (2.168) through (2.170)]. If the desired quantities, P_x^h and P_z^h, can be simultaneously extracted from the data (as in recoil polarization experiments with a focal plane polarimeter [212, 215–217]), corrections for temporal fluctuations in the beam polarization are not necessary; however, if only one component or a combination thereof can be extracted from the data (as in this experiment), the run-by-run scattering asymmetries must be normalized to some common value of the beam polarization.

The beam polarization normalization procedure for our asymmetry data was as follows. As the beam polarization was measured only periodically with the Møller polarimeter (not continuously as can be done with a Compton polarimeter), we defined the beam polarization for a run to be the result of the most recent prior Møller measurement. The run-by-run asymmetries extracted from the data were then normalized to a common polarization of 80% according to

$$\xi^{\text{run}} \ \rightarrow \ \xi^{\text{run}} \frac{80\%}{P_L^{\text{run}}} , \tag{5.75}$$

where $P_L^{\rm run}$ denotes the polarization for that run. The run-by-run statistical errors, $\Delta\xi^{\rm run}$, were also scaled by the same factor so that the relative statistical errors, $\Delta\xi^{\rm run}/\xi^{\rm run}$, were not altered by the normalization procedure.

Corrections for Charge-Exchange in the Lead Curtain

As we alluded earlier in Section 5.5.4, a two-step ^{2}H$(\vec{e},e'\vec{p})$ + Pb$(\vec{p},\vec{n})$ charge-exchange reaction could occur in the lead curtain that shielded the entrance to the steel collimator. Contamination from this background process would either dilute the "real" asymmetry from the ^{2}H$(\vec{e},e'\vec{n})$ reaction or create a false asymmetry if the neutrons originating from this process were unpolarized or polarized, respectively.

The asymmetry that is measured by the polarimeter, denoted ξ_M, is

$$\xi_M = f_R\xi_R + f_B\xi_B \ , \tag{5.76}$$

where f_B denotes the contamination level from the two-step charge-exchange process, ξ_B is the asymmetry measured by the polarimeter for neutrons from charge-exchange reactions, $f_R = 1 - f_B$ denotes the fraction of detected neutrons originating from ^{2}H$(\vec{e},e'\vec{n})$ events, and ξ_R is the asymmetry measured by the polarimeter for neutrons from the ^{2}H$(\vec{e},e'\vec{n})$ reaction. The asymmetry for the background process can further be written as

$$\xi_B = (P_S^p{\rm cos}\chi_p + P_L^p{\rm sin}\chi_p)\, D_{SS}^{\rm Pb} A_y \ , \tag{5.77}$$

where P_S^p and P_L^p denote, respectively, the projections of the proton's recoil polarization from the ^{2}H$(\vec{e},e'\vec{p})$ reaction on the polarimeter momentum basis $\hat{\mathbf{S}}$- and $\hat{\mathbf{L}}$-axes, χ_p is the proton spin precession angle in the Charybdis field, $D_{SS}^{\rm Pb}$ is the polarization transfer coefficient for the Pb$(\vec{p},\vec{n})$ reaction, and A_y is the polarimeter analyzing power. Combining the above two equations yields

$$\xi_R = \frac{\xi_M - f_B\,(P_S^p{\rm cos}\chi_p + P_L^p{\rm sin}\chi_p)\, D_{SS}^{\rm Pb} A_y}{1 - f_B} \ ; \tag{5.78}$$

therefore, if f_B, P_S^p, P_L^p, χ_p, $D_{SS}^{\rm Pb}$, and A_y are known or measured, ξ_R can be calculated.

Q^2 [(GeV/c)^2]	χ [deg]	Event Type	LH2 Event Rate [Events/mC]	LD2 Event Rate [Events/mC]	Contamination Level f_B [%]
0.447	-40	(n,n)	0.0136186 ± 0.0474556	25.22 ± 0.69	0.065 ± 0.225
0.447	-40	(n,p)	0.0153290 ± 0.0156948	25.60 ± 0.48	0.072 ± 0.073
0.447	$+40$	(n,n)	$0.000348490 \pm 0.037245724$	25.22 ± 0.69	0.0017 ± 0.1764
0.447	$+40$	(n,p)	$0.00931185 \pm 0.01152664$	25.60 ± 0.48	0.043 ± 0.054
1.136	0	(n,n)	0.113989 ± 0.032222	66.22 ± 11.20	0.21 ± 0.07
1.136	0	(n,p)	0.241862 ± 0.022201	94.40 ± 3.30	0.31 ± 0.03
1.136	± 90	(n,n)	0.129271 ± 0.058252	68.85 ± 3.56	0.22 ± 0.10
1.136	± 90	(n,p)	0.102187 ± 0.041925	96.41 ± 5.04	0.13 ± 0.05
1.169	-40	(n,n)	0.0763208 ± 0.0593706	36.38 ± 0.63	0.25 ± 0.20
1.169	-40	(n,p)	0.0415675 ± 0.0356346	53.31 ± 0.82	0.093 ± 0.080
1.169	$+40$	(n,n)	0.0000000 ± 0.0583505	37.78 ± 4.95	0.00 ± 0.18
1.169	$+40$	(n,p)	0.0564658 ± 0.0346586	54.14 ± 6.26	0.12 ± 0.08
1.474	0	(n,n)	0.471412 ± 0.037293	25.45 ± 1.16	2.21 ± 0.20
1.474	0	(n,p)	1.347672 ± 0.038132	38.21 ± 2.80	4.21 ± 0.33
1.474	± 90	(n,n)	No Data Taken[1]	29.53 ± 1.11	— ($\sim$0)
1.474	± 90	(n,p)	No Data Taken[1]	43.59 ± 3.25	— ($\sim$0)
1.474	-40	(n,n)	0.0708928 ± 0.0232466	28.78 ± 0.82	0.29 ± 0.10
1.474	-40	(n,p)	0.0486817 ± 0.0167822	45.43 ± 1.11	0.13 ± 0.04
1.474	$+40$	(n,n)	0.0328949 ± 0.0167065	29.71 ± 1.26	0.13 ± 0.07
1.474	$+40$	(n,p)	0.0308003 ± 0.0126484	46.52 ± 1.22	0.079 ± 0.033

[1] No liquid hydrogen data were taken at $Q^2 = 1.474$ (GeV/c)^2 with the Charybdis field set for the neutron spin precession angles of $\chi = \pm 90°$; however, at this field setting, the majority of the protons should have been swept from the opening to the steel collimator.

Table 5.6: Estimated contamination levels from the two-step ^{2}H$(\vec{e}, e'\vec{p})$ + Pb$(\vec{p},\vec{n})$ charge-exchange process.

In order to estimate the contamination levels, data taken with a liquid hydrogen target were analyzed, and the (n,n) and (n,p) event rates extracted from the liquid hydrogen data were compared with the (n,n) and (n,p) event rates extracted from the liquid deuterium data. To account for the difference in the proton densities in liquid hydrogen and liquid deuterium, we applied the following "density correction factor", C_ρ, to the event rates extracted from the liquid hydrogen data

$$C_\rho = \frac{(\rho_{\mathrm{LD2}}/A_{\mathrm{LD2}})}{(\rho_{\mathrm{LH2}}/A_{\mathrm{LH2}})} \, . \tag{5.79}$$

Here, ρ_{LD2} (ρ_{LH2}) and A_{LD2} (A_{LH2}) denote the liquid deuterium (liquid hydrogen) densities and atomic numbers, respectively. Using the values reported in [359], $\rho_{\mathrm{LD2}} = 0.169$ g cm^{-3}, $\rho_{\mathrm{LH2}} = 0.0708$ g cm^{-3}, $A_{\mathrm{LD2}} = 2.0140$, and $A_{\mathrm{LH2}} = 1.00794$, we find

$C_\rho = 1.1946$. The contamination levels, f_B, were then estimated to be

$$f_B = C_\rho \left(\frac{\text{LH2 Event Rate}}{\text{LD2 Event Rate}} \right) . \tag{5.80}$$

The (n,n) and (n,p) event rates extracted from the liquid deuterium and liquid hydrogen data and the resulting estimates of the contamination levels are listed in Table 5.6. As can be seen there, the contamination levels are negligible ($\lesssim 0.3\%$) for $\chi = \pm 40°$ and $\chi = \pm 90°$ precession at all of our Q^2 points (as the Charybdis field swept the majority of protons away from the front face of the lead curtain at the entrance to the steel collimator), and $\sim$0.3% and $\sim$3% for $\chi = 0°$ precession at $Q^2 = 1.136$ and 1.474 $(\text{GeV}/c)^2$, respectively. Accordingly, we did not apply charge-exchange corrections to any of the $\chi = \pm 40°$ and $\pm 90°$ asymmetries or the $Q^2 = 1.136$ $(\text{GeV}/c)^2$ $\chi = 0°$ asymmetries; however, we did apply a +2.3% and +4.4% correction to the $Q^2 = 1.474$ $(\text{GeV}/c)^2$ (n,n) and (n,p) asymmetries, respectively.[22]

Summary of Results

The final asymmetry data for the cuts listed in Table 5.5 plus cuts of $[-1,1]$ ns and $[-1,8]$ ns on cTOF and rTOF, respectively, are summarized in Table 5.7. To illustrate the quality of the asymmetry data, run-by-run plots of the (n,n) and (n,p) asymmetries for the $Q^2 = 1.136$ $(\text{GeV}/c)^2$ $\chi = 0°$ and $\pm 90°$ data sets are shown in Figs. 5-74 and 5-75; by convention, the sign of the asymmetries from runs with the $\lambda/2$-plate in have been reversed. For aesthetic purposes, histograms of the $\chi = 0°$ (n,n) and (n,p) asymmetries are shown in Fig. 5-76; these histograms clearly demonstrate that the distributions of the asymmetries are of an appropriate Gaussian shape.

[22] We corrected the $Q^2 = 1.474$ $(\text{GeV}/c)^2$ asymmetries according to Eq. (5.78) assuming $D_{SS}^{\text{Pb}} = 0$. D_{SS}^{Pb} was measured at $T_p = 795$ MeV by Prout *et al.* [418] and found to be consistent with 0 (i.e., $D_{SS}^{\text{Pb}} = 0.014 \pm 0.013$). The difference between the corrected asymmetries for $D_{SS}^{\text{Pb}} = 0.014 \pm 0.013$ and $D_{SS}^{\text{Pb}} = 0$ for (n,n) and (n,p) events was found to be a negligible 0.022% and 0.042%, respectively.

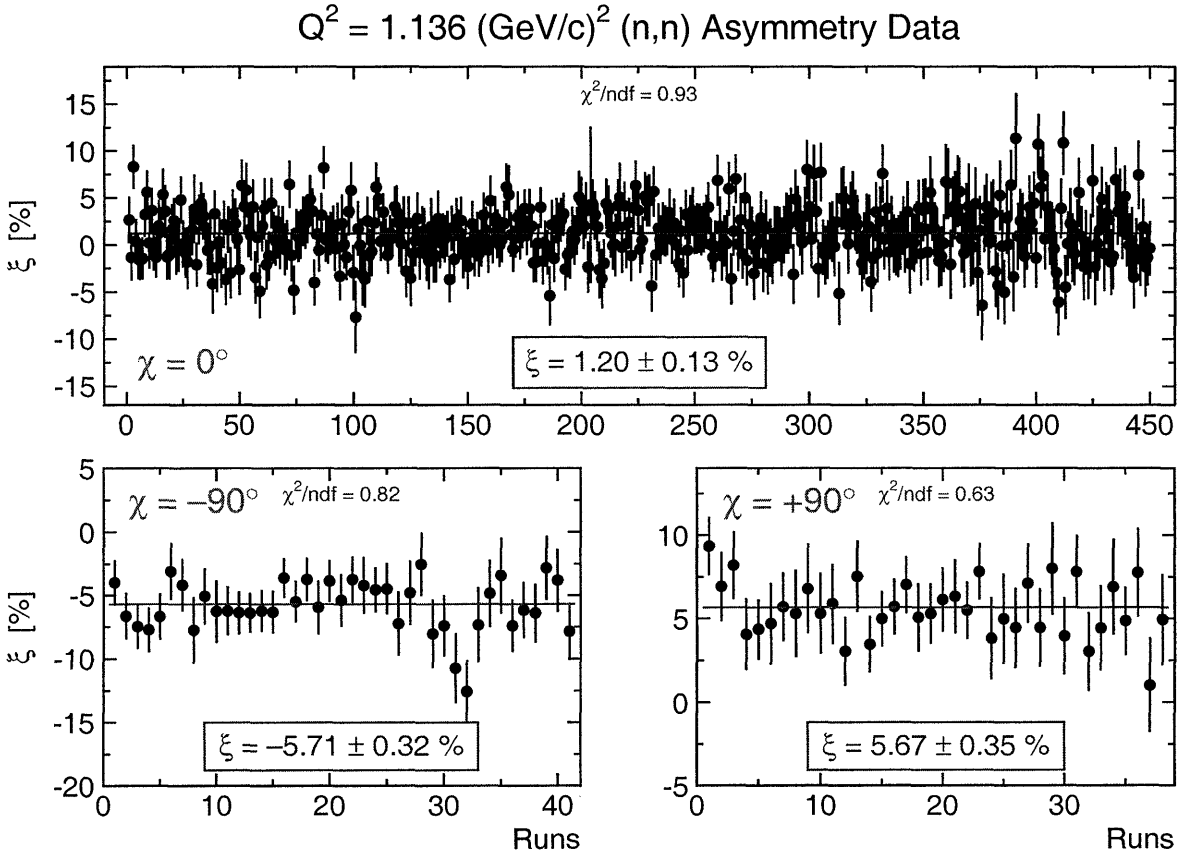

Figure 5-74: $Q^2 = 1.136$ (GeV/c)^2 $\chi = 0°$ and $\pm 90°$ (n, n) asymmetries normalized to a beam polarization of 80%.

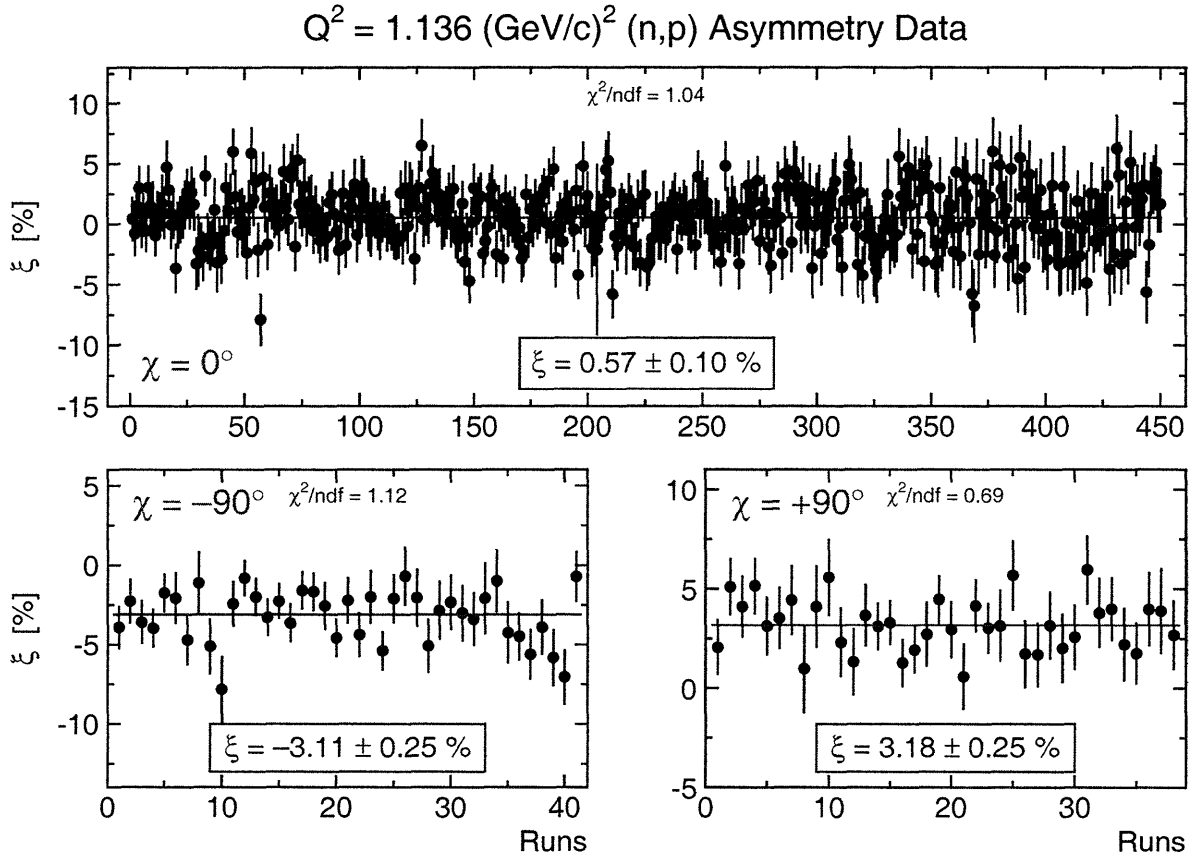

Figure 5-75: $Q^2 = 1.136$ (GeV/c)^2 $\chi = 0°$ and $\pm 90°$ (n, p) asymmetries normalized to a beam polarization of 80%.

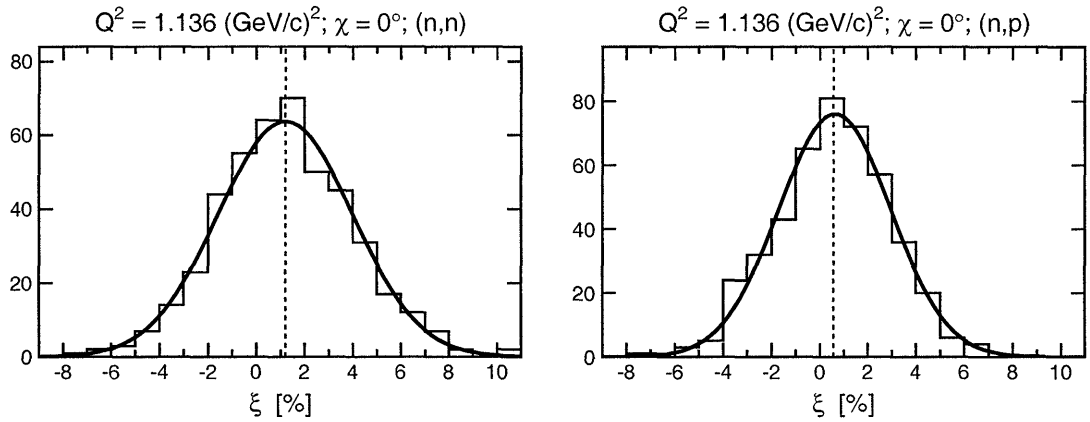

Figure 5-76: Histograms of the $Q^2 = 1.136$ (GeV/c)^2 $\chi = 0°$ (n,n) and (n,p) asymmetries. The solid curves are Gaussian fits, and the dashed lines are the mean values of the asymmetries given in Table 5.7.

Central Q^2 [(GeV/c)^2]	χ	(n,n) ξ [%]	(n,p) ξ [%]
0.447	$-40°$	-4.51 ± 0.22	-2.97 ± 0.19
0.447	$+40°$	6.38 ± 0.28	4.98 ± 0.29
1.136	$0°$	1.20 ± 0.13	0.57 ± 0.10
1.136	$-90°$	-5.71 ± 0.32	-3.11 ± 0.25
1.136	$+90°$	5.67 ± 0.35	3.18 ± 0.25
1.169	$-40°$	-2.92 ± 0.29	-1.42 ± 0.22
1.169	$+40°$	4.75 ± 0.31	2.76 ± 0.25
1.474	$0°$	1.29 ± 0.19	0.64 ± 0.17
1.474	$-90°$	-4.64 ± 0.47	-2.92 ± 0.50
1.474	$+90°$	5.07 ± 0.49	2.14 ± 0.43
1.474	$-40°$	-2.26 ± 0.20	-0.88 ± 0.18
1.474	$+40°$	4.03 ± 0.24	2.11 ± 0.21

Table 5.7: Final (n,n) and (n,p) asymmetry data. The $Q^2 = 1.474$ (GeV/c)^2 $\chi = 0°$ (n,n) and (n,p) asymmetries were corrected for contamination from charge-exchange reactions in the lead curtain.

5.7 Extraction of Uncorrected Values for G_{En}/G_{Mn}

We conclude this chapter in this section by extracting the values of G_{En}/G_{Mn} from the asymmetry data presented in the previous section assuming assuming elastic electron scattering from a free neutron and infinitesimal pointlike HMS and NPOL acceptances and neglecting nuclear physics corrections for FSI, MEC, and IC.

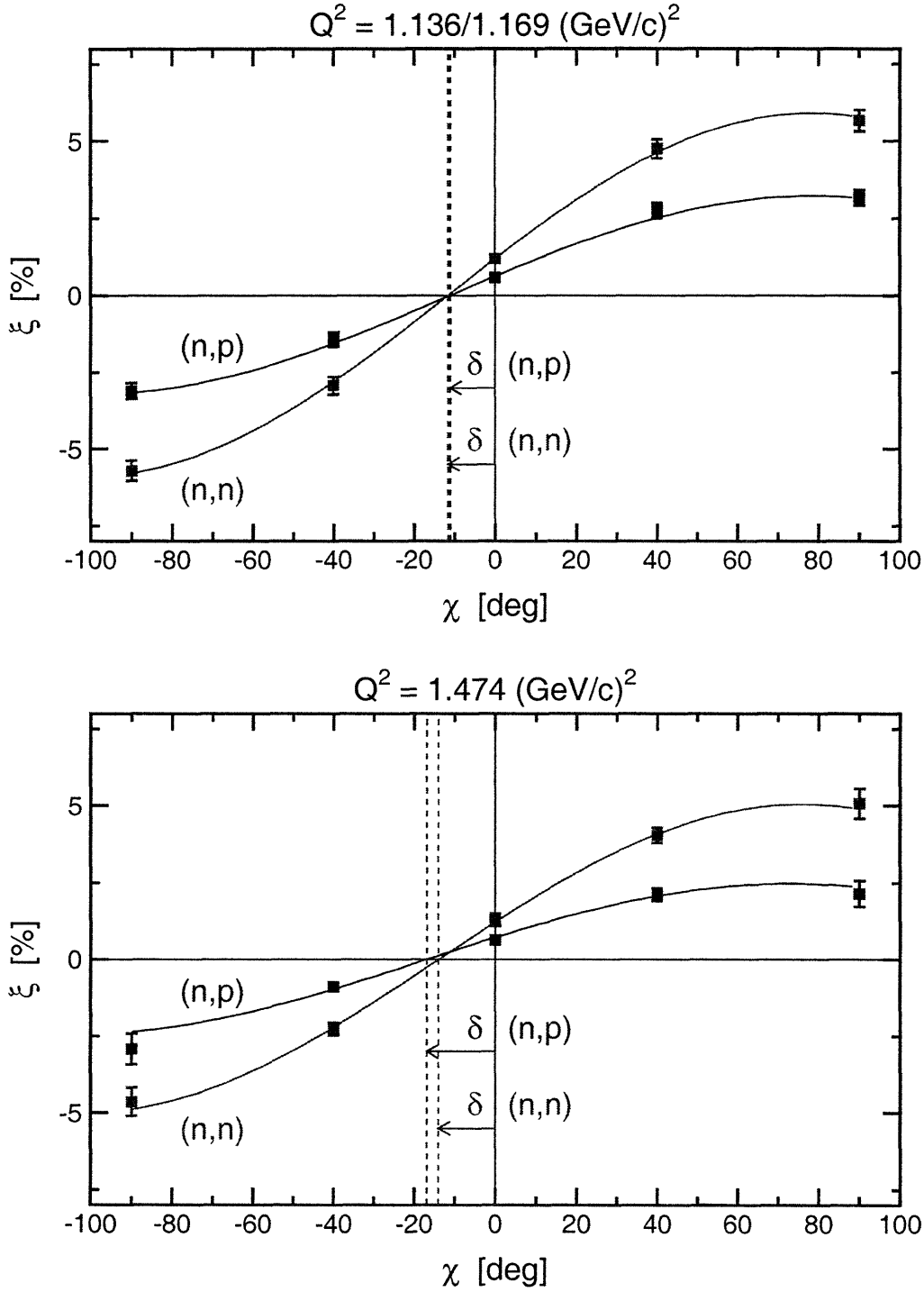

Figure 5-77: (color) Results of sinusoidal fits to the $Q^2 = 1.136/1.169$ and 1.474 $(\mathrm{GeV}/c)^2$ (n,n) and (n,p) asymmetries.

Central Q^2	δ [deg]		G_{En}/G_{Mn}		G_{En}/G_{Mn}
$[(\mathrm{GeV}/c)^2]$	(n,n)	(n,p)	(n,n)	(n,p)	Combined[1]
0.447	—	—	-0.0580 ± 0.0106	-0.0854 ± 0.0138	-0.0681 ± 0.0084
1.136/1.169[2]	11.7 ± 1.2	11.2 ± 1.7	-0.124 ± 0.013	-0.118 ± 0.019	-0.122 ± 0.011
1.474	14.0 ± 1.6	16.9 ± 2.9	-0.166 ± 0.020	-0.203 ± 0.037	-0.174 ± 0.017

[1] Weighted average of G_{En}/G_{Mn} from (n,n) and (n,p) events.
[2] Result obtained via averaging of the (nominal) central electron kinematics for the two Q^2 points.

Table 5.8: Phase shift fit parameter δ and uncorrected results for G_{En}/G_{Mn} at each of the Q^2 points.

We follow the prescription outlined in Section 2.3.6. The $Q^2 = 1.136/1.169$ $(\mathrm{GeV}/c)^2$ and 1.474 $(\mathrm{GeV}/c)^2$ asymmetries are plotted in Fig. 5-77 as a function of the neutron spin precession angle χ; these were fitted to

$$\xi(\chi) = P_1 \sin(\chi + P_2) \ , \tag{5.81}$$

where the fit parameter of interest, P_2, is just equivalent to δ in Eq. (2.174). It should be noted that the data are fit well by the sinusoids (with small values of χ^2), and we observe excellent global agreement between the asymmetries extracted from (n,n) and (n,p) events in the polarimeter. After the extraction of δ from the fits, the values of G_{En}/G_{Mn} were evaluated using Eq. (2.175) and the (nominal) central values for the electron kinematics listed in Table 3.1. The sinusoidal δ phase-shift analysis could not be conducted for the $Q^2 = 0.447$ $(\mathrm{GeV}/c)^2$ asymmetry data as data were taken only with the two $\pm 40^\circ$ precession angles; therefore, the uncorrected values for G_{En}/G_{Mn} were evaluated using Eq. (2.176) with $\chi_1 = -40^\circ$, $\chi_2 = 40^\circ$, and the (nominal) central values for the electron kinematics.

The results of this exercise are summarized in Table 5.8.

5.8 Summary

In this chapter, we began our discussion of the E93-038 analysis procedures. We described how events and tracks were reconstructed in the HMS and NPOL, and

we detailed how the scattering asymmetries in the polarimeter were extracted from time-of-flight spectra. Before concluding this chapter, we stress a very important issue. The uncorrected results for G_{En}/G_{Mn} that we presented in Section 5.7 assumed infinitesimal HMS and NPOL point acceptances and $n(\vec{e}, e'\vec{n})$ elastic scattering at the central values of the kinematics. These results are *not rigorous* as the HMS and NPOL have finite angular acceptances, quasielastic ^{2}H$(\vec{e}, e'\vec{n})$ scattering was employed, and the kinematics vary over the experimental acceptance.

As a first step towards a *rigorous* extraction of G_{En}/G_{Mn} from the experimental asymmetries, we discuss, in the next chapter, the two independent simulation programs that were developed to average Arenhövel's theoretical ^{2}H$(\vec{e}, e'\vec{n})$ recoil polarization calculations (discussed earlier in Section 2.3.7) over the experimental acceptance.

Chapter 6

Simulation Programs

In this chapter, we describe the two simulation programs, the `Acceptance` program and `GENGEN`, that were developed to extract the acceptance-averaged and nuclear physics corrected values of G_{En}/G_{Mn} from the measured experimental asymmetries. These simulation programs were developed specifically for E93-038 — we did not employ a standard community-recognized Monte Carlo code, such as `MCEEP` [419], for this task because a *rigorous simulation* of this experiment mandated the inclusion of a detailed model of all elements of the neutron polarimeter, and modification of a standard code would likely have proven to be as time-consuming as the development of a "home-grown" simulation program. Further, the development and maintenance of a home-grown Monte Carlo simulation code proved to be an extremely valuable educational tool; indeed, the author of this thesis profited immensely from this experience.

We begin with an overview of the physics models and algorithms that were written for the `GENGEN` Monte Carlo simulation program. After we have described this simulation program in sufficient detail, we document the validity of our simulation by demonstrating that `GENGEN` sufficiently reproduces experimental kinematic distributions and the response of the polarimeter. Next, we provide an overview of the `Acceptance` simulation program. Unlike `GENGEN`, the `Acceptance` program was not a Monte Carlo simulation program; instead, this program was designed to extract the corrections for the finite experimental acceptance and nuclear physics effects di-

rectly from actual experimental data. Again, we provide an overview of the physics models and algorithms that this program employed, and we discuss the advantages and disadvantages of using experimental data, as opposed to simulated data, for the acceptance-averaging procedure.

6.1 Overview of GENGEN

The GENGEN simulation program was developed under the leadership of Kelly beginning in 1999, and documentation for an early version of this code (dating to the year 2000) may be found in [420]. The original goal of this simulation program was to generate pseudodata in order to assess the readiness of early versions of the analysis programs (i.e., the E93-038 ENGINE and the Analyzer) that were being developed prior to the start of the experiment. Following the conclusion of the experiment, large portions of the original code were modified and many new routines were written as the demands for a rigorous extraction of the acceptance-averaged and nuclear physics corrected values for G_{En}/G_{Mn} from simulated data became apparent. GENGEN was written almost entirely in FORTRAN; more than 100 subroutines comprising approximately 9,000 lines of code were written specifically for this simulation by a number of authors. In addition, many routines written for other major codes, such as EPIPROD [421], MCEEP [419], and SAID [188], were incorporated into the GENGEN code structure. The version of GENGEN that we used for the final analysis presented in this thesis, 2.9, included realistic models for the primary $^2\mathrm{H}(\vec{e}, e'\vec{n})$ scattering event in the target, the acceptance of the HMS, neutron spin precession in the Charybdis dipole field, spin-dependent neutron scattering in the lead curtain, elastic and quasielastic np scattering in the front and rear arrays of the polarimeter, tracking of the incident neutron and the recoil proton from the front array to the rear array of the polarimeter, and the response of the polarimeter to interactions in the front and rear arrays.

A simplified schematic diagram of the structure of the GENGEN code is shown in Fig. 6-1. After we have provided an overview of the major features of the simulation, we turn to a detailed discussion of the underlying algorithms. Because we

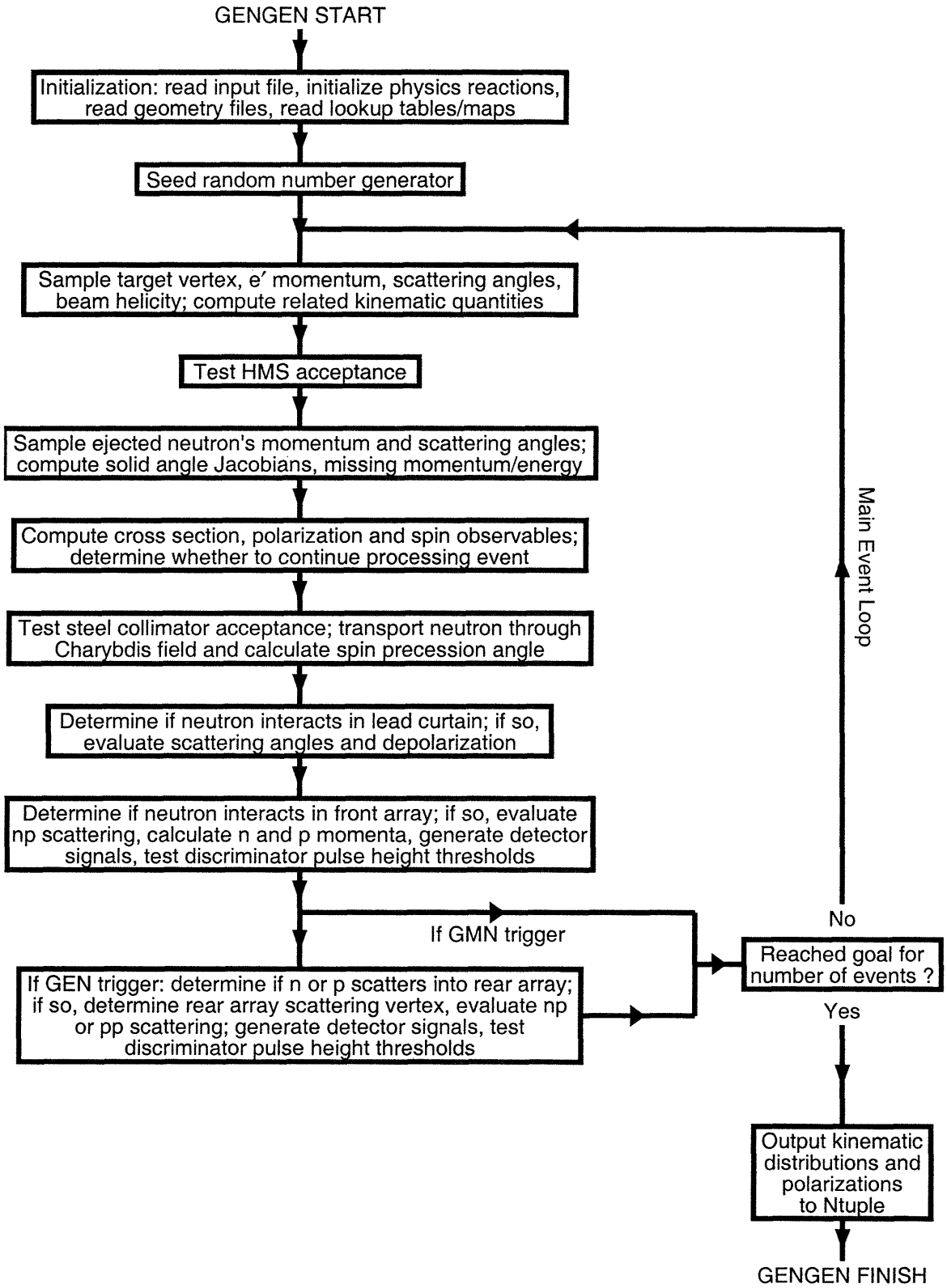

Figure 6-1: Schematic flowchart for the GENGEN Monte Carlo simulation program.

developed our own Monte Carlo simulation program instead of employing a standard community-recognized Monte Carlo code, we believe it is important that we document the most important physics algorithms that were written for our simulation.

6.1.1 Sampling Options

`GENGEN` permitted the user to perform either *importance sampling* or *uniform sampling.*

If the user chose to perform uniform sampling, events were generated uniformly over the available kinematic phase space, and a weight for each event was computed according to a model cross section. Alternatively, if the user chose to perform importance sampling, events (each of equal weight) were generated according to their relative probability via the standard acceptance-rejection method for Monte Carlo methods (see, e.g., [410]). As will be described in detail later, for each trial event, the simulation compared the trial cross section computed according to some model with a constant test cross section and a random number generated on the interval $[0, 1]$. If the ratio of the trial cross section to the test cross section was smaller than the random number, the event was rejected. As we will show later, the differential cross section for the $^2\mathrm{H}(\vec{e}, e'\vec{n})$ reaction tends to vary rapidly by several orders of magnitude over the acceptance (e.g., over the range of missing momentum); therefore, the majority of the trial events were rejected when importance sampling was enabled. Accordingly, the simulation efficiency[1] for importance sampling was significantly less than that for uniform sampling.

In addition to the choice between uniform and importance sampling, the user was permitted to perform the simulation in either the "`GMN` trigger" mode or the "`GEN` trigger" mode. If the user chose to employ the `GMN` trigger, a successful event required valid events in the HMS and the front array of NPOL; use of the `GEN` trigger was more rigorous as this mode of the simulation also required a valid event in the rear array of NPOL. As expected, the simulation was significantly less efficient when

[1] We define the simulation efficiency to be the ratio of the number of accepted events to the number of trial events generated by the simulation.

operated with the GEN trigger instead of the GMN trigger.

6.1.2 Physics Options

GENGEN permitted the user to choose from several different major physics options; these are summarized below.

- Elastic scattering from a stationary nucleon, quasielastic scattering from a neutron in a deuteron (with Fermi motion), or inelastic pion production on a neutron could be simulated.
- The differential cross section for the primary electron scattering reaction in the target and the recoil polarization observables could be computed according to the GENGEN PWBA model, a model employing Arenhövel's PWBA calculations, or a model employing Arenhövel's FSI+MEC+IC calculations.
- Neutron spin precession in the Charybdis dipole field could be simulated.
- Neutron scattering in the lead curtain could be simulated if the user was interested in evaluating the depolarization of the neutron flux entering the front array of NPOL due to nuclear interactions.
- Elastic and quasielastic nucleon-nucleon scattering in the front and rear arrays of the polarimeter were simulated, and (n, n) and (n, p) events were simulated simultaneously when the GEN trigger was enabled. As in the data analysis, an (n, n) event was defined to be detection of the scattered neutron in the rear array, and an (n, p) event was defined to be detection of the recoil proton in the rear array (i.e., an event in which the recoil proton had sufficient energy to penetrate the scintillators in the front array and the correct scattering angle to enter the rear array).

6.1.3 Output Options

If the user chose to perform uniform sampling, at the conclusion of the simulation, GENGEN output an HBOOK Ntuple file containing histograms of kinematic distributions

and recoil polarization observables. In version 2.9, distributions for 157 physics variables and 290 variables related to the response of the polarimeter were written to the Ntuple if the user chose to employ uniform sampling; the weight for each event was one of the variables written to the Ntuple. If, instead, the user chose to perform importance sampling, GENGEN output a .rzdat pseudodata file which could then be processed with the standard analysis programs (i.e., the Analyzer and the casym asymmetry program).

6.2 GENGEN Algorithms

We now begin a detailed description of the GENGEN algorithms. The order of our discussions will loosely follow the flowchart shown in Fig. 6-1; however, it should be noted that a number of different simulation features not displayed in this figure will be discussed.

6.2.1 Initialization

GENGEN began by interpreting a number of different environmental variables established by the user; these permitted the user to specify the filename for the main input file, the type of desired output (i.e., HBOOK Ntuple or .rzdat file), the goal for the number of simulated events, and the filenames for a number of different data files needed for initialization of the various physics algorithms.

The simulation then proceeded to a generic initialization phase; during this phase, GENGEN began by reading the user-defined main input file. The main input file permitted the user to specify, among many things, filenames for the output, the desired mode of operation (e.g., uniform or importance sampling, GMN or GEN trigger), central values for the electron kinematics and associated sampling ranges, physics options, TOSCA field maps for the Charybdis dipole field, detector timing and pulse height resolution parameters, detector pulse height thresholds, etc. In addition to reading the main input file, GENGEN also read a number of other data files needed for the processing of events in the main event loop; for example, files containing kinematic lookup

tables for the $^2\mathrm{H}(\vec{e}, e'\vec{n})$ structure functions, cross section data for $n + \mathrm{Pb}$ scattering, and the NPOL detector geometry were read during the initialization phase.

In addition to reading these data files, `GENGEN` also performed a number of different computations needed for the initialization of several different physics algorithms; these initial computations will be described in detail when we discuss the corresponding physics algorithm. It should be noted that our description of the initialization phase of the simulation was certainly not intended to be exhaustive; we have omitted reference to several non-physics routines needed for the basic functionality of the simulation that were called during the initialization phase.

6.2.2 Random Number Generator and Seeding

The `GENGEN` random number generator, based closely on one given in [422] (i.e., the `RAN1` algorithm), produced a random deviate on the interval $[0, 1]$ using the method of L'Ecuyer to combine two long-period multiplicative congruential generators to produce a period of about 2.3×10^{18}. Sequential correlations were suppresed with Bays-Durham shuffling, and integer overflows were avoided through the use of Schrage's method.

The random number generator was seeded in one of two different ways following completion of the numerous initialization routines. First, if the user was performing the simulation interactively, the random number generator was seeded with the CPU clock time. Second, if the simulation was being conducted on a non-interactive Linux batch farm machine (as was done for all simulation work for the final production analysis reported in this thesis), the random number generator was seeded with the `JOBID` for the process. Each Linux batch farm job is assigned a unique six-digit `JOBID`; therefore, no two simulations we conducted for the final production analysis were seeded identically.

After the random number generator was seeded, the seeds were locked and could not be accessed or modified at any later time.

6.2.3 Target Vertex and Electron Kinematics Sampling

Following the seeding of the random number generator, GENGEN entered the main event loop. For all simulation work reported in this thesis, the energy of the incident electron beam was taken to be constant and assumed the value specified in the main input file. The target vertex and the remaining electron kinematics were sampled via the following algorithm.

First, the vertex position for the $^2\mathrm{H}(\vec{e}, e'\vec{n})$ interaction in the target was sampled uniformly along the length of the 15-cm target and within the raster pattern, and the reconstructed time for the interaction was sampled from a Gaussian distribution with a standard deviation specified in the input file. Second, the kinematics for the scattered electron were sampled according to the following scheme. A point within the HMS aperture was chosen randomly[2], and the electron scattering angles $\theta_{e'}$ and $\phi_{e'}$ were computed after properly accounting for the vertex position in the extended target. The magnitude of the scattered electron's momentum, $|\mathbf{p}_{e'}|$, was sampled uniformly within a user-specified range of $\Delta p/p$ values, and then the four-momentum transfer and the invariant mass were computed.

The momenta of the incoming and scattered electron, the four-momentum transfer, and all other kinematic quantities derived from the electron kinematics were then stored for later use by other algorithms in the main event loop.

6.2.4 HMS Acceptance Test

After the electron kinematics were sampled, the acceptance of the HMS was enforced with a standard Hall C algorithm, the mc_hms routine, that is part of the more general SIMC simulation code [423] that has been used for the simulation of many Hall C experiments employing the HMS and/or SOS.

A brief overview of the HMS acceptance test that was enforced by the mc_hms routine is as follows. First, electrons were transported from the interaction vertex

[2]The point within the HMS aperture was sampled uniformly assuming the primary electron scattering event occurred in the center of the (extended) target. This point will become important later.

in the target to the octogonal collimator; those events with trajectories falling outside the acceptance of the collimator were rejected and not processed in any further detail. Second, for those events surviving the octogonal collimator test, `mc_hms` transported the scattered electrons through the HMS's quadrupole and dipole fields using a standard Hall C transport map; if the scattered electron's trajectory fell outside the apertures of any of these magnets, the event was rejected. Finally, for those events surviving transport through the magnets, acceptance tests through the detector package were conducted; tests were enforced for all elements of the detector package (i.e., the drift chambers, the hodoscopes, the Čerenkov detector, and the calorimeter), and any events with trajectories falling outside the physical dimensions of the detectors were rejected.

6.2.5 Neutron Momentum Sampling

For those events surviving the HMS acceptance tests, `GENGEN` continued by sampling the ejected neutron's momentum at the target. Two different sampling procedures were conducted.

First, for quasielastic ^{2}H$(e, e'n)$ scattering or pion production on a moving nucleon, the ejected neutron's momentum vector was sampled randomly within a specified range. In the former case, the ejected neutron's in-plane and out-of-plane scattering angles were sampled uniformly within specified ranges defined *relative to the center of the target.* After these scattering angles were sampled and a unit vector along the ejected neutron's momentum, $\hat{\mathbf{p}}_n$, was constructed, the magnitude of the momentum was computed by solving the quadratic equation for $|\mathbf{p}_n|$ given in Eq. (5.37). In the latter case, both the magnitude of the neutron's momentum and the in-plane and out-of-plane scattering angles were sampled within a user-specified range (again, relative to the center of the target).

Second, for pion production on a stationary nucleon, the in-plane and out-of-plane scattering angles were sampled uniformly within user-specified ranges (again, relative to the center of the target). Similar to Eq. (5.37), it can easily be shown in a few lines of algebra that the neutron's energy, E_n, is given by the solution to the quadratic

equation

$$AE_n^2 + BE_n + C = 0 \ , \tag{6.1}$$

where

$$A = (m_\pi + \omega)^2 - (\mathbf{q} \cdot \hat{\mathbf{p}}_n)^2 \ , \tag{6.2}$$

$$B = -2(\omega + m_n)D \ , \tag{6.3}$$

$$C = (\mathbf{q} \cdot \hat{\mathbf{p}}_n)^2 m_n^2 + D^2 \ , \tag{6.4}$$

$$D = \frac{1}{2}\left(2m_n^2 - m_\pi^2 - Q^2 + 2m_n\omega\right) \ , \tag{6.5}$$

and m_π denotes the pion mass.

Following the construction of the ejected neutron's momentum, the missing energy, missing momentum, missing mass, and the neutron's scattering angles relative to $\mathbf{q}$, θ_{nq} and ϕ_{nq}, were computed and stored for later use.

6.2.6 Computation of the ^{2}H$(\vec{e}, e'\vec{n})^1$H Differential Coincidence Cross Section and Recoil Polarization

After the kinematics for the scattered electron and the ejected neutron were completely specified, the differential cross section and the recoil polarization for the electron scattering event in the target were computed. In what follows below, we describe the algorithms that we used for the final production analysis [i.e., those algorithms that computed the differential cross section and recoil polarization according to Arenhövel's models for the quasielastic ^{2}H$(\vec{e}, e'\vec{n})$ reaction]. We did not use the `GENGEN` PWBA model for the final analysis; however, we refer the interested reader to [420] for a detailed discussion of the formalism for this algorithm.

Lookup Tables for Arenhövel's ^{2}H$(\vec{e}, e'\vec{n})^1$H Structure Functions

In order to employ the Arenhövel PWBA and FSI+MEC+IC models for computation of the ^{2}H$(\vec{e}, e'\vec{n})$ five-fold differential coincidence cross section and recoil polarization observables, we requested calculations of the eighteen structure functions for the

Central Q^2 $[(\mathrm{GeV}/c)^2]$	E_e [GeV]	$E_{e'}$ Range [GeV]	$\theta_{e'}$ Range [deg]
0.447	0.884	0.611 – 0.688	50.65 – 54.65
1.136	2.326	1.632 – 1.838	28.93 – 32.93
1.169	2.415	1.700 – 1.914	28.15 – 32.15
1.474	3.395	2.476 – 2.788	21.55 – 25.55

Table 6.1: Range of electron kinematics for the Arenhövel structure function calculations.

$^2\mathrm{H}(\vec{e}, e'\vec{n})$ reaction (recall the discussion in Section 2.3.7). These structure functions can be calculated solely from E_e, $E_{e'}$, $\theta_{e'}$, and $\Theta_{np}^{\mathrm{c.m.}}$ [192], and after specification of $\phi_{np}^{\mathrm{c.m.}}$, the full five-fold differential coincidence cross section and recoil polarization can be calculated according to Eqs. (2.177) and (2.179), respectively; therefore, it was necessary to request calculations over a dense kinematic grid that comfortably bracketed the range of electron kinematics satisfying all analysis cuts.

Calculations of the structure functions were requested, and subsequently provided, for the range of electron kinematics listed in Table 6.1. Arenhövel provided a separate calculation (i.e., a separate data file) for each $(E_e, E_{e'}, \theta_{e'})$ combination. Each of these data files contained the PWBA and FSI+MEC+IC structure function calculations for the specified electron kinematics calculated over a grid of $\Theta_{np}^{\mathrm{c.m.}}$ values ranging from $\Theta_{np}^{\mathrm{c.m.}} = 0°$ to 180°. For each Q^2 point, separate calculations were requested for 25 different $E_{e'}$ values spanning a $\Delta p/p \in [-5\%, +7\%]$ interval and 11 different $\theta_{e'}$ values spanning a $\pm 2°$ interval about the central value of the scattering angle. Also, for reasons that will become readily apparent later, PWBA and FSI+MEC+IC calculations were requested and subsequently provided for multiplicative factors of two different parameterizations of G_{En}. First, calculations were requested for G_{En} given by different multiplicative factors of the standard Galster parameterization,

$$G_{En} = -\mathrm{GSF}\frac{\tau}{1 + 5.6\tau}G_{Mn} \ , \tag{6.6}$$

where GSF = 0.50, 0.75, 1.00, 1.25, and 1.50. [GSF denotes "Galster Scale Factor".] Second, to investigate the influence of a different Q^2 dependence for G_{En} on the

acceptance-averaged results for G_{En}/G_{Mn}, calculations were requested for G_{En} given by different multiplicative factors of a modified Galster parameterization,

$$G_{En} = -\text{GSF}\frac{a\tau}{1+b\tau}G_{Mn} \ , \tag{6.7}$$

where a and b were chosen to be 0.894 and 3.55, respectively, and, again, GSF = 0.50, 0.75, 1.00, 1.25, and 1.50; the motivation for these values of a and b will be explained later (in Section 7.3.2). All of the calculations we received from Arenhövel assumed the dipole parameterization for G_{Mn}, G_{Ep}, and G_{Mp}.[3]

We received a total of 11,000 separate calculations for the kinematics listed in Table 6.1 (4 Q^2 points, 2 parameterization of G_{En} for each Q^2 point, 5 GSF values for each parameterization of G_{En}, 25 different grid values of $E_{e'}$, and 11 different grid values of $\theta_{e'}$). After receipt of the calculations, lookup tables for the structure functions indexed by $E_{e'}$, $\theta_{e'}$, and $\Theta_{np}^{\text{c.m.}}$ were constructed for each different Q^2, PWBA or FSI+MEC+IC, and GSF combination.

For each event, the five-fold differential coincidence cross section and recoil polarization were computed via three-dimensional cubic spline interpolation among the $E_{e'}$, $\theta_{e'}$, and $\Theta_{np}^{\text{c.m.}}$ kinematic grid elements. A general overview of cubic spline interpolation is given in Appendix D, and in what follows below, we discuss the implementation of our three-dimensional cubic spline interpolation algorithm in `GENGEN` and then document our algorithm's performance.

Implementation of Interpolation Algorithm in `GENGEN`

During the initialization of the simulation, `GENGEN` read the $(E_{e'}, \theta_{e'}, \Theta_{np}^{\text{c.m.}})$ kinematic grid elements and structure functions from the lookup table specified by the user in the main input file and then constructed three-dimensional cubic splines for each structure function via 18 separate calls (for the 18 structure functions) to a tricubic spline algorithm. The three-dimensional cubic splines were then stored in memory

[3] Although the recent polarized results for G_{Ep}/G_{Mp} [215,216] suggest that G_{Ep} and G_{Mp} do not scale similarly according to the dipole parameterization, we were interested in simulating quasifree neutron events and not quasifree proton events.

for later use during the main event loop.

After the kinematics for the electron and the neutron at the target were completely specified, the five-fold differential coincidence cross section and the recoil polarization were computed according to the following scheme. First, the ρ_L, ρ_{LT}, ρ_T, ρ_{TT}, ρ'_{LT}, and ρ'_T kinematic factors needed for computation of the cross section and the recoil polarization were computed according to Eqs. (2.107) through (2.109), and $\Theta_{np}^{\text{c.m.}}$ was computed according to Eq. (2.136). Second, the values of the structure functions for the event-wise $(E_{e'}, \theta_{e'}, \Theta_{np}^{\text{c.m.}})$ kinematics were computed via three-dimensional interpolation among the kinematic grid elements, and the cross section and recoil polarization were then computed according to Eqs. (2.177) and Eqs. (2.181) through (2.185), respectively (the latter computations required, of course, $\phi_{np}^{\text{c.m.}}$ as an additional input parameter). The cross section was transformed from the differential element $\mathrm{d}\Omega_{np}^{\text{c.m.}}$ to the differential element $\mathrm{d}\Omega_n$ via computation of the Jacobian given in Eq. (2.141), and the recoil polarization components were transformed from the n-p center of mass frame to the laboratory frame according to the prescription for the relativistic Wigner rotation discussed in Section 2.3.7.

Interpolation Performance

Although algorithms for two-dimensional cubic spline interpolation are readily available in standard references such as [422], we were not able to locate any such algorithms for three-dimensional cubic spline interpolation; therefore, we developed new algorithms specifically for this application, and, here, we document their performance.

First, in Fig. 6-2, we compare interpolated results for the f_L structure function with those provided by Arenhövel at the kinematic grid points for the FSI+MEC+IC model and G_{En} given by the Galster parameterization. The interpolated results clearly appear to be reasonable and agree well with the grid results which, in some cases, vary by several orders of magnitude over a relatively small change in a particular kinematic variable. Second, in Fig. 6-3, we compare interpolated results for the helicity-dependent polarization components P_x^h and P_z^h (at $\phi_{np}^{\text{c.m.}} = 0°$) with reference calculations provided by Arenhövel for the FSI+MEC+IC model and G_{En}

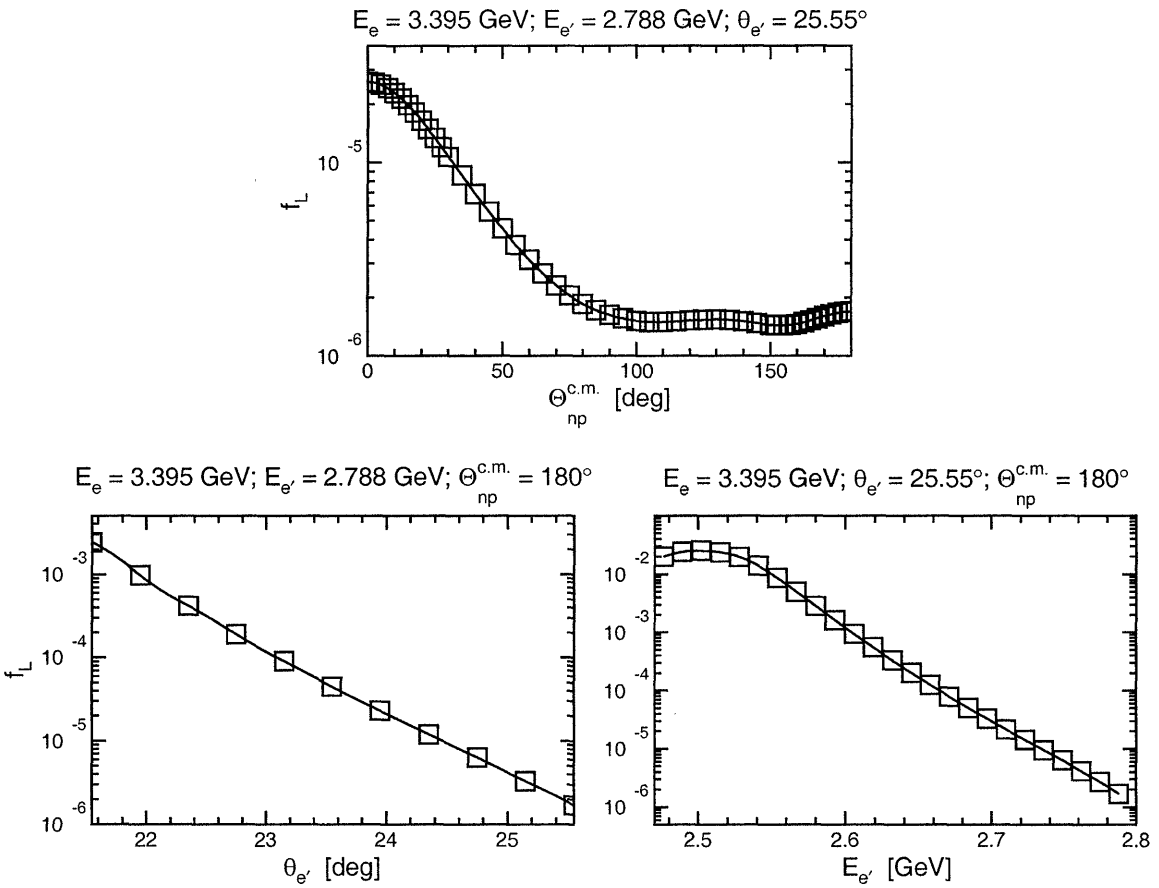

Figure 6-2: Comparison of interpolated results (lines) with Arenhövel's calculations (open squares) of the f_L structure function for the specified kinematics, the FSI+MEC+IC model, and G_{En} given by the Galster parameterization.

given by the Galster parameterization. Again, we see excellent agreement between the interpolated results and Arenhövel's reference calculations, and the behavior of the interpolated results as a function of $\Theta_{np}^{\text{c.m.}}$ clearly appears to be reasonable.

6.2.7 Electron and Neutron Solid Angle Jacobians

As we alluded in Section 6.2.3, it is important to realize that the five-fold differential coincidence cross section is differential in $d\Omega_{e'}$ and $d\Omega_n$, where these differential solid angles are defined by the scattered electron's and neutron's *actual scattering angles, not the in-plane and out-of-plane scattering angles sampled relative to the center of the target* by `GENGEN`; therefore, the value of the coincidence cross section computed

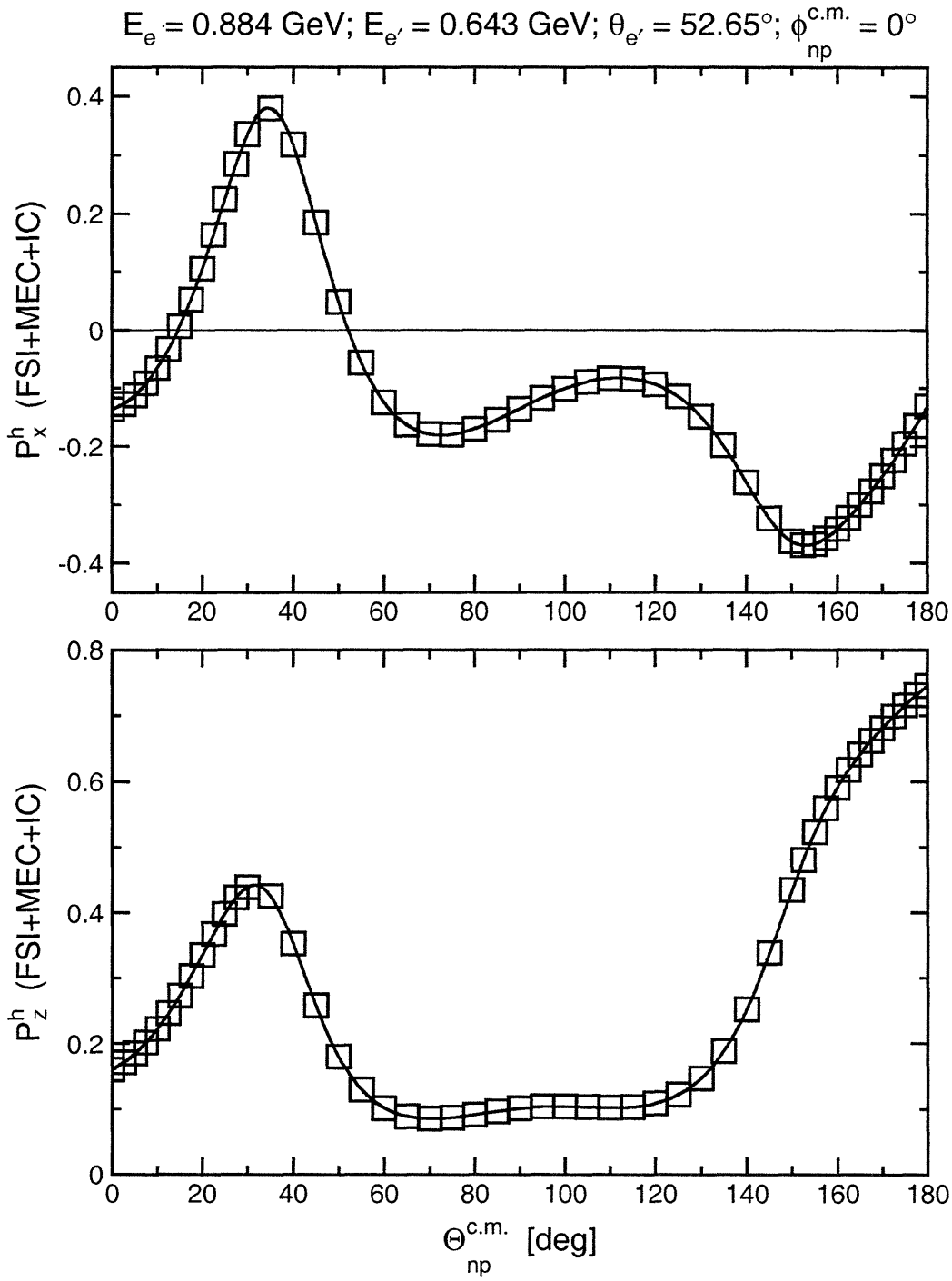

Figure 6-3: Comparison of interpolated results (lines) with Arenhövel's calculations (open squares) of P_x^h and P_z^h for the specified kinematics, the FSI+MEC+IC model, and G_{En} given by the Galster parameterization.

for the scattering angles sampled relative to the center of the target must be scaled by appropriate Jacobian factors for the actual solid angles of both the scattered electron and the neutron.

As described in detail by Ulmer [419], if the differential solid angle for the "actual scattering angles" is denoted $\mathrm{d}\Omega_a$, and the differential solid angle for the "sampled scattering angles" is denoted $\mathrm{d}\Omega_s$, the appropriate Jacobian factor is

$$\mathcal{J} = \frac{\mathrm{d}\Omega_a}{\mathrm{d}\Omega_s} \, . \tag{6.8}$$

A derivation of the exact formula for this Jacobian may be found in [419]; we do not repeat this derivation here as the details are fairly complicated and would not contribute to any further understanding of the task at hand. Instead, we simply remark that `GENGEN` computed the Jacobian for the scattered electron's solid angle, denoted $\mathcal{J}_{e'}$, and the Jacobian for the neutron's solid angle, denoted $\mathcal{J}_n$, using several routines written for `MCEEP`. Thereafter, the value of the cross section computed via interpolation of the structure functions was appropriately scaled according to

$$\frac{\mathrm{d}^5\sigma}{\mathrm{d}E_{e'}\mathrm{d}\Omega_{e'}\mathrm{d}\Omega_n} \rightarrow \left(\frac{\mathrm{d}^5\sigma}{\mathrm{d}E_{e'}\mathrm{d}\Omega_{e'}\mathrm{d}\Omega_n}\right) \mathcal{J}_{e'}\mathcal{J}_n \, . \tag{6.9}$$

6.2.8 Acceptance-Rejection Method for Importance Sampling

If the user chose to perform the simulation in the importance sampling mode, the trial kinematics were subjected to the following *acceptance-rejection test.* The test that determined if the event was accepted or rejected was

$$\left(\frac{\mathrm{d}^5\sigma}{\mathrm{d}E_{e'}\mathrm{d}\Omega_{e'}\mathrm{d}\Omega_n}\right) \mathcal{J}_{e'}\mathcal{J}_n < r\sigma_{\mathrm{test}} \quad \Longrightarrow \quad \text{event rejected,}$$

$$\left(\frac{\mathrm{d}^5\sigma}{\mathrm{d}E_{e'}\mathrm{d}\Omega_{e'}\mathrm{d}\Omega_n}\right) \mathcal{J}_{e'}\mathcal{J}_n \geq r\sigma_{\mathrm{test}} \quad \Longrightarrow \quad \text{event accepted,}$$

where r denotes a random number sampled uniformly on the interval $[0, 1]$ and σ_{test} denotes a value for a test cross section.

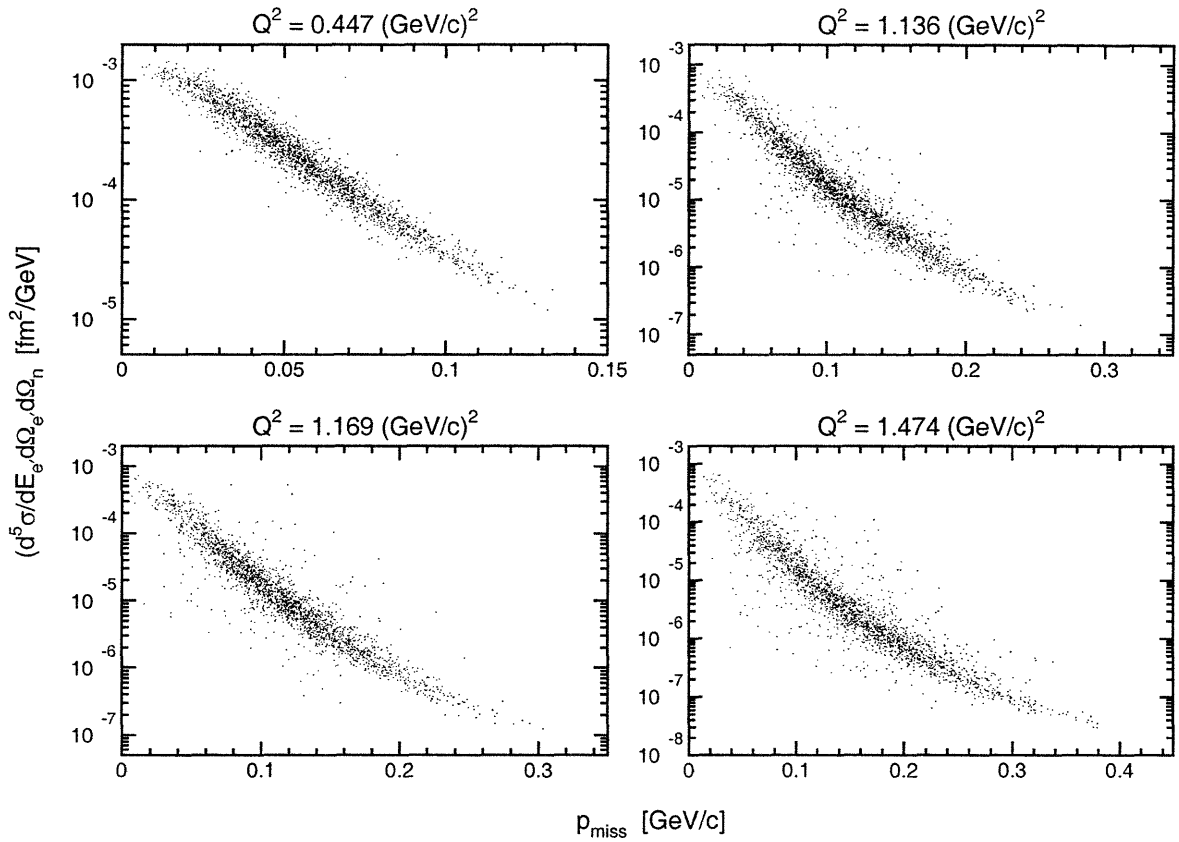

Figure 6-4: Five-fold ^{2}H$(\vec{e}, e'\vec{n})$ coincidence cross section computed according to Arenhövel's FSI+MEC+IC model with G_{En} given by the Galster parameterization plotted versus the range of sampled missing momentum.

Values for the five-fold coincidence cross section computed via interpolation of Arenhövel's FSI+MEC+IC structure functions are plotted in Fig. 6-4 versus the range of sampled missing momentum. As claimed earlier, we see here that the cross section varies by approximately two, four, and five orders of magnitude over the range of the missing momentum sampled for the $Q^2 = 0.447$, 1.136/1.169 and 1.474 $(\mathrm{GeV}/c)^2$ kinematic ranges, respectively; this rapid variation of the cross section with the missing momentum led to a drastic reduction in the simulation efficiency that was observed when `GENGEN` was operated in the importance sampling mode even if the value of the test cross section was optimized.

Although importance sampling is more rigorous, uniform sampling was employed for the final production analysis (simply due to the fact that the computation times for

the importance sampling mode were prohibitively long). When GENGEN was operated in the uniform samplig mode, the product of the five-fold coincidence cross section and the solid angle Jacobians for the scattered electron and the ejected neutron were stored as the event weight.

6.2.9 Construction of the Neutron's Spin

Following the computation of the five-fold coincidence cross section and recoil polarization and, if applicable, the acceptance-rejection test for the cross section, the spin of the neutron was constructed via the *maximum entropy approach*; this technique, proposed by Kelly [424], is described below.

Maximum Entropy Approach

For some random variable x, the entropy is, by definition,

$$S = -\langle \ln p(x) \rangle = -\int \mathrm{d}x \, \ln p(x) \, p(x) \; , \tag{6.10}$$

where $p(x)$ denotes the probability density function for x. A straightforward calculation demonstrates that maximization of S, subject to the constraints

$$\int_{-1}^{1} \mathrm{d}x \, p(x) = 1 \; , \qquad \int_{-1}^{1} \mathrm{d}x \, x \, p(x) = \bar{x} \; , \tag{6.11}$$

yields a conditional probability density function for x of the form

$$p(x|\bar{x}) = \frac{\lambda}{2} \frac{\exp[\lambda x]}{\sinh \lambda} \; , \tag{6.12}$$

where λ is the solution to the transcendental equation

$$\coth \lambda - \frac{1}{\lambda} = \bar{x} \; . \tag{6.13}$$

Now, suppose the polarization of an ensemble of particles is known, and it is desired to sample the spin of a particle chosen randomly from such an ensemble. A

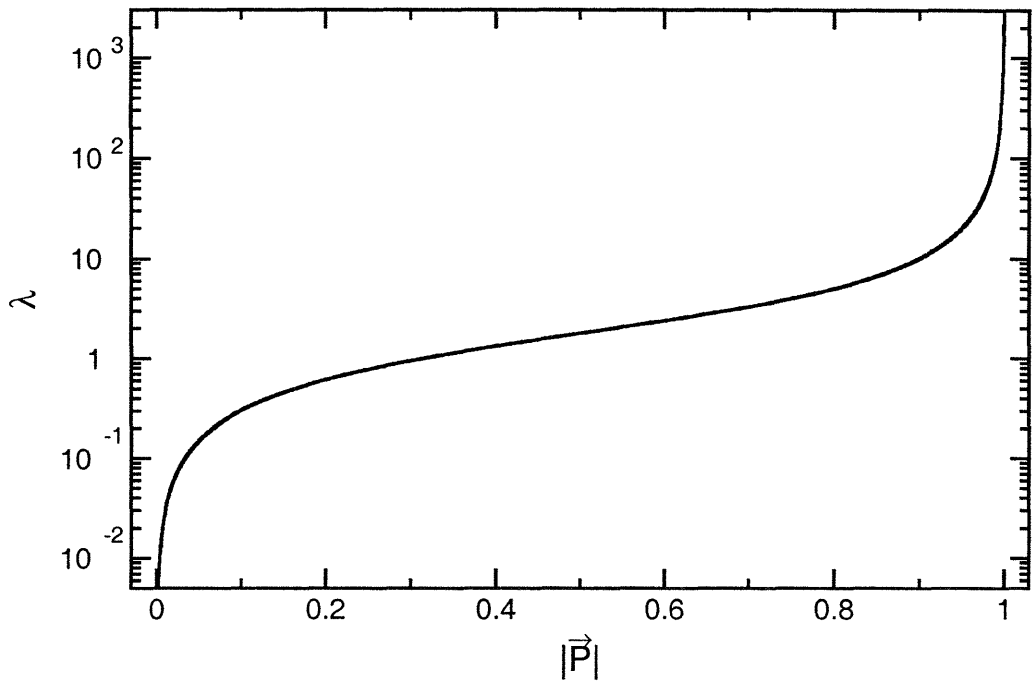

Figure 6-5: λ plotted as a function of $|\mathbf{P}|$ for Eq. (6.16).

probability density function for $x = \cos\theta$, where θ denotes the polar angle between the ensemble's polarization vector and the particle's spin, can be constructed via the above-described procedure. If we denote the ensemble's polarization as $\mathbf{P}$, where $P = |\mathbf{P}|$ satisifes $0 \leq P \leq 1$, and the spin of the particle as $\boldsymbol{\sigma}$, it follows that the conditional probability density for the spin, $p(\boldsymbol{\sigma}|\mathbf{P})$, subject to the constraints

$$\int \mathrm{d}\Omega\; p(\boldsymbol{\sigma}|\mathbf{P}) = 1\;, \qquad \int \mathrm{d}\Omega\; p(\boldsymbol{\sigma}|\mathbf{P})\; \boldsymbol{\sigma}\cdot\hat{\mathbf{P}} = \langle \boldsymbol{\sigma}\cdot\hat{\mathbf{P}} \rangle = P\;, \tag{6.14}$$

where $\hat{\mathbf{P}}$ is a unit vector along $\mathbf{P}$, is given by

$$p(\boldsymbol{\sigma}|\mathbf{P}) = \frac{\lambda}{4\pi} \frac{\exp[\lambda\; \boldsymbol{\sigma}\cdot\mathbf{P}]}{\sinh\lambda}\;. \tag{6.15}$$

As above, the parameter λ is the solution to the transcendental equation

$$\coth\lambda - \frac{1}{\lambda} = |\mathbf{P}|\;. \tag{6.16}$$

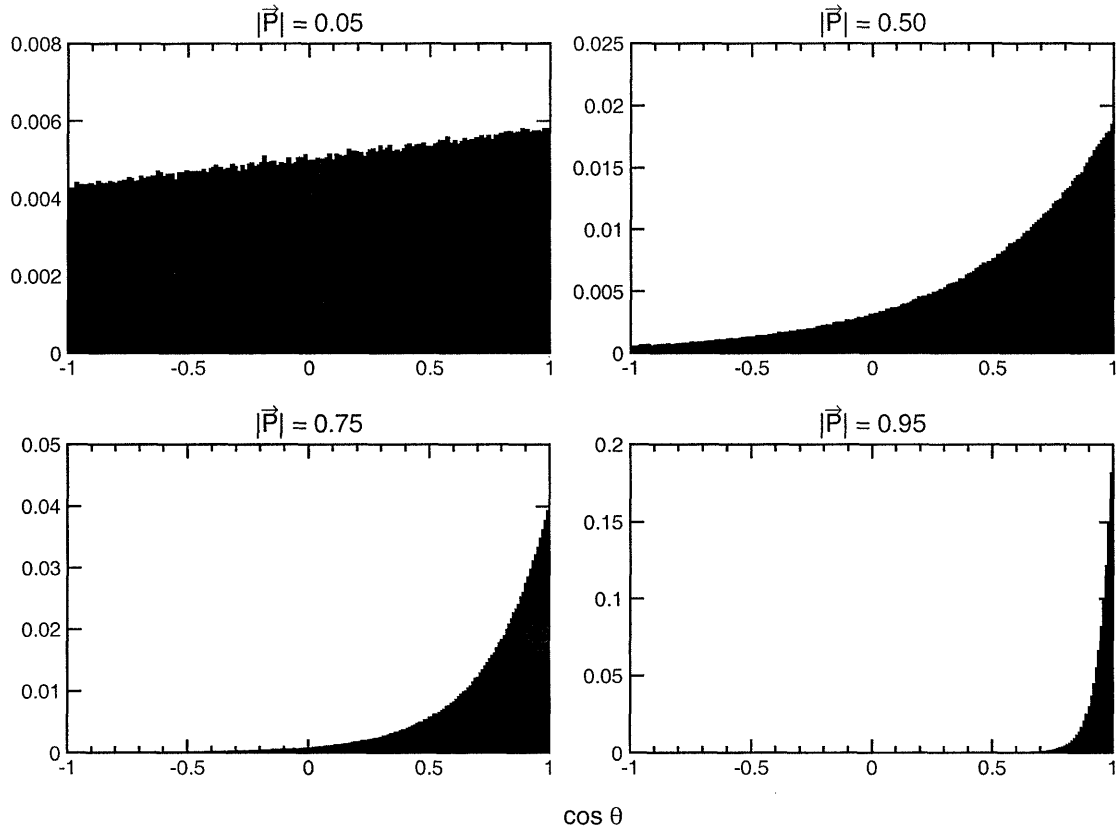

Figure 6-6: Simulated distributions of $\cos\theta$ for various values of $|\mathbf{P}|$. The histograms are normalized to unit content.

Implementation

During the initialization phase of the simulation, GENGEN constructed a numerical table of λ versus $|\mathbf{P}|$ according to Eq. (6.16) (as λ is the solution to a transcendental equation). When it was necessary to construct the spin of a particle (e.g., following the computation of the neutron's recoil polarization at the target), the magnitude of the polarization was computed, and GENGEN determined the appropriate value for λ. The spin of the particle was then constructed via the acceptance-rejection method.

To illustrate this sampling method, first, λ is plotted versus $|\mathbf{P}|$ in Fig. 6-5; here, we see that λ varies rapidly by several orders of magnitude over the range of possible values of $|\mathbf{P}|$. Second, simulated distributions of $\cos\theta$ for various values of $|\mathbf{P}|$ are shown in Fig. 6-6; these distributions clearly appear to be of the appropriate shape and, as would be expected, become broader (narrower) as $|\mathbf{P}| \to 0$ ($|\mathbf{P}| \to 1$).

6.2.10 Neutron Spin Transport Through Charybdis Field

Following the computation of the neutron's recoil polarization and the construction of the spin via the maximum entropy algorithm, GENGEN determined whether the neutron would pass through the opening to the steel collimator unimpeded; events with neutrons that did not pass through the opening in the steel collimator were rejected.

For those events surviving the steel collimator test, the recoil polarizaton and spin were transported through the Charybdis dipole field using a magnetic transport routine written by Taylor [425]. During the initialization phase, GENGEN read the x-, y-, and z-components of the field from a user-specified TOSCA map. As discussed previously in Section 4.2.2, the TOSCA field maps did not correspond exactly to the power supply currents used during the experiment; therefore, the field components were scaled by the ratio of the field integral for the desired current to the field integral for the TOSCA map current. Also, it is important to recall that the field integrals derived from the measured field maps and the TOSCA calculations agreed very well (recall Table 4.2).

An overview of the spin precession algorithm is as follows. The algorithm began by determining where the neutron first entered the field. After determination of this position, the algorithm calculated the transit time, Δt, between each (evenly-spaced) grid point in z. The spin was then transported through the field along each grid point in z. At each point, the algorithm determined the x- and y-coordinates for the neutron's position (assuming a straight trajectory) and then determined via interpolation the values of the x- and y-components of the field at that point (the z-components of the field at the grid points were, of course, specified in the field map). The spin and polarization vectors were then transported point-by-point along the z grid points via the modified midpoint method (see, e.g., [422]) according to

$$\mathbf{s}_0 = \text{spin at entry point } (x_0, y_0, z_0) \tag{6.17}$$

$$\mathbf{s}_1 = \mathbf{s}_0 + \Delta t \frac{\mathrm{d}\mathbf{s}}{\mathrm{d}t}\Big|_{(x_0,y_0,z_0)} \tag{6.18}$$

$$\mathbf{s}_{j+1} = \mathbf{s}_{j-1} + 2\Delta t \frac{\mathrm{d}\mathbf{s}}{\mathrm{d}t}\Big|_{(x_j, y_j, z_j)} \qquad \text{for } j = 1, 2, \ldots, N-1 \tag{6.19}$$

where $\mathrm{d}\mathbf{s}/\mathrm{d}t$ was computed according to Eq. (4.37) and N denotes the total number of grid points in z.

Finally, after the neutron was transported through the entire field, the precessed spin and polarization vectors were stored, and the precession angles were computed.

6.2.11 Interactions in the Lead Curtain

Neutron interations in the lead curtain were simulated with a spin-dependent multiple scattering algorithm that employed quasifree scattering from a lead nucleus modeled as a Fermi gas. In what follows below, we describe the formalism for our model, and we discuss its implementation in `GENGEN`.

Notation and Coordinate Systems

The algorithms evaluated spin-dependent nucleon-nucleon scattering in the *rest frame* of a nucleon chosen randomly from the Fermi gas. Before proceeding to a discussion of the underlying formalism for these algorithms, it is necessary to establish a certain amount of notation; the notation we employ follows the standard conventions for polarization phenomena in nucleon-nucleon scattering adopted by Bystricky, Lehar, and Winternitz [426].

First, in the *center-of-mass frame*, $(\hat{\mathbf{l}}, \hat{\mathbf{m}}, \hat{\mathbf{n}})$ basis vectors are defined according to

$$\hat{\mathbf{l}} = \frac{\hat{\mathbf{k}}_f + \hat{\mathbf{k}}_i}{|\hat{\mathbf{k}}_f + \hat{\mathbf{k}}_i|}\,, \qquad \hat{\mathbf{m}} = \frac{\hat{\mathbf{k}}_f - \hat{\mathbf{k}}_i}{|\hat{\mathbf{k}}_f - \hat{\mathbf{k}}_i|}\,, \qquad \hat{\mathbf{n}} = \frac{\hat{\mathbf{k}}_i \times \hat{\mathbf{k}}_f}{|\hat{\mathbf{k}}_i \times \hat{\mathbf{k}}_f|}\,, \tag{6.20}$$

where $\hat{\mathbf{k}}_i$ and $\hat{\mathbf{k}}_f$ are, respectively, unit vectors along the incident nucleon's and scattered nucleon's three-momentum in the center-of-mass frame.

Second, in the *rest frame of the target nucleon*, $(\hat{\mathbf{s}}, \hat{\mathbf{n}}, \hat{\mathbf{k}})$, $(\hat{\mathbf{s}}', \hat{\mathbf{n}}, \hat{\mathbf{k}}')$, and $(\hat{\mathbf{s}}'', \hat{\mathbf{n}}, \hat{\mathbf{k}}'')$ basis vectors for the incident nucleon, scattered nucleon, and recoil target nucleon,

respectively, are defined according to

$$\hat{\mathbf{k}} = \frac{\mathbf{k}}{|\mathbf{k}|} , \qquad \hat{\mathbf{k}}' = \frac{\mathbf{k}'}{|\mathbf{k}'|} , \qquad \hat{\mathbf{k}}'' = \frac{\mathbf{k}''}{|\mathbf{k}''|} , \tag{6.21}$$

$$\hat{\mathbf{n}} = \frac{\mathbf{k} \times \mathbf{k}'}{|\mathbf{k} \times \mathbf{k}'|} , \tag{6.22}$$

$$\hat{\mathbf{s}} = \hat{\mathbf{n}} \times \hat{\mathbf{k}} , \qquad \hat{\mathbf{s}}' = \hat{\mathbf{n}} \times \hat{\mathbf{k}}' , \qquad \hat{\mathbf{s}}'' = \hat{\mathbf{n}} \times \hat{\mathbf{k}}'' , \tag{6.23}$$

where $\hat{\mathbf{k}}$, $\hat{\mathbf{k}}'$, and $\hat{\mathbf{k}}''$ are, respectively, unit vectors along the incident nucleon's, scattered nucleon's, and recoil target nucleon's three-momentum in the target nucleon's rest frame.

Finally, we will label the incident nucleon, target nucleon, scattered nucleon, and recoil target nucleon as particles '1', '2', '3', and '4', respectively, and all subscripts or superscripts bearing such indicies in the remainder of this subsection should be interpreted as referring to the so-defined nucleon.

Interaction Probabilities

The high quality n+Pb total cross section data obtained from transmission measurements at the Los Alamos Meson Physics Facility by Finlay *et al.* [427] are plotted in Fig. 6-7 versus the incident neutron kinetic energy T_n; the error bars are smaller than the symbols for the data points.[4] Unfortunately, data are only available for values of T_n ranging from approximately 5 to 600 MeV [whereas T_n ranged up to ~700 and 900 MeV at $Q^2 = 1.136/1.169$ and 1.474 $(\mathrm{GeV}/c)^2$, respectively; see Fig. 5-68]; therefore, an extrapolation of the total cross section data to T_n values ranging from 600 to 1000 MeV was performed. We fitted a second-order polynomial to the existing total cross section data ranging from 300 to 600 MeV; the result of this fit and the subsequent extrapolation to higher energies is shown as the dashed line in Fig. 6-7. As we shall see later in Chapter 7, the corrections for interactions in the lead curtain are small and effectively cancel in the form factor ratio; therefore, the results are

[4]The neutron beam was produced by spallation of an 800 MeV proton beam from the LAMPF accelerator incident on a thick tungsten target.

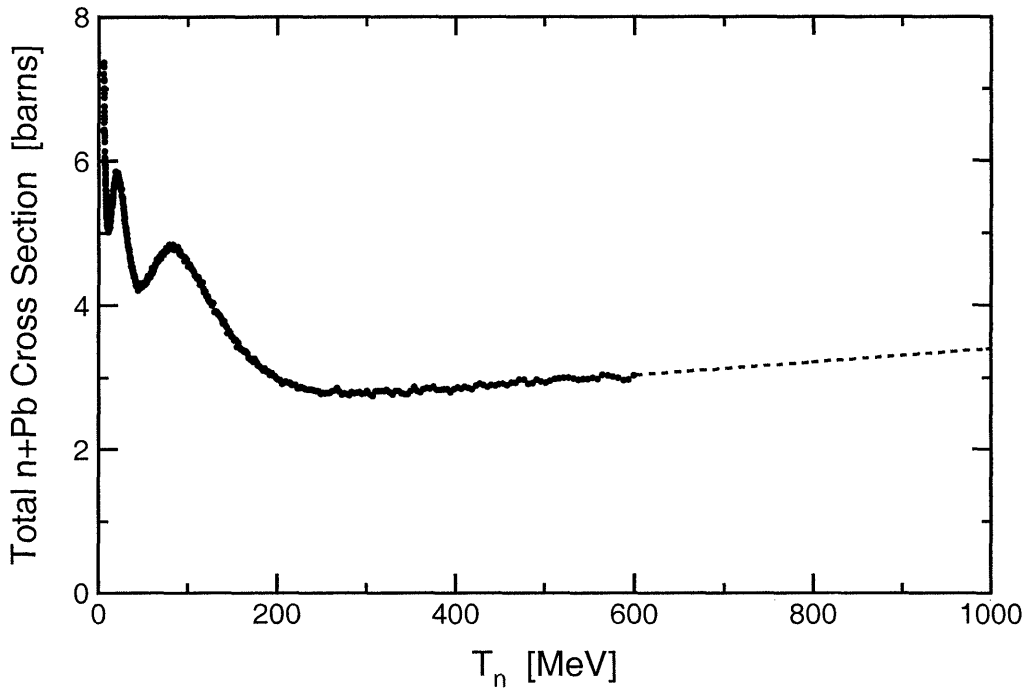

Figure 6-7: Total $n + \mathrm{Pb}$ cross section data plotted versus the neutron kinetic energy T_n. The dashed line represents the extrapolation of the existing data to $600 < T_n < 1000$ MeV.

insensitive to the actual interaction probabilities (and, hence, to deviations in the actual $n + \mathrm{Pb}$ cross section from the extrapolation).

GENGEN read the Finlay *et al.* $n + \mathrm{Pb}$ cross section data from a data file during the initialization phase of the simulation and subsequently stored these data in memory. For each event incident on the lead curtain, the code determined the value of the total cross section either via a lookup call to the data table or extrapolation. GENGEN then determined if an interaction occurred in the lead curtain by computing an interaction depth ℓ according to

$$\ell = -\lambda \ln r \ , \tag{6.24}$$

where $\lambda = 1/n\sigma$ is the mean free path, σ is the total cross section, and $n = 0.03295$ barn^{-1} cm^{-1} is the number density for ^{208}Pb [427], and r is a uniform random devi-

ate.[5] A test scattering vertex was then computed using the three components of the neutron's momentum, the coordinates for the previous vertex,[6] and the interaction depth ℓ. If the x, y, and z coordinates of the scattering vertex were within the physical dimensions of the lead curtain, GENGEN proceeded to evaluate the interaction (as described below). If the x or y coordinates fell outside of the lead curtain's physical dimensions but the z coordinate lay inside, the code assumed the neutron scattered into the walls of the shielding hut, and the event was not processed in any further detail. Finally, if the z coordinate fell outside of the lead curtain's physical dimensions, the algorithm assumed the neutron escaped the lead curtain.

Selection of *nn* and *np* Scattering Events

The cross sections for elastic nn and np scattering, denoted σ_{nn} and σ_{np}, respectively, were computed using an interface to routines provided by Arndt that are part of the SAID [188] program; the formalism for these algorithms and their implemententation in the GENGEN code structure will be described very shortly.

We estimated the probability for an interaction of the neutron with a neutron (proton) in the Fermi gas model of the lead nucleus, P_{nn} (P_{np}), to be

$$P_{nn} = \frac{N_n \sigma_{nn}}{N_n \sigma_{nn} + N_p \sigma_{np}} , \qquad P_{np} = \frac{N_p \sigma_{np}}{N_n \sigma_{nn} + N_p \sigma_{np}} , \tag{6.25}$$

where $N_n = 126$ and $N_p = 82$ for ^{208}Pb. The nn and np cross sections computed by these routines are plotted versus T_n in Fig. 6-8. It should be noted that the values of σ_{np} computed by GENGEN agree reasonably well with those compiled by Lechanoine-LeLuc and Lehar [428]. [Data for nn cross sections do not, of course, exist.] For $T_n \sim 600$ MeV, σ_{nn} (σ_{np}) is on the order of 50 (30) mb; therefore, the dominant process in the simulation was quasifree scattering from neutrons (as $P_{nn} \sim 0.72$).

[5] The total cross section is on the order of 3 barns for the relevant range of kinetic energies; therefore, the mean free path is approximately 10 cm, and the probability for an interaction in the lead curtain is ~50%.

[6] As multiple scattering was simulated, the previous vertex was the primary scattering vertex in the target for the first attempt at generating an interaction in the lead curtain, or the most recent scattering vertex in the lead curtain if at least one interaction had already occurred.

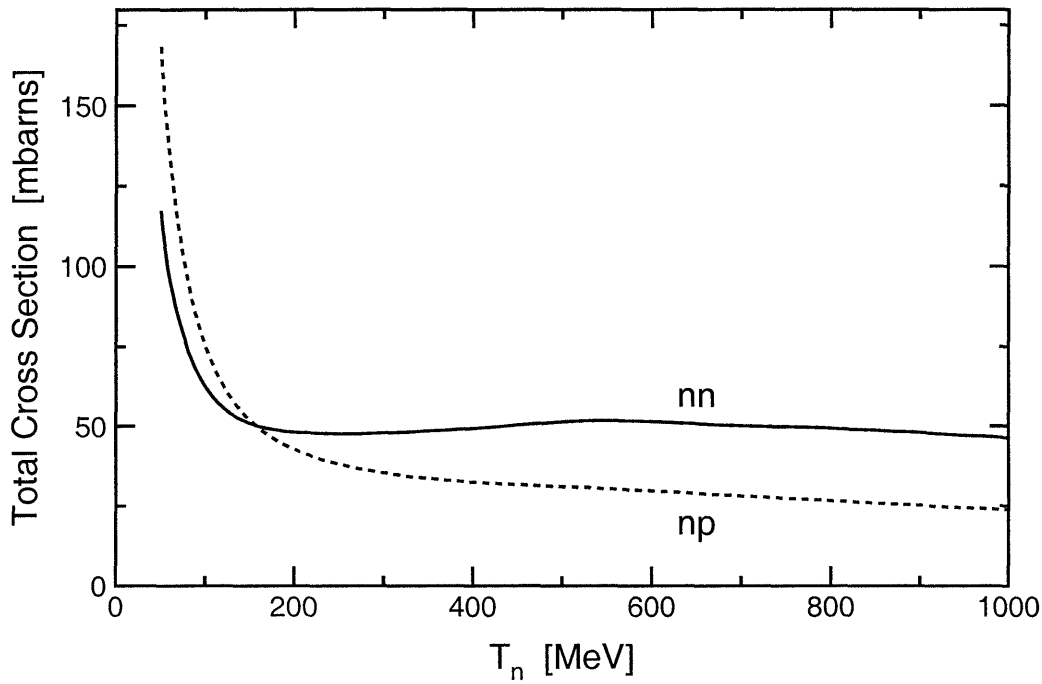

Figure 6-8: Total cross sections computed by GENGEN for elastic nn (solid line) and np (dashed line) scattering plotted versus T_n.

After GENGEN computed P_{nn} and P_{np}, a uniform random deviate was sampled and used to determine if an nn or np interaction occurred.

Overview of Formalism for NN Scattering

The brief overview of the formalism for polarized elastic nucleon-nucleon scattering which we present below closely follows and incorporates different discussions of this problem given by Wolfenstein and Ashkin [361], Schumacher and Bethe [429], Bystricky, Lehar, and Winternitz [426], Bleszynski, Bleszynski, and Whitten, Jr. [430], and Lechanoine-LeLuc and Lehar [428]. A detailed discussion of this formalism is much beyond the scope of this thesis; therefore, we primarily only quote relevant aspects of the formalism.

A complete description of spin-dependent nucleon-nucleon scattering is given by a matrix specifying the scattering amplitudes for all possible momentum and spin states of the scattered nucleon and the recoil target nucleon as a function of the incident nucleon's momentum and spin; this matrix, termed quite generally the *nucleon-nucleon*

scattering matrix, is conventionally written as

$$\mathcal{M} = \frac{1}{2}\Big[(a+b) + (a-b)\sigma_{1n}\sigma_{2n} + (c+d)\sigma_{1m}\sigma_{2m} + (c-d)\sigma_{1l}\sigma_{2l} + e(\sigma_{1n} + \sigma_{2n})\Big] \,, \tag{6.26}$$

where $\boldsymbol{\sigma}_1$ and $\boldsymbol{\sigma}_2$ are the usual Pauli spin matrices for particles 1 and 2, σ_{1n} denotes, for example, the projection of $\boldsymbol{\sigma}_1$ on the unit vector $\hat{\mathbf{n}}$, and the amplitudes a, b, c, d, and e are *complex-valued* functions of two kinematic variables (e.g., total energy and scattering angle in the center of mass frame, incident kinetic energy and scattering angle in the laboratory frame, etc.); the only assumptions that are necessary for the construction of $\mathcal{M}$ solely in terms of five amplitudes are parity conservation, time-reversal invariance, the Pauli principle, and isospin invariance.

Now, if we define an xyz coordinate system in the center-of-mass frame such that the z-axis is parallel to the *incident nucleon's momentum* and the y-axis is parallel to $\hat{\mathbf{n}}$, *helicity states* of the incident and scattered nucleon (i.e., particles 1 and 3) *defined relative to the above-defined z-axis* can be written as

$$\chi(\lambda_1) = \begin{pmatrix} \frac{1}{2} + \lambda_1 \\ \frac{1}{2} - \lambda_1 \end{pmatrix} \,, \tag{6.27}$$

and

$$\begin{aligned} \chi'(\lambda_3) &= \exp\left[\frac{-i\sigma_n \theta_{\text{scat}}^{\text{c.m.}}}{2}\right] \chi(\lambda_3) \\ &= \begin{pmatrix} \left(\frac{1}{2} + \lambda_3\right) \cos\frac{\theta_{\text{scat}}^{\text{c.m.}}}{2} - \left(\frac{1}{2} - \lambda_3\right) \sin\frac{\theta_{\text{scat}}^{\text{c.m.}}}{2} \\ \left(\frac{1}{2} + \lambda_3\right) \sin\frac{\theta_{\text{scat}}^{\text{c.m.}}}{2} + \left(\frac{1}{2} - \lambda_3\right) \cos\frac{\theta_{\text{scat}}^{\text{c.m.}}}{2} \end{pmatrix} \,, \end{aligned} \tag{6.28}$$

where $\lambda_1 = \pm\frac{1}{2}$ and $\lambda_3 = \pm\frac{1}{2}$ denote the helicity of particles 1 and 3 relative to their respective momenta and $\theta_{\text{scat}}^{\text{c.m.}}$ denotes the scattering angle in the center of mass frame. As is conventional, the helicity states of particles 2 and 4 are defined with a different phase (in addition to the fact that particles 1 and 2 and particles 3 and 4 are oriented

180° relative to each other in the center-of-mass frame) as

$$\begin{aligned}\chi'(\lambda_2) &= (-1)^{\frac{1}{2}-\lambda_2}\exp\left[-i\pi\right]\chi(\lambda_2) \\ &= (-1)^{\frac{1}{2}-\lambda_2}\begin{pmatrix} -\frac{1}{2}+\lambda_2 \\ \frac{1}{2}+\lambda_2 \end{pmatrix} ,\end{aligned} \tag{6.29}$$

and

$$\begin{aligned}\chi'(\lambda_4) &= (-1)^{\frac{1}{2}-\lambda_4}\exp\left[\frac{-i\sigma_n(\theta_{\rm scat}^{\rm c.m.}+\pi)}{2}\right]\chi(\lambda_4) \\ &= (-1)^{\frac{1}{2}-\lambda_4}\begin{pmatrix} -\left(\frac{1}{2}+\lambda_4\right)\sin\frac{\theta_{\rm scat}^{\rm c.m.}}{2} - \left(\frac{1}{2}-\lambda_4\right)\cos\frac{\theta_{\rm scat}^{\rm c.m.}}{2} \\ \left(\frac{1}{2}+\lambda_4\right)\cos\frac{\theta_{\rm scat}^{\rm c.m.}}{2} - \left(\frac{1}{2}-\lambda_4\right)\sin\frac{\theta_{\rm scat}^{\rm c.m.}}{2} \end{pmatrix} .\end{aligned} \tag{6.30}$$

Assuming parity conservation, time reversal invariance, and the Pauli principle, it can be shown (see, e.g., [426]) that five unique *helicity amplitudes*, denoted symbolically as $\langle\lambda_3\lambda_4|\mathcal{M}|\lambda_1\lambda_2\rangle$, can be defined according to

$$M_1 \equiv \langle++|\mathcal{M}|++\rangle = \langle--|\mathcal{M}|--\rangle , \tag{6.31}$$

$$M_2 \equiv \langle++|\mathcal{M}|--\rangle = \langle--|\mathcal{M}|++\rangle , \tag{6.32}$$

$$M_3 \equiv \langle+-|\mathcal{M}|+-\rangle = \langle-+|\mathcal{M}|-+\rangle , \tag{6.33}$$

$$M_4 \equiv \langle+-|\mathcal{M}|-+\rangle = \langle-+|\mathcal{M}|+-\rangle , \tag{6.34}$$

$$\begin{aligned}M_5 &\equiv \langle++|\mathcal{M}|+-\rangle = \langle-+|\mathcal{M}|--\rangle = \langle--|\mathcal{M}|+-\rangle \\ &= \langle-+|\mathcal{M}|++\rangle = -\langle--|\mathcal{M}|-+\rangle = -\langle+-|\mathcal{M}|++\rangle \\ &= -\langle++|\mathcal{M}|-+\rangle = -\langle+-|\mathcal{M}|--\rangle ,\end{aligned} \tag{6.35}$$

where only the signs of the nucleon helicities are indicated above. Finally, again as shown in detail in [426], the $M_1, \ldots, M_5$ helicity amplitudes can be written in terms of the nucleon-nucleon scattering matrix amplitudes $a, \ldots, e$ as

$$M_1 = \frac{1}{2}\left[a\cos\theta_{\rm scat}^{\rm c.m.} + b - c + d + ie\sin\theta_{\rm scat}^{\rm c.m.}\right] , \tag{6.36}$$

$$M_2 = \frac{1}{2}[a\cos\theta^{\text{c.m.}}_{\text{scat}} - b + c + d + ie\sin\theta^{\text{c.m.}}_{\text{scat}}] \ , \tag{6.37}$$

$$M_3 = \frac{1}{2}[a\cos\theta^{\text{c.m.}}_{\text{scat}} + b + c - d + ie\sin\theta^{\text{c.m.}}_{\text{scat}}] \ , \tag{6.38}$$

$$M_4 = \frac{1}{2}[-a\cos\theta^{\text{c.m.}}_{\text{scat}} + b + c + d - ie\sin\theta^{\text{c.m.}}_{\text{scat}}] \ , \tag{6.39}$$

$$M_5 = \frac{1}{2}[-a\sin\theta^{\text{c.m.}}_{\text{scat}} + ie\cos\theta^{\text{c.m.}}_{\text{scat}}] \ , \tag{6.40}$$

which can be inverted to give

$$a = \frac{1}{2}[(M_1 + M_2 + M_3 - M_4)\cos\theta^{\text{c.m.}}_{\text{scat}} - 4M_5\sin\theta^{\text{c.m.}}_{\text{scat}}] \ , \tag{6.41}$$

$$b = \frac{1}{2}[M_1 - M_2 + M_3 + M_4] \ , \tag{6.42}$$

$$c = \frac{1}{2}[-M_1 + M_2 + M_3 + M_4] \ , \tag{6.43}$$

$$d = \frac{1}{2}[M_1 + M_2 - M_3 + M_4] \ , \tag{6.44}$$

$$ie = \frac{1}{2}[(M_1 + M_2 + M_3 - M_4)\sin\theta^{\text{c.m.}}_{\text{scat}} + 4M_5\cos\theta^{\text{c.m.}}_{\text{scat}}] \ . \tag{6.45}$$

All relevant cross section and polarization observables are defined in terms of a, b, c, d, and e and can, as a result, be computed provided the M_1, M_2, M_3, M_4, and M_5 helicity amplitudes are known. Below, we provide the formulas for observables relevant for polarized-nucleon, unpolarized-nucleon scattering (as we were interested in evaluating the depolarization of the polarized neutron flux by interactions with unpolarized Pb nuclei).

First, the differential cross section in the *rest frame of the target nucleon*, denoted σ (for short), is given by

$$\sigma = \frac{1}{2}\left[|M_1|^2 + |M_2|^2 + |M_3|^2 + |M_4|^2 + 4|M_5|^2\right] \ . \tag{6.46}$$

Second, the induced polarization[7], P, or, equivalently, the analyzing power, A_y, is given by

$$\sigma P = -\Im\left[M_5^*(M_1 + M_2 + M_3 - M_4)\right] \ . \tag{6.47}$$

[7]The induced polarization is the polarization induced in the $\hat{\mathbf{n}}$ direction in elastic unpolarized-nucleon, unpolarized-nucleon scattering.

Third, the polarization of the scattered nucleon (i.e., particle 3), as referred to the $(\hat{\mathbf{s}}', \hat{\mathbf{n}}, \hat{\mathbf{k}}')$ basis, is given by

$$P_{3,s'} = \frac{P_{1,s}\mathcal{D}_{ss'} + P_{1,k}\mathcal{D}_{ks'}}{1 + PP_{1,n}} \ , \tag{6.48}$$

$$P_{3,n} = \frac{P + P_{1,n}\mathcal{D}_{nn}}{1 + PP_{1,n}} \ , \tag{6.49}$$

$$P_{3,k'} = \frac{P_{1,s}\mathcal{D}_{sk'} + P_{1,k}\mathcal{D}_{kk'}}{1 + PP_{1,n}} \ , \tag{6.50}$$

where $(P_{1,s}, P_{1,n}, P_{1,k})$ denotes the polarization of the incident nucleon (i.e., particle 1) as referred to the $(\hat{\mathbf{s}}, \hat{\mathbf{n}}, \hat{\mathbf{k}})$ basis, and the $\mathcal{D}_{ij}$ are elements of the *depolarization tensor*. The elements of the depolarization tensor *in the target nucleon's rest frame* can be written in terms of the helicity amplitudes explicitly as

$$\begin{aligned}\sigma\mathcal{D}_{ss'} &= -\Re\left[M_5^*(M_1 - M_2 + M_3 + M_4)\right]\sin\theta_1 \\ &\quad + \Re\left[M_1^* M_3 + M_2^* M_4\right]\cos\theta_1 \ ,\end{aligned} \tag{6.51}$$

$$\begin{aligned}\sigma\mathcal{D}_{ks'} &= \Re\left[M_5^*(M_1 - M_2 + M_3 + M_4)\right]\ \cos\theta_1 \\ &\quad + \frac{1}{2}\left[|M_1|^2 - |M_2|^2 + |M_3|^2 - |M_4|^2\right]\sin\theta_1 \ ,\end{aligned} \tag{6.52}$$

$$\sigma\mathcal{D}_{nn} = \Re\left[M_1^* M_3 - M_2^* M_4\right] + 2\ |M_5|^2 \ , \tag{6.53}$$

$$\begin{aligned}\sigma\mathcal{D}_{sk'} &= -\Re\left[M_5^*(M_1 - M_2 + M_3 + M_4)\right]\ \cos\theta_1 \\ &\quad - \Re\left[M_1^* M_3 + M_2^* M_4\right]\ \sin\theta_1 \ ,\end{aligned} \tag{6.54}$$

$$\begin{aligned}\sigma\mathcal{D}_{kk'} &= -\Re\left[M_5^*(M_1 - M_2 + M_3 + M_4)\right]\ \sin\theta_1 \\ &\quad + \frac{1}{2}\left[|M_1|^2 - |M_2|^2 + |M_3|^2 - |M_4|^2\right]\ \cos\theta_1 \ ,\end{aligned} \tag{6.55}$$

where θ_1 denotes the incident nucleon's scattering angle in the target nucleon's rest frame.

Finally, the last observable of interest, the polarization of the recoil target nucleon (i.e., particle 4), as referred to the $(\hat{\mathbf{s}}'', \hat{\mathbf{n}}, \hat{\mathbf{k}}'')$ basis, is given by

$$P_{4,s''} = \frac{P_{1,s}\mathcal{K}_{ss''} + P_{1,k}\mathcal{K}_{ks''}}{1 + PP_{1,n}} \ , \tag{6.56}$$

$$P_{4,n} = \frac{P + P_{1,n}\mathcal{K}_{nn}}{1 + PP_{1,n}} \,, \tag{6.57}$$

$$P_{4,k''} = \frac{P_{1,s}\mathcal{K}_{sk''} + P_{1,k}\mathcal{K}_{kk''}}{1 + PP_{1,n}} \,, \tag{6.58}$$

where the $\mathcal{K}_{ij}$ are elements of the *polarization transfer tensor*. As with the depolarization tensor, the elements of the polarization transfer tensor in the target nucleon's rest frame can be written in terms of the helicity amplitudes explicitly as

$$\begin{aligned}
\sigma\mathcal{K}_{ss''} &= -\Re\left[M_5^*(-M_1 + M_2 + M_3 + M_4)\right] \sin\theta_2 \\
&\quad - \Re\left[M_1^* M_4 + M_2^* M_3\right] \cos\theta_2 \,, && (6.59) \\
\sigma\mathcal{K}_{ks''} &= -\Re\left[M_5^*(-M_1 + M_2 + M_3 + M_4)\right] \cos\theta_2 \\
&\quad + \frac{1}{2}\left[-|M_1|^2 + |M_2|^2 + |M_3|^2 - |M_4|^2\right] \sin\theta_2 \,, \\
\sigma\mathcal{K}_{nn} &= -\Re\left[M_1^* M_4 - M_2^* M_3\right] + 2\,|M_5|^2 \,, && (6.60) \\
\sigma\mathcal{K}_{sk''} &= \Re\left[M_5^*(-M_1 + M_2 + M_3 + M_4)\right] \cos\theta_2 && (6.61) \\
&\quad - \Re\left[M_1^* M_4 + M_2^* M_3\right] \sin\theta_2 && (6.62) \\
\sigma\mathcal{K}_{kk''} &= -\Re\left[M_5^*(-M_1 + M_2 + M_3 + M_4)\right] \sin\theta_2 \\
&\quad - \frac{1}{2}\left[-|M_1|^2 + |M_2|^2 + |M_3|^2 - |M_4|^2\right] \cos\theta_2 \,, && (6.63)
\end{aligned}$$

where θ_2 denotes the target nucleon's recoil angle in its rest frame.

The above definitions and prescriptions for the cross section, analyzing power, and polarization observables for the scattered nucleon and the recoil target nucleon specify all of the quantities that were needed for our evaluation of spin-dependent neutron scattering in the lead curtain. We now proceed to discuss the implementation of this formalism in `GENGEN`.

Implementation

During the initialization phase of the simulation, routines from the `SAID` program [188] we received from Arndt computed the helicity amplitudes for *nn*, *np*, and *pp* scattering over a kinematic grid indexed by the incident nucleon's laboratory frame kinetic

energy, T, and scattering angle, θ_{scat}.[8] After calls to these routines, the differential cross section and analyzing power were computed for each combination of kinetic energy and scattering angle according to the formalism just discussed [i.e., Eqs. (6.46) and (6.47), respectively]. Lookup tables for the analyzing power indexed by the kinetic energy and scattering angle were then constructed and stored in memory.

Next, the total cross section for a fixed value of the kinetic energy was computed via numerical integration of the differential cross section over the possible range of scattering angles (i.e., from 0° to 90°). Lookup tables for the cumulative probability distribution for the scattering angle, $p(\theta_{\text{scat}} < \overline{\theta};\ T)$, at some value of the kinetic energy, defined to be

$$p(\theta_{\text{scat}} < \overline{\theta};\ T) = \frac{\int_0^{\overline{\theta}} \mathrm{d}\theta_{\text{scat}}\ \sigma(\theta_{\text{scat}};\ T)}{\int_0^{\pi/2} \mathrm{d}\theta_{\text{scat}}\ \sigma(\theta_{\text{scat}};\ T)}\ , \tag{6.64}$$

were then constructed and stored in memory for each combination of kinetic energy and scattering angle.

Spin-dependent neutron interactions in the lead curtain were then evaluated with the following collection of algorithms:

- First, the magnitude of the target nucleon's momentum, $|\mathbf{p}_2|$, was sampled from a Fermi gas distribution according to

$$|\mathbf{p}_2| = (r k_F^3/3)^{1/2}\ , \tag{6.65}$$

  where r is a uniform random deviate and the Fermi momentum, k_F, for ^{208}Pb was taken to be 265 MeV/c [431]; the direction of $\mathbf{p}_2$ was sampled randomly on a unit sphere.

- Second, the momentum for the scattered neutron and the recoil target nucleon were evaluated via the following procedure:

[8] As stated earlier, the nucleon-nucleon scattering matrix amplitudes $a, \ldots, e$, or, equivalently, the helicity amplitudes, are complex-valued functions of *two* kinematic variables; the routines we received from Arndt required the incident nucleon's kinetic energy and the scattering angle as input for computation of the helicity amplitudes.

- The four-momentum of the incident neutron and the target nucleon were transformed from the laboratory frame to the target nucleon's rest frame via the standard Lorentz transformations. The transformation of the incident neutron's spin and polarization required a Wigner rotation.

- After a random deviate r was chosen, the polar scattering angle, θ_{scat}, was obtained via interpolation within the lookup tables containing the cumulative $p(\theta_{\text{scat}} < \overline{\theta};\ T)$ probability distributions for the scattering angle constructed during initialization. The scattered neutron's energy was then computed in the target nucleon's rest frame using the interpolated value for θ_{scat}.

- The azimuthal scattering angle, ϕ_{scat}, was then constructed via the following acceptance-rejection method. A value for ϕ_{scat} was chosen randomly on the interval $[0°, 360°]$; the interpolated value for θ_{scat} and the sampled value for ϕ_{scat} then uniquely defined the scattered neutron's momentum in the target nucleon's rest frame. The analyzing power, A_y, was obtained via interpolation within the lookup tables constructed during initialization, and an asymmetry, α, defined to be

$$\alpha = \frac{1 + A_y \mathbf{s}_{12} \cdot \hat{\mathbf{n}}}{2\pi}\ , \tag{6.66}$$

  where $\mathbf{s}_{12}$ denotes the spin of the incident neutron (particle 1) in the rest frame of the target nucleon (particle 2), was computed. The asymmetry was then compared with a uniform random deviate r. If $r \leq \alpha$, the sampled value for ϕ_{scat} was accepted; otherwise, a new value was constructed and tested.

- After the scattered neutron's momentum was constructed in the target nucleon's rest frame, the components were transformed from the target nucleon's rest frame to laboratory frame via the standard Lorentz transformations; the recoil target nucleon's momentum in the laboratory frame was then evaluated via momentum conservation.

- Pauli blocking was enforced; that is, if the magnitude of either the scattered neutron's momentum or the recoil target nucleon's momentum fell below the Fermi momentum, the interaction was not processed in any further detail, and the momentum, spin, and polarization were restored to their original values.

- Third, the $(\hat{\mathbf{s}}, \hat{\mathbf{n}}, \hat{\mathbf{k}})$, $(\hat{\mathbf{s}}', \hat{\mathbf{n}}, \hat{\mathbf{k}}')$, and $(\hat{\mathbf{s}}'', \hat{\mathbf{n}}, \hat{\mathbf{k}}'')$ basis vectors [defined previously in Eqs. (6.21) through (6.23)] were constructed in the target nucleon's rest frame. Helicity amplitudes were computed for the kinematics in this reference frame, and the elements of the depolarization tensor and the polarization transfer tensor were computed from the helicity amplitudes according to the formulas provided above. Following the computation of the $\mathcal{D}_{ij}$ and $\mathcal{K}_{ij}$ elements, the polarization components of the scattered neutron and the recoil target nucleon were computed according to Eqs. (6.48) through (6.50) and Eqs. (6.56) through (6.58), respectively. Following the evaluation of the polarizations, the spins were sampled via the maximum entropy approach; the polarizations and spins were then transformed from the target nucleon's rest frame to the experimental frame via an appropriate Wigner rotation.

After the neutron escaped the lead curtain, the final values of the momentum, polarization, and spin evaluated by the above sequence of algorithms were stored and subsequently presented to the front array of the polarimeter.

6.2.12 Interactions in the Front and Rear Arrays

After `GENGEN` transported the neutron through the Charybdis field and the lead curtain, the code determined if the neutron interacted in the front array. To do so, a mean free path of $\lambda = 100$ cm was assumed for all neutron kinetic energies, and an interaction depth, ℓ, was chosen, again, according to Eq. (6.24). A scattering vertex was then computed using the three components of the neutron's momentum, the

coordinates for the previous vertex[9], and the interaction depth ℓ. If the coordinates for the scattering vertex fell within the physical dimensions of the front array, an *np* interaction was evaluated; otherwise, GENGEN assumed the neutron did not interact in the front array, and the event was not processed in any further detail.

For those events with an interaction in the front array, GENGEN determined if the neutron scattered elastically from a free proton in a hydrogen atom or quasielastically from a proton bound in a carbon nucleus; we assumed that the neutron scattered from a bound proton ~85% of the time.[10] The momenta of the scattered neutron and the recoil proton were constructed with algorithms similar to those employed for the evaluation of scattering in the lead curtain.[11]

We employed a rather simple model for the recoil proton's propagation and energy loss in the scintillator material (i.e., we did not attempt a full-scale GEANT-type[12] simulation of the interaction between the recoil proton and the plastic scintillator material). In particular, we used the Cecil, Anderson, and Madey [406] range-energy formulas given previously in Eqs. (5.19) and (5.20). Following the evaluation of the *np* interaction, we assumed the proton traveled in a straight line; our simple model did not account for the possibility of small-angle scattering of the proton due to, for example, Coulomb interactions. The range, R, was computed for the proton's initial kinetic energy and compared to the distance, d, that the proton would need to travel along the straight line in order to escape the front array. If $d \leq R$, GENGEN assumed the proton was completely stopped in the front array, and the energy deposition in each detector the proton traversed was converted into units of MeVee via Eq. (5.13). If, instead, $d > R$, our simple model then calculated the proton's final velocity assuming

[9]The previous vertex was the primary scattering vertex in the target (final scattering vertex in the lead curtain) if the neutron did not (did) interact in the lead curtain.

[10]The quoted ratio of hydrogen to carbon in BICRON 400 plastic scintillator is 1.103 [385]; therefore, the ratio of free to bound protons in the scintillators is ~15%.

[11]Technically, the algorithms developed for evaluation of interactions in the lead curtain were based on the pre-existing algorithms written for the evaluation of interactions in the front and rear arrays.

[12]GEANT [432], part of the larger CERNLIB [394] library, is a simulation program that describes the passage of elementary particles through matter. One of the principal applications of GEANT is for simulations of particle tracking through an experimental setup for the simulation of detector response.

the deceleration was constant along the path through the scintillator (the energy deposition in each detector the proton traversed was computed and converted into MeVee); in order to account for attenuation in the scintillators, the pulse heights recorded by each PMT were subjected to an exponential attenuation determined by the distance of the *np* interaction from each PMT. The timing signals for each PMT were generated based on the time that the particle first encountered the detector plus a propagation time for the light in the scintillators. Both the pulse height and timing signals were subjected to Gaussian fluctuations with standard deviations specified by the user. Also, if the pulse heights fell below the thresholds on the discriminators, the event was not processed any further.

If the user chose to conduct the simulation with the `GMN` trigger, successful evaluation of an interaction in the front array marked the end of an event, and the simulation returned to the start of the main event loop. If, instead, the user chose to operate `GENGEN` with the `GEN` trigger, both the scattered neutron and the recoil proton were tracked into the rear array. The code determined which particle, if either, interacted in the rear array, and if an interaction occurred, pulse height and timing signals for the rear array were generated in an identical fashion to that employed for the front array (i.e., completely identical algorithms were used). Successful evaluation of an interaction in the rear array marked the end of a `GEN` trigger event, and the simulation then returned to the start of the main event loop.

6.2.13 Output

Events were generated until a user-specified goal was achieved. The simulation results were then either written to an `HBOOK` Ntuple file or an `.rzdat` file for inspection by the user. In addition, a file summarizing the kinematics, physics options, mode of operation, detector resolution parameters, statistics (e.g., number of trial events, simulation efficiency, etc.) was output.

6.3 GENGEN Performance

A rigorous and reliable extraction of the corrections for the finite experimental acceptance and nuclear physics effects from simulated data is feasible if the simulated acceptance reasonably matches the experimental acceptance; therefore, in this section, we document the performance of GENGEN by comparing simulated distributions of important kinematic quantities with those derived from experimental data. All of the simulated data that we present were extracted from simulations we performed that employed uniform sampling and the GEN trigger; in addition, neutron scattering in the lead curtain was enabled. The five-fold differential coincidence cross section was computed according to Arenhövel's FSI+MEC+IC model with G_{En} given by the standard Galster parameterization.

As is documented in what follows, the GENGEN distributions agree reasonably well with those distributions extracted from the experimental data; therefore, we were confident that our final acceptance-averaged and nuclear physics corrected results for G_{En}/G_{Mn} that we extracted from our simulated data (described in the next chapter) were reliable.

For ease of reference, all figures showing comparisons between the GENGEN simulated and experimental distributions appear at the end of this chapter.

6.3.1 Comparison of Electron Variable Distributions

We begin by comparing simulated and experimental distributions of W and Q^2 for (n,n) and (n,p) events in Figs. 6-9 through 6-12. Here, we see relatively good agreement between the simulated and experimental distributions.

6.3.2 Comparison of ^{2}H$(e,e'n)$ Reaction Variable Distributions

Next, we continue by comparing simulated and experimental distributions of variables related to the ^{2}H$(e,e'n)$ quasielastic reaction; in particular, we compare simulated

and experimental distributions of $p_{\rm miss}$, θ_{nq}, and ϕ_{nq} for (n,n) and (n,p) events in Figs. 6-13 through 6-18. With the exception of the ϕ_{nq} distributions, we again see excellent agreement between the simulated and experimental distributions. Although much effort was expended in an attempt to resolve the discrepancy between the ϕ_{nq} distributions, we must admit that the origin of this discrepany was never understood; however, the effects of this discrepancy on the extraction of the corrections for the finite experimental acceptance and nuclear physics effects should be small as the acceptance-averaged helicity-dependent polarization components P_x^h and P_z^h should be largely insensitive to those structure functions multiplied by $\sin\phi_{nq}$ or $\cos\phi_{nq}$ [see Eqs. (2.184) through (2.185)] as these should average to 0 over the entire event sample.

6.3.3 Comparison of Polarimeter Scattering and Response Variable Distributions

Finally, we conclude our documentation of the `GENGEN` performance by comparing simulated and experimental distributions for a number of variables related to the polarimeter in Figs. 6-19 through 6-28. A number of comments are in order here.

First, in Figs. 6-19 through 6-24, we compare simulated and experimental distributions for variables related to NN scattering in the polarimeter: $\theta_{\rm scat}$, $\phi_{\rm scat}$, and $\beta_{\rm scat}$. Here, we see reasonable agreement; the slight discrepancies seen in these figures may possibly be the result of an incomplete model of NN scattering in the polarimeter (e.g., omission of inelastic channels). Second, simulated and experimental distributions of detector pulse heights for the detector recording the interaction in the front and rear array detectors are compared in Figs. 6-25 through 6-28. Here, we see that the pulse height distributions in the front array for (n,n) events agree fairly well; however, we see only qualitative agreement for (n,p) events. The (n,p) pulse height distributions are of the form expected for penetration of the recoil proton from the front array to the rear array (i.e., the recoil proton traversing only the short dimension of a front array detector), but our simple model was not capable of describing all possible energy loss processes. The rear array pulse height distributions for both

(n,n) and (n,p) events agree qualitatively; however, the structure that is seen in the experimental distributions at large pulse height values may be due to overflow in the ADCs (which was not, of course, simulated in GENGEN).

6.3.4 Simulation of Pion-Production Events

Although GENGEN was capable of simulating pion-production reactions in the target, this component of the simulation was not as refined as the elastic and quasielastic cases. Nevertheless, it is worth presenting some sample results from pion-production simulations that we peformed recently; however, the results presented here should be considered "preliminary".

Distributions of the invariant mass and the missing momentum extracted from pion-production simulations at $Q^2 = 1.474$ (GeV/c)^2 are presented in Fig. 6-29 (again, presented at the end of this chapter). These results suggest that our cuts on W and $p_{\rm miss}$, $W < 1.04$ (GeV/c)^2 and $p_{\rm miss} < 100$ MeV/c, were well chosen as these preliminary results suggest that nearly all pion-production events lie above these thresholds.

6.4 Overview of Acceptance Program

The Acceptance program, written by Semenov [414,433], was developed as an alternative to the GENGEN Monte Carlo simulation program and, in fact, produced the first acceptance-averaged and nuclear physics corrected results for G_{En}/G_{Mn} (although results from GENGEN followed several months later).

The Acceptance program was nearly identical to the casym program that was described in the previous chapter, and an overview of this program is as follows. First, as in the casym program, the Acceptance program began with a series of initialization routines that read user-specified cuts from an ASCII input file and initialized the output HBOOK file for distributions of the recoil polarization spectra and other kinematic variables. Also, the necessary three-dimensional cubic splines for the 18 structure functions were constructed via a call to the same interpolation routines developed

for GENGEN. Second, the Acceptance program began processing the event-by-event data in the .paw files; as in casym, each event was subjected to the final analysis cuts discussed in the previous chapter. For those events surviving the analysis cuts, the recoil polarization was computed using the reconstructed kinematics computed by the data analysis programs and the structure function interpolation algorithms. Third, the resulting values of the recoil polarization were transported through the Charybdis field with the same magnetic transport routines employed by GENGEN, and the polarizations presented to the front array of the polarimeter were accumulated and histogrammed. Finally, following the analysis of an entire run, histograms of the recoil polarization and other variables relevant for the acceptance-averaging analysis were written to an output HBOOK file for examination by the user.

Although the Acceptance program was, technically, not a true Monte Carlo simulation, *a significant advantage of this approach is that a model for the experimental acceptance is not needed as the experimental acceptance is automatically enforced when using those events employed for data analysis.* On the other hand, a slight disadvantage of this method is that the event-by-event kinematics reconstructed by the analysis codes are not, of course, "perfect". Also, we note that the Acceptance program was not capable of simulating interactions in the lead curtain.

6.5 Summary

In this chapter, we provided an overview of the two simulation programs that we developed to extract *rigorous* acceptance-averged and nuclear physics corrected values for G_{En}/G_{Mn} from our experimental asymmetry data. In the next chapter, we conclude our discussion of the E93-038 data analysis by presenting and comparing the final results obtained with these two simulation programs.

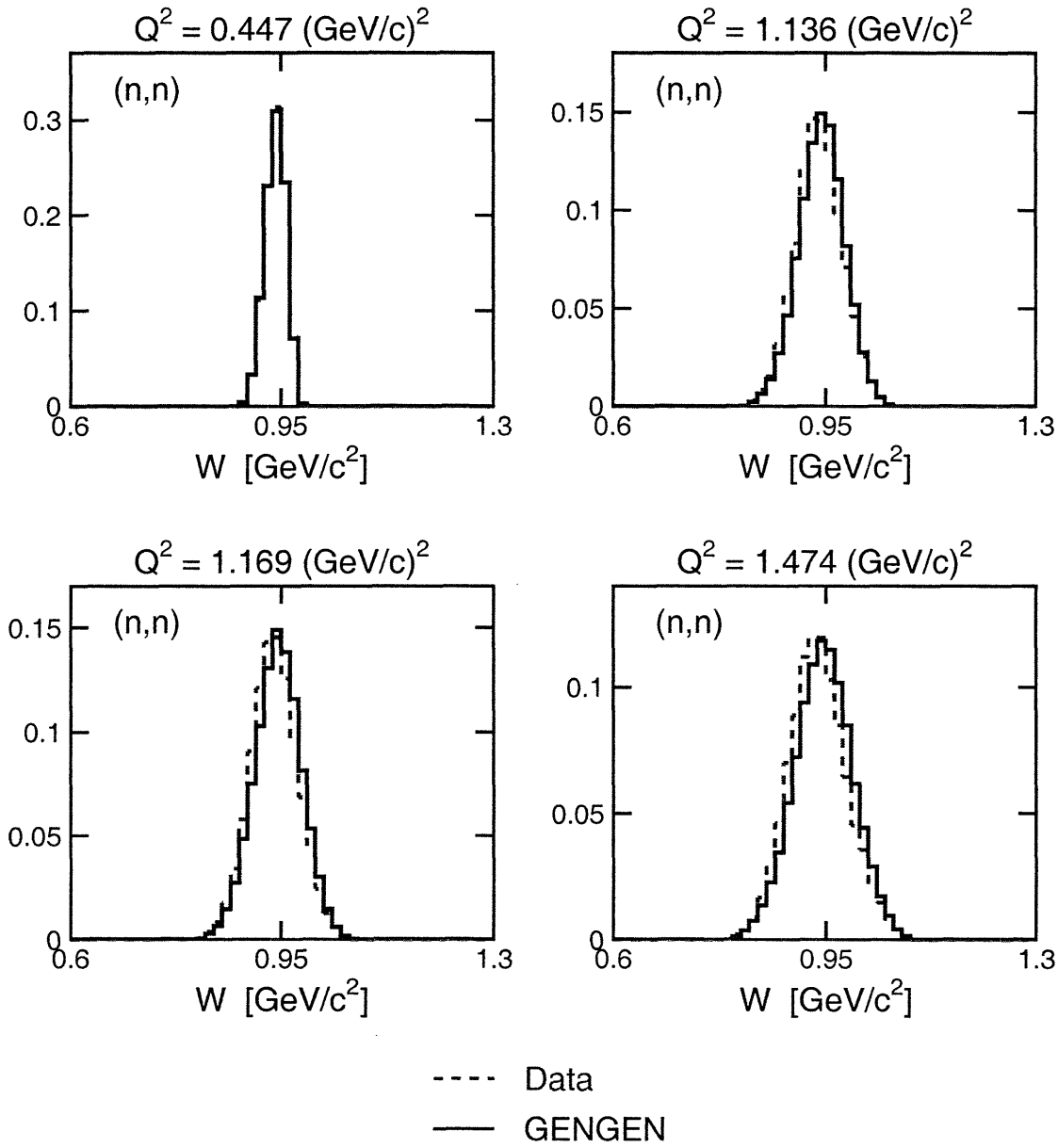

Figure 6-9: (color) Comparison of GENGEN simulated (blue solid lines) and experimental (red dashed lines) distributions of W for (n, n) events. The histograms are normalized to unit content.

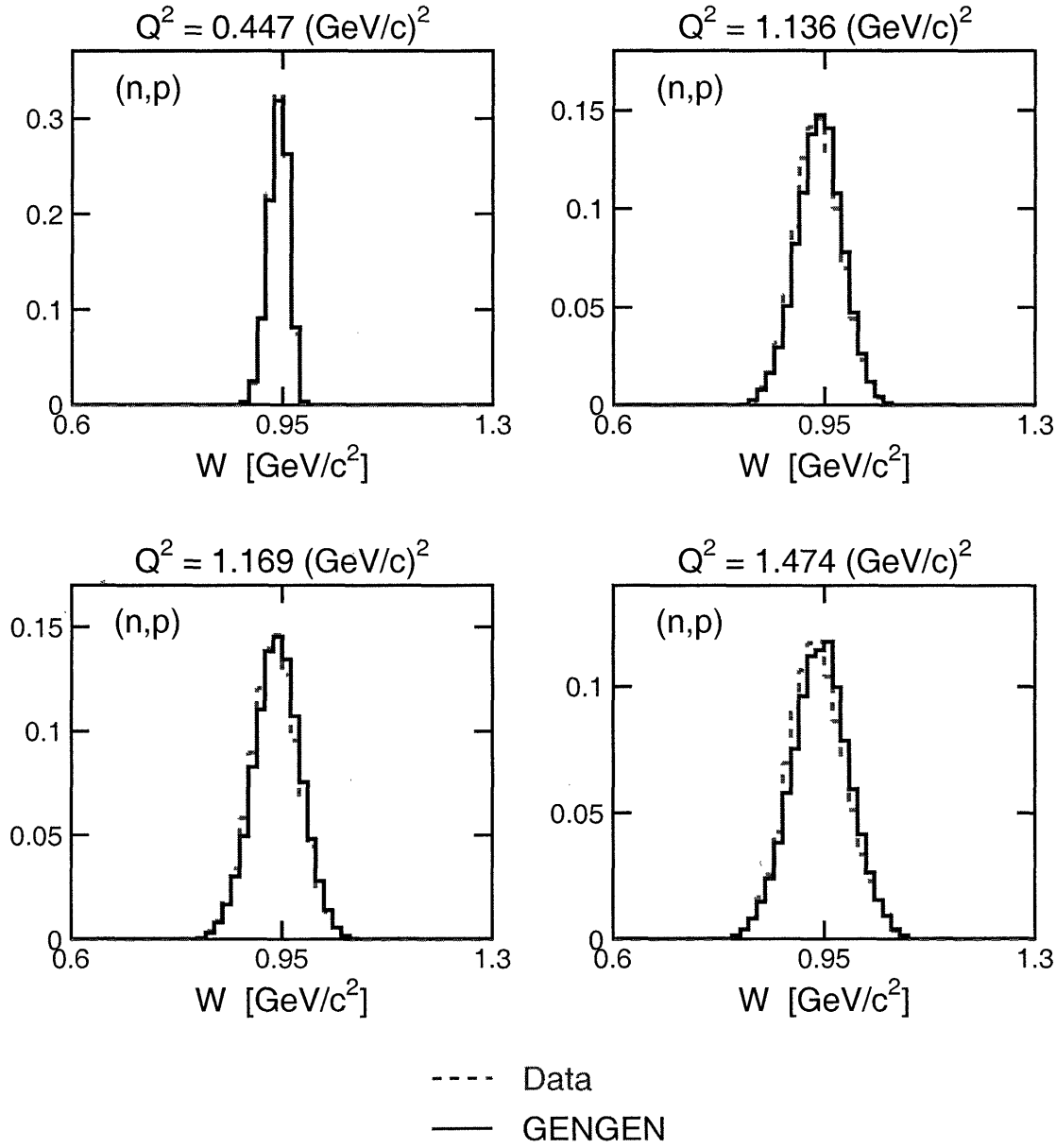

Figure 6-10: (color) Comparison of GENGEN simulated (blue solid lines) and experimental (red dashed lines) distributions of W for (n,p) events. The histograms are normalized to unit content.

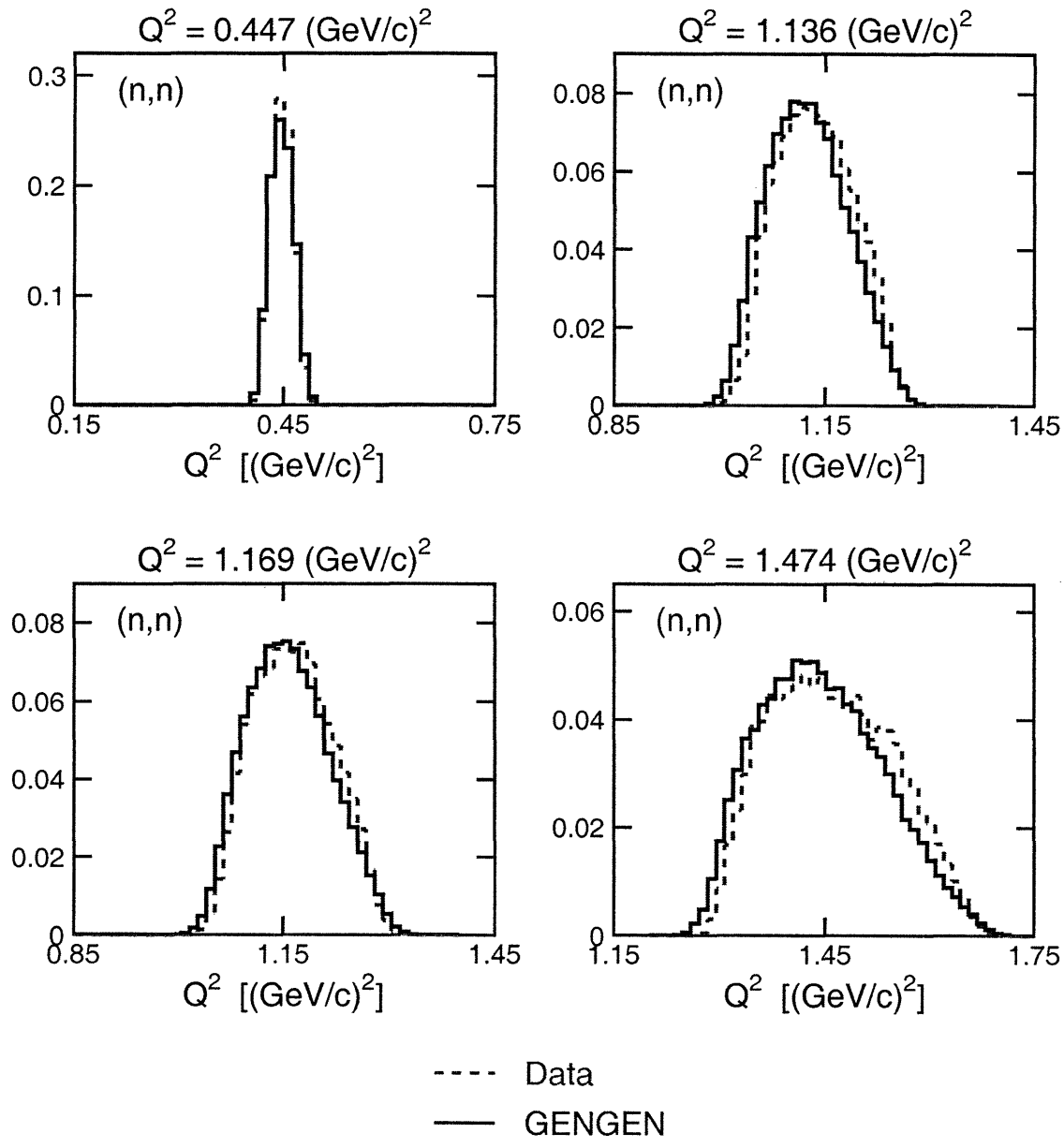

Figure 6-11: (color) Comparison of GENGEN simulated (blue solid lines) and experimental (red dashed lines) distributions of Q^2 for (n, n) events. The histograms are normalized to unit content.

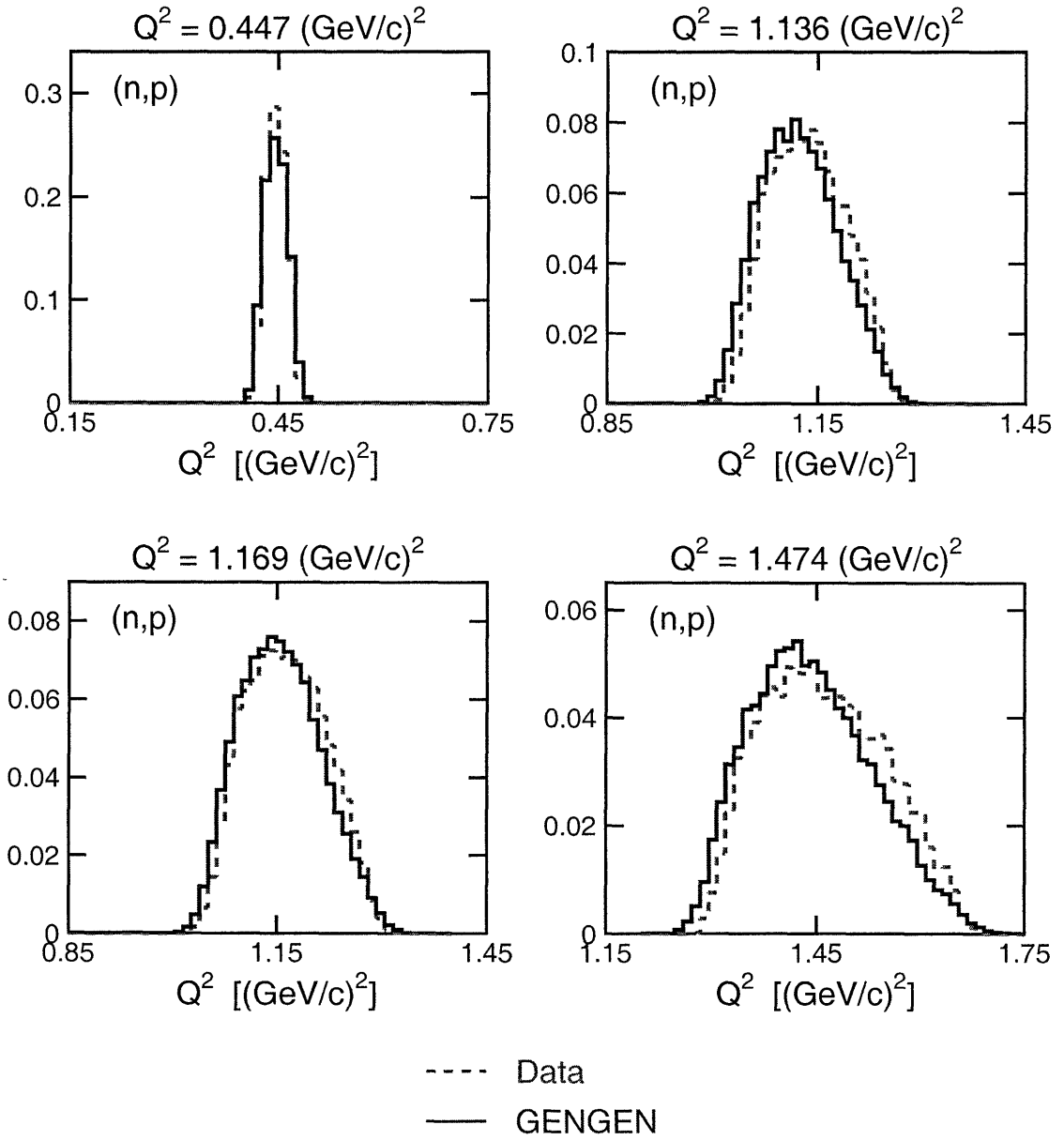

Figure 6-12: (color) Comparison of GENGEN simulated (blue solid lines) and experimental (red dashed lines) distributions of Q^2 for (n,p) events. The histograms are normalized to unit content.

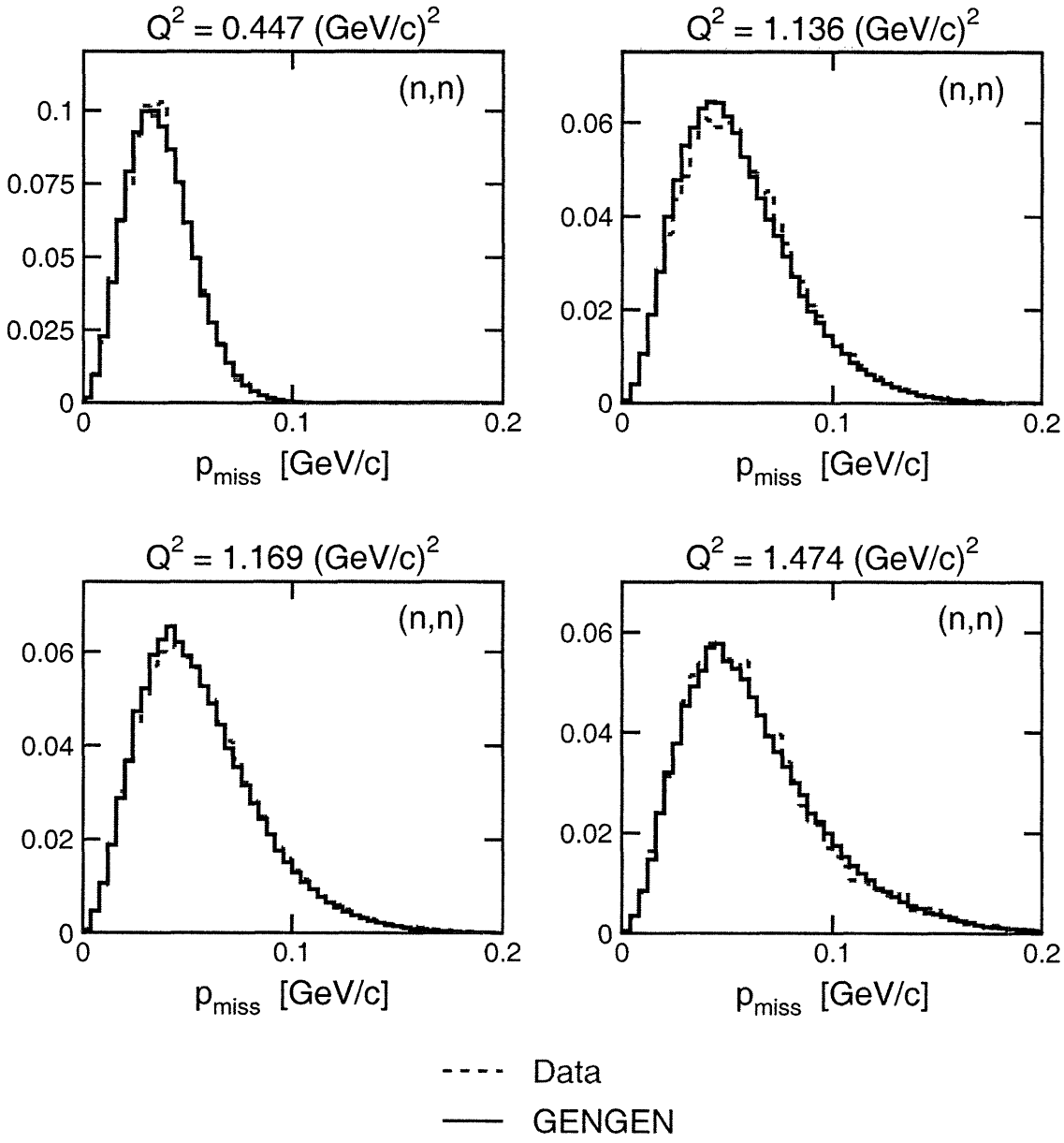

Figure 6-13: (color) Comparison of GENGEN simulated (blue solid lines) and experimental (red dashed lines) distributions of p_{miss} for (n, n) events. The histograms are normalized to unit content.

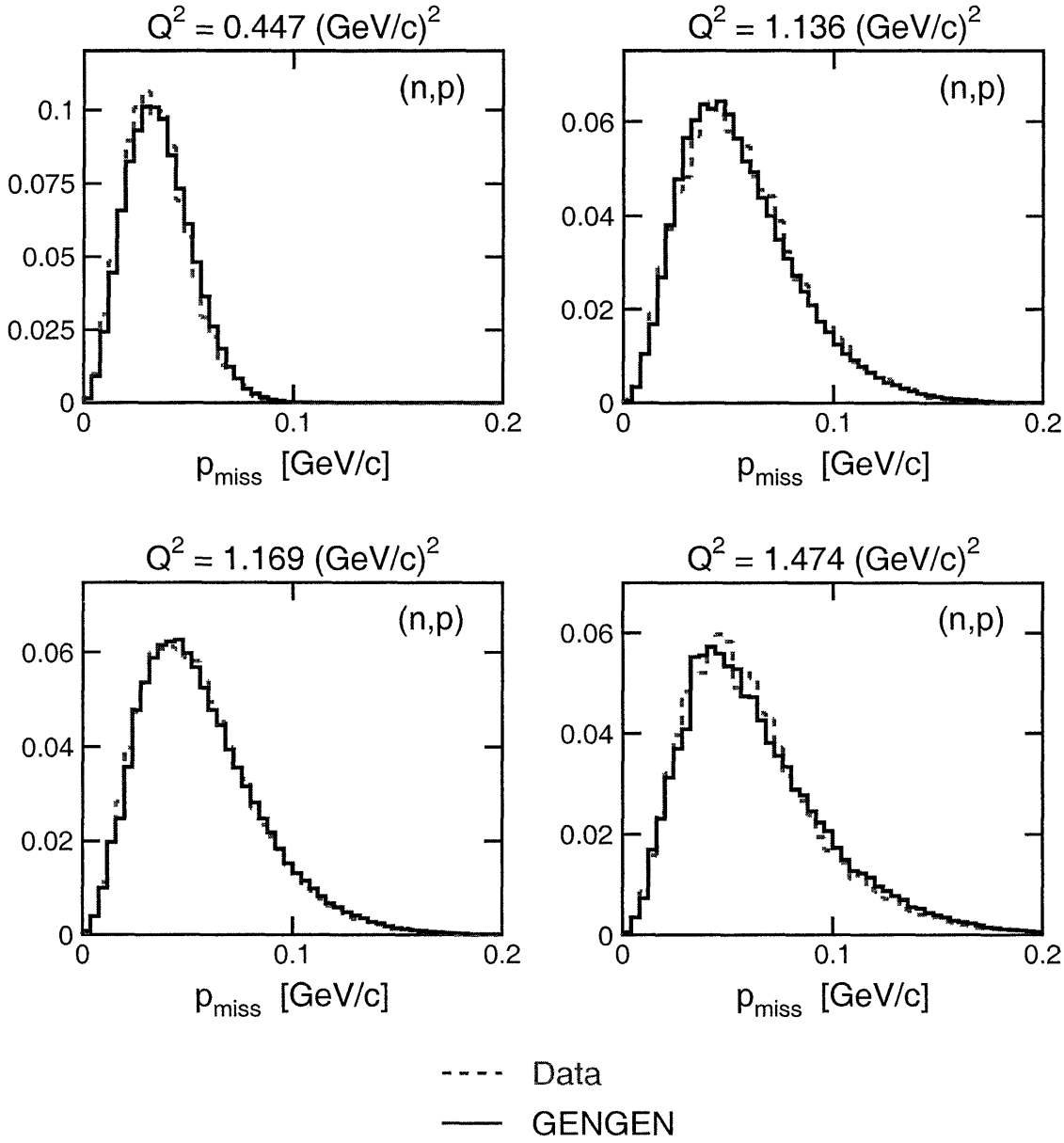

Figure 6-14: (color) Comparison of GENGEN simulated (blue solid lines) and experimental (red dashed lines) distributions of p_{miss} for (n,p) events. The histograms are normalized to unit content.

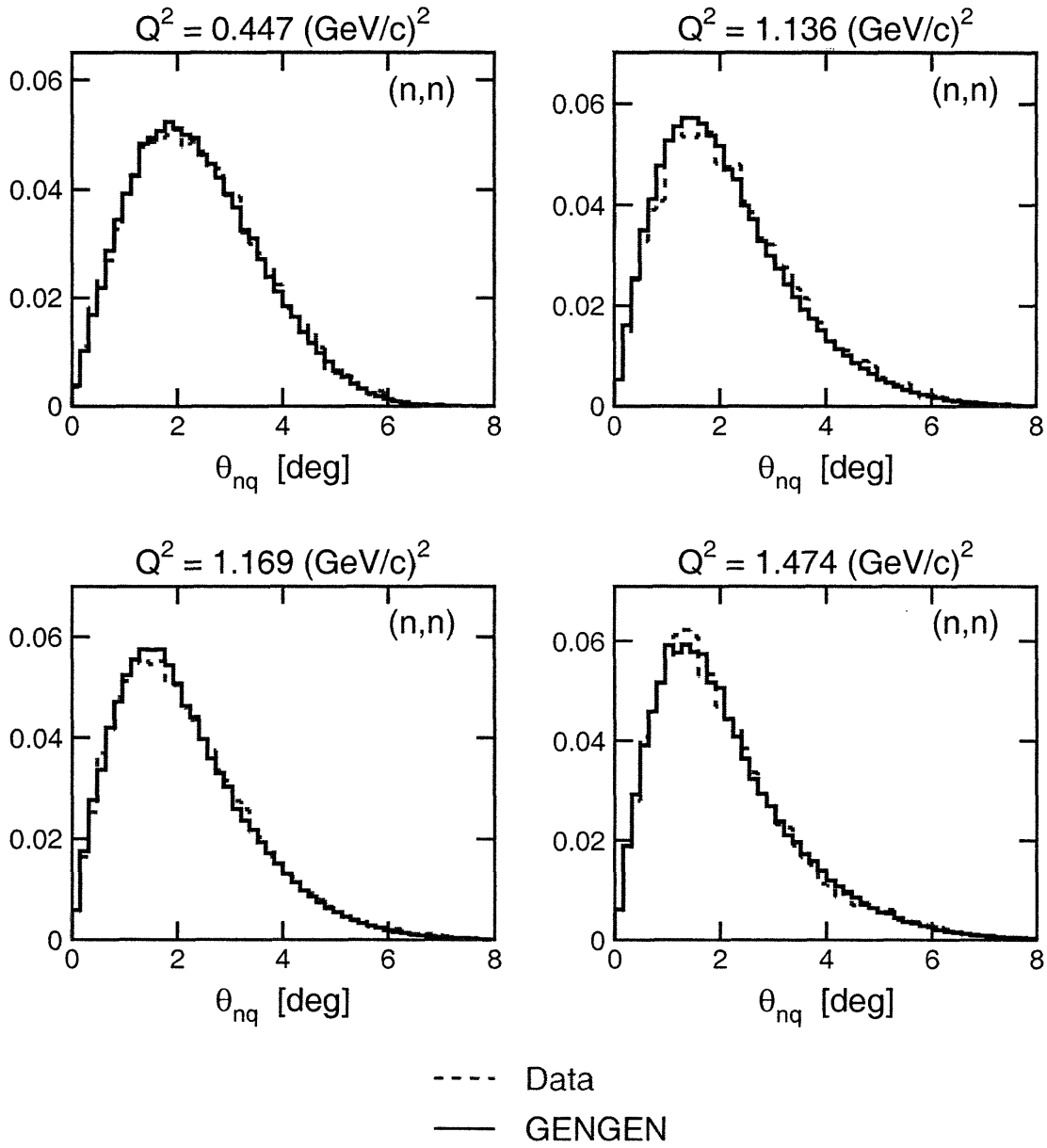

Figure 6-15: (color) Comparison of GENGEN simulated (blue solid lines) and experimental (red dashed lines) distributions of θ_{nq} for (n, n) events. The histograms are normalized to unit content.

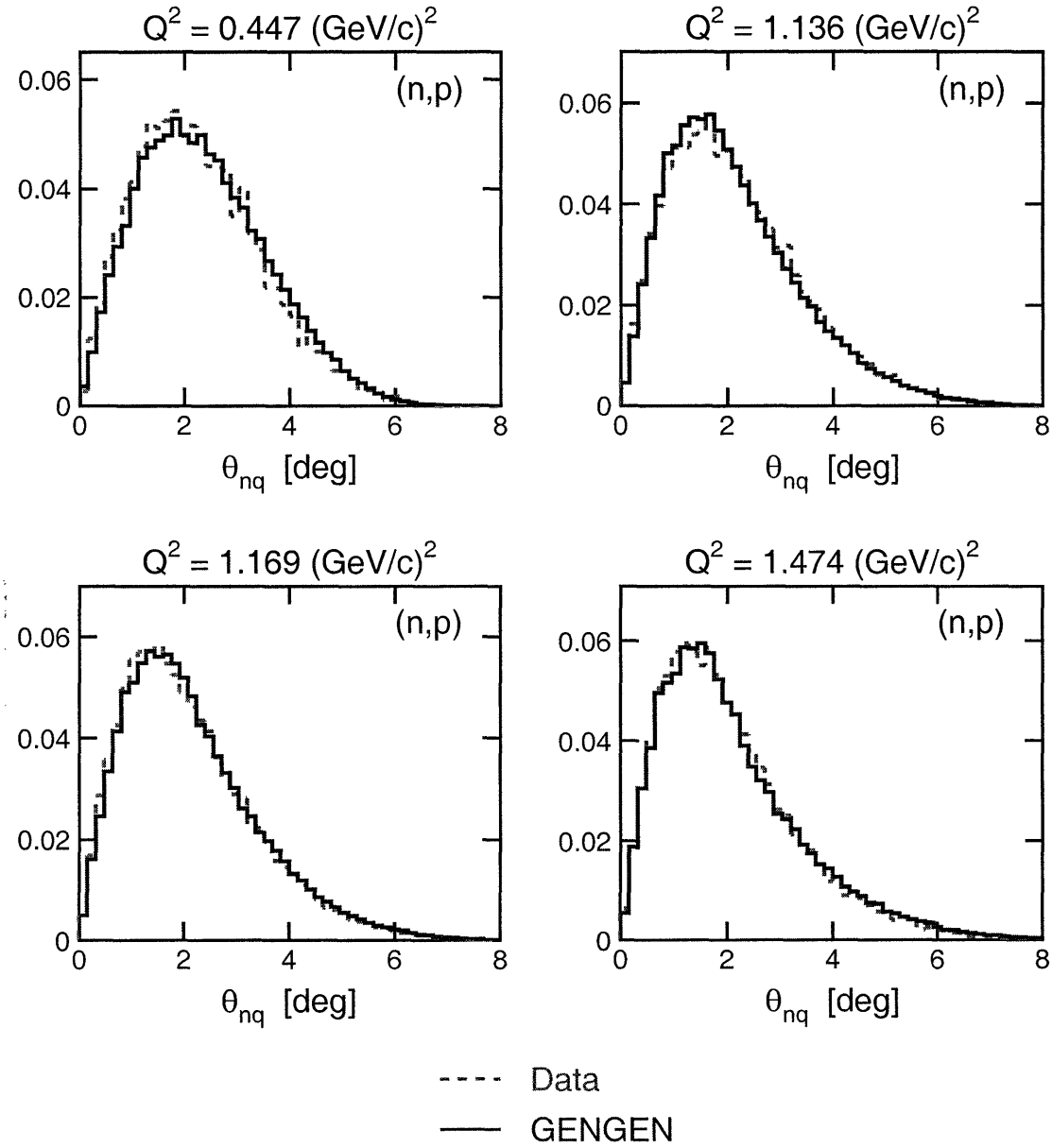

Figure 6-16: (color) Comparison of GENGEN simulated (blue solid lines) and experimental (red dashed lines) distributions of θ_{nq} for (n,p) events. The histograms are normalized to unit content.

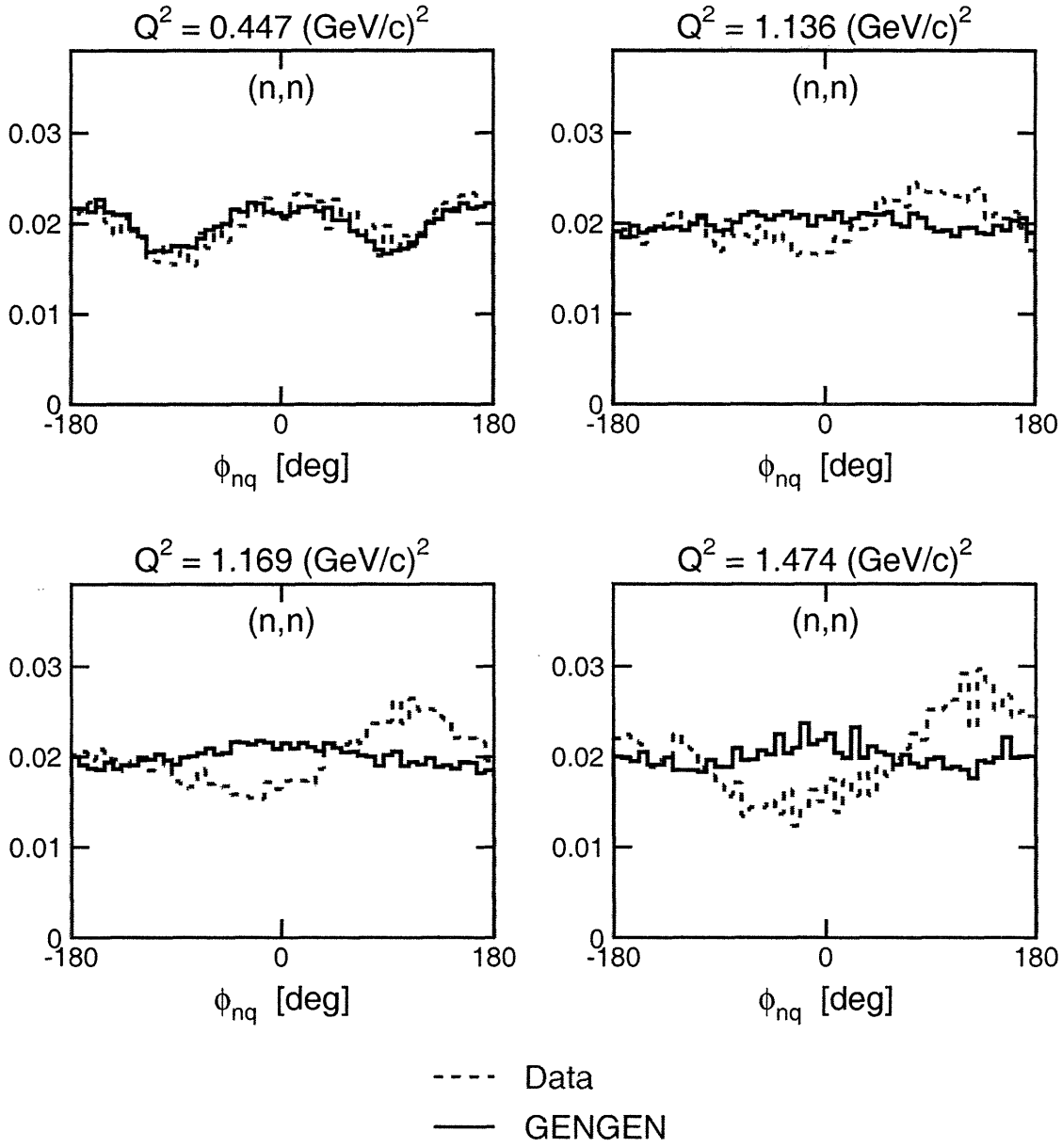

Figure 6-17: (color) Comparison of GENGEN simulated (blue solid lines) and experimental (red dashed lines) distributions of ϕ_{nq} for (n, n) events. The histograms are normalized to unit content.

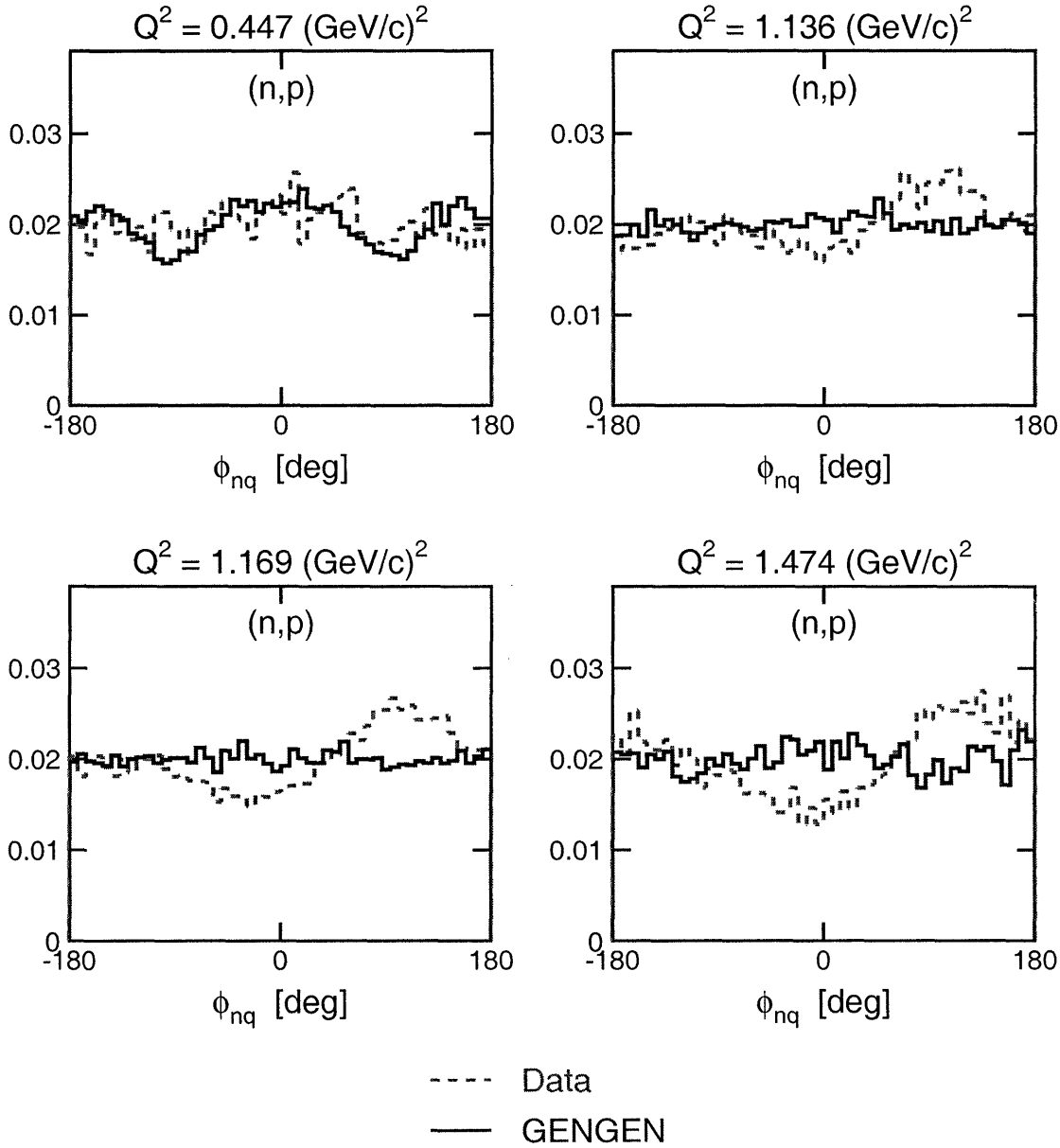

Figure 6-18: (color) Comparison of GENGEN simulated (blue solid lines) and experimental (red dashed lines) distributions of ϕ_{nq} for (n,p) events. The histograms are normalized to unit content.

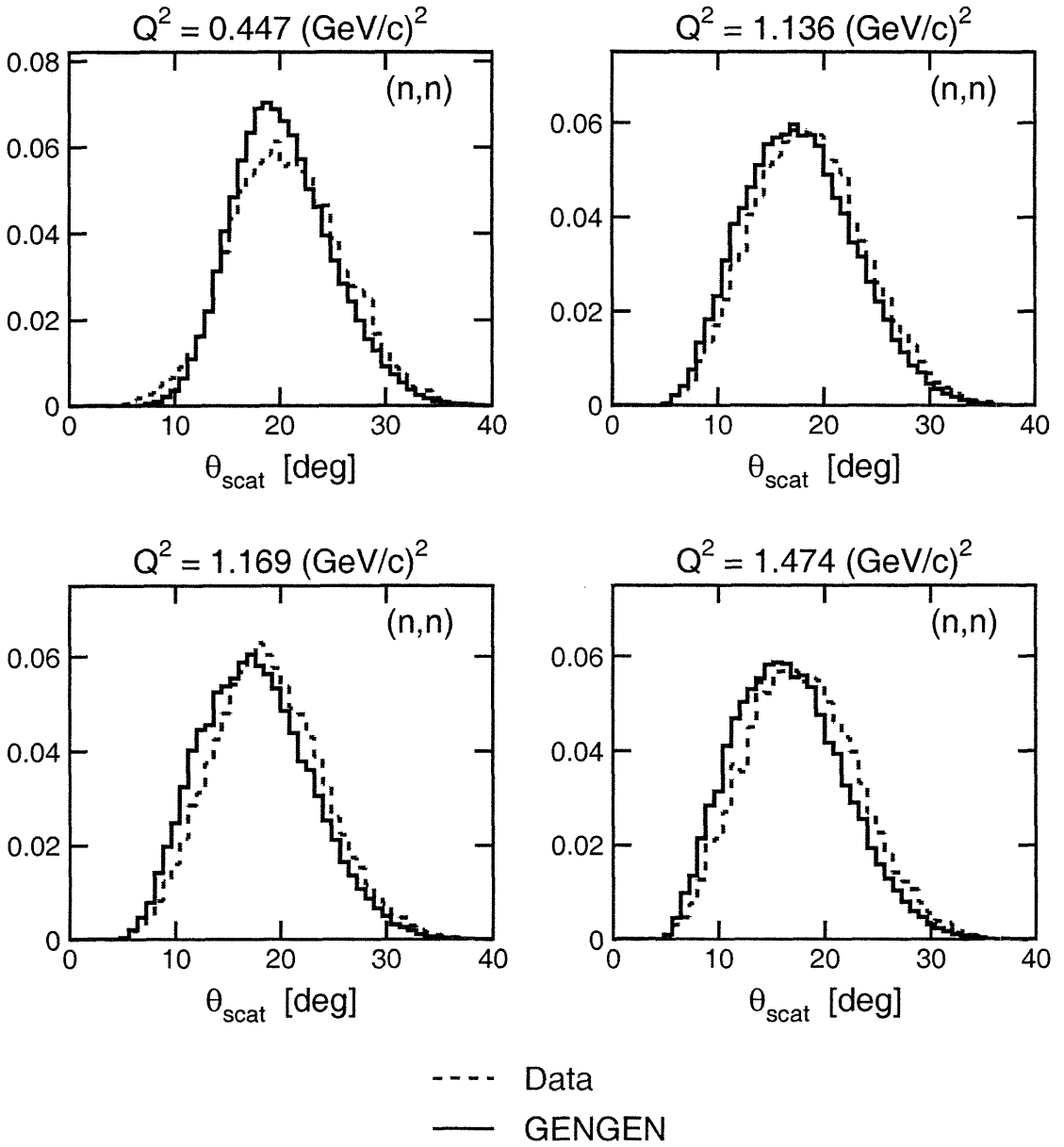

Figure 6-19: (color) Comparison of GENGEN simulated (blue solid lines) and experimental (red dashed lines) distributions of $\theta_{\rm scat}$ for (n, n) events. The histograms are normalized to unit content.

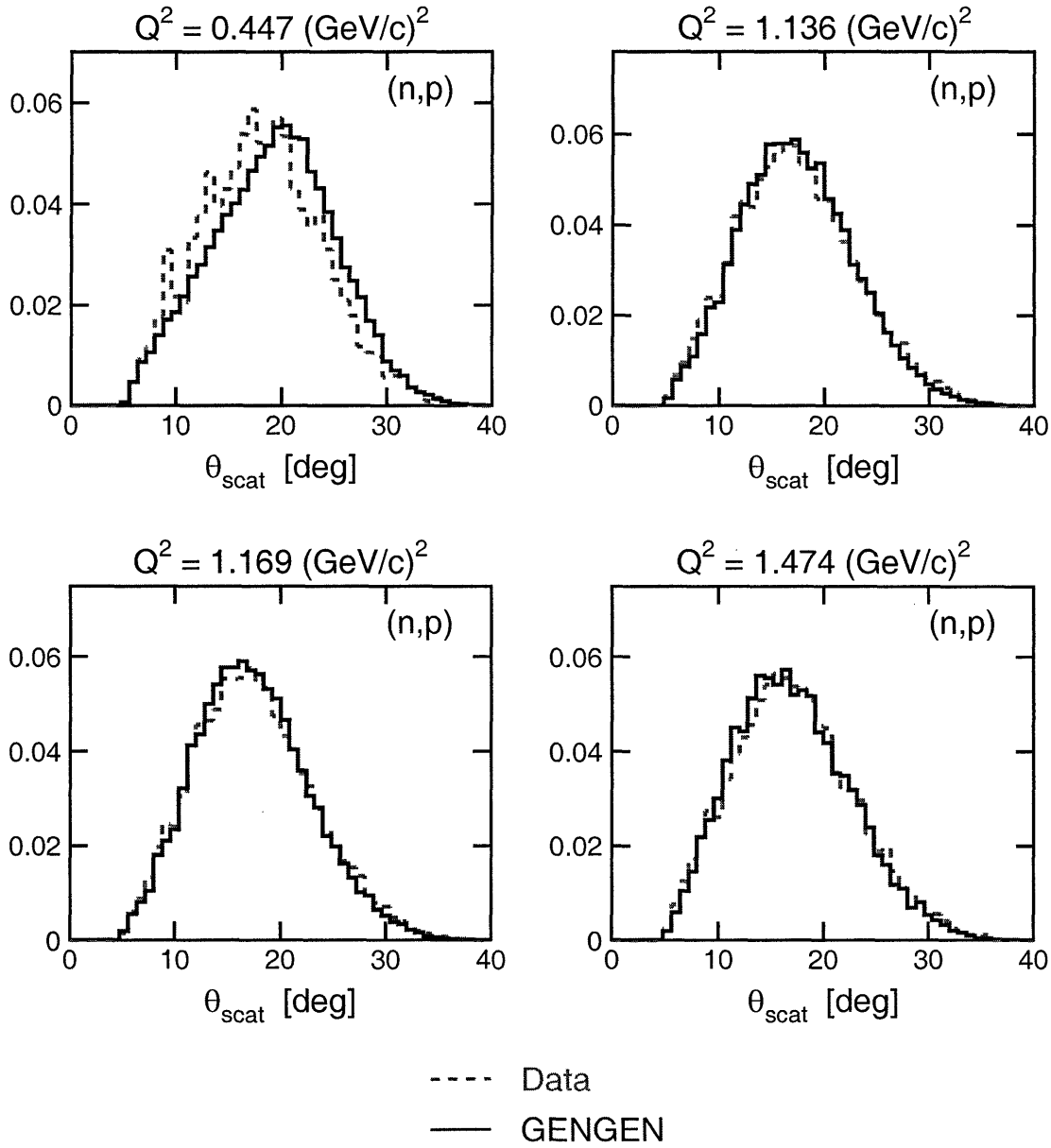

Figure 6-20: (color) Comparison of GENGEN simulated (blue solid lines) and experimental (red dashed lines) distributions of $\theta_{\rm scat}$ for (n,p) events. The histograms are normalized to unit content.

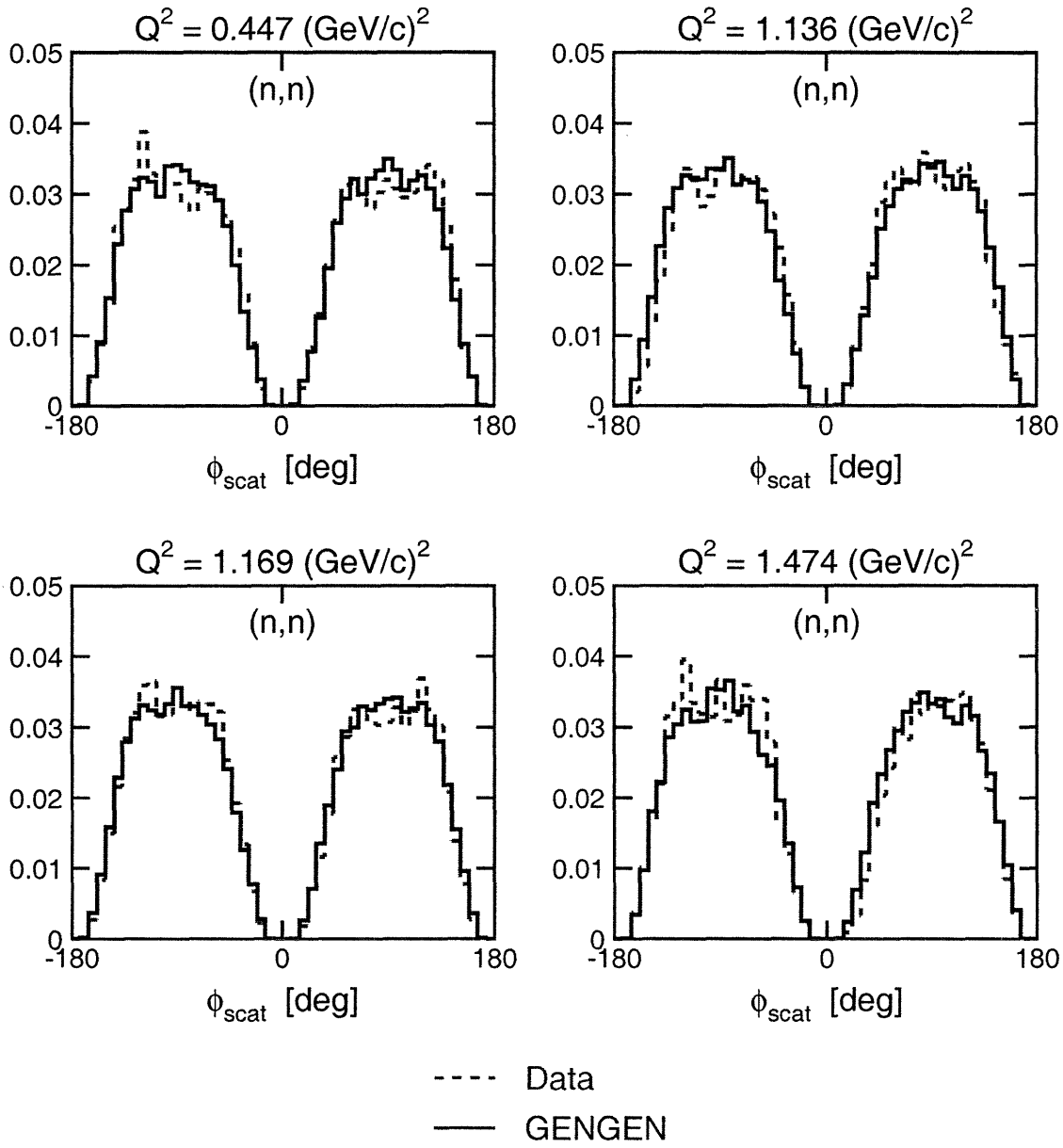

Figure 6-21: (color) Comparison of GENGEN simulated (blue solid lines) and experimental (red dashed lines) distributions of $\phi_{\rm scat}$ for (n, n) events. The histograms are normalized to unit content.

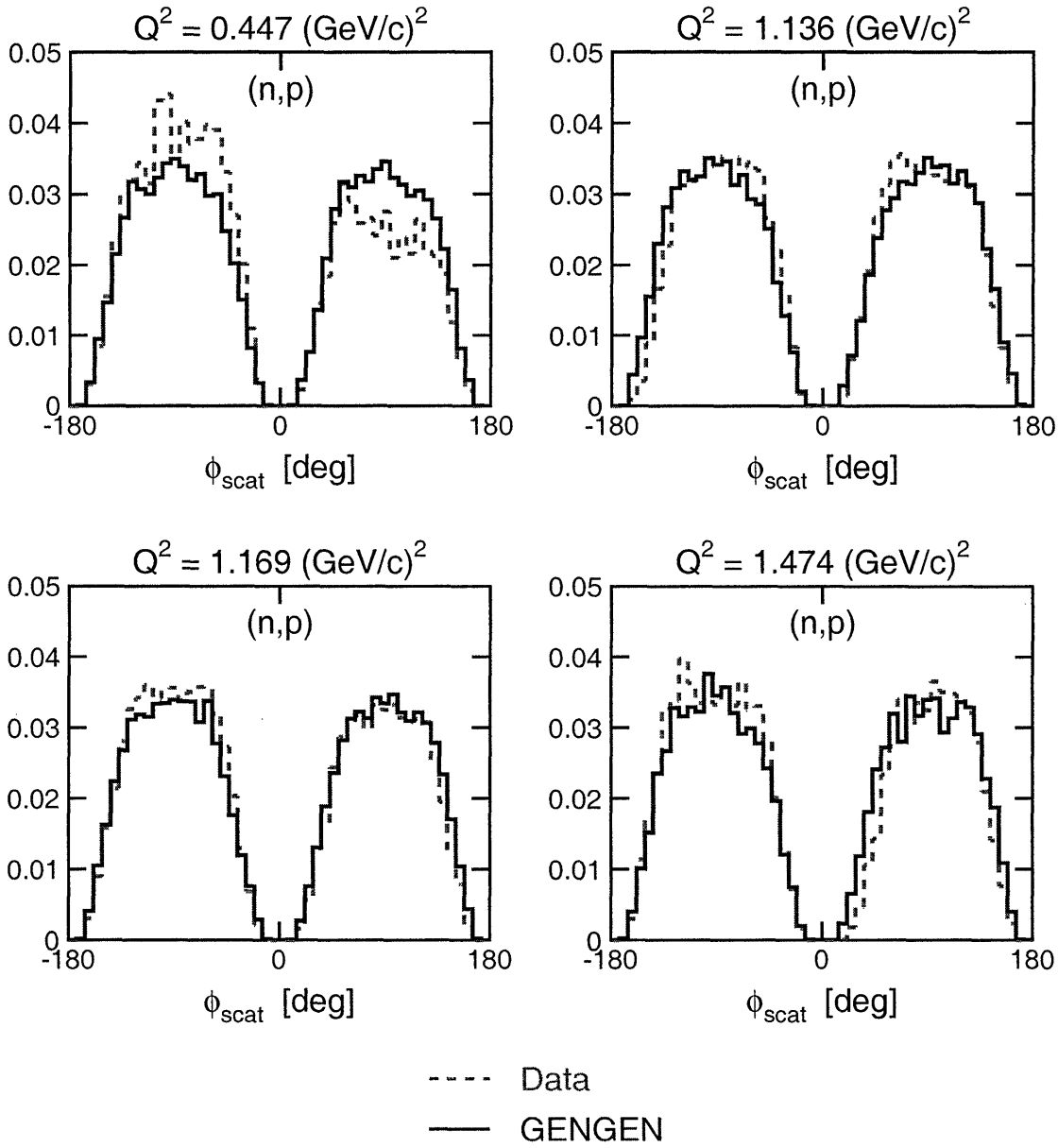

Figure 6-22: (color) Comparison of GENGEN simulated (blue solid lines) and experimental (red dashed lines) distributions of ϕ_{scat} for (n,p) events. The histograms are normalized to unit content.

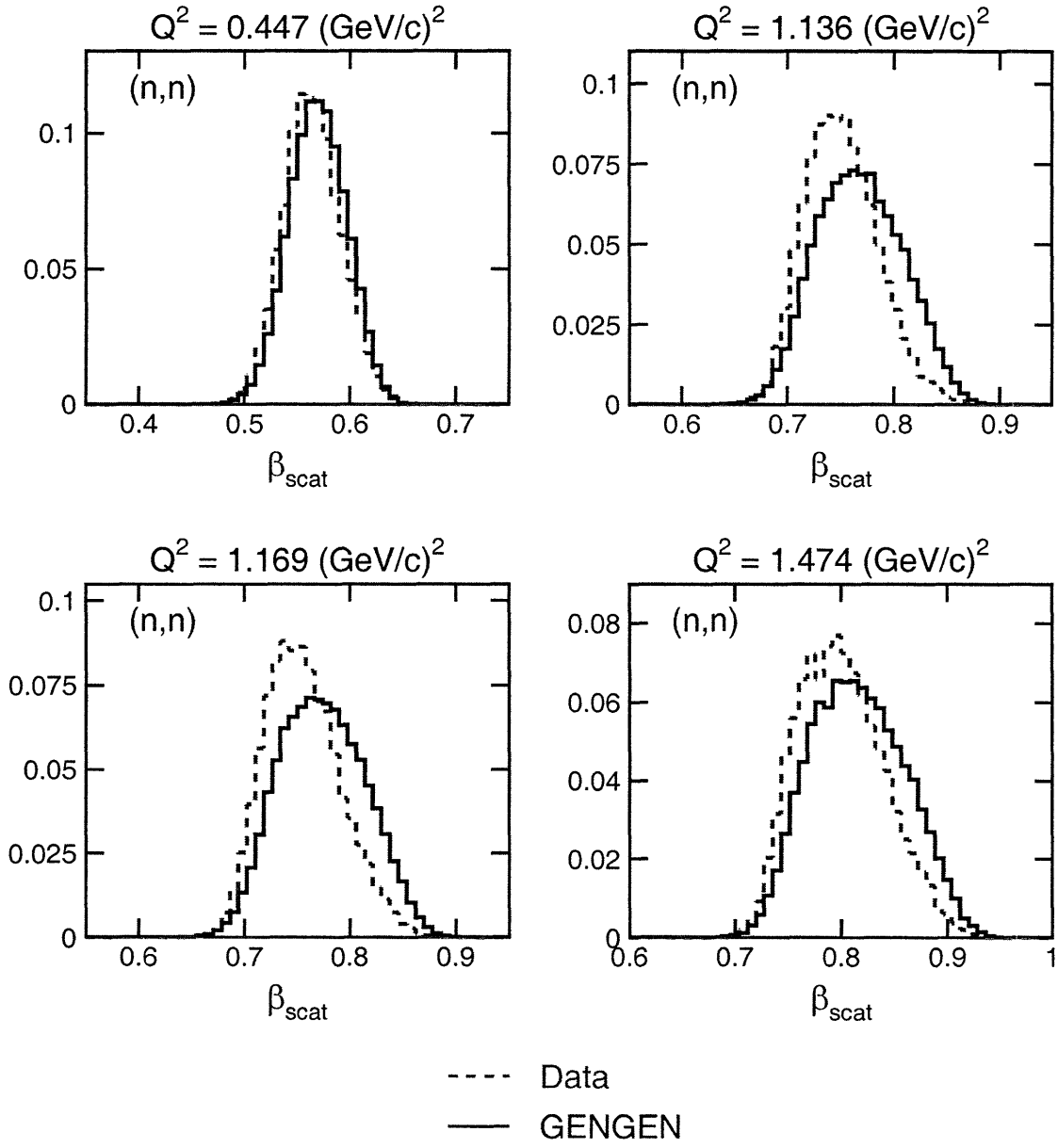

Figure 6-23: (color) Comparison of GENGEN simulated (blue solid lines) and experimental (red dashed lines) distributions of β_{scat} for (n, n) events. The histograms are normalized to unit content.

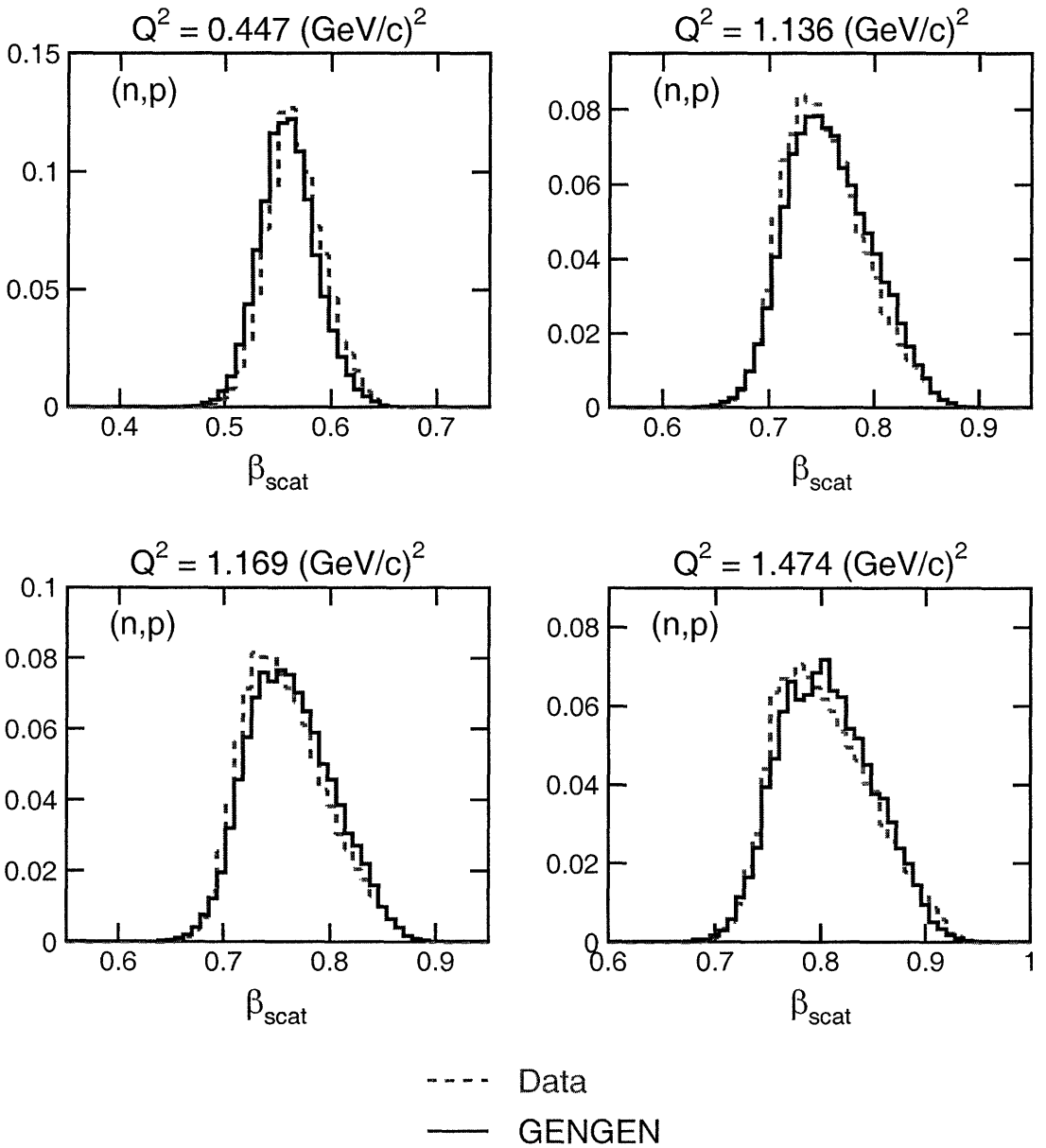

Figure 6-24: (color) Comparison of GENGEN simulated (blue solid lines) and experimental (red dashed lines) distributions of β_{scat} for (n,p) events. The histograms are normalized to unit content.

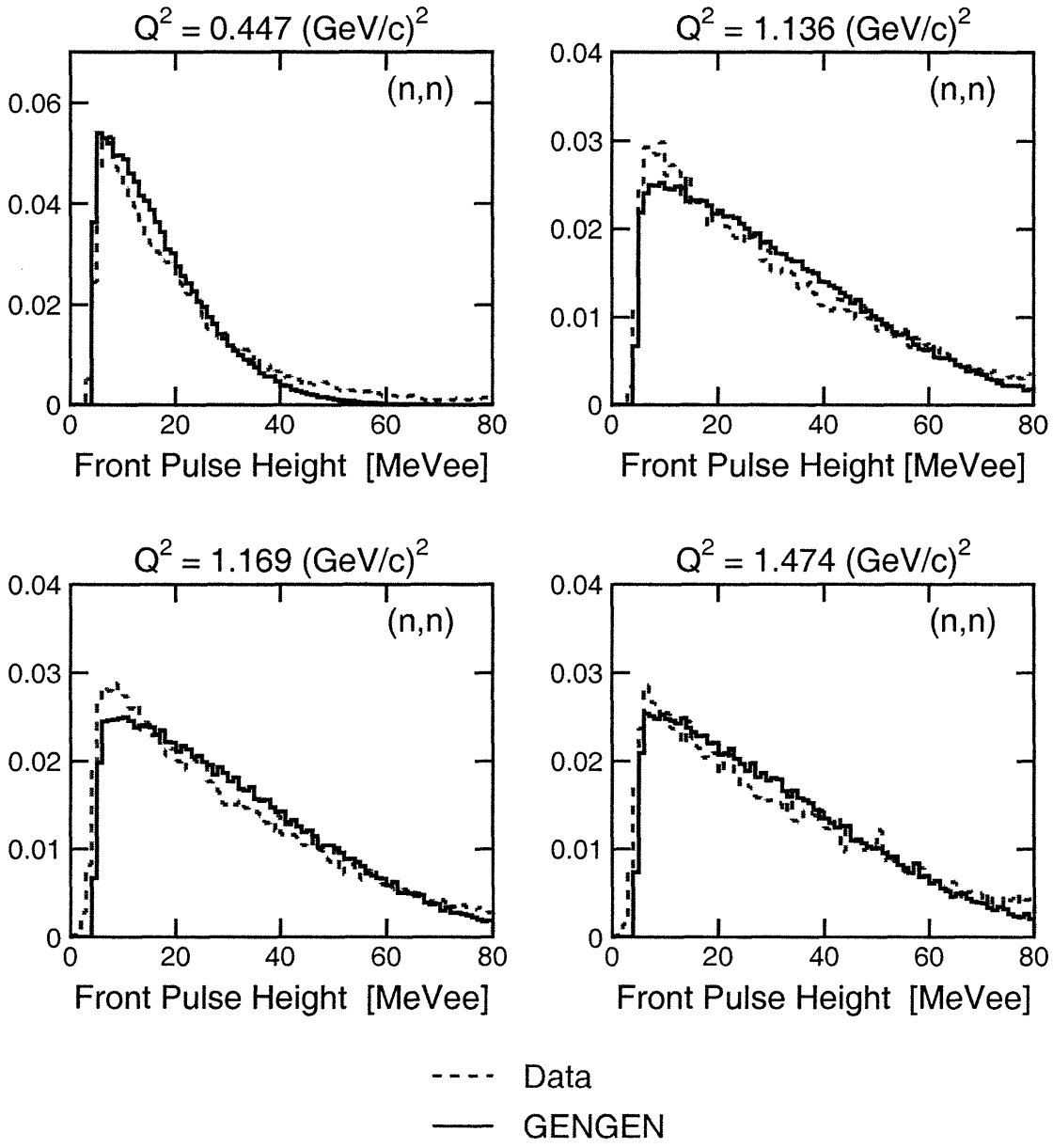

Figure 6-25: (color) Comparison of GENGEN simulated (blue solid lines) and experimental (red dashed lines) distributions of detector pulse height distributions for the detector recording the interaction in the front array for (n, n) events. The histograms are normalized to unit content.

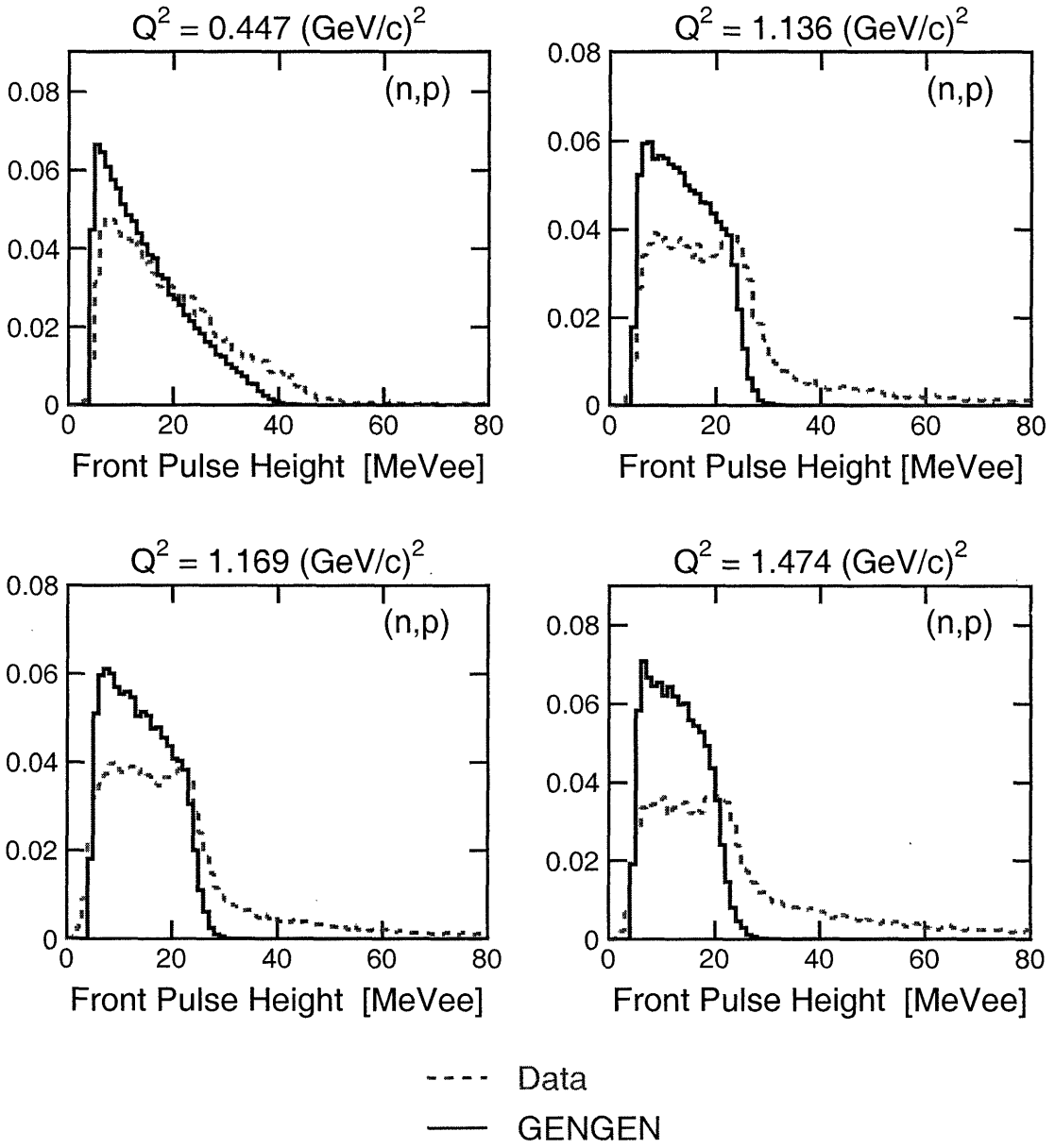

Figure 6-26: (color) Comparison of GENGEN simulated (blue solid lines) and experimental (red dashed lines) distributions of detector pulse height distributions for the detector recording the interaction in the front array for (n, p) events. The histograms are normalized to unit content.

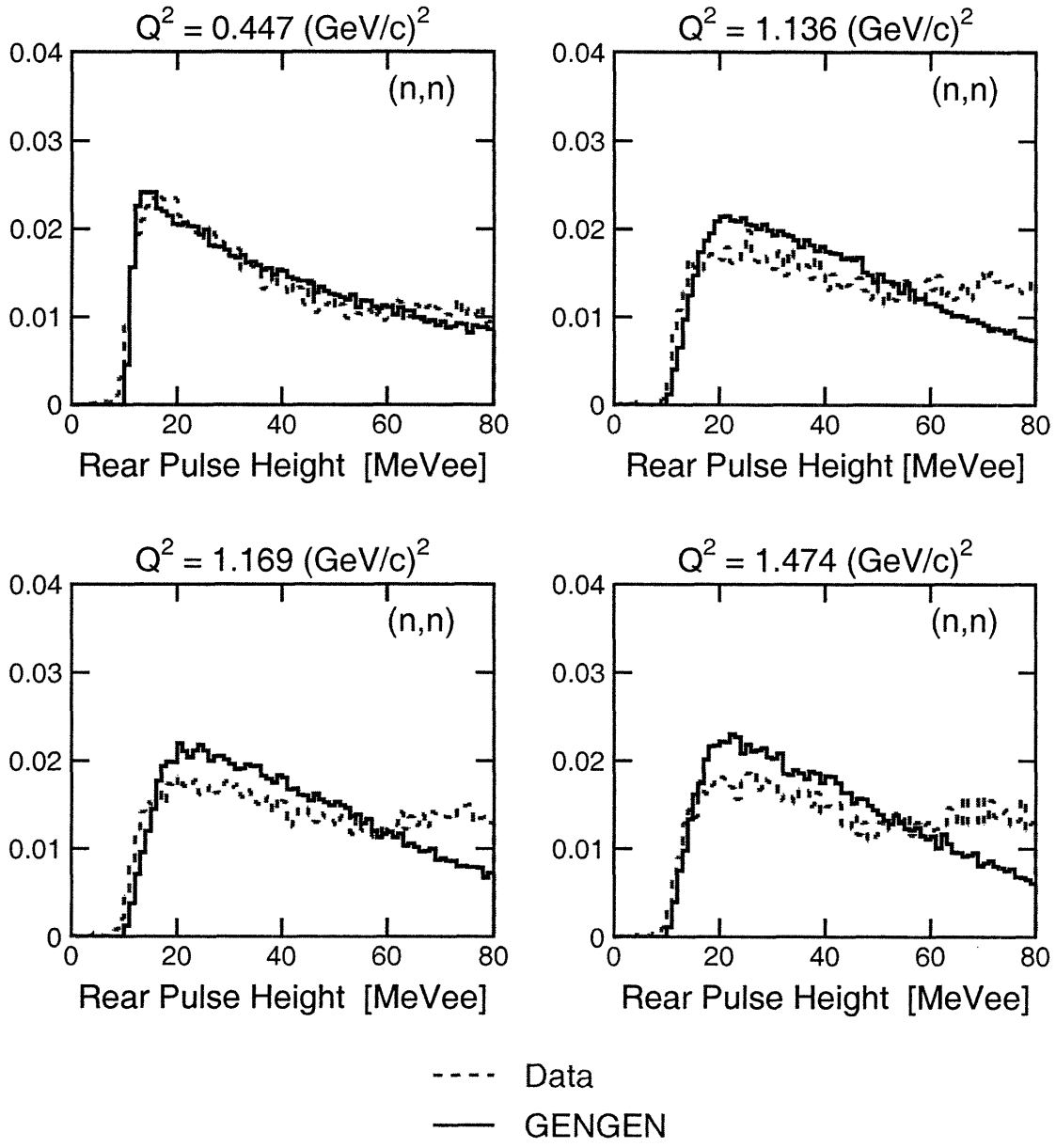

Figure 6-27: (color) Comparison of GENGEN simulated (blue solid lines) and experimental (red dashed lines) distributions of detector pulse height distributions for the detector recording the interaction in the rear array for (n, n) events. The histograms are normalized to unit content.

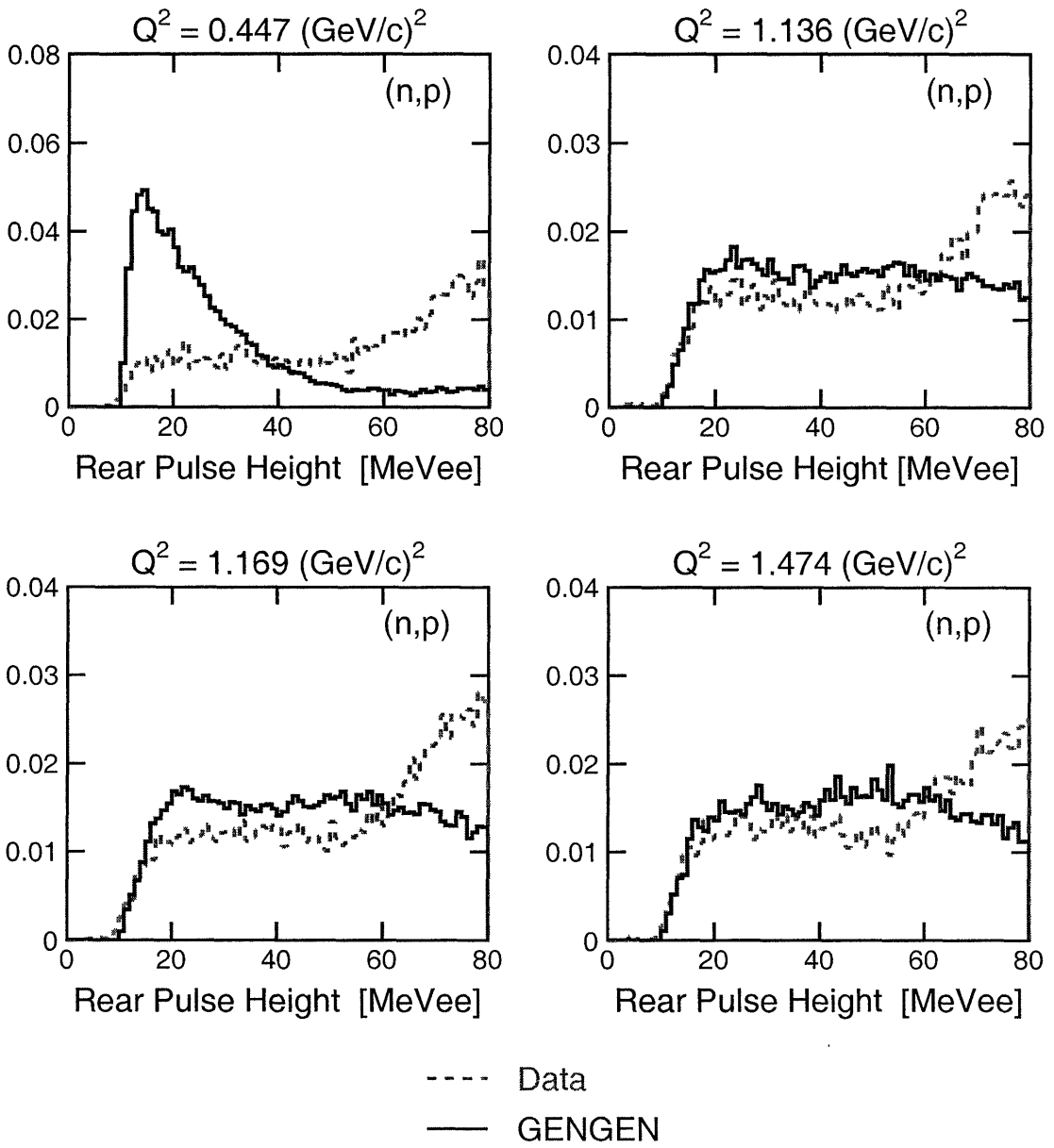

Figure 6-28: (color) Comparison of GENGEN simulated (blue solid lines) and experimental (red dashed lines) distributions of detector pulse height distributions for the detector recording the interaction in the rear array for (n, p) events. The histograms are normalized to unit content.

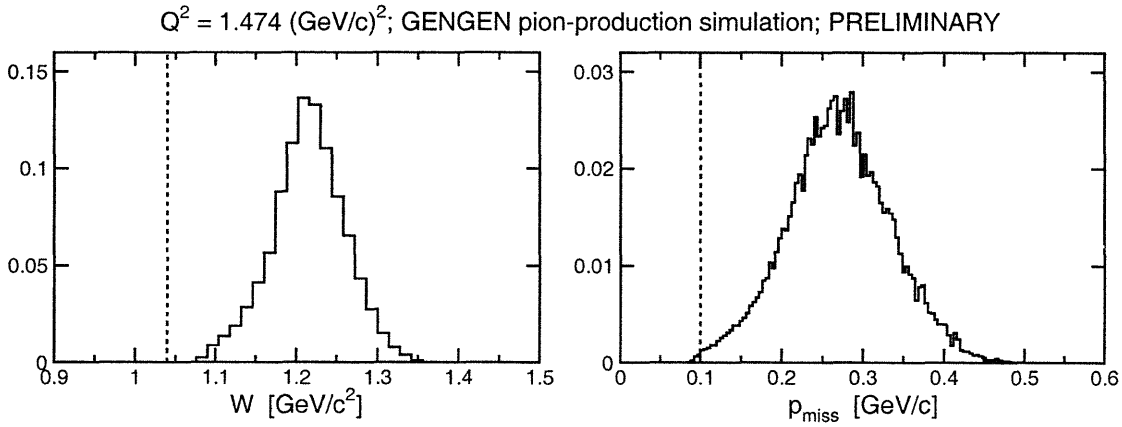

Figure 6-29: Distributions for W (left panel) and p_{miss} (right panel) from a *preliminary* GENGEN pion-production simulation at $Q^2 = 1.474$ (GeV/c)^2. The dashed lines denote the cuts of $W < 1.04$ GeV/c^2 and $p_{\mathrm{miss}} < 100$ MeV/c that were used for the final production data analysis. The histograms are normalized to unit content.

Chapter 7

Extraction of Final Results

We conclude our discussion of the E93-038 analysis procedures in this chapter by extracting the final acceptance-averaged and nuclear physics corrected results for G_{En}/G_{Mn} and G_{En} from the measured experimental asymmetries presented in Chapter 5. Final results obtained with both the `Acceptance` program and `GENGEN` are presented and compared.

An overview of the layout of this chapter is as follows. First, we begin in Section 7.1 by discussing the expected sensitivity of our results to nuclear physics effects (i.e., FSI, MEC, and IC). Second, in Section 7.2, we present sample output from the simulation programs (e.g., spectra of acceptance-averaged polarizations, spin precession angles, etc.), and we compare the cut-dependencies of the simulated acceptance-averaged polarizations with those of the experimental asymmetries. Third, in Section 7.3, we provide a detailed overview of the final analysis procedure, and we then extract the final acceptance-averaged and nuclear physics corrected values for G_{En}/G_{Mn} via a comparison of the experimental asymmetries and the simulated acceptance-averaged polarizations. Fourth, we provide estimates for the magnitudes of the various systematic uncertainties in Section 7.4. Finally, we conclude this chapter in Section 7.5 by presenting our final results for G_{En}, and we then "come full circle" by re-comparing the current world data on the nucleon form factors with the predictions of the various theoretical models discussed in Chapter 2.

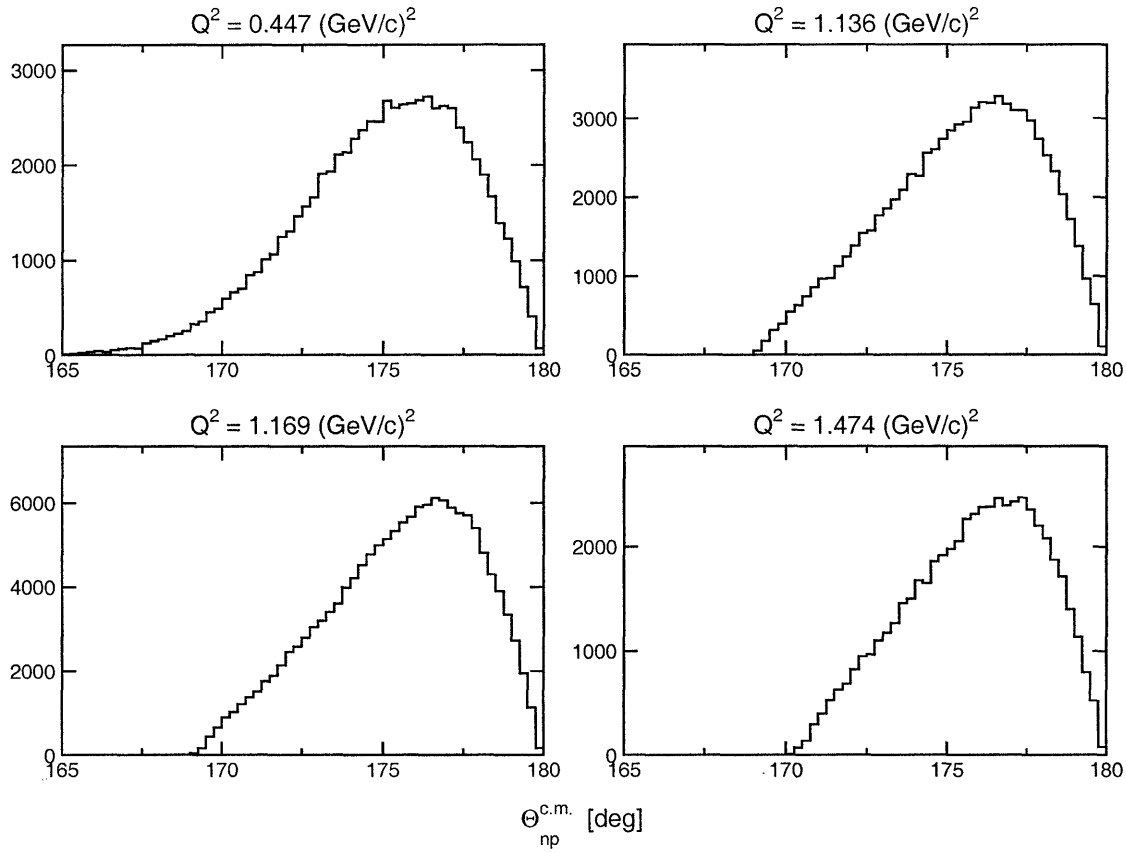

Figure 7-1: $\Theta_{np}^{\text{c.m.}}$ spectra after all cuts.

7.1 Sensitivity to Nuclear Physics Effects

In this section, we discuss the expected sensitivity of our results to FSI, MEC, and IC by comparing Arenhövel's PWBA and FSI+MEC+IC calculations of P_x^h and P_z^h over the range of accepted $\Theta_{np}^{\text{c.m.}}$ values.

7.1.1 Experimental $\Theta_{np}^{\text{c.m.}}$ Acceptance

Distributions of $\Theta_{np}^{\text{c.m.}}$ for those events surviving all analysis cuts are shown in Fig. 7-1. We see here that the majority of the accepted events were within $\sim$10°–15° of perfect quasifree emission in the *n*-*p* center-of-mass frame. Within the finite resolution of the detectors and the reconstruction algorithms, there are, of course, no events at $\Theta_{np}^{\text{c.m.}} = 180°$.

E_e [GeV]	$E_{e'}$ [GeV]	$\theta_{e'}$ [deg]	$E_{np}^{\text{c.m.}}$ [MeV]	Q^2 [(GeV/c)^2]	PWBA P_x^h/P_z^h	FSI+MEC+IC P_x^h/P_z^h	Relative Difference
0.884	0.643	52.65	116	0.447	0.1830	0.1754	4.153%
2.326	1.718	30.93	281	1.136	0.1923	0.1886	1.924%
2.415	1.789	30.15	289	1.169	0.1920	0.1884	1.875%
3.395	2.606	23.55	359	1.474	0.1875	0.1845	1.600%

Table 7.1: Comparison of Arenhövel's PWBA and FSI+MEC+IC calculations of P_x^h/P_z^h for $\Theta_{np}^{\text{c.m.}} = 180°$, $\phi_{np}^{\text{c.m.}} = 0°$, and the central values of the electron kinematics at the four Q^2 points. [$E_{np}^{\text{c.m.}}$ is the n-p energy in the n-p CM frame.]

7.1.2 Comparison of Arenhövel's PWBA and FSI+MEC+IC Calculations

In Figs. 7-2 through 7-5, we present close-up comparisons of Arenhövel's PWBA and FSI+MEC+IC calculations of P_x^h and P_z^h over the range $160° \leq \Theta_{np}^{\text{c.m.}} \leq 180°$ for the central electron kinematics at the four Q^2 points and $\phi_{np}^{\text{c.m.}} = 0°$. As can be seen clearly via inspection of these figures, there are differences between the PWBA and FSI+MEC+IC calculations of P_x^h even for perfect quasifree emission; indeed, a difference between these calculations even at the highest central Q^2 point of 1.474 (GeV/c)^2 can be seen.

In order to obtain a rough estimation of the expected magnitude of the corrections due to FSI+MEC+IC (not including those due to the finite experimental acceptance), we have, in Table 7.1, listed numerical values for the PWBA and FSI+MEC+IC calculations of the P_x^h/P_z^h polarization ratio for $\Theta_{np}^{\text{c.m.}} = 180°$, $\phi_{np}^{\text{c.m.}} = 0°$, and the central values of the electron kinematics at the four Q^2 points. As tabulated there, the relative differences between the PWBA and FSI+MEC+IC results for the P_x^h/P_z^h polarization ratio at $Q^2 = 0.447$, 1.136/1.169, and 1.474 (GeV/c)^2 are 4.2%, 1.9%, and 1.6%, respectively. As the differences between the PWBA and FSI+MEC+IC calculations increase away from perfect quasifree emission, the relative differences listed in Table 7.1 should be interpreted as *lower bounds* for the expected magnitude of the corrections for FSI, MEC, and IC.

A similar simple order-of-magnitude estimate for the magnitude of the corrections for the finite experimental acceptance cannot be made.

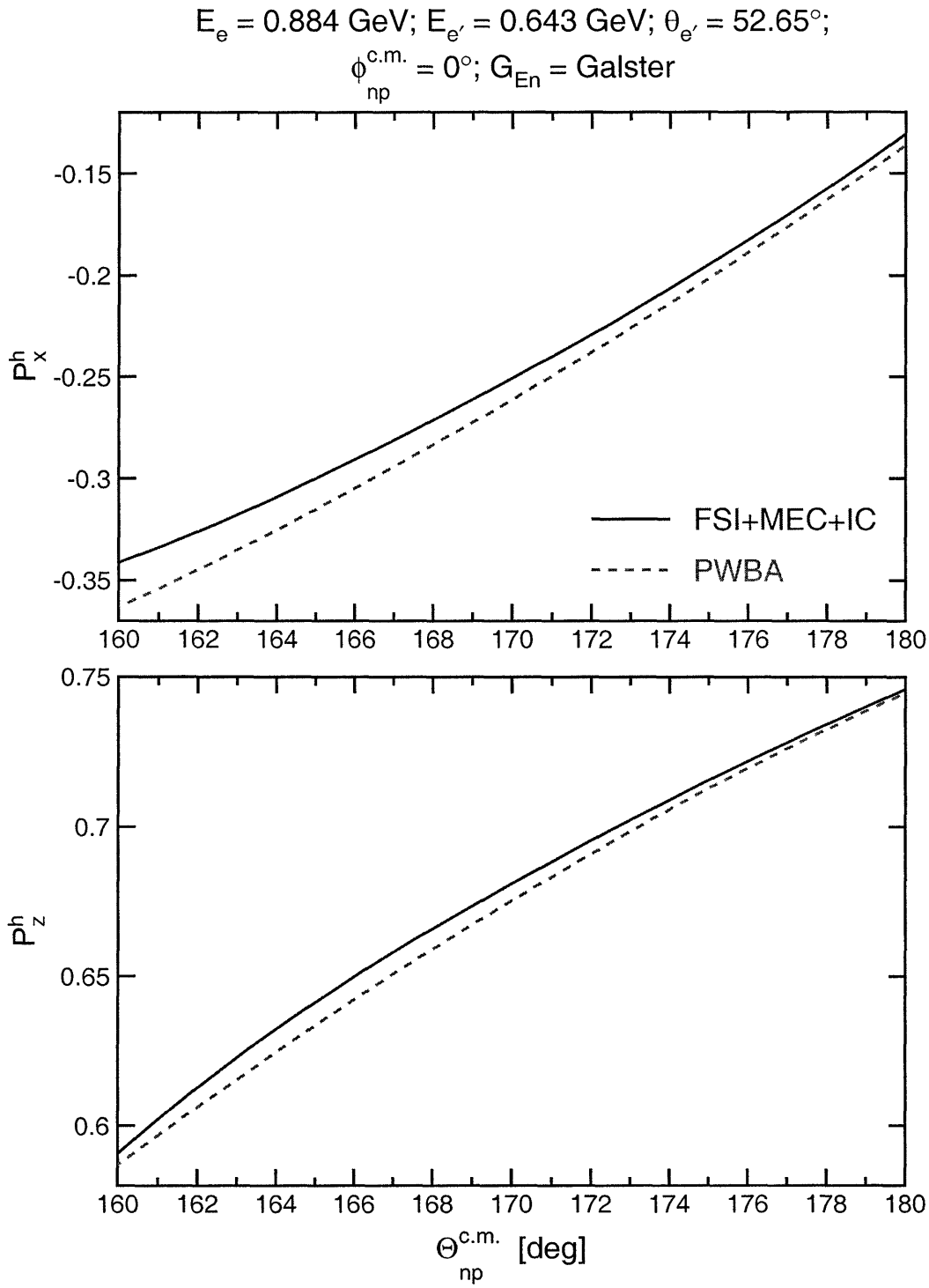

Figure 7-2: (color) Comparison of Arenhövel's PWBA (red dashed lines) and FSI+MEC+IC (blue solid lines) calculations of P_x^h (top panel) and P_z^h (bottom panel) for the central electron kinematics at $Q^2 = 0.447$ (GeV/c)^2.

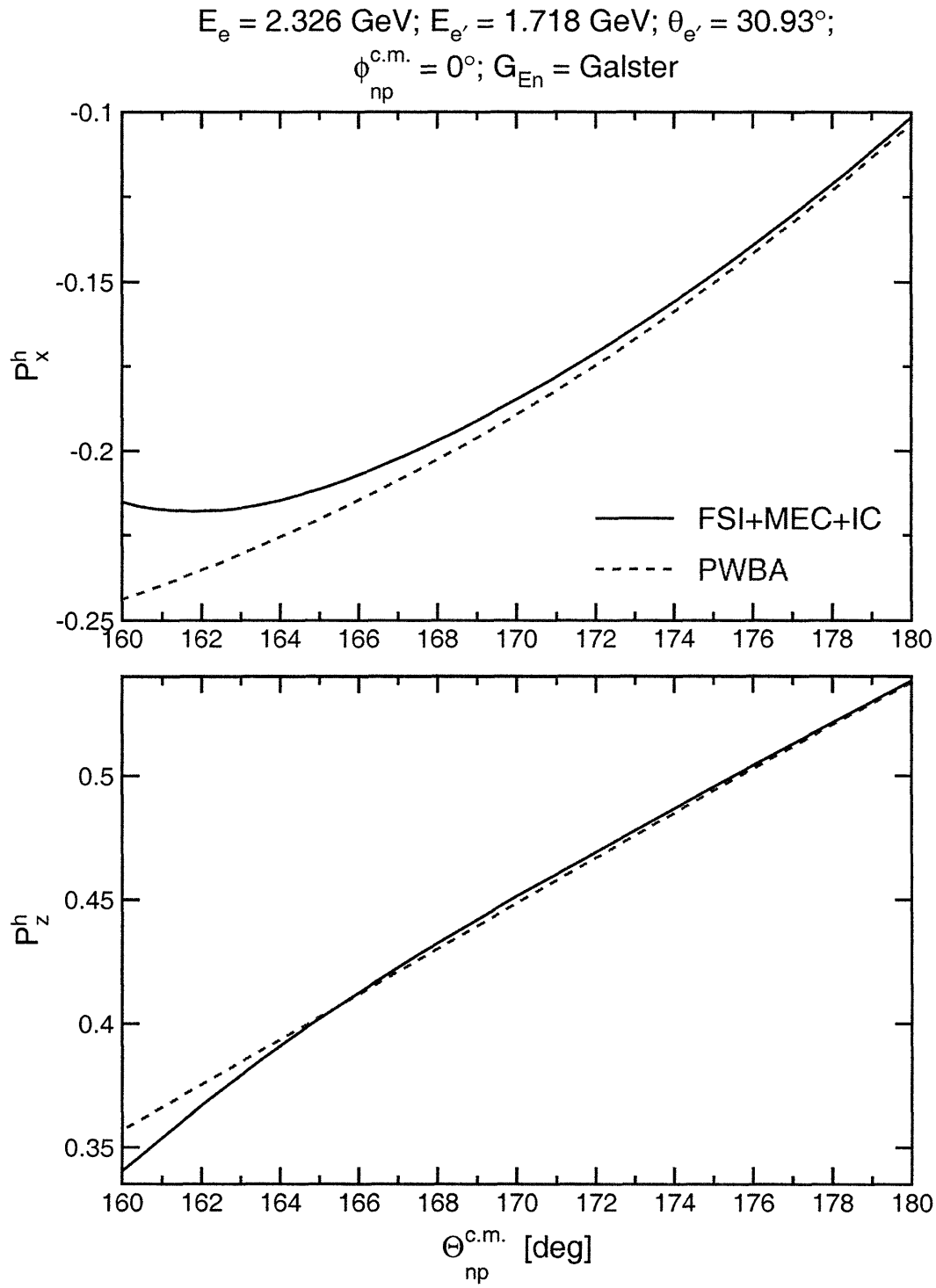

Figure 7-3: (color) Comparison of Arenhövel's PWBA (red dashed lines) and FSI+MEC+IC (blue solid lines) calculations of P_x^h (top panel) and P_z^h (bottom panel) for the central electron kinematics at $Q^2 = 1.136$ (GeV/c)^2.

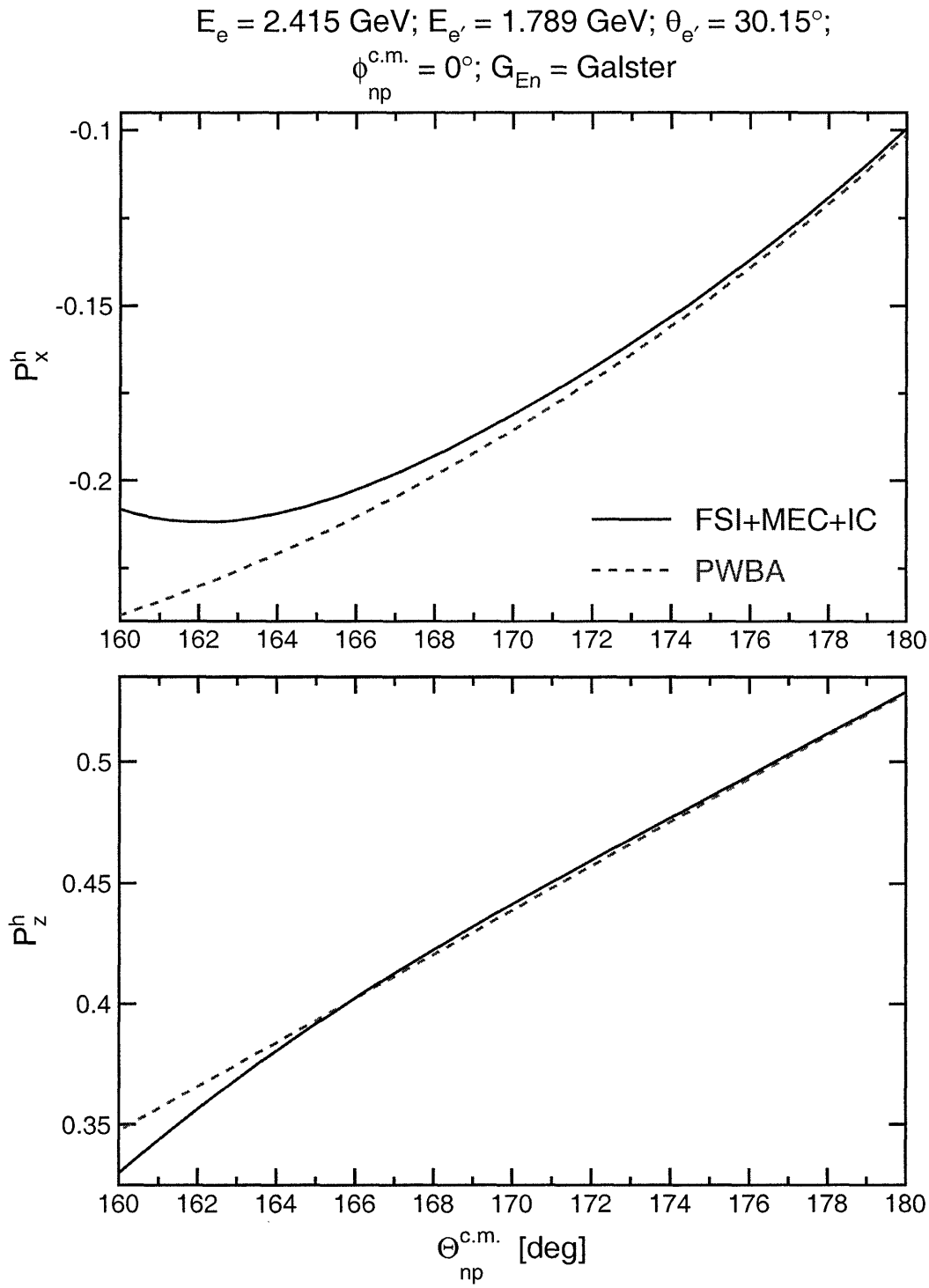

Figure 7-4: (color) Comparison of Arenhövel's PWBA (red dashed lines) and FSI+MEC+IC (blue solid lines) calculations of P_x^h (top panel) and P_z^h (bottom panel) for the central electron kinematics at $Q^2 = 1.169$ (GeV/c)^2.

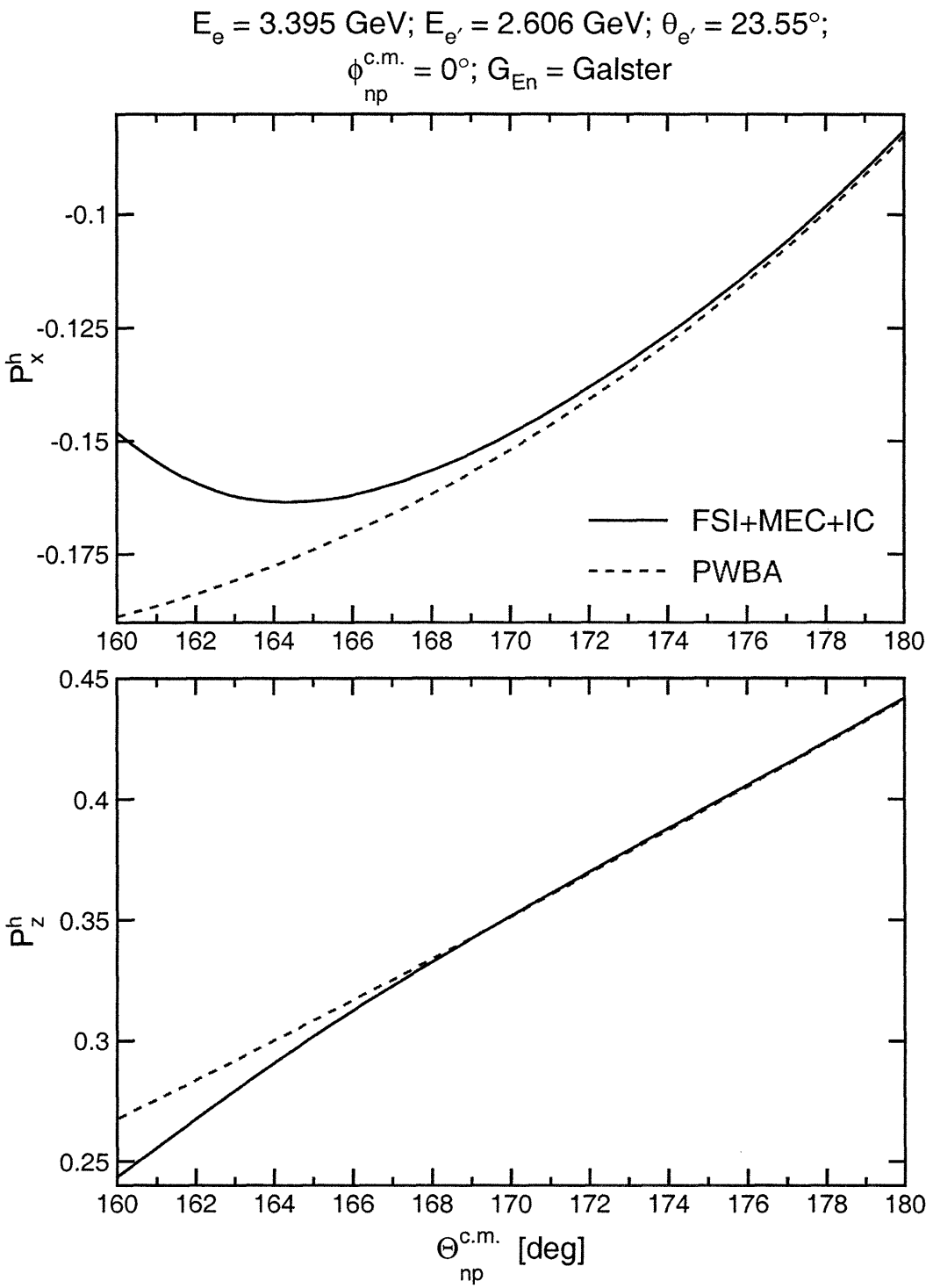

Figure 7-5: (color) Comparison of Arenhövel's PWBA (red dashed lines) and FSI+MEC+IC (blue solid lines) calculations of P_x^h (top panel) and P_z^h (bottom panel) for the central electron kinematics at $Q^2 = 1.474$ (GeV/c)^2.

7.2 Sample Simulation Output

In this section, we present sample output from the Acceptance program and GENGEN. In particular, we show sample distributions of the recoil polarization at the target (i.e., prior to precession in the Charybdis field), sample distributions of the neutron spin precession angle, and sample distributions of the sideways component of the recoil polarization presented to the front array of the polarimeter. Neutron scattering in the lead curtain was disabled (in GENGEN) for the simulation results presented in this section; however, we will, later, compare distributions of the polarization presented to the front array of the polarimeter for those events which did and did not suffer an interaction in the lead curtain.

It is not, of course, possible to show all possible distributions that were generated with the two simulation programs; instead, the purpose of the discussion that follows below is to illustrate the quality of the recoil polarization data that we were able to extract from the two simulations.

7.2.1 ^{2}H($\vec{e}$,$e'\vec{n}$)^{1}H Recoil Polarization at the Target

We begin by presenting sample simulated distributions (after all cuts) of the projection of the $^2\mathrm{H}(\vec{e}, e'\vec{n})$ recoil polarization at the target on the *polarimeter momentum basis* $\hat{\mathbf{S}}$- and $\hat{\mathbf{L}}$-axes; henceforth, the projection of the recoil polarization on these axes *at the target* will be denoted P_S and P_L, respectively. For purposes of brevity, we present sample distributions of P_S and P_L only for simulations performed for the central $Q^2 = 1.474$ (GeV/c)^2 point in Fig. 7-6. The distributions shown here were extracted from simulations that employed the Arenhövel FSI+MEC+IC model and assumed G_{En} is given by the (standard) Galster parameterization. We note that the distributions appear to be reasonable and are of the expected Gaussian shape. Also, what is perhaps most important is that the Acceptance program and GENGEN distributions clearly agree qualitatively (despite the differences in the bin sizes).

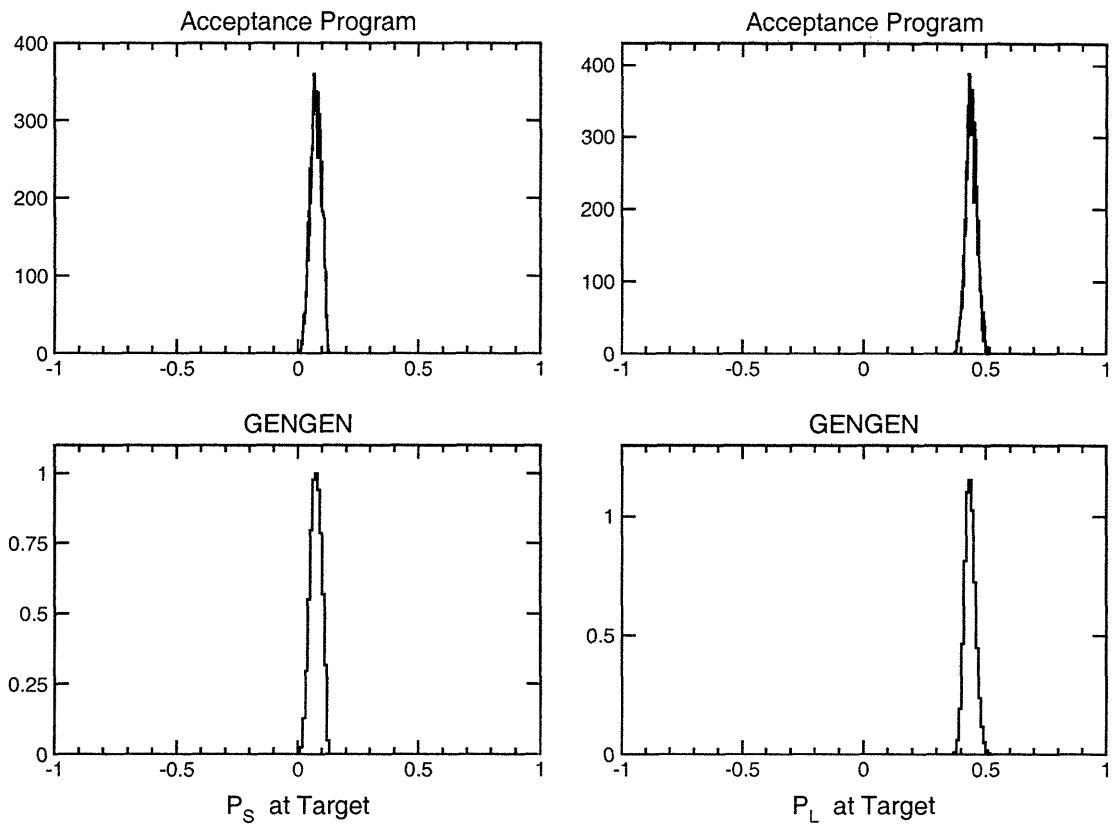

Figure 7-6: Sample distributions of the recoil polarization components P_S (left panels) and P_L (right panels) at the target extracted from simulated data generated by the `Acceptance program` (top panels) and `GENGEN` (bottom panels) for the central $Q^2 = 1.474$ (GeV/c)^2 point. The simulations employed the Arenhövel FSI+MEC+IC model and assumed the Galster parameterization for G_{En}.

7.2.2 Neutron Spin Precession Angles

Next, we present sample simulated distributions (after all cuts) of the neutron spin precession angle, χ, in the Charybdis dipole field. Again, for purposes of brevity, we present only sample distributions of χ extracted from simulations performed for the central $Q^2 = 1.474$ (GeV/c)^2 point in Figs. 7-7 and 7-8. Again, these distributions appear to be reasonable and are of the expected Gaussian shape, and the `Acceptance` program and `GENGEN` distributions agree qualitatively (despite the differences in the bin sizes). Also, the distributions are well centered around the nominal spin precession angles of $\chi = \pm 40°$ and $\pm 90°$.

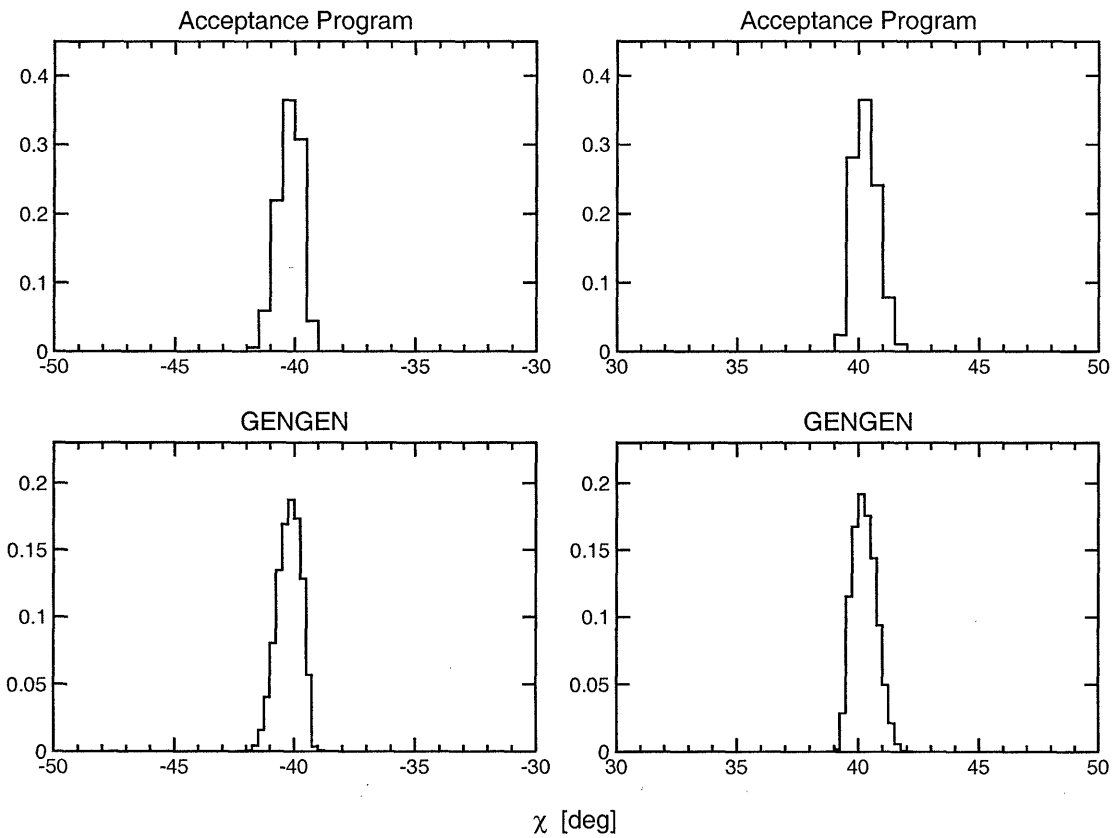

Figure 7-7: Sample distributions of neutron spin precession angles χ for $-40°$ (left panels) and $+40°$ (right panels) precession extracted from simulated data generated by the `Acceptance program` (top panels) and `GENGEN` (bottom panels) for the central $Q^2 = 1.474$ (GeV/c)^2 point.

7.2.3 Recoil Polarization Presented to the Polarimeter

Finally, we present sample distributions (after all cuts) of the recoil polarization presented to the polarimeter *after precession in the Charybdis field* through the nominal $\chi = \pm 40°$ and $\pm 90°$ spin precession angles extracted from simulations performed for the central $Q^2 = 1.474$ (GeV/c)^2 point in Figs. 7-9 and 7-10. The distributions shown here are histograms of the projection of the precessed recoil polarization vector on the polarimeter momentum basis $\hat{\mathbf{S}}$-axis; henceforth, we will denote this component of the polarization that is presented to the front array of the polarimeter as P'_S (the prime will indicate the polarization vector was transported through the Charybdis field and, if applicable, the lead curtain).

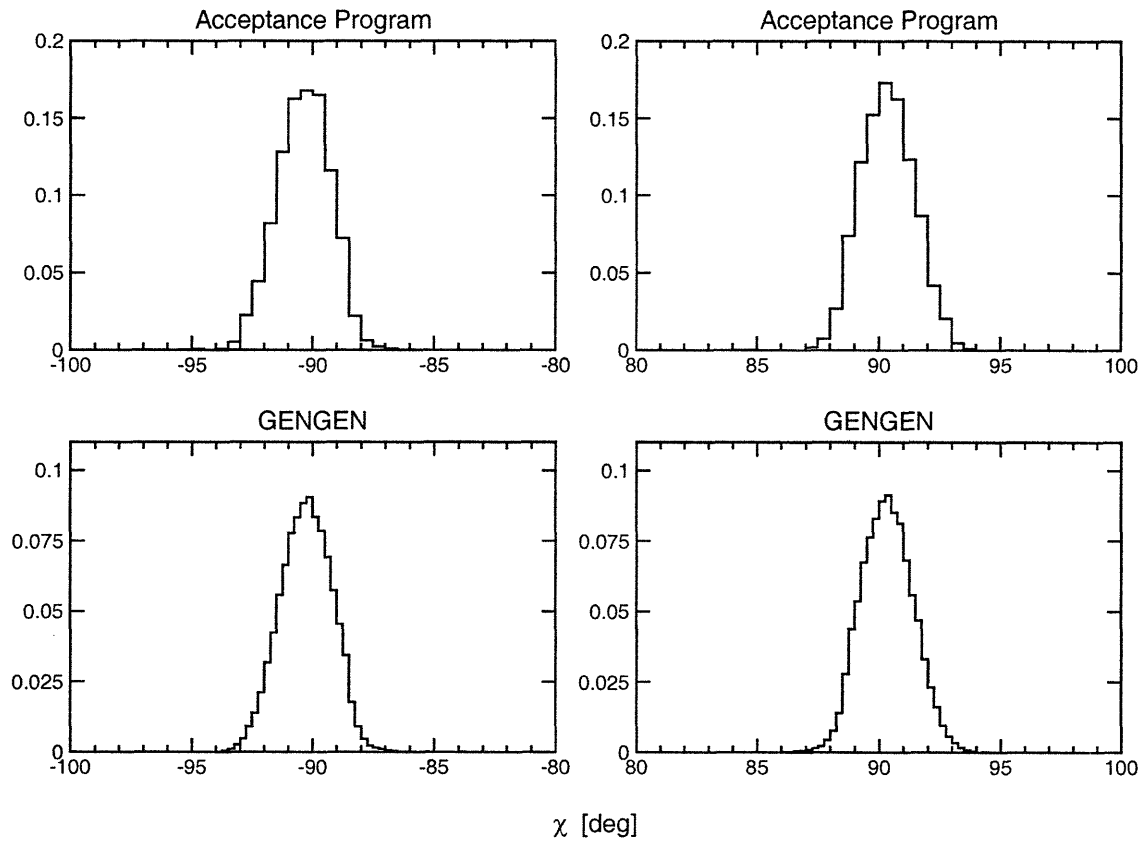

Figure 7-8: Sample distributions of neutron spin precession angles χ for $-90°$ (left panels) and $+90°$ (right panels) precession extracted from simulated data generated by the `Acceptance program` (top panels) and `GENGEN` (bottom panels) for the central $Q^2 = 1.474$ (GeV/c)^2 point.

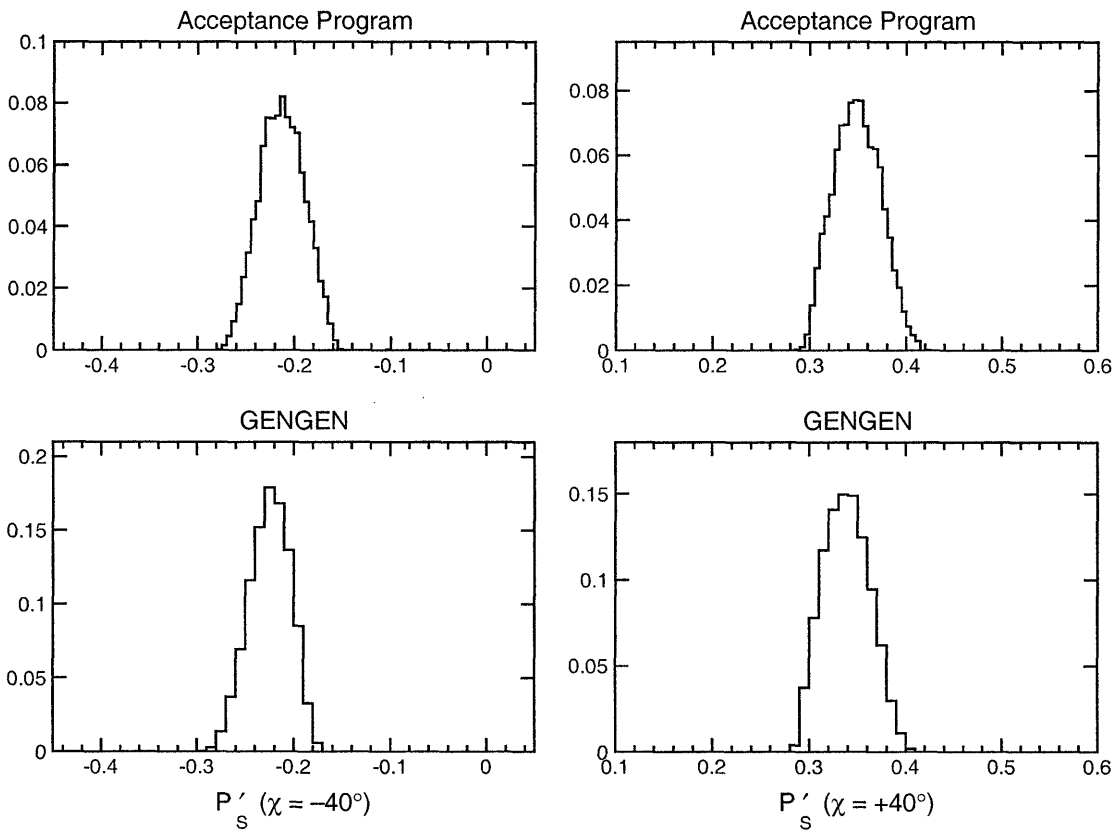

Figure 7-9: Sample distributions of P'_S after precession through $\chi = -40°$ (left panels) and $\chi = +40°$ (right panels) precession extracted from simulated data generated by the `Acceptance program` (top panels) and `GENGEN` (bottom panels) for the central $Q^2 = 1.474$ (GeV/c)^2 point.

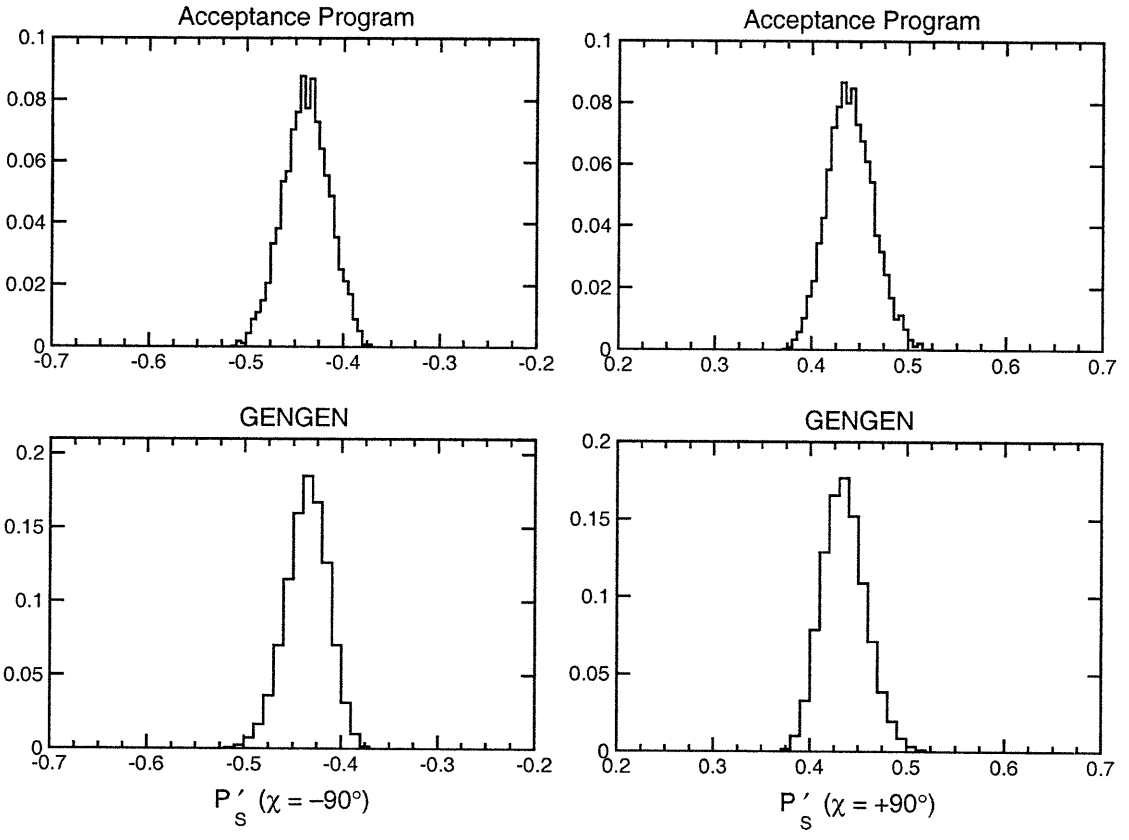

Figure 7-10: Sample distributions of P'_S after precession through $\chi = -90°$ (left panels) and $\chi = +90°$ (right panels) precession extracted from simulated data generated by the `Acceptance program` (top panels) and `GENGEN` (bottom panels) for the central $Q^2 = 1.474$ (GeV/c)^2 point.

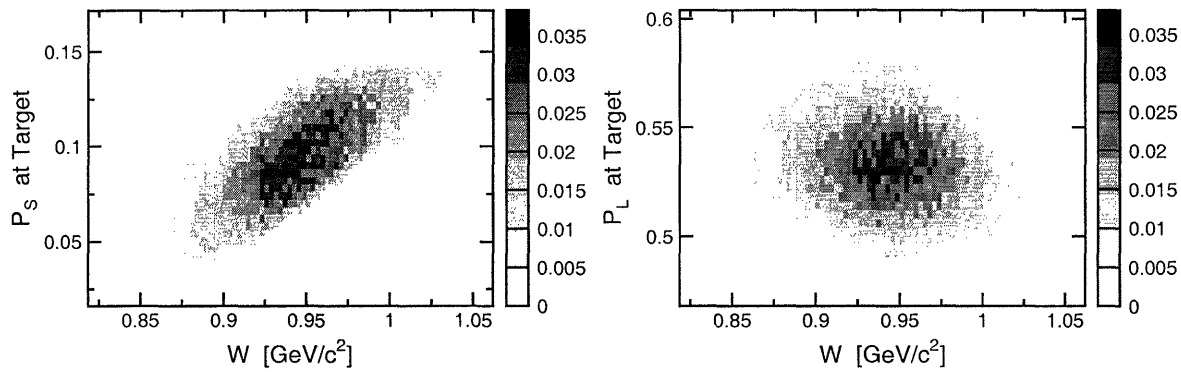

Figure 7-11: (color) Two-dimensional distributions of the recoil polarization components P_S (left panel) and P_L (right panel) at the target versus the invariant mass W at $Q^2 = 1.136$ (GeV/c)^2. These distributions were extracted from simulated data generated by GENGEN that employed the Arenhövel FSI+MEC+IC model and assumed the Galster parameterization for G_{En}.

7.2.4 Comparison of Simulated Polarizations and Experimental Asymmetries

We conclude our presentation of sample simulation output in this subsection by comparing the simulated acceptance-averaged polarizations with the asymmetries extracted from the experimental data. In order to make a meaningful comparison, we compare the behavior of the acceptance-averaged polarizations and the experimental asymmetries as a function of the cut on the invariant mass W; in particular, we investigate whether the simulated polarizations and the experimental asymmetries scale similarly with the cut on W.

To illustrate this investigation, we begin by presenting two-dimensional histograms of the recoil polarization components P_S and P_L at the target (i.e., prior to precession) versus the invariant mass W at $Q^2 = 1.136$ (GeV/c)^2 in Fig. 7-11. The distributions presented here were extracted from GENGEN simulated data; the distributions extracted from the Acceptance program are identical. Here, we see a strong linear correlation between P_S and W; a correlation also exists between P_L and W, but it is much weaker. It is imperative that these correlations are also present in the asymmetries extracted from the experimental data if the corrections for the finite

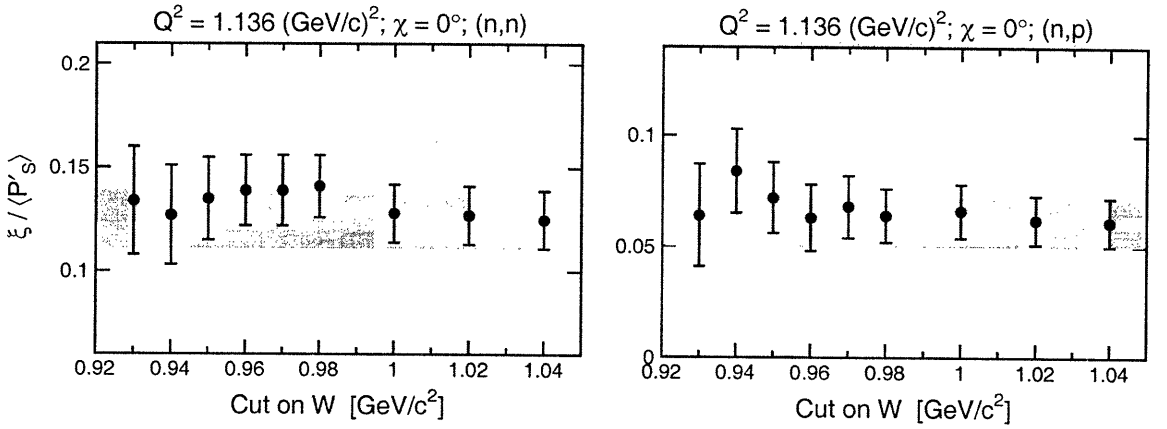

Figure 7-12: (color) Ratio of the asymmetries ξ extracted from the experimental data to the acceptance-averaged polarizations $\langle P'_S \rangle$ as a function of the cut on W for (n,n) [left panel] and (n,p) [right panel] events for $\chi = 0°$ precession at $Q^2 = 1.136$ $(\mathrm{GeV}/c)^2$. The yellow shaded bands indicate the statistical errors of the ratio for the nominal cut on W of 1.04 GeV/c^2.

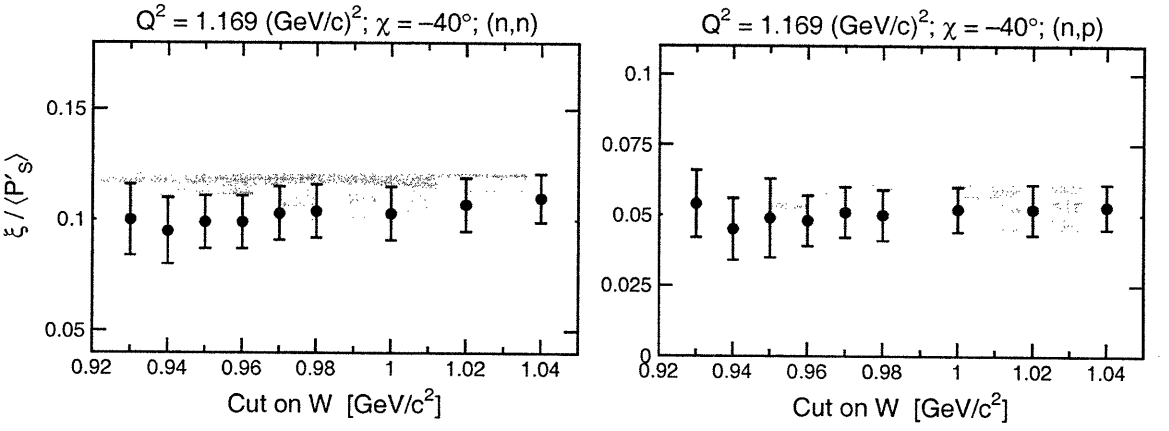

Figure 7-13: (color) Ratio of the asymmetries ξ extracted from the experimental data to the acceptance-averaged polarizations $\langle P'_S \rangle$ as a function of the cut on W for (n,n) [left panel] and (n,p) [right panel] events for $\chi = -40°$ precession at $Q^2 = 1.169$ $(\mathrm{GeV}/c)^2$. The yellow shaded bands indicate the statistical errors of the ratio for the nominal cut on W of 1.04 GeV/c^2.

experimental acceptance and nuclear physics effects extracted from the data are to be trusted; therefore, we present two examples of such an investigation. First, we compare the $Q^2 = 1.136$ $(\mathrm{GeV}/c)^2$ $\chi = 0°$ experimental asymmetries with the $\chi = 0°$ simulated acceptance-averaged polarizations in Fig. 7-12; there, we have plotted the ratio of the asymmetries extracted from the experimental data to the acceptance-

averaged polarizations, $\xi/\langle P'_S \rangle$, as a function of the cut on W. Indeed, we observe the desired behavior; within the statistical errors, the experimental asymmetries and the acceptance-averaged polarizations scale similarly with the cut on W. Second, in Fig. 7-13, we compare the same quantities for the $Q^2 = 1.169$ $(\mathrm{GeV}/c)^2$ $\chi = -40°$ experimental and simulated data. Again, within statistical errors, we observe the desired behavior. A more detailed and comprehensive discussion of these types of comparisons was given by Plaster and Kelly in [434].

7.3 Extraction of Acceptance-Averaged and Nuclear Physics Corrected Results for G_{En}/G_{Mn}

We now proceed to a discussion of the extraction of the acceptance-averaged and nuclear physics corrected values for G_{En}/G_{Mn} from the experimental asymmetries and the simulated acceptance-averaged polarizations. Following an overview of the analysis procedure that we employed, we compare the final results obtained with the `Acceptance` program and `GENGEN`.

7.3.1 Overview of Procedure

An overview of the final analysis procedure we employed is as follows:

1. Acceptance-averaged polarizations, $\langle P'_S \rangle$, computed according to Arenhövel's PWBA and FSI+MEC+IC models were extracted from the simulated data for each spin precession angle at each Q^2 point and for each multiplicative factor, GSF = 0.50, 0.75, 1.00, 1.25, and 1.50, of the Galster parameterization (recall the discussion in Section 6.2.6).

2. In the *pairwise analysis method*, for each GSF, we compared the ratio of the experimental asymmetries with the ratio of the simulated acceptance-averaged polarizations for the different spin precession techniques (i.e., $\chi = 0°$, $\pm 90°$ and

$\chi = \pm 40°$) and computed a χ^2 value for each spin precession technique and each event type [i.e., (n,n) or (n,p) events] according to

$$\chi^2 = \frac{(\eta_{\rm sim} - \eta_{\rm exp})^2}{(\Delta\eta_{\rm sim})^2 + (\Delta\eta_{\rm exp})^2} \ , \tag{7.1}$$

where

$$\eta_{\rm sim} = \begin{cases} \dfrac{\langle P'_S(0°)\rangle}{\langle P'_S(\pm 90°)\rangle} & \text{for } \chi = 0°,\ \pm 90° \text{ precession,} \\ \\ \dfrac{\langle P'_S(-40°)\rangle}{\langle P'_S(+40°)\rangle} & \text{for } \chi = \pm 40° \text{ precession,} \end{cases}$$

$$\eta_{\rm exp} = \begin{cases} \dfrac{\xi(0°)}{\xi(\pm 90°)} & \text{for } \chi = 0°,\ \pm 90° \text{ precession,} \\ \\ \dfrac{\xi(-40°)}{\xi(+40°)} & \text{for } \chi = \pm 40° \text{ precession,} \end{cases}$$

and $\Delta\eta_{\rm sim}$ and $\Delta\eta_{\rm exp}$ denote, respectively, the statistical errors of $\eta_{\rm sim}$ and $\eta_{\rm exp}$. The resulting values of χ^2 were fitted as a function of the GSF to a parabola-like function,

$$f(x) = \left(\frac{x - P_1}{P_2 + P_3 x}\right)^2 \ , \tag{7.2}$$

where the P_i were fit parameters, and the optimal value of the GSF was extracted from the solution to $f(x) = 0$.

3. In the *global analysis method*, we simultaneously compared the asymmetries with the simulated acceptance-averaged polarizations for all spin precession angles (i.e., $\chi = -90°,\ -40°,\ 0°\ , +40°$, and $+90°$) all event types [i.e., (n,n) and (n,p) events] and calculated a global χ^2 value for each GSF according to

$$\chi^2\left(A_y^{(n,n)}, A_y^{(n,p)}\right)_{\rm GSF} = \sum_{\text{all } \chi;\ (n,n);\ (n,p)} \frac{\left(\xi - A_y^{(n,n),\ (n,p)}\langle P'_S\rangle\right)^2}{(\Delta\xi)^2 + (\Delta\langle P'_S\rangle)^2} \ , \tag{7.3}$$

where the summation was performed over all 10 asymmetries and acceptance-averaged polarizations [i.e., 5 different spin precession angles and for (n,n) and (n,p) events], and $A_y^{(n,n)}$ and $A_y^{(n,p)}$ denote, respectively, the analyzing powers for (n,n) and (n,p) events. The analyzing powers were treated as free fit parameters, and the resulting global χ^2 values were fitted as a function of the GSF to the same parabolic-like function; as in the pairwise analysis, the optimal value of the GSF was extracted from the minimal χ^2 value. *It should be noted that the global analysis method could not be used for the analysis of the $Q^2 = 0.447$ $(GeV/c)^2$ data set as asymmetry data were only taken with the two $\chi = \pm 40^\circ$ spin precession angles.*

7.3.2 Acceptance Averaging Analysis Iterations

We performed two iterations of the above-described analysis procedure.

First, the `Acceptance` program and `GENGEN` simulations were performed with Arenhövel's PWBA and FSI+MEC+IC calculations that assumed different multiplicative factors of the *standard Galster parameterization* for the Q^2 dependence of G_{En}. The optimal values of the GSF that we extracted via the above-described procedure were then used to compute the optimal values for G_{En}/G_{Mn} according to

$$G_{En}/G_{Mn} = \mathrm{GSF}_{\mathrm{optimal}} \times \underbrace{\left(-\frac{\langle\tau\rangle}{1+5.6\langle\tau\rangle}\right)}_{\text{standard Galster}} , \tag{7.4}$$

where $\langle\tau\rangle = \langle Q^2\rangle/4m^2$ and $\langle Q^2\rangle$ denotes the *acceptance-averaged value* of Q^2; the acceptance-averaged values of Q^2 were determined to be $\langle Q^2\rangle = 0.447$, 1.126, 1.158, and 1.450 $(\mathrm{GeV}/c)^2$, respectively, for the central $Q^2 = 0.447$, 1.136, 1.169, and 1.474 $(\mathrm{GeV}/c)^2$ data sets. We then obtained the values for G_{En} from this first analysis iteration by multiplying our optimal values for G_{En}/G_{Mn} by the best-fit values for

G_{Mn} reported by Kelly[1] [20,424] at $\langle Q^2 \rangle = 0.447$, 1.132^2, and 1.450 $(\mathrm{GeV}/c)^2$; these were found to be $G_{Mn}/\mu_n G_D = 1.003 \pm 0.006$, 1.057 ± 0.017, and 1.044 ± 0.024, respectively. We then fitted our results for G_{En} from this first analysis iteration and the then-available current world data[3] on G_{En} to a modified Galster parameterization,

$$G_{En}(Q^2) = -\frac{a\mu_n\tau}{1+b\tau}\, G_D(Q^2)\ , \tag{7.5}$$

where a and b were free fit parameters and $G_D(Q^2)$ denotes the dipole parameterization; the best-fit parameters we found at that time were $a = 0.894 \pm 0.023$ and $b = 3.55 \pm 0.37$.

Second, after we finished the first analysis iteration, we then requested the second set of calculations from Arenhövel that assumed this modified Galster parameterization for the Q^2 dependence of G_{En} as we were interested in investigating whether the Q^2 dependence of G_{En} would have any effect on the acceptance-averaged result. The `Acceptance` program and `GENGEN` simulations were then both repeated using these new calculations. We repeated the entire analysis procedure described above, and the optimal values of the GSF that we extracted from our analysis were used to compute the optimal values for G_{En}/G_{Mn} according to

$$G_{En}/G_{Mn} = \mathrm{GSF}_{\mathrm{optimal}} \times \underbrace{\left(-\frac{-0.894\langle\tau\rangle}{1+3.55\langle\tau\rangle}\right)}_{\text{modified Galster}}\ . \tag{7.6}$$

In what follows below, we report relevant details from the second (and final) analysis iteration. The pairwise analysis method was employed for the extraction of the final values for G_{En}/G_{Mn} at $\langle Q^2 \rangle = 0.447$ $(\mathrm{GeV}/c)^2$, while the global analysis method was used for the extraction of the final values for G_{En}/G_{Mn} at $\langle Q^2 \rangle = 1.132$ and 1.474 $(\mathrm{GeV}/c)^2$. We have chosen not to present the results from the first analysis

[1]Kelly's [20,424] results for G_{Mn} were extracted from fits to the nucleon form factor data that employed linear expansions in complete sets of basis functions as the fit function. The results used here are those that were obtained using an expansion in Laguerre-Gaussian basis functions.

[2]The $\langle Q^2 \rangle = 1.132$ $(\mathrm{GeV}/c)^2$ value denotes the sample-size weighted average of the $\langle Q^2 \rangle = 1.126$ and 1.158 $(\mathrm{GeV}/c)^2$ data sets.

[3]At the conclusion of the first analysis iteration (March 2003), the new data on G_{En} reported recently by Bermuth *et al.* [205] and Warren *et al.* [209] were not yet available.

PWBA Results for G_{En}/G_{Mn}			
Simulation	(n,n)	(n,p)	Combined
`Acceptance`	-0.0606 ± 0.0110	-0.0872 ± 0.0139	-0.0709 ± 0.0086
`GENGEN`	-0.0610 ± 0.0110	-0.0885 ± 0.0138	-0.0716 ± 0.0086
FSI+MEC+IC Results for G_{En}/G_{Mn}			
Simulation	(n,n)	(n,p)	Combined
`Acceptance`	-0.0645 ± 0.0114	-0.0919 ± 0.0142	-0.0751 ± 0.0089
`GENGEN`	-0.0649 ± 0.0113	-0.0933 ± 0.0143	-0.0758 ± 0.0088

Table 7.2: Comparison of the pairwise analysis results at $\langle Q^2 \rangle = 0.447$ (GeV/c)^2 obtained with the `Acceptance` program and `GENGEN`.

iteration as the procedures for the two iterations were completely identical and the differences between the first and second analysis iterations were negligible.[4]

7.3.3 Acceptance-Averaging Analysis Results

$\langle Q^2 \rangle = 0.447$ (GeV/c)^2 Pairwise Analysis

The results of the $\langle Q^2 \rangle = 0.447$ (GeV/c)^2 pairwise analysis χ^2 fits to Eq. (7.1) obtained with `GENGEN` are shown in Fig. 7-14, and the values for G_{En}/G_{Mn} we obtained with the `Acceptance` program and `GENGEN` are compared in Table 7.2. As can be seen there, the agreement between the results from the two simulation programs is better than 1%. The final results for G_{En}/G_{Mn} we quote at $\langle Q^2 \rangle = 0.447$ (GeV/c)^2 are the average of the results obtained with the `Acceptance` program and `GENGEN`:

$$G_{En}/G_{Mn} = -0.0713 \pm 0.0086 \quad \text{(PWBA)} ,$$
$$G_{En}/G_{Mn} = -0.0755 \pm 0.0089 \quad \text{(FSI + MEC + IC)} .$$

The quoted errors are the statistical errors; systematic errors will be discussed in the next section of this chapter.

[4]The fact that the differences between the first and second analysis iterations differed little can be understood intuitively as follows. Both parameterizations for G_{En} are essentially linear (i.e., have small second derivatives) in the vicinity of our Q^2 points and the acceptance is fairly symmetric about the acceptance averaged values of Q^2; therefore, the actual slope of G_{En} should have little influence on the acceptance-averaged result.

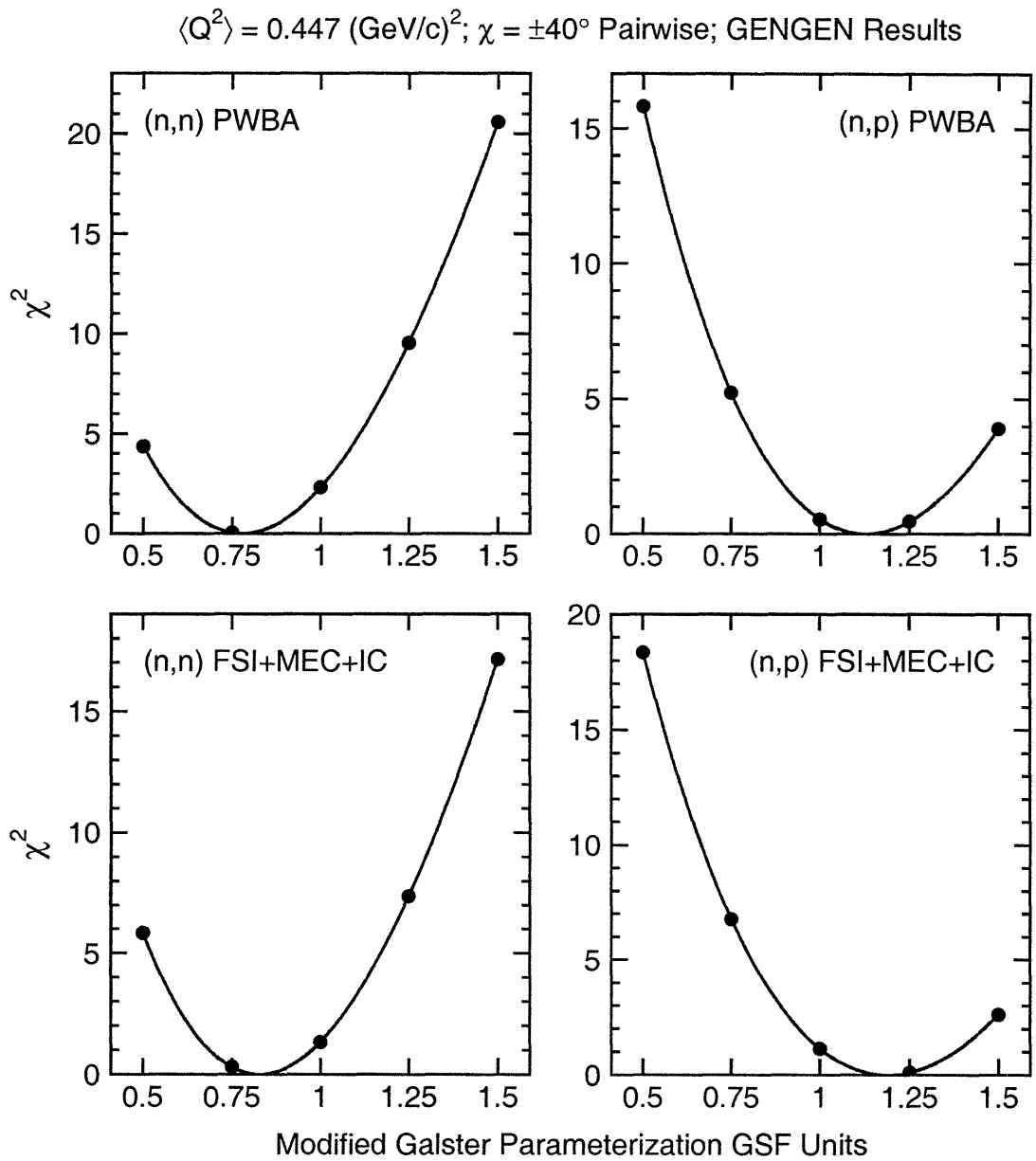

Figure 7-14: Results of the pairwise χ^2 analysis at $\langle Q^2 \rangle = 0.447$ (GeV/c)^2. The top [bottom] panels are the χ^2 fits for the PWBA [FSI+MEC+IC] calculations, and the left [right] panels are the χ^2 fits for (n,n) $[(n,p)]$ events.

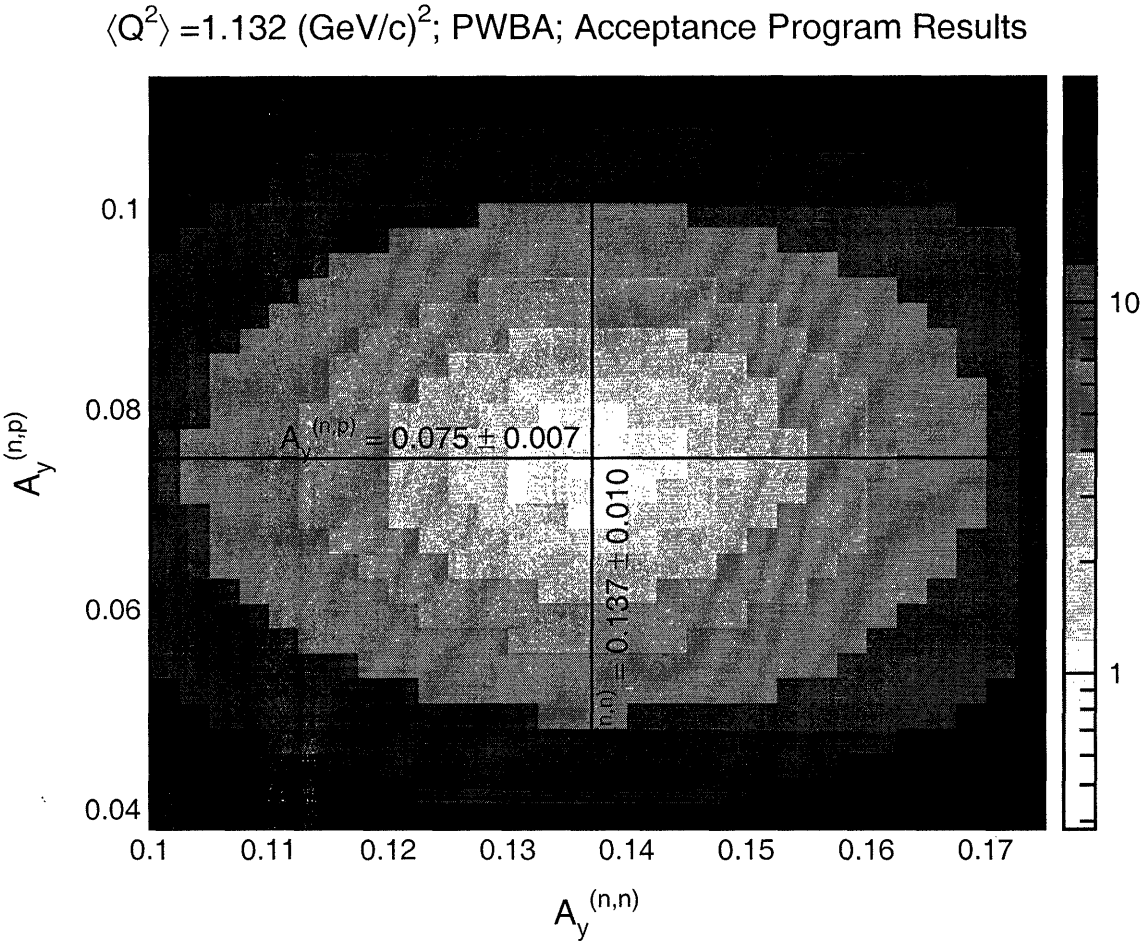

Figure 7-15: (color) Two-dimensional global analysis $\chi^2(A_y^{(n,n)}, A_y^{(n,p)})$ distributions for the PWBA analysis at $\langle Q^2 \rangle = 1.132$ (GeV/c)^2 obtained with the `Acceptance` program.

$\langle Q^2 \rangle = 1.132$ (GeV/c)^2 Global Analysis

Results from the $\langle Q^2 \rangle = 1.132$ (GeV/c)^2 global analysis obtained with the `Acceptance` program are shown in Figs. 7-15 through 7-17. The two-dimensional global analysis $\chi^2(A_y^{(n,n)}, A_y^{(n,p)})$ distributions for the PWBA and FSI+MEC+IC analysis are shown in Figs. 7-15 and 7-16, respectively, and Fig. 7-17 shows the fits of the resulting χ^2 values as a function of the GSF to Eq. (7.1) (with a vertical offset parameter added) after the analyzing powers were extracted from the two-dimensional $\chi^2(A_y^{(n,n)}, A_y^{(n,p)})$ distributions.

The values for G_{En}/G_{Mn} we obtained with the `Acceptance` program and `GENGEN`

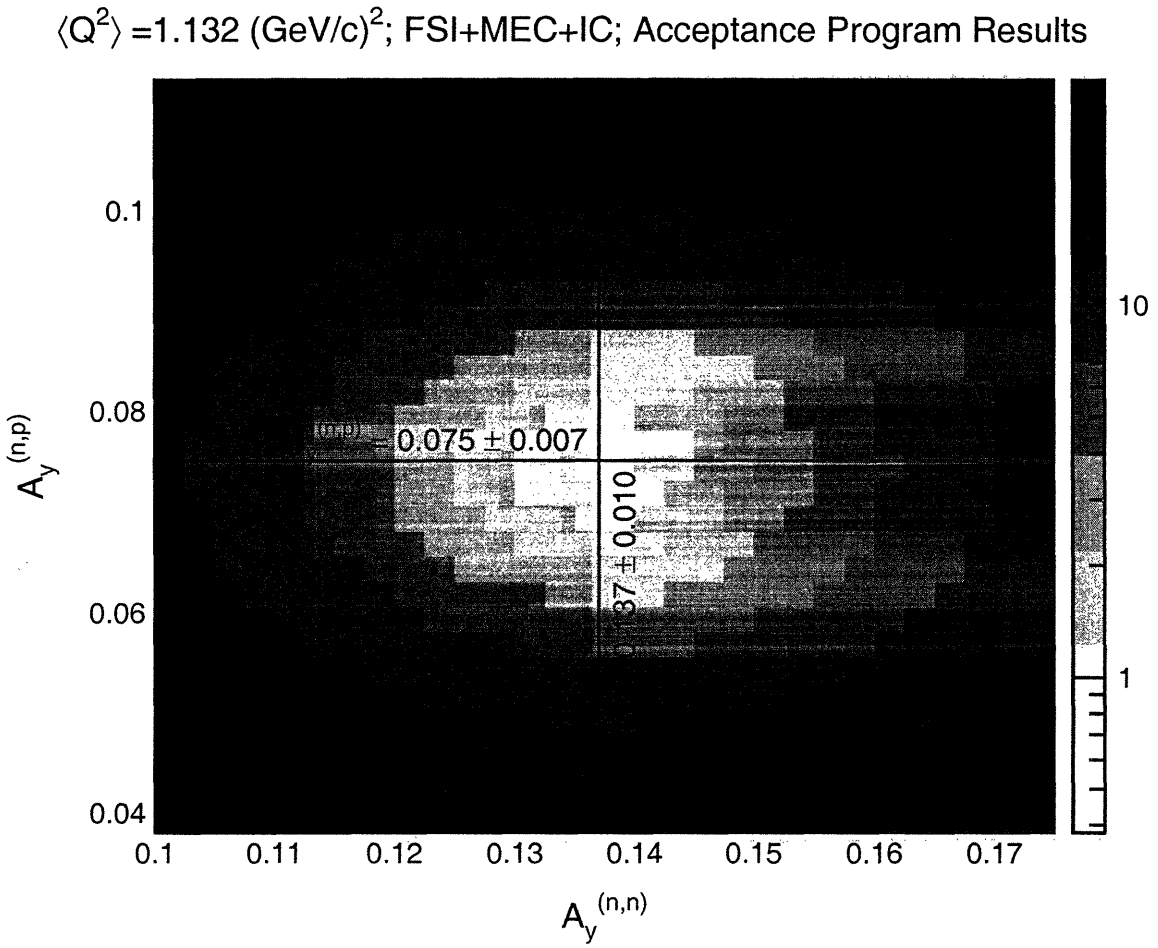

Figure 7-16: (color) Two-dimensional global analysis $\chi^2(A_y^{(n,n)}, A_y^{(n,p)})$ distributions for the FSI+MEC+IC analysis at $\langle Q^2 \rangle = 1.132$ (GeV/c)^2 obtained with the `Acceptance` program.

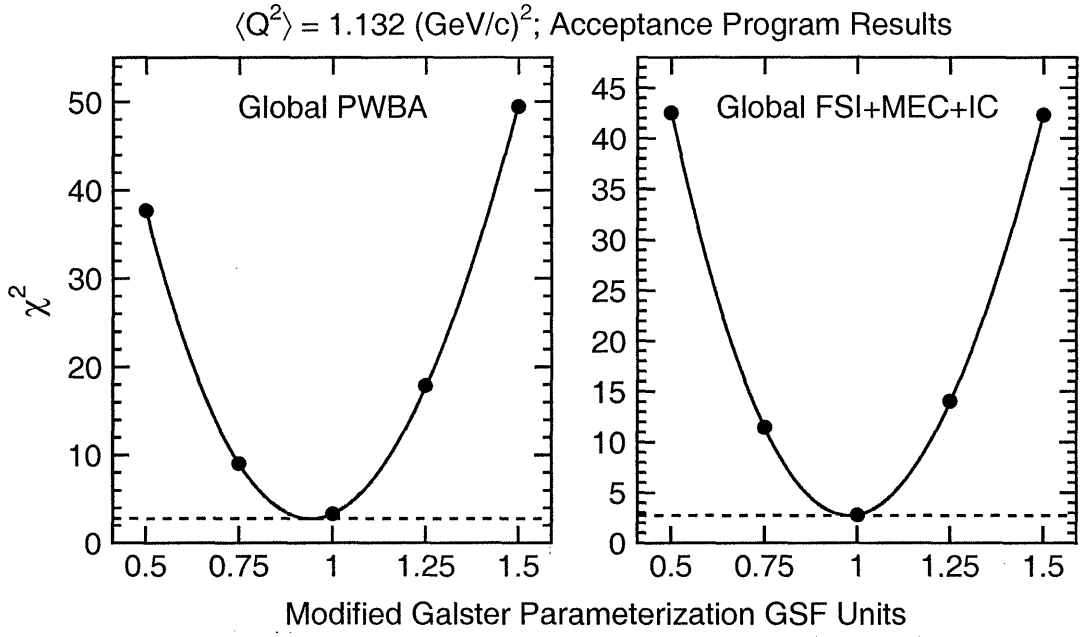

Figure 7-17: Results of the $\langle Q^2 \rangle = 1.132$ (GeV/c)^2 global analysis χ^2 fits after the analyzing powers were extracted from the two-dimensional $\chi^2(A_y^{(n,n)}, A_y^{(n,p)})$ distributions. The results shown here were obtained with the `Acceptance` program.

	Results for G_{En}/G_{Mn}	
Simulation	PWBA	FSI+MEC+IC
`Acceptance`	-0.126 ± 0.010	-0.131 ± 0.011
`GENGEN`	-0.125 ± 0.010	-0.130 ± 0.011

Table 7.3: Comparison of the global analysis results at $\langle Q^2 \rangle = 1.132$ (GeV/c)^2 obtained with the `Acceptance` program and `GENGEN`.

are compared in Table 7.3. As can be seen there, the agreement between the results from the two simulation programs is better than 1%. The final results for G_{En}/G_{Mn} we quote at $\langle Q^2 \rangle = 1.132$ (GeV/c)^2 are the average of the results obtained with the `Acceptance` program and `GENGEN`:

$$G_{En}/G_{Mn} = -0.126 \pm 0.010 \quad \text{(PWBA)} ,$$
$$G_{En}/G_{Mn} = -0.131 \pm 0.011 \quad \text{(FSI + MEC + IC)} .$$

Again, the errors quoted here are statistical.

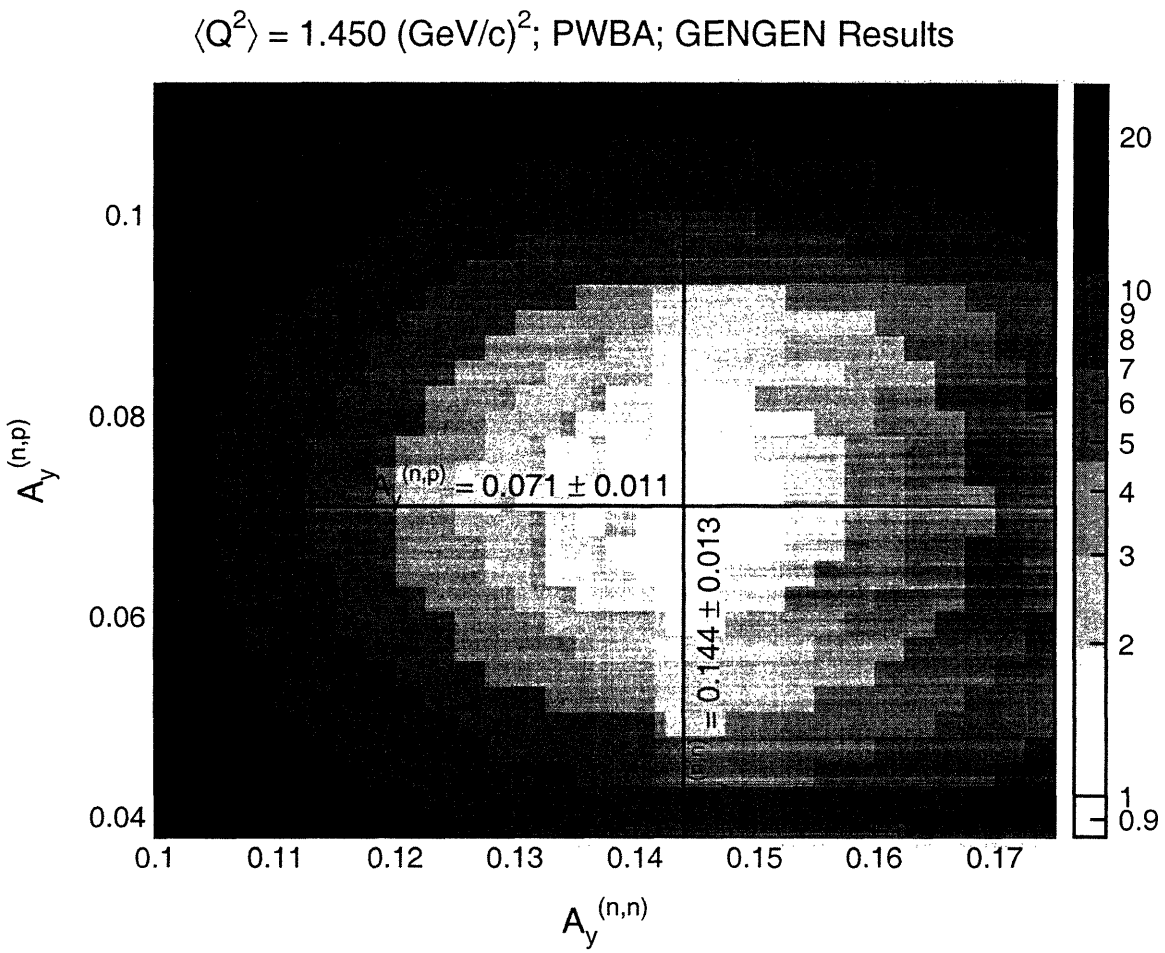

Figure 7-18: (color) Two-dimensional global analysis $\chi^2(A_y^{(n,n)}, A_y^{(n,p)})$ distributions for the PWBA analysis at $\langle Q^2 \rangle = 1.450$ (GeV/c)^2 obtained with GENGEN.

$\langle Q^2 \rangle = 1.450$ (GeV/c)^2 Global Analysis

Results from the $\langle Q^2 \rangle = 1.450$ (GeV/c)^2 global analysis obtained with GENGEN are shown in Figs. 7-18 through 7-20. Figs. 7-18 and 7-19 show the two-dimensional global analysis $\chi^2(A_y^{(n,n)}, A_y^{(n,p)})$ distributions for the PWBA and FSI+MEC+IC analysis, respectively, and Fig. 7-20 shows the fits of the resulting χ^2 values as a function of the GSF to Eq. (7.1) (with a vertical offset parameter added) after the analyzing powers were extracted from the two-dimensional $\chi^2(A_y^{(n,n)}, A_y^{(n,p)})$ distributions.

The values for G_{En}/G_{Mn} we obtained with the Acceptance program and GENGEN are compared in Table 7.4. As can be seen there, the agreement between the results from the two simulation programs is better than 2%. The final results for G_{En}/G_{Mn}

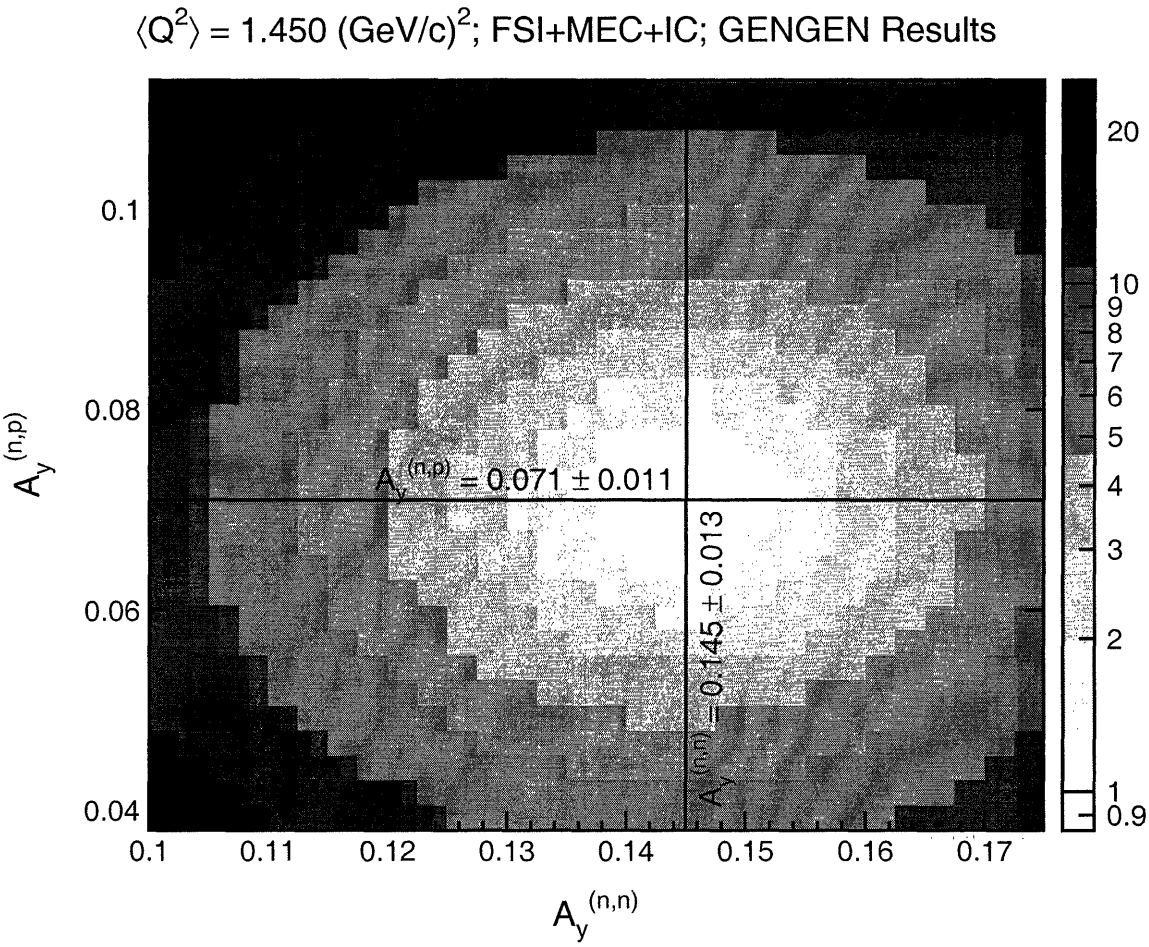

Figure 7-19: (color) Two-dimensional global analysis $\chi^2(A_y^{(n,n)}, A_y^{(n,p)})$ distributions for the FSI+MEC+IC analysis at $\langle Q^2 \rangle = 1.450$ (GeV/c)^2 obtained with GENGEN.

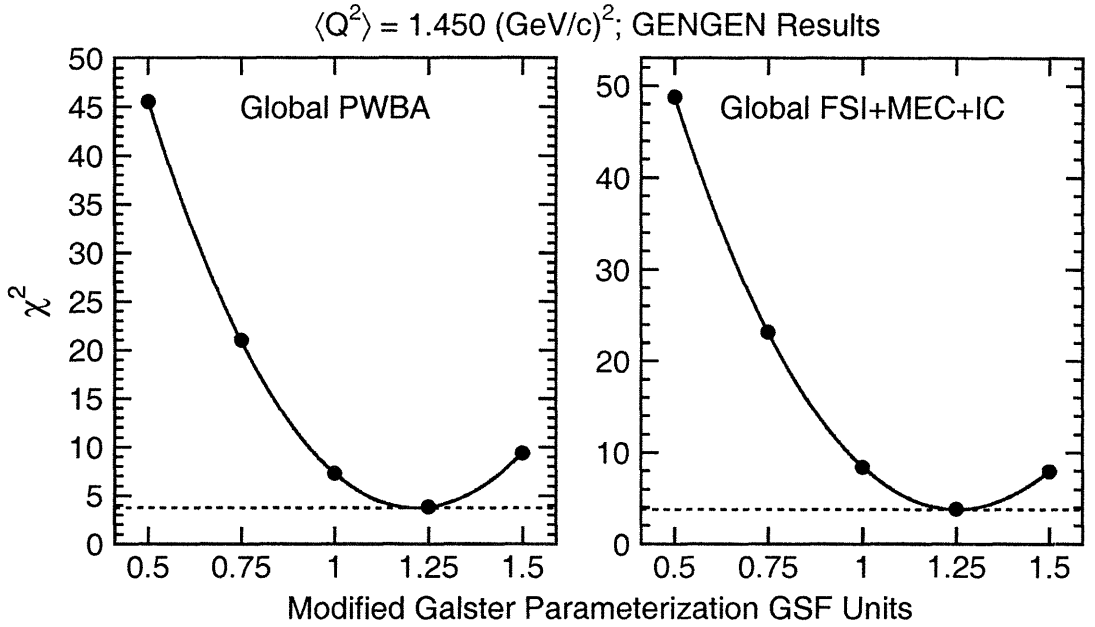

Figure 7-20: Results of the $\langle Q^2 \rangle = 1.450$ (GeV/c)^2 global analysis χ^2 fits after the analyzing powers were extracted from the two-dimensional $\chi^2(A_y^{(n,n)}, A_y^{(n,p)})$ distributions. The results shown here were obtained with `GENGEN`.

	Results for G_{En}/G_{Mn}	
Simulation	PWBA	FSI+MEC+IC
`Acceptance`	-0.184 ± 0.018	-0.191 ± 0.018
`GENGEN`	-0.182 ± 0.017	-0.187 ± 0.018

Table 7.4: Comparison of the global analysis results at $\langle Q^2 \rangle = 1.450$ (GeV/c)^2 obtained with the `Acceptance` program and `GENGEN`.

we quote at $\langle Q^2 \rangle = 1.450$ (GeV/c)^2 are the average of the results obtained with the `Acceptance` program and `GENGEN`:

$$G_{En}/G_{Mn} = -0.183 \pm 0.018 \quad \text{(PWBA)} ,$$
$$G_{En}/G_{Mn} = -0.189 \pm 0.018 \quad \text{(FSI + MEC + IC)} .$$

Again, the errors quoted here are statistical.

7.3.4 Summary of Results for G_{En}/G_{Mn}

The final acceptance-averaged and nuclear physics corrected results for G_{En}/G_{Mn} with their statistical errors that we report for our three Q^2 points are:

$$G_{En}/G_{Mn} = -0.0755 \pm 0.0089 \qquad \langle Q^2 \rangle = 0.447 \text{ (GeV/}c\text{)}^2$$
$$G_{En}/G_{Mn} = -0.131 \pm 0.011 \qquad \langle Q^2 \rangle = 1.132 \text{ (GeV/}c\text{)}^2$$
$$G_{En}/G_{Mn} = -0.189 \pm 0.018 \qquad \langle Q^2 \rangle = 1.450 \text{ (GeV/}c\text{)}^2$$

7.4 Systematic Uncertainties

In this section, we provide brief overviews of the procedures that were employed for the estimation of the various systematic uncertainties. The values of the systematic uncertainties for the two different spin precession techniques (i.e., $\chi = 0°$, $\pm 90°$ and $\pm 40°$) at each Q^2 point are considered.

7.4.1 Beam Polarization

A detailed discussion of the estimation of the contribution of the uncertainty in the beam polarization to the systematic uncertainty in G_{En}/G_{Mn} was given by Plaster and Madey in [435]; here, we summarize the most important features and results of this analysis.

Overview

As discussed in detail in Section 2.3.6, a significant advantage of the spin precession recoil polarimetry technique is that the G_{En}/G_{Mn} form factor ratio is relatively insensitive to the analyzing power of the polarimeter and the beam polarization. The analyzing power cancels exactly in the form factor ratio, and the beam polarization also cancels if the beam polarization is stable during measurements of the scattering asymmetries at the different spin precession angles; however, *fluctuations in the beam polarization between measurements introduce a systematic uncertainty.*

We estimated the magnitude of this systematic uncertainty via the following procedure. First, for the $\chi = 0°$, $\pm 90°$ precession technique, the form factor ratio $g \equiv G_{En}/G_{Mn}$ can be written as [recall Eq. (2.176)]

$$g = -K \frac{\xi(0°)}{\xi(\pm 90°)} \ , \tag{7.7}$$

where K is shorthand notation for the various kinematic factors. Now, if we denote the beam polarization during measurements of $\xi(0°)$ $[\xi(\pm 90°)]$ as $P_L^{0°}$ $[P_L^{\pm 90°}]$, the form factor ratio can be written as

$$g = -K \ \frac{\xi(0°)}{P_L^{0°}} \ \frac{P_L^{\pm 90°}}{\xi(\pm 90°)} \ ; \tag{7.8}$$

therefore, it follows that the systematic uncertainty in g due to uncertainty in the beam polarization, denoted $(\Delta g/g)_{\rm pol}$, can be written as

$$\left(\frac{\Delta g}{g}\right)^2_{\rm pol} = \left(\frac{\Delta P_L^{0°}}{P_L^{0°}}\right)^2 + \left(\frac{\Delta P_L^{\pm 90°}}{P_L^{\pm 90°}}\right)^2 \ . \tag{7.9}$$

If we define $P_L^{0°} = P_L^{\pm 90°} \equiv P_L$ and $\Delta P_L^{0°} = \Delta P_L^{\pm 90°} \equiv \Delta P_L$, the above reduces to

$$\left(\frac{\Delta g}{g}\right)^2_{\rm pol} = 2\left(\frac{\Delta P_L}{P_L}\right)^2 \ . \tag{7.10}$$

Second, for the $\chi = \pm 40°$ precession technique, the form factor ratio can be written as [again, see Eq. (2.176)]

$$g = -K \ \tan\chi \ \left(\frac{1+\eta}{1-\eta}\right) \ , \tag{7.11}$$

where $\eta \equiv \xi(-\chi)/\xi(+\chi)$. Again, if we denote the beam polarization during measurements of $\xi(-\chi)$ $[\xi(+\chi)]$ as P_L^- $[P_L^+]$, the form factor ratio can be written as

$$g = -K \ \tan\chi \ \left[\frac{1+\eta\frac{P_L^+}{P_L^-}}{1-\eta\frac{P_L^+}{P_L^-}}\right] \ ; \tag{7.12}$$

therefore, it follows that the systematic uncertainty in g due to uncertainty in the beam polarization is given by

$$\left(\frac{\Delta g}{g}\right)^2_{\text{pol}} = \frac{4\eta^2}{(\eta^2-1)^2}\left[\left(\frac{\Delta P_L^-}{P_L^-}\right)^2 + \left(\frac{\Delta P_L^+}{P_L^+}\right)^2\right] . \tag{7.13}$$

Again, if we define $P_L^- = P_L^+ \equiv P_L$ and $\Delta P_L^- = \Delta P_L^+ \equiv \Delta P_L$, the above reduces to

$$\left(\frac{\Delta g}{g}\right)^2_{\text{pol}} = \frac{4\eta^2}{(\eta^2-1)^2}\left[2\left(\frac{\Delta P_L}{P_L}\right)^2\right] . \tag{7.14}$$

It is interesting to note that

$$\left(\frac{\Delta g}{g}\right)^2_{\text{pol, }\pm\chi} = M\ \left(\frac{\Delta g}{g}\right)^2_{\text{pol, }\chi=0°,\ \pm 90°} , \tag{7.15}$$

where the multiplicative factor M is defined to be

$$M \equiv \frac{4\eta^2}{(\eta^2-1)^2} . \tag{7.16}$$

For the $\chi = \pm 40°$ asymmetries reported in Table 5.7, we found $M = 6.32$, 3.31, and 2.38 at $\langle Q^2 \rangle = 0.447$, 1.132, and 1.450 $(\text{GeV}/c)^2$ respectively.

Procedure

In order to assess the magnitude of this systematic uncertainty, we needed an estimate of the uncertainty in the beam polarization ΔP_L. To combine beam polarization measurements conducted during asymmetry measurements for a particular Q^2 point and spin precession technique, "clusters" of polarization measurements (i.e., measurements of the beam polarization conducted during similar conditions at the polarized source) were identified by Seo[5] [436]. The mean value of the polarization for each cluster was calculated, and a common offset was added to each individual polarization measurement in order to center the measurements about the nominal polarization of 80%. After each cluster was centered about the nominal polarization of 80%, the

[5]Wonick Seo was a masters thesis student at Kyungpook National University.

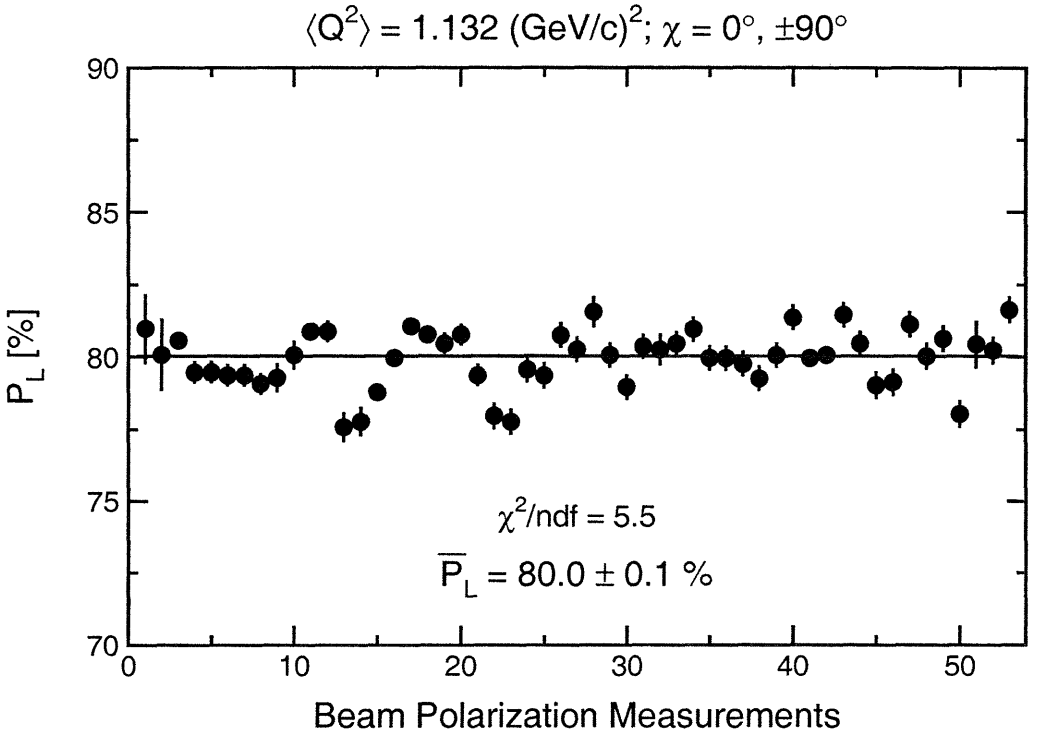

Figure 7-21: Beam polarization measurements for the $\langle Q^2 \rangle = 1.132$ (GeV/c)^2 $\chi = 0°$, $\pm 90°$ data set normalized to the nominal 80% beam polarization. The horizontal axis enumerates the measurements (roughly one measurement per day).

statistical error for the entire data set was calculated, and the relative uncertainty in the polarization was defined to be

$$\frac{\Delta P_L}{P_L} = \frac{\delta \overline{P}_L}{\overline{P}_L} \sqrt{\chi^2} \,, \tag{7.17}$$

where $\overline{P_L}$ denotes the mean value of the polarization, $\delta \overline{P_L}$ denotes the statistical error in $\overline{P_L}$, and χ^2 denotes the value of the reduced χ^2 from the fit of the individual clusters of polarization measurements to the mean. An example of such an analysis for the $\langle Q^2 \rangle = 1.132$ (GeV/c)^2 data set is shown in Fig. 7-21; the beam polarization data from the other Q^2 points that were used for the analysis of this systematic uncertainty look very similar and are not shown here for purposes of brevity.

$\langle Q^2 \rangle$ [(GeV/c)^2]	χ	$\Delta P_L/P_L$ [%]	M	$(\Delta g/g)_{\rm pol}$ [%]
0.447	$\pm 40°$	0.47	6.3	1.6
1.132	$\pm 40°$	0.26	3.3	0.7
1.132	$0°$, $\pm 90°$	0.30	—	0.4
1.450	$\pm 40°$	0.55	2.4	1.2
1.450	$0°$, $\pm 90°$	0.22	—	0.3

Table 7.5: Estimated values for the systematic uncertainty in $g = G_{En}/G_{Mn}$ due to fluctuations in the beam polarization.

Results for Systematic Uncertainties

The results of this analysis for the different spin precession techniques at all of the Q^2 points are presented in Table 7.5. The systematic uncertainties in $\Delta g/g$ are small (relative to the statistical errors in $\Delta g/g$) and on the order of 1.6% or less.

7.4.2 Charge-Exchange in the Lead Curtain

An estimation of the contamination levels (previously discussed in Section 5.6.5) and the systematic uncertainty due to two-step $^2\mathrm{H}(\vec{e}, e'\vec{p}) + \mathrm{Pb}(\vec{p}, \vec{n})$ charge-exchange reactions in the lead curtain was a major concern during both the experiment and during the analysis of the data (as evidenced by the number of internal reports written on this subject [437–440]). Here we attempt to summarize the salient features of this analysis.

Overview

As discussed previously in Section 5.6.5, the "real" asymmetry for $^2\mathrm{H}(\vec{e}, e'\vec{n})$ events, ξ_R, can be written in terms of the asymmetry measured by the polarimeter, ξ_M, as

$$\xi_R = \frac{\xi_M - f_B \left(P_S^p \cos\chi_p + P_L^p \sin\chi_p\right) D_{SS}^{\rm Pb} A_y}{1 - f_B} \ , \tag{7.18}$$

where f_B is the contamination level from charge-exchange reactions, P_S^p and P_L^p are the projections of the proton's recoil polarization from the $^2\mathrm{H}(\vec{e}, e'\vec{p})$ reaction on the polarimeter momentum basis $\hat{\mathbf{S}}$- and $\hat{\mathbf{L}}$-axes, χ_p is the proton spin precession angle in

the Charybdis field, $D_{SS}^{\rm Pb}$ is the polarization transfer coefficient for the Pb$(\vec{p},\vec{n})$ reaction, and A_y is the polarimeter analyzing power. In order to estimate the systematic uncertainty due to charge-exchange reactions, values for f_B, P_S^p, P_L^p, χ_p, $D_{SS}^{\rm Pb}$, and A_y are needed. The values for f_B have already been summarized in Table 5.6, and the values for A_y extracted from the acceptance-averaging analysis were given in the previous section of this chapter.

Values for P_S^p and P_L^p were estimated as follows. Assuming the one-photon exchange approximation, P_S^p and P_L^p can be written in terms of the proton form factors as

$$P_S^p = -\frac{2\sqrt{\tau(1+\tau)}G_{Ep}G_{Mp}\tan\frac{\theta_{e'}}{2}}{G_{Ep}^2 + G_{Mp}^2\left[\tau + 2\tau(1+\tau)\tan^2\frac{\theta_{e'}}{2}\right]}\ , \tag{7.19}$$

$$P_L^p = \frac{2\tau\sqrt{(1+\tau)[1+\tau\sin^2(\theta_{e'}/2)]}G_{Mp}^2\sec\frac{\theta_{e'}}{2}\tan\frac{\theta_{e'}}{2}}{G_{Ep}^2 + G_{Mp}^2\left[\tau + 2\tau(1+\tau)\tan^2\frac{\theta_{e'}}{2}\right]}\ , \tag{7.20}$$

For G_{Ep} and G_{Mp}, we employed the empirical parameterizations reported by Brash *et al.* in [441]; Brash *et al.* re-analyzed the world data set on G_{Mp} using the recent polarized results for $\mu_p G_{Ep}/G_{Mp}$ [215,216] as a constraint. A brief overview of their analysis procedure is as follows. First, the polarized results were fitted to a simple linear parameterization, with the result

$$r = \frac{G_{Ep}}{(G_{Mp}/\mu_p)} = 1.0 - (0.130 \pm 0.005)[Q^2 - (0.04 \pm 0.09)]\ . \tag{7.21}$$

Second, Brash *et al.* used $r = 1$ for $Q^2 < 0.04$ (GeV/c)^2, Eq. (7.21) for $0.04 < Q^2 < 7.7$ (GeV/c)^2, and $r = 0$ for $Q^2 > 7.7$ (GeV/c)^2 to extract G_{Mp} from cross section data; their empirical parameterization for G_{Mp}, based on a fit to their re-analyzed values of G_{Mp}, provides excellent agreement with data and is given by

$$G_{Mp} = \frac{\mu_p}{1 + AQ + BQ^2 + CQ^3 + DQ^4 + EQ^5}\ , \tag{7.22}$$

where $A = 0.116 \pm 0.040$, $B = 2.874 \pm 0.098$, $C = 0.241 \pm 0.107$, $D = 1.006 \pm 0.069$, and $E = 0.345 \pm 0.017$.

A value for χ_p was estimated as follows. Unfortunately, a proton deflection/spin precession algorithm was never written for the GENGEN simulation; therefore, it was necessary to estimate values for χ_p in the following way. As discussed in [162], the precession angles for a proton, χ_p, and a neutron, χ, in a uniform magnetic field can be written in terms of the field integral, $\int B \, \mathrm{d}\ell$, as

$$\chi_p = (g_p - 2)\mu_N \int B \, \mathrm{d}\ell \, , \tag{7.23}$$

$$\chi = g_n \mu_N \int B \, \mathrm{d}\ell \, , \tag{7.24}$$

where the Lande g-factors are $g_p/2 = 2.79$ and $g_n/2 = -1.91$ and μ_N denotes the nuclear magneton. For a fixed value of the field integral (i.e., identical magnetic fields and path lengths), it follows that

$$\frac{\chi_p}{\chi} = \frac{g_p - 2}{g_n} = -0.937 \, ; \tag{7.25}$$

therefore, we assumed $\chi_p = \mp 37.5°$ and $\mp 84.3°$ for field integrals corresponding to neutron spin precession angles of $\chi = \pm 40°$ and $\pm 90°$, respectively. We stress that this is merely an approximation — this simple estimation does not account for the deflection of the proton. *Although we did not obtain a rigorous estimate for χ_p via simulation, the contaminations levels for $\chi \neq 0°$ are very small; therefore, we believe our results should be relatively insensitive to the exact value of χ_p.*

Procedure

We estimated the magnitude of the charge-exchange systematic uncertainty via the following procedure:

1. For the $\langle Q^2 \rangle = 0.447$ ($\chi = \pm 40°$), 1.132 ($\chi = 0°$, $\pm 90°$ and $\pm 40°$), and 1.450 ($\chi = \pm 40°$) $(\mathrm{GeV}/c)^2$ data sets, the contamination levels are very small ($<$ 0.26%). Unfortunately, we do not have data for D_{SS}^{Pb} at $\langle Q^2 \rangle = 0.447$ and 1.132

$(\mathrm{GeV}/c)^2$ (i.e., $T_p \sim 240$ and 610 MeV, respectively); however, data for D_{SS}^{Pb} do exist at $\langle Q^2 \rangle = 1.450$ $(\mathrm{GeV}/c)^2$ (i.e., $T_p \sim 790$ MeV) [6].

As the contamination levels are very small for these cases, we employed the following procedure to estimate the charge-exchange systematic uncertainty. We used the measured contamination levels, the calculated values of P_S^p and P_L^p, the estimated values of χ_p, and the analyzing powers to calculate the "corrected asymmetries", ξ_R, for three values of D_{SS}^{Pb}: -1, 0, $+1$. Using the corrected asymmetries, we extracted the final acceptance-averaged and nuclear physics corrected values for $g = G_{En}/G_{Mn}$ for each value of D_{SS}^{Pb} via the acceptance-averaging procedure discussed in the previous section of this chapter.

To estimate the systematic uncertainty, we assumed that $D_{SS}^{\mathrm{Pb}} \in [-1, 0]$ for the range of proton energies sampled at $\langle Q^2 \rangle = 0.447$ and 1.132 $(\mathrm{GeV}/c)^2$. The magnitude of the charge-exchange systematic uncertainty was then estimated to be

$$\left(\frac{\Delta g}{g}\right) \sim \frac{1}{2}\left|\frac{g(D_{SS}^{\mathrm{Pb}}=0) - g(D_{SS}^{\mathrm{Pb}}=-1)}{g(D_{SS}^{\mathrm{Pb}}=0)}\right| . \tag{7.26}$$

We acknowledge that our estimation of the charge-exchange systematic uncertainty for the $\langle Q^2 \rangle = 1.450$ $(\mathrm{GeV}/c)^2$ $\chi = \pm 40^\circ$ data set via this procedure may overestimate the systematic uncertainty as data for D_{SS}^{Pb} do exist for the range of proton energies sampled at this Q^2; *however, the systematic uncertainty is already very small (0.01%).*

2. At $\langle Q^2 \rangle = 1.450$ $(\mathrm{GeV}/c)^2$ ($\chi = 0^\circ$, $\pm 90^\circ$), the $\chi = 0^\circ$ contamination levels were not negligible, and the asymmetries were corrected as described in Section 5.6.5. To estimate the magnitude of the charge-exchange systematic uncertainty for this case, we employed the following procedure. The value of D_{SS}^{Pb} for $T_p =$ 795 MeV was found to be 0.014 ± 0.013 [418]; therefore, we assumed D_{SS}^{Pb} was zero for this case (as the measured result is essentially consistent with zero, and assuming $D_{SS}^{\mathrm{Pb}} = 0$ greatly simplified the calculations).

[6] Data for D_{SS}^{Pb} have been published for $T_p = 197$ MeV [442] and 795 MeV [418].

$\langle Q^2 \rangle$ [(GeV/c)^2]	χ	$(\Delta g/g)$ [%]
0.447	$\pm 40°$	< 0.1
1.132	$\pm 40°$	< 0.1
1.132	$0°$, $\pm 90°$	0.1
1.450	$\pm 40°$	< 0.1
1.450	$0°$, $\pm 90°$	0.2

Table 7.6: Estimated values for the systematic uncertainty in $g = G_{En}/G_{Mn}$ due to charge-exchange reactions in the lead curtain.

Assuming D_{SS}^{Pb} is known, the largest contribution to the uncertainty is expected to be that in the contamination level f_B; therefore, to assess the uncertainties in the corrected asymmetries due to the uncertainties in f_B, we calculated the corrected asymmetries for the one-sigma limits of f_B, $f_B - \Delta f_B$ and $f_B + \Delta f_B$, where, Δf_B denotes the statistical uncertainty in f_B. We then extracted acceptance-averaged and nuclear physics corrected values for G_{En}/G_{Mn} for these corrected asymmetries, and the magnitude of the charge-exchange systematic uncertainty was then estimated to be

$$\left(\frac{\Delta g}{g}\right) \sim \frac{1}{2}\left|\frac{g(f_B + \Delta f_B) - g(f_B - \Delta f_B)}{g(f_B)}\right| . \tag{7.27}$$

Results for Systematic Uncertainties

Detailed results of the above-described analysis procedure were given by Plaster in [440]. Here, we simply quote the results for the charge-exchange systematic uncertainty in $\Delta g/g$ in Table 7.6. As can be seen there, our estimates for this systematic uncertainty are small ($< 0.2\%$) for all of our Q^2 points.

7.4.3 Depolarization in the Lead Curtain

As discussed earlier in Section 6.2.11, neutron interactions in the lead curtain were simulated in `GENGEN` in order to assess the effects of a possible depolarization of the incident neutron flux on our results.

Interaction Probabilities

As discussed in Section 6.2.11, the total n + Pb cross section is approximately 3 barns for neutron kinetic energies ranging from approximately 200 to 1000 MeV. The cross section rises slowly with kinetic energy; therefore, the interaction probability was expected to be highest for our $\langle Q^2 \rangle = 1.450$ (GeV/c)^2 data. Our simulation results were consistent with this expectation; the interaction probabilities for the simulated 10.16-cm lead curtain were found to be 30.8%, 42.5%, 43.0%, and 46.7% at $\langle Q^2 \rangle = 0.447$, 1.126, 1.158, and 1.450 (GeV/c)^2, respectively.

Contamination Levels

Henceforth, accepted events (i.e., those passing all cuts) which *did not* suffer an interaction in the lead curtain will be designated "No Lead Events", whereas accepted events which *did* suffer an interaction in the lead curtain will be designated "Lead Events". Clearly, these two categories are mutually exclusive; their sum will be designated "All Events".

Sample simulated cTOF spectra extracted from `GENGEN` simulations at the four Q^2 points are plotted in Fig. 7-22; the spectra shown here have been summed over both (n,n) and (n,p) events in the polarimeter. This figure shows clearly that the contamination level within the $[-1,1]$ ns cTOF window rises with T_n and is not negligible at $\langle Q^2 \rangle = 1.450$ (GeV/c)^2. Although the n + Pb cross section is essentially the same for the range of neutron kinetic energies seen at our Q^2 points, the fact that the contamination increases with kinetic energy is not unexpected and can be explained as follows. Angular distributions[7] for nn and np scattering computed by the `SAID` [188] code incorporated in `GENGEN` are shown in Fig. 7-23 for the central values of the kinetic energy at each Q^2 point. The angular distributions for the

[7]By angular distributions we mean the differential cross section weighted by the appropriate Jacobian factor for spherical coordinates. Assuming no ϕ dependence, the total cross section, σ, is given by

$$\sigma = 2\pi \int_0^\pi \mathrm{d}\theta \, \sin\theta \, \frac{\mathrm{d}\sigma}{\mathrm{d}\Omega} \; ; \tag{7.28}$$

therefore, the probability density for scattering into some angle θ is $\sin\theta(\mathrm{d}\sigma/\mathrm{d}\Omega)$.

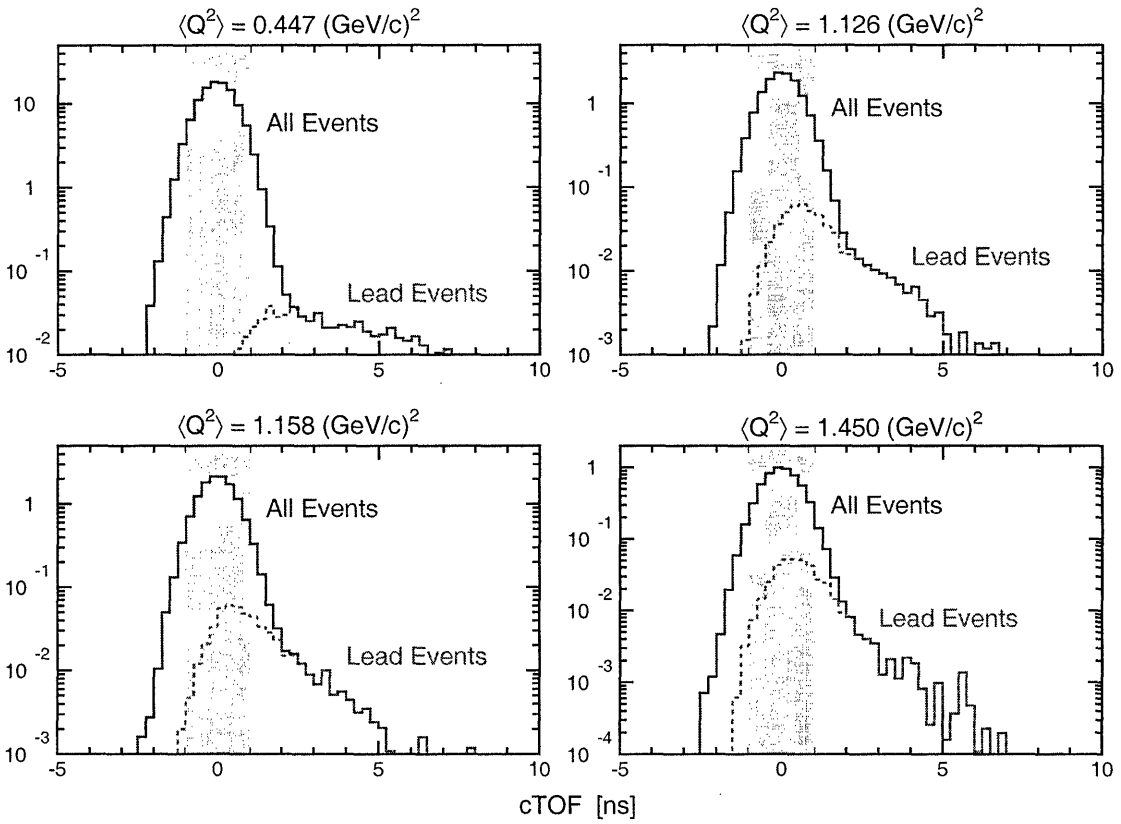

Figure 7-22: (color) Sample simulated cTOF spectra. The solid blue histograms are cTOF spectra for "All Events", the dashed red histograms are cTOF spectra for "Lead Events", and the vertical yellow bands denote the $[-1, 1]$ ns cut on cTOF. See text for definition of event types. The units of the ordinate are arbitrary.

kinetic energy at $Q^2 = 0.447$ (GeV/c)^2 peak at large scattering angles (i.e., neutrons will primarily scatter away from the front array) while the angular distributions for the larger kinetic energies peak at smaller scattering angles.

The contamination levels within the $[-1, 1]$ ns cTOF window that we extracted from our simulated data were 0.04%, 3.8%, 4.2%, and 9.3% at $\langle Q^2 \rangle = 0.447$, 1.126, 1.158, and 1.450 (GeV/c)^2. Also, as expected, we found that the contamination levels increase as the cTOF window is widened; indeed, we believe that interactions in the lead curtain may partly be responsible for the small tail that is present on the slow side of the experimental cTOF peaks.

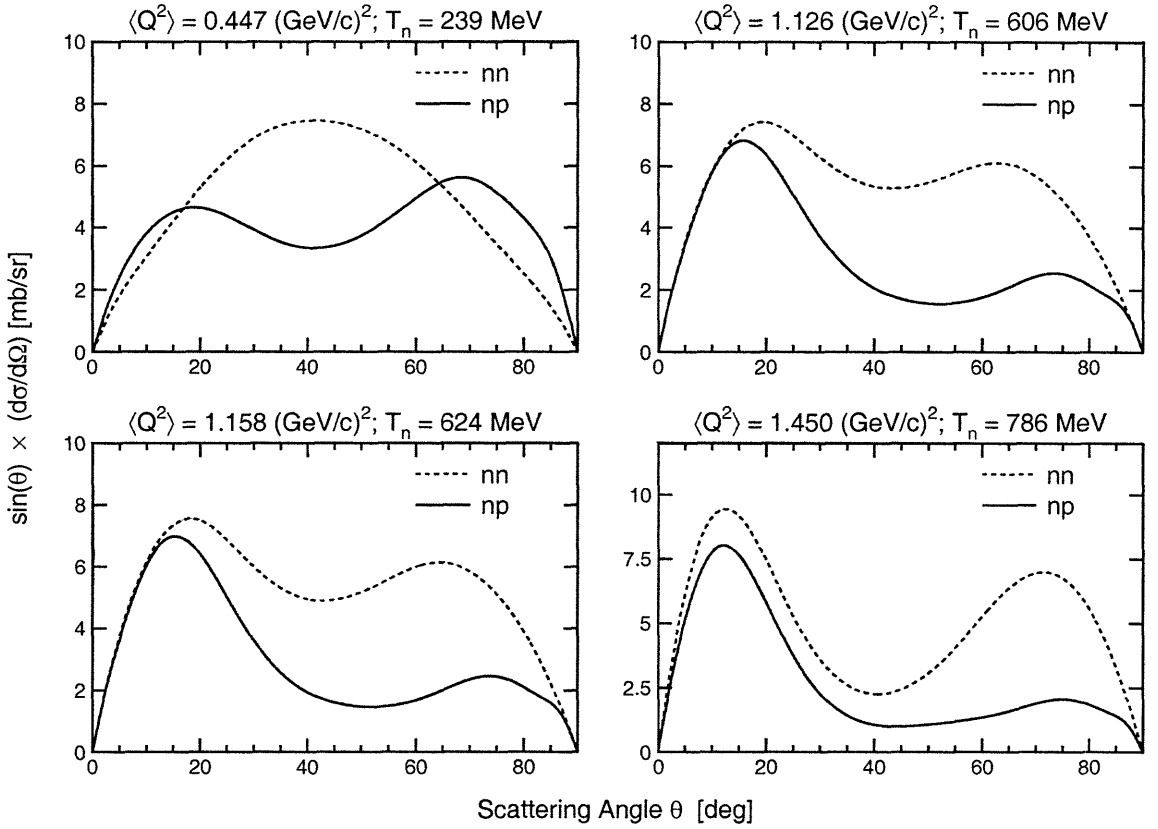

Figure 7-23: Angular distributions for nn (dashed lines) and np (solid lines) scattering computed by the SAID [188] code incorported in GENGEN for the central neutron kinetic energies at each Q^2 point.

Scattering Vertex Distributions

The lead curtain was not a point target but instead a large 72.6 cm × 37.3 cm × 10.16 cm slab; therefore, an item of interest was the distribution of the interaction positions within the lead curtain's volume. In Fig. 7-24 we show a scatter plot of the (x, y)-coordinates and a histogram of the z-coordinate for the final scattering vertex in the lead curtain; the coordinates refer to the polarimeter basis. Consistent with expectations, we see that the final scattering vertex was essentially distributed uniformly throughout the x-y plane; however, due to multiple scattering, the distribution of the final z-coordinate is skewed towards the exit end.

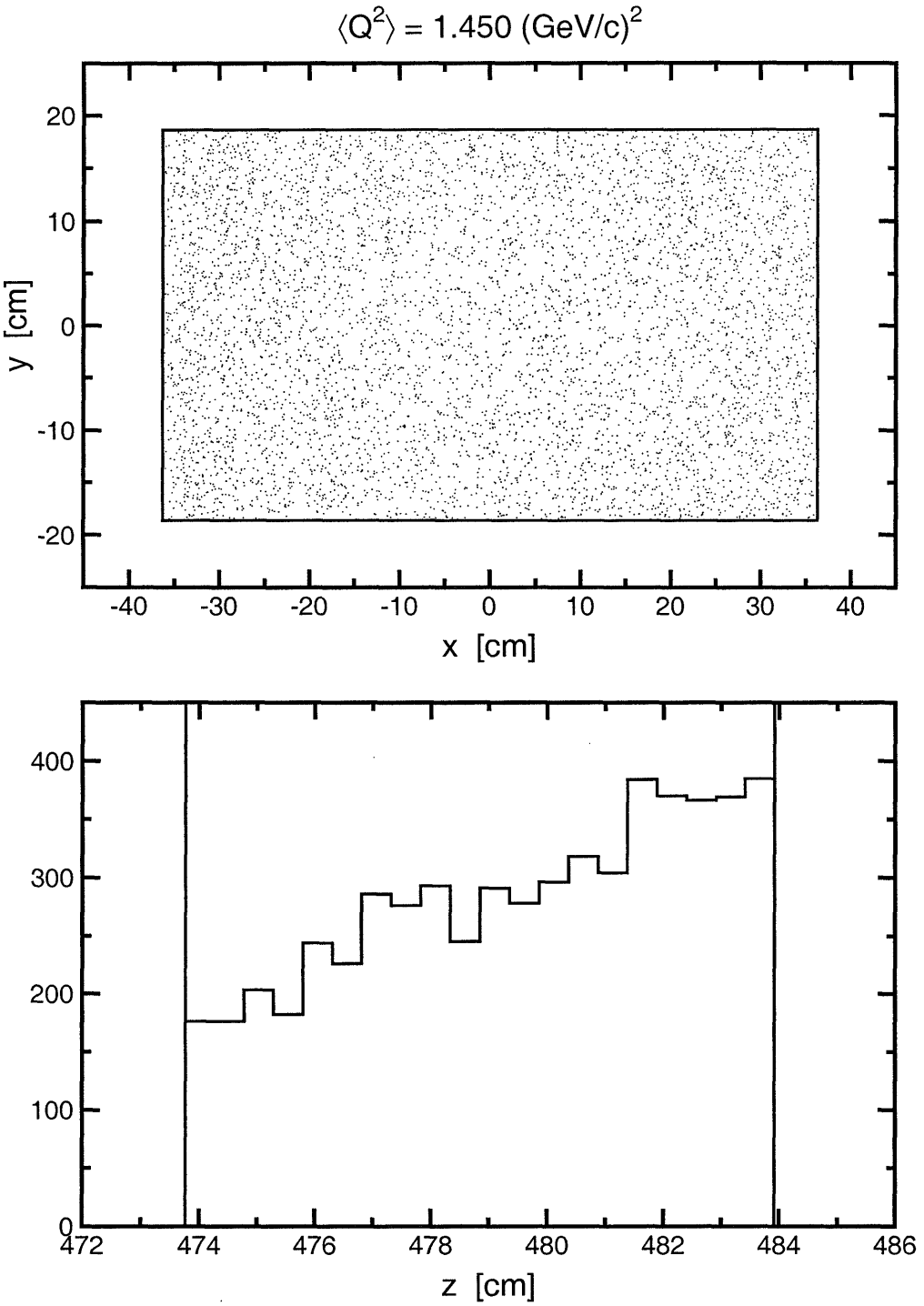

Figure 7-24: Scatter plot (top panel) of the (x, y)-coordinates and a histogram (bottom panel) of the z-coordinate for the final scattering vertex in the lead curtain from a simulation at $\langle Q^2 \rangle = 1.450$ (GeV/c)^2. The solid lines denote the physical dimensions of the lead curtain, and the coordinate systems refer to the polarimeter basis.

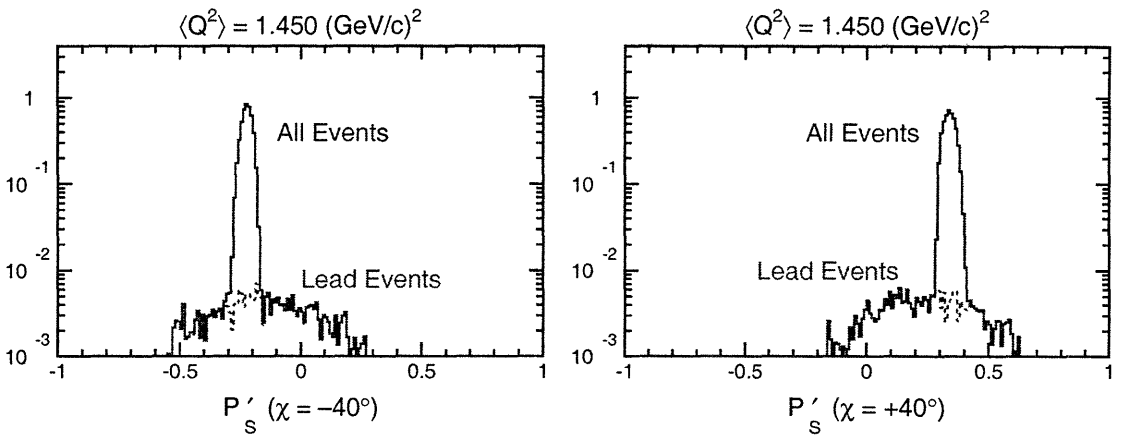

Figure 7-25: (color) Sample simulated P'_S spectra at $\langle Q^2 \rangle = 1.450$ (GeV/c)^2 for $\chi = \pm 40°$ precession. The solid blue histograms are P'_S spectra for "All Events" and the dashed red histograms are P'_S spectra for "Lead Events". See text for definition of event types. The units of the ordinate are arbitrary.

Polarization Spectra

The quantity of interest is the polarization that is presented to the front array of the polarimeter after the neutron has traversed the Charybdis dipole field and the lead curtain. Sample simulated P'_S spectra extracted from GENGEN simulations at $\langle Q^2 \rangle = 1.450$ (GeV/c)^2 for $\chi = \pm 40°$ spin precession are shown in Fig. 7-25; as in the cTOF spectra, these spectra have been summed over both (n,n) and (n,p) events in the polarimeter. As can be seen clearly in this figure, the distribution of the polarization for neutrons that suffered an interaction in the lead curtain is a broad continuum; indeed, this continuum depolarizes the overall neutron flux that is presented to the front array of the polarimeter.

Results for Systematic Uncertainties

The acceptance-averaged polarization ratios for "All Events" and "No Lead Events" for the different spin precession techniques [i.e., $\langle P'_S(0°) \rangle / \langle P'_S(\pm 90°) \rangle$ for $\chi = 0°, \pm 90°$ precession and $\langle P'_S(-40°) \rangle / \langle P'_S(+40°) \rangle$ for $\chi = \pm 40°$ precession] at each of the Q^2 points extracted from the GENGEN simulated data are presented in Table 7.7. The polarization ratios for "All Events" and "No Lead Events" are nearly identical as

$\langle Q^2 \rangle$ [(GeV/c)^2]	χ	Event Type	Polarization Ratio
0.447	$\pm 40°$	All Events	-0.66760 ± 0.00010
0.447	$\pm 40°$	No Lead Events	-0.66766 ± 0.00010
1.132	$0°, -90°$	All Events	-0.17836 ± 0.00022
1.132	$0°, -90°$	No Lead Events	-0.17826 ± 0.00013
1.132	$0°, +90°$	All Events	0.17808 ± 0.00025
1.132	$0°, +90°$	No Lead Events	0.17805 ± 0.00013
1.132	$\pm 40°$	All Events	-0.65073 ± 0.00042
1.132	$\pm 40°$	No Lead Events	-0.65133 ± 0.00020
1.450	$0°, -90°$	All Events	-0.17136 ± 0.00054
1.450	$0°, -90°$	No Lead Events	-0.17022 ± 0.00023
1.450	$0°, +90°$	All Events	0.17133 ± 0.00054
1.450	$0°, +90°$	No Lead Events	0.17029 ± 0.00023
1.450	$\pm 40°$	All Events	-0.66388 ± 0.00084
1.450	$\pm 40°$	No Lead Events	-0.66412 ± 0.00033

Table 7.7: Comparison of simulated acceptance-averaged polarization ratios for "All Events" and "No Lead Events".

$\langle Q^2 \rangle$ [(GeV/c)^2]	χ	$(\Delta g/g)$ [%]
0.447	$\pm 40°$	< 0.1
1.132	$\pm 40°$	0.1
1.132	$0°, \pm 90°$	< 0.1
1.450	$\pm 40°$	< 0.1
1.450	$0°, \pm 90°$	0.6

Table 7.8: Estimated values for the systematic uncertainty in $g = G_{En}/G_{Mn}$ due to depolarization in the lead curtain.

the depolarization due to interactions in the lead curtain tends to cancel in the polarization ratio. The magnitude of the residual non-cancellation is taken to be the systematic uncertainty in G_{En}/G_{Mn}, and these results are summarized in Table 7.8.

7.4.4 Instrumental Asymmetry

As we stated in Section 5.6.4 and proved in Appendix C, the scattering asymmetries extracted from the cross ratio are insensitive to possible differences in the relative acceptances and efficiencies of the top and bottom halves of the rear array. To demonstrate this quantitatively, we used a slightly modified version of the most

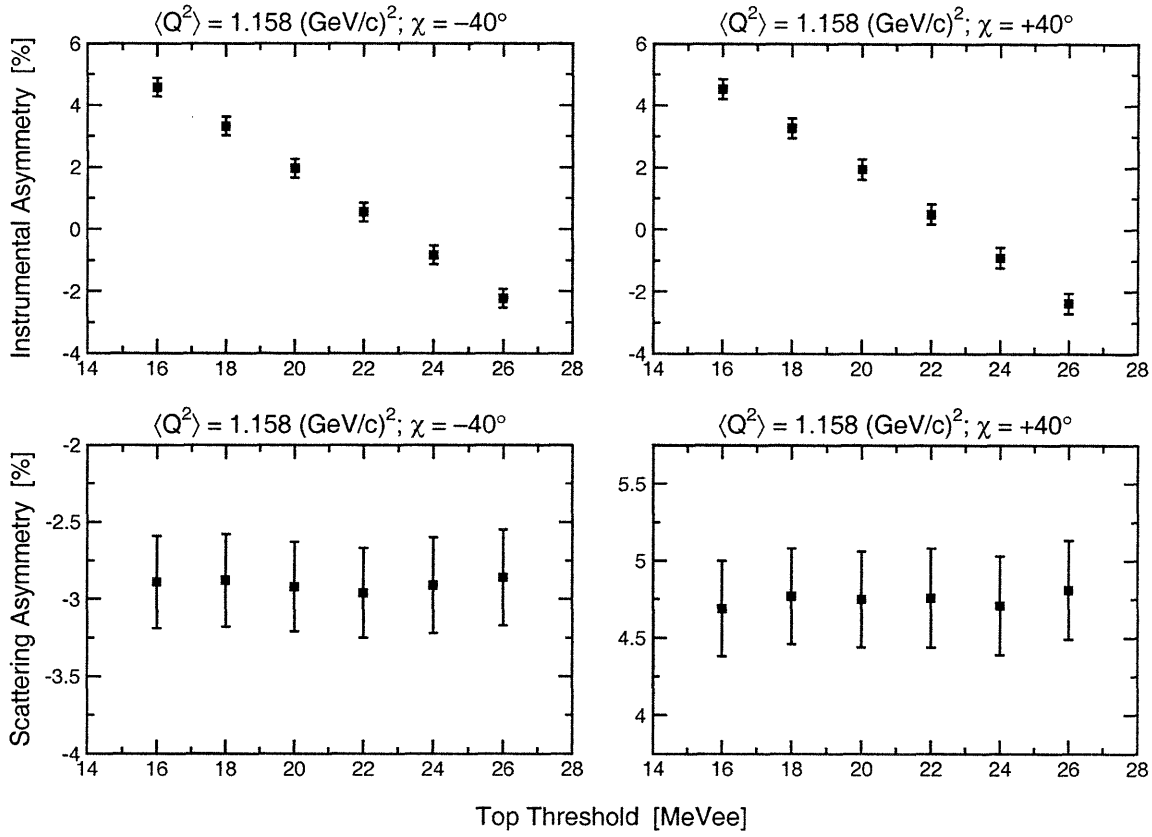

Figure 7-26: Variation of the instrumental asymmetry (top panels) and the physical scattering asymmetry (bottom panels) with the threshold applied to the top rear array (with the threshold on the bottom rear array held constant at 20 MeVee) for the entire $\chi = -40°$ (left panels) and $\chi = +40°$ (right panels) data sets at $\langle Q^2 \rangle = 1.158$ $(\mathrm{GeV}/c)^2$. Note the differences in the vertical scales.

recent version of the `casym` program to extract (n, n) asymmetries from the entire $\langle Q^2 \rangle = 1.158$ $(\mathrm{GeV}/c)^2$ data set for varied thresholds on the top rear array of the polarimeter while holding the threshold on the bottom rear array constant at the nominal value of 20 MeVee.

The results of this exercise are shown in Fig. 7-26. There, for $\chi = \pm 40°$ precession, we have plotted the *instrumental asymmetry* and the physical scattering asymmetry versus the threshold applied to the top rear array; the instrumental asymmetry, ξ_{inst}, is defined in terms of the *geometric ratio*, r_{geom}, as

$$\xi_{\mathrm{inst}} = \frac{r_{\mathrm{geom}} - 1}{r_{\mathrm{geom}} + 1}\,, \tag{7.29}$$

where the geometric ratio,

$$r_{\text{geom}} = \left(\frac{N_{RU} N_{LU}}{N_{RD} N_{LD}} \right)^{1/2} , \tag{7.30}$$

is the ratio of the geometric means for scattering up and scattering down in the polarimeter.

It is clear that we have obtained the desired result; the instrumental asymmetry varies linearly with the threshold, while the scattering asymmetry is insensitive (within statistical errors) to variations in the threshold. Accordingly, we do not quote a systematic error here.

7.4.5 Positioning and Traceback

The form factor ratio $g = G_{En}/G_{Mn}$ is a function not only of the recoil polarization components but also, of course, the electron kinematics; therefore, an uncertainty in the electron scattering angle, $\Delta\theta_{e'}$, introduces a systematic uncertainty in g. There are two contributions to this uncertainty:

- positioning: the offset in the scattering angle from the nominal value [$\equiv (\Delta\theta_e)_{\text{pos}}$], and

- traceback: the uncertainty in the reconstruction of the scattering angle from the focal plane to the target [$\equiv (\Delta\theta_e)_{\text{tra}}$].

In what follows below, we derive the relationship between $\Delta\theta_{e'}$ and the resulting systematic uncertainty in g and then present the results of this analysis.

Formalism

From Eq. (2.176), we have

$$\frac{G_{En}}{G_{Mn}} = -\left[\tau \left(1 + \tau \sin^2 \frac{\theta_{e'}}{2} \right) \right]^{1/2} \sec \frac{\theta_{e'}}{2} \left[\frac{\sin\chi_1 - \eta \sin\chi_2}{\eta \cos\chi_2 - \cos\chi_1} \right] . \tag{7.31}$$

In accordance with notation employed during early stages of the analysis, we rewrite the kinematic factors in the above equation as

$$\left[\tau\left(1+\tau\sin^2\frac{\theta_{e'}}{2}\right)\right]^{1/2}\sec\frac{\theta_{e'}}{2} \equiv \frac{K_L}{K_S}\ , \tag{7.32}$$

where the K_L and K_S kinematic factors are given by

$$K_L = 2\tau\left\{(1+\tau)\left[1+\tau\sin^2\frac{\theta_{e'}}{2}\right]\right\}^{1/2}\sec\frac{\theta_{e'}}{2}\tan\frac{\theta_{e'}}{2}\ , \tag{7.33}$$

$$K_S = 2[\tau(1+\tau)]^{1/2}\tan\frac{\theta_{e'}}{2}\ . \tag{7.34}$$

The remaining usual factors can, of course, be written in terms of $\theta_{e'}$ as

$$\tau = \frac{Q^2}{4m^2}\ , \tag{7.35}$$

$$Q^2 = 4E_eE_{e'}\sin^2\frac{\theta_{e'}}{2}\ , \tag{7.36}$$

$$E_{e'} = \frac{E_e}{1+2\frac{E_e}{m}\sin^2\frac{\theta_{e'}}{2}}\ . \tag{7.37}$$

The contribution of the uncertainty in the electron scattering angle, $\Delta\theta_{e'}$, to the systematic uncertainty in g, $(\Delta g)_{\theta_{e'}}$, is defined to be

$$(\Delta g)^2_{\theta_{e'}} \equiv \left(\frac{\partial g}{\partial\theta_{e'}}\right)^2(\Delta\theta_{e'})^2\ , \tag{7.38}$$

where

$$\frac{\partial g}{\partial\theta_{e'}} = \frac{\partial g}{\partial K_L}\frac{\mathrm{d}K_L}{\mathrm{d}\theta_{e'}} + \frac{\partial g}{\partial K_S}\frac{\mathrm{d}K_S}{\mathrm{d}\theta_{e'}} \equiv AC + BD\ , \tag{7.39}$$

and A, B, C, and D are defined to be

$$A \equiv \frac{\partial g}{\partial K_L} = \frac{g}{K_L}\ , \tag{7.40}$$

$$B \equiv \frac{\partial g}{\partial K_S} = -\frac{g}{K_S}\ , \tag{7.41}$$

$$C \equiv \frac{\mathrm{d}K_L}{\mathrm{d}\theta_{e'}}\ , \tag{7.42}$$

$$D \equiv \frac{\mathrm{d}K_S}{\mathrm{d}\theta_{e'}} \ . \tag{7.43}$$

It then follows that

$$C = \frac{\partial K_L}{\partial \tau}\frac{\partial \tau}{\partial \theta_{e'}} + \frac{\partial K_L}{\partial \theta_{e'}} \equiv EF + G, \tag{7.44}$$

$$D = \frac{\partial K_S}{\partial \tau}\frac{\partial \tau}{\partial \theta_{e'}} + \frac{\partial K_S}{\partial \theta_{e'}} \equiv HF + I, \tag{7.45}$$

where E, F, G, H, and I are given by

$$E \equiv \frac{\partial K_L}{\partial \tau} = \frac{\sec\frac{\theta_{e'}}{2}\tan\frac{\theta_{e'}}{2}}{\left\{(1+\tau)[1+\tau\sin^2\frac{\theta_{e'}}{2}]\right\}^{1/2}}\left[2+3\tau+(3+4\tau)\tau\sin^2\frac{\theta_{e'}}{2}\right] \ , \tag{7.46}$$

$$F \equiv \frac{\partial \tau}{\partial \theta_{e'}} = \frac{\left(\frac{E_e}{m}\right)^2 \sin\frac{\theta_{e'}}{2}\cos\frac{\theta_{e'}}{2}}{\left[1+2\left(\frac{E_e}{m}\right)\sin^2\frac{\theta_{e'}}{2}\right]^2} \ , \tag{7.47}$$

$$G \equiv \frac{\partial K_L}{\partial \theta_{e'}} = \frac{\tau(1+\tau)^{1/2}}{\left[1+\tau\sin^2\frac{\theta_{e'}}{2}\right]^{1/2}}\left\{\tau\sin^2\frac{\theta_{e'}}{2}\sec\frac{\theta_{e'}}{2} + \right.$$
$$\left. + \ \sec^3\frac{\theta_{e'}}{2}\left[1+\tau\sin^2\frac{\theta_{e'}}{2}\right]\left[1+\sin^2\frac{\theta_{e'}}{2}\right]\right\} \ , \tag{7.48}$$

$$H \equiv \frac{\partial K_S}{\partial \tau} = \frac{(1+2\tau)\tan\frac{\theta_{e'}}{2}}{[\tau(1+\tau)]^{1/2}} \ , \tag{7.49}$$

$$I \equiv \frac{\partial K_S}{\partial \theta_{e'}} = [\tau(1+\tau)]^{1/2}\sec^2\frac{\theta_{e'}}{2} \ . \tag{7.50}$$

We have now completely specified $(\Delta g)^2_{\theta_{e'}}$ in terms of A, B, E, F, G, H, and I. As is obvious via inspection of Eqs. (7.39), (7.40), and (7.41), $(\Delta g/g)^2_{\theta_{e'}}$ *is independent of* g.

Results for Systematic Uncertainties

For the purposes of this analysis, we assumed $(\Delta\theta_{e'})_{\mathrm{pos}} = 1.2$ mrad and $(\Delta\theta_{e'})_{\mathrm{tra}} = 1.3$ mrad. The value for $(\Delta\theta_{e'})_{\mathrm{pos}}$ was provided by Christy [443], and the value for

$\langle Q^2 \rangle$ [(GeV/c)^2]	χ	$(\Delta g/g)$ [%]
0.447	$\pm 40^\circ$	0.2
1.132	$\pm 40^\circ$	0.3
1.132	0°, $\pm 90^\circ$	0.3
1.450	$\pm 40^\circ$	0.4
1.450	0°, $\pm 90^\circ$	0.4

Table 7.9: Estimated values for the systematic uncertainty in $g = G_{En}/G_{Mn}$ due to uncertainty in the electron scattering angle $\Delta\theta_{e'}$.

$(\Delta\theta_{e'})_{\rm tra}$ was derived from an analysis of the HMS matrix element data that were taken during this experiment [444]. With these values, we then calculated the values of $(\Delta g/g)_{\theta_{e'}}$ for $(\Delta\theta_{e'})_{\rm pos}$ and $(\Delta\theta_{e'})_{\rm tra}$ and added the results in quadrature; these results are tabulated in Table 7.9. This results in an *overestimation* of $(\Delta g/g)_{\theta_{e'}}$ as $(\Delta\theta_{e'})_{\rm pos}$ and $(\Delta\theta_{e'})_{\rm tra}$ are correlated; however, the values for $(\Delta g/g)_{\theta_{e'}}$ are already small and on the order of 0.2% to 0.4%.

7.4.6 Precession Angle

A complete assessment of the systematic uncertainty due to uncertainties in the neutron spin precession angle, $(\Delta g/g)_\chi$, was given by Taylor [425]; here, we provide a brief overview of the relevant features.

In the same spirit as the `Acceptance` program, $(\Delta g/g)_\chi$ was estimated using the reconstructed kinematics from the experimental data as the source of the neutron three-momentum vectors incident on the Charybdis field. A spin vector was generated uniformly on a unit sphere and then transported through the Charybdis field using the same magnetic transport algorithms employed by the `Acceptance` program and `GENGEN`.

Histograms of the precession angle (similar to those shown in Figs. 7-7 and 7-8) were accumulated, and the resulting distributions were fitted to double Gaussians in order to accommodate the slightly asymmetric tails that are seen in these distributions. The mean spin precession angles and associated errors were extracted from these fits, and the resulting error in $(\Delta g/g)_\chi$ was obtained by propagating the un-

$\langle Q^2 \rangle$ [(GeV/c)^2]	Nominal χ	Mean $\lvert\chi\rvert$	$(\Delta g/g)$ [%]
0.447	$\pm 40°$	40.17 ± 0.30	1.1
1.132	$\pm 40°$	40.19 ± 0.08	0.3
1.132	$0°$, $\pm 90°$	89.99 ± 0.22	0.1
1.450	$\pm 40°$	40.26 ± 0.14	0.5
1.450	$0°$, $\pm 90°$	90.34 ± 0.24	0.1

Table 7.10: Estimated values for the mean spin precession angles and the resulting systematic uncertainties in $\Delta g/g$.

certainty in the mean value of χ through Eq. (2.176). Specifically, for $\chi = 0°$, $\pm 90°$ precession, we have

$$\left(\frac{\Delta g}{g}\right)_{\chi} = \eta \, \Delta\chi \, , \tag{7.51}$$

where $\eta = \xi(0°)/\xi(\pm 90°)$, and for $\pm\chi$ precession we have

$$\left(\frac{\Delta g}{g}\right)_{\chi} = \sec\chi \, \csc\chi \, \Delta\chi \, . \tag{7.52}$$

The final values for the mean spin precession angles and the systematic uncertainties reported by Taylor [425] are listed in Table 7.10.

7.4.7 Radiative Corrections

Radiative corrections were calculated specifically for the kinematics of this experiment by Afansasev [445] according to the formalism developed by Afansasev, Akushevich, and Merenkov [446] for model-independent radiative corrections in elastic $N(\vec{e}, e'\vec{N})$ and $\vec{N}(\vec{e}, e'N)$ scattering. Their approach employed an "exact" calculation[8] of the lowest-order model-independent correction; this lowest-order correction includes the QED processes of the radiation of an unobserved real photon, vacuum polarization, and electron-photon vertex corrections. The calculation of model-dependent corrections (e.g., box-type diagrams, emission by hadrons, etc.) require assumptions about

[8] As discussed in detail by Afanasev, Akushevich, and Merenkov [446], the statement that their calculation was "exact" implied that their calculation was performed without introduction of an artificial parameter for the separation of momentum space into soft and hard parts. Also, the integration over the photon phase space was performed without approximations such as the leading logarithm approximation.

$\langle Q^2 \rangle$ [(GeV/c)^2]	χ	$(\Delta g/g)$ [%]
0.447	$\pm 40°$	0.7
1.132	$\pm 40°$	0.1
1.132	$0°$, $\pm 90°$	0.1
1.450	$\pm 40°$	0.1
1.450	$0°$, $\pm 90°$	0.1

Table 7.11: Estimated values for the systematic uncertainty in $g = G_{En}/G_{Mn}$ due to radiative corrections.

hadron interactions that are subject to theoretical uncertainties; therefore, the model-dependent corrections are more difficult to control but were stated to be much smaller compared to electron radiation.

The primary effect of radiative corrections on the recoil polarization components is depolarization of the electron such that both components of the recoil polarization should be increased by ~1.9%, ~3.7%, and ~4.4% at $\langle Q^2 \rangle = 0.447$, 1.132, and 1.450 (GeV/$c$)^2; however, these effects nearly cancel in the form factor ratio such that the net effect is small at $\langle Q^2 \rangle = 0.447$ (GeV/c)^2 and negligible at the two higher Q^2 points. The systematic uncertainties we quote for radiative corrections were taken to be the residual non-cancellation of the corrections in the form factor ratio; these uncertainties are summarized in Table 7.11.

7.4.8 Scattering from Target Cell Windows

Data were taken with the dummy target cells discussed previously in Section 3.3.5. As stated there, the dummy target cell windows were approximately 8 times as thick as the cell windows for the cryogenic target cell windows. Even so, essentially no coincidence events falling within the $[-1, 1]$ ns cTOF window after cuts were found in our analysis of the dummy target data; therefore, we consider contamination from this process to be completely negligible.

	$\langle Q^2 \rangle$ [(GeV/c)^2]				
Source	0.447[1]	1.132[1]	1.132[2]	1.450[1]	1.450[2]
Beam Polarization	1.6	0.7	0.4	1.2	0.3
Charge-Exchange in Lead Curtain	< 0.1	< 0.1	0.1	< 0.1	0.2
Depolarization in Lead Curtain	< 0.1	0.1	< 0.1	< 0.1	0.6
Positioning and Traceback	0.2	0.3	0.3	0.4	0.4
Precession Angle	1.1	0.3	0.1	0.5	0.1
Radiative Corrections	0.7	0.1	0.1	0.1	0.1
Time Calibration	2.0	2.0	2.0	2.0	2.0
Total of Above Sources	2.9	2.2	2.1	2.4	2.2

[1] $\chi = \pm 40°$ precession.
[2] $\chi = 0°,\ \pm 90°$ precession.

Table 7.12: Compilation of our estimated systematic uncertainties in $\Delta g/g$ [%]. The total systematic error that is quoted for each Q^2 point and spin precession technique is the quadrature sum of the individual systematic errors.

7.4.9 Time Calibration

As a cross check, during various stages of the analysis, the data analyses conducted at the different Q^2 points by those individuals identified in Table 5.4 were independently checked by other individuals. In general, excellent agreement was always found between the independent analyses; however, we did find that the results were sensitive at approximately the 2% level (or less) to the subset of data the individual employed for the time calibration of the polarimeter. Although these analysis comparisons were not conducted for the very final analysis pass reported in this thesis, we believe that we should still quote a 2% time calibration systematic uncertainty for all of our Q^2 points for safety's sake.

7.4.10 Summary of Systematic Errors

A summary of our best estimates for the various systematic uncertainties in $g = G_{En}/G_{Mn}$ are compiled in Table 7.12. Our final values for the total systematic uncertainties, 2% to 3%, are much smaller than our relative statistical errors [11.8%, 8.4%, and 9.5% at $\langle Q^2 \rangle = 0.447$, 1.132, and 1.450 (GeV/$c$)^2, respectively].

Analysis	Quantity	$\langle Q^2 \rangle$ [(GeV/c)^2] 0.447	1.132	1.450
$n(\vec{e}, e'\vec{n})$	G_{En}/G_{Mn}	$-0.0681 \pm 0.0084 \pm 0.0020$	$-0.122 \pm 0.011 \pm 0.003$	$-0.174 \pm 0.017 \pm 0.004$
^{2}H$(\vec{e}, e'\vec{n})^1$H PWBA	G_{En}/G_{Mn}	$-0.0713 \pm 0.0086 \pm 0.0021$	$-0.126 \pm 0.010 \pm 0.003$	$-0.183 \pm 0.018 \pm 0.004$
^{2}H$(\vec{e}, e'\vec{n})^1$H FSI+MEC+IC	G_{En}/G_{Mn}	$-0.0755 \pm 0.0089 \pm 0.0022$	$-0.131 \pm 0.011 \pm 0.003$	$-0.189 \pm 0.018 \pm 0.004$
Values from [20]	$G_{Mn}/\mu_n G_D$	1.003 ± 0.006	1.057 ± 0.017	1.044 ± 0.024
$n(\vec{e}, e'\vec{n})$	G_{En}	$0.0492 \pm 0.0061 \pm 0.0015$	$0.0367 \pm 0.0033 \pm 0.0011$	$0.0375 \pm 0.0037 \pm 0.0012$
^{2}H$(\vec{e}, e'\vec{n})^1$H PWBA	G_{En}	$0.0515 \pm 0.0062 \pm 0.0015$	$0.0379 \pm 0.0033 \pm 0.0011$	$0.0395 \pm 0.0039 \pm 0.0013$
^{2}H$(\vec{e}, e'\vec{n})^1$H FSI+MEC+IC	G_{En}	$0.0546 \pm 0.0064 \pm 0.0016$	$0.0394 \pm 0.0033 \pm 0.0011$	$0.0408 \pm 0.0039 \pm 0.0013$

Table 7.13: Summary of final results for G_{En}/G_{Mn} and G_{En}.

7.5 Final Results

In this section, we present our final results for G_{En} and then compare the current world data on the nucleon form factors with the various theoretical predictions discussed in Chapter 2.

7.5.1 Final Results for G_{En}

Our final results for G_{En}/G_{Mn} and G_{En} extracted from the different analyses assuming:

- elastic $n(\vec{e}, e'\vec{n})$ scattering and infinitesimal HMS and NPOL point acceptances
- quasielastic $^2\mathrm{H}(\vec{e}, e'\vec{n})^1\mathrm{H}$ scattering and the experimental acceptance-averaged Arenhövel PWBA model
- quasielastic $^2\mathrm{H}(\vec{e}, e'\vec{n})^1\mathrm{H}$ scattering and the experimental acceptance-averaged Arenhövel FSI+MEC+IC model

are tabulated in Table 7.13 and compared in Fig. 7-27. The first set of errors are statistical, and the second set of errors are the systematic errors; the systematic errors we quote for G_{En} are the quadrature sum of the total systematic errors listed in Table 7.12 and the relative uncertainties in G_{Mn}.

7.5.2 Current World Data on G_{En}

Our new $^2\mathrm{H}(\vec{e}, e'\vec{n})^1\mathrm{H}$ data [218] at $Q^2 = 0.447$, 1.132, and 1.450 $(\mathrm{GeV}/c)^2$ and the new JLab $^2\vec{\mathrm{H}}(\vec{e}, e'n)^1\mathrm{H}$ data at $Q^2 = 0.5$ and 1.0 $(\mathrm{GeV}/c)^2$ reported recently by Warren *et al.* [209] are compared with the current world data on G_{En} [195, 202–205, 207, 210, 213, 214] in Fig. 7-28. In general, our new datum at $Q^2 = 0.447$ $(\mathrm{GeV}/c)^2$ agrees well with the existing low Q^2 data, and our new datum at $Q^2 = 1.132$ $(\mathrm{GeV}/c)^2$ agrees within errors with the Warren *et al.* result at $Q^2 = 1.0$ $(\mathrm{GeV}/c)^2$. Finally, our new datum at $Q^2 = 1.450$ $(\mathrm{GeV}/c)^2$ is the first precise measurement of G_{En} in the $Q^2 > 1$ $(\mathrm{GeV}/c)^2$ region and now provides a serious constraint on the behavior of G_{En}

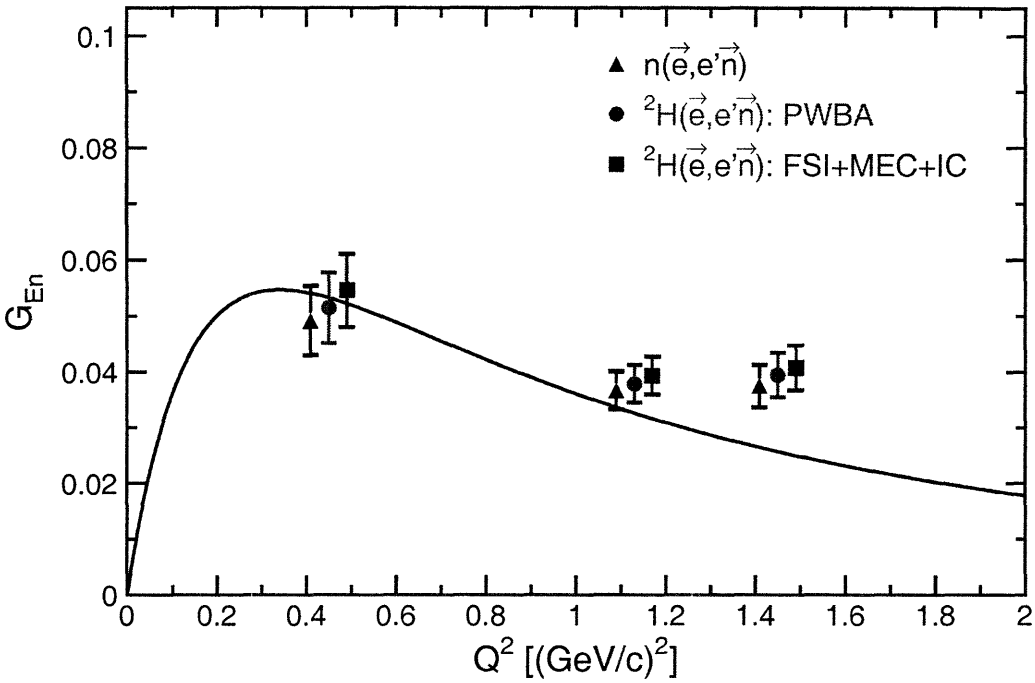

Figure 7-27: (color) Comparison of the final results for G_{En} extracted from analyses assuming $n(\vec{e}, e'\vec{n})$ elastic scattering and a point acceptance (black triangles), the acceptance-averaged $^2\mathrm{H}(\vec{e}, e'\vec{n})^1\mathrm{H}$ Arenhövel PWBA model (red circles), and the acceptance-averaged $^2\mathrm{H}(\vec{e}, e'\vec{n})^1\mathrm{H}$ Arenhövel FSI+MEC+IC model (blue squares). The error bars shown are the quadrature sum of the statistical and systematic errors, and the solid curve is the Galster parameterization.

in what was previously an essentially unexplored region of Q^2. Although Schiavilla and Sick's [195] theoretical extraction of G_{En} from an analysis of the world data on the deuteron quadrupole form factor yielded values for G_{En} over a wide range of Q^2 values from 0.01 to 1.64 $(\mathrm{GeV}/c)^2$, our error bar at $Q^2 = 1.45$ $(\mathrm{GeV}/c)^2$ is nearly a factor of three smaller than those of Schiavilla and Sick's in the same Q^2 region.

We fitted all of these data and the slope of G_{En} at the origin [142,144] [as measured via $e(n, n')$ scattering; recall the discussion in Section 2.2.7] to a modified Galster parameterization,

$$G_{En}(Q^2) = -\frac{a\mu_n\tau}{1+b\tau}\, G_D(Q^2)\ , \tag{7.53}$$

and the best fit parameters we report are $a = 0.886 \pm 0.022$ and $b = 3.29 \pm 0.31$. As can be seen in Fig. 7-29, our new fit suggests that G_{En} is substantially higher than that given by the Galster parameterization in the $Q^2 = 0.5$ to 2.0 $(\mathrm{GeV}/c)^2$ region.

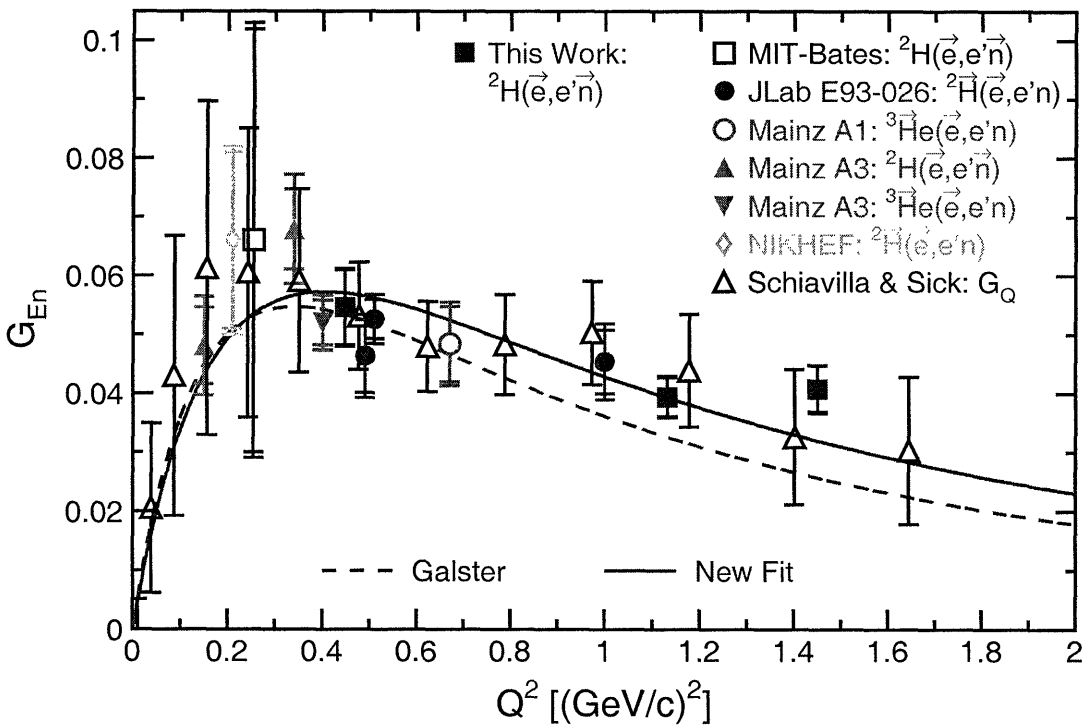

Figure 7-28: (color) Current world data on G_{En} [195, 202–205, 207, 209, 210, 213, 214, 218]. The black dashed curve is the original Galster parameterization, and the blue solid curve is the result of our modified Galster parameterization fit to these data.

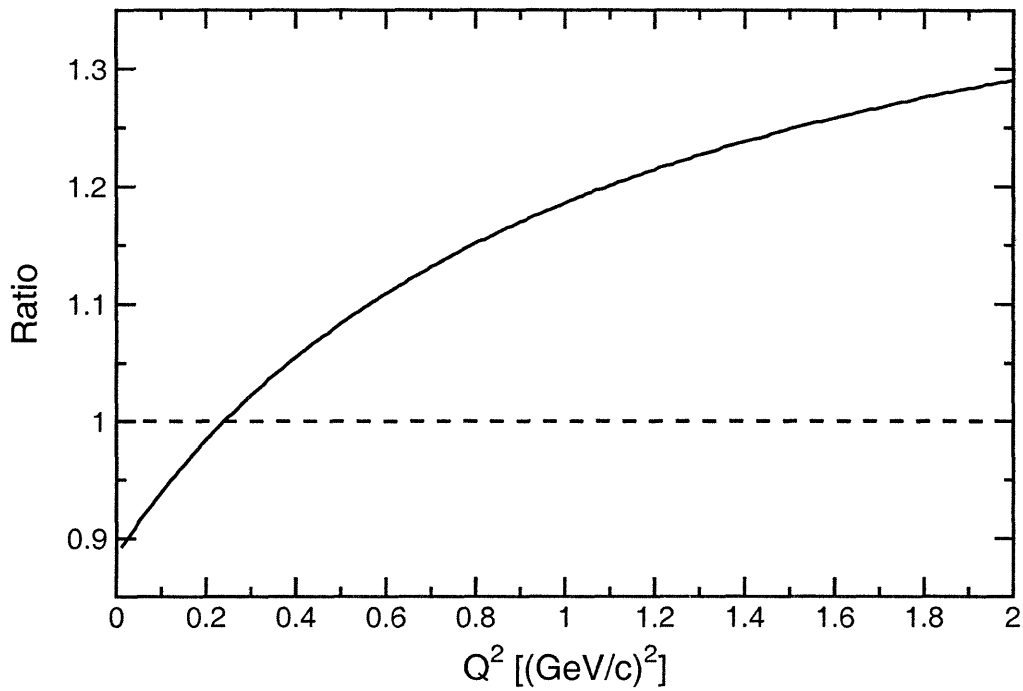

Figure 7-29: Ratio of our modified Galster parameterization to the original Galster parameterization plotted versus Q^2.

7.5.3 Comparison of Current World Data on Nucleon Form Factors with Theoretical Calculations

Finally, we now "come full circle" by re-comparing the current world data on the nucleon form factors with the predictions of the various theoretical model calculations discussed in Chapter 2. We present the same figure as was shown previously in Fig. 2-32; however, we have now added the new neutron data recently reported by Madey *et al.* [218] (i.e., the final results reported in this thesis) at $Q^2 = 0.45$, 1.13, and 1.45 $(\mathrm{GeV}/c)^2$ and the new neutron data reported by Warren *et al.* [209] at $Q^2 = 0.5$ and 1.0 $(\mathrm{GeV}/c)^2$ to this plot.

A number of observations are rather transparent, and we offer the following comments:

- First, we observe that essentially only one theoretical model calculation, that of Kaskulov and Grabmayr [275–277], denoted "OGE PC" and "OGE PC + π", achieves quantitative agreement with both the proton and neutron data.

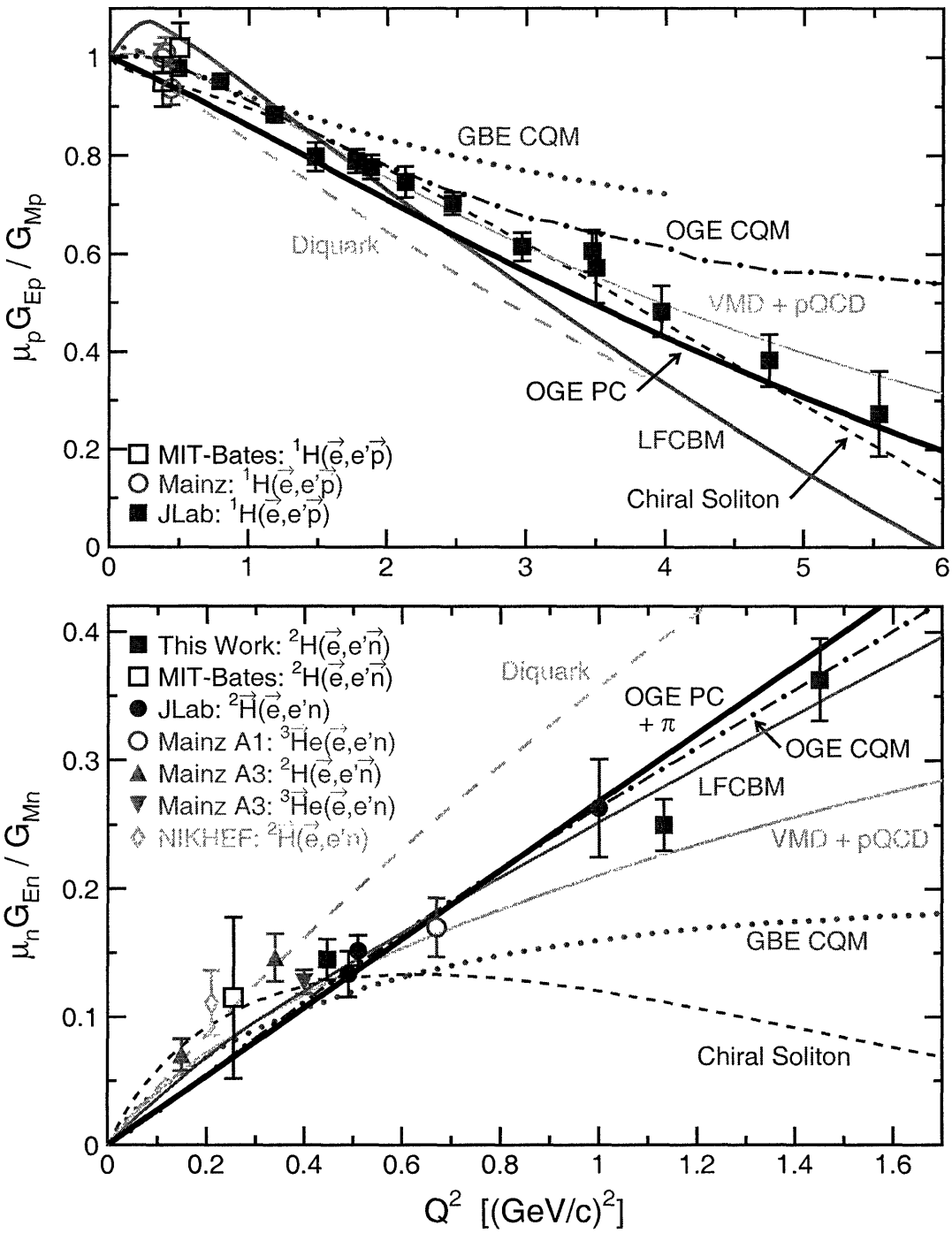

Figure 7-30: (color) Comparison of predictions from selected models (see text here and Section 2.4.8 for the glossary and references for the various model calculations) with experimental data for $\mu_p G_{Ep}/G_{Mp}$ (top panel) and $\mu_n G_{En}/G_{Mn}$ (bottom panel). The data shown for $\mu_p G_{Ep}/G_{Mp}$ are from [212, 215–217], and those for $\mu_n G_{En}/G_{Mn}$ are from [202–205, 207, 209, 210, 213, 214, 218]. All published polarized results for the nucleon form factors are now presented here.

Kaskulov and Grabmayr found that it was necessary to include the effects of the pion cloud in order to achieve agreement with the neutron data (otherwise their calculations drastically underpredict the neutron form factor ratio by nearly a factor of two). Indeed, the experimental data appear to support their claim that the pion cloud is an essential ingredient in the structure of the neutron[9]; however, it should be noted that their calculation was not truly relativistic, but, instead, nonrelativistic with relativistic corrections for the Lorentz boost to the wavefunction.

- Second, we observe that two other model calculations,
  - the light-front calculation of Cardarelli and Simula [153] and Simula [265] employing the OGE mechanism and constituent quark form factors, denoted "OGE CQM",
  - the light-front cloudy bag model of Miller [269] including the pion cloud, denoted "LFCBM",

  achieve quantitative agreement with the neutron data; however, the "OGE CQM" model predictions lie above the proton data, and the "LFCBM" calculation underpredicts the proton data.

- Finally, the remaining calculations,
  - the extended Gari-Krümpelmann "VMD + pQCD" model fits of Lomon [244, 245],
  - the "Chiral Soliton" calculation of Holzwarth [258, 259],
  - the calculation of Wagenbrunn *et al.* [272] and Boffi *et al.* [273] employing the point-form spectator approximation and a Goldstone boson exchange interaction, denoted "GBE CQM",

[9]Recently, Friedrich and Walcher [447] analyzed the current world data on the nucleon form factors with a phenomenological fit based on the constituent quark model. They reported that their analysis suggested all four nucleon form factors exhibit a similar structure at small momentum transfer (at radii of $\sim$2 fm) which they interpreted as evidence for the pion cloud.

– the light-cone quark spectator-diquark calculation of Ma, Qing, and Schmidt [281], denoted "Diquark",

do not achieve quantitative agreement with the new neutron data in the $Q^2 > 1$ $(\mathrm{GeV}/c)^2$ region. Lomon's [244, 245] "VMD + pQCD" fits can probably be repeated to accommodate the neutron data, but as we stated earlier, these fits have little absolute predictive power for Q^2 ranges in which data do not already exist. Although we cannot offer technical critiques of the other three calculations, it is clear that the new neutron data provide a challenging test to the theoretical basis of these models.

7.6 Summary

In this chapter, we concluded our discussion of the E93-038 analysis procedures by detailing the extraction of the final acceptance-averaged and nuclear physics corrected results for G_{En}/G_{Mn} from the experimental asymmetries. Complete details of the analysis procedure were presented, and we discussed the various systematic uncertainties in our data. Our final results were compared with the current world data on G_{En}, and we then recompared the existing world data on the nucleon form factors with the various theoretical calculations discussed previously in Chapter 2. This concludes our discussion of this experiment; we conclude this thesis with a very brief summary in the next chapter.

Chapter 8

Summary and Outlook

We attempted in this thesis to provide a comprehensive overview of the nucleon elastic electromagnetic form factors with special emphasis on the elusive neutron electric form factor. Interest in the nucleon form factors was reinvigorated in the 1990s with the advent of high duty-factor polarized electron beam facilities and advances in recoil polarimetry and polarized target technology. Interest in the nucleon form factors within the nuclear physics community remains high; the recent discovery of the dramatic linear decrease in the proton form factor ratio with Q^2 has generated much experimental and theoretical debate, and future high Q^2 measurements of the proton form factor ratio will no doubt generate further excitement.

As we described in detail in this thesis, measurements of the neutron form factors, in particular, those of the neutron electric form factor, have been notoriously difficult. After several decades of effort, experimentalists have finally achieved the first precise measurements of the neutron electric form factor in the largely unexplored $Q^2 > 1$ $(\mathrm{GeV}/c)^2$ region. A detailed description of the experimental arrangement and analysis of the data from an experiment designed to probe the charge structure of the neutron was presented in this thesis, and the final data for G_{En} presented here will stand as the highest Q^2 measurements of this quantity for several years to come.

Progress in the theoretical understanding of the nucleon electromagnetic structure has kept pace with the recent experimental data, and the new neutron form factor data presented in this thesis provide a challenging test for several models of

confinement which, prior to our new data, achieved qualitative agreement with the experimental data on the proton form factors and the then available experimental data on the neutron form factors. Indeed, our results invite experimental extensions of the neutron form factors to even higher values of Q^2, and we eagerly await the day when experimental data on the nucleon form factors will serve as an arbiter for lattice QCD calculations.

Appendix A

Relativistic Spin Rotation

Overview

In this appendix, we present an alternative formulation for the relativistic phenomenon of Wigner spin rotation. Many different formulations for Wigner rotation have been given (see, e.g., those given by Arenḥövel [192], Dmitrašinović [448], and Giebink [449]); the alternative formulation presented here is originally due to Kelly [424]. The formulation presented here was used in the `GENGEN` simulation for the Wigner rotations needed during the evaluation of nucleon-nucleon scattering (evaluated in the rest frame of the target nucleon).

Formalism

As the apparent direction of an intrinsic spin vector depends on the frame of reference, it is customary to specify the intrinsic spin of a massive particle in its rest frame. Suppose that $\boldsymbol{\sigma}$ is a unit vector that represents the spin orientation in the particle's rest frame. As discussed in Section 4.2.1, a spin four-vector can be formed in the rest frame as $s^\mu = (0, \boldsymbol{\sigma})$, where $s^\mu s_\mu = -1$. The spin four-vector can then be transformed from the rest frame to any arbitary frame via a boost that represents the momentum in that frame; however, the orientation of the spin will still be represented by the original $\boldsymbol{\sigma}$. The relationship between the apparent direction of the intrinsic spin in two reference frames, denoted S_1 and S_2, differing by a Lorentz boost can be determined by transforming each frame to a rest frame of the particle, using a boost

parallel to the momentum in that frame, and comparing the orientations of the two rest frames.

Without any loss of generality, we adopt a fixed coordinate system in which the z-axis is parallel to the boost vector from S_1 to S_2, the y-axis is normal to the plane spanned by the boost vector and the particle's three-momentum, and the direction of the x-axis is specified by the requirement that the x-, y-, and z-axes form a right-handed coordinate system. In this coordinate system, the four-momenta in S_1 and S_2 can be written as

$$p_i = m\gamma_i(1,\ \beta_i \sin\theta_i,\ 0,\ \beta_i \cos\theta_i)\ , \qquad (i = 1, 2) \tag{A.1}$$

where $\beta_i > 0$ denotes the magnitude of the particle's velocity in S_i, $\gamma_i = (1-\beta_i^2)^{-1/2}$, m is the particle's mass, and θ_i denotes the angle between the particle's three-momentum and the z-axis in S_i. *We assume that the components of the particle's spin are referred to this (fixed) coordinate system.*

To analyze the spin of the particle in its rest frame, we can either:

1. Rotate the coordinate system in S_1 through an angle θ_1 to align the z-axis with the three-momentum in S_1, boost to the rest frame along the rotated z-axis, and then rotate the coordinate system through an angle $-\theta_1$ to restore the coordinate system to its original orientation. This transformation will be denoted symbolically as $\mathcal{T}_1$.

2. Boost from S_1 to S_2 along the original z-axis, rotate the coordinate system in S_2 through an angle θ_2 to align the z-axis with the three-momentum in S_2, boost to the rest frame along the rotated z-axis, and then rotate the coordinate system through an angle $-\theta_1$ to restore the coordinate system to its original orientation. This transformation will be denoted symbolically as $\mathcal{T}_2$.

These transformations are illustrated schematically in Fig. A-1. As noted there, to eliminate clutter, the final rotation through an angle of $-\theta_1$ ($-\theta_2$) for $\mathcal{T}_1$ ($\mathcal{T}_2$) has been omitted from this diagram.

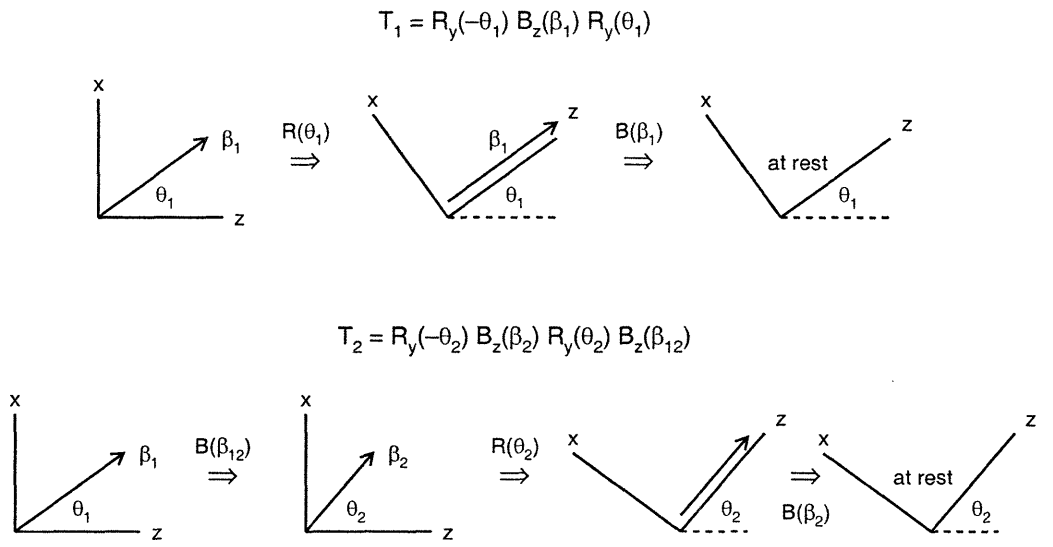

Figure A-1: Schematic diagrams of the sequence of boosts and rotations for the transformations $\mathcal{T}_1$ and $\mathcal{T}_2$ described in the text. To eliminate clutter, the final rotation of the coordinate axes through angles of $-\theta_1$ and $-\theta_2$ for $\mathcal{T}_1$ and $\mathcal{T}_2$, respectively, have been omitted from these diagrams.

We denote the transformation matrices for a rotation about the y-axis through an angle θ and a boost with boost parameter β [and Lorentz factor $\gamma = (1-\beta^2)^{-1/2}$] along the z-axis as $\mathcal{R}_y(\theta)$ and $\mathcal{B}_z(\beta)$, respectively. $\mathcal{R}_y(\theta)$ and $\mathcal{B}_z(\beta)$ can be written in component form explicitly as

$$\mathcal{R}_y(\theta) = \begin{pmatrix} 1 & 0 & 0 \\ 0 & \cos\theta & -\sin\theta \\ 0 & \sin\theta & \cos\theta \end{pmatrix}, \qquad \mathcal{B}_z(\beta) = \begin{pmatrix} \gamma & 0 & -\gamma\beta \\ 0 & 1 & 0 \\ -\gamma\beta & 0 & \gamma \end{pmatrix}, \tag{A.2}$$

where, for ease of notation, we have omitted the superfluous y-component from these matrices. With this notation, the complete Lorentz transformations for $\mathcal{T}_1$ and $\mathcal{T}_2$ can be written explicitly as

$$\mathcal{T}_1 = \mathcal{R}_y(-\theta_1) \cdot \mathcal{B}_z(\beta_1) \cdot \mathcal{R}_y(\theta_1) \tag{A.3}$$

$$\mathcal{T}_2 = \mathcal{R}_y(-\theta_2) \cdot \mathcal{B}_z(\beta_2) \cdot \mathcal{R}_y(\theta_2) \cdot \mathcal{B}_z(\beta_{12}) \tag{A.4}$$

where β_{12} denotes the boost parameter from S_1 to S_2 and $\gamma_{12} = (1 - \beta_{12}^2)^{-1/2}$. We note that these transformations are completely general and are valid for either $\beta_{12} < 0$ (i.e., $\theta_2 < \theta_1$) or $\beta_{12} > 0$ (i.e., $\theta_2 > \theta_1$).

As both $\mathcal{T}_1$ and $\mathcal{T}_2$ transform the components of the four-momentum from S_1 to the particle's rest frame, the transformations must differ at most by a planar rotation about their common y-axis, denoted $\mathcal{R}_y(\chi)$, such that

$$\mathcal{T}_2 = \mathcal{R}_y(\chi) \cdot \mathcal{T}_1 \ ; \tag{A.5}$$

therefore, the angle between the orientation of the spin vectors in S_1 and S_2 can be deduced via examination of the transformation

$$\begin{aligned} \mathcal{R}_y(\chi) &= \mathcal{T}_2 \cdot \mathcal{T}_1^{-1} \\ &= \mathcal{R}_y(-\theta_2) \cdot \mathcal{B}_z(\beta_2) \cdot \mathcal{R}_y(\theta_2) \cdot \mathcal{B}_z(\beta_{12}) \cdot \mathcal{R}_y(-\theta_1) \cdot \mathcal{B}_z(-\beta_1) \cdot \mathcal{R}_y(\theta_1) \ . \end{aligned} \tag{A.6}$$

Direct multiplication of these seven matrices would be a heinous task. Fortunately, a somewhat simpler (although not much simpler) method is to recognize the fact that successive rotations about the same axis add, such that

$$\begin{aligned} \mathcal{R}_y(\chi + \theta_2 - \theta_1) &= \mathcal{R}_y(\theta_2) \cdot \left(\mathcal{T}_2 \cdot \mathcal{T}_1^{-1}\right) \cdot \mathcal{R}_y(-\theta_1) \\ &= \mathcal{B}_z(\beta_2) \cdot \mathcal{R}_y(\theta_2) \cdot \mathcal{B}_z(\beta_{12}) \cdot \mathcal{R}_y(-\theta_1) \cdot \mathcal{B}_z(-\beta_1) \ . \end{aligned} \tag{A.7}$$

It is straightforward to show that the following relations between kinematic variables in S_1 and S_2 hold:

$$\gamma_2 = \gamma_1\gamma_{12}\left(1 - \beta_1\beta_{12}\cos\theta_1\right) \ , \tag{A.8}$$

$$\sin\theta_2 = \frac{\beta_1\gamma_1}{\beta_2\gamma_2}\sin\theta_1 \ , \tag{A.9}$$

$$\cos\theta_2 = \frac{\gamma_1\gamma_{12}}{\beta_2\gamma_2}\left(\beta_1\cos\theta_1 - \beta_{12}\right) \ . \tag{A.10}$$

With these identities, $\mathcal{R}_y(\chi+\theta_2-\theta_1)$ can be written as

$$\mathcal{R}_y(\chi+\theta_2-\theta_1) \equiv \begin{pmatrix} (\mathcal{R}_{\chi 21})_{00} & (\mathcal{R}_{\chi 21})_{01} & (\mathcal{R}_{\chi 21})_{03} \\ (\mathcal{R}_{\chi 21})_{10} & (\mathcal{R}_{\chi 21})_{11} & (\mathcal{R}_{\chi 21})_{13} \\ (\mathcal{R}_{\chi 21})_{30} & (\mathcal{R}_{\chi 21})_{31} & (\mathcal{R}_{\chi 21})_{33} \end{pmatrix} , \tag{A.11}$$

where

$$(\mathcal{R}_{\chi 21})_{00} = 1 , \tag{A.12}$$

$$(\mathcal{R}_{\chi 21})_{00} = 0 , \tag{A.13}$$

$$(\mathcal{R}_{\chi 21})_{00} = 0 , \tag{A.14}$$

$$(\mathcal{R}_{\chi 21})_{10} = 0 , \tag{A.15}$$

$$(\mathcal{R}_{\chi 21})_{11} = \frac{\beta_1 - \beta_{12}\cos\theta_1}{(1-\beta_1\beta_{12}\cos\theta_1)\sqrt{1-\dfrac{(1-\beta_1^2)(1-\beta_{12}^2)}{(1-\beta_1\beta_{12}\cos\theta_1)^2}}} , \tag{A.16}$$

$$(\mathcal{R}_{\chi 21})_{13} = -\frac{\beta_{12}(1-\beta_1^2)\sin\theta_1}{(1-\beta_1\beta_{12}\cos\theta_1)\sqrt{(1-\beta_1^2)\left(1-\dfrac{(1-\beta_1^2)(1-\beta_{12}^2)}{(1-\beta_1\beta_{12}\cos\theta_1)^2}\right)}} , \tag{A.17}$$

$$(\mathcal{R}_{\chi 21})_{30} = 0 , \tag{A.18}$$

$$(\mathcal{R}_{\chi 21})_{31} = \frac{\beta_{12}(1-\beta_1^2)\sin\theta_1}{(1-\beta_1\beta_{12}\cos\theta_1)\sqrt{(1-\beta_1^2)\left(1-\dfrac{(1-\beta_1^2)(1-\beta_{12}^2)}{(1-\beta_1\beta_{12}\cos\theta_1)^2}\right)}} , \tag{A.19}$$

$$(\mathcal{R}_{\chi 21})_{33} = \frac{\beta_1 - \beta_{12}\cos\theta_1}{(1-\beta_1\beta_{12}\cos\theta_1)\sqrt{1-\dfrac{(1-\beta_1^2)(1-\beta_{12}^2)}{(1-\beta_1\beta_{12}\cos\theta_1)^2}}} . \tag{A.20}$$

Although we do not present explicit details here, it can be shown that $\mathcal{R}_y(\chi+\theta_2-\theta_1)$ satisfies

$$\mathcal{R}_y(\chi+\theta_2-\theta_1)\cdot \text{transpose}\left\{\mathcal{R}_y(\chi+\theta_2-\theta_1)\right\} = \begin{pmatrix} 1 & 0 & 0 \\ 0 & 1 & 0 \\ 0 & 0 & 1 \end{pmatrix} , \tag{A.21}$$

$$\det\left\{\mathcal{R}_y(\chi+\theta_2-\theta_1)\right\} = 1 . \tag{A.22}$$

The above demonstrates that $\mathcal{R}_y(\chi + \theta_2 - \theta_1)$ is a proper orthogonal matrix or, in other words, a pure rotation; therefore, the net effect of three non-parallel coplanar boosts which transform a system from one rest frame to another according to the above-defined sequence is a pure rotation. The rotation angle of the spin relative to the rotation angle of the momentum, $\theta_2 - \theta_1$, can be identified by analyzing the above listed matrix elements. Is is clear that $(\mathcal{R}_{\chi 21})_{13}$ and $(\mathcal{R}_{\chi 21})_{31}$ carry the sign of $\beta_{12}\sin\theta_1$, while the sign of $(\mathcal{R}_{\chi 21})_{11}$ and $(\mathcal{R}_{\chi 21})_{33}$ depend upon the relative magnitudes of β_1 and β_{12}; therefore, we define

$$\begin{aligned}\Omega &= \tan^{-1}\frac{(\mathcal{R}_{\chi 21})_{31}}{(\mathcal{R}_{\chi 21})_{33}} \\ &= \tan^{-1}\left[\frac{\beta_{12}\sin\theta_1}{\gamma_1(\beta_1 - \beta_{12}\cos\theta_1)}\right] ,\end{aligned} \tag{A.23}$$

and the rotation angle, χ, *relative to a fixed set of coordinate axes* is then

$$\chi = \Omega + \theta_1 - \theta_2 , \tag{A.24}$$

or, written in full form,

$$\chi = \theta_1 - \tan^{-1}\left[\frac{\beta_1\sqrt{1-\beta_{12}^2}\sin\theta_1}{\beta_1\cos\theta_1 - \beta_{12}}\right] + \tan^{-1}\left[\frac{\beta_{12}\sqrt{1-\beta_1^2}\sin\theta_1}{\beta_1 - \beta_{12}\cos\theta_1}\right] . \tag{A.25}$$

The angle χ is the relativistic precession angle of the spin as referred to our above-defined fixed coordinate system. The components of the spin transform under this relativistic transformation according to

$$\begin{pmatrix} s_{x,2} \\ s_{y,2} \\ s_{z,2} \end{pmatrix} = \begin{pmatrix} \cos\chi & 0 & -\sin\chi \\ 0 & 1 & 0 \\ \sin\chi & 0 & \cos\chi \end{pmatrix} \begin{pmatrix} s_{x,1} \\ s_{y,1} \\ s_{z,1} \end{pmatrix} . \tag{A.26}$$

Obviously, χ must satisfy $\chi \to 0$ in the non-relativistic limit. The proof that our above expression for χ satisfies the non-relativistic limit is accomplished via use of

the identity

$$\tan^{-1}z_1 - \tan^{-1}z_2 = \tan^{-1}\left(\frac{z_1 - z_2}{1 + z_1 z_2}\right) . \tag{A.27}$$

With this identity, we can rewrite our above expression for χ as

$$\chi = \theta_1 + \tan^{-1}\left[\frac{\beta_1\beta_{12}\sqrt{1-\beta_1^2}\sin\theta_1\cos\theta_1 - \beta_{12}^2\sqrt{1-\beta_1^2}\sin\theta_1 - \beta_1^2\sqrt{1-\beta_{12}^2}\sin\theta_1 + \beta_1\beta_{12}\sqrt{1-\beta_{12}^2}\sin\theta_1\cos\theta_1}{\beta_1^2\cos\theta_1 - \beta_1\beta_{12} - \beta_1\beta_{12}\cos\theta_1 + \beta_{12}^2\cos\theta_1 + \beta_1\beta_{12}\sqrt{1-\beta_1^2}\sqrt{1-\beta_{12}^2}\sin^2\theta_1}\right] \tag{A.28}$$

In the non-relativistic boost limit of $|\beta_{12}| \to 0$ (but keeping β_1 intact), the above reduces to

$$\chi = \theta_1 + \tan^{-1}(-\tan\theta_1) = 0 . \tag{A.29}$$

This justifies our identification of χ as the relativistic spin precession angle.

Appendix B

Neutron Polarimeter Detector Geometry

In this appendix, we provide complete tables summarizing the detector geometry for the neutron polarimeter. We list each detector's center position and dimensions; the coordinate system employed refers to the *polarimeter basis* defined in Section 4.1.1. The tables begin on the next page.

Detector Array	Layer	Detector Number	Center Position [cm]			Dimensions [cm]		
			x	y	z	x	y	z
Front	1	1	0.0	−20.2	683.7	100.0	10.0	10.0
Front	1	2	0.0	−10.1	683.7	100.0	10.0	10.0
Front	1	3	0.0	0.0	683.7	100.0	10.0	10.0
Front	1	4	0.0	10.1	683.7	100.0	10.0	10.0
Front	1	5	0.0	20.2	683.7	100.0	10.0	10.0
Front	2	6	0.0	−20.2	693.9	100.0	10.0	10.0
Front	2	7	0.0	−10.1	693.9	100.0	10.0	10.0
Front	2	8	0.0	0.0	693.9	100.0	10.0	10.0
Front	2	9	0.0	10.1	693.9	100.0	10.0	10.0
Front	2	10	0.0	20.2	693.9	100.0	10.0	10.0
Front	3	11	0.0	−20.2	706.1	100.0	10.0	10.0
Front	3	12	0.0	−10.1	706.1	100.0	10.0	10.0
Front	3	13	0.0	0.0	706.1	100.0	10.0	10.0
Front	3	14	0.0	10.1	706.1	100.0	10.0	10.0
Front	3	15	0.0	20.2	706.1	100.0	10.0	10.0
Front	4	16	0.0	−20.2	716.3	100.0	10.0	10.0
Front	4	17	0.0	−10.1	716.3	100.0	10.0	10.0
Front	4	18	0.0	0.0	716.3	100.0	10.0	10.0
Front	4	19	0.0	10.1	716.3	100.0	10.0	10.0
Front	4	20	0.0	20.2	716.3	100.0	10.0	10.0
Bottom Rear	Outer	21	−50.95	−89.74	952.0	50.8	10.16	101.6
Bottom Rear	Outer	22	−12.75	−89.74	952.0	25.4	10.16	101.6
Bottom Rear	Outer	23	12.75	−89.74	952.0	25.4	10.16	101.6
Bottom Rear	Outer	24	50.95	−89.74	952.0	50.8	10.16	101.6
Bottom Rear	Middle	25	−50.95	−73.23	957.0	50.8	10.16	101.6
Bottom Rear	Middle	26	−12.75	−73.23	957.0	25.4	10.16	101.6
Bottom Rear	Middle	27	12.75	−73.23	957.0	25.4	10.16	101.6
Bottom Rear	Middle	28	50.95	−73.23	957.0	50.8	10.16	101.6
Bottom Rear	Inner	29	−50.95	−56.72	952.0	50.8	10.16	101.6
Bottom Rear	Inner	30	−12.75	−56.72	952.0	25.4	10.16	101.6
Bottom Rear	Inner	31	12.75	−56.72	952.0	25.4	10.16	101.6
Bottom Rear	Inner	32	50.95	−56.72	952.0	50.8	10.16	101.6
Top Rear	Inner	33	−50.95	56.72	952.0	50.8	10.16	101.6
Top Rear	Inner	34	−12.75	56.72	952.0	25.4	10.16	101.6
Top Rear	Inner	35	12.75	56.72	952.0	25.4	10.16	101.6
Top Rear	Inner	36	50.95	56.72	952.0	50.8	10.16	101.6
Top Rear	Middle	37	−50.95	73.23	957.0	50.8	10.16	101.6
Top Rear	Middle	38	−12.75	73.23	957.0	25.4	10.16	101.6
Top Rear	Middle	39	12.75	73.23	957.0	25.4	10.16	101.6
Top Rear	Middle	40	50.95	73.23	957.0	50.8	10.16	101.6
Top Rear	Outer	41	−50.95	89.74	952.0	50.8	10.16	101.6
Top Rear	Outer	42	−12.75	89.74	952.0	25.4	10.16	101.6
Top Rear	Outer	43	12.75	89.74	952.0	25.4	10.16	101.6
Top Rear	Outer	44	50.95	89.74	952.0	50.8	10.16	101.6

Table B.1: The NPOL detector geometry for the front and rear arrays. In the front array, the vertical spacing between detectors was 1 mm, and the horizontal spacing between layers was 2 mm. In the rear array, the horizontal spacing between detectors was 1 mm, and the vertical spacing between layers was 6.35 cm. The (x, y, z) coordinates and dimensions refer to the polarimeter basis.

Detector Array	Layer	Detector Number	Center Position [cm]			Dimensions [cm]		
			x	y	z	x	y	z
Front Veto/Tagger	1	45	0.0	−21.7	667.5	160.0	11.0	0.635
Front Veto/Tagger	1	46	0.0	−10.6	667.5	160.0	11.0	0.635
Front Veto/Tagger	1	47	0.0	0.5	667.5	160.0	11.0	0.635
Front Veto/Tagger	1	48	0.0	11.6	667.5	160.0	11.0	0.635
Front Veto/Tagger	1	49	0.0	22.7	667.5	160.0	11.0	0.635
Front Veto/Tagger	2	50	0.0	−22.7	673.3	160.0	11.0	0.635
Front Veto/Tagger	2	51	0.0	−11.6	673.3	160.0	11.0	0.635
Front Veto/Tagger	2	52	0.0	−0.5	673.3	160.0	11.0	0.635
Front Veto/Tagger	2	53	0.0	10.6	673.3	160.0	11.0	0.635
Front Veto/Tagger	2	54	0.0	21.7	673.3	160.0	11.0	0.635
Rear Veto/Tagger	1	55	0.0	−38.85	726.70	160.0	11.0	0.635
Rear Veto/Tagger	1	56	0.0	−27.75	726.70	160.0	11.0	0.635
Rear Veto/Tagger	1	57	0.0	−16.65	726.70	160.0	11.0	0.635
Rear Veto/Tagger	1	58	0.0	−5.55	726.70	160.0	11.0	0.635
Rear Veto/Tagger	1	59	0.0	5.55	726.70	160.0	11.0	0.635
Rear Veto/Tagger	1	60	0.0	16.65	726.70	160.0	11.0	0.635
Rear Veto/Tagger	1	61	0.0	27.75	726.70	160.0	11.0	0.635
Rear Veto/Tagger	1	62	0.0	38.85	726.70	160.0	11.0	0.635
Rear Veto/Tagger	2	63	0.0	−37.90	733.33	160.0	11.0	0.635
Rear Veto/Tagger	2	64	0.0	−26.80	733.33	160.0	11.0	0.635
Rear Veto/Tagger	2	65	0.0	−15.70	733.33	160.0	11.0	0.635
Rear Veto/Tagger	2	66	0.0	−4.60	733.33	160.0	11.0	0.635
Rear Veto/Tagger	2	67	0.0	6.50	733.33	160.0	11.0	0.635
Rear Veto/Tagger	2	68	0.0	17.60	733.33	160.0	11.0	0.635
Rear Veto/Tagger	2	69	0.0	28.70	733.33	160.0	11.0	0.635
Rear Veto/Tagger	2	70	0.0	39.80	733.33	160.0	11.0	0.635

Table B.2: The NPOL detector geometry for the front veto/tagger and rear veto/tagger arrays. The vertical spacing between detectors in the front (rear) veto/tagger array was 1 mm (0.95 mm). The (x, y, z) coordinates and dimensions refer to the polarimeter basis.

Appendix C

Cross Ratio Technique for Asymmetry Extraction

As we described in detail in Section 5.6, the physical scattering asymmetries in the polarimeter were extracted from the yields in the four decomposed rTOF spectra (i.e., the RU, LD, RD, and LU spectra) via the *cross ratio technique* of Ohlsen and Keaton [417]. As a review, the cross ratio, r, is defined to be the ratio of two geometric means,

$$r = \sqrt{\frac{N_{RU}N_{LD}}{N_{RD}N_{LU}}}\,, \tag{C.1}$$

where the notation is obvious, and the physical scattering asymmetry, ξ, is given by

$$\xi = \frac{r-1}{r+1} = \frac{\sqrt{N_{RU}N_{LD}} - \sqrt{N_{RD}N_{LU}}}{\sqrt{N_{RU}N_{LD}} + \sqrt{N_{RD}N_{LU}}}\,. \tag{C.2}$$

We stated there that the merit of the cross ratio technique is that ξ is insensitive to

- the number of particles incident on the polarimeter (i.e., target luminosities) for the different beam helicity states, and
- the relative efficiencies and acceptances of the top and bottom rear arrays of the polarimeter.

We now prove these claims.

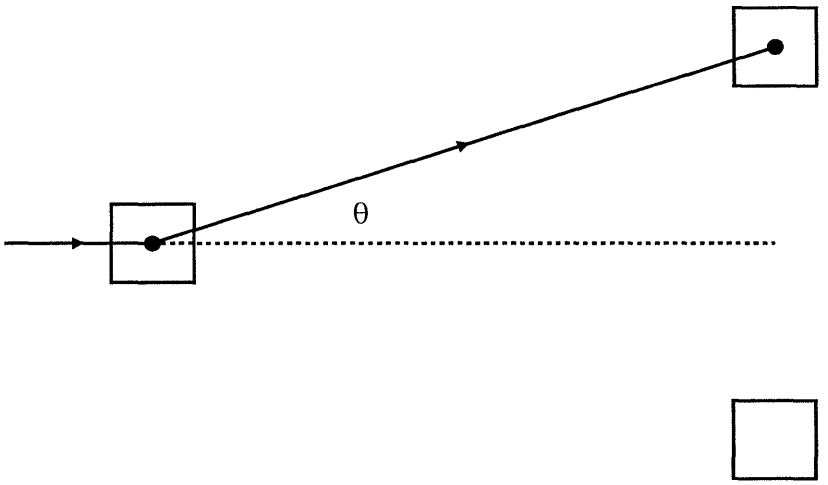

Figure C-1: A simple polarimeter.

Consider a simple polarimeter consisting of three detectors such as that shown in Fig. C-1. As we discussed in detail in Section 4.1.1, such a polarimeter is sensitive to the component of the spin that is perpendicular to the plane of this piece of paper, here denoted P_S. The differential cross section for elastic polarized-nucleon, unpolarized nucleon scattering, denoted $\sigma(\theta, \phi)$, was shown there to be of the form

$$\sigma(\theta, \phi) = \sigma_0(\theta) \left[1 + A_y(\theta) P_S \cos\phi\right] \ , \tag{C.3}$$

where $\sigma_0(\theta)$ is the unpolarized cross section and $A_y(\theta)$ is, as usual, the analyzing power. It then follows that the number of counts recorded by a detector at some scattering angle θ will be

$$N(\theta, \phi) = nN\Omega\epsilon\sigma(\theta, \phi) \ , \tag{C.4}$$

where n denotes the number of particles incident on the front array, N denotes the number of target/scatterer nuclei per unit area, Ω denotes the solid angle subtended by the detector, and ϵ denotes the detector's efficiency.

Now, we assume that the top and bottom rear array of this simple polarimeter are perfectly aligned; however, we permit the solid angles for the top and bottom detectors, Ω_t and Ω_b, respectively, and the efficiencies for the top and bottom detectors, ϵ_t and ϵ_b, respectively, to differ. We define $\phi = 0^\circ$ (180°) for scattering to the top

(bottom) detector. Now, if we denote the values of $N(\theta, \phi)$ for the top and bottom detectors as $N_t(\theta, \phi)$ and $N_b(\theta, \phi)$, respectively, it follows that

$$N_t(\theta, \phi = 0°) = nN\Omega_t\epsilon_t\sigma_0(\theta)\left[1 + A_y(\theta)P_S\right] \equiv N_{RU} \ , \tag{C.5}$$

$$N_b(\theta, \phi = 180°) = nN\Omega_b\epsilon_b\sigma_0(\theta)\left[1 - A_y(\theta)P_S\right] \equiv N_{RD} \ . \tag{C.6}$$

Now, if we flip the polarization of the incident nucleons (or, equivalently, flip the helicity of the electron beam) such that $P_S \rightarrow -P_S$, it follows that

$$N_t(\theta, \phi = 0°) = n'N'\Omega_t\epsilon_t\sigma_0(\theta)\left[1 - A_y(\theta)P_S\right] \equiv N_{LU} \ , \tag{C.7}$$

$$N_b(\theta, \phi = 180°) = n'N'\Omega_b\epsilon_b\sigma_0(\theta)\left[1 + A_y(\theta)P_S\right] \equiv N_{LD} \ , \tag{C.8}$$

where the primes indicate that the integrated charge and the effective target/scatterer thickness may vary between data taking with the helicity flipped.

We now define geometric means

$$\begin{aligned} U &\equiv \sqrt{N_{RU}N_{LD}} \\ &= \left[nn'NN'\Omega_t\Omega_b\epsilon_t\epsilon_b\right]^{1/2}\sigma_0(\theta)\left[1 + A_y(\theta)P_S\right] \ , \end{aligned} \tag{C.9}$$

$$\begin{aligned} D &\equiv \sqrt{N_{RD}N_{LU}} \\ &= \left[nn'NN'\Omega_t\Omega_b\epsilon_t\epsilon_b\right]^{1/2}\sigma_0(\theta)\left[1 - A_y(\theta)P_S\right] \ . \end{aligned} \tag{C.10}$$

From this, it immediately follows that

$$\frac{U}{D} = \frac{\sqrt{N_{RU}N_{LD}}}{\sqrt{N_{RD}N_{LU}}} = \frac{1 + A_y(\theta)P_S}{1 - A_y(\theta)P_S} \ , \tag{C.11}$$

where the n, n', N, N', Ω_t, Ω_b, ϵ_t, and ϵ_b have *cancelled* in the ratio. This can easily be rearranged into the form

$$P_S A_y(\theta) = \frac{\sqrt{N_{RU}N_{LD}} - \sqrt{N_{RD}N_{LU}}}{\sqrt{N_{RU}N_{LD}} + \sqrt{N_{RD}N_{LU}}} = \frac{r - 1}{r + 1} \ , \tag{C.12}$$

where r is the cross ratio as defined in Eq. (C.1). From this, it is obvious that the physical scattering asymmetry, $\xi = A_y(\theta)P_S$, is insensitive to

- relative detector efficiencies for the top and bottom detectors,
- relative detector solid angles for the top and bottom detectors,
- relative integrated charge (or target luminosities) for the different beam helicity states, and
- possible variations in the target/scatterer thickness for the different beam helicity states (although this scenario was highly unlikely as the beam helicity was flipped at 30 Hz).

Our claims are proven.

Appendix D

Cubic Spline Interpolation

In this appendix, we provide a general overview of cubic spline interpolation. We begin with the simplest case, one-dimensional cubic spline interpolation, and then proceed to a discussion of its generalization to three dimensions. Much of our discussion follows that given in the standard reference for scientific programming in FORTRAN [422].

Suppose tabulated values for some arbitrary function $y_i \equiv y(x_i)$, $i = 1, \ldots, N$ exist, and the value of the function between some x_j and x_{j+1}, where the x_i are assumed to be monotonically increasing, is desired. The simplest interpolation scheme, *linear interpolation*, assumes that the underlying function, $y(x)$, varies linearly with x between x_j and x_{j+1}, such that

$$y(x) = y_j + \left(\frac{y_{j+1} - y_j}{x_{j+1} - x_j}\right)(x - x_j) \tag{D.1}$$

for $x_j \leq x \leq x_{j+1}$. In general, linear interpolation can be highly inaccurate as the interpolating function is piecewise linear; also, the second derivative of the interpolating function is zero everywhere within the (x_j, x_{j+1}) interval and undefined at the end points (i.e., at x_j and x_{j+1}).

The goal of *cubic spline interpolation* is to construct an interpolating function that is smooth in the first derivative and continuous in the second derivative, both within the interval and at the end points. To do so, suppose that, in contrast to

reality, in addition to the tabulated values of y_i, tabulated values of the function's second derivative, denoted y_i'', exist. Then, within each interval, a cubic polynomial can be added to the right-hand side of Eq. (D.1) such that the second derivative of this cubic polynomial yields the appropriate values for y_j'' and y_{j+1}'' at the end points; the interpolating function then possesses the desired behavior of a continous second derivative. Further, if the cubic polynomial is constructed such that its value vanishes at x_j and x_{j+1}, the addition of this polynomial to the simplistic formula for linear interpolation will not spoil the (perfect) agreement between the tabulated values of the function and the interpolated values at the endpoints.

The only way to construct this function is if

$$y(x) = Ay_j + By_{j+1} + Cy_j'' + Dy_{j+1}'' \ , \tag{D.2}$$

where

$$A = \frac{x_{j+1} - x}{x_{j+1} - x_j} \ , \tag{D.3}$$

$$B = 1 - A = \frac{x - x_j}{x_{j+1} - x_j} \ , \tag{D.4}$$

$$C = \frac{1}{6}\left(A^3 - A\right)\left(x_{j+1} - x_j\right)^2 \ , \tag{D.5}$$

$$D = \frac{1}{6}\left(B^3 - B\right)\left(x_{j+1} - x_j\right)^2 \ . \tag{D.6}$$

After a small amount of algebra, we find

$$y'(x) = \frac{y_{j+1} - y_j}{x_{j+1} - x_j} - \frac{3A^2 - 1}{6}(x_{j+1} - x_j)y_j'' + \frac{3B^2 - 1}{6}(x_{j+1} - x_j)y_{j+1}'' \ , \tag{D.7}$$

from which it follows that

$$y''(x) = Ay_j'' + By_{j+1}'' \ . \tag{D.8}$$

As $A = 1$ for $x = x_j$, $A = 0$ for $x = x_{j+1}$, $B = 0$ for $x = x_j$, and $B = 1$ for $x = x_{j+1}$, we see immediately that $y''(x) = y_j''$ at $x = x_j$ and $y''(x) = y_{j+1}''$ at $x = x_{j+1}$; therefore, we see that the second derivative of the interpolating polynomial assumes the correct

values at the end points. Also, we see that the second derivative is continuous at the boundary between two intervals [e.g., between (x_{j-1}, x_j) and (x_j, x_{j+1})].

The procedure outlined above assumes that tabulated values for the second derivative of the interpolating polynomial exist; however, in practice, such data rarely, if ever, exist. As such, it would appear that construction of Eq. (D.2) is impossible; however, no condition has, as of yet, been imposed on the behavior of the first derivative of the interpolating polynomial. Indeed, as we shall now show, requiring the first derivative of the interpolating polynomial to be continous across the boundary between two intervals permits the construction of a system of equations whose solutions are the y''_j.

The requisite system of equations is obtained by requiring the equation for $y'(x)$ evaluated at the end point $x = x_j$ for the interval (x_{j-1}, x_j) to be equal to the equation for $y'(x)$ evaluated at the end point $x = x_j$ for the interval (x_j, x_{j+1}). Imposing this requirement gives us, for $j = 2, \ldots, N-1$,

$$\frac{x_j - x_{j-1}}{6} y''_{j-1} + \frac{x_{j+1} - x_{j-1}}{3} y''_j + \frac{x_{j+1} - x_j}{6} y''_{j+1} = \frac{y_{j+1} - y_j}{x_{j+1} - x_j} - \frac{y_j - y_{j-1}}{x_j - x_{j-1}} . \quad \text{(D.9)}$$

Here, we have $N-2$ (linear) equations, but there are N unknowns; therefore, a non-unique two-parameter family of solutions exists. For a unique solution, two further constraints must be specified; these are, typically, taken to be the boundary conditions at x_1 and x_N. The two most common choices of boundary conditions are:

- requiring $y''_1 = y''_N = 0$, yielding what is known as a *natural cubic spline*; or

- setting y''_1 and y''_N to values calculated from the above equation for $y'(x)$ such that the first derivative of the interpolating polynomial assumes some specified values at x_1 and x_N.

We note that our interpolation algorithms in `GENGEN` constructed natural cubic splines. The above system of equations is not only linear, but tridiagonal (i.e., each y''_j is

coupled only to y''_{j-1} and y''_{j+1}).[1] Numerical algorithms for the solution of a tridiagonal system of equations are readily available in standard references (see, e.g., [422]) and can, as a result, be implemented fairly easily within an interpolation algorithm.

A computational scheme for one-dimensional cubic spline interpolation would be as follows. An initialization algorithm would compute the *splines* (i.e., the second derivatives of the interpolating function) for each grid point via solution of the tridiagonal system of equations given in Eq. (D.9). Following computation and storage of the splines, the value of the interpolating function between any two grid points could be determined any number of times via numerical evaluation of Eq. (D.2); the computational procedure for the final step is generally referred to as a *splint algorithm* (for *spl*ine *int*erpolation).

The extension of one-dimensional cubic spline interpolation to two, three, or even higher dimensions is straightforward. Here, we outline the generalization to three dimensions as three-dimensional interpolation of Arenhövel's calculations of the structure functions between the kinematic grid elements indexed by $(E_{e'}, \theta_{e'}, \Theta^{\text{c.m.}}_{np})$ was necessary.

Suppose now that tabulated values for an arbitary function, $f_{ijk} \equiv f(x_i, y_j, z_k)$, $i = 1, \ldots, L$, $j = 1, \ldots, M$, $k = 1, \ldots, N$, exist with the x_i, y_j, and z_k monotonically increasing in their indices. Just as one-dimensional splines must be constructed for one-dimensional cubic spline interpolation, three-dimensional cubic splines must be constructed for three-dimensional cubic spline interpolation. The generalization to three dimensions is straightforward and is accomplished by reducing the dimensionality from three to two to one in successive iterations; for example, a fixed value

[1] A system of linear equations is said to be tridiagonal if, when written in matrix form, non-zero elements appear only on the diagonal plus or minus one column. Specifically, such a system of equations can be written as

$$\begin{pmatrix} b_1 & c_1 & 0 & \ldots & & \\ a_2 & b_2 & c_2 & \ldots & & \\ & & & \ddots & & \\ & & & \ldots\ a_{N-1} & b_{N-1} & c_{N-1} \\ & & & \ldots\ 0 & a_N & b_N \end{pmatrix} \begin{pmatrix} u_1 \\ u_2 \\ \vdots \\ u_{N-1} \\ u_N \end{pmatrix} = \begin{pmatrix} r_1 \\ r_2 \\ \vdots \\ r_{N-1} \\ r_N \end{pmatrix} . \tag{D.10}$$

Here, the u_i index the y''_i, and the r_i index the right-hand side of Eq. (D.9).

of z_k defines a unique two-dimensional x-y plane, and a fixed value of y_j within this two-dimensional plane then defines a unique one-dimensional function $f(x, y_j, z_k)$. Two-dimensional cubic splines can then be constructed for each value of z_k, and one-dimensional cubic splines can be constructed for each (y_j, z_k) combination.

After construction of the three-dimensional cubic splines, the value of the three-dimensional interpolating function at any point (x, y, z) can be determined with a three-dimensional splint algorithm. After determining the values of i, j, and k that satisfy $x_i \leq x \leq x_{i+1}$, $y_j \leq y \leq y_{j+1}$, $z_k \leq z \leq z_{k+1}$, the N two-dimensional cubic splines constructed for each x-y plane can be evaluated; the output of this interpolation is the value of the interpolating function for each x-y plane combination. After this evaluation, one-dimensional splines can be constructed over these output values, and the final interpolated value of the function can be evaluated with a one-dimensional splint algorithm.

Appendix E

Jefferson Laboratory E93-038 Collaboration

The members of the Jefferson Laboratory E93-038 Collaboration are listed on the next page.

Members of the Collaboration

Collaboration spokespersons are underlined;
Ph.D. thesis students are in *italics*

A. Aghalaryan[19], A. Ahmidouch[11], B. D. Anderson[6], H. Arenhövel[5], R. Asaturyan[19], O. Baker[4], A. R. Baldwin[6], D. Barkhuff[9], H. Breuer[17], R. Carlini[16], E. Christy[4], S. Churchwell[2], L. Cole[4], *E. Crouse*[1], S. Danagoulian[11,16], D. Day[18], T. Eden[4,6], M. Elaasar[15], R. Ent[16], M. Farkondeh[9], H. Fenker[16], J. M. Finn[1], L. Gan[4], K. Garrow[16], A. Gasparian[4,11], P. Gueye[4], C. Howell[2], B. Hu[4], M. K. Jones[16], J. J. Kelly[17], C. Keppel[4], M. Khandaker[10], W.-Y. Kim[7], S. Kowalski[9], A. Lai[6], A. Lung[16], D. Mack[16], *G. MacLachlan*[12], R. Madey[6,16], D. M. Manley[6], P. Markowitz[3], J. Mitchell[16], H. Mkrtchyan[19], A. K. Opper[12], C. Perdrisat[1], *B. Plaster*[9], V. Punjabi[10], B. Raue[3], T. Reichelt[14], J. Reinhold[3], J. Roche[1], Y. Sato[4], N. Savvinov[17], A. Yu. Semenov[6], I. A. Semenova[6], W. Seo[7], N. Simicevic[8], G. Smith[16], S. Stepanyan[7,19], V. Tadevosyan[19], *S. Tajima*[2], L. Tang[4], S. Taylor[9], *W. Tireman*[6], P. Ulmer[13], W. Vulcan[16], J. Watson[6], S. Wells[8], F. Wesselmann[18], S. Wood[16], Chen Yan[16], *Chenyu Yan*[6], S. Yang[7], L. Yuan[4], W.-M. Zhang[6], H. Zhu[18], and X. Zhu[4]

[1] *The College of William and Mary, Williamsburg, Virginia 23187, USA*
[2] *Duke University, Durham, North Carolina 27708, USA*
[3] *Florida International University, Miami, Florida 33199, USA*
[4] *Hampton University, Hampton, Virginia, 23668, USA*
[5] *Johannes Gutenberg-Universität, D-55099 Mainz, Germany*
[6] *Kent State University Kent, Ohio 44242, USA*
[7] *Kyungpook National University, Taegu 702-701, Korea*
[8] *Louisiana Tech University, Ruston, Louisiana 71272, USA*
[9] *Massachusetts Institute of Technology, Cambridge, Massachusetts 02139, USA*
[10] *Norfolk State University, Norfolk, Virginia 23504, USA*
[11] *North Carolina A&T University, Greensboro, North Carolina 27411, USA*
[12] *Ohio University, Athens, Ohio 45701, USA*
[13] *Old Dominion University, Norfolk, Virginia 23508, USA*
[14] *Rheinische Friedrich-Wilhelms-Universität Bonn, D-53115 Bonn, Germany*
[15] *Southern University at New Orleans, New Orleans, Louisiana 70126, USA*
[16] *Thomas Jefferson National Accelerator Facility, Newport News, Virginia 23606, USA*
[17] *University of Maryland, College Park, Maryland 20742, USA*
[18] *University of Virginia, Charlottesville, Virginia 22904, USA*
[19] *Yerevan Physics Institute, Yerevan 375036, Armenia*

Bibliography

[1] T. DeForest, Jr. and J. D. Walecka, Adv. Phys. **15**, 1 (1966).

[2] E. M. Lyman, A. O. Hanson, and M. B. Scott, Phys. Rev. **84**, 626 (1951).

[3] R. Hofstadter and R. W. McAllister, Phys. Rev. **98**, 217 (1955).

[4] R. W. McAllister and R. Hofstadter, Phys. Rev. **102**, 851 (1956).

[5] E. E. Chambers and R. Hofstadter, Phys. Rev. **103**, 1454 (1956).

[6] E. D. Bloom, D. H. Coward, H. DeStaebler, J. Drees, G. Miller, L. W. Mo, R. E. Taylor, M. Breidenbach, J. I. Friedman, G. C. Hartmann, and H. W. Kendall, Phys. Rev. Lett. **23**, 930 (1969).

[7] M. Breidenbach, J. I. Friedman, H. W. Kendall, E. D. Bloom, D. H. Coward, H. DeStaebler, J. Drees, L. W. Mo, and R. E. Taylor, Phys. Rev. Lett. **23**, 935 (1969).

[8] M. E. Peskin and D. V. Schroeder, *An Introduction to Quantum Field Theory* (Perseus Books Publishing, 1995).

[9] R. P. Feynman, Phys. Rev. **76**, 749 (1949).

[10] R. P. Feynman, Phys. Rev. **76**, 769 (1949).

[11] L. L. Foldy, Phys. Rev. **87**, 688 (1952).

[12] L. L. Foldy, Phys. Rev. **87**, 693 (1952).

[13] G. Salzman, Phys. Rev. **99**, 973 (1955).

[14] M. N. Rosenbluth, Phys. Rev. **79**, 615 (1950).

[15] D. R. Yennie, M. M. Lévy, and D. G. Ravenhall, Rev. Mod. Phys. **29**, 144 (1957).

[16] J. P. Walecka, Nuovo Cimento **11**, 821 (1959).

[17] F. J. Ernst, R. G. Sachs, and K. C. Wali, Phys. Rev. **119**, 1105 (1960).

[18] R. G. Sachs, Phys. Rev. **126**, 2256 (1962).

[19] J. J. Kelly, `arXiv:hep-ph/0111251`

[20] J. J. Kelly, Phys. Rev. C **66**, 065203 (2002).

[21] L. W. Mo and Y. S. Tsai, Rev. Mod. Phys. **41**, 205 (1969).

[22] R. Hofstadter, F. Bumiller, and M. R. Yearian, Rev. Mod. Phys. **30**, 482 (1958).

[23] W. Albrecht, H. J. Behrend, F. W. Brasse, W. Flauger, H. Hultschig, and K. G. Steffen, Phys. Rev. Lett. **17**, 1192 (1966).

[24] F. Bumiller, M. Croissiaux, E. Dally, and R. Hofstadter, Phys. Rev. **124**, 1623 (1961).

[25] P. Lehmann, R. Taylor, and R. Wilson, Phys. Rev. **126**, 1183 (1962).

[26] D. J. Drickey and L. N. Hand, Phys. Rev. Lett. **9**, 521 (1962).

[27] B. Dudzelak, G. Sauvage, and P. Lehmann, Nuovo Cimento **28**, 18 (1963).

[28] K. Berkelman, M. Feldman, R. M. Littauer, G. Rouse, and R. R. Wilson, Phys. Rev. **130**, 2061 (1963).

[29] J. R. Dunning, K. W. Chen, N. F. Ramsey, J. R. Rees, W. Shaler, J. K. Walker, and R. Wilson, Phys. Rev. Lett. **10**, 500 (1963).

[30] L. N. Hand, D. G. Miller, and R. Wilson, Rev. Mod. Phys. **35**, 335 (1963).

[31] K. W. Chen, A. A. Cone, J. R. Dunning, Jr., S. G. F. Frank, N. F. Ramsey, J. K. Walker, and R. Wilson, Phys. Rev. Lett. **11**, 561 (1963).

[32] K. W. Chen, J. R. Dunning, Jr., A. A. Cone, N. F. Ramsey, J. K. Walker, and R. Wilson, Phys. Rev. **141**, 1267 (1966).

[33] D. Frèrejacque, D. Benaksas, and D. Drickey, Phys. Rev. **141**, 1308 (1966).

[34] T. Janssens, R. Hofstadter, E. B. Hughes, and M. R. Yearian, Phys. Rev. **142**, 922 (1966).

[35] W. Bartel, B. Dudelzak, H. Krehbiel, J. M. McElroy, U. Meyer-Berkhout, R. J. Morrison, H. Nguyen-Ngoc, W. Schmidt, and G. Weber, Phys. Rev. Lett. **17**, 608 (1966).

[36] H. J. Behrend, G. Hartwig, and H. Schopper, Nuovo Cimento **48**, 140 (1967).

[37] W. Albrecht, H. J. Behrend, H. Dorner, W. Flauger, and H. Hultschig, Phys. Rev. Lett. **18**, 1014 (1967).

[38] W. Bartel, B. Dudelzak, H. Krehbiel, J. M. McElroy, U. Meyer-Berkhout, R. J. Morrison, H. Nguyen-Ngoc, W. Schmidt, and G. Weber, Phys. Lett. **25B**, 236 (1967).

[39] J. Litt, B. Buschhorn, D. R. Coward, H. Destaebler, L. M. Mo, R. E. Taylor, B. C. Barish, S. C. Loken, J. Pine, J. I. Friedman, G. G. Hartmann, and H. W. Kendall, Phys. Lett. **31B**, 40 (1970).

[40] Ch. Berger, E. Gersing, G. Knop, B. Langenbeck, K. Rith, and F. Schumacher, Phys. Lett. **28B**, 276 (1968).

[41] Ch. Berger, V. Burkert, G. Knop, B. Langenbeck, and K. Rith, Phys. Lett. **35B**, 87 (1971).

[42] M. Goitein, R. J. Budnitz, L. Carroll, J. Chen, J. R. Dunning, Jr., K. Hanson, D. Imrie, C. Mistretta, J. K. Walker, R. Wilson, G. F. Dell, M. Fotino, J. M. Paterson, and H. Winick, Phys. Rev. Lett. **18**, 1016 (1967).

[43] M. Goitein, R. J. Budnitz, L. Carroll, J. R. Chen, J. R. Dunning, Jr., K. Hanson, D. C. Imrie, C. Mistretta, and R. Wilson, Phys. Rev. D **1**, 2449 (1970).

[44] L. E. Price, J. R. Dunning, Jr., M. Goitein, K. Hanson, T. Kirk, and R. Wilson, Phys. Rev. D **4**, 45 (1971).

[45] D. Ganichot, B. Grossetête, and D. B. Isabelle, Nucl. Phys. **A178**, 545 (1972).

[46] Yu. K. Akimov *et al.*, JETP (Sov. Phys.) **35**, 651 (1972).

[47] W. Bartel, F.-W. Büszer, W.-R. Dix, R. Felst, D. Harms, H. Krehbiel, P. E. Kuhlmann, J. McElroy, and G. Weber, Phys. Lett. **33B**, 245 (1970).

[48] W. Bartel, F.-W. Büsser, W.-R. Dix, R. Felst, D. Harms, H. Krehbiel, P. E. Kuhlmann, J. McElroy, J. Meyer, and G. Weber, Nucl. Phys. **B58**, 429 (1973).

[49] D. H. Coward *et al.*, Phys. Rev. Lett. **20**, 292 (1968).

[50] P. N. Kirk *et al.*, Phys. Rev. D **8**, 63 (1973).

[51] H. Theissen and W. Schütz, Z. Phys. **266**, 33 (1974).

[52] J. J. Murphy, II, Y. M. Shin, and D. M. Skopik, Phys. Rev. C **9**, 2125 (1974).

[53] F. Borkowski, P. Peuser, G. G. Simon, V. H. Walther, and R. D. Wendling, Nucl. Phys. **A222**, 269 (1974).

[54] F. Borkowski, G. G. Simon, V. H. Walther, and R. D. Wendling, Nucl. Phys. **B93**, 461 (1975).

[55] G. G. Simon, Ch. Schmitt, F. Borkowski, and V. H. Walther, Nucl. Phys. **A333**, 381 (1980).

[56] P. E. Bosted *et al.*, Phys. Rev. Lett. **42**, 38 (1990).

[57] R. G. Arnold *et al.*, Phys. Rev. Lett. **57**, 174 (1986).

[58] A. F. Sill *et al.*, Phys. Rev. D **48**, 29 (1993).

[59] R. C. Walker *et al.*, Phys. Lett. **224B**, 353 (1989).

[60] R. C. Walker *et al.*, Phys. Lett. **49**, 5671 (1994).

[61] P. E. Bosted *et al.*, Phys. Rev. Lett. **68**, 3841 (1992).

[62] L. Andivahis *et al.*, Phys. Rev. D **50**, 5491 (1994).

[63] R. Rosenfelder, Phys. Lett. B **479**, 381 (2000).

[64] H. Gao, Int. J. Mod. Phys. E **12**, 1 (2003).

[65] J. L. Friar, `arXiv:nucl-th/0207065`

[66] K. Melnikov and T. van Ritbergen, Phys. Rev. Lett. **84**, 1673 (2000).

[67] R. Hofstadter, Rev. Mod. Phys. **28**, 214 (1956).

[68] L. Durand, III, Phys. Rev. **115**, 1020 (1959).

[69] L. Durand, III, Phys. Rev. **123**, 1393 (1961).

[70] F. M. Renard, J. Tran Thanh Van, and M. Le Bellac, Nuovo Cimento, **38**, 565 (1965).

[71] F. M. Renard, J. Tran Thanh Van, and M. Le Bellac, Nuovo Cimento, **38**, 1688 (1965).

[72] V. Glaser and B. Jakšić, Nuovo Cimento **5**, 1197 (1957).

[73] M. Gourdin, Nuovo Cimento **28**, 533 (1963).

[74] R. M. Littauer, H. F. Schopper, and R. R. Wilson, Phys. Rev. Lett. **7**, 141 (1961).

[75] P. Stein, R. W. McAllister, B. D. McDaniel, and W. M. Woodward, Phys. Rev. Lett. **9**, 403 (1962).

[76] R. Hofstadter, C. de Vries, and R. Herman, Phys. Rev. Lett. **6**, 290 (1961).

[77] R. Hofstadter and R. Herman, Phys. Rev. Lett. **6**, 293 (1961).

[78] C. de Vries, R. Hofstadter, and R. Herman, Phys. Rev. Lett. **8**, 381 (1962).

[79] C. de Vries, R. Hofstadter, A. Johansson, and R. Herman, Phys. Rev. **134**, B848 (1964).

[80] J. Nuttall and M. L. Whippman, Phys. Rev. **130**, 2495 (1963).

[81] C. W. Akerlof, K. Berkelman, G. Rouse, and M. Tigner, Phys. Rev. **135**, B810 (1964).

[82] E. B. Hughes, T. A. Griffy, M. R. Yearian, and R. Hofstadter, Phys. Rev. **139**, B458 (1965).

[83] J. R. Dunning, Jr., K. W. Chen, A. A. Cone, G. Hartwig, N. F. Ramsey, J. K. Walker, and R. Wilson, Phys. Rev. Lett. **13**, 631 (1964).

[84] J. R. Dunning, Jr., K. W. Chen, A. A. Cone, G. Hartwig, H. F. Ramsey, J. K. Walker, and R. Wilson, Phys. Rev. **141**, 1286 (1966).

[85] P. Stein, M. Binkley, R. McAllister, A. Suri, and W. Woodward, Phys. Rev. Lett. **16**, 592 (1966).

[86] E. B. Hughes, T. A. Griffy, R. Hofstadter, and M. R. Yearian, Phys. Rev. **146**, 973 (1966).

[87] W. Albrecht, H.-J. Behrend, H. Dorner, W. Flauger, and H. Hultschig, Phys. Lett. **26B**, 642 (1968).

[88] R. Budnitz, J. Appel, L. Carroll, J. Chen, J. R. Dunning, Jr., M. Goitein, K. Hanson, D. Imrie, C. Mistretta, J. K. Walker, and R. Wilson, Phys. Rev. Lett. **19**, 809 (1967).

[89] R. J. Budnitz, J. Appel, L. Carroll, J. Chen, J. R. Dunning, Jr., M. Goitein, K. Hanson, D. Imrie, C. Mistretta, J. K. Walker, and R. Wilson, Phys. Rev. **173**, 1357 (1968).

[90] W. Bartel, F.-W. Büsser, W.-R. Dix, R. Felst, D. Harms, H. Krehbiel, P. E. Kuhlmann, J. McElroy, W. Schmidt, V. Walther, and G. Weber, Phys. Lett. **30B**, 285 (1969).

[91] W. Bartel, F.-W. Büsser, W.-R. Dix, R. Felst, D. Harms, H. Krehbiel, P. E. Kuhlman, J. McElroy, J. Meyer, and G. Weber, Phys. Lett. **39B**, 407 (1972).

[92] K. M. Hanson, J. R. Dunning, Jr., M. Goitein, T. Kirk, L. E. Price, and R. Wilson, Phys. Rev. D **8**, 753 (1973).

[93] S. Rock, R. G. Arnold, P. Bosted, B. T. Chertok, B. A. Mecking, I. Schmidt, Z. M. Szalata, R. C. York, and R. Zdarko, Phys. Rev. Lett. **49**, 1139 (1982).

[94] A. S. Esaulov, A. P. Rekalo, M. P. Rekalo, Yu. I. Titov, R. V. Akhmerov, and E. M. Smelov, Sov. J. Nucl. Phys. **45**, 258 (1987).

[95] R. G. Arnold *et al.*, Phys. Rev. Lett. **61**, 806 (1988).

[96] A. Lung *et al.*, Phys. Rev. Lett. **70**, 718 (1993).

[97] P. Markowitz *et al.*, Phys. Rev. C **48**, R5 (1993).

[98] W. Fabian and H. Arenhövel, Nucl. Phys. **A314**, 253 (1979).

[99] H. Arenhövel, Nucl. Phys. **A384**, 287 (1982).

[100] H. Anklin *et al.*., Phys. Lett. B **336**, 313 (1994).

[101] E. Hummel and J. A. Tjon, Phys. Rev. Lett. **63**, 1788 (1989).

[102] E. Hummel and J. A. Tjon, Phys. Rev. C **42**, 423 (1990).

[103] E. E. W. Bruins *et al.*, Phys. Rev. Lett. **75**, 21 (1995).

[104] H. Anklin *et al.*, Phys. Lett. B **428**, 248 (1998).

[105] G. Kubon *et al.*, Phys. Lett. B **524**, 26 (2002).

[106] B. Grossetête, D. Treille, and P. Lehmann, Nuovo Cimento **28**, 240 (1963).

[107] T. Hamada and J. D. Johnston, Nucl. Phys. **34**, 382 (1962).

[108] B. Grossetête, D. Drickey, and P. Lehmann, Phys. Rev. **141**, 1425 (1966).

[109] B. Grossetête, S. Jullian, and P. Lehmann, Phys. Rev. **141**, 1435 (1966).

[110] B. Bosco, B. Grossetête, and P. Quarati, Phys. Rev. **141**, 1441 (1966).

[111] D. Benaksas, D. Drickey, and D. Frèrejacque, Phys. Rev. Lett. **13**, 353 (1964).

[112] D. Benaksas, D. Drickey, and D. Frèrejacque, Phys. Rev. **148**, 1327 (1966).

[113] F. A. Bumiller, F. R. Buskirk, J. W. Stewart, and E. B. Dally, Phys. Rev. Lett. **25**, 1774 (1970).

[114] H. Feshbach and E. Lomon, Rev. Mod. Phys. **39**, 611 (1967).

[115] F. Gross, Phys. Rev. **142**, 1025 (1966); Phys. Rev. **152**, 1517(E) (1966).

[116] B. M. Casper and F. Gross, Phys. Rev. **155**, 1607 (1967).

[117] S. Galster, H. Klein, J. Moritz, K. H. Schmidt, D. Wegener, and J. Bleckwenn, Nucl. Phys. B **32**, 221 (1971).

[118] R. W. Berard, F. R. Buskirk, E. B. Dally, J. N. Dyer, X. K. Maruyama, R. L. Topping, and T. J. Traverso, Phys. Lett. **47B**, 355 (1973).

[119] G. G. Simon, C. Schmitt, and V. H. Walther, Nucl. Phys. **A364**, 285 (1981).

[120] R. V. Reid, Ann. Phys. **50**, 411 (1968).

[121] W. Fabian and H. Arenhövel, Nucl. Phys. **A258**, 461 (1976).

[122] W. Fabian and H. Arenhövel, Phys. Rev. Lett. **37**, 550 (1976).

[123] S. Platchkov, A. Amroun, S. Auffret, J. M. Cavedon, P. Dreux, J. Duclos, B. Frois, D. Goutte, H. Hachemi, J. Martino, X. H. Phan, and I. Sick, Nucl. Phys. **A510**, 740 (1990).

[124] M. Lacombe, B. Loiseau, R. Vinh Mau, J. Cote, P. Pires, and R. de Tourreil, Phys. Lett. **101B**, 139 (1981).

[125] R. G. Arnold, C. E. Carlson, and F. Gross, Phys. Rev. C **21**, 1426 (1980).

[126] B. Mosconi and P. Ricci, Few-Body Systems **6**, 63 (1989).

[127] J. Jourdan, I. Sick, and J. Zhao, Phys. Rev. Lett. **79**, 5186 (1997).

[128] E. E. W. Bruins *et al.*, Phys. Rev. Lett. **79**, 5187 (1997).

[129] L. Hulthén and M. Sugawara, Handbuch der Physik, edited by S. Flugge (Springer-Verlag, Berlin, 1957), Vol. 39, p. 1.

[130] I. McGee, Phys. Rev. **151**, 772 (1966).

[131] S. Auffret, J. M. Cavedon, J. C. Clemens, B. Frois, D. Goutte, M. Huet, Ph. Leconte, J. Martino, Y. Mizuno, X. H. Phan, S. Platchkov, and I. Sick, Phys. Rev. Lett. **54**, 649 (1985).

[132] R. Cramer, M. Renkhoff, J. Drees, U. Ecker, D. Jagoda, K. Koseck, G. R. Pingel, B. Remenschnitter, A. Ritterskamp, B. Boden, V. Burkert, G. Knop, M. Lenen, R. Sauerwein, and D. Schablitzky, Z. Phys. C **29**, 513 (1985).

[133] R. G. Arnold *et al.*, Phys. Rev. Lett. **58**, 1723 (1987).

[134] R. B. Wiringa, R. A. Smith, and T. A. Ainsworth, Phys. Rev. C **29**, 1207 (1984).

[135] M. M. Nagels, T. A. Rijken, and J. de Swaart, Phys. Rev. D **17**, 768 (1978).

[136] L. L. Foldy, Rev. Mod. Phys. **30**, 471 (1958).

[137] V. E. Krohn and G. R. Ringo, Phys. Rev. **148**, 1303 (1966).

[138] V. E. Krohn and G. R. Ringo, Phys. Rev. D **8**, 1305 (1973).

[139] Yu. A. Aleksandrov, J. Vávra, M. Vrana, I. Kulda, T. A. Machekhina, P. Mikula, R. Michalec, V. M. Nazarov, A. I. Okorokov, V. F. Peresedov, V. V. Runov, L. N. Sedlakova, and B. Chalupa, Sov. Phys. JETP **62**, 19 (1985).

[140] H. Leeb and C. Teichtmeister, Phys. Rev. C **48**, 1719 (1993).

[141] Yu. A. Alexandrov, Phys. Rev. C **49**, R2297 (1994).

[142] S. Kopecky, P. Riehs, J. A. Harvey, and N. W. Hill, Phys. Rev. Lett. **74**, 2427 (1995).

[143] L. Koester, W. Waschkowski, L. V. Mitsyna, G. S. Samosvat, P. Prokofjevs, and J. Tambergs, Phys. Rev. C **51**, 3363 (1995).

[144] S. Kopecky, J. A. Harvey, N. W. Hill, M. Krenn, M. Pernicka, P. Riehs, and S. Steiner, Phys. Rev. C **56**, 2229 (1997).

[145] V. F. Sears, Phys. Rep. **141**, 281 (1986).

[146] L. Koester, W. Nistler, and W. Waschkowski, Phys. Rev. Lett. **36**, 1021 (1976).

[147] L. Koester, W. Waschkowski, and A. Klüver, Physica B **137**, 282 (1986).

[148] Yu. A. Alexandrov, Nucl. Instr. and Meth. A **284**, 134 (1989).

[149] Yu. A. Alexandrov, T. A. Machekhina, L. N. Sedlakova, and L. E. Fyrkin, Sov. J. Nucl. Phys. **20**, 623 (1975).

[150] Yu. A. Alexandrov, M. Vrana, Garcia J. Manrique, T. A. Manchekhina, and L. N. Sedlakova, Sov. J. Nucl. Phys. **44**, 900 (1986).

[151] N. Isgur, Phys. Rev. Lett. **83**, 272 (1999).

[152] F. Cardarelli and S. Simula, Phys. Lett. B **467**, 1 (1999).

[153] F. Cardarelli and S. Simula, Phys. Rev. C **62**, 065201 (2000).

[154] D. B. Leinweber, A. W. Thomas, and R. D. Young, Phys. Rev. Lett. **86**, 5011 (2001).

[155] A. Bincer, Phys. Rev. **107**, 1467 (1957).

[156] J. H. Scofield, Phys. Rev. **113**, 1599 (1959).

[157] J. H. Scofield, Phys. Rev. **141**, 1352 (1966).

[158] N. Dombey, Rev. Mod. Phys. **41**, 236 (1969).

[159] A. I. Akhiezer and M. P. Rekalo, Sov. J. Part. Nucl. **4**, 277 (1974).

[160] R. G. Arnold, C. E. Carlson, and F. Gross, Phys. Rev. C **23**, 363 (1981).

[161] T. W. Donnelly in *Modern Topics in Electron Scattering*, edited by B. Frois and I. Sick (World Scientific, 1991).

[162] R. Hagedorn, *Relativisic Kinematics* (The Benjamin Cummings Publishing Company, Inc., 1963).

[163] T. W. Donnelly and A. S. Raskin, Ann. Phys. **169**, 247 (1986).

[164] A. S. Raskin and T. W. Donnelly, Ann. Phys. **191**, 78 (1989).

[165] J. J. Kelly, Adv. Nucl. Phys. **23**, 75 (1996).

[166] H. Arenhövel, W. Leidemann, and E. L. Tomusiak, Z. Phys. A **331**, 123 (1988).

[167] B. Blankleider and R. M. Woloshyn, Phys. Rev. C **29**, 538 (1984).

[168] J. L. Friar, B. F. Gibson, G. L. Payne, A. M. Bernstein, and T. E. Chupp, Phys. Rev. C **42**, 2310 (1990).

[169] C. Ciofi degli Atti, E. Pace, and G. Salmè, Phys. Rev. C **46**, R1591 (1992).

[170] R.-W. Schulze and P. U. Sauer, Phys. Rev. C **48**, 38 (1993).

[171] I. R. Afnan and N. D. Birrell, Phys. Rev. C **16**, 823 (1977).

[172] J. Berakdar, Phys. Rev. Lett. **85**, 4036 (2000).

[173] L. D. Faddeev, Sov. Phys. JETP **12**, 1014 (1961).

[174] J. M. Laget, Phys. Lett. **273B**, 367 (1991).

[175] C. Y. Cheung and R. M. Woloshyn, Phys. Lett. **127B**, 147 (1983).

[176] E. L. Tomusiak and H. Arenhövel, Phys. Lett. **206B**, 187 (1988).

[177] H. Arenhövel, W. Leidemann, and E. L. Tomusiak, Phys. Rev. C **46**, 455 (1992).

[178] H. Arenhövel, W. Leidemann, and E. L. Tomusiak, Phys. Rev. C **52**, 1232 (1992).

[179] W. Leidemann, E. L. Tomusiak, and H. Arenhövel, Phys. Rev. C **43**, 1022 (1991).

[180] W. Leidemann and H. Arenhövel, Phys. Lett. **184B**, 7 (1987).

[181] H. Arenhövel, private communication (2001, 2002, 2003).

[182] A. F. J. Siegert, Phys. Rev. **52**, 787 (1937).

[183] R. J. Blin-Stoyle in *Mesons in Nuclei Volume I*, edited by M. Rho and D. Wilkinson (North-Holland Publishing Company, 1979).

[184] T. Wilbois, G. Beck, and H. Arenhövel, Few-Body Syst. **15**, 39 (1993).

[185] R. Machleidt, K. Holinde, and Ch. Elster, Phys. Rep. **149**, 1 (1987).

[186] R. B. Wiringa, V. G. J. Stoks, and R. Schiavilla, Phys. Rev. C **51**, 38 (1995).

[187] S. M. Wong, *Nuclear Physics* (John Wiley and Sons, Inc., 1998).

[188] R. A. Arndt, I. I. Strakovsky, and R. L. Workman, Int. J. Mod. Phys. A **18**, 449 (2003).

[189] H. Arenhövel, Phys. Lett. **199B**, 13 (1987).

[190] M. P. Rekalo, G. I. Rakh, and A. P. Rekalo, J. Phys. G: Nucl. Part. Phys. **15**, 1223 (1989).

[191] The Madison Convention, in *Polarization Phenomena in Nuclear Reactions*, edited by H. H. Barschall and W. Haeberli (University of Wisconsin Press, 1970).

[192] H. Arenhövel, "Kinematics of Deuteron Electrodisintegration", unpublished.

[193] D. Abbott *et al.*, Phys. Rev. Lett. **84**, 5053 (2000).

[194] D. M. Nikolenko *et al.*, Phys. Rev. Lett. **90**, 072501 (2003).

[195] R. Schiavilla and I. Sick, Phys. Rev. C **64**, 041002(R) (2001).

[196] C. E. Jones-Woodward *et al.*, Phys. Rev. C **44**, R571 (1991).

[197] A. K. Thompson *et al.*, Phys. Rev. Lett. **68**, 2901 (1992).

[198] H. Gao *et al.*, Phys. Rev. C **50**, R546 (1994).

[199] W. Xu *et al.*, Phys. Rev. Lett. **85**, 2900 (2000).

[200] W. Xu *et al.*, Phys. Rev. C **67**, 012201(R) (2003).

[201] M. Meyerhoff *et al.*, Phys. Lett. B **327**, 201 (1994).

[202] J. Becker *et al.*, Eur. Phys. J. A **6**, 329 (1999).

[203] J. Golak, G. Ziemer, H. Kamada, H. Watala, and W. Glöckle, Phys. Rev. C **63**, 034006 (2001).

[204] D. Rohe *et al.*, Phys. Rev. Lett. **83**, 4257 (1999).

[205] J. Bermuth *et al.*, Phys. Lett. B **564**, 199 (2003).

[206] J. Golak, W. Glöckle, H. Kamada, H. Witala, R. Skibiński, and A. Nogga, Phys. Rev. C **65**, 044002 (2002).

[207] I. Passchier *et al.*, Phys. Rev. Lett. **82**, 4988 (1999).

[208] H. Zhu *et al.*, Phys. Rev. Lett. **87**, 081801 (2001)

[209] G. Warren *et al.*, `arXiv:nucl-ex/0308021`, submitted to Phys. Rev. Lett.

[210] T. Eden *et al.*, Phys. Rev. C **50**, R1749 (1994).

[211] R. Madey, A. R. Baldwin, P. J. Pella, J. Schambach, and R. M. Sellers, IEEE Trans. Nucl. Sci. **36**, 231 (1989).

[212] B. D. Milbrath *et al.*, Phys. Rev. Lett. **80**, 452 (1998); **82**, 2221(E) (1999).

[213] M. Ostrick *et al.*, Phys. Rev. Lett. **83**, 276 (1999).

[214] C. Herberg *et al.*, Eur. Phys. J. A **5**, 131 (1999).

[215] M. K. Jones *et al.*, Phys. Rev. Lett. **84**, 1398 (2000).

[216] O. Gayou *et al.*, Phys. Rev. Lett. **88**, 092301 (2002).

[217] Th. Pospischil *et al.*, Eur. Phys. J. A **12**, 125 (2001).

[218] R. Madey, A. Yu. Semenov, S. Taylor, B. Plaster *et al.*, Phys. Rev. Lett. **91**, 122002 (2003).

[219] J. Arrington, Phys. Rev. C. **68**, 034325 (2003).

[220] J. Arrington, `arXiv:nucl-ex/0309011`, submitted to Phys. Rev. C.

[221] A. Afanasev, I. Akushevich, and N. P. Merenkov, `arXiv:hep-ph/0208260`

[222] P. A. M. Guichon and M. Vanderhaeghen, Phys. Rev. Lett. **91**. 142303 (2003).

[223] P. G. Blunden, W. Melnitchouk, and J. A. Tjon, Phys. Rev. Lett. **91**, 142304 (2003).

[224] Jefferson Laboratory proposal E01-109, E. Brash, M. K. Jones, C. F. Perdrisat, and V. Punjabi, spokespersons.

[225] Jefferson Laboratory proposal E01-001, J. Arrington and R. Segel, spokespersons.

[226] MIT-Bates Linear Accelerator proposal E01-01, J. R. Calarco, H. Kolster, and H. Gao, spokespersons.

[227] MIT-Bates Linear Accelerator proposal E00-02, J. R. Calarco and H. Gao, spokespersons.

[228] S. G. Karshenboim, arXiv:hep-ph/0008137

[229] Jefferson Laboratory proposal E02-013, G. Cates, K. McCormick, B. Reitz, B. Wojtsekhowski, spokespersons.

[230] Jefferson Laboratory proposal E94-017, W. Brooks and M. Vineyard, spokespersons.

[231] G. G. Petratos, Nucl. Phys. **A666&667**, 61c (2000).

[232] S. J. Brodsky and G. R. Farrar, Phys. Rev. D **11**, 1309 (1975).

[233] G. P. Lepage and S. J. Brodsky, Phys. Rev. Lett. **43**, 545 (1979).

[234] G. P. Lepage and S. J. Brodsky, Phys. Rev. D **22**, 2157 (1980).

[235] J. P. Ralston and P. Jain, arXiv:hep-ph/0302043

[236] G. A. Miller and M. R. Frank, Phys. Rev. C **65**, 065205 (2002).

[237] H. Goldstein, *Classical Mechanics* (Addison-Wesley Publishing Company, 1980).

[238] A. V. Belitsky, X. Ji, and F. Yuan, Phys. Rev. Lett. **91**, 092003 (2003).

[239] J. J. Sakurai, *Currents and Mesons* (University of Chicago Press, 1969).

[240] R. P. Feynman, *Photon-Hadron Interactions* (Addison-Wesley, 1972).

[241] F. Iachello, A. D. Jackson, and A. Lande, Phys. Lett. **43B**, 191 (1973).

[242] M. Gari and W. Krümpelmann, Z. Phys. A **322**, 689 (1985).

[243] M. F. Gari and W. Krümpelmann, Phys. Lett. B **274**, 159 (1992).

[244] E. L. Lomon, Phys. Rev. C **64**, 035204 (2001).

[245] E. L. Lomon, Phys. Rev. C **66**, 045501 (2002).

[246] G. B. Arfken and H. J. Weber, *Mathematical Methods for Physicists* (Academic Press, 1995).

[247] G. Höhler, E. Pietarinen, I. Sabba-Stefanescu, F. Borskowski, G. G. Simon, V. H. Walther, and R. D. Wendling, Nucl. Phys. **B114**, 505 (1976).

[248] P. Mergell, U.-G. Meissner, and D. Drechsel, Nucl. Phys. A **596**, 367 (1996).

[249] H.-W. Hammer, U.-G. Meissner, and D. Drechsel, Phys. Lett. B **385**, 343 (1996).

[250] R. Calabrese, Nucl. Phys. **A666&667**, 84c (2000).

[251] T. H. R. Skyrme, Proc. R. Soc. London **A260**, 127 (1961).

[252] T. H. R. Skyrme, Nucl. Phys. **31**, 556 (1962).

[253] E. Braaten, S.-M. Tse, and C. Willcox, Phys. Rev. Lett. **56**, 2008 (1986).

[254] E. Braaten, S.-M. Tse, and C. Willcox, Phys. Rev. D **34**, 1482 (1986).

[255] E. Witten, Nucl. Phys. **B223**, 422 (1983).

[256] E. Witten, Nucl. Phys. **B223**, 433 (1983).

[257] G. S. Adkins, C. R. Nappi, and E. Witten, Nucl. Phys. **B228**, 552 (1983).

[258] G. Holzwarth, Z. Phys. A **356**, 339 (1996).

[259] G. Holzwarth, `arXiv:hep-ph/0201138`

[260] K. J. Barnes, P. Carruthers, and F. von Hippel, Phys. Rev. Lett. **14**, (1965).

[261] N. Isgur, G. Karl, and D. W. L. Sprung, Phys. Rev. D **23**, 163 (1981).

[262] P. A. M. Dirac, Rev. Mod. Phys. **21**, 392 (1949).

[263] G. A. Miller, arXiv:nucl-th/0206027

[264] F. Cardarelli, E. Pace, G. Salmè, and S. Simula, Phys. Lett. B **357**, 267 (1995).

[265] S. Simula, arXiv:nucl-th/0105024

[266] S. Godfrey and N. Isgur, Phys. Rev. D **32**, 185 (1985).

[267] S. Capstick and N. Isgur, Phys. Rev. D **34**, 2809 (1986).

[268] H. J. Melosh, Phys. Rev. D **9**, 1095 (1974).

[269] G. A. Miller, Phys. Rev. C **66**, 032201(R) (2002).

[270] V. B. Berestetskii and M. V. Terent'ev, Sov. J. Nucl. Phys. **25**, 347 (1977).

[271] P. L. Chung and F. Coester, Phys. Rev. D **44**, 229 (1991).

[272] R. F. Wagenbrunn, S. Boffi, W. Klink, W. Plessas, and M. Radici, Phys. Lett. B **511**, 33 (2001).

[273] S. Boffi, L. Ya. Glozman, W. Klink, W. Plessas, M. Radici, and R. F. Wagenbrunn, Eur. Phys. J. A **14**, 17 (2002).

[274] L. Ya. Glozman, W. Plessas, K. Varga, and R. F. Wagenbrunn, Phys. Rev. D **58**, 094030 (1998).

[275] M. M. Kaskulov and P. Grabmayr, Phys. Rev. C **67**, 042201(R) (2003).

[276] M. M. Kaskulov and P. Grabmary, arXiv:nucl-th/0308105

[277] M. M. Kaskulov, private communication (2003).

[278] F. E. Close, Phys. Lett. **43B**, 422 (1973).

[279] R. D. Field and R. P. Feynman, Phys. Rev. D **15**, 2590 (1977).

[280] B.-Q. Ma, Phys. Lett. B **375**, 320 (1996).

[281] B.-Q. Ma, Phys. Rev. C **65**, 035205 (2002).

[282] D. G. Richards, `arXiv:nucl-th/0006020`

[283] S. J. Dong, K. F. Liu, and A. G. Williams, Phys. Rev. D **58**, 074504 (1998).

[284] A. Tang, W. Wilcox, and R. Lewis, `arXiv:hep-lat/0307006`

[285] J. D. Ashley, D. B. Leinweber, A. W. Thomas, and R. D. Young, `arXiv:hep-lat/0308024`

[286] K. A. Aniol *et al.*, Phys. Rev. Lett. **82**, 1096 (1999).

[287] W. Bertozzi, J. Friar, J. Heisenberg, and J. W. Negele, Phys. Lett. **41B**, 408 (1972).

[288] A. V. Radyushkin, Phys. Lett. B **380**, 417 (1996).

[289] A. V. Radyushkin, Phys. Lett. B **385**, 333 (1996).

[290] A. V. Radyushkin, Phys. Rev. D **56**, 5524 (1997).

[291] X. Ji, Phys. Rev. Lett. **78**, 610 (1997).

[292] X. Ji, Phys. Rev. D **55**, 7114 (1997).

[293] C. W. Leemann, D. R. Douglas, and G. A. Krafft, Ann. Rev. Nucl. Part. Sci. **51**, 413 (2001).

[294] C. K. Sinclair, Jefferson Laboratory Technical Note TJNAF-TN-97-021.

[295] M. Poelker, P. Adderley, J. Clark, A. Day, J. Grames, J. Hansknecht, P. Hartmann, R. Kazimi, P. Rutt, C. Sinclair, and M. Steigerwald, Proceedings of the 14th International Spin Physics Symposium, edited by K. Hatanaka, T. Nakano, K. Imai, and H. Ejiri, A.I.P. Conf. Proc. **570**, 943 (2001).

[296] J. E. Clendenin, Stanford Linear Accelerator Center Technical Note SLAC-PUB-95-6842 (1995).

[297] M. J. Alguard *et al.*, Phys. Rev. Lett. **37**, 1621 (1976).

[298] M. J. Alguard *et al.*, Phys. Rev. Lett. **41**, 70 (1976).

[299] G. Baum *et al.*, Phys. Rev. Lett. **45**, 2000 (1980).

[300] G. Baum *et al.*, Phys. Rev. Lett. **51**, 1135 (1983).

[301] E. L. Garwin *et al.*, Helv. Phys. Acta **47**, 393 (1974).

[302] G. Lampel and C. Weisleuch, Solid State Comm. **16**, 877 (1975).

[303] C. Y. Prescott *et al.*, Phys. Lett. **77B**, 347 (1978).

[304] C. Y. Prescott *et al.*, Phys. Lett. **84B**, 524 (1979).

[305] W. Heil *et al.*, Nucl. Phys. **B327**, 1 (1989).

[306] P. A. Souder *et al.*, Phys. Rev. Lett. **65**, 694 (1990).

[307] B. Mueller *et al.*, Phys. Rev. Lett. **78**, 3824 (1997).

[308] R. Hasty *et al.*, Science **290**, 2117 (2000).

[309] D. T. Spayde *et al.*, Phys. Rev. Lett. **84**, 1106 (2000).

[310] T. M. Ito *et al.*, `arXiv:nucl-ex/0310001`, submitted to Phys. Rev. Lett.

[311] K. A. Aniol *et al.*, Phys. Lett. B **509**, 211 (2001).

[312] Jefferson Laboratory proposal E00-006, D. Beck, spokesperson.

[313] Jefferson Laboratory proposal E99-115, K. Kumar, spokesperson.

[314] Jefferson Laboratory proposal E00-114, D. Armstrong and R. Michaels, spokespersons.

[315] Jefferson Laboratory proposal E03-011, R. Michaels, P. A. Souder, and G. M. Urciuoli.

[316] MAMI Experiment A4, D. von Harrach, spokesperson, F. E. Maas, contact person.

[317] Stanford Linear Accelerator Center experiment 158, K. Kumar, E. Hughes, and P. A. Souder, spokespersons.

[318] Jefferson Laboratory proposal 02-020, J. D. Bowman, R. Carlini, J. M. Finn, S. Kowalski, and S. Page, spokespersons.

[319] G. Fishman and G. Lampel, Phys. Rev. B **16**, 820 (1977).

[320] I. Goroff and L. Kleinman, Phys. Rev. **132**, 1080 (1963).

[321] F. H. Pollak and M. Cardona, Phys. Rev. **172**, 816 (1968).

[322] T. Maruyama, E. L. Garwin, R. Prepost, G. H. Zapalac, J. S. Smith, and J. D. Walker, Phys. Rev. Lett. **66**, 2376 (1991).

[323] T. Maruyama, E. L. Garwin, R. Prepost, and G. H. Zapalac, Phys. Rev. B **46**, 4261 (1992).

[324] M. Poelker and J. Hansknecht, Proceedings of the IEEE Particle Accelerator Conference (PAC 2001), edited by P. Lucas and S. Webber, 95 (2001).

[325] M. Poelker, private communication (2003).

[326] C. K. Sinclair, Proceedings of the IEEE Particle Accelerator Conference (PAC 1999), edited by A. U. Luccio and W. W. MacKay, 65 (1999).

[327] H. Tang, R. Alley, J. Clendenin, J. Frisch, G. Mulhollan, P. Saez, D. Schultz, and K. Witte, Stanford Linear Accelerator Center Technical Note SLAC-PUB-6918 (1995).

[328] W. Diamond, Jefferson Laboratory Technical Note CEBAF-PR-87-011.

[329] J. D. Jackson, *Classical Electrodynamics* (John Wiley and Sons, Inc., 1999).

[330] J. Grames, Proceedings of the IEEE Particle Accelerator Conference (PAC 2001), edited by P. Lucas and S. Webber, 2392 (2001).

[331] The JLab Spin Rotation Calculator Web Site:
`http://clasweb.jlab.org/spin_rotation/`

[332] J. Arrington, Ph.D. thesis, California Institute of Technology (1998).

[333] K. Gustafsson, Ph.D. thesis, University of Maryland (2000).

[334] W. Tireman, Ph.D. thesis, Kent State University (2003).

[335] H. Zhu, Ph.D. thesis, University of Virginia (2000).

[336] C. Yan, P. Adderley, D. Barker, J. Beaufait, K. Capek, R. Carlini, J. Dahlberg, E. Feldl, K. Jordan, B. Kross, W. Oren, R. Wojcik, and J. VanDyke, Nucl. Inst. and Meth. A **365**, 261 (1995).

[337] K. Unser, Proceedings of the Accelerator Instrumentation Workshop, edited by W. Barry and P. Kloeppel, A.I.P. Conf. Proc. **252**, 266 (1992).

[338] R. Wojcik and C. Yan, Nucl. Inst. and Meth. A **484**, 690 (2002).

[339] C. Yan, P. Adderley, R. Carlini, C. Cuevas, W. Vulcan, and R. Wines, Nucl. Inst. and Meth. A **365**, 46 (1995).

[340] C. Møller, Annalen der Physik **14**, 531 (1932).

[341] M. Hauger *et al.*, Nucl. Inst. and Meth. A **462**, 382 (2001).

[342] L. L. DeRaad and Y. Ng, Phys. Rev. D **11**, 1586 (1975).

[343] B. Wagner, H. G. Andresen, K. H. Steffens, W. Hartmann, W. Heil, and E. Reichert, Nucl. Inst. and Meth. A **294**, 541 (1990).

[344] J. Arrington, E. J. Beise, B. W. Filippone, T. G. O'Neill, W. R. Dodge, G. W. Dodson, K. A. Dow, and J. D. Zumbro, Nucl. Inst. and Meth. A **311**, 39 (1992).

[345] L. G. Levchuk, Nucl. Inst. and Meth. A **345**, 496 (1994).

[346] L. deBever, J. Jourdan, M. Loppacher, S. Robinson, I. Sick, and J. Zhao, Nucl. Inst. and Meth. A **400**, 379 (1997).

[347] R. A. Reck and D. L. Fry, Phys. Rev. **184**, 492 (1969).

[348] U. Fano, Opt. Soc. Amer. **39**, 859 (1949).

[349] I. Passchier, D. W. Higinbotham, C. W. de Jager, B. E. Norum, N. H. Papadakis, and N. P. Vodinas, Nucl. Inst. and Meth. A **414**, 446 (1998).

[350] D. P. Barber *et al.*, Nucl. Inst. and Meth. A **329**, 79 (1993).

[351] N. Falletto *et al.*, Nucl. Inst. and Meth. A **459**, 412 (2001).

[352] J. Alcorn *et al.*, submitted to Nucl. Inst. and Meth. A, `http://hallaweb.jlab.org/equipment/NIM-A.ps`

[353] S. Kowalski, private communication (2001, 2002, 2003).

[354] G. Smith, private communication (2001).

[355] `http://www.jlab.org/Hall-C/equipment/HMS.html`

[356] O. K. Baker, J. Beaufait, R. Carlini, J. Cha, S. Danagoulian, A. Johnson, B. Kross, S. Majewski, A. McCauley, W. Naing, G. Niculescu, I. Niculescu, T. S. Shin, and W. Vulcan, Nucl. Inst. and Meth. A **367**, 92 (1995).

[357] W. R. Leo, *Techniques for Nuclear and Particle Physics Experiments* (Springer-Verlag, Berlin, Germany, 1987).

[358] D. H. Perkins, *Introduction to High Energy Physics* (Addison-Wesley Publishing Company, Inc., Menlo Park, California, 1987).

[359] Review of Particle Physics Part I, Phys. Rev. D **66** (2002).

[360] L. Wolfenstein, Phys. Rev. **75**, 1664 (1949).

[361] L. Wolfenstein and J. Ashkin, Phys. Rev. **85**, 947 (1952).

[362] R. Madey and F. M. Waterman, Nucl. Inst. and Meth. **106**, 89 (1973).

[363] R. Madey, F. M. Waterman, and A. R. Baldwin, Nucl. Inst. and Meth. **133**, 61 (1976).

[364] A. R. Baldwin and R. Madey, Nucl. Inst. and Meth. **171**, 149 (1980).

[365] R. Madey, J. W. Watson, M. Ahmad, B. D. Anderson, A. R. Baldwin, A. L. Casson, W. Casson, R. A. Cecil, A. Fazely, J. M. Knudson, C. Lebo, W. Pairsuwan, P. J. Pella, J. C. Varga, and T. R. Wittin, Nucl. Inst. and Meth. **214**, 401 (1983).

[366] J. W. Watson, M. R. Plumley, P. J. Pella, B. D. Anderson, A. R. Baldwin, and R. Madey, Nucl. Inst. and Meth. A **272**, 750 (1988).

[367] B. D. Anderson, R. J. McCarthy, M. Ahmad, A. Fazely, A. M. Kalenda, J. N. Knudson, J. W. Watson, R. Madey, and C. C. Foster, Phys. Rev. C **26**, 8 (1982).

[368] B. D. Anderson, T. Chittrakarn, A. R. Baldwin, C. Lebo, R. Madey, P. C. Tandy, J. W. Watson, B. A. Brown, and C. C. Foster, Phys. Rev. C **31**, 1161 (1985).

[369] J. W. Watson, P. J. Pella, B. D. Anderson, A. R. Baldwin, T. Chittrakarn, B. S. Flanders, R. Madey, C. C. Foster, and I. J. Van Heerden, Phys. Lett. **B181**, 47 (1986).

[370] J. W. Watson, B. D. Anderson, and R. Madey, Can. J. Phys. **65**, 566 (1987).

[371] T. Eden *et al.* Nucl. Inst. and Meth. A **338**, 432 (1994).

[372] T. Eden, Ph.D. thesis, Kent State University (1993).

[373] R. Madey, private communcation (2001, 2003, 2003).

[374] R. Madey, A. Lai, and T. Eden, Proceedings of the Polarization Phenomena in Nuclear Physics Conference, edited by E. J. Stephenson and S. E. Vigdor, A.I.P. Conf. Proc. **339**, 47 (1995).

[375] I. Niculescu *et al.*, IEEE Trans. Nucl. Sci. **45**, 68 (1998).

[376] R. Madey, Bull. Am. Phys. Soc. **41**, 1260 (1996).

[377] R. Madey and T. Eden, "Beam Current Limitations for JLab E93-038", E93-038 internal report (June 23, 1999).

[378] R. Madey, A. Semenov, and P. Degtiarenko, "Beam Current Limitations for Updated JLab E93-038", E93-038 internal report (June 7, 2000).

[379] W. Vulcan, private communication (2003).

[380] J. J. Sakurai, *Modern Quantum Mechanics* (Addison-Wesley Publishing Company, Inc., 1994).

[381] V. Bargmann, L. Michel, and V. L. Telegdi, Phys. Rev. Lett. **2**, 435 (1959).

[382] S. Taylor, "Some Notes About Charybdis", E93-038 internal report (August 23, 2000).

[383] S. Taylor, "Field Integrals and Precession Angles for G_{En}", E93-038 internal report (February 16, 2001).

[384] S. Taylor, "Charybdis Map Update", E93-038 internal report (July 3, 2001).

[385] Technical data sheet for BICRON-400 plastic scintillators, available at: `http://www.bicron.com/`

[386] Technical data sheet for Phillips XP2262 photomultiplier tubes.

[387] Technical data sheets for Hamamatsu R1828-01 and R1250 photomultiplier tubes, available at:
http://usa.hamamatsu.com/hcpdf/catsandguides/PMTCAT_index.htm

[388] C. Howell, "Electronics for E93-038", E93-038 internal report (March 7, 2001).

[389] C. Howell, private communication (2001, 2002, 2003).

[390] W. A. Watson, J. Chen, G. Heyes, E. Jastrzembski, and D. Quarrie, Proceedings of the 8th Real-Time Computer Applications in Nuclear, Particle, and Plasma Physics Conference (RT 93), edited by B. Axen and R. Poutissou, 296 (1993).

[391] G. Heyes, W. A. Watson, E. Jastrzembski, J. Chen, D. Abbott, and D. Barker, Proceedings of the Computing in High-Energy Physics Conference (CHEP 94), edited by S. C. Loken, 122 (1994).

[392] S. Tajima, "Variable and Subroutine Names for E93038 Analyzer", E93-038 internal report (February 21, 2000).

[393] S. Tajima, "Physics Quantity Reconstruction in E93038 Analysis ENGINE", E93-038 internal report (May 25, 2000).

[394] The CERN Program Library,
http://wwwasd.web.cern.ch/wwwasd/cernlib/

[395] G. Niculescu, Ph.D. thesis, Hampton University (1998).

[396] D. Dutta, Ph.D. thesis, Northwestern University (1999).

[397] S. A. Wood, "The CEBAF Test Package: A Symbolic and Dynamic Test, Histogram, and Parameter Package for On- and Off-line Particle Physics Data Analysis" (August 3, 1995),
http://hallcweb.jlab.org/document/howtos/ctp_manual/

[398] "An Introduction to Q", LAMPF internal report MP-1-3401-3.

[399] D. C. Carey, K. L. Brown, and F. Rothacker, Stanford Linear Accelerator technical note SLAC-R-95-462 and Fermi National Accelerator Laboratory technical note FERMILAB-PUB-95-069 (May 1995).

[400] S. Penner, Rev. Sci. Inst. **32**, 150 (1961).

[401] K. Makino and M. Berz, Nucl. Inst. and Meth. A **427**, 338 (1999).

[402] M. Loffler *et al.*, Nucl. Inst. and Meth. **111**, 1 (1973).

[403] G. MacLachlan, "Delta Matrix Element Optimization", E93-038 internal report (May 5, 2002).

[404] R. Madey, F. M. Waterman, A. R. Baldwin, J. N. Knudson, J. D. Carlson, and J. Rapaport, Nucl. Inst. and Meth. **151**, 445 (1978).

[405] O. Klein and Y. Nishina, Z. Phys. **52**, 853 (1929).

[406] R. A. Cecil, B. D. Anderson, and R. Madey, Nucl. Inst. and Meth. **161**, 439 (1979).

[407] W. Tireman, "Pulse Height Calibration of the Neutron Polarimeter with a ^{228}Th Source", E93-038 internal report (October 9, 2001).

[408] W. Tireman, "Comparison between Pulse Height Calibrations for NPOL during E93-038", E93-038 internal report (October 10, 2001).

[409] J. J. Kelly, "Time Calibration Procedures for the E93-038 Polarimeter Version 2.2", E93-038 internal report (May 1, 2001).

[410] P. R. Bevington and D. K. Robinson, *Data Reduction and Error Analysis for the Physical Sciences* (The McGraw-Hill Companies, Inc., 1992).

[411] J. J. Kelly, "NPOL Analysis Program for E93-038", `http://www.physics.umd.edu/enp/e93038/npol_calculations.htm`

[412] S. Tajima, "Physics Quantity Reconstruction for E93-038", E93-038 internal report (December 17, 2001).

[413] S. Tajima, Ph.D. thesis, Duke University (2003).

[414] A. Semenov, private communication (2001, 2002, 2003).

[415] R. Madey and A. Semenov, "Event Types in E93-038", E93-038 internal report (June 15, 2001).

[416] Jefferson Laboratory proposal PR02-009, R. Madey and S. Kowalski, spokespersons.

[417] G. G. Ohlsen and P. W. Keaton, Jr., Nucl. Inst. and Meth. **109**, 41 (1973).

[418] D. L. Prout *et al.*, Phys. Rev. C **63**, 014603 (2000).

[419] P. E. Ulmer, `MCEEP` computer code,
`http://www.physics.odu.edu/~ulmer/mceep/mceep.html`

[420] J. J. Kelly, "`GENGEN`: event generator for G_{En} using the $d(\vec{e}, e'\vec{n})$ reaction (Version 2.5)", E93-038 internal report (September 1, 2000).

[421] J. J. Kelly, `EPIPROD` computer code,
`http://www.physics.umd.edu/enp/jjkelly/EPIPROD/epiprod.html`

[422] W. H. Press, B. P. Flannery, S.A. Teukolsky, and W.T. Vetterling, *Numerical Recipes in FORTRAN* (Cambridge University Press, 1992).

[423] J. Arrington, `SIMC` computer code,
`http://www.jlab.org/~johna/SIMC_documents/simc/simc.html`

[424] J. J. Kelly, private communication (2001, 2002, 2003).

[425] S. Taylor, "More on spin precession ...", E93-038 internal report (June 20, 2002).

[426] J. Bystricky, F. Lehar, and P. Winternitz, J. Phys. (France) **39**, 1 (1978).

[427] R. W. Finlay, W. P. Abfalterer, G. Fink, E. Montei, T. Adami, P. W. Lisowski, G. L. Morgan, and R. C. Haight, Phys. Rev. C **47**, 237 (1993).

[428] C. Lechanoine-LeLuc and F. Lehar, Rev. Mod. Phys. **65**, 47 (1993).

[429] C. R. Schumacher and H. A. Bethe, Phys. Rev. **121**, 1534 (1961).

[430] E. Bleszynski, M. Bleszynski, and C. A. Whitten, Jr., Phys. Rev. C **26**, 2063 (1982).

[431] S. Frullani and J. Mougey, Adv. Nucl. Phys. **14**, 1 (1984).

[432] `GEANT 4` computer code,
`http://wwwasd.web.cern.ch/wwwasd/geant4/`

[433] A. Semenov, I. Semenova, and R. Madey, "Extraction of G_{En} Values with an `Acceptance` Program", E93-038 internal report (April 18, 2003).

[434] B. Plaster and J. J. Kelly, "`GENGEN`: The E93-038 Monte Carlo Simulation Program", E93-038 internal report (April 16, 2003).

[435] B. Plaster and R. Madey, "The Contribution of the Uncertainty in the Beam Polarization to the Systematic Uncertainty in G_{En}/G_{Mn}", E93-038 internal report (December 13, 2001).

[436] W. Seo, Masters thesis, Kyungpook National University (2001).

[437] R. Madey, W. Tireman, and B. Plaster, "False Asymmetry and Dilution from the First-Pass Analysis of the Two-Step Process $^2\mathrm{H}(\vec{e},e'\vec{p})+\mathrm{Pb}(\vec{p},\vec{n})$", E93-038 internal report (February 25, 2002).

[438] R. Madey, W. Tireman, and B. Plaster, "False Asymmetry and/or Dilution from the Second-Pass Analysis of the Two-Step Process $^2\mathrm{H}(\vec{e},e'\vec{p})+\mathrm{Pb}(\vec{p},\vec{n})$", E93-038 internal report (May 21, 2002).

[439] B. Plaster, "An Estimation of the Charge-Exchange Systematic Uncertainty", E93-038 internal report (June 9, 2003).

[440] B. Plaster, "An Estimation of the Charge-Exchange Systematic Uncertainty (Version II)", E93-038 internal report (July 29, 2003).

[441] E. J. Brash, A. Kozlov, Sh. Li, and G. M. Huber, Phys. Rev. C **65**, 051001(R) (2002).

[442] C. Hautala *et al.*, Phys. Rev. C **65**, 034612 (2002).

[443] M. E. Christy, private communication (2001).

[444] M. K. Jones, private communication (2001).

[445] A. Afanasev, private communication (2002).

[446] A. Afanasev, I. Akushevich, and N. Merenkov, Phys. Rev. D **64**, 113009 (2001).

[447] J. Friedrich and Th. Walcher, Eur. Phys. J A **17**, 607 (2003).

[448] V. Dmitrašinović, Phys. Rev. C **47**, 2195 (1993).

[449] D. R. Giebink, Phys. Rev. C **32**, 502 (1985).